UNIVERSITAT POLITÈCNICA DE CATALUNYA

BARCELONA**TECH**

ESCOLA TÈCNICA SUPERIOR D'ENGYNIERS DE CAMINS, CANALS I PORTS DE BARCELONA

Department of Civil and Environmental Engineering

THERMOMECHANICAL MODELLING OF GROUND RESPONSE UNDER ENVIRONMENTAL ACTIONS

DOCTORAL THESIS SUBMITTED BY

Sergio Samat

Supervised by:

Jean Vaunat

Abstract

Natural disasters, such as landslides triggered by heavy rains, rock deformations and soil cracking in presence of temperature changes and other phenomena related to climatic actions, show the relevance of investigating the effects of the interactions between the atmosphere and the earth ground surface where main human activities develop. The prediction of such hazard requires an adequate knowledge of the changes in hydro-geological conditions under climatic actions. Having advanced constitutive models able to predict the thermo-hydro-mechanical response of natural soils in unsaturated and non-isothermal conditions is also necessary to this end.

The topic of this dissertation is the modeling of the soil-atmosphere interactions and its application to several geotechnical problems. Soil-atmosphere interactions encompass heat and mass exchanges (air, water). They have been modeled following Noilhan (1988) approach which includes evaporation and transpiration, sensible heat exchange, net radiation and heat convected by air and water flow. The modeling of these interactions is integrated within a thermodynamic investigation of behaviour of three-phase porous medium in order to provide a general comprehension of the addressed problem. A thermo-hydro-mechanical code provided with a specific boundary condition for heat and mass exchange between the ground and the atmosphere have been enhanced, particularly by the addition of a module to cope with transpiration according to vegetation characteristics.

Soil-vegetation-atmosphere interaction model have been coupled with thermo-hydro-mechanical models in the framework of the finite element code. In order to ensure good computational characteristics, the models have been derived from the general frameworks of poro-mechanics and hyperplasticity for saturated, unsaturated and non-isothermal geological media and implemented using modern algorithms based on the optimization techniques such as the interior-point algorithms.

Studies of several cases have been carried out with the model, all validated with field data. They include: (a) the change in moisture content in an experimental field of the National Meteorological service in France, (b) the response of a foundation of collapsible silt layer and (c) the stability of a rock cliff located at Roque Gageac site - France. Results show the ability of the model to represent properly water and heat exchange between the soil and

the atmosphere and to successfully overcome difficult modeling issues such as the occurrence of traction failure due temperature gradients and plastic zone under the foundation. Some practical conclusions have been also shown concerning the bearing capacity of a foundation on an unsaturated soil layer and the stability of rock block interpreted as a cantilever bean under climatic actions.

Resumen

Desastres naturales, tales como el desencadenamiento de deslizamientos, deformación en macizos rocosos y fisuración de suelos en presencia de cambio de temperatura y otros fenómenos relacionados a acciones climáticas, evidencian la importancia de investigar los efectos de las interacciones entre la atmosfera y la superficie de la tierra, donde se desarrollan las principales actividades humanas.

La predicción de tales deslizamientos requiere un conocimiento adecuado de los cambios de las condiciones hidrogeológicas bajo acciones climáticas. Con este fin es necesario disponer de modelos constitutivos avanzados capaces de predecir la respuesta termo-hidro-mecánica de suelos naturales en condiciones parcialmente saturadas y no isotérmicas

El objeto de esta tesis es el modelado de las interacciones suelo-atmósfera y su aplicación a diversos problemas geotécnicos. Las interacciones suelo-atmosfera contemplan el intercambio de calor y masa (aire, agua). Ellas has sido modeladas siguiendo el enfoque propuesto por Noilhan (1988) que incluye flujos de evaporación y transpiración, el calor sensible intercambiado, la radiación neta y el calor de convección debido a flujos aire y agua. El modelado de estas interacciones se integra dentro de un estudio termodinámico del comportamiento del medio poroso no saturado con tal de proveer un entendimiento general del problema abordado. Un código termo-hidro-mecánico provisto con una condición de contorno específica para el intercambio de calor y masa entre el suelo y la atmosfera ha sido mejorado, en particular un modulo para modelar la transpiración de acuerdo a las características de la vegetación ha sido añadido.

El modelo de interacción suelo-vegetación-atmosfera ha sido acoplado con modelos termo-hidro-mecánicos en el marco de un código de elementos finitos. A fin de asegurar buenas características computacionales, los modelos han sido desarrollados desde marcos generales de la poro-mecánica y la hiperplasticidad para medios geológicos saturados, parcialmente saturados y no-isotérmicos e implementados usando algoritmos modernos basados en técnicas de optimización como algoritmos de punto-interior.

El estudio de varios casos ha sido llevado a cabo con el modelo propuesto, todos ellos validados con datos de campo. Incluyendo: (a) el cambio del contenido de humedad en un campo experimental del servicio Meteorológico Nacional en Francia, (b) la respuesta de

una fundación de una capa limo-arcillosa colapsable y (c) la estabilidad de un acantilado ubicado en Roque Gageac - Francia. Los resultados muestran la habilidad del modelo para representar adecuadamente los intercambios de agua y calor entre el suelo y la atmosfera y superar satisfactoriamente problemas complejos de modelación tales como la falla por tracción debido a gradientes de temperatura y zonas plásticas bajo fundación. Se presentan conclusiones prácticas a cerca de la capacidad de carga de una fundación sobre una capa de suelo parcialmente saturada y la estabilidad de un bloque de roca interpretado como una viga voladizo sometida a acciones climáticas.

Resum

Desastres naturals, tals com el desencadenament d'esllavissades, deformació en massissos rocosos, fissuració de sòls en presència de canvis de temperatura i altres fenòmens relacionats amb accions climàtiques, evidencien la importància d'investigar els efectes de les interaccions entre l'atmosfera i la superfície de la Terra, on es desenvolupen les principals activitats humanes.

La predicció de tals esllavissades requereix un coneixement adequat dels canvis de les condicions hidrogeològiques sota accions climàtiques. Amb aquest fi és necessari disposar de models constitutius avançats capaços de predir la resposta temo-hidro-mecànica de sòls naturals en condicions parcialment saturades i no isotèrmiques.

L'objectiu d'aquesta tesi és la modelització de les interaccions sòl-atmosfera i la seva aplicació a diversos problemes geotècnics. Les interaccions sòl-atmosfera contemplen l'intercanvi de calor i massa (aire, aigua). Elles han estat modelades seguint l'enfoc proposat per Noilhan (1988) que inclou fluxos d'evaporació i transpiració, la calor sensible intercanviada, la radiació neta i la calor de convecció degut a fluxos d'aire i aigua. La modelització d'aquestes interaccions s'integra dins d'un estudi termodinàmic del comportament del medi porós no saturat per tal de proveir un enteniment general del problema abordat. Un codi termo-hidro-mecànic proveït amb una condició de contorn específica per l'intercanvi de calor i massa entre el sòl i l'atmosfera ha estat millorat, en particular un mòdul per modelitzar la transpiració d'acord amb les característiques de la vegetació ha estat afegit.

El model d'interacció sòl-vegetació-atmosfera ha estat acoblat amb models termo-hidro-mecànics en el marc d'un codi d'elements finits. Per tal d'assegurar bones característiques computacionals, els models han estat desenvolupats des de marcs generals de la poro-mecànica i la hiperplasticitat per a medis geològics saturats, parcialment saturats i no-isotèrmics i implementats utilitzant algoritmes moderns basats en tècniques d'optimització amb algoritmes de punt-interior.

L'estudi de diversos casos ha estat dut a terme amb el model proposat, tots ells han estat validats amb dades de camp. Incloent: (a) el canvi del contingut d'humitat en un camp experimental del servei Meteorològic Nacional a França, (b) la resposta d'una fonamentació d'una capa llimo-argilosa col·lapsable i (c) l'estabilitat d'un penya-segat

situat a Roque Gageac – França. Els resultats mostren l'habilitat del model per representar adequadament els intercanvis d'aigua i calor entre el sòl i l'atmosfera i superar satisfactòriament problemes complexes de modelització tals com la ruptura per tracció degut a gradients de temperatura i zones plàstiques sota una fonamentació. Es presenten conclusions pràctiques referents a la capacitat de càrrega d'una fonamentació sobre una capa de sòl parcialment saturada i l'estabilitat d'un bloc de roca interpretat com una biga en voladís sotmesa a accions climàtiques.

A mi Madre

Acknowledgments

I would like to express my deepest gratitude to my adviser Jean Vaunat, for letting me work with him closely along these years in a nice environment and for his endless patience with me. This stage would not have been possible without his guidance and support.

Secondly, I would like to thank Prof. Antonio Gens Sole, for his advice and support during the crucial period of the initial years of the thesis and Prof. Eduardo Alonso for trusting me to tackle a job about the interactions between the climatic actions and the soil. I would also like to extend my gratitude to Enrique Romero, Josep Suriol, Maarten Saaltink, Antonio Rodríguez Ferran, Carlos López, Sebastià Olivella, Marcel Hürlimann, Ferhun Caner and the team of professors of the discrete mathematics department Enrique Bendito, Andres Encinas and Angeles Carmona, from whom I received valuable comments and fruitful interactions.

Thirdly, I would like to thank Prof. Juan Manuel Fiore and Prof. Marcelo Sanchez for encouraging me to start doctoral studies away from home.

I am also grateful to my colleagues and friends within the department Ricardo Madrid, Núria Pinyol, Nubia González, Anna Ramon, Olga Mavrouli, Benoit Garitte, Dani Tarrago, Teresa Yubero, Zhifeng Zhan, Dani Garolera, Francesca Casini, Jean-Michel Pereira, Rodrigo Gómez, Christian Hoffmann, Ernesto Castellanos, Serena Chighini, Jubert Pineda, Claudia Abancó.

I would like to thank especially to Andrés Idiart, Juan Muñoz and Abel Jacinto who have shared their experience with me and have helped creating a nice environment during my stay at UPC.

The greatest appreciation is for my family in San Juan. They have been the true support for me and the reason why I was able to accomplish this dream. To my father, for teaching me to persevere in my desires, for shaping into the person I am today and for instilling values that remain unchanged no matter the circumstances. To Marcela and Jorge, for staying by my site in spite of the distance and for their unconditional support.

To my family in law in Warsaw, the affection received from the begging have been the best aid to mitigate the distance and time apart from my family in Argentina. Finally, I would like to give special mention to my wife Marta. Her encouragement has been vital to overcome the most difficult times of this journey.

TABLE OF CONTENTS

LIST OF FIGURES

19

25

LIST OF TABLES

LIST OF BOXES

CHAPTER 1

INTRODUCTION AND ORGANIZATION OF THE THESIS

Natural disasters, such as landslides triggered by heavy rains, rock deformations and soil cracking in presence of temperature changes and other phenomena related to climatic actions, show the relevance of investigating the effects of the interactions between the atmosphere and the earth ground surface where main human activities develop.

An example of such disasters is the case of the failure observed in Naples on September 15th 2001 and mentioned by Gens (2010). In this case, a heavy rainstorm with a rainfall intensity of 130–160 mm during 3 hour caused the failure of a foundation on a natural loose pyroclastic material which had remained stable for a long time. It was observed that maximum collapse settlement reached 200mm, which corresponded to an estimated water table rise of 12m.

Another remarkable case is to the collapse of a large zone of the Pereira Barreto town (Gens (2010)) located on the right-hand bank of Tietê River, near the confluence with the Paraná River in the North West of Sao Paulo State in Brazil.

The town is founded on a thick layer of collapsible colluvial soil that overlies a residual soil with a thin gravel layer separating colluvium and residual soil.

The ground water table rise caused collapse settlements of more than 100mm that affected buildings founded in the zone identified as collapsible by SPT and CPT tests in the shoreline of the hydroelectric plant.

The prediction of such hazard requires a good knowledge of the changes in hydro-geological conditions under climatic actions as well as the availability of advanced models able to predict the thermo-hydro-mechanical response of natural soils in unsaturated and non-isothermal conditions.

This dissertation aims to provide advances in the modeling of realistic cases of soil-atmosphere interactions. For this purpose several directions have been followed: (a) development of a module for soil-vegetation-atmosphere interactions, (b) development of advance constitutive model frameworks and constitutive laws for the response of geological material to mechanical and environmental (suction, temperature) actions. (c) development of robust integration algorithms based on optimization techniques and modern algorithms.

The dissertation is divided in nine chapters. Chapter 1 and Chapter 9 contain the introduction and final conclusions of the thesis.

Chapter 2 addresses the formulation of a model for soil-atmosphere interactions in a thermodynamic framework of the equations governing the thermo-hydro-mechanical behaviour of porous media (Olivella (1994), Houlsby (2005), Gens (2010)).

It includes a boundary condition modelling different exchange fluxes between the soil and the atmosphere: water ($j^w{}_{atm}$), air ($j^a{}_{atm}$) and energy $\left(j_{E_{atm}}\right)$ (Penman (1948), Monteith (1965) and Noilhan (1996)).

A sensitivity analysis on soil, atmosphere and vegetation properties is then presented and several conclusions drawn on the main parameters governing soil-vegetation-atmosphere interactions.

Chapter 3 presents a theory of plasticity derived from thermomechanical principles. Two consolidated frameworks are revisited: (a) poro-elastoplasticity and (b) hyperplasticity. Both frameworks are merge into one thermomechanical consistent framework able to model soil response in partially saturated conditions.

Thermomechanical bases, for biphasic porous materials are first addressed. It leads to identify and couple different types of energies (elastic energy, trapped energy and dissipation energy) within the general theoretical framework of plasticity.

The study of three-phase porous media is addressed by extending the proposed thermomechanical approach.

Derivation of the conjugate variables defining the response of unsaturated soils is first presented, then state equations linking the different conjugate variables are derived by proposing general layouts for the energy functions g_s and f_s.

A kinematical hardening model is presented to reproduce hysteretic retention curves behaviour.

Chapter 4 contains developments of particular constitutive models of practical importance for soil-vegetation-atmosphere interactions problems. Those models are derived within the thermomechanical framework studied in chapter 3.

The addressed models are:

- Water retention with and without hysteresis
- Thermo-hydro-mechanical elastic law
- Suction dependent critical state models of type: (a) Barcelona Basic Model " BBM-like", Alonso (1990) and (b) Hyperplastic CASM Model "HP-CASM", Yu (2006)
- Temperature and suction dependent frictional models: Drucker-Prager and Matsuoka-Nakai yield criterion.

For the water retention curve, a simplified van Genuchten law is proposed. This law admits a closed-form integration and allows for the derivation of an energy potential for the air-liquid interface. In this regard, a force potential is presented to model the retention hysteresis.

For the BBM-like and HP-CASM models dissipation potentials, as function of primary environmental variables, have been then presented.

Elastic potentials presented by Houlsby (2005) have been extended in order to consider the effects of: (a) suction due to partial saturation, (b) thermal strains due to temperature changes and (c) water retention dependency on mean stress.

Finally two cohesive-frictional models have been reviewed within the hyperplastic framework: the Drucker-Prager and the Matsuoka-Nakai models, with special attention paid to the expression of dissipation function and its consequences in terms of material dilatant behaviour.

Chapter 5 addresses the numerical integration of constitutive model studied in chapter 4. The advantage of formulating elastoplastic models by defining the internal and the dissipation potentials is exploited at time of integration by using mathematical programming tools.

Lagrange functionals ($\mathcal{L}^{g_s}$) are minimized leading to proper variational structures. These structures will allow to determine optimal points which are the solution for the return plastic mapping. Two types of integration algorithms will be addressed and their advantages and benefits discussed:

a) Return mapping by the closest-point projection

b) Return mapping by the interior-point method

Moreover, an additional method, Line-search method, has been included to control the time step-size taken at each correction.

Chapter 6 aims to analyze an experimental fallow field under climatic actions. The field is extensively instrumented in order to register soil water content and temperature measurements, at different depths in the upper soil layer. Evaporation, long and short wave radiation, biomass variation are also measured.

The soil-atmosphere interaction will show to have a great influence on the topsoil layer. It will also show the relevance of transpiration flow over evaporation flow in the summertime. It will be seen that this relevance is reversed in winter time.

The numerical results appeared to well reproduce the field measurements of water content (θ) and temperature (T) at different depths, thus validating the soil-atmosphere model studied in chapter 2.

Chapter 7 addresses the response of a shallow foundation under climatic actions. The BVP model is initially calibrated by comparison with a physical model at laboratory scale carried out in the centrifuge of the laboratory of the National Minister of Civil Works.

The thermo-hydro-mechanical formulation developed in chapter 2 is used to address the numerical model.

It includes a modified version of the Barcelona Basic Model (BBM2-generalized) and the simplified van Genuchten retention law presented in chapter 4.

Results show the ability of the model to reproduce hydraulic collapse upon wetting of the silty layer and the force-displacement curve of the foundation.

A procedure to evaluate the bearing capacity factors in non-saturated conditions is addressed. It is based on Potts (2001) proposal to compute the bearing capacity factors of shallow foundations.

Then the prototype (field scale) is modelled under climatic actions to study their effects on the response of the shallow foundation. Then, in order to study the displacements of the foundation under climatic actions, it is first loaded to a service load equal to 1/3 of the ultimate load and then subjected to climatic actions. A sensitivity study of soil permeability is finally addressed.

Chapter 8 deals with the thermo-mechanical study of a rock massif located in the south of France subjected to climatic actions registered in a meteorological station located in the area of the massif. The elastic response of the massif is modelled with a hyperelastic linear law while the plastic response is modelled with the Drucker-Prager model presented in chapter 4.

The interior-point algorithm presented in chapter 5 is used to integrate the constitutive model due to its property of solving partial loading-unloading problems until the final solution is reached.

Results evidence the ability of the model to compute stress response under compression, extension and traction path, which are of significative magnitude at the massif face.

Stability of the most critical part of the massif is finally addressed by deriving a plastic limit envelope according to Drucker yield criterion.

Chapter 9 addresses the final conclusions and advances future lines of research.

CHAPTER 2

MODELING OF SOIL-VEGETATION-ATMOSPHERE INTERACTIONS

2.1) Introduction

The interactions between the ground and the atmosphere play a central role in the analysis of the natural risks associated to slope movements. Since a long time, precipitations, together with toe erosion and seism, have been recognized as one of the main triggering factors of landslides. However, there are relatively little cases where direct relationships could be established between occurrence and features of landslides and the characteristics of the rainfall (intensity, duration, frequency and spectrum history). As pointed by (Leroueil, 2001), slopes respond mainly to changes in pore pressure. The relationship between the pore pressure and the rainfall is complex. It depends, on the one hand, on soil permeability and consolidation parameters and, on the other hand, on the interactions with the atmosphere, including infiltration, runoff, evaporation and evapotranspiration. Vegetation plays often a non-negligible role by intercepting part of the rainfall, limiting the runoff, releasing back vapor to the atmosphere, providing the soil with root reinforcement, creating settlements or increasing soil permeability by desiccation.

The objective of the present chapter of the dissertation is to provide an insight on the study of the interaction "soil-water-energy balance" over the slopes of soils within a thermomechanical framework for porous media. The main components of the soil-water-energy balance are summarized in Fig. 2.1 and will be developed in this chapter.

The chapter is composed by five sections in addition to the introduction and the conclusions. The second section introduces the notation used along the chapter. The third section introduces the energy balance and mass balances of water and air considering the terms belonging to a boundary soil-atmosphere. The fourth section addresses the modeling of the interaction fluxes between the soil and the atmosphere considering a

41

fallow field. The fifth section addresses a thermomechanical formulation for a multiphase porous medium following (Olivella, 1995), (Gens A. , 2010) and (Houlsby & Puzrin, 2005). Finally, the sixth section presents relevant conclusions of the soil-vegetation-atmosphere interaction obtained by sensitive analysis of synthetic problems.

2.2) Notation and Terminology

Notation for Atmospheric and Vegetation Fluxes	
E_p	Potential evaporation
Δ	Slope of relation temperature vs. saturated water vapor pressure
R_n	Net incoming solar radiation
Γ	Psychrometric constant
Λ	Latent heat of vaporization
E_a	Vapor pressure deficit
$j_{E_{atm}}$	Heat flux
r_a	Aerodynamic resistance
r_l	Plant surface resistance
LAI	Leaf Area Index
E_{m_v}	Aerodynamic resistance
Veg	Vegetation fraction
E_v	Actual Evaporation (Evapo-transpiration)
ρ_{v_a}	Absolute humidity at the atmosphere
ρ_v	Absolute humidity at the ground
K	Karman's constant
ϕ	*S*tability factor
v_a	Wind velocity
z_a	Screen height
z_o	Roughness length (high over soil surface at which v_a and ρ_{va} are measured)
Ψ	Water potential
ψ_m	Matrix potential

ψ_g	Gravitational potential
π	Osmotic (solute) potential
P_r	Water pressure potential (related to the turgor pressure)
r_s	Surface stomatal resistance
$r_{s_{min}}$	Minimum surface stomatal resistance
F_1	Coefficient for photo synthetically active radiation
F_2	Stress factor coefficient
F_3	Vapor pressure density coefficient
F_4	Air temperature coefficient
θ_w	wilting point
θ_{fc}	Field capacity
θ_a	Anaerobiosis point
R_g	Global radiation
R_{g_l}	Limit global radiation
ψ_{l_c}	Water potential at the bulk leaf
ψ_{c_r}	Critical threshold for the water potential
ψ_{c_c}	Water potential at stomatal closure
r_{s_f}	Soil-root resistance
r_{p_c}	Plant-canopy resistance
ψ_{r_f}	Water potential at root layer
ψ_p	Plant pressure potential
C_p	Specific heat at constant pressure
C_r	Relative plant growth
L_A	Leaf surface
V_c	Plant volume / Cell volume
P_c	Plant weight
F_c	Ratio of leaf surface over plant weight
A_n	Ratio of net assimilation
M_p	Maximum canopy weight
S	Cell surface

_____

L_c	Relative hydraulic conductivity of the cell
P	Precipitation
P_T	Turgor pressure
Y_c	Yield critical threshold
V_{wc}	Volume of the cell wall chamber
m_c	Irreversible extensibility coefficient
T_g^c	Rate of increase of cell wall chamber
q_g	Flux of gas
γ_g	Gas leakage coefficient
j^a_{atm}	Atmospheric flux of air
j^w_{atm}	Atmospheric flux of water
ω_g^w	Mass fraction of vapor in the gas phase
j_{sr}	Surface runoff
γ_w	Water leakage coefficient
H_s	Sensible heat flux
H_c	Convected heat flux
C_a	Specific heat of gas
ρ_{ga}	Atmospheric density
T_a	Atmospheric temperature
T_o	Ground temperature
h_v	Free energy of vapor
h_{la}	Free energy of liquid water
h_{a0}	Free energy of air
R_a	Atmospheric long wave radiation
A_l	Albedo
σ_{SB}	Stephan Boltzmann constant
ε_{MS}	Emissivity
E_T	Actual transpiration flux

_____

Notation for thermomechanical approach to three-phase porous medium	
E_s	Specific internal energy per unit mass of solid phase
E_i	Specific internal energy of air-water interface
E_l	Specific internal energy of liquid phase
E_g	Specific internal energy of gas phase
ρ_s	Density of solid skeleton
ϕ	Porosity
ρ	Dry density
ρ_l	Density of pore liquid
ρ_g	Density of pore gas
w_l	Partial fraction of liquid density per unit mass of skeleton
w_g	Partial fraction of gas density per unit mass of skeleton
$j_{\widetilde{E}_s}$	Net flow of energy in the porous skeleton
j_{E_l}	Net flow of energy in the liquid
j_{E_g}	Net flow of energy in the gas
i_c	Conductive heat flux
ϑ_i^k	Partial fraction $\left(\rho_i^k \phi_i\right)$ per unit mass of dry density
ϕ_l	Liquid porosity
ϕ_g	Gas porosity
q_l	Darcy flux of liquid
q_g	Darcy flux of gas
i_g^w	Diffusive flux of vapor Fick-type
i_l^a	Diffusive flux of dissolved air Fick-type
v_i	Solid velocity
v_s	Unit volume of solid
j_g^w	Net flow of vapor
j_l^a	Net flow of dissolved air
v_{gi}^w	Diffusion velocity of vapor
v_i^a	Air velocity
v_l^w	Unit volume of water

v_g^w	Unit volume of vapor
$v_{l_i}^a$	Diffusion velocity of dissolved air
v_i^w	Water velocity
ρ_i^k	Partial density of species k in phase i
v_g^a	Unit volume of air
v_l^a	Unit volume of dissolved air
L	Power input to the porous volume
v_i^c	Absolute velocity of air-liquid skin
E_g^w	Specific internal energy of vapor
E_l^a	Specific internal energy of dissolved air
θ_g^w	Apparent mass density of vapor
θ_l^a	Apparent mass density of dissolved air
p_l	Liquid pressure
p_g	Gas pressure
T_i	Force of air-liquid interface
g_i	Gravity
t_i	Traction force at solid skeleton
S_l	Degree of saturation
σ_{ij}	Stress tensor
d_{ij}	Strain rate tensor
ω_{ij}	Rotational tensor
$\mathfrak{H}$	Specific entropy of porous medium
$\widetilde{\mathfrak{H}}_s$	Specific entropy of porous skeleton
$\mathfrak{H}_l$	Specific entropy of liquid
$\mathfrak{H}_g$	Specific entropy of gas
$\mathfrak{H}_i$	Specific entropy of air-liquid interface
$j_{\widetilde{\mathfrak{H}}_s}$	Net flow of entropy in the mineral and in the air-liquid interface
$j_{\mathfrak{H}_l}$	Net flow of entropy in the liquid
$j_{\mathfrak{H}_g}$	Net flow of entropy in the gas
d	Dissipation of porous medium

$j_{\mathfrak{H}i}$	Net flow of entropy in the air-liquid interface
T	Temperature in the porous medium

2.3)   Presentation of soil-atmosphere interactions

The generic term of "soil-water balance" was introduced by Blight (1997) to express the flux of mass that crosses the interface between the ground and the atmosphere. It would in fact be more accurate to call it "soil-water-energy balance" as the flow of heat coming from and released back to the atmosphere proved to be determinant. This flow affects the evapo-transpiration taking place on ground surface and sometimes affects considerably the proper thermo-mechanical response of slope exposed to strong changes in temperature, Samat (2011). The most relevant fluxes of heat, water and air taking place at both the atmosphere and the upper soil layer interacting with the atmosphere that built the "soil-water-energy balance", are summarized in Fig. 2.1.
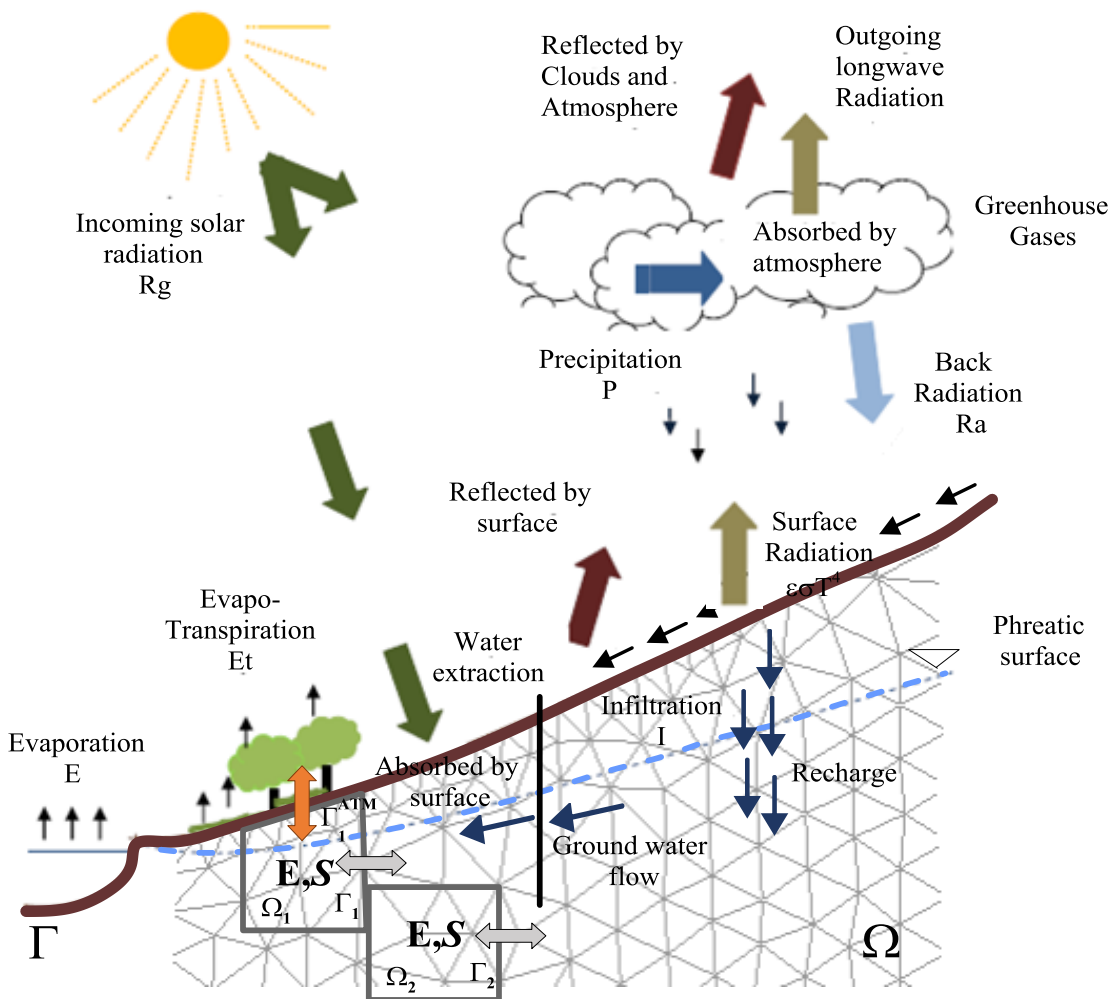
Figure 2.1: Fluxes of the "Soil-Water-Energy Balance", after Bear (1972) & Blight (1997).

47

Regarding the energy flux, the main atmospheric flux is due to the radiation. This flux reaches the earth surface in such a way that it can be represented by three clearly differentiated components: (a) the first component reaches directly the soil surface through the atmosphere with a shortwave length and is usually named direct solar radiation R_g, (b) the second component is modified by the interaction with the atmosphere (part of it is reflected by the clouds and/or absorbed by the atmosphere). It reaches the soil surface in the form of a longwave and is usually named atmospheric radiation R_a and (c) finally, the third component corresponds to the reflected radiation by the soil surface: ground radiation.

The remaining heat fluxes contributing to the total heat flux are: (a) on the one side, the flux convected to the atmosphere as consequence of the free energies responses of liquid water, vapor and air to the atmospheric heat H_c and (b) on the other side the flux advected through the atmosphere by temperature changes H_s.

Thus, taking into consideration all the present phases in a porous medium and their interactions and accepting the thermal equilibrium between them, the energy balance for a general porous volume with a boundary Γ^{atm} in the border with the atmosphere $\left(\text{such that: } \Gamma_1 = \Gamma^{atm} \cup \Gamma\right)$ Fig. 2.1 can be detailed as:
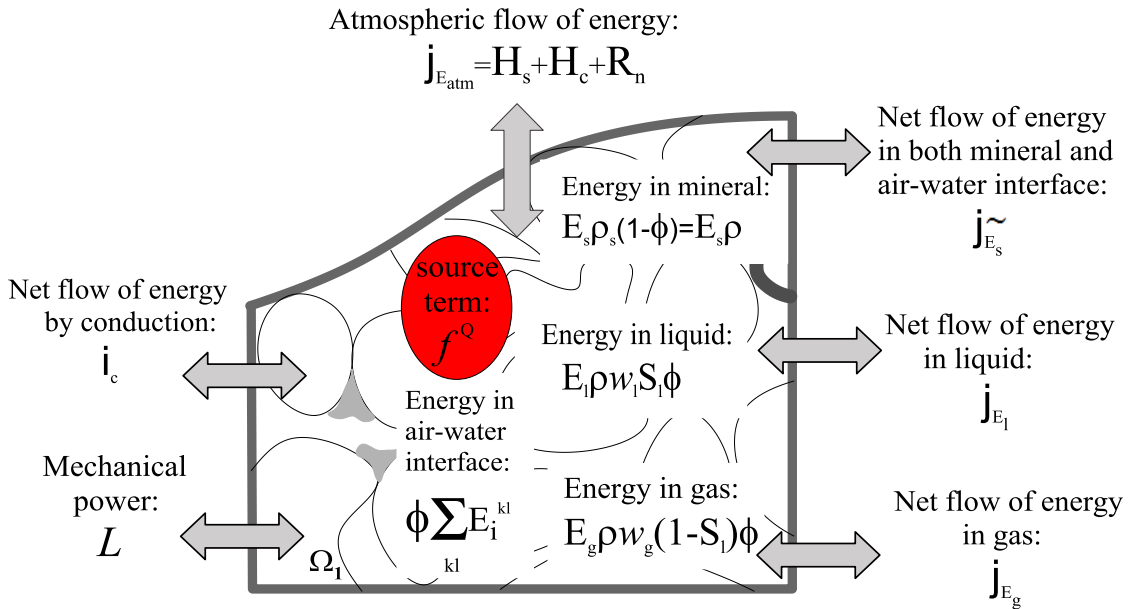
Figure 2.2: Energy storage and energy fluxes involved in a three-phase porous medium in contact with the atmosphere, after Noilhan (1996) , Gens (2010), Gran (2015).

The storage energy in the porous skeleton is defined by the energy in the mineral $E_s\rho_s(1-\phi)$ and the energy in the air-water interface $\phi\sum E_i^{kl}$. The storage energy in the pore liquid and in the pore gas are given by the terms $E_l\rho w_l S_l\phi$ and $E_g\rho w_g(1-S_l)\phi$, respectively. Where ρ is the dry density and $w_l = {\rho_l}/{\rho}$, $w_g = {\rho_g}/{\rho}$ are the partial fractions of liquid and gas unit masses per unit mass of skeleton.

The net flows through the boundary Γ_1 are: (a) the net flow of energy in the mineral and in the air-water interface $j_{\widetilde{E}_s}$, (b) the net flow of energy in the liquid j_{E_l}, (c) the net flow of energy in the gas j_{E_g} and (d) the net flow of energy by conduction i_c.

The first law of thermodynamics states that the rate of increase of internal energy in the porous volume Ω is equal to the power input to the volume given by: (a) energy input at the boundaries and (b) the rate of work of body forces.

Ascribing $\widetilde{E}_s$, E_l and E_g as the specific energy of the skeleton, the specific energy of the liquid phase and the specific energy of the gas phase, respectively, L as the power input to the porous volume and i_c as the heat flux , the first law of thermodynamics is stated as:

$$\int_\Omega \frac{\partial}{\partial t}\left(\widetilde{E}_s\rho + E_l\rho w^w S_l\phi + E_g\rho w^a(1-S_l)\phi\right)d\Omega + \int_\Gamma \left(j_{\widetilde{E}_s} + j_{E_l} + j_{E_g}\right)n_i d\Gamma \qquad (2.1)$$

$$+ \int_{\Gamma^{atm}}(j_{E^{atm}})n_i d\Gamma^{atm} + \int_\Omega f^Q\, d\Omega = \int_\Omega L d\Omega - \int_\Gamma i_{c_i}\, n_i d\Gamma$$

where flows of energy in the atmospheric boundary Γ^{atm} take particular forms which depend on the atmospheric variables.

The water flux $j^{w atm}$ at the atmospheric boundary Γ^{atm} is the result of the sum of: net precipitation, evaporation, transpiration, water flux drained at soil surface due to full saturation or gravity and flux of water vapor advective in the gas phase.

Mass balance of water expressed with: soil porosity, degree of saturation and density ratios w_l^w - w_l^w, is given by:

$$\int_\Omega \frac{\partial}{\partial t}\left(\rho w_l^w S_l\phi + \rho w_g^w\phi(1-S_l)\right)d\Omega + \int_\Gamma \underbrace{\left(j_l^w + j_g^w\right)}_{j^w}n_i d\Gamma + \int_{\Gamma^{atm}}(j^{w atm})n_i d\Gamma^{atm} \qquad (2.2)$$

$$+ \int_\Omega f^w d\Omega = 0$$

where f^{w} is a sink/source term and j^{w} is the total flux of water, advective and diffusive within porous medium. Expressions for the flow of water in the atmospheric boundary are studied in detail in section 2.4.1.

The air flux at the atmospheric boundary Γ^{atm} is given by the existing gradient between the gas pressure at the soil surface and the atmospheric pressure $\mathrm{j}^{\mathrm{a_{atm}}}$.

Mass balance of air expressed with: soil porosity, degree of saturation and density ratios $w_{\mathrm{g}}^{\mathrm{a}}$ - $w_{\mathrm{l}}^{\mathrm{a}}$, is given by:

$$\int_{\Omega} \frac{\partial}{\partial t}\left(\rho w_{\mathrm{g}}^{\mathrm{a}}(1-S_{\mathrm{l}})\phi + \rho w_{\mathrm{l}}^{\mathrm{a}}\phi S_{\mathrm{l}}\right) d\Omega + \int_{\Gamma} \underbrace{\left(j_{\mathrm{g}}^{\mathrm{a}} + j_{\mathrm{l}}^{\mathrm{a}}\right)}_{j^{\mathrm{a}}} n_{i} d\Gamma + \int_{\Gamma^{\mathrm{atm}}} (j^{\mathrm{a_{atm}}})n_{i}d\Gamma^{\mathrm{atm}} \qquad (2.3)$$

$$+ \int_{\Omega} f^{\mathrm{a}}d\Omega = 0$$

where f^{a} is a sink/source term and j^{a} is the total flux of air within porous medium which considers the air dissolved in the liquid. Expression for the flow of air in the atmospheric boundary is studied in detail at section 2.4.2.

In the following section, mathematical expressions for the atmospheric fluxes giving rise to the "natural boundary condition" concerning the soil-atmosphere interactions are addressed.

2.4) Formulation of atmospheric fluxes at boundary Γ^{atm}

The atmospheric actions by the fluxes $\mathrm{j}^{\mathrm{w_{atm}}}$, $\mathrm{j}^{\mathrm{a_{atm}}}$ and $\mathrm{j}_{\mathrm{E_{atm}}}$ on ground surface encompass exchanges of mass of fluids and heat at Γ^{atm}, Gran (2015).

They include evaporation, transpiration, rainfall, solar radiation, atmospheric radiation, wind, among others, Carreras (1991) and Noilhan (1988). In particular, the vegetation cover is imposed at the upper soil layer in terms of transpiration (water uptake at root level by plants) and heat exchanges.

At the last instance, atmospheric fluxes acting at the soil-atmosphere boundary Γ^{atm} are controlled by the three state variables: liquid pressure, gas pressure and temperature.

2.4.1) Description of atmospheric water flux $j^{W\text{atm}}$

Atmospheric water flux is defined as the sum of: (a) precipitation P, (b) ground evapo-transpiration E_v, (c) advective flux of vapor $j_g^{W\text{atm}}$ and (d) surface runoff j_{sr}, fluxes acting at the ground surface.

Precipitation P corresponds to the net rainfall reaching the ground surface since part of the real rainfall is intercepted by the canopy $P = P_r - I$.

Evaporation is the process whereby liquid water is converted to water vapor (vaporization) and removed from the evaporating surface; water evaporates from a variety of surfaces, such as lakes, rivers, pavements and soils.

Transpiration is the result of the vaporization of liquid water contained in plant tissues to the atmosphere. Crops predominately lose their water through stomata, which are small openings on the plant leaf through which gases and water vapor passes.

Apart from the water availability in the topsoil, the potential evaporation from a cropped soil is mainly determined by the fraction of the solar radiation reaching the soil surface. This fraction decreases over the growing period as the crop develops and the crop canopy shades more and more of the ground area. When the crop is small, water is predominately lost by soil evaporation, but once the crop is well developed and completely covers the soil, transpiration becomes the main process.

The determination of evapo-transpiration has been of concern to agriculturalists and hydrologists. The most usual methods consider that the actual evapo-transpiration E_{vt} is equal to the maximum value allowed by the heat present in the medium, called the "potential evapo-transpiration" E_p.

It is essentially true for irrigated fields or for climates with positive water balance. For arid, semi-arid and non-irrigated areas the availability of water may limit evapo-transpiration and the actual E_{vt} flux may drop below the potential E_p flux.

2.4.1.1) Modeling Evaporation and Transpiration

The most rational approach to calculate potential evaporation E_p was introduced by Penman (1948). It is based on the energy balance at the soil surface and is given by the expression,

$$E_p \left({}^{kg}\!/_{m^2} \right) = \frac{\Delta \cdot R_n + \gamma \lambda(T, \sigma_s) \cdot E_a}{\lambda(T, \sigma_s) \cdot (\Delta + \gamma)} \qquad (2.4)$$

where $\Delta \left({}^{Pa}\!/_{\circ C} \right)$ is the slope of the temperature versus saturated water vapor pressure curve at the prevailing air temperature, $\lambda \left({}^{J}\!/_{m^2} \right)$ is the latent heat of vaporization of water, γ is the psychrometric constant $\left(= 66 \; {}^{Pa}\!/_{\circ C} \right)$ and $E_a \; ({}^{mm}\!/_d)$ is a term accounting for the vapor pressure deficit. E_a is given by the expression $\left(= 0.165 \cdot (p_v^{sat} - p_v^a) \cdot \left(0.8 + {}^{v_a}\!/_{100} \right) \right)$ where p_v^a (hPa) is the actual vapor pressure of air, p_v^{sat} (hPa) the saturated vapor pressure of air and v_a (km/d) the wind velocity.

Penman equation for evaporation flux has been adopted as standard by the Food and Agriculture Organization (FAO).

An updated version of Eq. 2.4 has been proposed by Monteith (1965) to include the contribution of transpiration flux. The potential evapo-transpiration flux reads:

$$E_p \left({}^{kg}\!/_{m^2} \right) = \frac{\Delta \cdot {}^{(R_n - j_e)}\!/_{\lambda(T, \sigma_s)} + \gamma \cdot Ea}{\Delta + \gamma \cdot \left(1 + {}^{r_s}\!/_{r_a} \right)} \qquad (2.5)$$

where j_e is the conductive energy flux (sensible heat). r_a is the aerodynamic resistance of ground surface and r_s is the plant surface resistance. r_s is computed as ${}^{r_l}\!/_{LAI_{eff}}$, where $r_l[s/m]$ is the bulk stomatal resistance of the well-illuminated leaf and LAI_{eff} is the effective leaf area index.

The equation has been validated on a reference cropped field, defined by the following characteristics: (a) crop of grass with a fixed height of 0.12m, (b) an albedo equal to 0.23 and (c) a surface resistance equal to $69 \; {}^s\!/_m$.

Blaney and Criddle (1950), Turc (1954), Thornthwaite (1954) proposed alternative expressions to predict the actual evaporation E_v with less parameters. In this regard, Thornthwaite proposed the following empirical equation:

$$E_{m_v} = 16.2 \cdot \left(\frac{10 T_m}{\Sigma \left({}^T\!/_5 \right)^{1.5}} \right)^a \qquad (2.6)$$

Where E_{m_v} (mm) is the monthly evaporation, T_m (°C) is the mean monthly temperature, T is the mean daily temperature and a is a side constrained expression $a \le 0.5$ given by the polynomial:

$$a = 6.75e-8 \cdot \left(\sum \left(T/5\right)^{1.5}\right)^3 - 7.7e-6 \cdot \left(\sum \left(T/5\right)^{1.5}\right)^2 + 0.08 \cdot \sum \left(T/5\right)^{1.5} \quad (2.7)$$
$$+ 0.49$$

The Thornthwaite work was carried out in humid regions and his proposal may not be suitable for arid sites.

More recent theories allow evaluating the actual evapo-transpiration flux as the ratio potential/resistance in a electrical analogy (sellers et al., (1986)). More specifically, they interpret the latent heat, the sensible heat and the vapor fluxes as resulting from a system driven by two potentials: the jump in temperature and relative humidity across the surface and a number of resistances provided by both the soil and the plant. An illustration of such theory is presented in Fig. 2.3.
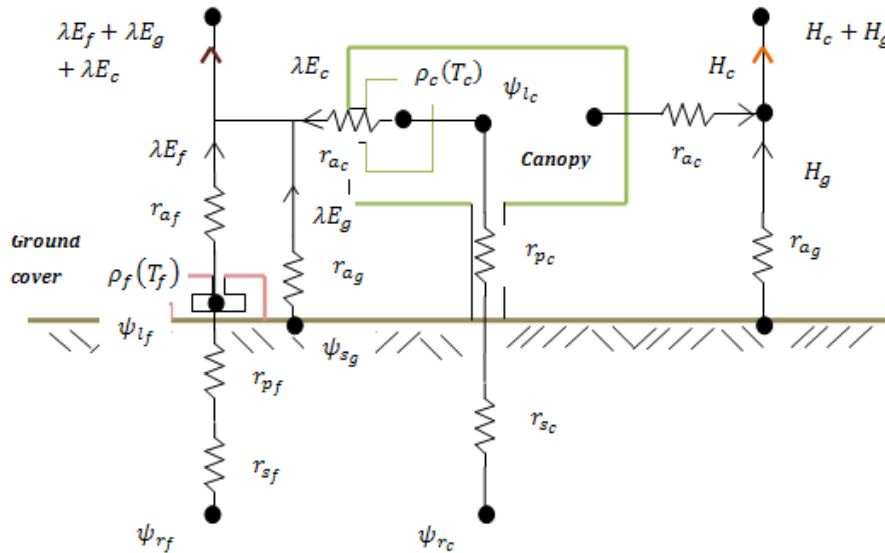
Figure 2.3: Resistances Model for the Atmospheric-Vegetation-Soil Upper layer

The layer in contact with the soil surface is composed of a network defined by a set of resistances and water potentials, through which the evapo-transpiration fluxes develops. Two vegetation systems are considered to act in parallel with ground evaporation E_g: a simple grass cover – non lignified – (left side of the figure) and a canopy (central part). The non lignified system is described by several resistances to flow movement, put in series: r_{s_f} (soil/plant), r_{p_f} (plant) and r_{a_f} (plant/atmosphere) that control the transpiration flux E_f under the gradient existing between ground water potential at the level of plant root ψ_{r_f} and water potential prevailing above at the level of plant leafs ψ_{l_f}. ρ_f is the absolute humidity at the ground cover level.

Similarly, the canopy system is described by resistances r_{s_c} (soil/canopy), r_{p_c} (canopy) and r_{a_c} (canopy/atmosphere), transpiration flux E_c and water potentials ψ_{r_c} (water potential at depth of canopy roots) and ψ_{l_c} (water potential at leafs elevation). ρ_c is the absolute humidity at the canopy level.

The figure depicts the heat balance of the system that includes the sensible heat fluxes H_c and H_g as well as the latent heat λ convected by evapo-transpiration.

Within this framework, Noilhan (1996) proposed a formulation where the evaporation flux is driven by the difference in vapor concentration at leaf level, between the air and the leaf, according to the expression:

$$E_v \left[\frac{k_g}{m^2 s}\right] = (1 - veg) \cdot \underbrace{\frac{k^2 v_a \emptyset}{\ln\left(\frac{z_a}{z_o}\right)^2}}_{1/r_a} \left(\rho_{va}(T_{atm}) - \rho_v\big(s, T(j_e)\big)\right) \qquad (2.8)$$

where the term $r_a [s\,m^{-1}]$ is the aerodynamic resistance, k is the von Karman's constant (often taken as 0.4), ϕ is a stability factor, veg is the vegetalized surface per unit area of ground (to remove transpiration from Eq. 2.8) and ρ_{va} and ρ_v are the absolute humidity of the atmosphere and the ground respectively, $(1 - veg)$ is the complement to the vegetation fraction, v_a is the wind velocity, z_o is the ground surface roughness length (often assimilated to canopy height), z_a is the screen height (height at which the wind velocity and the absolute humidity of the atmosphere are measured).

The absolute humidity (ρ_{va}) should be strictly measured at height z_o. Instead, it is computed from the state variables just below ground surface assuming a constant profile of wind speed between the ground surface and z_o, see Fig. 2.4.
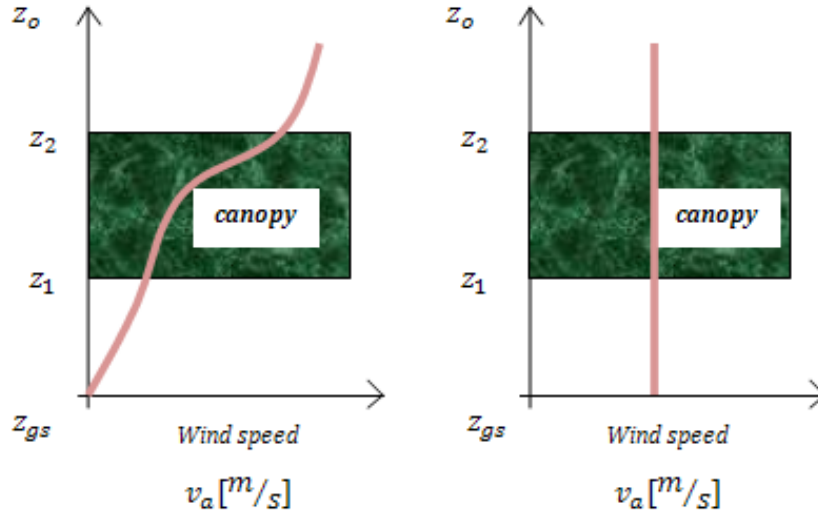
Figure 2.4: Profiles of wind speed above, within, and below the canopy vegetation: (a) real profile, (b) simplified assumed profile.

The ground absolute humidity ρ_v is computed from gas density ρ_g and vapor mass fraction θ_g^w by the expression $\rho_v = \rho_g \cdot \theta_g^w(s, T(j_e))$. The vapor mass fraction can be in turn determined through the psychrometric law:

$$\theta_g^w = \left(\theta_g^w\right)^\circ \cdot \exp\left(\frac{-s \cdot M_w}{R \cdot T(j_e) \cdot \rho_l}\right) \tag{2.9}$$

where *s* is the suction existing at the soil surface. From Eq. 2.9 the total evaporation flux can be rewritten as an explicit function of the mass fraction of water vapor:

$$E = (1 - veg) \cdot \underbrace{\frac{k^2 v_a \emptyset}{\ln\left(\frac{z_a}{z_o}\right)^2}}_{1/r_a} \underbrace{\left(\rho_{va} - \rho_g \cdot \theta_g^w(s, T(j_e))\right)}_{\text{potential}} \tag{2.10}$$

$\underbrace{}_{\text{Evaporation flux}}$

Vaporization from the crop stomata, is a complex process that starts with the soil water being taken by the vegetation at the root level and ends with the water being expelled via the stomata.

It encompasses interactions between the soil and the vegetation, on the one hand, and the vegetation and the atmosphere on the other hand.

The transpiration flux strictly represents the loss of water vapor from leaves. This flux is controlled at the level of leafs by the release of vapor molecules by stomata Fig. 2.5, whose opening and closure are activated by specialized cells called "guard cells".

Figure 2.5: Guard cells and Open stomata of a tobacco leaf, after Damon et al. (2007).

Transpiration flux maintains a depressed water column in the plant that traduces in an intake of water at the level of roots. There is thus a continuous stream of water from the roots to the upper parts of the plant that provides the plant with both the minerals and the required water mass to carry out photosynthesis.

More than 90% of water taken by the roots is lost by transpiration while the remaining 10% participate to plant growth.

There are many factors involved in the transport of water and minerals in plants where the xylem (lignified tissue) is the principal water-conducting tissue (Embryophyta). Among them, the following environmental factors have important effects on transpiration process: (a) light, it speeds up transpiration by warming the leaf and opening stomata; (b) air humidity, it is related to the driving potential for transpiration at the level of leafs. A decrease in air humidity increases transpiration because of the greater difference in water concentration; (c) wind, it increases the rate of transpiration because of the constant removal of humid air close to the leafs; (d) temperature, it provides heat for water evaporation; (e) soil water content, it is related to the driving potential for transpiration at the level of roots. The intake of water by the roots provides the plant with water and nutrients, keeps the osmotic pressure at the required level for maintaining the turgor pressure within plants cells and thus allowing the stomata to play its regulator role for the

transpiration Fig. 2.6; (f) Carbon Dioxide concentration – It has a negative effect on transpiration. High carbon dioxide levels in the air around the plant usually cause the guard cells to lose turgor pressure and the stomata to close.
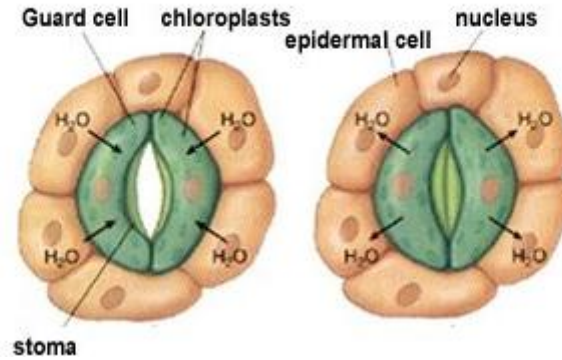
Figure 2.6: Water diffuses into guard cells which cause them to open. On hot/dry days, the guard cells have less water, they relax and the stoma closes.

Potassium ions play an important role in transpiration as they are an important factor of guard cell activity. The blue part of the spectrum's light triggers the active transport of potassium into the cell, which increases the solute concentration and causes inward water movement due to osmosis. When potassium ions passively leave the cells, they carry water molecules, which makes diminishing turgor pressure and cause stomatal closure.

Notwithstanding the complexity of living systems, from a pure modeling point of view, the upward movement of water in plants is considered as related to the gradient of water potential ψ expressed by the sum:

$$\psi = \pi + P_r + \psi_m + \psi_g \qquad (2.11)$$

where ψ_g is the gravity potential, ψ_m the matrix potential (related to water surface tension), π the osmotic potential (due to difference in solute concentration) and P_r the water pressure potential. According to the "cohesion-tension" theory, early developed by (Dixon & Joly, 1894), these potentials interact to maintain an upward gradient of total water potential from roots to plant leafs, see Fig. 2.7. Four transport mechanisms are distinguished, see for example Taiz L. & Zeiger, E., (2010):

a) At leaf level, transpiration occurs as the result of gradient in relative humidity between leaf and atmosphere. Because transpiration is the main mechanism of nutrient transport, plants must transpire even in presence of water deficit. To provide the conditions for permanent transpiration, stomata regulate the outflow

_____

of water molecules through the opening and closing of guard cells in order to maintain the relative humidity close to saturation in the air between the mesophyll cell of leafs, Fig. 2.7. During stomata closure, water total potential ψ_{leaf} is close to zero (HR = 100%). At time of stomata opening, vapor goes out and ψ_{leaf} becomes negative.

b) Transpiration flux is balanced by water income from the xylem. Xylem contains sap, which is water with essentially inorganic ions, thus having a negative osmotic potential π. In addition, capillary actions balance gravity $(\psi_m + \psi_g = 0)$ and, because xylem walls are stiff, they do not apply any pressure on the sap $(P_r = 0)$. Water will then move to the leafs when ψ_{leaf} becomes lower than xylem osmotic pressure. The difference between both potentials generates matric suction in the xylem.

c) Water lost by the xylem is balanced by an inflow of water coming from the root. Because nutrients are consumed during sap transport, osmotic potential is more negative at roots than at leafs level. This gradient is compensated by matrix suction gradient leading to an upward gradient in water total potential. Root cells are indeed provided with flexible membrane that pressurized the inner fluid $(P_r > 0)$.

d) Roots take water from the soil thanks to the existence of the gradient of osmotic suction that counteracts the gradient of water pressure/suction.

According to this theory, transpiration is essentially a flux-controlled process to which the plants have to adapt by regulating water potentials through chemo-thermo-hydro-mechanical actions at cell level. In front of the complexity of the coupled CTHM processes in living systems, a common approach in agricultural engineering considers modeling transpiration by applying directly the vapor flux existing at canopy level, Sellers et al. (1986); Noilhan & Planton, (1988).

This type of model expresses the transpiration flux at canopy level as driven by the difference between vapour density of the atmosphere (ρ_v) and the leaf. Because relative humidity within the leaf is close to 100%, the latter is taken equal to vapour density at saturation ρ_{va}, that depends only on leaf temperature (taken equal to atmosphere temperature T_{at}):

$$E_T \left[\frac{k_g}{m^2 s} \right] = veg \cdot \frac{1}{(r_a + r_s)} \cdot \left(\rho_{va\,sat}(T_{at}) - \rho_{va}(T_{at}) \right) \tag{2.12}$$
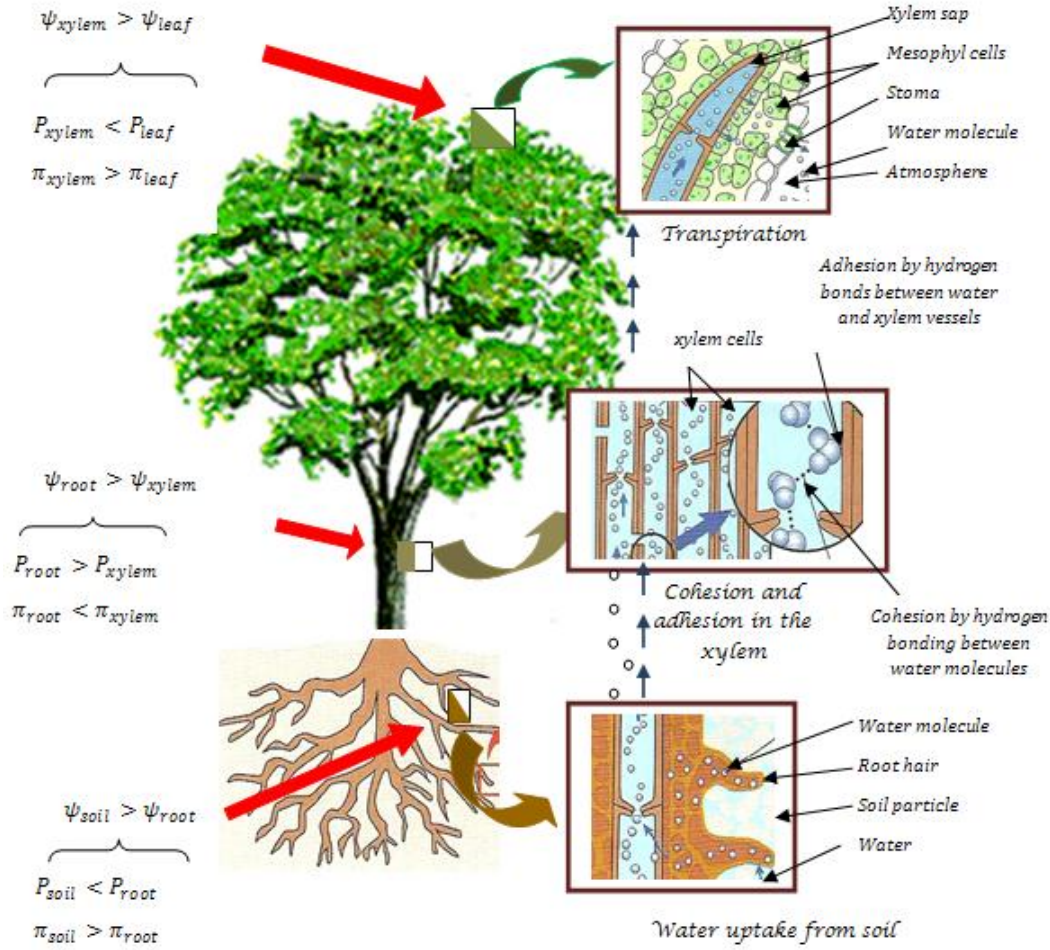
Figure 2.7: Transpiration-Cohesion-Tension mechanism (Transpiration Pull Theory) for the "Soil–Plant–Air" System.

$r_a[S/m]$ is the atmosphere resistance on top of the leaf, taken equal to the aerodynamic resistance previously defined, $r_s[S/m]$ is the leaf resistance provided by the stomata (Jarvis, 1976) and *veg* is the vegetation fraction. r_a and r_s are supposed to act in series. According to Noilhan & Mahfouf (1996), the stomatal resistance r_s is defined by four functions F_1, F_2, F_3 and F_4 of common use in agricultural engineering:

$$r_s = \frac{r_{s_{min}}}{LAI} \cdot \left[\frac{F_1(R_g)}{F_2(\theta) \cdot F_3(P_{v_{at}}) \cdot F_4(T_{at})} \right] \tag{2.13}$$

$r_{s_{min}}$ is the minimum surface resistance and depends on plant type. For different forest canopies, it has been observed that the relation $r_{s_{min}}/LAI$ remains nearly constant.

_____

Function $F_1(R_g)$ takes into account the effects of the photosynthetically active radiation R_g, assumed equal to 55% of the global radiation. It is evaluated following Dickinson proposal (Dickinson, 1984):

$$F_1 = \frac{1 + \left(\frac{1.1}{LAI} \cdot \frac{R_g}{R_{gl}}\right)}{\left(\frac{1.1}{LAI} \cdot \frac{R_g}{R_{gl}}\right) + \frac{r_{s_{min}}}{r_{s_{max}}}} \qquad (2.14)$$

where R_{gl} provides the upper limit of R_g and ranges between $30 \, {}^W/_{m^2}$ for a forest to $100 \, {}^W/_{m^2}$ for a crop.

Function $F_2(\theta)$ expresses the plant capacity to extract water from the soil at a given water content θ and is called the stress factor. It is approximated by a broken line with four segments :

$$F_2 = \begin{cases} 0 & \text{if } \theta \leq \theta_w \\ \dfrac{\theta - \theta_w}{\theta_{fc} - \theta_w} & \text{if } \theta_w \leq \theta < \theta_{fc} \\ 1 & \text{if } \theta_{fc} \leq \theta < \theta_a \\ \dfrac{1 - \theta}{1 - \theta_a} & \theta \geq \theta_a \end{cases} \qquad (2.15)$$

θ_w is the water content at the wilting point. It is the threshold below which plants cannot extract any more water and has been identified as corresponding to suction around 1.5 MPa (Jacquemin & Noilhan, 1990). θ_{fc} provides the "field capacity", defined as the water content remaining in a soil column after downward gravity drainage. It has been associated by Richards (1950) to values of suction between 0.01 MPa to 0.05 MPa and by Wetzel & Chang (1987) to an upper threshold of hydraulic conductivity, estimated equal to 0.1 mm/day (note that these values are characteristics to agricultural soils, mainly composed by silty/sandy fractions and medium porosity).

Bear et al. (1968) proposed to define θ_{fc} from the profile of soil water content in the soil column once completed bottom free drainage, Fig. 2.8. It corresponds to the value of water content attained at the depth where suction profile starts to be influenced by the free drainage condition. At higher depths, an increase in water content is registered. At lower depths, water content remains essentially constant. θ_{fc} is interpreted as the water content for which all the drainable porosity is empty. This concept is similar to the concept of microscopic water content developed by Romero et al. (1999), Romero & Vaunat (2000) and Alonso et al. (2010).

_____
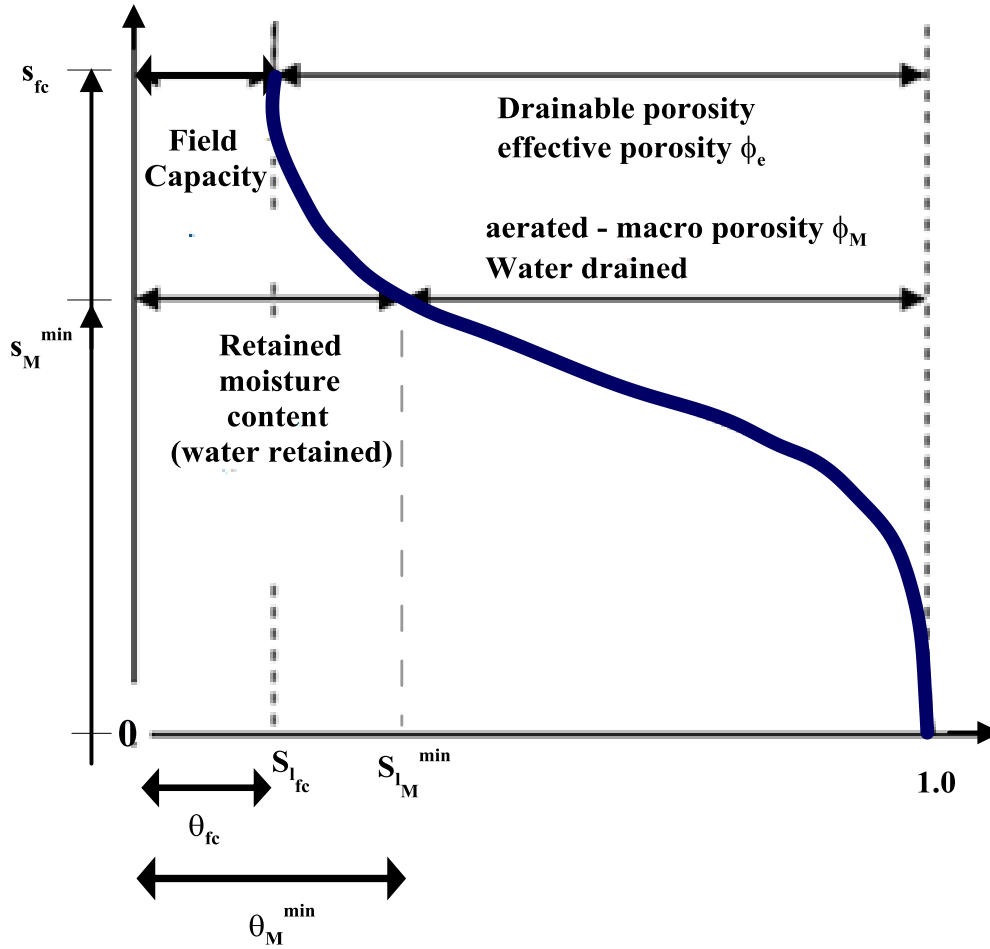
Figure 2.8: Field Capacity and effective porosity (after Bear 1972).

Finally the last threshold (θ_a) corresponds to the anaerobiosis point and represents the water content at which plants metabolism starts to lose efficiency because of too much water and loss of oxygen in the soil.

The function $F_3\left(P_{v_{at}}\right)$ accounts for stomata closure when a deficit of vapor pressure exists in the air (dry environment). It is evaluated through the equation

$$F_3 = 1 - \gamma \cdot \left(p_{v_{sat}} - p_v\right) \tag{2.16}$$

where $\gamma\left[^1/_{MPa}\right]$ is an empirical parameter. The surface resistance dependence on F_3 becomes a relatively important environmental constraint for the transpiration of moist broadleaf forest and seem to be less important for short canopies.

The last function $F_4(T_{at})$ introduces the dependence of r_s on air temperature. The function used is a modified version of Dickinson proposal (Dickinson, 1984) and is modified to avoid eventual, physically meaningless, negative values (Noilhan & Mahfouf, 1996):

$$F_4 = \exp(-0.0016 \cdot (298 - T_a)^2) \tag{2.17}$$

It is important to emphasize the empirical basis of the definition of functions F_1 to F_4, whose expression is no more than a phenomenological description of the evapotranspiration flux for a whole canopy. Typical values of the different parameters are provided in Table 2.1 for distinct types of vegetation.

Table 2.1: Vegetation Parameters for Land Surface Scheme, after (Noilhan & Planton, 1988).

Case	vegetation	z_o (m)	LAI $\left(\mathrm{m^2}/\mathrm{m^2}\right)$	$r_{s_{min}}$ (s/m)	veg
1	Maize	0.1	2	40	0.8
2	Soja	0.02	1	40	0.7
3	Maize	0.02	0.3	40	0.4
4	Forest	1	2.3	100	0.99
5	Maize	0.1	2	40	0.7
6	Oats	0.15	3	450	0.9

Alternative formulations express the stress factor (F_2) as a function of "leaf water potential" which depends on plant physiology and soil moisture. Jarvis (1976) suggests a negative exponential relationship between stomatal conductance and leaf water potential while Choudhury and Idso (Choudhury & Idso, 1985) derived an empirical function from data obtained at a field-grown wheat:

$$F_2 = 1 + \left(\frac{\psi_{lc}}{\psi_{cr}}\right)^{5.5} \tag{2.18}$$

ψ_{lc} is the water potential of the bulk leaf and ψ_{cr} is the critical limit for ψ_{lc} beyond which the transpiration rate is strongly limited by water stress ($\cong -2\mathrm{MPa}$ for a cereal crop). More recently, de Ridder & Schayes (1997) proposed a hyperbolic dependence of the form:

$$F_2 = \left(1 - \frac{\psi_{lc}}{\psi_{cc}}\right)^{-1} \tag{2.19}$$

where $\psi_{cc}(\cong -2.5\mathrm{MPa})$ represents the value of leaf water potential at which a complete stomatal closure occurs.

Along this lines, Lynn & Carlson (1990) had proposed years before a model composed by two resistances – the soil/root ($\mathrm{r_{sf}}$) and plant/canopy $\left(\mathrm{r_{pc}}\right)$ resistances – and three water

potentials – soil water potential in the root layer (ψ_{rf}), plant pressure potential (ψ_P) and leaf water potential (ψ_{lc}), see Fig. 2.9. The model is based on Jarvis assumption (Jarvis, 1976) that the flow of water from the soil to the leaf (j_{sl}) is equal to the potential transpiration flux E_T, which leads to the expression:

$$L_e E_T \left[\frac{J}{m^2 s}\right] = L_e \frac{\psi_{rf} - \psi_{lc}}{r_{sf} + r_{pc}} = \frac{\rho C_p}{\gamma \cdot (r_l + r_a)} \cdot (p_{at} - p_l) \qquad (2.20)$$
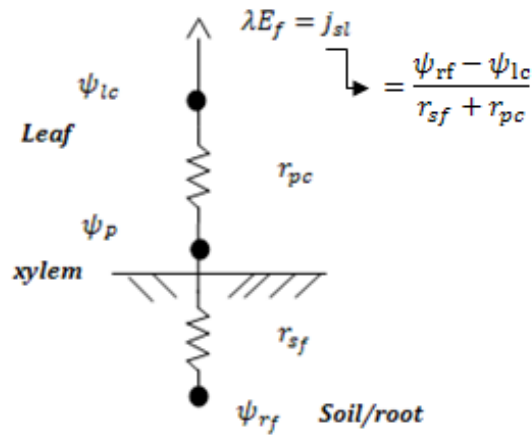
Figure 2.9: Water Transfer in plants as proposed by Landsberg (1976).

In Eq. 2.20, p_{at} is the atmosphere pressure surrounding the leaf , p_l the leaf vapor pressure, $\rho \left[\frac{kg}{m^3}\right]$ the air density, $C_p \left[\frac{J}{k_g K}\right]$ is the specific heat at constant pressure, $\gamma \left[\frac{MPa}{K}\right] = \frac{p_{at} C_p}{0.622 L_e}$, $r_l [\frac{s}{m}]$ is the leaf resistance and $r_a [\frac{s}{m}]$ is the atmosphere aerodynamic resistance.

Eq. 2.20 can also be expressed in terms of the absolute humidity of the atmosphere surrounding the leaf ρ_{at} and the absolute humidity at the leaf ρ_l, recognizing the relationship $\rho_v = \frac{p_v \cdot \varepsilon^v}{p}$, with $\varepsilon^v = \frac{m_d M_w}{VM_d}$ in which M_w and M_d are the molecular mass of vapor and dry air, respectively:

$$E_T \left[\frac{kg}{m^2 s}\right] = \left(\frac{p}{L_e \cdot \varepsilon^v}\right) \cdot \frac{\rho C_p}{\gamma \cdot (r_l + r_a)} \cdot (\rho_{at} - \rho_l) \qquad (2.21)$$

In this model, the leaf resistance r_l is computed by considering a parallel action of cuticular and stomatal resistances r_{cut} and r_s:

$$\frac{1}{r_l} = \frac{1}{r_s} + \frac{1}{r_{cut}} \tag{2.22}$$

Table 2.2 summarizes the revisited formulations to compute evapotranspiration fluxes from macroscopic viewpoints. In this work, the Noilhan (1988) formulation will be followed without entering in the complexity of the chemo-thermo-hydro-mechanical processes controlling the water potential in the plant system.

This formulation provides a value for the actual transpiration in contrast to the potential one provided by Montheith (1965), Lynn (1990).

Table 2.2: Summary of the referred expressions for computation of Evaporation and Transpiration fluxes.

Penman (1948)	Potential - Evaporation	$E_p = \dfrac{\Delta \cdot R_n + \gamma \lambda(T, \sigma_s) \cdot E_a}{\lambda(T, \sigma_s) \cdot (\Delta + \gamma)}$	$\left[\dfrac{k_g}{m^2 d}\right]$	$\Delta \left(\frac{P_a}{°C}\right)$	slope T-p_v^{sat}
				R_n	net radiation
				$\lambda \left(\frac{J}{m^2}\right)$	latent heat of vaporization
				(γ)	psychrometric constant
Penman-Monteith (1965)	Potential - Evapo-transpiration	$E_p = \dfrac{\Delta \cdot \frac{(R_n - j_e)}{\lambda(T, \sigma_s)} + \gamma \cdot Ea}{\Delta + \gamma \cdot (1 + \frac{r_s}{r_a})}$	$\left[\dfrac{k_g}{m^2 d}\right]$	$E_a \left(\frac{mm}{}\right)$	vapor flux due to pressure deficit
				j_e	conductive energy flux
				r_a	aerodynamic resistance
				r_s	plant surface resistance
Thornthwaite (1954)	Real - Evaporation	$E_{m_v} = 16.2 \cdot \left(\dfrac{10 T_m}{\Sigma\left(\frac{T}{5}\right)^{1.5}}\right)^a$	$\left[\dfrac{mm}{m_s}\right]$	$T_m(°C)$	mean monthly temperature
				T	mean daily temperature
				a	polynomial value ≤ 0.5
Sellers - Noilhan (1980)	Real - Evaporation	$E_v = (1 - veg) \cdot \dfrac{k^2 v_a \emptyset}{\ln\left(\frac{Z_a}{Z_o}\right)^2} \left(\rho_{va}(T_{atm}) - \rho_v(s, T(j_e))\right)$	$\left[\dfrac{k_g}{m^2 s}\right]$	veg	vegetalized surface per unit area of ground
				$\emptyset$	stability factor
				ρ_{va}	atmosphere's absolute humidity
Noilhan - Planton (1988)	Real - Transpiration	$E_T = veg \cdot \dfrac{1}{(r_a + r_s)} \cdot \left(\rho_{va\,sat}(T_{at}) - \rho_{va}(T_{at})\right)$	$\left[\dfrac{k_g}{m^2 s}\right]$	ρ_v	ground's absolute humidity
				r_a	aerodynamic resistance
				r_s	leaf surface resistance
Jarvis. Lynn &	Potential -	$E_T = \dfrac{\psi_{rf} - \psi_{lc}}{r_{sf} + r_{pc}} = \dfrac{\rho\, C_p}{L_e \gamma \cdot (r_l + r_a)} \cdot (p_{at} - p_l)$	$\left[\dfrac{k_g}{m^2 s}\right]$	p_l	leaf vapor pressure
				p_{at}	atmosphere pressure
				ρ	air density

Carlson (1990)	Transpiration			C_p	specific heat
				$r_l [{}^S/_m]$	leaf resistance
				$r_a [{}^S/_m]$	atmosphere aerodynamic resistance

More recent developments coming from bioengineering present more fundamental formulations based on the modeling of cell tissue response in function of both solute and suction changes to better cope with the transpiration flux. A brief review of these developments is presented below, section 2.4.1.2.

2.4.1.2)   Effect of plant growth

The intake of water by the roots provides the plant with water and nutrients that favor its growth. As consequence, roots depth and density change over time and therefore the characteristics of the vadose zone are affected.

Plant growth is a complex process that can be tackled from two sides: 1) at the plant level, by measuring macroscopic parameters such as stem diameters and canopy height, volume and weight and 2) at the cell level, by studying their growth and differentiation.

The "macroscopic" approach is based on the expression of the change in plant volume V_c or plant weight P_c. It is expressed by:

$$C_r = \frac{1}{V_c} \frac{dV_c}{dt} = \frac{1}{P_c} \frac{dP_c}{dt} \tag{2.23}$$

where C_r is the relative growth magnitude.

Several expressions exist for C_r. This first approach relates C_r to the morphological factor $F_c = {}^{L_A}/_{P_c}$, ratio of leaf surface L_A over plant weight. By defining the rate of net assimilation as $A_n = \left(1/_{L_A}\right) \cdot {}^{dP_c}/_{dt}$, C_r can be rewritten as:

$$C_r = A_n \cdot F_c \tag{2.24}$$

L_A can be expressed by the product $LAI \cdot S_c$ where LAI is the leaf area index and S_c the projected area of plant canopy on ground surface. In this approach, the rate of net assimilation $A_n [\text{MPa}]$ between times t_1 and t_2 is estimated by the Eq. 2.25a while the morphological factor $F_c [1/_{\text{MPa}}]$ is given by Eq. 2.25b,

_____

$$A_n = \frac{P_c^2 - P_c^1}{L_A^2 - L_A^1} \cdot \frac{\ln\left(L_A^2 / L_A^1\right)}{\Delta_t} \quad ; \quad F_c = \frac{1}{2} \cdot \left(\frac{L_A^1}{P_c^1} + \frac{L_A^2}{P_c^2}\right) \tag{2.25}$$

The relative plant growth between times t_1 and t_2 is thus given by:

$$C_r = \frac{((P_c^2)^2 P_c^1 - (P_c^1)^2 P_c^2)}{(L_A^1 P_c^2 + L_A^2 P_c^1)^{-1}(P_c^1 P_c^2) 2\Delta t} \cdot \frac{\ln\left(L_A^2 / L_A^1\right)}{(L_A^2 - L_A^1)} \tag{2.26}$$

Equation 2.26 provides a constant evolution for the relative growth. This is a limitation of the model as growth tends generally to decrease as plant size increases. To overcome this limitation, the second approach states the following dependency for C_r:

$$C_r = \frac{k(M_p - P_c)}{M_p} \tag{2.27}$$

where k is a proportionality constant and M_p the maximum weight that the canopy can reach. From Eq. 2.23 and Eq. 2.27, the expression of plant growth becomes:

$$P_c = \frac{M_p}{1 + \exp(b - kt)} \tag{2.28}$$

b/k is the time at which the half of maximum weight is reached. Equation 2.28 predicts an evolutive growth with an initial phase of fast growth followed by an aging phase.

Other expressions exist for plant growth like the Richard's function, polynomials models and log-polynomials models. This type of models are completed by the statement of an alometric relation (Uso, Mateu, Karjalainen, & Salvador, 1997) between roots volume and the total canopy volume $\left(V_r / V_c\right)$ that finally allows to define the change in root depth and density.

The "microscopic" approach is based on the statement of an equation for cellular growth. In the simplest models, cells increase their volume when their wall yields under the effect of water entry. The rate of water absorption by the cell depends on the gradient of the water potential ψ, cell surface S and specific hydraulic conductivity of the cell membrane $L_p[cm/s \cdot MPa]$. Then, the increment of the cell volume V_c can be expressed as a function of the net rate of water uptake:

$$\underbrace{\frac{dV_c}{V_c dt}}_{\substack{\text{Rate of increase of} \\ \text{water volume}}} = S \cdot L_p \cdot \frac{\Delta \psi}{V_c} = \underbrace{L_c (\Delta \pi - P_T)}_{\substack{\text{Net rate of water} \\ \text{uptake}}} \qquad (2.29)$$

Rate of increase of water volume

Net rate of water uptake

where, $L_c = \frac{S \cdot L_p}{V_c} [1/_{s \cdot MPa}]$ is the relative hydraulic conductivity of the cell and P_T the

turgor pressure. The turgor is the force exerted by the cell membrane on the inner fluid to maintain equilibrium. P_T is thus equal to the difference between the external and internal fluid pressure P_r^o applied on the membrane. The cell proliferates in volume when an irreversible dilation occurs at cell membrane, accompanied by tissue softening and corresponding lose of turgor pressure. Because of the reduction of P_T, water is allowed to enter into the cell increasing the cellular volume until the turgor pressure is recovered.

The cellular expansion is then expressed as a function of the distance between the turgor pressure and the critical threshold Y_c:,

$$T_g^c = \underbrace{\frac{dV_{wc}}{V_{wc} dt}}_{\substack{\text{Rate of increase} \\ \text{of wall chamber} \\ \text{volume}}} = \underbrace{m_c \cdot (P_T - Y_c)}_{\substack{\text{Irreversible} \\ \text{expansion rate}}} \qquad (2.30)$$

Rate of increase of wall chamber volume

Irreversible expansion rate

where V_{wc} is the volume of the cell wall chamber, m_c is the irreversible extensibility coefficient and Y_c is the "critical turgor pressure", threshold at which the cell starts to grow. Equations 2.29 and 2.30 allow to express the steady-state turgor pressure (membrane pressure at which cell stops to grow):

$$P_T = \frac{L_c \Delta \pi + m_c Y_c}{m + L_c} \qquad (2.31)$$

The rate of cellular growth can then be re-written as,

$$\frac{dV_c}{V_c dt} = \frac{m_c L_c \cdot (\Delta \pi - Y_c)}{m_c + L_c} \qquad (2.32)$$

and the cell volume at any time is given by:

$$V_c = V_c^o \cdot \exp \left(\frac{m_c L_c \cdot (\Delta \pi - Y_c)}{m_c + L_c} \cdot t \right) \qquad (2.33)$$

Equations 2.29 to 2.31 are the "Lockhart Equations" (Lockhart, 1965).

_____

They represent the first model developed to tackle the cellular growth of plants. It is expressed as a function of the osmotic potential π, the relative hydraulic conductivity of the cell L_c, the irreversible extensibility coefficient m_c and the threshold turgor pressure Y_c. Further works have introduced the effect of external stimuli, such as the light or hormones as variables controlling these factors.

More recently, advanced models have been proposed based on the mechanics of hollow cylinders (or hollow spheres) to model the decrease in turgor pressure. All these models present the advantages of relating plant growth to osmotic pressure through a mechanical model and may be implemented as constitutive laws in chemo-thermo-hydro-mechanical processes.

Further improvements regarding the interaction between the vegetation cover and the ground should indeed compute transpiration flux by a suitable treatment of osmotic suction through the correct formulation of chemical equations controlling solutes transport. This approach leads to a better representation of most of the observed vegetation effects.

Exchange fluxes of vapor between the ground and the atmosphere includes finally the vapor advected by the air phase crossing ground surface. The advective flux of vapor at the air phase is evaluated by invoking both the mass fraction of vapor and the flux of gas and is computed through the equation,

$$j_g^{w_{atm}} = \begin{cases} \omega_g^w \cdot q_g & \text{if } P_g > P_{ga} \\ \rho_{va}/\rho_{ga} \cdot q_g & \text{if } P_g \leq P_{ga} \end{cases} \tag{2.34}$$

where ρ_{ga} is the atmospheric gas density and $q_g \left[\frac{k_g}{m^2 s} \right]$ the flux of gas driven by the existent gradient between the gas pressure at the soil surface and the atmospheric pressure.

2.4.1.3) Modeling runoff flux

The surface runoff j_{sr} flux, is the flow rate of water that do not enter into the ground but drain over the soil surface. Its effect is simulated by considering that the infiltration can only enter in the soils if the atmospheric pressure is higher than the ground pore pressure, according to the condition:

$$j_{sr} = \begin{cases} \gamma_w \cdot (P_l - P_{ga}) & \text{if } P_l > P_{ga} \\ 0 & \text{if } P_l \leq P_{ga} \end{cases} \tag{2.35}$$

where $\gamma_w [^S/_m]$ is the ground surface liquid leakage coefficient. It is remarked that ponding is not explicitly simulated in the present work.

Total atmospheric water flux crossing the ground surface finally results in:

$$j^{w_{atm}} = P + E_v + j_g^{w_{atm}} + j_{sr} \tag{2.36}$$

2.4.2) Description of atmospheric air flux $j^{a_{atm}}$

Atmospheric flux of air is defined by the existent gradient between the gas pressure at the soil surface and the atmospheric pressure. It is given in terms of the gas flux and the mass fraction of atmospheric dry air.

Accordingly, the flux of the gas phase q_g is expressed in terms of the atmospheric pressure p_{at} as:

$$q_g \left[\frac{k_g}{m^2 s} \right] = \gamma_g \cdot (P_g - P_{at}) \tag{2.37}$$

where $\gamma_g [^S/_m]$ is a leakage coefficient. This flux carries two species the dry air and the vapour, then the flux of atmospheric dry air reads:

$$j^{a_{atm}} = \omega_g^a \cdot q_g = (1 - \omega_g^w) \cdot q_g \tag{2.38}$$

where ω_g^w is the mass fraction of atmospheric humidity.

2.4.3) Description of atmospheric energy flux $j_{E_{atm}}$

The atmospheric energy flux $j_{E_{atm}}$ reaching the ground surface is given by the sum of three components: (a) the sensible heat flux H_s, (b) the heat flux H_c convected by the mass fluxes (an important term here is the latent heat of vaporization carried by water mass flux) and the net radiation R_n.

Sensible heat flux is computed through the aerodynamic diffusion relation:

$$H_s \left[\frac{J}{m^2 s} \right] = \rho_{ga} C_a \cdot \frac{k^2 v_a \emptyset}{\left(\ln \left(\frac{z_a}{z_0} \right) \right)^2} \cdot (T_a - T_0) \tag{2.39}$$

where $C_a \left[\frac{J}{k_g K} \right]$ is the specific gas heat, ρ_{ga} the atmosphere density, T_a the atmospheric

temperature and T_0 is the ground temperature. For its part, the convected heat flux is evaluated taking into account the internal energy of liquid water, vapor and air:

$$H_c \left[\frac{J}{m^2 s} \right] = h_v \left(E_v + j_g^{w_{atm}} \right) + h_l \left(P + j_l^{w_{atm}} \right) + h_a j^{a_{atm}} \tag{2.40}$$

where $h_v \left[\frac{J}{k_g} \right]$, $h_l \left[\frac{J}{k_g} \right]$ and $h_a \left[\frac{J}{k_g} \right]$ are the free energies of vapor, liquid water and air, respectively.

The last flux summing up to the total flux of atmospheric energy is from my point of view the most relevant concerning the "soil-water-energy balance", it is the net radiation R_n.

It can be measured directly or evaluated from considerations about solar and atmosphere radiations. In the last case the flux is evaluated by the expression:

$$R_n \left[\frac{J}{m^2 s} \right] = (1 - A_l(S_l)) \cdot R_g + \varepsilon_{MS}(S_l) \cdot R_a - \varepsilon_{MS} \sigma_{SB} T^4 \tag{2.41}$$

where $R_g \left[\frac{J}{m^2 s} \right]$ is the direct solar short wavelength radiation and $R_a \left[\frac{J}{m^2 s} \right]$ the long wavelength atmospheric radiation, $A_l(S_l)$ is the ground albedo (reflection coefficient) which depends on degree of saturation, $\varepsilon_{MS}(S_l)$ is the ground emissivity which depends on the saturation degree and σ_{SB} the Stefan-Boltzmann constant $\left(5.67 \times 10^{-8} \left[\frac{J}{s \cdot m^2 \cdot K^4} \right] \right)$.

The dependences $A_l(S_l)$ and $\varepsilon(S_l)$ are materialized through the expressions:

$$A_l = A_d + (A_d - A_w) \cdot \left(S_l^2 - 2S_l \right) \tag{2.42}$$
$$\varepsilon_{MS} = 0.9 + 0.05 \cdot S_l$$

where A_d and A_w are the dry and wet albedos respectively.

Long wave atmospheric radiation R_a can eventually be computed as a function of the atmospheric temperature, in absence of measurements.

Eq. 2.43 presents one of the existent empirical proposals to compute R_a:

$$R_a = \sigma_{SB} \cdot T_{at}^4 \cdot \left(0.605 + 0.048\sqrt{1370\rho_{va}}\right) \tag{2.43}$$

where T_{at} is the atmospheric temperature and ρ_{va} the absolute humidity.

Finally, it is recalled that in absence of measures of atmospheric radiation it is possible to built harmonic approximations according to sinusoidal and co-sinusoidal functions, (Gran, 2015).

The total flux of atmospheric energy $j_{E_{atm}}$ that crosses the ground surface is finally given by the sum:

$$j_{E_{atm}} = H_s + H_c + R_n \tag{2.44}$$

Figure 2.10 summarizes the fluxes acting at the "soil-water-energy balance" boundary Γ^{atm}.
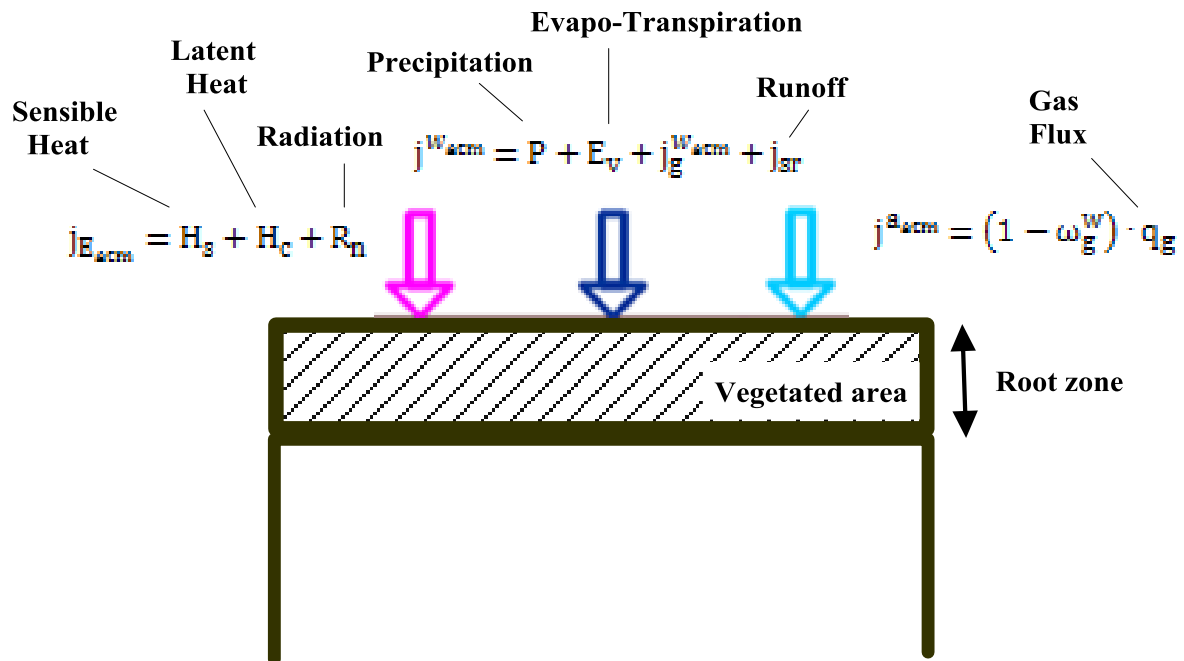
Figure 2.10: Summary of the fluxes acting at the "soil-water-energy-balance".

_____

2.5)   Formulation of the THM response of three-phase porous medium by thermomechanical approach

The behavior of the porous media from a mathematical viewpoint can be addressed in two ways: (a) following proposals in classical literature, in which governing equations of the problem are presented and detailed, (b) properly setting the energy balance and dissipation of the porous medium, and then proceeding with the analysis following standard methods in thermodynamics.

The first procedure is detailed in appendix 1 of this dissertation following the formulation presented by Olivella (1995) and further extended by Sanchez (2004). The second procedure is discussed below.

In theory of porous media balance equations are established considering all the present phases in the medium and their interactions. In this chapter the required coupled THM formulation for non-isothermal processes is presented based on the approaches proposed by Olivella et.al. (1994) and Houlsby et.al. (2006).

The formulation assumes thermal equilibrium between the phases. This assumption seems reasonable at the light of the characteristic times of most geotechnical problems.

The energy balance equation is formulated for a three-phase porous medium: (a) solid, (b) liquid and (c) gas. This equation postulates that the change of internal energy for the three soil phases is equal to the sum of: (a) mechanical power , (b) net inflow-outflow of heat energy and (c) sink-source contribution, see Fig. 2.11.

The storage energy in the porous skeleton is composed by the energy in the mineral $E_s\rho_s(1-\phi)$ and the energy in the air-water interface $\phi\sum E_i^{kl}$. The storage energy in the pore liquid and in the pore gas are given by the terms $E_l\rho w_l S_l\phi$ and $E_g\rho w_g(1-S_l)\phi$, respectively. Where ρ is the dry density and $w_l = {\rho_l}/{\rho}$, $w_g = {\rho_g}/{\rho}$ are the partial fractions of liquid and gas unit masses per unit mass of skeleton.

The net flows are: (a) the net flow of energy in the mineral and in the air-water interface $j_{\widetilde{E}_s}$, (b) the net flow of energy in the liquid j_{E_l}, (c) the net flow of energy in the gas j_{E_g} and (d) the net flow of energy by conduction i_c, Fig. 2.11.

_____

If a boundary Γ^{atm} of a volume of porous medium is in the border with the atmosphere (such that: $\Gamma^{atm} \in \Gamma$) the expression for the flow of energy in this border takes a particular form which depends on the atmospheric variables.
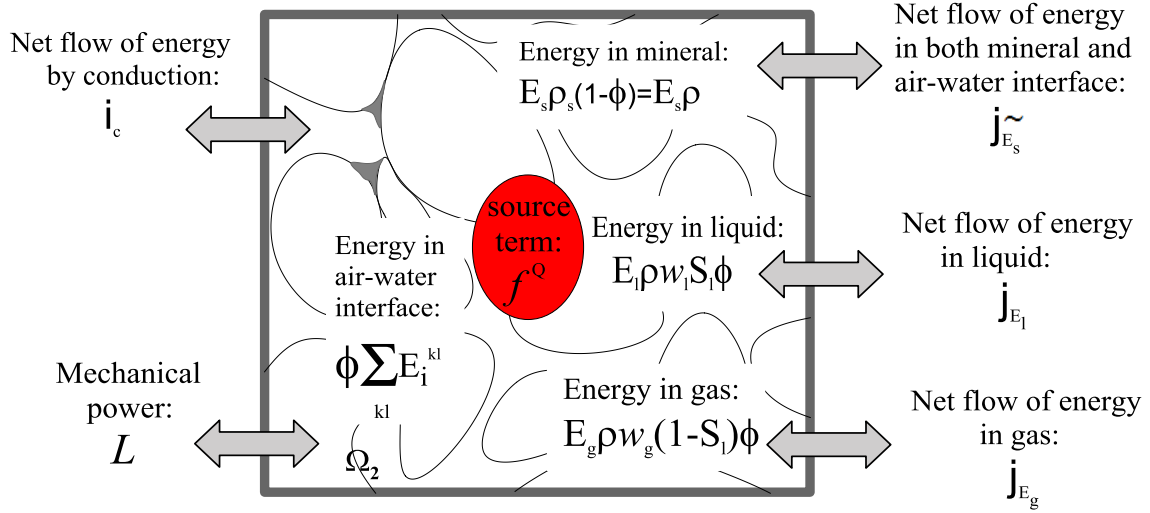
Figure 2.11: Energy storage and energy fluxes involved in a three-phase porous medium, for a volume totally embedded in the porous medium (after Gens, 2009).

Before proceeding further, some definitions are presented to be used along the development. Eq. 2.45 presents ϑ fractions in terms of unit mass densities, degree of saturation and porosity:

$$\vartheta_l^w = \frac{\rho_l^w}{\rho} S_l \phi \quad ; \quad \vartheta_g^w = \frac{\rho_g^w}{\rho}(1 - S_l)\phi \quad ; \quad \vartheta_l^a = \frac{\rho_l^a}{\rho} S_l \phi \quad ; \quad \vartheta_g^a = \frac{\rho_g^a}{\rho}(1 - S_l)\phi \qquad (2.45)$$

Eq. 2.46 shows different expressions for the mass of fluids present in the porous skeleton:

$$\rho w_l^w \phi S_l \quad = \quad \rho \vartheta_l^w \quad = \quad \rho_l^w \phi_l \qquad (2.46)$$

$$\rho w_g^w \phi(1 - S_l) \quad = \quad \rho \vartheta_g^w \quad = \quad \rho_g^w \phi_g$$

$$\rho w_g^a \phi(1 - S_l) \quad = \quad \rho \vartheta_l^a \quad = \quad \rho_g^a \phi_g$$

$$\rho w_l^a \phi S_l \quad = \quad \rho \vartheta_g^a \quad = \quad \rho_l^a \phi_l$$

Eq. 2.47 presents different expressions for the macro porosity of a three-phase porous medium in terms of both: (a) partial porosities and (b) degree of saturation:

$$\phi = \phi_l + \phi_g = \phi S_l + \phi(1 - S_l) \qquad (2.47)$$

73

_____

Eq. 2.48 presents expressions of advective and diffusive fluxes for the flows in a three-phase porous medium:

$$q'_{l_i} \quad = \quad \rho_l^w \phi_l (\vartheta_i^w - v_i) \quad = \quad \rho_l^w q_{l_i} \tag{2.48}$$

$$i_{g_i}^{w'} \quad = \quad \rho_g^w \phi_g (v_{g_i}^w - v_i^a) \quad = \quad \rho_g^w i_{g_i}^w$$

$$q'_{g_i} \quad = \quad \rho_g^a \phi_g (v_i^a - v_i) \quad = \quad \rho_g^a q_{g_i}$$

$$i_{l_i}^{a'} \quad = \quad \rho_l^a \phi_l (v_{l_i}^a - v_i^w) \quad = \quad \rho_l^a i_{l_i}^a$$

Before addressing the laws of thermodynamics it is convenient to review the balance laws of each phase: solid, liquid and gas.

Mass balance of solid skeleton is stated in terms of dry density $\rho = \rho_s (1 - \phi)$ leading to:

$$\int_\Omega \frac{\partial \rho}{\partial t} d\Omega + \int_\Gamma \rho v_i n_i d\Gamma = 0 \tag{2.49}$$

using the divergence theorem of Gauss and due to the arbitrary character of $d\Omega$, Eq. 2.49 can be rewritten in local form:

$$\frac{\partial \rho}{\partial t} + (\rho v_i)_{,i} = 0 \tag{2.50}$$

the development of each term of Eq. 2.50 leads to the conservation law:

$$\frac{\partial \rho}{\partial t} + \rho_{,i} v_i + \rho v_{i,i} \quad = \quad 0 \tag{2.51}$$

$$\frac{d\rho}{dt} + \rho v_{i,i} \quad = \quad 0$$

Eq. 2.51b establishes a relation between the rate of change of dry density and the solid dilation rate. Furthermore, noting that:

$$\frac{d\rho}{dt} = \frac{d\rho_s}{dt}(1 - \phi) - \rho_s \frac{d\phi}{dt} \quad ; \quad \phi = \phi_l + \phi_g \tag{2.52}$$

mass continuity of solid skeleton Eq. 2.51b can be re-expressed in terms of solid matrix density ρ_s and porosity ϕ:

$$\frac{d\rho_s}{dt} \frac{\left(1 - (\phi_l + \phi_g)\right)}{\rho_s} - \frac{d}{dt}(\phi_l + \phi_g) + \left(1 - (\phi_l + \phi_g)\right) v_{i,i} = 0 \tag{2.53}$$

Eq. 2.53 can also be expressed in terms of unit volume $v_s = {}^1\!/\!\rho_s$:

_____

$$\phi v_{i,i} = -\rho \frac{dv_s}{dt} - \frac{d\phi}{dt} + v_{i,i} \tag{2.54}$$

Mass balance of water stated in terms of density ratio w_k^i , porosity and degree of saturation is:

$$\int_\Omega \frac{\partial}{\partial t}\left(\rho w_l^w S_l \phi + \rho w_g^w \phi (1 - S_l)\right) d\Omega + \int_\Gamma \underbrace{\left(j_l^w + j_g^w\right)}_{j^w} n_i d\Gamma + \int_\Omega f^w d\Omega = 0 \tag{2.55}$$

where f^w is a sink/source term and j^w is the total flux of water, advective and diffusive, given by:

$$j^w = \underbrace{\rho w_l^w S_l \phi v_i + \rho w_l^w \phi S_l (v_i^w - v_i)}_{j_l^w} \tag{2.56}$$
$$+ \underbrace{\rho w_g^w (1 - S_l) \phi v_i + \rho w_g^w \phi (1 - S_l)\left(v_{g_i}^w - v_i^a\right)}_{j_g^w}$$

or in terms of ϑ fractions:

$$j^w = \underbrace{\rho \vartheta_l^w v_i + \underbrace{\rho \vartheta_l^w (v_i^w - v_i)}_{q_{l_i}'}}_{j_l^w} + \underbrace{\rho \vartheta_g^w v_i + \underbrace{\rho \vartheta_g^w\left(v_{g_i}^w - v_i^a\right)}_{i_{g_i}^{w'}}}_{j_g^w}$$

divergence theorem of Gauss allows to rewrite Eq. 2.55 as:

$$\int_\Omega \frac{\partial}{\partial t}\left(\rho w_l^w S_l \phi + \rho w_g^w \phi (1 - S_l)\right) + \left(j_l^w + j_g^w\right)_{,i} d\Omega + \int_\Omega f^w d\Omega = 0 \tag{2.57}$$

because $d\Omega$ in Eq. 2.57 is arbitrary it can be written in local form:

$$\frac{\partial}{\partial t}\left(\rho w_l^w S_l \phi + \rho w_g^w \phi (1 - S_l)\right) + \left(j_l^w + j_g^w\right)_{,i} + f^w = 0 \tag{2.58}$$

or in terms of ϑ fractions:

$$\frac{\partial}{\partial t}\left(\rho \vartheta_l^w + \rho \vartheta_g^w\right) + \left(j_l^w + j_g^w\right)_{,i} + f^w = 0$$

developing each term of Eq. 2.58b leads to the conservation law:

$$\frac{\partial \rho}{\partial t}\vartheta_l^w + \rho \frac{\partial \vartheta_l^w}{\partial t} + \frac{\partial \rho}{\partial t}\vartheta_g^w + \rho \frac{\partial \vartheta_g^w}{\partial t} + \rho_{,i}(\vartheta_l^w + \vartheta_g^w)v_i + \rho\left(\vartheta_{l,i}^w + \vartheta_{g,i}^w\right)v_i \tag{2.59}$$
$$+ \rho(\vartheta_l^w + \vartheta_g^w)v_{i,i} + q_{l_i,i}' + i_{g_i,i}^{w'} = 0$$

or similarly,

$$\frac{d\rho}{dt}(\vartheta_l^w + \vartheta_g^w) + \rho\left(\frac{d\vartheta_l^w}{dt} + \frac{d\vartheta_g^w}{dt}\right) + \rho \vartheta_l^w v_{i,i} + \rho \vartheta_g^w v_{i,i} + q_{l_i,i}' + i_{g_i,i}^{w'} = 0$$

_____

which on account of the skeleton mass conservation leads to the relations for water specie at each phase $(\blacksquare)_l^w$ and $(\blacksquare)_g^w$:

$$\rho\frac{d\vartheta_l^w}{dt} + q'_{l_i,i} = 0 \quad ; \quad \rho\frac{\partial\vartheta_g^w}{\partial t} + i_{g_i,i}^{w'} = 0 \tag{2.60}$$

Moreover, water mass continuity equation Eq. 2.59 can be rewritten in terms of fluid densities $\{\rho_k^w : k = l, g\}$ and partial porosities $\{\phi_k : k = l, g\}$, leading to:

$$\frac{d\rho_l^w}{dt}\phi_l + \rho_l^w\frac{d\phi_l}{dt} + \frac{d\rho_g^w}{dt}\phi_g + \rho_g^w\frac{d\phi_g}{dt} + \rho_l^w\phi_l v_{i,i} + \rho_g^w\phi_g v_{i,i} + \left(\rho_l^w q_{l_i}\right)_{,i} \tag{2.61}$$
$$+ \left(\rho_g^w i_{g_i}^w\right)_{,i} = 0$$

the equality at Eq. 2.61 should be fulfilled for each species (water in liquid state) and (vapor), then:

$$\frac{d\rho_l^w}{dt}\frac{\phi_l}{\rho_l^w} + \frac{d\phi_l}{dt} + \phi_l v_{i,i} + \frac{\rho_{l,i}^w}{\rho_l^w}q_{l_i} + q_{l_i,i} \quad = \quad 0 \tag{2.62}$$

$$\frac{d\rho_g^w}{dt}\frac{\phi_g}{\rho_g^w} + \frac{d\phi_g}{dt} + \phi_g v_{i,i} + \frac{\rho_{g,i}^w}{\rho_g^w}i_{g_i}^w + i_{g_i,i}^w \quad = \quad 0$$

where each equation is identically zero. They can also be expressed in terms of unit volumes $v_l^w = {}^1\!/_{\rho_l^w}$, $v_g^w = {}^1\!/_{\rho_g^w}$:

$$q_{l_i,i} \quad = \quad \frac{dv_l^w}{dt}\rho_l^w\phi_l + \frac{d\phi_l}{dt} + \phi_l v_{i,i} + q'_{l_i}v_{l,i}^w \tag{2.63}$$

$$i_{g_i,i}^w \quad = \quad \frac{dv_g^w}{dt}\rho_g^w\phi_g + \frac{d\phi_g}{dt} + \phi_g v_{i,i} + i_{g_i}^{w'}v_{g,i}^w$$

In a similar approach a mass balance of air stated in terms of density ratio, porosity and degree of saturation is:

$$\int_\Omega \frac{\partial}{\partial t}\left(\rho w_g^a(1 - S_l)\phi + \rho w_l^a\phi S_l\right)d\Omega + \int_\Gamma \underbrace{\left(j_g^a + j_l^a\right)}_{j^a}n_i d\Gamma + \int_\Omega f^a d\Omega = 0 \tag{2.64}$$

where f^a is a sink/source term and j^a is the total flux of air given by:

_____

$$j^a = \underbrace{\rho w_g^a(1 - S_l)\phi v_i + \rho w_g^a \phi(1 - S_l)(v_i^a - v_i)}_{j_g^a} \tag{2.65}$$

$$+ \underbrace{\rho w_l^a S_l \phi v_i + \rho w_l^a \phi S_l(v_{l_i}^a - v_i^w)}_{j_l^a}$$

or in terms of ϑ fractions:

$$j^a = \underbrace{\rho\vartheta_g^a v_i + \underbrace{\rho\vartheta_g^a(v_i^a - v_i)}_{q'_{g_i}}}_{j_g^a} + \underbrace{\rho\vartheta_l^a v_i + \underbrace{\rho\vartheta_l^a(v_{l_i}^a - v_i^w)}_{i_{l_i}^{a'}}}_{j_l^a}$$

by using the divergence theorem and the fact that dΩ is arbitrary Eq. 2.64 can be rewritten in local form:

$$\frac{\partial}{\partial t}\left(\rho w_g^a(1 - S_l)\phi + \rho w_l^a \phi S_l\right) + \left(j_g^a + j_l^a\right)_{,i} + f^a = 0 \tag{2.66}$$

or in terms of ϑ fractions:

$$\frac{\partial}{\partial t}\left(\rho\vartheta_g^a + \rho\vartheta_l^a\right) + \left(j_g^a + j_l^a\right)_{,i} + f^a = 0$$

the development of each term of Eq. 2.66b leads to the conservation law:

$$\frac{\partial\rho}{\partial t}\vartheta_g^a + \rho\frac{\partial\vartheta_g^a}{\partial t} + \frac{\partial\rho}{\partial t}\vartheta_l^a + \rho\frac{\partial\vartheta_l^a}{\partial t} + \rho_{,i}\left(\vartheta_g^a + \vartheta_l^a\right)v_i + \rho\left(\vartheta_{g,i}^a + \vartheta_{l,i}^a\right)v_i \tag{2.67}$$

$$+ \rho\left(\vartheta_g^a + \vartheta_l^a\right)v_{i,i} + q'_{g_{i,i}} + i_{l_{i,i}}^{a'} = 0$$

or similarly,

$$\frac{d\rho}{dt}\left(\vartheta_g^a + \vartheta_l^a\right) + \rho\left(\frac{d\vartheta_g^a}{dt} + \frac{d\vartheta_l^a}{dt}\right) + \rho\vartheta_g^a v_{i,i} + \rho\vartheta_l^a v_{i,i} + q'_{g_{i,i}} + i_{l_{i,i}}^{a'} = 0$$

which on account of the skeleton mass conservation leads to the relations for air specie at each phase $(\blacksquare)_g^a$ and $(\blacksquare)_l^a$:

$$\rho\frac{d\vartheta_g^a}{dt} + q'_{g_{i,i}} = 0 \quad ; \quad \rho\frac{d\vartheta_l^a}{dt} + i_{l_{i,i}}^{a'} = 0 \tag{2.68}$$

Gas mass continuity Eq. 2.67 can be rewritten in terms of fluid densities $\{\rho_k^a : k = l, g\}$ and partial porosities $\{\phi_k : k = l, g\}$, leading to:

$$\frac{d\rho_g^a}{dt}\phi_g + \rho_g^a\frac{d\phi_g}{dt} + \frac{d\rho_l^a}{dt}\phi_l + \rho_l^a\frac{d\phi_l}{dt} + \rho_g^a\phi_g v_{i,i} + \rho_l^a\phi_l v_{i,i} + \left(\rho_g^a q_{g_i}\right)_{,i} + \left(\rho_l^a i_{l_i}^a\right)_{,i} \tag{2.69}$$

$$= 0$$

Eq. 2.69 should be fulfilled for each species (air in gas) and (air in liquid), then:

$$\frac{d\rho_g^a}{dt}\frac{\phi_g}{\rho_g^a} + \frac{d\phi_g}{dt} + \phi_g v_{i,i} + \frac{\rho_{g,i}^a}{\rho_g^a}q_{g_i} + q_{g_{i,i}} \quad = \quad 0 \tag{2.70}$$

$$\frac{d\rho_l^a}{dt}\frac{\phi_l}{\rho_l^a} + \frac{d\phi_l}{dt} + \phi_l v_{i,i} + \frac{\rho_{l,i}^a}{\rho_l^a}i_{l_i}^a + i_{l_{i,i}}^a \quad = \quad 0$$

where each equation is identically zero. They can also be expressed in terms of unit volumes $v_g^a = 1/\rho_g^a$, $v_l^a = 1/\rho_l^a$:

$$q_{g_{i,i}} \quad = \quad \frac{dv_g^a}{dt}\rho_g^a\phi_g - \frac{d\phi_g}{dt} - \phi_g v_{i,i} + q_{g_i}' v_{g,i}^a \tag{2.71}$$

$$i_{l_{i,i}}^a \quad = \quad \frac{dv_l^a}{dt}\rho_l^a\phi_l + \frac{d\phi_l}{dt} + \phi_l v_{i,i} + i_{l_i}^{a\prime} v_{l,i}^a$$

The combined continuity equation for the solid skeleton and the pore fluids can be obtained by adding equations 2.53, 2.62 and 2.70, leading to:

$$v_{i,i} + q_{l_{i,i}} + i_{g_{i,i}}^w + q_{g_{i,i}} + i_{l_{i,i}}^a + \frac{\rho_{l,i}^w}{\rho_l^w}q_{l_i} + \frac{\rho_{g,i}^w}{\rho_g^w}i_{g_i}^w + \frac{\rho_{g,i}^a}{\rho_g^a}q_{g_i} + \frac{\rho_{l,i}^a}{\rho_l^a}i_{l_i}^a \tag{2.72}$$

$$+ \left(\frac{d\rho_l^w}{dt}\frac{1}{\rho_l^w} + \frac{d\rho_l^a}{dt}\frac{1}{\rho_l^a}\right)\phi S_l + \left(\frac{d\rho_g^w}{dt}\frac{1}{\rho_g^w} + \frac{d\rho_g^a}{dt}\frac{1}{\rho_g^a}\right)\phi(1 - S_l)$$

$$+ \frac{(1 - \phi)}{\rho_s}\frac{d\rho_s}{dt} = 0$$

where results from skeleton mass conservation has been used to drop off material derivative of ϕ.

If pore water compressibility is considered much more higher than gas compressibility and solid grains, the combined continuity equation Eq. 2.72 is reduced to:

$$v_{i,i} + q_{l_{i,i}} + i_{g_{i,i}}^w + q_{g_{i,i}} + i_{l_{i,i}}^a + \frac{\rho_{g,i}^a}{\rho_g^a}q_{g_i} + \frac{\rho_{l,i}^a}{\rho_l^a}i_{l_i}^a + \frac{d\rho_l^a}{dt}\frac{1}{\rho_l^a}\phi S_l + \frac{d\rho_g^a}{dt}\frac{1}{\rho_g^a}\phi(1 - S_l) \tag{2.73}$$

$$+ \frac{(1 - \phi)}{\rho_s}\frac{d\rho_s}{dt} = 0$$

If pore fluids and solid grains are assumed to be incompressible Eq. 2.72 is reduced to:

$$v_{i,i} + q_{l_{i,i}} + i_{g_{i,i}}^w + q_{g_{i,i}} + i_{l_{i,i}}^a = 0 \tag{2.74}$$

First law of thermodynamics states that the rate of increase of internal energy in the porous volume Ω is equal to the power input to the volume given by: (a) energy input at the boundaries and (b) the rate of work of body forces.

Assuming thermal equilibrium between the phases (equal temperature in all the phases) and ascribing $\widetilde{E}_s$, E_l and E_g as the specific energy of the skeleton, the specific energy of the liquid phase and the specific energy of the gas phase, respectively, $\mathcal{L}$ as the power input to the porous volume and i_c as the heat flux, the first law of thermodynamics is stated as:

$$\int_\Omega \frac{\partial}{\partial t}\left(\widetilde{E}_s\rho + E_l\rho w^w S_l\phi + E_g\rho w^a(1-S_l)\phi\right)d\Omega + \int_\Gamma \left(j_{\widetilde{E}_s} + j_{E_l} + j_{E_g}\right)n_i d\Gamma \qquad (2.75)$$

$$+ \int_\Omega f^Q\, d\Omega = \int_\Omega L d\Omega - \int_\Gamma i_{c_i}\, n_i d\Gamma$$

The specific internal energy of the porous skeleton accounts for the energy of the solid skeleton in addition to the energy of the air-liquid interface (due to the partial saturation condition):

$$\begin{aligned}
E &= \left(E_s + \phi\sum_{kl} E_i^{kl}\right) + \rho_l\frac{E_l}{\rho} + \rho_g\frac{E_g}{\rho} \qquad (2.76)\\
&= \widetilde{E}_s + w^w E_l + w^a E_g
\end{aligned}$$

where $\rho = \rho_s \cdot (1-\phi)$ is the dry density of the medium, w^w and w^a are the mass fractions of water and air per unit volume of skeleton respectively and $\widetilde{E}_s$ is the specific energy of the solid matrix and the interfaces exerted by the interactions between solid, air and liquid E_i^{kl}.

The energy flux of porous skeleton due to the porous skeleton motion is given by the expression:

$$\begin{aligned}
j_{\widetilde{E}_s} &= \left[\left(E_s + \phi\sum_{kl} E_i^{kl}\right)v_i + \phi\sum_{kl} E_i^{kl}(v_i^c - v_i)\right]\rho_s(1-\phi) \qquad (2.77)\\
&= \left(E_s + \phi\sum_{kl} E_i^{kl}\right)\rho v_i + \underbrace{\phi\sum_{kl} E_i^{kl}\rho(v_i^c - v_i)}_{j_{E_i}'}
\end{aligned}$$

where v_i^c is the absolute velocity of the air-liquid interface.

According to mixture theory, the specific internal energy of the liquid phase is:

$$E_l\rho_l = (E_l^w w_l^w + E_l^a w_l^a) \cdot \rho \qquad (2.78)$$

where E_l^w and E_l^a are the specific internal energies of air and water in the liquid phase and w_l^a and w_l^w are the unit mass fractions of dissolved air and water in liquid phase per unit mass of skeleton, respectively.

Furthermore, the energy flux of pore liquid due to water motion is given by the expression:

$$j_{E_l} = (i_l^w + \theta_l^w q_l)E_l^w + (i_l^a + \theta_l^a q_l)E_l^a + E_l \rho_l S_l \phi v_i \qquad (2.79)$$

$$= E_l \rho w_l S_l \phi v_i + \underbrace{E_l \rho w_l \phi S_l (v_{l_i} - v_i) + i_l^w E_l^w + i_l^a E_l^a}_{j'_{E_l}}$$

$$= E_l \rho w_l \phi S_l v_{l_i} + i_l^w E_l^w + E_l^a \rho w_l^a \phi S_l (v_{l_i}^a - v_{l_i})$$

or in term of ϑ fractions:

$$j_{E_l} = E_l \rho \vartheta_l^w v_{l_i} + i_l^w E_l^w + E_l^a \rho \vartheta_l^a (v_{l_i}^a - v_{l_i})$$

where θ_l^w and θ_l^a are the apparent mass densities of liquid water and dissolved air as used in Code_Bright notation, J'_{E_i} is the energy flux with respect to the solid phase, i_l^w and i_l^a are the diffusive fluxes of water and air in liquid phase and q_l is the Darcy flux of liquid.

In the same way, the specific internal energy of the gas phase is:

$$E_g \rho_g = (E_g^w w_g^w + E_g^a w_g^a) \cdot \rho \qquad (2.80)$$

where E_g^w and E_g^a are the specific internal energies of water and air in the gas phase and w_g^w and w_g^a are the unit mass fractions of water vapor and air in gas phase per unit mass of skeleton, respectively.

Then the energy flux of pore gas due to air motion is given by the expression:

$$j_{E_g} = (i_g^w + \theta_g^w q_g)E_g^w + (i_g^a + \theta_g^a q_g)E_g^a + E_g \rho_g S_g \phi v_i \qquad (2.81)$$

$$= E_g \rho w_g (1 - S_l) \phi v_i + \underbrace{E_g \rho w_g \phi (1 - S_l)(v_{g_i} - v_i) + i_g^w E_g^w + i_g^a E_g^a}_{j'_{E_g}}$$

$$= E_g \rho w_g \phi (1 - S_l) v_{g_i} + E_g^w \rho w_g^w \phi (1 - S_l)(v_{g_i}^w - v_{g_i}) + i_g^a E_g^a$$

or in term of ϑ fractions:

$$j_{E_g} = E_g \rho \vartheta_g^a v_{g_i} + E_g^w \rho \vartheta_g^w (v_{g_i}^w - v_{g_i}) + i_g^a E_g^a$$

where θ_g^w and θ_g^a are the apparent mass densities of water vapor and gas air as used in Code_Bright notation, $J'_{E_{gi}}$ is the energy fluxes with respect to the solid phase, i_g^w and i_g^a are the diffusive fluxes of water and air in gas phase and q_g is the Darcy flux of gas.

_____

Both the energy flux of liquid and the energy flux of gas can be rewritten with respect to the motion of the solid phase instead of absolute motion, leading to:

$$j'_{E_l} = \underbrace{E_l \rho w_l \phi S_l (v_{l_i} - v_i)}_{j'_{E1_l}} + \underbrace{i_l^w E_l^w + E_l^a \rho w_l^a \phi S_l (v_{l_i}^a - v_{l_i})}_{j'_{E2_l}} \tag{2.82}$$

$$j'_{E_g} = \underbrace{E_g \rho w_g \phi (1 - S_l)(v_{g_i} - v_i)}_{j'_{E1_g}} + \underbrace{E_g^w \rho w_g^w \phi (1 - S_l)(v_{g_i}^w - v_{g_i}) + i_g^a E_g^a}_{j'_{E2_g}}$$

or in terms of ϑ fractions:

$$j'_{E_l} = \underbrace{E_l \rho \vartheta_l^w (v_{l_i} - v_i)}_{j'_{E1_l}} + \underbrace{i_l^w E_l^w + E_l^a \rho \vartheta_l^a (v_{l_i}^a - v_{l_i})}_{j'_{E2_l}} \tag{2.83}$$

$$j'_{E_g} = \underbrace{E_g \rho \vartheta_g^a (v_{g_i} - v_i)}_{j'_{E1_g}} + \underbrace{E_g^w \rho \vartheta_g^w (v_{g_i}^w - v_{g_i}) + i_g^a E_g^a}_{j'_{E2_g}}$$

where the diffusive fluxes are: (a) water vapor $i_g^w = \vartheta_g^w (v_{g_i}^w - v_{g_i})$ and (b) dissolved air $i_l^a = \vartheta_l^a (v_{l_i}^a - v_{l_i})$, respectively.

Then the first law of thermodynamics Eq. 2.75 can be rewritten as:

$$\int_\Omega \frac{\partial}{\partial t} \left(\left(E_s \rho + \phi \rho \sum_{kl} E_i^{kl} \right) + E_l \rho w_l S_l \phi + E_g \rho w_g (1 - S_l) \phi \right) d\Omega \tag{2.84}$$

$$+ \int_\Gamma \left[\left(\left(E_s \rho + \phi \rho \sum_{kl} E_i^{kl} \right) + E_l \rho w^w S_l \phi + E_g \rho w^a (1 - S_l) \phi \right) v_i \right.$$

$$\left. + \left(j'_{E_i} + j'_{E_l} + j'_{E_g} \right) \right] n_i d\Gamma + \int_\Omega f^Q \, d\Omega = \int_\Omega L d\Omega - \int_\Gamma i_{c_i} n_i d\Gamma$$

The rate of work input $\mathcal{L}$ to a three phase porous material is defined by: (a) the tractions t_i (forces per unit area) acting on the boundary of the solid skeleton $\Gamma(1 - \phi)$, (b) the pore pressures p_l and p_g of the fluids in the soil pores acting on the complementary fraction of the boundary $\Gamma\phi$, (c) the forces in the contractile skin T_i generated by the summed effect of surface tensions due to different pore air and water pressures (d) the body forces per unit volume of solid skeleton ρg_i and (e) the body forces per unit volume of pore fluids $\rho \phi S_l w_l$ and $\rho \phi (1 - S_l) w_g$.

81

Then, the work done per unit area by the tractions on $\Gamma(1 - \phi)$ is $(1 - \phi)t_i v_i$, the work done by the pore pressures on $\Gamma\phi$ is expressed as $-n_i\phi\left(S_l p_l v_i^w + (1 - S_l)p_g v_i^a\right)$, the work done by the tractions in the contractile skin is $T_i v_i^c$ and the work done per unit volume by the body forces of the skeleton and of the pore fluids are $\rho g_i v_i$ and $\rho\phi\left(S_l w_l v_i^w + (1 - S_l)w_g v_i^a\right)$, respectively, Fig. 2.12.
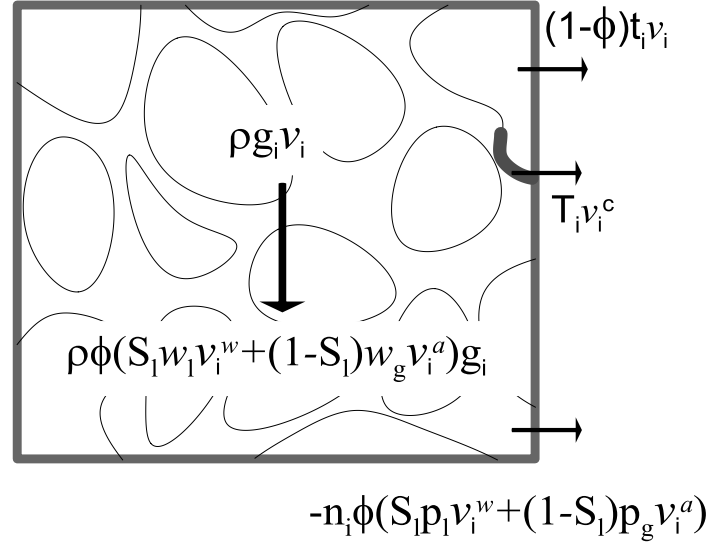
Figure 2.12: Boundary and body forces on a representative elementary volume (REV) of porous medium.

where v_i^c is the velocity of the contractile skin defined by the air-water interface.

The work done by the pore pressures can be developed in order to highlight the partial pressures in each specie p_l^w, p_l^a, p_g^w and p_g^a linked by the Dalton's partial pressures law leading to $-n_i\phi\left(S_l\left(p_l^w v_{l_i}^w + p_l^a v_{l_i}^a\right) + (1 - S_l)\left(p_g^w v_{g_i}^w + p_g^a v_{g_i}^a\right)\right)$.

Then, the power input to the porous volume Ω is implicitly given by:

$$\int_\Omega L d\Omega = \int_\Gamma \left[(1 - \phi)t_i v_i - \phi\left(S_l\left(p_l^w v_{l_i}^w + p_l^a v_{l_i}^a\right) + (1 - S_l)\left(p_g^w v_{g_i}^w + p_g^a v_{g_i}^a\right)\right)n_i \right. \tag{2.85}$$
$$\left. + T_i v_i^c\right]d\Gamma + \int_\Omega \left[\rho v_i + \rho\phi\left(S_l w_l v_i^w + (1 - S_l)w_g v_i^a\right)\right]g_i d\Omega$$

_____

the forces per unit area t_i, pore pressures p_l and p_g and the forces per unit of porous volume in the contractile skin summed to T_i are related to the total stress σ_{ij} by:

$$(1 - \phi)t_i v_i = \sigma_{ij}n_i v_i + n_i\phi S_l p_l v_i^w + n_i\phi(1 - S_l)p_g v_i^a - n_i p_l q_{l_i} - n_i p_g q_{g_i} - T_i v_i \qquad (2.86)$$

where n_i is the outward unit vector to the surface Γ of the representative element volume Ω and T_i is the traction vector due to the air-water interface.

Replacing Eq. 2.86 in Eq. 2.85 leads to the expression of the power input to the porous volume Ω in terms of the stress tensor and the artificial seepage velocities:

$$\int_\Omega L d\Omega = \int_\Gamma \left[\sigma_{ij}v_i - p_l^w q_{l_i} - p_g^a q_{g_i} - p_l^a i_{l_i}^a - p_g^w i_{g_i}^w + T_{ij}(v_i^c - v_i) \right] n_i \, d\Gamma \qquad (2.87)$$

$$+ \int_\Omega \left[\rho v_i + \rho\phi\left(S_l w_l v_i^w + (1 - S_l)w_g v_i^a\right) \right]g_i d\Omega$$

Then the energy balance of the three phase porous medium Eq. 2.84 becomes:

$$\int_\Omega \frac{\partial}{\partial t}\left(\left(E_s\rho + \phi\rho\sum_{kl} E_i^{kl} \right) + E_l\rho w_l S_l\phi + E_g\rho w_g(1 - S_l)\phi \right) d\Omega \qquad (2.88)$$

$$+ \int_\Gamma \left[\left(\left(E_s\rho + \phi\rho\sum_{kl} E_i^{kl} \right) + E_l\rho w_l S_l\phi + E_g\rho w_g(1 - S_l)\phi \right) v_i \right.$$

$$\left. + \left(j_{E_i}' + j_{E_l}' + j_{E_g}' \right) \right] n_i d\Gamma + \int_\Omega f^Q \, d\Omega$$

$$= \int_\Gamma \left[\sigma_{ij}v_i - p_l^w q_{l_i} - p_g^a q_{g_i} - p_l^a i_{l_i}^a - p_g^w i_{g_i}^w + T_{ij}(v_i^c - v_i) \right] n_i \, d\Gamma$$

$$+ \int_\Omega \left[\rho v_i + \rho\phi\left(S_l w_l v_i^w + (1 - S_l)w_g v_i^a\right) \right]g_i d\Omega + \int_\Gamma i_{c_i} n_i d\Gamma$$

applying the divergence theorem of Gauss to Eq. 2.88 and the fact that Ω is arbitrary, the local form of the energy balance (Gens A. , 2010) in terms of ϑ fractions is:

$$\frac{\partial}{\partial t}\left(\left(E_s\rho + \phi\rho\sum_{kl} E_i^{kl}\right) + E_l\rho\vartheta_l + E_g\rho\vartheta_g\right)$$

(2.89)

$$+ \left[\left(\left(E_s\rho + \phi\rho\sum_{kl} E_i^{kl}\right) + E_l\rho\vartheta_l + E_g\rho\vartheta_g\right)v_i\right]_{,j}$$

$$+ \left(j'_{E_i} + j'_{E_l} + j'_{E_g}\right)_{,i} + f^Q$$

$$= \left[\sigma_{ij}v_i - p_l^w q_{l_i} - p_g^a q_{g_i} - p_l^a i_{l_i}^a - p_g^w i_{g_i}^w + T_{ij}(v_i^c - v_i) - i_{c_i}\right]_{,i}$$

$$+ \left[\rho v_i + \rho\phi\left(S_l w_l v_i^w + (1 - S_l)w_g v_i^a\right)\right]g_i$$

By expanding the derivatives in the left hand side of Eq. 2.89 and using the results obtained in Eq. 2.51b, Eq. 2.60 and Eq. 2.68 one arrives to:

$$\frac{d}{dt}\left(\left(\underbrace{E_s\rho + \phi\rho\sum_{kl} E_i^{kl}}_{\widetilde{E}_s\rho} + E_l\rho\vartheta_l + E_g\rho\vartheta_g\right)\right)$$

(2.90)

$$+ \left[\left(E_s + \phi\sum_{kl} E_i^{kl}\right)\rho v_{i,i} + E_l\rho\vartheta_l v_{i,i} + E_g\rho\vartheta_g v_{i,i}\right]$$

$$+ \left(j'_{E_i} + j'_{E_l} + j'_{E_g}\right)_{,i} + f^Q$$

$$= \rho\frac{dE_s}{dt} + \rho\phi\frac{dE_i}{dt} + \rho\vartheta_l\frac{dE_l}{dt} + \rho\vartheta_g\frac{dE_g}{dt} + E_{i,i}\phi\rho(v_i^c - v_i) + E_{l,i}^w q'_{l_i}$$

$$+ E_{l,i}^a i_{l_i}^{a'} + E_{g,i}^a q'_{g_i} + E_{g,i}^w i_{g_i}^{w'}$$

the right hand side of Eq. 2.89 may be rearranged as follows:

$$\left[\sigma_{ij}v_i - p_l^w q_{l_i} - p_g^a q_{g_i} - p_l^a i_{l_i}^a - p_g^w i_{gi}^w + T_{ij}(v_i^c - v_i) - i_{c_i}\right]_{,i} + [\rho v_i \tag{2.91}$$

$$+\rho\phi(S_l w_l v_i^w + (1 - S_l)w_g v_i^a)]g_i$$

$$= \left(\sigma_{ij,i} + \rho\left(1 + \phi(S_l w_l + (1 - S_l)w_g)g_i\right)\right)v_i + \sigma_{ij}v_{i,i} - p_{l,i}^w q_{l_i} - p_l^w q_{l_{i,i}}$$

$$-p_{g,i}^a q_{g_i} - p_g^a q_{g_{i,i}} - p_{l,i}^a i_{l_i}^a - p_l^a i_{l_{i,i}}^a - p_{g,i}^w i_{gi}^w - p_g^w i_{gi,i}^w$$

$$+T_{ij,i}(v_i^c - v_i) + T_{ij}(v_i^c - v_i)_{,i} + \rho w_l q_{l_i} g_i + \rho w_g q_{g_i} g_i - i_{c_{i,i}}$$

$$= \left(\sigma_{ij,i} + \rho\left(1 + \phi(S_l w_l + (1 - S_l)w_g)g_i\right)\right)v_i + T_{ij,i}(v_i^c - v_i) + \sigma_{ij}v_{i,i}$$

$$+ \left(\rho w_l g_i - p_{l,i}\right)q_{l_i} + \left(\rho w_g g_i - p_{g,i}\right)q_{g_i} - p_{l,i}^a i_{l_i}^a - p_{g,i}^w i_{gi}^w$$

$$-p_l^w q_{l_{i,i}} - p_g^a q_{g_{i,i}} - p_l^a i_{l_{i,i}}^a - p_g^w i_{gi,i}^w + T_{ij}(v_i^c - v_i)_{,i} - i_{c_{i,i}}$$

The solid skeleton velocity $v_{i,i}$ can be splitted in its symmetrical and non-symmetrical parts giving rise to the strain rate tensor and the rotational tensor:

$$d_{ij} = \frac{1}{2}\left(v_{i,j} + v_{j,i}\right) \tag{2.92}$$

$$\omega_{ij} = \frac{1}{2}\left(v_{i,j} - v_{j,i}\right)$$

using Eq. 2.92 and replacing Eq. 2.90-Eq. 2.91 in Eq. 2.89 leads to:

$$\rho\frac{dE_s}{dt} + \rho\phi\frac{dE_i}{dt} + \rho\vartheta_l\frac{dE_l}{dt} + \rho\vartheta_g\frac{dE_g}{dt} + E_{i,i}\phi\rho(v_i^c - v_i) + E_{l,i}^w q_{l_i}' + E_{l,i}^a i_{l_i}^{a\prime} + E_{g,i}^a q_{gi}' \tag{2.93}$$

$$+ E_{g,i}^w i_{gi}^{w\prime}$$

$$= \left(\sigma_{ij,i} + \rho\left(1 + \phi(S_l w_l + (1 - S_l)w_g)g_i\right)\right)v_i + T_{ij,i}(v_i^c - v_i)$$

$$+ \sigma_{ij}\omega_{ij} + \sigma_{ij}d_{ij} + \left(\rho w_l g_i - p_{l,i}\right)q_{l_i} + \left(\rho w_g g_i - p_{g,i}\right)q_{g_i} - p_{l,i}^a i_{l_i}^a$$

$$- p_{g,i}^w i_{gi}^w - p_l^w q_{l_{i,i}} - p_g^a q_{g_{i,i}} - p_l^a i_{l_{i,i}}^a - p_g^w i_{gi,i}^w + T_{ij}(v_i^c - v_i)_{,i} - i_{c_{i,i}}$$

because rigid movements do not produce any change in the internal energy, then:

$$\left(\sigma_{ij,i} + \rho\left(1 + \phi(S_l w_l + (1 - S_l)w_g)g_i\right)\right)v_i = 0 \tag{2.94}$$

$$\sigma_{ij}\omega_{ij} = 0$$

$$T_{ij,i}(v_i^c - v_i) = 0$$

for any value of v_i, ω_{ij} and $(v_i^c - v_i)$.

From Eq. 2.94b it is concluded that the antisymmetric part of σ_{ij} is zero. As consequence the stress tensor is symmetric. From Eq. 2.94a the balance of momentum for the three-phase porous medium is obtained:

_____

$$\sigma_{ij,i} + \rho\big(1 + \phi(S_l w_l + (1 - S_l)w_g)g_i\big) = 0 \qquad (2.95)$$

Eq. 2.94c states the momentum balance for the air-liquid interface as $T_{ij,i} = 0$. This result is physically accepted due to the thinness of the interface skin. Then Eq. 2.93 is reduced to:

$$\begin{aligned}
\rho\frac{dE_s}{dt} + \rho\phi\frac{dE_i}{dt} &+ \rho\vartheta_l\frac{dE_l}{dt} + \rho\vartheta_g\frac{dE_g}{dt} + E_{i,i}\phi\rho(v_i^c - v_i) + E_{l,i}^w q_{l_i}' + E_{l,i}^a i_{l_i}^{a'} + E_{g,i}^a q_{g_i}' \qquad (2.96)\\
&+ E_{g,i}^w i_{g_i}^{w'}\\
&= \sigma_{ij}d_{ij} + \big(\rho w_l g_i - p_{l,i}\big)q_{l_i} + \big(\rho w_g g_i - p_{g,i}\big)q_{g_i} - p_{l,i}^a i_{l_i}^a - p_{g,i}^w i_{g_i}^w\\
&\quad - p_l^w q_{l_{i,i}} - p_g^a q_{g_{i,i}} - p_l^a i_{l_{i,i}}^a - p_g^w i_{g_{i,i}}^w + T_{ij}(v_i^c - v_i)_{,i} - i_{c_{i,i}}
\end{aligned}$$

Restrictions to the intensive variables defining the energy balance of Eq. 2.96 are introduced invoking the positive character of dissipation energy of the porous medium (second law of thermodynamics).

The existence of a state function, the specific entropy $\mathfrak{H}$, is assumed such that the rate of entropy production is non-negative (Houlsby & Puzrin, 2005). Ascribing $\widetilde{\mathfrak{H}}_s$, $\mathfrak{H}_l$ and $\mathfrak{H}_g$ as the specific entropy of the skeleton, the specific entropy of pore liquid phase and the specific entropy of pore gas phase, the specific entropy of the porous medium is $\mathfrak{H} = \widetilde{\mathfrak{H}}_s + w_l\mathfrak{H}_l + w_g\mathfrak{H}_g$ where $\widetilde{\mathfrak{H}}$ not only accounts for the entropy of the solid matrix but also for the air-liquid interface entropy given by the interactions between solid, gas and liquid phases.

The storage entropy in a porous skeleton is composed of: (a) the entropy in the mineral $\mathfrak{H}_s\rho_s(1 - \phi)$, (b) the entropy in the air-liquid interface $\phi\sum\mathfrak{H}_i^{kl}$, (c) the entropy in the pore liquid $\mathfrak{H}_l\rho w_l S_l\phi$ and (d) the entropy in the pore gas $\mathfrak{H}_g\rho w_g(1 - S_l)\phi$.

Net flows of entropy are defined by: (a) the net flow of entropy in the mineral and in the air-liquid interface $j_{\widetilde{\mathfrak{H}}_s}$, (b) the net flow of entropy in the liquid $j_{\mathfrak{H}_l}$, (c) the net flow of entropy in the gas $j_{\mathfrak{H}_g}$ and the net flow of entropy by conduction $\big(^{i_c}\!/_T\big)$, see Fig. 2.13.
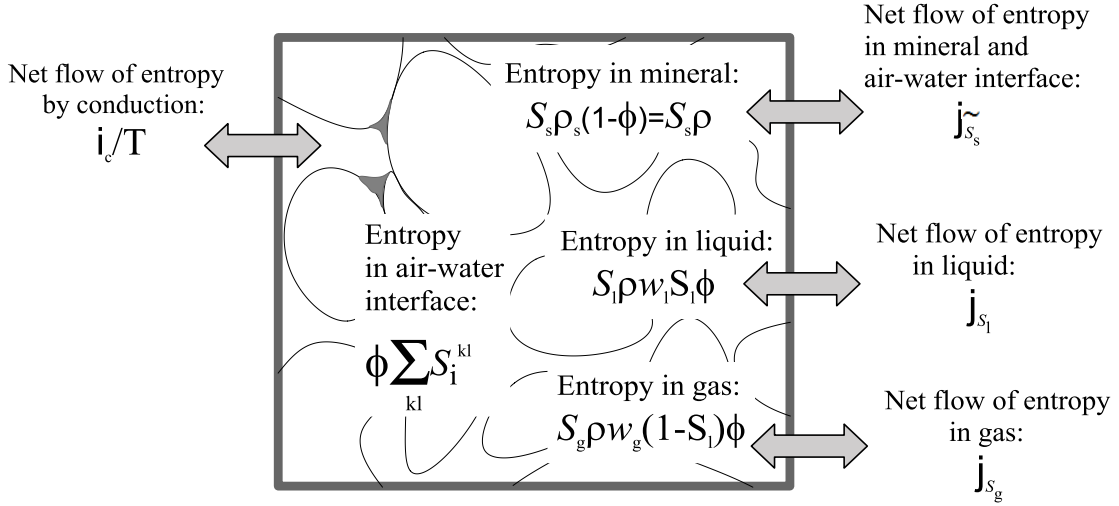
Figure 2.13: Storage and fluxes of entropy in a three-phase porous medium.

Fundamental inequality for the entropy states that the rate of increase of entropy of the porous medium plus the entropy fluxes at each phase across the boundary is greater than or equal to the entropy flux into Ω, thus:

$$\int_\Omega \frac{\partial}{\partial t}\left(\widetilde{\mathfrak{H}}_s\rho + \mathfrak{H}_l\rho w_l S_l \phi + \mathfrak{H}_g\rho w_g(1-S_l)\phi\right)d\Omega + \int_\Gamma \left(j_{\widetilde{\mathfrak{H}}_s} + j_{\mathfrak{H}_l} + j_{\mathfrak{H}_g}\right)n_i d\Gamma \qquad (2.97)$$

$$\geq \int_\Omega \frac{\partial}{\partial t}\left(\widetilde{\mathfrak{H}}_{s_r}\rho + \mathfrak{H}_{l_r}\rho w_l S_l \phi + \mathfrak{H}_{g_r}\rho w_g(1-S_l)\phi\right)d\Omega$$

$$+ \int_\Gamma \left(j_{\widetilde{\mathfrak{H}}_{s_r}} + j_{\mathfrak{H}_{l_r}} + j_{\mathfrak{H}_{g_r}}\right)n_i d\Gamma \equiv \int_\Gamma -\frac{i_{c_i}}{T}n_i d\Gamma$$

where the subscript $\blacksquare_r$ makes reference to the reversible part of entropy given by the rate of entropy supplied to the porous material element from its surroundings.

The rate of entropy production within the porous element corresponds to the irreversible part of the entropy which satisfies the positivity condition d $\geq$ 0.

The specific entropy of the porous skeleton accounts not only for the specific entropy of the solid but also for the specific entropy of the air-liquid interface, thus:

$$\begin{aligned}\mathfrak{H} &= \left(\mathfrak{H}_s + \phi\sum_{kl}\mathfrak{H}_i^{kl}\right) + \rho_l\frac{\mathfrak{H}_l}{\rho} + \rho_g\frac{\mathfrak{H}_g}{\rho} \qquad (2.98)\\ &= \widetilde{\mathfrak{H}}_s + w_l\mathfrak{H}_l + w_g\mathfrak{H}_g\end{aligned}$$

The entropy flux of porous skeleton due to its motion is defined by:

_____

$$
\begin{aligned}
j_{\tilde{\mathfrak{H}}_s} &= \left[\left(\mathfrak{H}_s + \phi \sum_{kl} \mathfrak{H}_i^{kl}\right) v_i + \phi \sum_{kl} \mathfrak{H}_i^{kl}(v_i^c - v_i)\right]\rho_s(1-\phi) \\
&= \left(\mathfrak{H}_s + \phi \sum_{kl} \mathfrak{H}_i^{kl}\right)\rho v_i + \underbrace{\phi \sum_{kl} \mathfrak{H}_i^{kl}\rho(v_i^c - v_i)}_{j'_{\mathfrak{H}_i}}
\end{aligned}
\tag{2.99}
$$

In addition, the entropy fluxes of liquid and gas phases due to their motions are given by:

$$
j_{\mathfrak{H}_l} = \mathfrak{H}_l \rho \vartheta_l^w v_i + \underbrace{\mathfrak{H}_l \rho \vartheta_l^w(v_{l_i} - v_i) + i_l^w \mathfrak{H}_l^w + \mathfrak{H}_l^a \rho \vartheta_l^a(v_{l_i}^a - v_{l_i})}_{j'_{\mathfrak{H}_l}}
\tag{2.100}
$$

$$
j_{\mathfrak{H}_g} = \mathfrak{H}_g \rho \vartheta_g^a v_i + \underbrace{\mathfrak{H}_g \rho \vartheta_g^a(v_{g_i} - v_i) + \mathfrak{H}_g^w \rho \vartheta_g^w(v_{g_i}^w - v_{g_i}) + i_g^a E_g^a}_{j'_{\mathfrak{H}_g}}
$$

where $j'_{\mathfrak{H}_l}$ and $j'_{\mathfrak{H}_g}$ are the entropy fluxes of liquid and gas with respect to the motion of the solid phase.

Applying the divergence theorem to Eq. 2.97 and due to the arbitrariness of Ω the local form of the fundamental inequality of entropy is:

$$
\begin{aligned}
&\frac{\partial}{\partial t}\left(\left(\mathfrak{H}_s \rho + \phi \rho \sum_{kl} \mathfrak{H}_i^{kl}\right) + \mathfrak{H}_l \rho \vartheta_l + \mathfrak{H}_g \rho \vartheta_g\right) \\
&\qquad + \left[\left(\left(\mathfrak{H}_s \rho + \phi \rho \sum_{kl} \mathfrak{H}_i^{kl}\right) + \mathfrak{H}_l \rho \vartheta_l + \mathfrak{H}_g \rho \vartheta_g\right) v_i\right]_{,i} \\
&\qquad + \left(j'_{\mathfrak{H}_i} + j'_{\mathfrak{H}_l} + j'_{\mathfrak{H}_g} + \frac{i_{c_i}}{T}\right)_{,i} \geq 0
\end{aligned}
\tag{2.101}
$$

expanding the derivatives at Eq. 201 it can be re-written as:

$$\frac{d}{dt}\left(\left(\underbrace{\mathfrak{H}_s\rho + \phi\rho\sum_{kl}\mathfrak{H}_i^{kl}}_{\widetilde{\mathfrak{H}}_s\rho}\right) + \mathfrak{H}_l\rho\vartheta_l + \mathfrak{H}_g\rho\vartheta_g\right) \tag{2.102}$$

$$+\left[\left(\mathfrak{H}_s\rho + \phi\rho\sum_{kl}\mathfrak{H}_i^{kl}\right)\rho v_{i,i} + \mathfrak{H}_l\rho\vartheta_l v_{i,i} + \mathfrak{H}_g\rho\vartheta_g v_{i,i}\right]$$

$$+\left(j'_{\mathfrak{H}_i} + j'_{\mathfrak{H}_l} + j'_{\mathfrak{H}_g} + \frac{i_{c_i}}{T}\right)_{,i}$$

$$= \rho\frac{d\mathfrak{H}_s}{dt} + \rho\phi\frac{d\mathfrak{H}_i}{dt} + \rho\vartheta_l\frac{d\mathfrak{H}_l}{dt} + \rho\vartheta_g\frac{d\mathfrak{H}_g}{dt} + \mathfrak{H}_{i,i}\phi\rho(v_i^c - v_i)$$

$$+ \mathfrak{H}_{l,i}^w q'_{l_i} + \mathfrak{H}_{l,i}^a i_{l_i}^{a'} + \mathfrak{H}_{g,i}^a q'_{g_i} + \mathfrak{H}_{g,i}^w i_{g_i}^{w'} + \frac{i_{c_{i,i}}}{T} - \frac{i_{c_i}T_{,i}}{T^2} = \frac{\rho d}{T} \geq 0$$

where the total dissipation d considers: (a) the dissipations at the fluid phases, (b) the mechanical dissipation d_s and (c) the thermal dissipation $\left(-\frac{i_{c_k}T_{,k}}{T}\right)$. Combination of Eq. 2.96 and Eq. 2.102 leads to:

$$\rho\frac{dE_s}{dt} + \rho\phi\frac{dE_i}{dt} + \rho\vartheta_l\frac{dE_l}{dt} + \rho\vartheta_g\frac{dE_g}{dt} + \rho d \tag{2.103}$$

$$= \sigma_{ij}d_{ij} - p_l^w q_{l_{i,i}} - p_g^a q_{g_{i,i}} - p_l^a i_{l_{i,i}}^a - p_g^w i_{g_{i,i}}^w + T_{ij}(v_i^c - v_i)_{,i}$$

$$+ \rho T\frac{d\mathfrak{H}_s}{dt} + \rho\phi T\frac{d\mathfrak{H}_i}{dt} + \rho\vartheta_l T\frac{d\mathfrak{H}_l}{dt} + \rho\vartheta_g T\frac{d\mathfrak{H}_g}{dt} - \frac{i_{c_i}T_{,i}}{T}$$

$$+ (\rho w_l g_i - p_{l_i})q_{l_i} + (\rho w_g g_i - p_{g_i})q_{g_i} - p_{l_i}^a i_{l_i}^a - p_{g_i}^w i_{g_i}^w$$

$$- (E_{i,i} - T\mathfrak{H}_{i,i})\phi\rho(v_i^c - v_i) - \left(E_{l,i}^w - T\mathfrak{H}_{l,i}^w\right)q'_{l_i} - \left(E_{l,i}^a - T\mathfrak{H}_{l,i}^a\right)i_{l_i}^{a'}$$

$$- \left(E_{g,i}^a - T\mathfrak{H}_{g,i}^a\right)q'_{g_i} - \left(E_{g,i}^w - T\mathfrak{H}_{g,i}^w\right)i_{g_i}^{w'}$$

which on account of Eq. 2.54, Eq. 2.63 and Eq. 2.71 can be rewritten as:

$$\rho \frac{dE_s}{dt} + \rho\phi \frac{dE_i}{dt} + \rho\vartheta_l \frac{dE_l}{dt} + \rho\vartheta_g \frac{dE_g}{dt} + \rho d \qquad (2.104)$$

$$= \left(\sigma_{ij} - \left(p_g + S_l(p_g - p_l)\right)\delta_{ij}\right)d_{ij} + \phi(p_g - p_l)\frac{dS_l}{dt}$$

$$+ T_{ij}(v_i^c - v_i)_{,i} - \rho\left(p_lS_l + p_g(1 - S_l)\right)\frac{dv_s}{dt} - \rho\vartheta_l^w p_l^w \frac{dv_l^w}{dt}$$

$$- \rho\vartheta_l^a p_l^a \frac{dv_l^a}{dt} - \rho\vartheta_g^a p_g^a \frac{dv_g^a}{dt} - \rho\vartheta_g^w p_g^w \frac{dv_g^w}{dt} + \rho T \frac{d\mathfrak{H}_s}{dt} + \rho\phi T \frac{d\mathfrak{H}_i}{dt}$$

$$+ \rho\vartheta_l T \frac{d\mathfrak{H}_l}{dt} + \rho\vartheta_g T \frac{d\mathfrak{H}_g}{dt} - \frac{i_{c_i}T_{,i}}{T} + (\rho w_l g_i - p_{l,i})q_{l_i}$$

$$+ (\rho w_g g_i - p_{g,i})q_{g_i} - p_{l,i}^a i_{l_i}^a - p_{g,i}^w i_{g_i}^w - (E_{i,i} - T\mathfrak{H}_{i,i})\phi\rho(v_i^c - v_i)$$

$$- \left(E_{l,i}^w - T\mathfrak{H}_{l,i}^w + p_l^w v_{l,i}^w\right)q_{l_i}' - \left(E_{l,i}^a - T\mathfrak{H}_{l,i}^a + p_l^a v_{l,i}^a\right)i_{l_i}^{a'}$$

$$- \left(E_{g,i}^a - T\mathfrak{H}_{g,i}^a + p_g^a v_{g,i}^a\right)q_{g_i}' - \left(E_{g,i}^w - T\mathfrak{H}_{g,i}^w + p_g^w v_{g,i}^w\right)i_{g_i}^{w'}$$

Eq. 2.104 expressed in terms of the internal energy of the porous medium per mass of skeleton E is:

$$\frac{dE}{dt} + d = \frac{1}{\rho}\left(\sigma_{ij} - \left(p_g + S_l(p_g - p_l)\right)\delta_{ij}\right)d_{ij} + \frac{1}{\rho}\phi(p_g - p_l)\frac{dS_l}{dt} \qquad (2.105)$$

$$+ \frac{1}{\rho}T_{ij}(v_i^c - v_i)_{,i} - \left(p_lS_l + p_g(1 - S_l)\right)\frac{dv_s}{dt} - \vartheta_l^w p_l^w \frac{dv_l^w}{dt}$$

$$- \vartheta_l^a p_l^a \frac{dv_l^a}{dt} - \vartheta_g^a p_g^a \frac{dv_g^a}{dt} - \vartheta_g^w p_g^w \frac{dv_g^w}{dt} + T \frac{d\mathfrak{H}_s}{dt} + \phi T \frac{d\mathfrak{H}_i}{dt}$$

$$+ \vartheta_l T \frac{d\mathfrak{H}_l}{dt} + \vartheta_g T \frac{d\mathfrak{H}_g}{dt} + E_i \frac{d\phi}{dt} + E_l \frac{d\vartheta_l}{dt} + E_g \frac{d\vartheta_g}{dt} - \frac{1}{\rho}\frac{i_{c_i}T_{,i}}{T}$$

$$+ \frac{1}{\rho}(\rho w_l g_i - p_{l,i})q_{l_i} + \frac{1}{\rho}(\rho w_g g_i - p_{g,i})q_{g_i} - \frac{1}{\rho}p_{l,i}^a i_{l_i}^a - \frac{1}{\rho}p_{g,i}^w i_{g_i}^w$$

$$- (E_{i,i} - T\mathfrak{H}_{i,i})\phi(v_i^c - v_i) - \frac{1}{\rho}\left(E_{l,i}^w - T\mathfrak{H}_{l,i}^w + p_l^w v_{l,i}^w\right)q_{l_i}'$$

$$- \frac{1}{\rho}\left(E_{l,i}^a - T\mathfrak{H}_{l,i}^a + p_l^a v_{l,i}^a\right)i_{l_i}^{a'} - \frac{1}{\rho}\left(E_{g,i}^a - T\mathfrak{H}_{g,i}^a + p_g^a v_{g,i}^a\right)q_{g_i}'$$

$$- \frac{1}{\rho}\left(E_{g,i}^w - T\mathfrak{H}_{g,i}^w + p_g^w v_{g,i}^w\right)i_{g_i}^{w'}$$

Equation 2.105 establishes the relationship between physical variables of porous medium (right hand side) and rate of energy and dissipation of the porous medium (left hand side).

2.5.1) Constitutive Equations

The rate of internal energy of the porous skeleton dE/dt can be expressed by differentiating it with respect to its internal variables: strain rate d_{ij}, degree of saturation S_l, solid unit volume v_s, unit volume of specie k in fluid phase i v_i^k, solid entropy $\mathfrak{H}_s$, air-liquid skin entropy $\mathfrak{H}_i$, liquid phase entropy $\mathfrak{H}_l$, gas phase entropy $\mathfrak{H}_g$, porosity ϕ, liquid fraction ϑ_l, gas fraction ϑ_g, plastic strain α_{ij} and plastic saturation α_l, so that:

$$
\begin{aligned}
E \quad = \quad & E\big(d_{ij}, S_l, v_s, v_l^w, v_l^a, v_g^a, v_g^w, \mathfrak{H}_s, \mathfrak{H}_i, \mathfrak{H}_l, \mathfrak{H}_g, \phi, \vartheta_l, \vartheta_g, \alpha_{ij}, \alpha_l\big) \qquad (2.106) \\
= \quad & E_s\big(d_{ij}, S_l, \alpha_{ij}, v_s, \mathfrak{H}_s\big) + \phi E_i\big(d_{ij}, S_l, \alpha_l, \mathfrak{H}_i\big) + \vartheta_l E_l(v_l^w, v_l^a, \mathfrak{H}_l) \\
& \qquad + \vartheta_g E_g\big(v_g^a, v_g^w, \mathfrak{H}_g\big)
\end{aligned}
$$

so that the material derivative can be developed as:

$$
\begin{aligned}
\frac{dE}{dt} = & \frac{\partial E}{\partial d_{ij}}\dot{d}_{ij} + \frac{\partial E}{\partial S_l}\frac{dS_l}{dt} + \frac{\partial E}{\partial v_s}\frac{dv_s}{dt} + \frac{\partial E}{\partial v_l^w}\frac{dv_l^w}{dt} + \frac{\partial E}{\partial v_l^a}\frac{dv_l^a}{dt} + \frac{\partial E}{\partial v_g^a}\frac{dv_g^a}{dt} + \frac{\partial E}{\partial v_g^w}\frac{dv_g^w}{dt} \quad (2.107) \\
& + \frac{\partial E}{\partial \mathfrak{H}_s}\frac{d\mathfrak{H}_s}{dt} + \frac{\partial E}{\partial \mathfrak{H}_i}\frac{d\mathfrak{H}_i}{dt} + \frac{\partial E}{\partial \mathfrak{H}_l}\frac{d\mathfrak{H}_l}{dt} + \frac{\partial E}{\partial \mathfrak{H}_g}\frac{d\mathfrak{H}_g}{dt} + \frac{\partial E}{\partial \phi}\frac{d\phi}{dt} + \frac{\partial E}{\partial \vartheta_l}\frac{d\vartheta_l}{dt} \\
& + \frac{\partial E}{\partial \vartheta_g}\frac{d\vartheta_g}{dt} + \frac{\partial E}{\partial \alpha_{ij}}\frac{d\alpha_{ij}}{dt} + \frac{\partial E}{\partial \alpha_l}\frac{d\alpha_l}{dt} \\
= & \frac{\partial E_s}{\partial d_{ij}}\dot{d}_{ij} + \frac{\partial E_s}{\partial \alpha_{ij}}\frac{d\alpha_{ij}}{dt} + \frac{\partial E_s}{\partial v_s}\frac{dv_s}{dt} + \frac{\partial E_s}{\partial \mathfrak{H}_s}\frac{d\mathfrak{H}_s}{dt} + E_i\frac{d\phi}{dt} + \phi\frac{\partial E_i}{\partial S_l}\frac{dS_l}{dt} + \phi\frac{\partial E_i}{\partial \alpha_l}\frac{d\alpha_l}{dt} \\
& + \phi\frac{\partial E_i}{\partial \mathfrak{H}_i}\frac{d\mathfrak{H}_i}{dt} + E_l\frac{d\vartheta_l}{dt} + \vartheta_l^w\frac{\partial E_l^w}{\partial v_l^w}\frac{dv_l^w}{dt} + \vartheta_l^a\frac{\partial E_l^a}{\partial v_l^a}\frac{dv_l^a}{dt} + \vartheta_l\frac{\partial E_l}{\partial \mathfrak{H}_l}\frac{d\mathfrak{H}_l}{dt} \\
& + E_g\frac{d\vartheta_g}{dt} + \vartheta_g^a\frac{\partial E_g^a}{\partial v_g^a}\frac{dv_g^a}{dt} + \vartheta_g^w\frac{\partial E_g^a}{\partial v_g^w}\frac{dv_g^w}{dt} + \vartheta_g\frac{\partial E_g}{\partial \mathfrak{H}_g}\frac{d\mathfrak{H}_g}{dt}
\end{aligned}
$$

where relations 2.78 and 2.80 have been used.

In the same way, the dissipation energy of the porous skeleton d is also expressed in terms of its internal variables, given by: i_{c_i}/T, q_{l_i}, q_{g_i}, $i_{l_i}^a$, $i_{g_i}^w$ in addition the internal variables of the internal energy, thus:

$$
d \qquad\qquad\qquad\qquad\qquad\qquad\qquad\qquad\qquad\qquad\qquad\qquad (2.108)
$$

$$
= d\left(\alpha_{ij}, \alpha_l, v_s, v_l^w, v_l^a, v_g^a, v_g^w, \mathfrak{H}_s, \mathfrak{H}_i, \mathfrak{H}_l, \mathfrak{H}_g, \phi, \vartheta_l, \vartheta_g, \frac{d\alpha_{ij}}{dt}, \frac{d\alpha_l}{dt}, i_{c_i}/T, q_{l_i}, q_{g_i}, i_{l_i}^a, i_{g_i}^w\right)
$$

introducing the notation $\eta_i = {}^{i_{c_i}}/_T$ and assuming d as an homogeneous and first order function, the material derivative is developed as:

$$d = \frac{\partial d}{\partial \, {}^{d\alpha_{ij}}/_{dt}} \frac{d\alpha_{ij}}{dt} + \frac{\partial d}{\partial \, {}^{d\alpha_l}/_{dt}} \frac{d\alpha_l}{dt} + \frac{\partial d}{\partial \eta_i} \frac{d\eta_i}{dt} + \frac{\partial d}{\partial q_{l_i}} \frac{dq_{l_i}}{dt} + \frac{\partial d}{\partial q_{g_i}} \frac{dq_{g_i}}{dt} + \frac{\partial d}{\partial i_{l_i}^a} \frac{di_{l_i}^a}{dt} \qquad (2.109)$$

$$+ \frac{\partial d}{\partial i_{g_i}^w} \frac{di_{g_i}^w}{dt}$$

substituting Eq. 2.107 and Eq. 2.109 in Eq. 2.105 and after collecting terms, leads to:

$$0 = \left(\frac{1}{\rho} \left(\sigma_{ij} - \left(p_g + S_l(p_g - p_l) \right) \delta_{ij} \right) - \frac{\partial E_s}{\partial d_{ij}} \right) \dot{d}_{ij} + \left(\frac{1}{\rho} \phi(p_g - p_l) - \frac{\partial E_i}{\partial S_l} \right) \frac{dS_l}{dt} \qquad (2.110)$$

$$- \left(\left((p_l S_l + p_g(1 - S_l) \right) + \frac{\partial E_s}{\partial v_s} \right) \frac{dv_s}{dt} - \vartheta_l^w \left(p_l^w + \frac{\partial E_l^w}{\partial v_l^w} \right) \frac{dv_l^w}{dt}$$

$$- \vartheta_l^a \left(p_l^a + \frac{\partial E_l^a}{\partial v_l^a} \right) \frac{dv_l^a}{dt} - \vartheta_g^a \left(p_g^a + \frac{\partial E_g^a}{\partial v_g^a} \right) \frac{dv_g^a}{dt}$$

$$- \vartheta_g^w \left(p_g^w + \frac{\partial E_g^w}{\partial v_g^w} \right) \frac{dv_g^w}{dt} + \left(T - \frac{\partial E_s}{\partial \mathfrak{H}_s} \right) \frac{d\mathfrak{H}_s}{dt} + \phi \left(T - \frac{\partial E_i}{\partial \mathfrak{H}_i} \right) \frac{d\mathfrak{H}_i}{dt}$$

$$+ \vartheta_l \left(T - \frac{\partial E_l}{\partial \mathfrak{H}_l} \right) \frac{d\mathfrak{H}_l}{dt} + \vartheta_g \left(T - \frac{\partial E_g}{\partial \mathfrak{H}_g} \right) \frac{d\mathfrak{H}_g}{dt}$$

$$- \left(\frac{\partial E}{\partial \alpha_{ij}} + \frac{\partial d}{\partial \, {}^{d\alpha_{ij}}/_{dt}} \right) \frac{d\alpha_{ij}}{dt} - \left(\frac{\partial E}{\partial \alpha_l} + \frac{\partial d}{\partial \, {}^{d\alpha_l}/_{dt}} \right) \frac{d\alpha_l}{dt}$$

$$- \left(\frac{\partial d}{\partial \eta_i} + \frac{1}{\rho} T_{,i} \right) \eta_i + \left(\frac{1}{\rho} \left(\rho w_l g_i - p_{l,i} \right) - \frac{\partial d}{\partial q_{l_i}} \right) q_{l_i}$$

$$+ \left(\frac{1}{\rho} \left(\rho w_g g_i - p_{g,i} \right) - \frac{\partial d}{\partial q_{g_i}} \right) q_{g_i} - \left(\frac{1}{\rho} p_{l,i}^a + \frac{\partial d}{\partial i_{l_i}^a} \right) i_{l_i}^a$$

$$- \left(\frac{1}{\rho} p_{g,i}^w + \frac{\partial d}{\partial i_{g_i}^w} \right) i_{g_i}^w - \frac{1}{\rho} \left(E_{l,i}^w - T\mathfrak{H}_{l,i}^w + p_l^w v_{l,i}^w \right) q_{l_i}'$$

$$- \frac{1}{\rho} \left(E_{l,i}^a - T\mathfrak{H}_{l,i}^a + p_l^a v_{l,i}^a \right) i_{l_i}^{a\prime} - \frac{1}{\rho} \left(E_{g,i}^a - T\mathfrak{H}_{g,i}^a + p_g^a v_{g,i}^a \right) q_{g_i}'$$

$$- \frac{1}{\rho} \left(E_{g,i}^w - T\mathfrak{H}_{g,i}^w + p_g^w v_{g,i}^w \right) i_{g_i}^{w\prime}$$

Eq. 2.110 must be satisfied for any value of $\dot{d}_{ij}$, $\frac{dS_l}{dt}$, $\frac{dv_s}{dt}$, $\frac{dv_l^w}{dt}$, $\frac{dv_l^a}{dt}$, $\frac{dv_g^a}{dt}$,

$\frac{dv_g^w}{dt}$, $\frac{d\mathfrak{H}_s}{dt}$, $\frac{d\mathfrak{H}_i}{dt}$, $\frac{d\mathfrak{H}_l}{dt}$, $\frac{d\mathfrak{H}_g}{dt}$, $\frac{d\alpha_{ij}}{dt}$, $\frac{d\alpha_l}{dt}$, η_i, q_{l_i}, q_{g_i}, q_{l_i}, $i_{l_i}^a$, $i_{g_i}^w$, since all those

variables are independent of each other. Then it follows that:

Mechanical Constitutive law

Description	State equation for the solid skeleton of a three-phase porous medium.	N⁰. of Eqs.
Equations	$$\frac{1}{\rho}\underbrace{\left(\sigma_{ij} - \left(p_g + S_l(p_g - p_l)\right)\delta_{ij}\right)}_{\sigma'_{ij}} = \frac{\partial E_s}{\partial d_{ij}}$$ E_s Internal energy of solid skeleton d_{ij} Strain tensor σ_{ij} Total stress tensor p_g Gas pressure p_l Liquid pressure	6

Skeleton compressibility law

Description	State equation for the pore pressure of a three-phase porous medium.	N⁰. of Eqs.
Equations	$$-\underbrace{\left(p_l S_l + p_g(1 - S_l)\right)}_{p} = \frac{\partial E_s}{\partial v_s}$$ E_s Internal energy of solid skeleton v_s Unit volume of solid skeleton p Pore pressure p_g Gas pressure p_l Liquid pressure	1

Mechanical hardening law

Description	Complementary State equation for the Generalized stress tensor of a three-phase porous medium (Ziegler's orthogonality)	No. of Eqs.
Equations	$$\frac{\partial E_s}{\partial \alpha_{ij}} = -\frac{\partial d}{\partial \, {}^{d\alpha_{ij}}\!/\!_{dt}} \equiv x_{ij}$$ E_s Internal energy of solid skeleton d Dissipation of porous medium α_{ij} Plastic strain tensor ${}^{d\alpha_{ij}}\!/\!_{dt}$ Material derivative of plastic strain tensor x_{ij} Generalized stress tensor	6

Retention curve law

Description	State equation for water retention law.	No. of Eqs.
Equations	$$\frac{1}{\rho}\phi \underbrace{(p_g - p_l)}_{s} = \frac{\partial E_i}{\partial S_l}$$ E_i Internal energy of air-liquid interface S_l Degree of saturation s Suction p_g Gas pressure p_l Liquid pressure ϕ porosity	1

Hardening law for air-liquid interface

Description	Complementary state equation for the generalized suction (Ziegler's orthogonality).	Nº. of Eqs.
Equations	$$\phi \frac{\partial E_i}{\partial \alpha_l} = - \frac{\partial d}{\partial \, d\alpha_l / dt} \equiv x_s$$ E_i Internal energy of air-liquid interface d Dissipation α_l Irreversible degree of saturation ϕ Porosity x_s Generalized suction	1

Partial liquid pressure

Description	State equation for partial pressure in liquid water of a three-phase porous medium.	Nº. of Eqs.
Equations	$$-p_l^w = \frac{\partial E_l^w}{\partial v_l^w}$$ E_l^w Internal energy of liquid water v_l^w Unit volume of liquid water p_l^w Partial pressure at liquid water	1

Partial pressure in dissolved air

Description	State equation for partial pressure in dissolved air of a three-phase porous medium.	Nº. of Eqs.
Equations	$$-p_l^a = \frac{\partial E_l^a}{\partial v_l^a}$$ E_l^a Internal energy of dissolved air v_l^a Unit volume of dissolved air p_l^a Partial pressure at dissolved air	1

Partial pressure in dry air

Description	State equation for partial pressure in dry air of a three-phase porous medium.	N⁰. of Eqs.
Equations	$$-p_g^a = \frac{\partial E_g^a}{\partial v_g^a}$$ E_g^a Internal energy of dry air v_g^a Unit volume of dry air p_g^a Partial pressure at dry air	1

Partial pressure of vapor

Description	State equation for partial pressure in water vapor of a three-phase porous medium.	N⁰. of Eqs.
Equations	$$-p_g^w = \frac{\partial E_g^w}{\partial v_g^w}$$ E_g^w Internal energy of water vapor v_g^w Unit volume of water vapor p_g^w Partial pressure of water vapor	1

Constitutive law for Temperature

Description	State equation for Temperature at any phase of a three-phase porous medium.	N⁰. of Eqs.
Equations	$$T = \frac{\partial E_s}{\partial \mathfrak{H}_s} = \frac{\partial E_i}{\partial \mathfrak{H}_i} = \frac{\partial E_l}{\partial \mathfrak{H}_l} = \frac{\partial E_g}{\partial \mathfrak{H}_g}$$ E_s Internal energy of solid skeleton E_i Internal energy of air-liquid interface E_l Internal energy of liquid phase E_g Internal energy of gas phase $\mathfrak{H}_s$ Specific entropy of solid skeleton $\mathfrak{H}_i$ Specific entropy of air-liquid interface $\mathfrak{H}_l$ Specific entropy of liquid phase $\mathfrak{H}_g$ Specific entropy of gas phase	1

Constitutive law for heat conduction

Description	State equation for heat conduction law.	Nº. of Eqs.
Equations	$$-\frac{1}{\rho}T_{,i} = \frac{\partial d}{\partial \eta_i}$$ d — Dissipation η_i — Ratio ${}^{i}c_i/{}_T$ T — Temperature	3

Constitutive law for liquid conduction

Description	State equation for liquid water conduction law.	Nº. of Eqs.
Equations	$$\frac{1}{\rho}\left(\rho w_l g_i - p_{l,i}\right) = \frac{\partial d}{\partial q_{l_i}}$$ d — Dissipation q_{l_i} — Liquid water flux of Darcy's type p_l — Liquid pressure	3

Constitutive law for gas conduction

Description	State equation for dry air conduction law.	Nº. of Eqs.
Equations	$$\frac{1}{\rho}\left(\rho w_g g_i - p_{g,i}\right) = \frac{\partial d}{\partial q_{g_i}}$$ d — Dissipation q_{g_i} — Dry air flux of Darcy's type p_g — Gas pressure	3

Diffusion of dissolved air

Description	State equation for dissolved air diffusion law.	Nº. of Eqs.
Equations	$$\frac{1}{\rho}\mathrm{p}^{a}_{l,i} = -\frac{\partial d}{\partial \mathrm{i}^{a}_{l_i}}$$ d Dissipation $\mathrm{i}^{a}_{l_i}$ Diffusive flux of dissolved air in liquid phase p^{a}_{l} Partial pressure of dissolved air	3

Diffusion of water vapor

Description	State equation for water vapor diffusion law.	Nº. of Eqs.
Equations	$$\frac{1}{\rho}\mathrm{p}^{w}_{g,i} = -\frac{\partial d}{\partial \mathrm{i}^{w}_{g_i}}$$ d Dissipation $\mathrm{i}^{w}_{g_i}$ Diffusive flux of water vapor in gas phase p^{w}_{g} Partial pressure of vapor	3

The rest of terms in Eq. 2.110 are identically zero, since in virtue of the laws derived above:

$$\mathrm{E}^{k}_{j,i} = \frac{\partial \mathrm{E}^{k}_{j}}{\partial v^{k}_{j}}v^{k}_{j,i} + \frac{\partial \mathrm{E}^{k}_{j}}{\partial \mathfrak{H}^{k}_{j}}\mathfrak{H}^{k}_{j,i} = -\mathrm{p}^{k}_{j}v^{k}_{j,i} + \mathrm{T}\mathfrak{H}^{k}_{j,i} \tag{2.111}$$

where $(k \equiv w, \mathrm{a})$ and $\mathrm{j} \equiv (\mathrm{l}, \mathrm{g})$.

For simplicity, terms concerning air-liquid skin velocity v^{c}_{i} have been dropped in Eq. 2110 under the assumption that air-liquid skin moves with the solid skeleton leading to $v^{c}_{i} - v_{i} = 0$.

2.6) Ground response to the interaction with the atmosphere

In this section some consequences of the soil-atmosphere interactions are illustrated based on real situations in order to better understand these interactions.

Balance between infiltration and evapotranspiration causes hydric changes in the upper zone of the ground, called "active zone" or "zone of seasonal moisture changes". The

thickness of this zone is typically lower than 3 m (Nelson & Miller, 1992), although Blight (1997) reported water content variations until depth of 6 m. Fig. 2.14 shows the example of two extreme profiles of water contents (winter and summer) as measured by TDRs in a road embankment (Carmaux, France). Measurements clearly indicate that climate actions do not causes changes in water content below a depth equal to 4 m for the material under consideration.
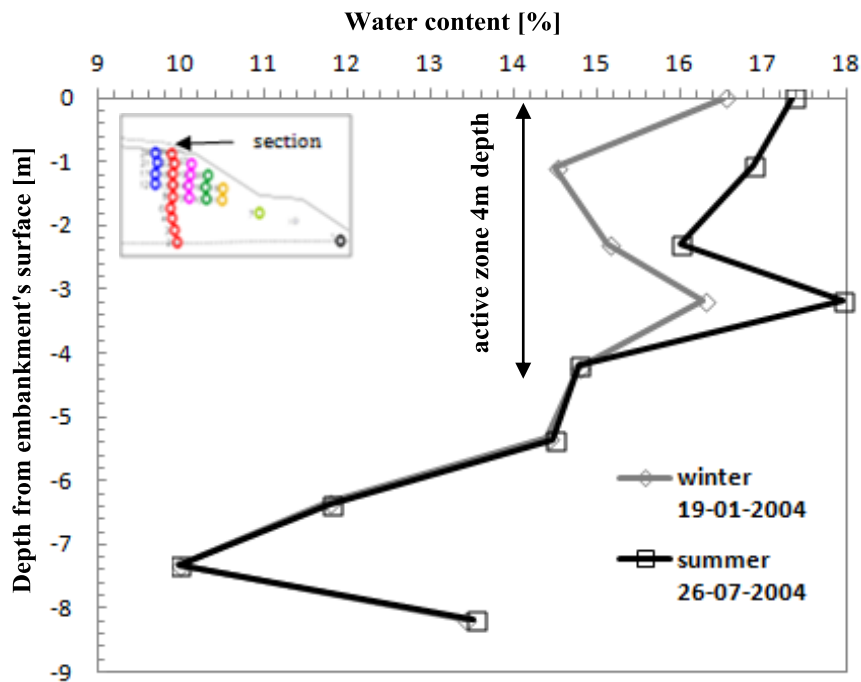
Figure 2.14: Seasonal changes in water content measures at a section of Carmaux embankment in France.

Pore pressure fluctuations at the bottom of the active zone act as a forcing condition for the underlying ground and, in absence of other effects (artesian recharge, recharge due to river level variation, etc.), further govern the groundwater response. The estimation of hydric changes in the active layer has thus a geotechnical relevance that goes well beyond the estimation of the characteristics of the superficial vadose zone.

Permeability plays obviously a central role in groundwater response as it controls the amount of percolated water and thus the balance between infiltration and evapo-transpiration. For example, Fig. 2.15 shows the effects of soil permeability on predicted hydric changes within a layer of silt at Le Fauga site (see chapter 6 for the description of the material and field conditions).

99
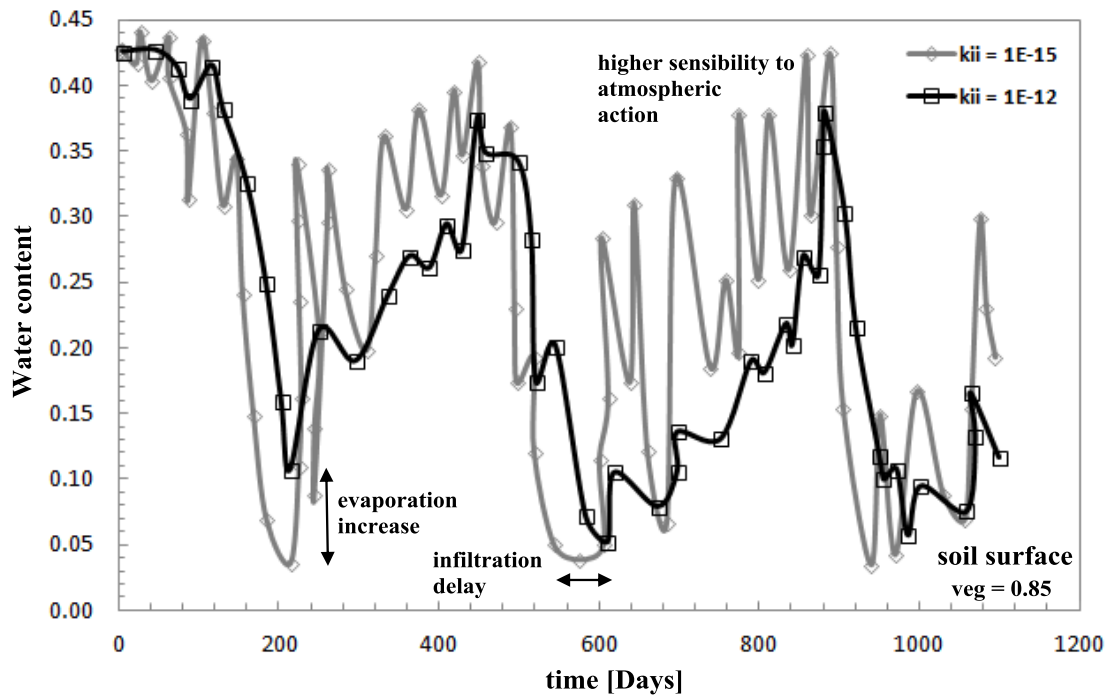
Figure 2.15: Influence of permeability on hydric time evolution at the surface of a silt layer (Le Fauga-France).Filtered data from the obtained results.

Lower water contents are predicted if a higher permeability is considered. Fig. 2.15 states that: a) a greater resistance of the soil to percolation enhances evaporation and b) the rate of infiltration decreases as percolation resistance increases. Moreover it is concluded that the soil sensitivity to atmospheric actions increases as the resistance to percolation increases. Figure 2.16 confirms the mentioned conclusions and also shows that the impact of statements a and b decreases as the depth increases.
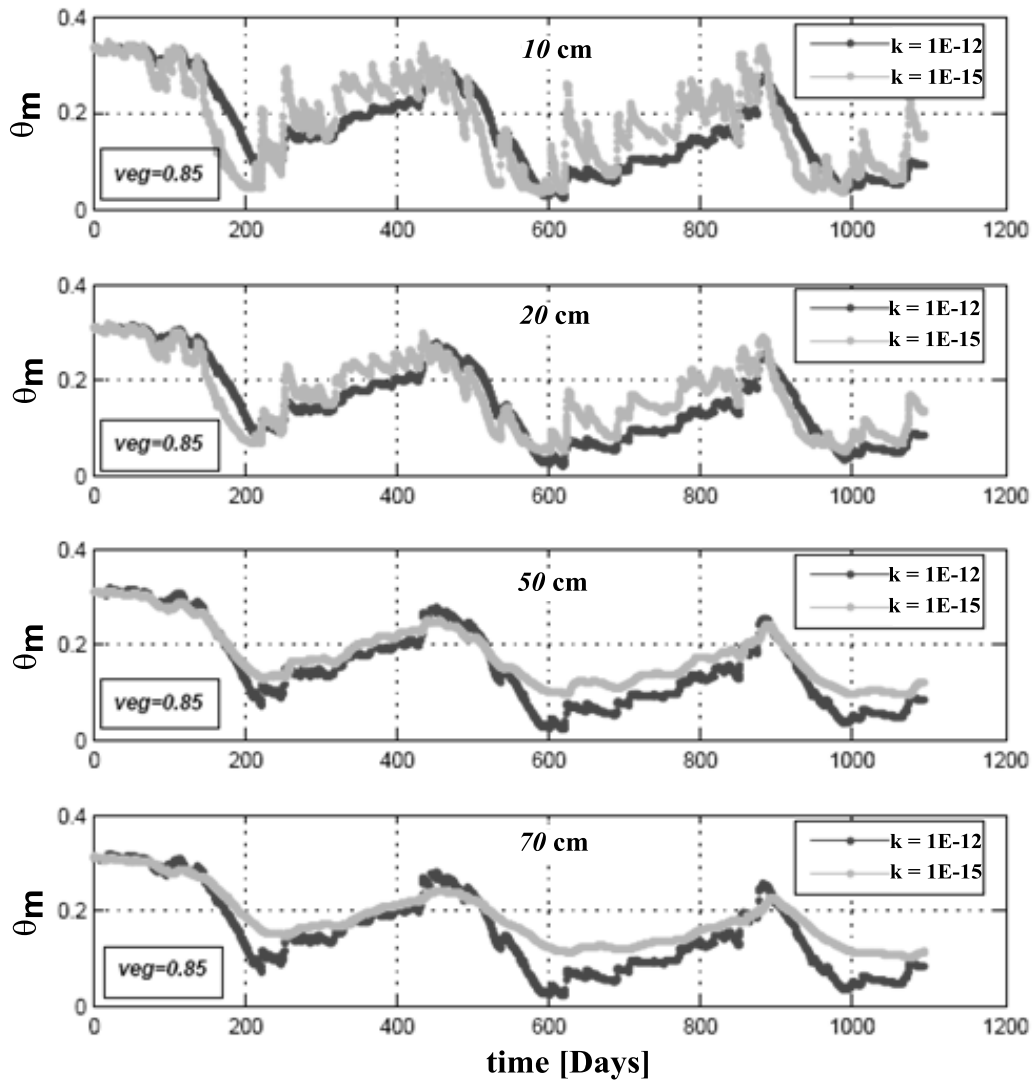
Figure 2.16: Influence of permeability on hydric time evolution at several depths within a layer of silt (10, 20, 30, 40, 50 60 and 70 cm).

Additionally, high permeability may affect the energy balance as it favors a deeper percolation of surface water (at atmosphere temperature). This effect is illustrated in Fig. 2.17 for the case of the silt layer at Le Fauga site. At 50 cm depth, differences in temperature may be appreciated between the simulations with $k_{ii} = 10^{-12}$ m2 and $k_{ii} = 10^{-15}$ m2.
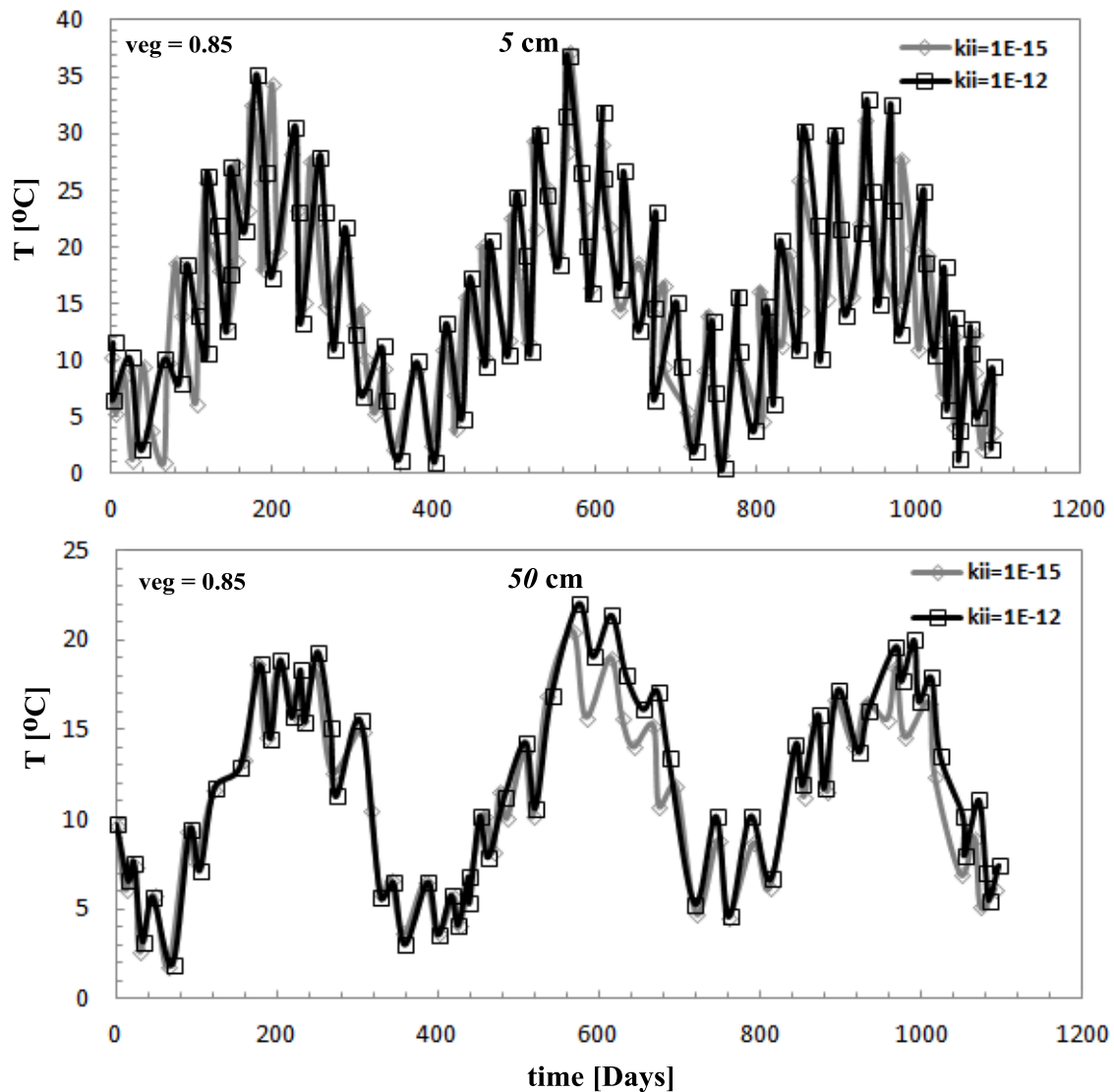
Figure 2.17: Permeability influence of the upper soil layer for a vegetation fraction ($veg = 0.85$) at Le Fauga site. Response of the Temperature evolution. Filtered data from the obtained results.

Leroueil (2001) indicated however that permeability cannot explain alone the overall response of groundwater and particularly the delay and attenuation of pore pressure changes with depth. This response is essentially governed by the processes of saturation/desaturation and consolidation/swelling that take place in the ground below the active zone. Retention curve and stiffness are the main material parameters that govern these processes, otherwise largely controlled by soil stratigraphy and bedrock depth and inclination. Water pressures distribution influences in turn soil stiffness and strength, which lastly determines the stability of the slope. Reverse hydro-mechanical coupling such as pore-pressure build-up by loading inside the moving mass (Picarelli, (1986); Sassa, (1985)) or the dependence of permeability on deformation and,

particularly, on fissures and other localized discontinuities may also play a non-negligible role in rainfall induced failures.

Figure 2.18 shows the effect of the vegetation fraction over suction profiles predicted by the presented model. The effect is shown by obtaining the suction profiles in a maize field at two different stages of ageing: a) a growing field with 55% of the ground covered by maize plants with 30% of leafs and b) a mature field with 85% of the ground totally covered by the leafs of the plants.

The unsaturated zone is 1 m deeper in the last case because of the higher amount of water extracted by roots in the mature fallow field.
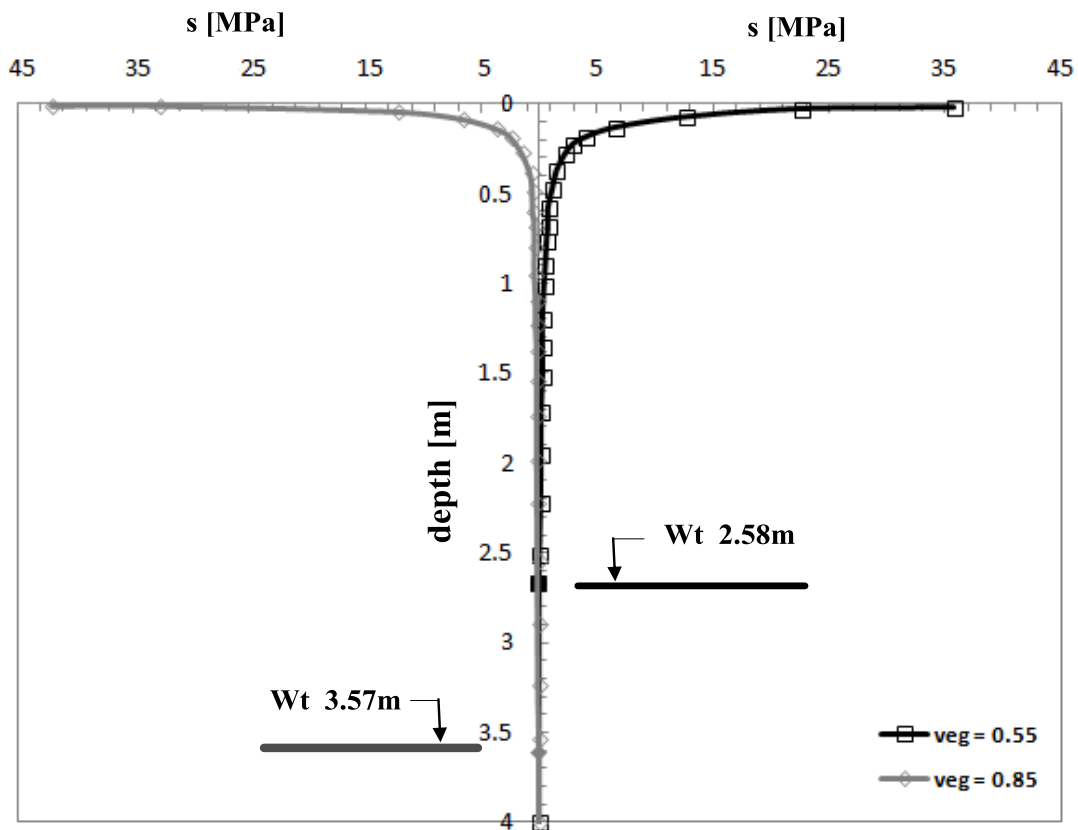
Figure 2.18: Water content profiles beneath two different vegetated surfaces: (a) Maize field during plant growth (parameter used: $R_{S_{min}} = 40\,^S/_m$, $LAI = 0.3\,^{m^2}/_{m^2}$, $z_a = 10\,m$, $veg = 0.55$); (b) Mature maize field (parameters used: $R_{S_{min}} = 40\,^S/_m$, $LAI = 1\,^{m^2}/_{m^2}$, $z_a = 10\,m$, $veg = 0.85$).

It addition to the amount of water extracted by a plant, the depth and density of roots has a significant influence on the thickness of active zone. Fig. 2.19 shows a comparison between two simulations with changing root depth (0.65 and 0.95 cm, respectively) in a silt layer of an experimental field (extensively developed in chapter 6).

It is observed that water content reaches systematically lower values as root depth increases.
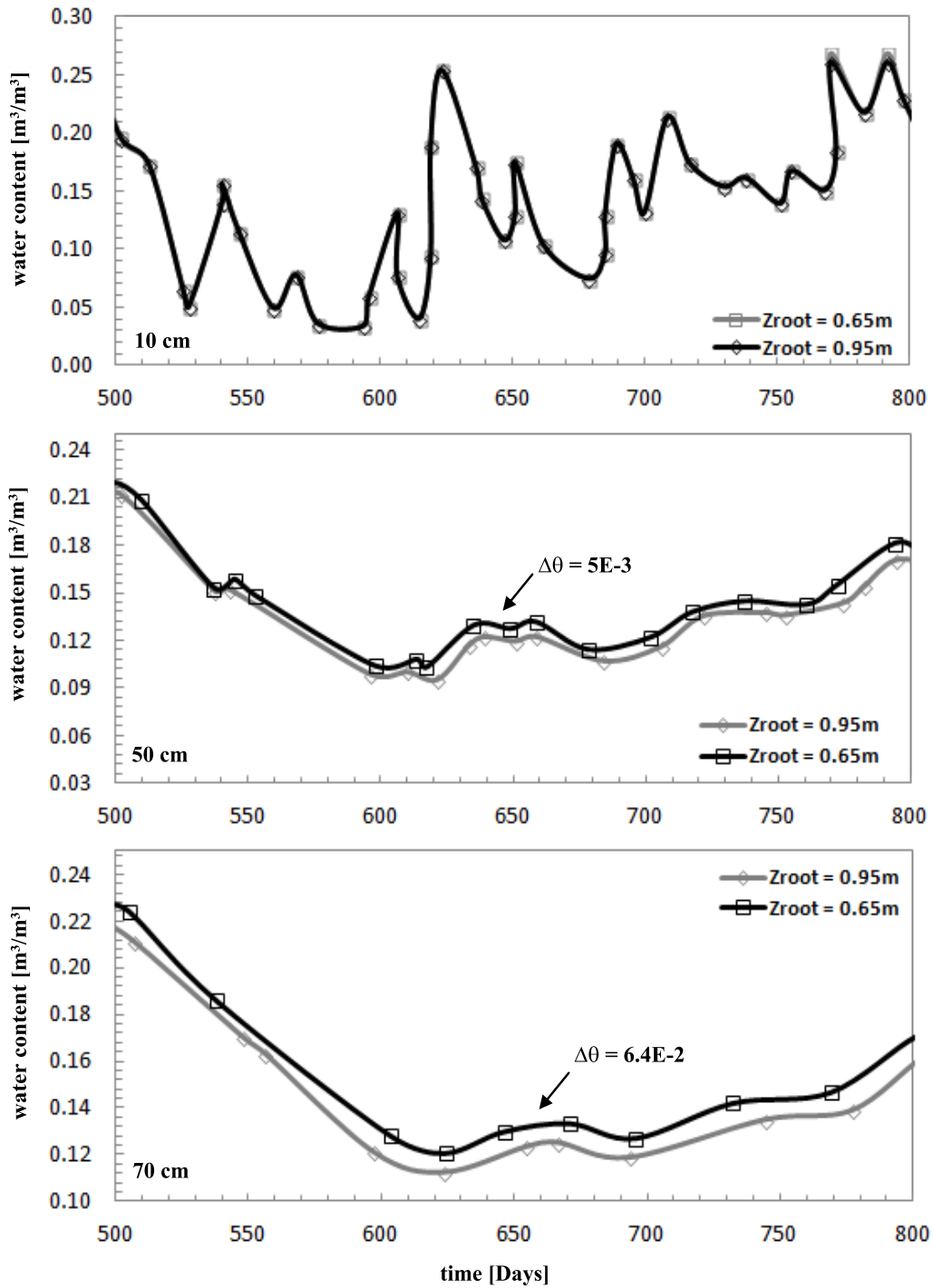
Figure 2.19: Water content evolutions "at 10cm depth"; "at 50cm depth" and "at 70cm depth" at Le Fauga site for two different rooting depths. (a) Root depth at $z_r = 0.95\ m$; (b) Root depth at $z_r = 0.65\ m$. Filtered data from the obtained results.

_____

The water content evolution at a depth of 10cm in Fig. 2.16a shows few differences between the two compared cases. However, as depth increases differences between the registered water contents in both cases become more and more evident.

It reveals that the response of the higher soil layers are mainly controlled by evaporation fluxes while as depth increases the transpiration fluxes become more relevant and therefore control the soil response.

As far as root density is concerned Fig. 2.20 shows the soil response in terms of water content when two different densities: a) zDr=1 and b) zDr=0.5 of the rooting system are considered. It evidences a delay in water extraction by the roots as well as a decrease in the magnitude of such extraction (transpiration).
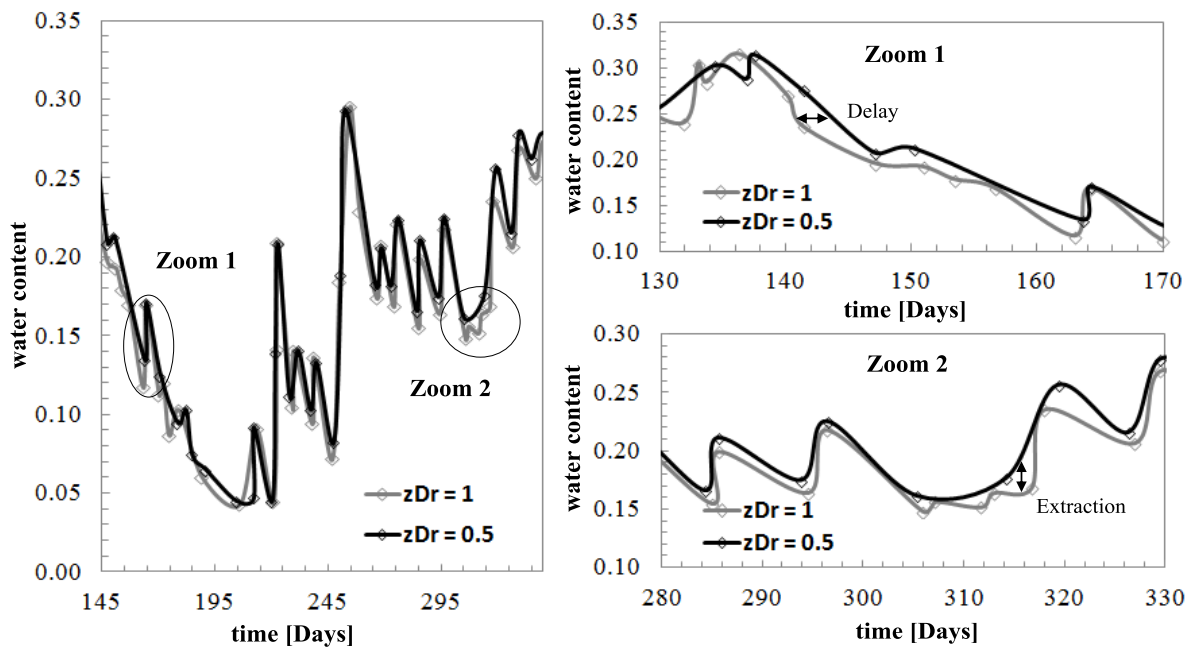
Figure 2.20: Density of Rooting Influence on the Water Content evolution at the upper soil layer ($10cm$) for a vegetation fraction($veg = 0.85$).

Extend of root zone depends on both plant and soil characteristics. As pointed out by Penman (1963): "If root development is such that the roots can continue to grow downwards in pursuit of a retreating water table, it will be possible to lower the water table permanently, provided that the mean annual transpiration is a little greater from the deep-rooted vegetation than that of any shallow-rooted vegetation it has replaced", the common assumption that root develops vertically leads to unphysical conclusions.

Dobson and Moffat (1995) showed indeed that the tree/root architecture is often horizontal with root depths limited to 2m and lateral spread that may exceed 20m. The tree/root architecture pattern is also affected by the type of soil: root depth is higher in sandy soils than in clayed soils. In the last case it is much common to find root systems developed at width than at depth.

2.7)   Conclusions

In this chapter the soil-atmosphere interaction has been presented in a coupled THM formulation of mass and heat flow in deformable porous media. This approach provides an overview of the cause of problems studied in this dissertation.

The modeling account for the net radiation reaching the soil surface. Net radiation flux has proved to be of great relevance for evaporation, producing thermal strains. It will be seen in chapter 8 that it could also be the cause of ground deformation.

Magnitude of this flux depends on the magnitudes of current atmospheric variables (wind velocity, relative humidity, atmospheric temperature).

Transpiration flux which acts on the root zone of vegetated areas depends on the soil water content available at the root zone. Stress factor affecting leaf surface resistance is the controlling factor for this flux.

The fluxes on the soil-atmosphere interface have been implemented in a thermomechanical formulation for THM behavior of porous media. It is based on first and second laws of thermodynamics and allows to derive the momentum balance equation for the skeleton and for the air-liquid interface, involving the average stress-like tensor T_{ij}. Moreover, following standard procedures in thermomechanics, the state equations (constitutive laws) of the three-phase porous medium have been obtained.

All those elements set up bases for the study in this dissertation of different geotechnical problems of soil-atmosphere interactions.

A sensitive study of the effect of some factors has been presented at the end of this chapter. It includes the effects of permeability and vegetation characteristics which affect the water content profiles in the active zone.

As future work, it is foreseen to introduce the effect of life cycle of plants which affects suction profile at the root zone. To do that, a model for plant growth at cellular level can be envisaged.

CHAPTER 3

A THERMODYNAMIC FRAMEWORK TO MODEL PARTIALLY SATURATED POROUS MEDIA

3.1) Introduction

Modelling the mechanical response of the ground (including failure) under climatic actions requires having at hand thermo-hydro-mechanical models suitable to provide objective numerical solutions, particularly in presence of materials displaying softening. One way to insure necessary conditions for well-posed models relies on the derivation of constitutive laws from thermodynamics potentials. The objective of this chapter is to propose a framework for such derivation in presence of the effect of temperature and internal pressures in three-phase media. The framework essentially merges concepts developed in poromechanics (Coussy, (2004) and hyperplasticity (Collins & Houlsby, 1997) extended to three-phase media.

3.2) Notation and Terminology

Symbols used in the remaining part of the chapter are summarized hereinafter.

Table 3.3: Notation and Terminology

Latin symbols	
C_{ijkl}	Stiffness matrix
d	Dissipation energy of the medium
d_s	Dissipation energy of solid skeleton (including interfaces between phases)

_____

e	Void ratio
f_i	Helmholtz energy function of interfaces between phases only
f_s	Helmholtz energy function of solid skeleton (including interfaces between phases)
$f_{\bar{s}}$	Helmholtz energy function of solid skeleton only
f_{s_1}	Elastic Helmholtz energy function of solid skeleton (including interfaces between phases)
f_{s_2}	Trapped Helmholtz energy function of solid skeleton (including interfaces between phases)
f^y	Yield function
G	Shear modulus
g_s	Gibbs free energy function of solid skeleton (including interfaces between phases)
g_{s_1}	Elastic Gibbs free energy function of solid skeleton (including interfaces between phases)
g_{s_2}	Trapped Gibbs free energy function of solid skeleton (including interfaces between phases)
L	Characteristics length of the porous network
l_i	Characteristics length of the part of the porous network filled with fluid *i*
L	Rate of total work
L^d	Rate of dissipative work
L_s	Rate of work of the porous skeleton (including interfaces between phases)
L_s^e	Reversible part of the rate of work of the porous skeleton (including interfaces between phases)
L_s^p	Irreversible part of the rate of work of the porous skeleton (including interfaces between phases)
m_{f^i}	Mass concentration of fluid *i* with respect to total porous medium volume
n_i	Apparent molar density of species *i*
p	Mean stress
p'	Mean effective stress (Bishop effective stress with $\chi = S_l$ in three-phase porous media)
p^c	Preconsolidation pressure in Cam Clay Model
σ'_{ij}	Effective stress tensor (Bishop effective stress tensor with $\chi = S_l$ in

	three-phase porous media)
p_f	Fluid pressure
p_g	Gas pressure
p_l	Liquid pressure
q	Deviatoric stress
q_k	Heat flux through the medium (solid and, eventually, fluid phases)
q'_k	Heat flux through the soil skeleton (including eventual interfaces)
s	Suction
S_l	Degree of liquid saturation
S_e^l	Effective degree of liquid saturation
S_m^l	Residual degree of liquid saturation
T	Temperature
E_i	Internal energy of interface between phases only
E_s	Internal energy of solid skeleton (including interfaces between phases)
v_i	Seepage velocity
x_{ij}	Generalized dissipative stress tensor in one-phase porous media
x'_{ij}	Generalized dissipative stress tensor in multi-phase porous media
x_p	Generalized dissipative fluid pressure
x_s	Generalized dissipative suction

Greek symbols	
α_{ij}	Internal variables of solid skeleton (including interfaces between phases)
α_l	Internal variable of the liquid-gas interface
α_p	Internal variable of fluid
δ_{ij}	Kronecker symbol
ε_{ij}	Strain tensor
ε_{ij}^e	Elastic strain tensor
ε_{ij}^p	Plastic strain tensor
ε_p	Volumetric strain
ε_w	Hydraulic strain
ϕ	Porosity

ϕ_0	Initial porosity
γ_{lg}	Surface tension gas-liquid
κ^*	Slope of the elastic branch in the plane $\{\varepsilon_p - \ln(p')\}$
λ^*	Slope of the inelastic branch in the plane $\{\varepsilon_p - \ln(p')\}$
μ_i	Molar chemical potential of species i
ρ_g	Gas density
ρ'_{ij}	Back stress tensor (shift stress)
ρ_s	Back suction (shift suction)
σ_{ij}	Total stress tensor
σ'_{ij}	Effective stress tensor (Bishop effective stress tensor with $\chi = S_l$ in three-phase porous media)
σ''_{ij}	Net stress tensor

Others symbols	
$\mathfrak{H}$	Entropy of the porous medium
$\mathfrak{H}_s$	Entropy of the solid skeleton (including interfaces between phases)
$\mathfrak{H}_{s_r}$	Reversible part of the entropy of the solid skeleton and interfaces between phases
$\mathfrak{H}_{s_i}$	Irreversible part of the entropy of the solid skeleton and interfaces between phases
$\mathfrak{H}_{i_{kl}}$	Entropy of interface between phase k and l
$\mathfrak{H}_{i_{r,kl}}$	Reversible part of interface between phase k and l
$\mathfrak{H}_{i_{i,kl}}$	Irreversible part of the entropy of interface between phase k and l
$\mathfrak{H}_i$	Entropy of all interfaces
$\mathfrak{H}_{i_r}$	Reversible part of the entropy of all interfaces
$\mathfrak{H}_{i_i}$	Irreversible part of the entropy of all interfaces

3.3) **Theoretical restrictions on plasticity theory**

Elastoplastic models for geomaterials may be either purely empirical, based on curve fitting of laboratory tests, or based on some more fundamental postulates. The two approaches are often combined leading to the rational formulation of constitutive laws of materials. A common framework is the theory of elasto-plasticity which is able to

accommodate an almost limitless variety of models. Unlike elastic models, elastoplastic models construct stress-strain relationships in a finite space (either in stress or in strain), which limit has been attempted to be related to restrictions provided by the second law of thermodynamics.

Perhaps the older and best known restriction is the *Drucker's stability postulate* (Drucker D. , 1951). Initially considered as a thermodynamics restriction, this postulate appears later to be a "constitutive" assumption allowing "quasi-thermodynamic" classification of materials. The postulate states that the second order plastic work should be positive or null,

$$\delta\sigma_{ij}\delta\varepsilon_{ij}^{p} \geq 0 \qquad (3.1)$$

where $\delta\sigma_{ij}$ and $\delta\varepsilon_{ij}^{p}$ are increments of applied stress and the resulting plastic strain. Equation 3.1 states the orthogonality between the yield surface and the plastic strain increment (or the flow rule). This condition is also called associativity of the flow rule. Most of the materials of geological origin do not respect this condition as the flow is usually non associated.

An alternative restriction is the *Postulate of Plasticity* of Il'iushin (1961). It states that the work done during a cycle of strain must be positive or zero.

$$\oint \sigma_{ij}d\varepsilon_{ij} \geq 0 \qquad (3.2)$$

This condition is less restrictive than Drucker's postulate, as it allows strain softening behavior. However, like Drucker postulate, Il'iushin postulate provides a condition stricter to that compared with the second law of thermodynamics.

The hyper-plasticity approach uses an extremum principle introduced by Ziegler (1977) called "*the orthogonality condition*". It states that the dissipation function acts as a potential. The dissipated work $\left(L^{d} = x_{ij}\dot{\alpha}_{ij} = d\right)$ defines a new tensor, the "dissipative generalized stress x_{ij}". The direction of this tensor is determined assuming that, in the vicinity of the rate of plastic strain $\left(\dot{\alpha}_{ij}\right)$, the dissipation function admits a power series expansion. The dissipative generalized stress corresponds to the second coefficient of Taylor's series, leading to the expression:

$$x_{ij} = \frac{\partial d}{\partial\dot{\alpha}_{ij}} \qquad (3.3)$$

According to Eq. 3.3, x_{ij} is orthogonal to iso-value surfaces of the dissipation, Fig. 3.21.
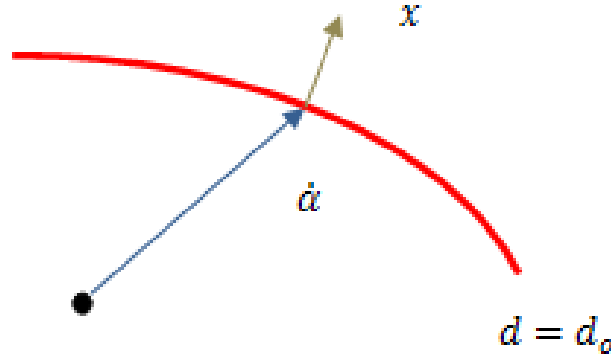
Figure 3.21: Orthogonality of dissipative forces and rates

The orthogonality condition is equivalent to the principle of maximal dissipation rate enunciated by Ziegler (1977): "Provided the dissipative force x_{ij} is prescribed, the actual rate $\dot{\alpha}_{ij}$ maximizes the dissipation rate $\left(L^d = x_{ij}\dot{\alpha}_{ij}\right)$ subjected to the side condition". This condition is more restrictive than the second law of thermodynamics which states that dissipation is positive but not necessarily maximal, and less strict that Drucker's and Il'iushin postulates. It allows particularly to model materials that present stress or strain softening along specific paths.

The development of the orthogonality principle will be revisited later in section 3.4.1 when the dissipation function is considered.

3.4)   Thermodynamics of Two-phase Media (Mechanic Part)

A soil element treated as a porous medium can be understood as the superimposition of two continuous media: the skeleton and the fluid filling the porous space. The former corresponds to the solid skeleton and is composed by the solid matrix and the disconnected porous space emptied of fluid. The latter is the fluid saturating the connected porous space (Biot, 1941). Assuming small strains, the natural arguments of the internal energy for the porous continuum are $\left(\varepsilon_{ij}, \varphi_m, m_f, \mathfrak{H}, \alpha_{ij}, \alpha_p\right)$ (Coussy O. , 2004)

$$\mathrm{E} = \mathrm{E}\left(\varepsilon_{ij}, \varphi_m, m_f, \mathfrak{H}, \alpha_{ij}, \varphi_m^p\right) \tag{3.4}$$

where m_f is the mass concentration of fluid, $\mathfrak{H}$ is the entropy of the porous continuum and both φ_m-φ_m^p are the volume of solid matrix and the internal kinematic variable of this matrix, which account for the solid compressibility. The fluid is a mixture composed of

several species (j) with molar apparent density n_j and chemical potential μ_j. From the isothermal Gibbs-Duhem equality, fluid pressure p_f is related to n_j and μ_j by:

$$\phi\dot{p}_f - \sum_j n_j\dot{\mu}_j = 0 \qquad (3.5)$$

where ϕ is the porosity. Because the system exchanges moles of species (j) with adjacent systems in the continuum, it is considered as an open thermodynamic system. The first law of thermodynamics (energy balance) can be then written in local rate form as:

$$\dot{E} = \sigma_{ij}\dot{\varepsilon}_{ij} + p\dot{\phi}_m + \sum_j \mu_j\dot{n}_j - q_{k,k} \qquad (3.6)$$

Where q_k is the heat flux vector through the medium (solid and flux phases), representing the heat exchange between the soil element and its surroundings, p is the mean total stress conjugate to the volume rate of solid $\left(\equiv \dot{\rho}_s/\rho_s\right)$ and $\mu_j\dot{n}_j$ is the supplied energy associated with the change in molar content n_j of j species.

The internal energy of the skeleton E_s is defined as the difference between the internal energy of the medium E and the internal energy of the fluid phases: $E_s = E - \left(\sum_j \mu_j n_j - \phi p_f\right)$. From Eq. 3.6, the rate of E_s can be written in terms of pore pressure and porosity:

$$\dot{E}_s = \sigma_{ij}\dot{\varepsilon}_{ij} + p\dot{\phi}_m + p_f\left(\dot{\phi} + \phi v_{i,i}\right) - q'_{k,k} \qquad (3.7)$$

where q'_k is the flux of heat through the solid phase only. When the stiffness of the solid grains is much higher than that of the porous medium (a common figure in Soil Mechanics), the skeleton matrix can be assumed incompressible . Moreover from the mass conservation of skeleton it is known that $\dot{\phi} = -\dot{\varepsilon}_{ii}(1 - \phi)$ which after replacement in Eq. 3.7 leads to:

$$\dot{E}_s = \underbrace{\left(\sigma_{ij} - p_f\delta_{ij}\right)}_{\sigma'_{ij}}\dot{\varepsilon}_{ij} - q'_{k,k} \qquad (3.8)$$

where σ'_{ij} is the Terzaghi's effective stress.

The second law of thermodynamics (dissipation must be positive) is formulated assuming the existence of a state function $\mathfrak{H}$ "the entropy of the porous medium per unit of skeleton mass", such that the rate of entropy production is non-negative. The entropy for the bi-phase medium per unit of skeleton mass is composed of two terms: (a) the entropy of the

_____

solid skeleton $\mathfrak{H}_s$ and (b) the entropy of the fluid phase $\mathfrak{H}_f$ such that $\mathfrak{H} = \mathfrak{H}_s + \phi\omega_f\mathfrak{H}_f$. The term $\omega_f = {}^{\rho_f}\!/_\rho$ is the mass fraction of the fluid phase per unit of skeleton mass.

The local form of the second law of thermodynamics takes then the following form:

$$T\big(\dot{\mathfrak{H}}_s + \phi\omega_f\dot{\mathfrak{H}}_f\big) \geq T\big(\dot{\mathfrak{H}}_{s_r} + \phi\omega_f\dot{\mathfrak{H}}_{f_r}\big) \equiv -T\left(\frac{q'_k}{T}\right)_{,k} = -q'_{k,k} + \frac{q'_k T_{,k}}{T} \tag{3.9}$$

where the subscript r makes reference to the reversible part of entropy given by the rate of entropy supplied to the material element from its surroundings. The rate of entropy production within the element is the irreversible part expressed by the difference between $\big(\dot{\mathfrak{H}}_{s_i} = \dot{\mathfrak{H}}_s - \dot{\mathfrak{H}}_{s_r}\big)$ and $\big(\dot{\mathfrak{H}}_{f_i} = \dot{\mathfrak{H}}_f - \dot{\mathfrak{H}}_{f_r}\big)$, and by virtue of Eq. 3.9 satisfies the inequality:

$$\begin{aligned} d &\equiv T\big(\dot{\mathfrak{H}}_s - \dot{\mathfrak{H}}_{s_r}\big) + T\phi\omega_f\big(\dot{\mathfrak{H}}_f - \dot{\mathfrak{H}}_{f_r}\big) \geq 0 \\ &= T\dot{\mathfrak{H}}_s + T\phi\omega_f\dot{\mathfrak{H}}_f + q_{k,k} - \frac{q'_k T_{,k}}{T} \end{aligned} \tag{3.10}$$

where d is the dissipation function of the porous medium. If the thermal dissipation is neglected Eq. 3.11 reveals that the divergence of the thermal flux corresponds to the reversible part of entropy in both the solid matrix and the fluid phase:

$$q_{k,k} = -\big(T\dot{\mathfrak{H}}_{s_r} + T\phi\omega_f\dot{\mathfrak{H}}_{f_r}\big) \tag{3.11}$$

while the divergence of the heat flux in the solid skeleton only $(q'_{k,k})$ corresponds to the difference between the total heat flux in the medium $q_{k,k}$ and the heat flux of the fluid phases $-T\phi\omega_f\dot{\mathfrak{H}}_{f_r}$.

As for the internal energy, the dissipation of the solid skeleton is defined by the difference between the dissipation of the whole medium and the dissipation of bulk fluid:

$$d_s = d - T\phi\omega_f\dot{\mathfrak{H}}_{f_i} = T\dot{\mathfrak{H}}_s + q'_{k,k} \equiv T\dot{\mathfrak{H}}_{s_i} \geq 0 \tag{3.12}$$

Expressed in this form, the thermodynamics inequality is called Planck's inequality (Truesdell, 1969). In the case in which isothermal deformations are considered, $(T = constant)$, it is convenient to replace the entropy $(\mathfrak{H}_s)$ by the temperature (T) in the expression for the energy function. This can be achieved using the "Legendre transformation" to define the Helmholtz free energy of the porous skeleton, dual to internal energy (E_s) with respect to the entropy $(\mathfrak{H}_s)$:

$$f_s\big(\varepsilon_{ij}, T\big) = E_s - T\mathfrak{H}_s \tag{3.13}$$

As discussed by Houlsby & Puzrin (2000), if the thermal dissipation $q_k T_{,k}/T$ is neglected in Eq. 3.10 (isothermal conditions), the rate form of f_s under isothermal conditions and maximal dissipation yields to:

$$\dot{f}_s = \sigma'_{ij}\dot{\varepsilon}_{ij} - q'_{k,k} = \sigma'_{ij}\dot{\varepsilon}_{ij} - T(\dot{\mathfrak{H}}_s - \dot{\mathfrak{H}}_s^r) = \sigma'_{ij}\dot{\varepsilon}_{ij} - d_s \tag{3.14}$$

or

$$\sigma'_{ij}\dot{\varepsilon}_{ij} = \dot{f}_s + d_s \tag{3.15}$$

The left hand term of Eq. 3.15 expands to $(\sigma_{ij}\dot{\varepsilon}_{ij} + p\dot{\phi})$ for the case of compressible solid phase. In a poroplastic material, the energy dissipation arises from changes in the internal variables, and the skeleton dissipation (d_s) is stated to be a function of those variables. It is then possible to express the rate of Helmholtz energy of the skeleton (f_s) by differentiating with respect to its internal variables:

$$\dot{f}_s + d_s = \frac{\partial f_s}{\partial \varepsilon_{ij}}\dot{\varepsilon}_{ij} + \frac{\partial f_s}{\partial \alpha_{ij}}\dot{\alpha}_{ij} + \frac{\partial d_s}{\partial \dot{\alpha}_{ij}}\dot{\alpha}_{ij} \tag{3.16}$$

By introducing Eq. 3.16 in Eq. 3.15 and collecting terms, the following equation arises:

$$0 = \left(\sigma'_{ij} - \frac{\partial f_s}{\partial \varepsilon_{ij}}\right)\dot{\varepsilon}_{ij} + \left(\frac{\partial f_s}{\partial \alpha_{ij}} + \frac{\partial d_s}{\partial \dot{\alpha}_{ij}}\right)\dot{\alpha}_{ij} \tag{3.17}$$

As the last equation must be satisfied for any combination of $\dot{\varepsilon}_{ij}$ and $\dot{\alpha}_{ij}$ and because the quantities in the brackets are independent of each others, each term at Eq. 3.17 must be equal to zero, yielding the state equation:

$$\sigma'_{ij} = \frac{\partial f_s}{\partial \varepsilon_{ij}} \tag{3.18}$$

and the sufficient condition:

$$\frac{\partial f_s}{\partial \alpha_{ij}} + \frac{\partial d_s}{\partial \dot{\alpha}_{ij}} = 0 \tag{3.19}$$

As discussed by Houlsby & Puzrin (2000). It is moreover assumed that Eq. 3.19 is a necessary condition. This new restriction is not governed by any of the thermodynamic requirements but is simply a constitutive assumption. Comparison between equations 3.12 and 3.19 leads to the definition of the classical generalized stress-like variable in hyperplasticity (Collins & Houlsby, 1997):

$$\tilde{x}_{ij}\left(\equiv \frac{\partial d_s}{\partial \dot{\alpha}_{ij}}\right) = -\frac{\partial f_s}{\partial \alpha_{ij}} \tag{3.20}$$

This variable provides a stress state of the porous skeleton in a shifted space in relation to the traditional true stress space. The advantages of this representation are addressed below and will be used further on the formulation of particular constitutive models developed in chapter 4.

Depending on the physical problem, it can be necessary to express the energy in terms of different intensive variables and thus to consider the Gibbs free energy of the porous medium instead of the Helmholtz energy $\left(g_s = f_s - \sigma'_{ij}\varepsilon_{ij}\right)$.

For an incompressible matrix and a decoupled poro-material Collins (1997) proposed the following form for g_s:

$$g_s(\sigma_{ij}, \alpha_{ij}) = g_{s_1}(\sigma'_{ij}) - \sigma'_{ij}\alpha_{ij} + g_{s_2}(\alpha_{ij}) \qquad (3.21)$$

Equation 3.21 together with the state equation make the strain tensor reads,

$$\varepsilon_{ij} = -\frac{\partial g_s}{\partial \sigma'_{ij}} = \underbrace{-\frac{\partial g_{s_1}}{\partial \sigma'_{ij}}}_{\varepsilon^e_{ij}} + \alpha_{ij} \qquad (3.22)$$

while the complementary state equation allows to derive the expression of the dissipative generalized stress tensor:

$$\tilde{x}'_{ij} = -\frac{\partial g_s}{\partial \alpha_{ij}} = \sigma'_{ij} - \underbrace{\frac{\partial g_{s_2}}{\partial \alpha_{ij}}}_{\rho'_{ij}} \qquad (3.23)$$

where ρ'_{ij} is a function of the internal variables and plays the role of a shift or back stress during kinematical hardening. It is important to note that the back stress does not influence the elastic response. The last equation defines the "fundamental relationship" that relates the generalized stresses x'_{ij} to the true stresses σ'_{ij}.

3.4.1) Dissipation (Orthogonality Principle) and Yield Function

The generalized stress variable $\tilde{x}_{ij}$ defined above at Eq. 3.20 has the character of stress-like due to the fact that $\dot{\alpha}_{ij}$ is a kinematic strain-like variable. Then the dissipation of the solid skeleton can be rewritten as

$$d_s = T\dot{\mathfrak{H}}_i = \tilde{x}_{ij}\dot{\alpha}_{ij} \qquad (3.24)$$

Equation 3.24 reveals a dependency of the dissipation function on the rate of plastic strains. Furthermore, for the class of rate-independent materials the last function is

homogeneous of first order in the rate of internal variables. For this class of functions Euler's second order expansion gives

$$d_{\mathrm{s}} = \frac{\partial d_{\mathrm{s}}}{\partial \dot{\alpha}_{ij}} \dot{\alpha}_{ij} = x_{ij}\dot{\alpha}_{ij} \tag{3.25}$$

Subtracting equations 3.24 and 3.25 leads to

$$0 = \left(\tilde{x}_{ij} - x_{ij}\right) \cdot \dot{\alpha}_{ij} \tag{3.26}$$

Equation 3.26 is geometrically interpreted as an orthogonality between the vectors $\left(\tilde{x}_{ij} - x_{ij}\right)$ and $\dot{\alpha}_{ij}$. Ziegler argue that the difference between $\tilde{x}_{ij}$ and x_{ij} can be assumed as zero leading to

$$\tilde{x}_{ij} = x_{ij} = \frac{\partial d_{\mathrm{s}}}{\partial \dot{\alpha}_{ij}} \tag{3.27}$$

which is read as the generalized stress is perpendicular to the level surface of dissipation d_{s} and established the Ziegler's postulate known as "Orthogonality principle".

This principle has been mentioned above as a restriction to plasticity theory. It has also been remarked that it represents a stricter condition than the second law of thermodynamics because it requires the dissipation to be maximal as well as positive. The property of maximum is more clearly seen if Eq. 3.27 is understood as the result of the extremum problem $\partial/\partial \dot{\alpha}_{ij} \left\{x_{ij}\dot{\alpha}_{ij} - \mathrm{d}_{\mathrm{s}}(\dot{\alpha}_{ij})\right\} = 0$.

From the orthogonality postulate (Eq. 3.27) the generalized stress x_{ij} is defined as the derivative of the skeleton dissipation with regard to the rate of plastic strain $\dot{\alpha}_{ij}$. Exchanging the role between those variables by the Legendre transformation gives rise to another function such that

$$\dot{\alpha}_{ij} = \frac{\partial \mathrm{F}^{y}}{\partial x_{ij}} \quad \text{and} \quad \mathrm{d}_{\mathrm{s}} + \mathrm{F}^{y} = x_{ij}\dot{\alpha}_{ij} \tag{3.28}$$

As mentioned above for the case of rate-independent porous materials the homogeneous degree one character of the dissipation makes the last transformation to be singular. This singularity is mathematically expressed as $\mathrm{F}^{y} = \lambda f^{y}$:

$$\lambda f^{y}\left(x_{ij}\right) = \mathrm{d}\left(\dot{\alpha}_{ij}\right) - x_{ij}\dot{\alpha}_{ij} = 0 \tag{3.29}$$

where λ is an arbitrary non-negative multiplicative constant (plastic multiplier in classical plasticity). The differentiation of the transformed function leads to the plastic flow rule:

$$\dot{\alpha}_{ij} = \lambda \frac{\partial f^y}{\partial x'_{ij}} \tag{3.30}$$

The plastic multiplier scales the magnitude of the plastic strain increment $\dot{\alpha}_{ij}$ and also satisfy the Kuhn-Tucker conditions:

$$\lambda \geq 0; \quad f^y \leq 0; \quad \lambda f^y = 0 \tag{3.31}$$

Then by taking into account the positive character of the skeleton dissipation and replacing the expression for the rate of plastic strain (flow rule) in the Eq. 3.29 the convexity condition for the yield function f^y is obtained,

$$x_{ij} \cdot \frac{\partial f^y}{\partial x'_{ij}} \geq 0 \tag{3.32}$$

where the plastic multiplier has been ignored since $(\gamma \geq 0)$. Equation 3.32 is read in geometric terms as the inner product between x_{ij} and $\frac{\partial f^y}{\partial x_{ij}}$ and says that the angle between both vectors should remain between -90º and 90º, which is the convexity requirement.

3.4.2) Trapped Energy – Hardening Plasticity

As pointed by Collins (2005), the hardening behavior in geo-materials can be explained by thermomechanical developments. In case of isothermal deformation, the energy balance of a porous skeleton is expressed by:

$$L_s = \dot{f}_s + d_s \tag{3.33}$$

Then the possible layouts assumed for f_s will be determinant in the study of plastic hardening.

In this regard time differentiation of Eq. 3.23 leads to the expression for the generalized stress evolution given by two terms: (a) the first coefficient accompanying $\dot{\varepsilon}^e_{ij}$ results in a stiffness moduli which is necessarily independent of $\dot{\alpha}_{ij}$ for decoupled materials, (b) the second coefficient accompanying $\dot{\alpha}_{ij}$ is also independent of $\dot{\varepsilon}^e_{ij}$ for decoupled materials. If those terms are integrated separately, then the integration results in the expressions for the true stress σ'_{ij} and the back-stress ρ'_{ij}, respectively. Furthermore, considering both the validity of the energy separation principle (Ulm & Coussy, 2003) and the assumption for decoupled materials, the integration of Eq. 3.23 leads to an expression for the Helmholtz function of the form, Collins (1997):

$$f_s = f_{s_1}\left(\varepsilon_{ij} - \alpha_{ij}, \varphi_m - \varphi_m^p\right) + f_{s_2}\left(\alpha_{ij}, \varphi_m^p\right) \tag{3.34}$$

or alternatively

$$f_s = f_{s_1}\left(\varepsilon_{ij} - \alpha_{ij}, \varphi_m - \varphi_m^p\right)$$

It is noted that f_{s_2} does not influence the elastic response. With this form of Helmholtz

energy the generalized stress is $x'_{ij} = \sigma'_{ij} - \rho_{ij}\left(\equiv \partial f_{s_2}/\partial \alpha_{ij}\right)$ or $x'_{ij} = \sigma'_{ij}$ for $\left(f_{s_2} = 0\right)$. Both

forms of the energy functions are valid and will define the amount of plastic work dissipated by the solid skeleton once a plastic process has started. From the last two equations, Eq. 3.33 and Eq. 3.34, the rate of total work of a porous skeleton medium can be written as:

$$L_s = L_s^e + L_s^p = \dot{f}_{s_1}\left(\varepsilon_{ij} - \alpha_{ij}, \varphi_m - \varphi_m^p\right) + \dot{f}_{s_2}\left(\alpha_{ij}, \varphi_m^p\right) + d_s\left(\dot{\alpha}_{ij}, \dot{\varphi}_m^p\right) \tag{3.35}$$

or alternatively for $f_{s_2} = 0$:

$$L_s = L_s^e + L_s^p = \dot{f}_{s_1}\left(\varepsilon_{ij} - \alpha_{ij}, \varphi_m - \varphi_m^p\right) + d_s\left(\dot{\alpha}_{ij}, \dot{\varphi}_m^p\right)$$

By cancelling out the elastic contribution at Eq. 3.35 and simplifying it to an incompressible solid phase, it reads:

$$L_s^p = \underbrace{\dot{f}_{s_2}\left(\alpha_{ij}\right)}_{\rho'_{ij}} + d_s\left(\dot{\alpha}_{ij}\right) \tag{3.36}$$

or alternatively for $f_{s_2} = 0$:

$$L_s^p = d_s\left(\dot{\alpha}_{ij}\right)$$

Equation 3.36a expresses that the rate of plastic work in the porous medium is given by the sum of the energy dissipated and the plastic stored energy depending on internal variables. The last energy can be positive or negative (unlike the dissipation energy d_s). Equation 3.36b says that the rate of plastic work in the porous medium coincides with the energy dissipated, so all the plastic work is dissipated $\left(f_{s_2} = 0\right)$.

Physically the last terms of the energy functions account for the trapped (or stored) energy that can be positive or negative and depicted the current state of kinematic hardening of the soil when $\left(f_{s_2} \neq 0\right)$. During a loading cycle the trapped energy is first stored and then recovered giving rise to the "kinematic hardening" of a material.

Table 3.4 summarizes the layout of both the energy functions and the dissipation functions when: (a) it is assumed that part of the plastic work is stored and another part is dissipated and (b) all plastic work is assumed to be dissipated.

Table 3.4: Layout of energy and dissipation functions according to the model's hardening

Hardening	Energy Function		Shift-stress	Dissipation Function
Kinematic	Gibbs: $$g_s = g_{s_1}(\sigma'_{ij}, p) - (\sigma'_{ij}\alpha_{ij} + p\sigma'_{ij}) + g_{s_2}(\alpha_{ij}, \varphi^p_m)$$		$$\rho_{ij} = \frac{\partial g_{s_2}}{\partial \alpha_{ij}}$$ $$\rho_p = \frac{\partial g_{s_2}}{\partial \varphi^p_m}$$	Critical state model (deformable solid phase): $$d_s = d_{s_1}(\dot{\alpha}_{ij}, \dot{\varphi}^p_m, \alpha_p)$$
	Helmholtz: $$f_s = f_{s_1}(\varepsilon_{ij} - \alpha_{ij}, \varphi_m - \varphi^p_m) + f_{s_2}(\alpha_{ij}, \varphi^p_m)$$		$$\rho_{ij} = \frac{\partial f_{s_2}}{\partial \alpha_{ij}}$$ $$\rho_p = \frac{\partial f_{s_2}}{\partial \varphi^p_m}$$	
Isotropic	Gibbs: $$g_s = g_{s_1}(\sigma'_{ij}, p) - (\sigma'_{ij}\alpha_{ij} + p\varphi^p_m)$$ with $\quad g_{s_2} = 0$		$$\rho_{ij} = 0$$ $$\rho_p = 0$$	Critical state model (deformable solid phase): $$d_s = d_{s_1}\left(\dot{\alpha}_{ij}, \dot{\varphi}^p_m, \alpha_p\right) + d_{s_2}(\dot{\alpha}_p, \alpha_p)$$
	Helmholtz: $$f_s = f_{s_1}(\varepsilon_{ij} - \alpha_{ij}, \phi_m - \varphi^p_m)$$ with $\quad f_{s_2} = 0$		$$\rho_{ij} = 0$$ $$\rho_p = 0$$	

3.5) Thermodynamics of Three-phase Media (Mechanical Part)

Three-phase porous media are composed by a solid matrix and two fluids that fill the porous space (water and air). The modeling of their behaviour requires to account for both the effects of the two fluid pressures and the thermo-hydro-mechanical couplings associated with the surface tension developed at the contact surfaces "fluid-fluid" and "fluid-solid" (Coussy O. , 2004).

Ascribing E_s as the specific energy of the porous skeleton (energy per unit mass of skeleton), E_l as the specific energy of the liquid phase (energy per unit mass of skeleton) and E_g as the specific energy of the gas phase (energy per unit mass of skeleton), the internal energy of the porous medium is:

$$\widetilde{E} = \rho E_s + \phi_l w_l \rho E_l + \phi_g w_g \rho E_g \tag{3.37}$$

where $w_k = \rho_k/\rho$. Eq. 3.37 expressed per unit mass of skeleton (known as dry density in soil mechanics) is:

$$\underbrace{\frac{\widetilde{E}}{\rho}}_{E} = E_s + \phi_l w_l E_l + \phi_g w_g E_g \tag{3.38}$$

It is noted that the internal energy of the porous skeleton not only accounts for the solid matrix but also for the interfaces exerted by the interactions between solid, air and liquid,

$$\widetilde{E}_s = \rho E_m + \phi\rho \sum_{kl} E_i^{kl} = \rho E_m + \phi\rho E_i \tag{3.39}$$

where E_m is the specific energy of the solid per unit mass of skeleton and E_i is the interface energy per unit mass of skeleton. Eq. 3.39 expressed per unit of skeleton mass leads to:

$$\underbrace{\frac{\widetilde{E}_s}{\rho}}_{E_s} = E_m + \phi \sum_{kl} E_i^{kl} = E_m + \phi E_i \tag{3.40}$$

Under the assumption of small strain, the internal energy of partially saturated porous continuum E admits as natural arguments: (a) the strain tensor ε_{ij}, (b) the mass concentration of each fluid m_{fj}, (c) the entropy of the skeleton $\mathfrak{H}_s$ and (d) the interval kinematic variables (α_{ij}, α_l). Through the Gibbs-Duhem equality, mass concentration of the different species within one fluid may be interchanged with the partial pressure of the fluid, through the equation:

$$\varphi_j \dot{p}_j - \sum_i n_{ij} \dot{\mu}_{ij} = 0 \tag{3.41}$$

where p_j is the partial pressure of the fluid (j), n_{ij} the molar density and μ_{ij} the molar chemical potential for the specie (i) in fluid (j). Furthermore, φ_j is the fluid porous volume of fluid j which evolves as variations of molar density of the fluid j are produced.

Because the system exchanges moles of species j with adjacent systems in the continuum, it is considered as an open thermodynamic system. The first law of thermodynamics (energy balance) can be then written in local rate form as:

$$\dot{E} = \sigma_{ij}\dot{\varepsilon}_{ij} + \sum_j \sum_i \mu_{ij}\dot{n}_{ij} - q_{k,k} \tag{3.42}$$

where q_k is the heat flux vector through the medium (solid and flux phases), representing the heat exchange between the soil element and its surroundings, and $\mu_{ij}\dot{n}_{ij}$ is the supplied energy associated with the change in molar content n_{ij} of i species in the fluid j.

The internal energy of the skeleton E_s is defined as the difference between the internal energies of both the medium E and the fluid phases, in addition to the fluid pressures acting on the internal walls of the skeleton

$$
\begin{aligned}
E_s &= E - \left(\phi_l w_l E_l - \varphi_l p_l + \phi_g w_g E_g - \varphi_g p_g \right) \\
&= E - \left[\sum_j \left(\sum_i \mu_{ij} n_{ij} - \varphi_j p_j \right) \right]
\end{aligned}
\tag{3.43}
$$

Then from Eqs. 3.42-3.43, the rate of E_s becomes expressed in terms of partial pore pressures and porosity:

$$
\begin{aligned}
\dot{E}_s &= \sigma_{ij}\dot{\varepsilon}_{ij} + p_l\dot{\varphi}_l + p_g\dot{\varphi}_g - q'_{k,k} \\
&= \sigma_{ij}\dot{\varepsilon}_{ij} + p_l\left(\dot{\phi}_l + \phi_l v_{i,i}\right) + p_g\left(\dot{\phi}_g + \phi_g v_{i,i}\right) - q'_{k,k}
\end{aligned}
\tag{3.44}
$$

where q'_k is the flux of heat through the solid phase only and the partial pressures p_l and p_g are the pressures exerted by the liquid and the gas phases respectively and ϕ_j is the j's fluid porous volume which evolves as variations of molar density and solid velocity. The term $\phi_k v_{i,i}$ accounts for the rate of porous volume exerted by the fluid k under solid velocity.

If the result from the compatibility relation for the mass balance of solid $v_{i,i} = -\dot{\varepsilon}_{ii}$ is considered the rates of fluid porous volume $\dot{\phi}_j$ are given by the expressions:

$$
\begin{aligned}
\dot{\phi}_l &= \phi\dot{S}_l - S_l\dot{\varepsilon}_{ii} + \phi S_l\dot{\varepsilon}_{ii} \\
\dot{\phi}_g &= -\phi\dot{S}_l - (1-S_l)\dot{\varepsilon}_{ii} + \phi(1-S_l)\dot{\varepsilon}_{ii}
\end{aligned}
\tag{3.45}
$$

replacing the last relations for the rate of porous volume in Eq. 3.44 leads to the expression for the rate of internal energy of the solid skeleton in terms of strain rate, saturation rate and the heat flux exerted at the solid phase,

$$
\dot{E}_s = \sigma_{ij}\dot{\varepsilon}_{ij} + p_l\left(\phi\dot{S}_l - S_l\dot{\varepsilon}_{ii}\right) + p_g\left(-\phi\dot{S}_l - (1-S_l)\dot{\varepsilon}_{ii}\right) - q'_{k,k}
\tag{3.46}
$$

From all the possible linear combinations of the terms at the last expression there are two which are commonly used in soil mechanics. The first combination leads to the set of constitutive variables used by the constitutive models BBM (Alonso, Gens, & Josa, 1990) and BBMW (Vaunat, Romero, & Jomi, 2000):

$$
\dot{E}_s = \Big(\underbrace{\sigma_{ij} - p_g \cdot \delta_{ij}}_{\sigma''_{ij}} \Big) \cdot \dot{\varepsilon}_{ij} - \Big(\underbrace{p_g - p_l}_{s} \Big) \Big(\underbrace{-\dot{\varepsilon}_{ii}S_l - \phi\dot{S}_l}_{-\dot{\varepsilon}_w} \Big) - q'_{k,k}
\tag{3.47}
$$

where $\sigma_{ij}{}''$ is the net stress and $\varepsilon_w = -\dot{\phi}_l$ is the hydraulic strain. The first term at the right hand side of Eq. 3.47 is the power input to deform the porous skeleton while the second term on this side represents the power input to change the saturation degree of such skeleton. The expression also shows that the work conjugated to suction is $\dot{\varepsilon}_w$.

Alternatively, the energy balance of the porous skeleton can be linearly re-combined leading to the set of constitutive variables used at the constitutive model proposed by Gallipoli (2003):

$$\dot{E}_s = \left(\underbrace{\sigma_{ij} - \left(p_g + S_l(p_g - p_l) \right) \cdot \delta_{ij}}_{\sigma'_{ij}} \right) \cdot \dot{\varepsilon}_{ij} - \phi \left(\underbrace{p_g - p_l}_{s} \right) \dot{S}_l - q'_{k,k} \tag{3.48}$$

where $\sigma_{ij}{}'$ is a particularization of Bishop effective stress where parameter χ is equal to the degree of liquid saturation.

In a three-phase medium, dissipation *d* occurs in the solid skeleton in the fluid phases and at the interface between phases. Furthermore, the existence of a state specific entropy function is assumed in such a way that the rate of entropy production is non-negative. Denoting $\mathfrak{H}_s$, $\mathfrak{H}_j$ and $\mathfrak{H}_i^{kl}$ as the entropy of the solid skeleton, the entropy of fluid j and the entropy of interface between phases k and l per unit volume of porous medium respectively, the specific entropy of the porous medium per unit mass of skeleton is $\mathfrak{H} = \mathfrak{H}_s + \phi \sum \mathfrak{H}_i^{kl} + \sum \omega_j \mathfrak{H}_j \phi$.

Then the local form of second law of thermodynamics can be expressed,

$$T \cdot \left(\dot{\mathfrak{H}}_s + \phi \sum_{kl} \dot{\mathfrak{H}}_i^{kl} + \sum_j \omega_j \phi \dot{\mathfrak{H}}_j \right) \geq T \cdot \left(\dot{\mathfrak{H}}_{s_r} + \phi \sum_{kl} \dot{\mathfrak{H}}_{i_r}^{kl} + \sum_j \omega_j \phi \dot{\mathfrak{H}}_{j_r} \right) \tag{3.49}$$

$$\equiv -T \left(\frac{q_k}{T} \right)_{,k} = -q_{k,k} + \frac{q_k T_{,k}}{T}$$

where $\omega_j = {\rho_j}/{\rho}$ is the mass fraction of the fluid phase j per unit of skeleton mass and the subscript r at the right hand side refers to the reversible part of the rate of entropy. It is the rate of entropy supplied to the material element from its surrounding. The rate of entropy production within the porous element corresponds to the irreversible part of the entropy. This irreversible part of the entropy defines the dissipation *d* of the porous medium which should satisfy the inequality,

$$d \quad \equiv \quad T(\dot{\mathfrak{H}}_s - \dot{\mathfrak{H}}_{s_r}) + \phi T(\dot{\mathfrak{H}}_i - \dot{\mathfrak{H}}_{i_r}) + \sum_j T\omega_j \phi(\dot{\mathfrak{H}}_j - \dot{\mathfrak{H}}_{j_r}) \geq 0 \qquad (3.50)$$

$$= \quad T\dot{\mathfrak{H}}_s + \phi T\dot{\mathfrak{H}}_i + \sum_j T\omega_j \phi \dot{\mathfrak{H}}_j + q_{k,k} - \frac{q_k T_{,k}}{T}$$

If the thermal dissipation is neglected Eq. 3.50 reveals that the divergence of the thermal flux corresponds to the reversible part of entropy in both the bulk phases and the interfaces:

$$q_{k,k} = -\left(T\dot{\mathfrak{H}}_{s_r} + \phi T\dot{\mathfrak{H}}_{i_r} + \sum_j T\omega_j \phi \dot{\mathfrak{H}}_{j_r} \right) \qquad (3.51)$$

while the divergence of the heat flux in the solid skeleton only ($q'_{k,k}$) corresponds to the difference between the total heat flux in the medium $q_{k,k}$ and the heat flux of the fluid phases $-\sum_j T\omega_j \phi \dot{\mathfrak{H}}_{j_r}$.

As for the energy, the entropy of solid skeleton is defined by the difference between the entropy of the whole medium and the entropies of bulk fluid phases, then the skeleton dissipation reads:

$$d_s = d - \sum_j T\omega_j \phi \dot{\mathfrak{H}}_{j_i} = T\dot{\mathfrak{H}}_s + \phi T\dot{\mathfrak{H}}_i + q'_{k,k} \equiv T\dot{\mathfrak{H}}_{s_i} + \phi T\dot{\mathfrak{H}}_{i_i} \geq 0 \qquad (3.52)$$

where $\dot{\mathfrak{H}}_{s_i}$ is the rate of the irreversible part of soil skeleton entropy and $\dot{\mathfrak{H}}_{i_i}$ is the rate of the irreversible part of interface skin entropy. From Eq. 3.52 it appears that the skeleton dissipation d_s represents the rate of entropy production within a skeleton element of the three-phase porous medium and should satisfy the inequality of being always positive.

Having defined the expressions of both the internal energy and the dissipation for the porous medium and under the consideration of a thermodynamic open system, both the expression of the internal energy and the dissipation for the porous skeleton are obtained by: (a) replacing the contributions of the fluid mass concentration to those energies and applying the corresponding partial pressures and (b) extracting the heat flux through the fluids phases. Those findings together with the assumption of validity of the "orthogonality condition" introduced by Ziegler (1977) promote the introduction of the term "Hyper-poro-plasticity" as formal basis for the formulation of constitutive models of porous media which exhibit different phases.

Going forward with the study, when isothermal conditions prevail, it is convenient to replace the entropy $\mathfrak{H}_s$ by the temperature T in the expression of the energy function by using the corresponding Legendre transformation. It results in the expression for the

Helmholtz free energy of the porous skeleton, dual to the internal energy E_s with respect to entropies $\mathfrak{H}_s$ and $\mathfrak{H}_i$:

$$f_s(\varepsilon_{ij}, T) = E_s - T(\mathfrak{H}_s + \phi\mathfrak{H}_i) \tag{3.53}$$

Taking into account Eq. 3.48 and Eq. 3.52 and again assuming isothermal conditions, the rate of f_s can be expressed as:

$$\dot{f}_s = \sigma'_{ij}\dot{\varepsilon}_{ij} - \phi s \dot{S}_l - T(\dot{\mathfrak{H}}_s + \phi\dot{\mathfrak{H}}_i) - q'_{k,k} \tag{3.54}$$
$$= \sigma'_{ij}\dot{\varepsilon}_{ij} - \phi s \dot{S}_l - T(\dot{\mathfrak{H}}_{s_i} + \phi\dot{\mathfrak{H}}_{i_i})$$

The last equation can be rearranged to give,

$$\sigma'_{ij}\dot{\varepsilon}_{ij} - \phi s \dot{S}_l = \dot{f}_s + d_s \tag{3.55}$$

In a poroplastic material, energy is dissipated during changes in the internal variables and the dissipation d_s is stated to be a function of them. Differentiating f_s and d_s with respect to the different variables leads to:

$$\dot{f}_s + d_s = \frac{\partial f_s}{\partial \varepsilon_{ij}}\dot{\varepsilon}_{ij} + \frac{\partial f_s}{\partial S_l}\dot{S}_l + \frac{\partial f_s}{\partial \alpha_{ij}}\dot{\alpha}_{ij} + \frac{\partial f_s}{\partial \alpha_l}\dot{\alpha}_l + \frac{\partial d_s}{\partial \dot{\alpha}_{ij}}\dot{\alpha}_{ij} + \frac{\partial d_s}{\partial \alpha_l}\dot{\alpha}_l \tag{3.56}$$

Combining Eq. 3.55 and Eq. 3.56 and collecting terms leads to the expression:

$$0 = \left(\sigma'_{ij} - \frac{\partial f_s}{\partial \varepsilon_{ij}}\right)\dot{\varepsilon}_{ij} - \left(\phi s + \frac{\partial f_s}{\partial S_l}\right)\dot{S}_l - \left(\frac{\partial f_s}{\partial \alpha_{ij}} + \frac{\partial d_s}{\partial \dot{\alpha}_{ij}}\right)\dot{\alpha}_{ij} - \left(\frac{\partial f_s}{\partial \alpha_l} + \frac{\partial d_s}{\partial \dot{\alpha}_l}\right)\dot{\alpha}_l \tag{3.57}$$

This equation must be satisfied for any combination of the variables $\dot{\varepsilon}_{ij}$, $\dot{S}_l$, $\dot{\alpha}_{ij}$ and $\dot{\alpha}_l$ since the quantities within the brackets are independent of each other. Each term of Eq. 3.57 should thus be equal to zero, leading to the state equations:

$$\sigma'_{ij} = \frac{\partial f_s}{\partial \varepsilon_{ij}} \quad ; \quad \phi s = -\frac{\partial f_s}{\partial S_l} \tag{3.58}$$

and the sufficient conditions:

$$\frac{\partial f_s}{\partial \alpha_{ij}} + \frac{\partial d_s}{\partial \dot{\alpha}_{ij}} = 0 \quad ; \quad \frac{\partial f_s}{\partial \alpha_l} + \frac{\partial d_s}{\partial \dot{\alpha}_l} = 0 \tag{3.59}$$

As for the two-phase media, conditions given by Eq. 3.59 are assumed to be also necessary conditions since they are not governed by any thermodynamics requirement but are simply constitutive equations. The generalized dissipative stress-like variables are defined by:

$$x'_{ij} = \frac{\partial d_s}{\partial \dot{\alpha}_{ij}} = -\frac{\partial f_s}{\partial \alpha_{ij}} \tag{3.60}$$

$$\phi x_s = -\frac{\partial d_s}{\partial \dot{\alpha}_l} = \frac{\partial f_s}{\partial \alpha_l}$$

Alternatively ε_{ij}, S_l, x'_{ij} and x_s can be derived from the Gibbs free energy $g_s(\sigma'_{ij}, \phi s, \alpha_{ij}, \alpha_l)$. In fact applying the proper Legendre transformation $g_s = \sigma'_{ij}\varepsilon_{ij} + \phi s S_l + x'_{ij}\alpha_{ij} + x_s\alpha_l - f_s$ the Gibbs energy for the uncompressible and decouple poro-material is obtained. If, additionally the decomposition proposed by Collins (1997) is assumed for g_s:

$$g_s = g_{s_1}(\sigma'_{ij}, \phi s) - \sigma'_{ij}\alpha_{ij} + \phi s \alpha_l + g_{s_2}(\alpha_{ij}, \alpha_l) \tag{3.61}$$

the strain tensor and the degree of saturation are obtained from the state equations:

$$\varepsilon_{ij} = -\frac{\partial g_s}{\partial \sigma'_{ij}} = \underbrace{-\frac{\partial g_{s_1}}{\partial \sigma_{ij}}}_{\varepsilon^e_{ij}} + \alpha_{ij} \tag{3.62}$$

$$S_l = \frac{\partial g_s}{\partial \phi s} = \underbrace{\frac{\partial g_{s_1}}{\partial \phi s}}_{S^e_l} + \alpha_l$$

while the complementary state equations allow to derive the expressions for the dissipative generalized stress and the dissipative suction:

$$x'_{ij} = -\frac{\partial f_s}{\partial \alpha_{ij}} = -\frac{\partial g_s}{\partial \alpha_{ij}} = \sigma'_{ij} - \underbrace{\frac{\partial g_{s_2}}{\partial \alpha_{ij}}}_{\rho'_{ij}} \tag{3.63}$$

$$x_s = \frac{\partial f_s}{\partial \alpha_l} = \frac{\partial g_s}{\partial \alpha_l} = \phi s + \underbrace{\frac{\partial g_{s_2}}{\partial \alpha_l}}_{-\rho_s}$$

where ρ'_{ij} is a function of the internal variable α_{ij} and plays the role of a shift (or back) stress, $-\rho_s$ is function of the internal variable α_l and acts as shift suction, providing the material with hydro-mechanical kinematical hardening. It is important to note that the back suction does not influence the elastic response. Equation 3.56 defines the "fundamental relationship" that links the generalized "effective" suction x_s and the true "effective" suction ϕs by the shift (or back) suction ρ_s.

_____

3.5.1) Interface Energy (Suction curve Model)

The Helmholtz free energy of the porous skeleton includes the energy of the skeleton and the energy of the interfaces between the different components, "fluid-fluid" and "solid-fluid" Coussy (2004). The additive character of energy functions allows writing the Helmholtz energy as:

$$f_s = f_{\bar{s}} - \phi f_i \tag{3.64}$$

where $f_{\bar{s}}$ represents the free energy of the solid skeleton while f_i is the overall interfacial energy developed per unit of porous volume. In the simple case where $f_{\bar{s}}$ is independent of the degree of saturation, the current suction is computed as:

$$\phi s = -\frac{\partial f_s}{\partial S_l} = \frac{\partial \phi f_i}{\partial S_l} \tag{3.65}$$

Under the assumptions of isothermal condition and non-deformable porous skeleton, f_i depends only on S_l and the suction s is directly the derivative of the interface energy with respect to the degree of saturation. In the case of deformable porous media, because interface menisci force depends on pore size, f_i depends both on S_l and ϕ:

$$f_s(\varepsilon_{ij}, S_l) = f_{\bar{s}}(\varepsilon_{ij}) - \phi f_i(S_l, \phi) \tag{3.66}$$

In order to identify a possible function for $f_i(S_l, \phi)$ a dimensional analysis was proposed by Coussy & Fleureau (2002) in which a certain length (l) was introduced to scale the porous volume according to $(\phi dA = l^3)$, so that:

$$\frac{\dot{\phi}}{\phi} = 3\frac{\dot{l}}{l} \tag{3.67}$$

Additionally, the dimensional analysis results in the relationship:

$$E_i = \frac{\gamma_{l,g}}{l} f\left(\frac{l_j}{l}\right) \tag{3.68}$$

where $\gamma_{l,g}$ is the surface tension liquid-gaz. Equation 3.68 relates the free energy of the interface E_i to the quotient between characteristic length l_j that describes the geometry of the porous network filled by phase j and l. The former length can be removed by differentiating Eq. 3.68:

$$\frac{\dot{E}_i}{E_i} = -\frac{\dot{l}}{l} \tag{3.69}$$

Replacing the length l by the porosity ϕ from Eq. 3.67 in Eq. 3.69 and by integrating the differential equation lead to an expression for the internal energy $E_i(S_l, \phi)$:

$$E_i = -\phi^{(-1/3)} E_i^u(S_l) \tag{3.70}$$

where $E_i^u(S_l)$ is the interface energy in the case in which the solid skeleton is undeformable. According to Eq. 3.70, the internal energy of the air-liquid interface in a deformable porous medium is equal to that stored in a non-deformable medium multiplied by a function of porosity. For non-isothermal conditions the interface free energy depends additionally on interface entropy $\mathfrak{H}_i$, according to the expression:

$$E_i = -\phi^{(-1/3)} E_i^u(S_l, \mathfrak{H}_i) \tag{3.71}$$

The interface energy can alternatively be expressed as function of temperature T instead of the entropy $\mathfrak{H}_i$ through the Legendre transformation$(f_i = E_i - T\mathfrak{H}_i)$. It results in the following expression for the Helmholtz free energy of the deformable porous skeleton:

$$
\begin{aligned}
f_s(\varepsilon_{ij}, S_l) &= f_{\bar{s}}(\varepsilon_{ij}) + \phi \left(\underbrace{\phi^{(-1/3)} f_i^u(S_l, T)}_{f_i^u(S_l, T, \phi)} \right) \\
&= f_{\bar{s}}(\varepsilon_{ij}) + \phi^{(2/3)} f_i^u(S_l, T)
\end{aligned}
\tag{3.72}
$$

Finally, suction is derived from Eq. 3.72 through the state equation:

$$\phi s = -\frac{\partial f_s}{\partial S_l} \equiv s = \underbrace{-\phi^{(-1/3)} \frac{\partial f_i^u}{\partial S_l}}_{WRC(S_l)} \tag{3.73}$$

Eq. 3.73 states the relationship existing between suction and degree of saturation at constant volume, called the water retention curve WRC(S_l). From Eq. 3.71 it comes out that:

$$\frac{1}{\phi} \frac{\partial E_i}{\partial S_l} = -\phi^{(-1/3)} \frac{\partial E_i^u}{\partial S_l} = WRC(S_l) \tag{3.74}$$

The interface energy in a deformable medium can thus be determined as the integral of the Water Retention Curve.

3.5.2) Different thermodynamic potentials in three-phase porous media

For the case of decoupled poro-materials and under isothermal conditions, several alternatives of energy potential functions can be formulated, all of them linked by the interchange of extensive and intensive variables through total or partial Legendre transformation. The potentials based on the natural variables $(\sigma'_{ij}, \alpha_{ij}, s, \alpha_l, T)$, $(\varepsilon_{ij}, \alpha_{ij}, s, \alpha_l, T)$, $(\varepsilon_{ij}, \alpha_{ij}, S_l, \alpha_l, T)$, $(\sigma'_{ij}, \alpha_{ij}, S_l, \alpha_l, T)$, and $(\sigma'_{ij}, x'_{ij}, s, x_s, T)$ are of particular interest for the formulation of thermo-hydro-mechanical constitutive models.

The potential based on the set of variables $(\sigma'_{ij}, \alpha_{ij}, s, \alpha_l, T)$ is the Gibbs free energy. As for any energy potential, it sums up the terms of bulk solid matrix and gas-liquid interfaces:

$$g_s = \underbrace{\left[g_{\bar{s}_1}(\sigma'_{ij}) - \phi g_{i_1}(\phi s)\right]}_{g_{s_1}} - \sigma'_{ij}\alpha_{ij} + \phi s \alpha_l + \underbrace{\left[g_{\bar{s}_2}(\alpha_{ij}) - \phi g_{i_2}(\alpha_l)\right]}_{g_{s_2}} \tag{3.75}$$

The first term within brackets on the right-hand side of Eq. 3.75 corresponds to the elastic free energy while the second term is due to dissipation in presence of kinematic hardening.

The potential based on the set of variables $(\varepsilon_{ij}, \alpha_{ij}, s, \alpha_l, T)$ is obtained by applying the partial Legendre transform on the Helmholtz free energy in order to exchange the hydraulic variable (S_l or ϕ_l) by suction. This potential is denoted f_s^g and is expressed through the transformation $f_s^g = g_s + \sigma'_{ij}\varepsilon_{ij}$. Within the theory of hyperporoplasticity, this potential is the sum of an elastic part, dependent only on elastic strain and reversible change in volumetric water content (or degree of saturation) and a dissipative term in presence of mechanical and hydraulic kinematical hardenings:

$$f_s^g = \underbrace{\left[f_{\bar{s}_1}(\varepsilon_{ij} - \alpha_{ij}) - \phi g_{i_1}(\phi s)\right]}_{f_{s_1}^g} + \phi s \alpha_l + \underbrace{\left[g_{\bar{s}_2}(\alpha_{ij}) - \phi f_{i_2}(\alpha_l)\right]}_{f_{s_2}^g} \tag{3.76}$$

The potential based on the first set of variables $(\varepsilon_{ij}, \alpha_{ij}, S_l, \alpha_l, T)$ is the Helmholtz free energy that sums up the terms of bulk solid skeleton and gas-liquid interfaces:

$$f_s = \underbrace{f_{\bar{s}_1}(\varepsilon_{ij} - \alpha_{ij}) - \phi f_{i_1}(S_l - \alpha_l)}_{f_{s_1}} + \underbrace{\left[f_{\bar{s}_2}(\alpha_{ij}) - \phi f_{i_2}(\alpha_l)\right]}_{f_{s_2}} \tag{3.77}$$

_____

The first term within brackets on the right-hand side of Eq. 3.77 corresponds to the elastic free energy while the second term is due to dissipation in presence of kinematic hardening.

The potential based on the set of variables $(\sigma'_{ij}, \alpha_{ij}, S_l, \alpha_l, T)$ is obtained by applying a partial Legendre transform on the Helmholtz free energy in order to exchange strain by stress only. This potential is denoted as g_s^f and is expressed by $g_s^f = f_s - \sigma'_{ij}\varepsilon_{ij}$. It can be decomposed within the theory of hyperporoplasticity into:

$$g_s^f = \underbrace{\left[g_{\bar{s}_1}(\sigma'_{ij}) - \phi f_{i_1}(S_l - \alpha_l)\right]}_{g_{s_1}^f} - \sigma'_{ij}\alpha_{ij} + \underbrace{\left[f_{\bar{s}_2}(\alpha_{ij}) - \phi f_{i_2}(\alpha_l)\right]}_{g_{s_2}^f} \qquad (3.78)$$

Finally, the potential based on the set of variables $(\sigma'_{ij}, x'_{ij}, s, x_s, T)$ is the Legendre transformation of the Gibbs free energy obtained by exchanging the internal variable α_{ij} and α_l with their intensive counterpart x_{ij} and x_s:

$$\tilde{g}_s = g_s + x'_{ij}\alpha_{ij} - x_s\alpha_l \qquad (3.79)$$

therefore it is decomposed into:

$$\tilde{g}_s = \underbrace{g_{\bar{s}_1}(\sigma'_{ij}) - \phi g_{i_1}(\phi s)}_{\tilde{g}_{s_1}} + \underbrace{\left[\tilde{g}_{\bar{s}_2}(x'_{ij}) - \phi\tilde{g}_{s_2}(x_l)\right]}_{\tilde{g}_{s_2}} \qquad (3.80)$$

In spite of the decoupled assumption, experimental evidences show that it is not always valid. In particular Alonso et.al. (1990) presented a dependency of the hardening parameter on suction for modeling a partial saturated medium using the BBM model. Thus, in this respect the Gibbs energy for hyperporoplastic medium presents the layout:

$$g_s = g_{s_1}(\sigma'_{ij}, \phi s) - \sigma'_{ij}\alpha_{ij} + \phi s\alpha_l + g_{s_2}(\alpha_{ij}, \alpha_l, \sigma'_{ij}, \phi s) \qquad (3.81)$$

where the hysteretic response of the capillary curve is considered. However not all the poro-materials present such a response, in this case the function layout is simplified to,

$$g_s = g_{s_1}(\sigma'_{ij}) - \sigma'_{ij}\alpha_{ij} + g_{s_2}(\alpha_{ij}, \sigma'_{ij}, \phi s) \qquad (3.82)$$

These energy functions provide the bases for the derivation of elasto-plastic models for partially saturated soils presented in Chapter 4. The state equations derived from these different expressions of the energy are summarized in Table 3.5.

Table 3.5: Summary of state equation for hyperplasticity in three-phase porous media using Bishop effective stress (with $\chi = S_l$).

Effective stress tensor	Strain tensor
$$\sigma'_{ij} = \frac{\partial f_s}{\partial \varepsilon_{ij}} = \frac{\partial f_s^g}{\partial \varepsilon_{ij}}$$	$$\varepsilon_{ij} = -\frac{\partial g_s}{\partial \sigma'_{ij}} = -\frac{\partial g_s^f}{\partial \sigma'_{ij}}$$
Effective suction	Degree of saturation
$$\phi s = -\frac{\partial f_s}{\partial S_l} = -\frac{\partial g_s^f}{\partial S_l}$$	$$S_l = \frac{\partial f_s^g}{\partial \phi s} = \frac{\partial g_s}{\partial \phi s}$$
Generalized stress tensor	Plastic strain tensor
$$x'_{ij} = -\frac{\partial f_s}{\partial \alpha_{ij}} = -\frac{\partial f_s^g}{\partial \alpha_{ij}} = -\frac{\partial g_s^f}{\partial \alpha_{ij}} = -\frac{\partial g_s}{\partial \alpha_{ij}}$$ $$x'_{ij} = \frac{\partial d_s}{\partial \dot{\alpha}_{ij}}$$	$$\alpha_{ij} = \frac{\partial \tilde{g}_s}{\partial x'_{ij}}$$ $$\dot{\alpha}_{ij} = \dot{\lambda}\frac{\partial f^y}{\partial x'_{ij}}$$
Generalized suction	Plastic degree of saturation
$$x_s = \frac{\partial f_s}{\partial \alpha_l} = \frac{\partial f_s^g}{\partial \alpha_l} = \frac{\partial g_s^f}{\partial \alpha_l} = \frac{\partial g_s}{\partial \alpha_l}$$ $$x_s = \frac{\partial d_s}{\partial \dot{\alpha}_l}$$	$$\alpha_l = \frac{\partial \tilde{g}_s}{\partial x_s}$$ $$\dot{\alpha}_l = \dot{\lambda}\frac{\partial f^y}{\partial x_s}$$

3.5.3) **Alternative formulation using net stress and suction**

An alternative formulation can be derived if Eq. 3.47 is used instead of Eq. 3.48. In this case, the work conjugated variables are the net stresses – conjugated to strains – and the suction – conjugated to the hydraulic strain. Following the same developments as for the pair (effective stress σ'_{ij}, effective suction ϕs), different rates of energy functions can be derived, each one associated to a state equation. They are summarized in Table 3.6.

Table 3.6: Summary of energy functions and state equations for hyperplasticity in three-phase porous media using net stresses.

Rate of internal energy
$$\dot{E}_s = \sigma''_{ij}\,\dot{\varepsilon}_{ij} + s\dot{\varepsilon}_w - q'_{k,k}$$
Rate of Helmholtz free energy (non-isothermal)
$$\dot{f}_s = \sigma''_{ij}\dot{\varepsilon}_{ij} + s\dot{\varepsilon}_w - (\mathfrak{H}_s + \phi\mathfrak{H}_i)\dot{T} - d_s$$
Rate of Gibbs free energy (non-isothermal)

$$\dot{g}_s = -\dot{\sigma}_{ij}^{''}\varepsilon_{ij} - \dot{s}\varepsilon_w - (\mathfrak{H}_s + \phi\mathfrak{H}_i)\dot{T} - d_s$$

Net stress tensor	Strain tensor
$$\sigma_{ij}^{''} = \frac{\partial f_s}{\partial\varepsilon_{ij}} = \frac{\partial f_s^g}{\partial\varepsilon_{ij}}$$	$$\varepsilon_{ij} = -\frac{\partial g_s}{\partial\sigma_{ij}^{''}} = -\frac{\partial g_s^f}{\partial\sigma_{ij}^{''}}$$
Suction	Hydraulic strain
$$s = \frac{\partial f_s}{\partial\varepsilon_w} = \frac{\partial g_s^f}{\partial\varepsilon_w}$$	$$\varepsilon_w = -\frac{\partial g_s}{\partial s} = -\frac{\partial f_s^g}{\partial s}$$
Generalized net stress tensor	Plastic strain tensor
$$x_{ij}^{''} = -\frac{\partial f_s}{\partial\alpha_{ij}} = -\frac{\partial f_s^g}{\partial\alpha_{ij}} = -\frac{\partial g_s^f}{\partial\alpha_{ij}} = -\frac{\partial g_s}{\partial\alpha_{ij}}$$ $$x_{ij}^{''} = \frac{\partial d_s}{\partial\dot{\alpha}_{ij}}$$	$$\alpha_{ij} = \frac{\partial\tilde{g}_s}{\partial x_{ij}^{''}}$$ $$\dot{\alpha}_{ij} = \dot{\lambda}\frac{\partial f^y}{\partial x_{ij}^{''}}$$
Generalized suction	Plastic hydraulic strain
$$x_s = -\frac{\partial f_s}{\partial\alpha_l} = -\frac{\partial f_s^g}{\partial\alpha_l} = -\frac{\partial g_s^f}{\partial\alpha_l} = -\frac{\partial g_s}{\partial\alpha_l}$$ $$x_s = \frac{\partial d_s}{\partial\dot{\alpha}_l}$$	$$\alpha_l = \frac{\partial\tilde{g}_s}{\partial x_s}$$ $$\dot{\alpha}_l = \dot{\lambda}\frac{\partial f^y}{\partial x_s}$$

3.6)   Illustration case: derivation of the Modified Cam-Clay Model

Because it is the first model developed in the framework of critical state mechanics (Schofield & Wroth, 1968), Cam-clay model represents a reference model in Soil Mechanics. In this section, this model is used to illustrate the way in which thermo-mechanical potentials can be used to derive constitutive models for porous media.

As presented in the last section, the use of Legendre transformation is omnipresent in the manipulation of the thermomechanical potentials, which implies that only smooth yield functions can be derived (the framework can however be extended to non-smooth yield surfaces by use of Legendre-Fenchel transformation). As a consequence, this section will deal with the Modified Cam Clay Model – MCCM – (Burland, 1965) instead of the Original Cam Clay model – OCCM (Roscoe & Schofield, 1963).

The model has been derived from a thermomechanical viewpoint by several researchers : (Houlsby G. , 1981), (Modaressi, Laloui, & Aubry, 1994), (Collins & Houlsby, 1997), (Coussy O. , 2004), (Houlsby & Puzrin, 2006), and (Zouain, Pontes, & Vaunat, 2009). It is important to note that, for such a simple model, model derivation from hyper-poro-

elastoplastic potentials apparently does not present advantages and even appears to be rather less direct than other procedures. However, the method offers certain advantages when deriving more sophisticated MCC models, because this can be easily done by introducing new dependencies in the governing functions.

Derivation of Modified Cam-clay model requires the definition of a free energy (in this case, Gibbs free energy g_s) and dissipation (d_s) functions. Notation used in the following text is summarized above in Table 3.3. Houlsby (1981) introduced the following Gibbs energy potential:

$$g_s = -\kappa^* p' \left[\ln\left(\frac{p'}{p^o}\right) - 1 \right] - \frac{q^2}{6G} - (p'\alpha_p + q\alpha_q) + \frac{p^c}{2}(\lambda^* - \kappa^*)\exp\left(\frac{\alpha_p}{\lambda^* - \kappa^*}\right) \qquad (3.83)$$

Direct differentiation of Equation 3.77 leads to the expressions for the strains:

$$\varepsilon_p = -\frac{\partial g_s}{\partial p'} = \kappa^* \ln\left(\frac{p'}{p^o}\right) + \alpha_p \qquad (3.84)$$

$$\varepsilon_q = -\frac{\partial g_s}{\partial q} = \frac{q}{3G} + \alpha_q$$

Where ε_p is the total volumetric strain and ε_q is the total deviatoric strain. Double differentiation of Gibbs potential function leads to the elastic compliance coefficient:

$$\frac{\partial^2 g_s}{\partial p' \, \partial p'} = \frac{\kappa^*}{p'} = \frac{1}{K} \qquad (3.85)$$

$$\frac{\partial^2 g_s}{\partial q \, \partial q} = \frac{1}{3G}$$

while the out of diagonal terms are null $\left(\frac{\partial^2 g_s}{\partial p' \, \partial q} = \frac{\partial^2 g_s}{\partial q \, \partial p'} = 0 \right)$. Houlsby (1981)

presented the alternatively Helmholtz free energy,

$$f_s = p^c \kappa^* \exp\left(\frac{\varepsilon_p - \alpha_p}{\kappa^*}\right) + \frac{3G}{2}(\varepsilon_q - \alpha_q)^2 + \frac{p^c}{2}(\lambda^* - \kappa^*)\exp\left(\frac{\alpha_p}{\lambda^* - \kappa^*}\right) \qquad (3.86)$$

whose direct differentiation provides the expression for stresses:

$$p' = \frac{\partial f_s}{\partial \varepsilon_p} = p^c \exp\left(\frac{\varepsilon_p - \alpha_p}{\kappa^*}\right) \qquad (3.87)$$

$$q = \frac{\partial f_s}{\partial \varepsilon_q} = 3G\varepsilon_q$$

Double differentiation of Helmholtz energy function leads then to the elastic stiffness coefficients:

$$\frac{\partial^2 f_s}{\partial \varepsilon_p \, \partial \varepsilon_p} = \frac{p'}{\kappa^*} = K \tag{3.88}$$

$$\frac{\partial^2 f_s}{\partial \varepsilon_q \, \partial \varepsilon_q} = 3G$$

while the out of diagonal terms are null $\left(\frac{\partial^2 f_s}{\partial \varepsilon_p \, \partial \varepsilon_q} = \frac{\partial^2 f_s}{\partial \varepsilon_q \, \partial \varepsilon_p} = 0 \right)$. The generalized stresses are computed by the complementary state equation

$$x_p' = -\frac{\partial g_s}{\partial \alpha_p} = p' - \frac{p^c}{2} \exp\left(\frac{\alpha_p}{\lambda^* - \kappa^*}\right) \tag{3.89}$$

$$x_q' = -\frac{\partial g_s}{\partial \alpha_q} = q$$

The difference between equations 3.87 and 3.89 provides the expressions for the volumetric ρ_p back stress and the deviatoric ρ_q back stress:

$$\rho_p = \frac{p^c}{2} \exp\left(\frac{\alpha_p}{\lambda^* - \kappa^*}\right) \tag{3.90}$$

$$\rho_q = 0$$

Eq. 3.90 indicates that the kinematic hardening of modified Cam-clay model is only volumetric.

As for the dissipation function, Houlsby (1981) and, later, Modaressi et al. (1994) proposed the following expression:

$$d_s = \frac{p^c}{2} \exp\left(\frac{\alpha_p}{\lambda^* - \kappa^*}\right) \left[\dot{\alpha}_p{}^2 + M^2 \dot{\alpha}_q{}^2\right]^{1/2} \tag{3.91}$$

where $\dot{\alpha}_p$ and $\dot{\alpha}_q$ are the rates of the internal history variables. The generalized stress variables x_p' and x_q' are obtained by differentiation of Eq. 3.91:

$$x_p' = \frac{\partial d_s}{\partial \dot{\alpha}_p} = \frac{p^c}{2} \exp\left(\frac{\alpha_p}{\lambda^* - \kappa^*}\right) \frac{\dot{\alpha}_p}{\sqrt{\dot{\alpha}_p{}^2 + M^2 \dot{\alpha}_q{}^2}} \tag{3.92}$$

$$x_q' = \frac{\partial d_s}{\partial \dot{\alpha}_q} = \frac{p^c}{2} \exp\left(\frac{\alpha_p}{\lambda^* - \kappa^*}\right) \frac{M^2 \dot{\alpha}_q}{\sqrt{\dot{\alpha}_p{}^2 + M^2 \dot{\alpha}_q{}^2}}$$

The expression of the yield function $f^y(x)$ in the dissipative stress space is obtained by eliminating the plastic strain rates in Eq. 3.92:

$$f^y = x_p{}^2 + \frac{x_q{}^2}{M^2} - \left(\frac{p^c}{2} \exp\left(\frac{\alpha_p}{\lambda^* - \kappa^*}\right)\right)^2 = 0 \tag{3.93}$$

The evolution of the internal history variables ("the flow rules") is then computed from Eq. 3.93:

$$\dot{\alpha}_p = \lambda \frac{\partial f^y}{\partial x_p} = 2\lambda x_p \tag{3.94}$$

$$\dot{\alpha}_q = \lambda \frac{\partial f^y}{\partial x_q} = \frac{2\lambda}{M^2} x_p$$

where λ is the plastic multiplier.

Finally, the use of the fundamental relation $(x = \sigma' - \rho)$ leads to the expression of the yield function in the true stress space:

$$f^y = \left(p' - \rho_p\right)^2 + \frac{q^2}{M^2} - \left(\frac{p^c}{2} \exp\left(\frac{\alpha_p}{\lambda^* - \kappa^*}\right)\right)^2 = 0 \tag{3.95}$$

Figure 3.22 shows the translation and the role of the back stress ρ into the formulation.

Figure 3.22: Modified Cam-clay Yield surface at Dissipation and True stress Spaces

From a formal point of view, the state equations and the orthogonality rule $(x = \bar{x})$ are necessary to specify the constitutive equations of an elasto-plastic porous material. Dissipation function or yield function can be alternatively the starting point of the derivation.

3.6.1)   Pressure Dependent Elastic Moduli

In the Critical State theory, elastic properties are usually assumed to be isotropic and pressure dependent. In the MCCM, the bulk modulus K is proportional to the mean pressure and the shear modulus is constant. Under this condition, Poisson's ratio v evolves quickly towards incompressible value ($v = 0.5$) when the mean pressure increases. An alternative to avoid this problematic response is to compute G from K by considering a constant value for v. This solution leads however to the formulation of a non-conservative elastic law as G depends of p' (a fact early recognized by experiments, see for example Zytinski et al., (1978)) but K is independent of q.

The hyper-elastic approach provides the basis to derive pressure dependent moduli within a conservative elastic law. Houlsby & Wroth (1991) proposed to express the shear modulus as a function of the volumetric strain ε_p through the expression $G = \varrho p^o \exp\left(\varepsilon_p / \kappa^*\right)$, where ϱ is a material parameter, κ the slope of the isotropic unloading-reloading line and p^0 a reference pressure. The incremental relationship derived from the associated potential evidences an anisotropic response of the soil, characterized non-zero diagonal terms in the tangent stiffness $\left(D^{f_s}\right)$. This model has been further extended by Borja et al. (1997) but still appeared to present some undesirable features. Einav and Puzrin (2004) proposed later a new form of coupling, but the associated potential shows to be valid only in a limited range of stress ratios $\eta = {}^q/_p$. Houlsby et al. (2005) proposed finally an expression for the Helmholtz energy function that overcomes the previous drawbacks. For the particular asymptotic case where the exponent of the function is equal to 1, the expression reads:

$$f_s = \kappa^* p^o \exp\left(\frac{\varepsilon_p}{\kappa^*} + \frac{3\varrho\varepsilon_q{}^2}{2\kappa^*}\right) \tag{3.96}$$

where ϱ is a material parameter that should be calibrated. By differentiation, p' and q have the following expressions:

$$p' = p^o \exp\left(\frac{\varepsilon_p}{\kappa^*} + \frac{3\varrho\varepsilon_q{}^2}{2\kappa^*}\right) \tag{3.97}$$

$$q = 3\varrho p^o \exp\left(\frac{\varepsilon_p}{\kappa^*} + \frac{3\varrho\varepsilon_q{}^2}{2\kappa^*}\right) \cdot \varepsilon_q$$

And the stiffness matrix modulus results in the form:

_____

$$C^{f_s} = p^o \exp\left(\frac{\varepsilon_p}{\kappa^*} + \frac{3\varrho\varepsilon_q^2}{2\kappa^*}\right) \cdot \begin{bmatrix} \dfrac{1}{\kappa^*} & \dfrac{3\varrho}{\kappa^*} \\ \dfrac{3\varrho}{\kappa^*} & 3\varrho\left(1 + \dfrac{3\varrho\varepsilon_q^2}{k^*}\right) \end{bmatrix} \tag{3.98}$$

By noting that $^q/_{p'} = 3\varrho\varepsilon_q = \eta$, the stiffness matrix may be rearranged into:

$$C^{f_s} = \begin{bmatrix} \dfrac{p'}{\kappa^*} & \dfrac{p'\eta}{\kappa^*} \\ \dfrac{p'\eta}{\kappa^*} & \left(\dfrac{\eta^2}{\kappa^*} + \dfrac{\eta}{\varepsilon_q}\right)p' \end{bmatrix} = \begin{bmatrix} \dfrac{p'}{\kappa^*} & \dfrac{q}{\kappa^*} \\ \dfrac{q}{\kappa^*} & \dfrac{q^2}{p'\kappa^*} + 3\varrho p' \end{bmatrix} \tag{3.99}$$

For isotropic stress states the shear modulus is reduced to a pressure dependent modulus and the off-diagonal terms at the stiffness matrix are zero. For other stress states, the off-diagonal terms are different from 0, which implies a "stress-induced" anisotropic elastic behaviour that naturally arises from the hyper-elastic formulation.

Now, if Gibbs free energy is taken equal to:

$$g_s = -\kappa^* p'\left[\ln\left(\frac{p'}{p^o}\right) - 1\right] - \frac{q^2}{6\varrho p'} \tag{3.100}$$

then the volumetric strain and the deviatoric strain are related to mean and deviatoric stresses by:

$$\varepsilon_p = -\frac{\partial g_s}{\partial p'} = \kappa^* \log\left(\frac{p'}{p^o}\right) - \frac{q^2}{6\varrho p'^2} \tag{3.101}$$

$$\varepsilon_q = -\frac{\partial g_s}{\partial q} = \frac{q^2}{3\varrho p'}$$

and the compliance matrix D^{g_s} obtained by double differentiation of the Gibbs energy (Eq. 3.100), results in:

$$D^{g_s} = \begin{bmatrix} \dfrac{\kappa^*}{p'} + \dfrac{q^2}{3\varrho p'^3} & -\dfrac{q}{3\varrho p'^2} \\ -\dfrac{q}{3\varrho p'^2} & \dfrac{1}{3\varrho p'} \end{bmatrix} \tag{3.102}$$

The pressure-dependent elastic behaviour can finally be introduced into the MCCM by modifying the Gibbs and Helmholtz free energies expressed by Eq. 3.83 and Eq. 3.86 according to Eq. 3.100 and Eq. 3.96:

_____

$$g_s \quad = \quad -\kappa^*p'\left[\ln\left(\frac{p'}{p^o}\right) - 1\right] - \frac{q^2}{6\varrho p'} - \left(p'\alpha_p + q\alpha_q\right) + \frac{p^c}{2}(\lambda^* - \kappa^*)\exp\left(\frac{\alpha_p}{\lambda^* - \kappa^*}\right) \qquad (3.103)$$

$$f_s \quad = \quad p^o\kappa^*\exp\left(\frac{\varepsilon_p - \alpha_p}{\kappa^*} + \frac{3\varrho}{2\kappa^*}\left(\varepsilon_q - \alpha_q\right)^2\right) + \frac{p^c}{2}(\lambda^* - \kappa^*)\exp\left(\frac{\alpha_p}{\lambda^* - \kappa^*}\right)$$

The generalized mean and deviatoric stresses are computed from the complementary state equations:

$$x'_p = -\frac{\partial g_s}{\partial \alpha_p} = p' - \frac{p^c}{2}\exp\left(\frac{\alpha_p}{\lambda^* - \kappa^*}\right) \qquad (3.104)$$

$$x'_q = -\frac{\partial g_s}{\partial \alpha_q} = q$$

From equations 3.97 and 3.104, the mean back stress ρ_p and deviatoric back stress ρ_q are given by:

$$\rho_p = \frac{p^c}{2}\exp\left(\frac{\alpha_p}{\lambda^* - \kappa^*}\right) \qquad (3.105)$$

$$\rho_q = 0$$

Expressions 3.105 are the same as those shown in Eq. 3.90 because only the elastic behavior has been revisited in this section. The derivation of conservative pressure-dependent MCCM is finally achieved by considering the dissipation function Eq. 3.91.

The performance of this model is illustrated hereinafter. Material parameters are taken from laboratory tests performed on clay samples taken from the subsoil of Barcelona Harbour. They are summarized in Table 3.7.

Table 3.7: Material properties for Barcelona Harbour Clay

$\kappa[-]$	$p_o[MPa]$	$\nu[-]$	M	λ
0.018	0.01	0.09	1	0.09

Figure 3.23 shows a loading–unloading path under isotropic conditions. As expected, in presence of a null deviatoric stress, the response is similar to that of the MCCM. Fig. 3.24 shows drained triaxial tests on normally consolidated and over-consolidated soil samples respectively. Despite of the stress induced anisotropy, the response of the sample is very similar to that of the simple MCCM.
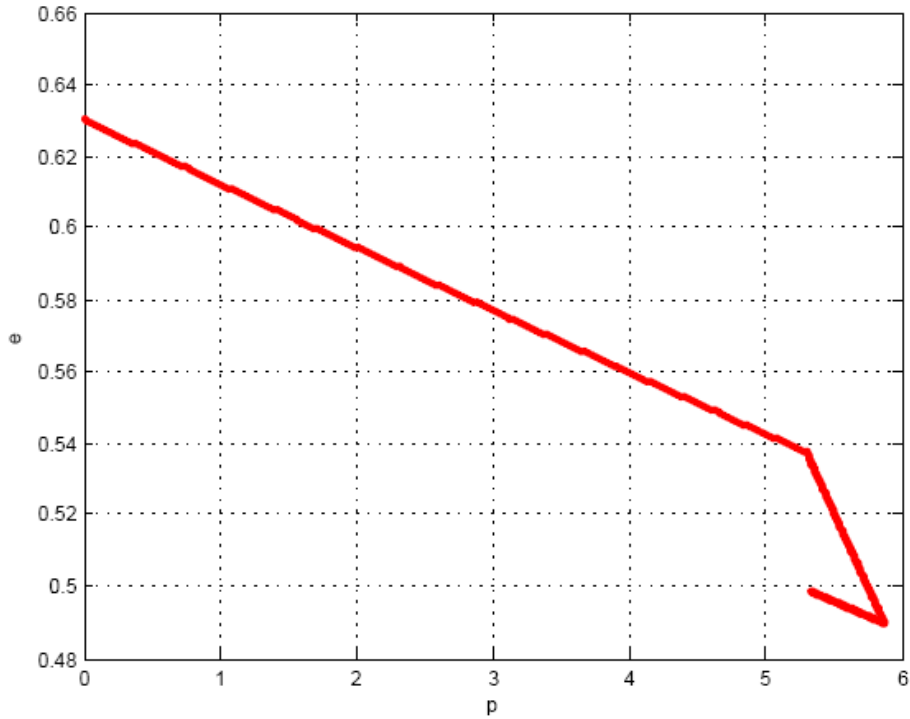
Figure 3.23: Relation between mean effective stress "p" and the void ratio "e". Loading-Unloading for Cam-Clay Mode with non-linear elastic modulus.
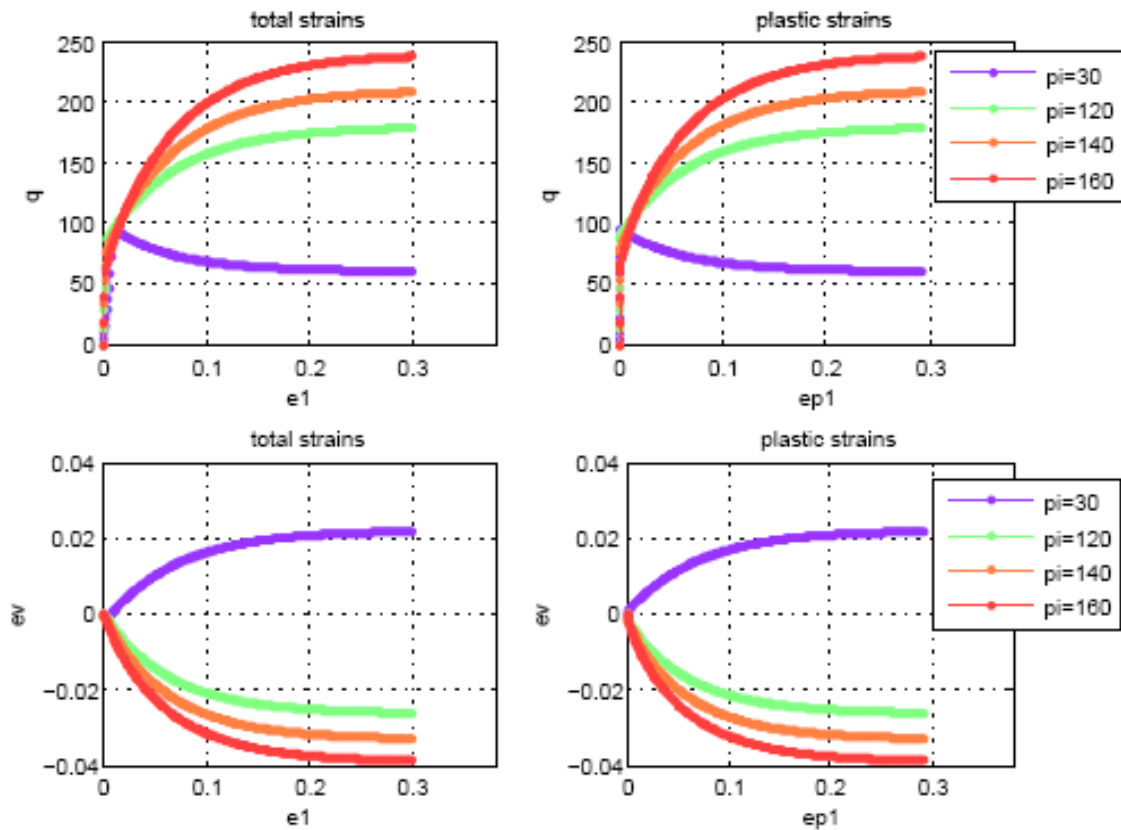
Figure 3.24: Conventional drained triaxial tests on normally and overconsolidated samples considering Cam-clay Model enhanced with a conservative non-linear elasticity.

140

3.6.2) Alternative formulation to the hyperplastic approach

As discussed in Collins & Houlsby (1997), it is possible to derive thermomechanical potentials for the Modified Cam Clay Model without introducing any back stress in the formulation. In this case, an extra term is introduced in the dissipation function:

$$d_s = \frac{p^c}{2} \exp\left(\frac{\alpha_p}{\lambda^* - \kappa^*}\right)\left[\left(\dot{\alpha}_p{}^2 + M^2\dot{\alpha}_q{}^2\right)^{1/2} + \dot{\alpha}_p\right] \tag{3.106}$$

while function f_{s_2} (and thus g_{s_2}) is stated identically null. Helmholtz and Gibbs free energies are thus expressed by:

$$f_s(\varepsilon_p, \varepsilon_q, \alpha_p, \alpha_q) \quad = \quad \kappa^* p^c \exp\left(\frac{\varepsilon_p - \alpha_p}{\kappa^*}\right) + \frac{3G}{2}\left(\varepsilon_q - \alpha_q\right)^2 \tag{3.107}$$

$$g_s(p', q, \alpha_p, \alpha_q) \quad = \quad -\kappa^* p'\left[\ln\left(\frac{p'}{p^c}\right) - 1\right] - \frac{q^2}{6G} - \left(p'\alpha_p + q\alpha_q\right)$$

It outcomes then from the state equations:

$$x'_p = -\frac{\partial g_s}{\partial \alpha_p} = p' \quad \text{or} \quad \rho_p = 0 \tag{3.108}$$

$$x'_q = -\frac{\partial g_s}{\partial \alpha_q} = q \quad \text{or} \quad \rho_q = 0$$

On the other side x'_p and x'_q are computed from the dissipation function as:

$$x'_p = \frac{\partial d_s}{\partial \dot{\alpha}_p} \quad = \quad \frac{p^c}{2}\exp\left(\frac{\alpha_p}{\lambda^* - \kappa^*}\right)\left[\left(\dot{\alpha}_p{}^2 + M^2\dot{\alpha}_q{}^2\right)^{-1/2}\dot{\alpha}_p + 1\right] \tag{3.109}$$

$$x'_q = \frac{\partial d_s}{\partial \dot{\alpha}_q} \quad = \quad M^2\frac{p^c}{2}\exp\left(\frac{\alpha_p}{\lambda^* - \kappa^*}\right)\left(\dot{\alpha}_p{}^2 + M^2\dot{\alpha}_q{}^2\right)^{-1/2}\dot{\alpha}_q$$

eliminating the plastic strain rates between the expressions at Eq. 3.109 leads to the expression for the yield surface:

$$f^y(x'_p, x'_q, \alpha_p) = \left(\frac{x'_p}{p_0} - 1\right)^2 + \left(\frac{x'_q}{Mp_0}\right)^2 - 1 = 0 \tag{3.110}$$

141

where $p_0 = {p^c}/{2} \exp\left({\alpha_p}/{\lambda^* - \kappa^*}\right)$. Or in terms of the true stresses at the true stress space,

$$f^y(p', q, \rho_p) = \frac{q^2}{M^2} + (p' - p_0)^2 - p_0^2 = \frac{q^2}{M^2} - p'(2p_0 - p') = 0 \qquad (3.111)$$

The formulations described along the chapter will be used further in chapter 4 to formulate extensions of MCCM model to unsaturated conditions.

This alternative formulation presents the advantages of a simple derivation of the state equations at the expense of introducing a hardening law which is not normal to the dissipation and therefore may affect algorithmic properties.

3.7) Conclusions

This chapter presents a review of the theory of plasticity from thermo-mechanical principles. Two consolidated frameworks: (a) poro-elastoplasticity and (b) hyperplasticity have been examined.

The poro-elastoplastic framework offers a more physical viewpoint of the processes occurring in porous medium. It also gives a formal procedure for the disconnection of the fluid phase from the porous medium leaving the two following components separated: (a) the solid skeleton and (b) the pore fluid. This separation leads to the independent study of each phase.

 The hyperplastic framework gives an adequate perspective to address: (a) material hardening and (b) plastic flow direction without losing associativity of the flow rule in the so called dissipative stress space.

Both frameworks have been examined and merged into a thermomechanical consistent framework (hyperporoplasticity) able to model soil response in partially saturated conditions. The hyperporoplasticity maintains the characteristics of the two original theories.

In the first place, a review of biphasic porous materials behavior from a thermomechanical viewpoint, merging concepts of poro-elastoplasticity and hyperplasticity, has been addressed.

This first study allowed to understand the basis of each approach as well as the existing connection between the elements of classical plasticity modeling and the different types of energies (elastic energy, trapped energy and dissipation energy).

Study of three-phase porous media from the hyperporoplastic approach has allowed to derived the set of constitutive variables commonly used in modeling of partially saturated soils. It has also given rise to obtain the state equations linking the conjugate variables.

An interesting result derived with the hyperporoplastic approach is the kinematical hardening related to the formulation of the retention curve. The obtained result extends the fundamental relationship linking variables at true space and variables at dissipative space, to consider the shift (or back) suction. This extension leads to model hysteresis of the capillary curve.

A general structure has been proposed for the energy functions g_s and f_s in partially saturated conditions.

Several thermo-hydro-mechanical models are addressed in the next chapter specifying expressions for the energy and dissipation potentials.

CHAPTER 4

FORMULATION OF PARTICULAR THERMO-HYDRO-MECHANICAL MODELS WITHIN THE FRAMEWORK OF HYPER-PORO-PLASTICITY

4.1) Introduction

This chapter deals with the formulation of a specific constitutive models, relevant for geotechnical problems where environmental actions play a central role. Those models are consistently derived from the thermo-mechanical framework developed in the last chapter for partially saturated porous media.

The first two sections of the chapter focus on the formulation of the retention curve. First, the hyperelastic formulation is recalled and particularized in order to derive a non-hysteretic, van Genuchten like, retention curve. Then, a hyperplastic hydraulic law that enables the model hysteresis in the retention curve is presented.

The second part of the chapter is devoted to the formulation of several variants of hyperplastic models adapted from Barcelona Basic Model obtained by combining in different way effective stress or net stress, hysteretic and non hysteretic water retention curves and mixed volumetric/kinematical or purely kinematical hardening.

The third part is devoted to the definition of hyperplastic law for frictional materials, of special interest to model shear failure of soils under environmental actions. The first constitutive law considers a Drucker-Prager yield criterion with a cohesive component. Special attention has been devoted to the smoothing of the apex along the hydrostatic axis as well as to model yield degradation with temperature. The second model is based on Matsuoka-Nakai yield criterion following the works of (Houlsby & Puzrin, 2006) and (Collins & Houlsby, 1997). New points have been addressed such as the formulation of

different dilatancy rules and the possibility to extend the model in order to include non linear yield shape in the meridian plane.

4.2) Notation and Terminology

S_l	degree of saturation
S	Suction
$s^0(T)$	Air entry value for the capillary curve
N	Material parameter for the capillary curve
M	Material parameter for the capillary curve
g_i^d	Gibbs energy function of the gas-liquid interface
p'	Mean effective stress
Q	Deviator stress
K	Bulk modulus
G	Shear modulus
Φ	Porosity
E	Void ratio
g_s	Gibbs energy function of the skeleton
f_s	Helmholtz energy function of the skeleton
f_s^g	Energy function for the skeleton
ε_p	Total volumetric strain
ε_q	Total deviator strain
ε_p^e	Elastic volumetric strain
ε_q^e	Elastic deviator strain
σ_{ij}'	Bishop effective stress tensor
ε_{ij}	strain tensor
b_s	Dilatancy coefficient
T	Temperature
T_i	Reference Temperature
δ_{ij}	Kronecker delta
ρ_s^0	Reference suction
S_0	Reference degree of saturation
s_{I0}	Reference suction for the drying branch
f_i	Helmholtz energy for the gas-liquid interface

f_{i_2}	Trapped Helmholtz energy for the gas-liquid interface
g_{i_2}	Trapped Gibbs energy for the gas-liquid interface
α_l	Plastic degree of saturation
κ_w	Slope of the scanning curve
λ_w	Slope of the main drying and wetting curves
ρ_s	Back suction
s_D	Hardening parameter for the main suction decrease curve
s_I	Hardening parameter for the main suction increase curve
w^y	Flow potential for the capillary curve
Ξ	Bonding variable
K	Slope of the loading – reloading line
Λ	Slope of the virgin compression line
p^0	Reference pressure
α_p	volumetric plastic strain
α_q	deviator strain
C^{fg}	Stiffness matrix
D^{gs}	Compliance matrix
P	Material parameter
V	Unsaturated specific volume
v_s	Saturated specific volume
A	Material parameter for BBM[1] model
B	Material parameter for BBM[1] model
e_s	Saturated void ratio
p_0	Partially saturated pre-consolidation pressure
p_0^*	Saturated pre-consolidation pressure
N	Origin of the virgin loading branch in saturated conditions
f^y	yield function
x'_p	generalized mean stress
x_q	generalized deviator stress
d_s	dissipation function
σ''_{ij}	Net stress tensor
ε_w	Hydraulic strain
p''	mean net stress
x''_p	generalized mean net stress

_____

$x_q^{''}$	generalized deviatoric net stress
p_s	Resistance to pure traction
p_{at}	Atmospheric pressure
J	Square root of the second stress invariant
ϕ'	friction angle
c	Cohesion
ψ	dilation angle
α_{ij}'	Plastic strain tensor
$\dot{\alpha}_{ij}'$	Rate plastic strain tensor
x_{ij}'	Generalized effective stress tensor
x_p	Generalized mean pressure
d	Dissipation function
Λ	Lagrange multiplier
r_c	Temperature dependent resistance parameter
T_o	Reference temperature
c	Dilatancy constraint
υ	Target distance of the rounded hyperbolic
σ_{kk}	trace of stress tensor
x_{kk}	trace of the generalized stress tensor
I_1	first invariant of stress tensor
I_2	second invariant of stress tensor
I_3	third invariant of stress tensor

4.3)   Hyper-elasticity: energy functions for environmental actions

Within hyperporoplasticity, hyperelasticity is the simplest framework that allows introducing thermal and hydraulic effects preserving thermodynamics principles. It is described in this section as an introduction to the more complex models described in the remaining part of the chapter.

One of the most extended constitutive relationship between suction and degree of saturation is the van Genuchten law (van Genuchten, 1980). This law presents the drawback that there is no closed form to integrate it along a specific path, which prevents

the explicit definition of a potential from which it can be derived. An alternative expression will thus be considered here. Van Genuchten (1980) equation reads:

$$S_l = \left[1 + \left(\frac{s}{s^o}\right)^n\right]^{-m} \tag{4.1}$$

where n, m and $s^o(T)$ are fitting parameters. Regardless mechanical coupling and hysteretic behavior, and according to Eq. 3.70, the energy function related to the gas-liquid interface can only be obtained by integration of Eq. 4.1 from the dry state to the saturated state:

$$g_i^d(s) = -\int_0^s \left(\frac{1}{1 + \left(\frac{s}{s^o}\right)^n}\right)^m ds \tag{4.2}$$

Or, by substituting $s/_{s^o} = -y^{(1/n)}$ in the Eq. 4.2:

$$g_i^d(s) = -\frac{s^o}{n}\int_0^{-\left(s/_{s^o}\right)^n} (1-y)^{-m} \cdot y^{(1/n-1)} dy \tag{4.3}$$

Equation 4.3 corresponds to a particular form of the Incomplete Beta-function. In the most general case, no closed-form expression exists for this integral. However for the particular case$\left(1/_n - 1 = 0\right)$, integration of Eq. 4.3 gives,

$$g_i^d(s) = -\frac{s^o}{1-m}\left[\left(1 + \frac{s}{s^o}\right)^{(1-m)}\right] \tag{4.4}$$

Leading to the following expression for the degree of saturation:

$$S_l = -\frac{\partial g_i^d}{\partial s} = \left(1 + \frac{s}{s^o}\right)^{-m} \tag{4.5}$$

Equation 4.5 provides a simplified van Genuchten-like model for the water retention curve. Figures 4.25 and 4.26 show the shape of this curve for different values of m and s_0 parameters.
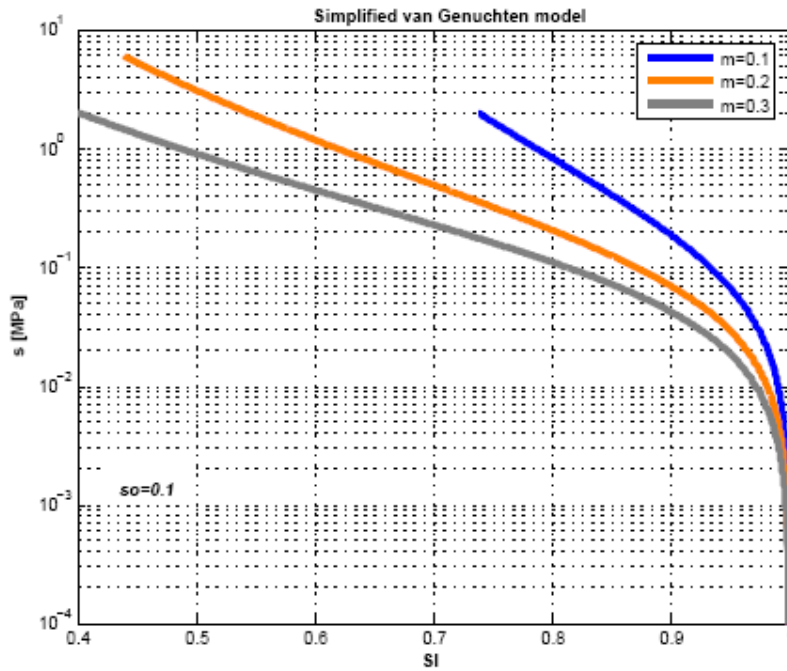
Figure 4.25: Shape of a simplified van Genuchten curve for different values of m parameter (at constant s0).
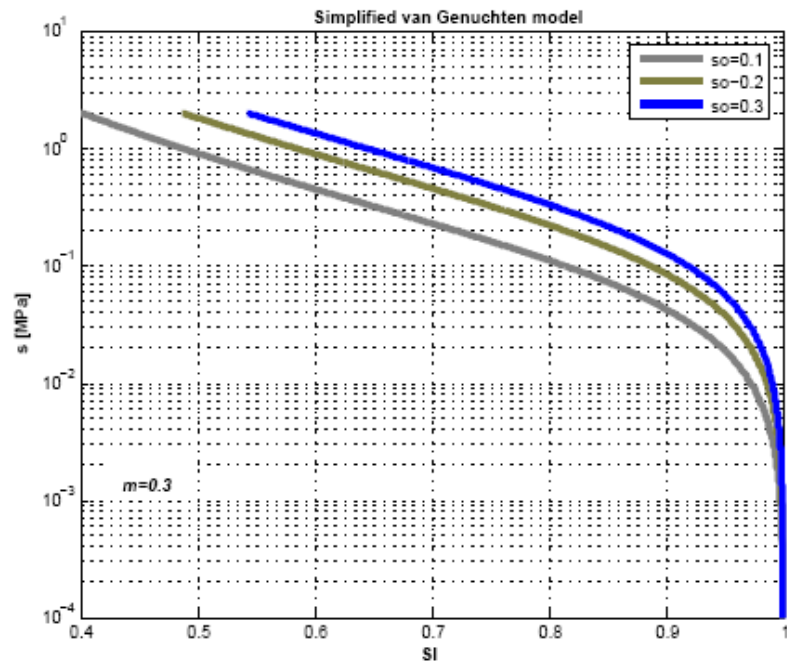
Figure 4.26: Shape of a simplified van Genuchten curve for different values of s0 parameter (at constant m).

This simplified version is suitable to be merged in a hydro-mechanical hyperelastic model, given by the following Gibbs free energy $\left(g_s(p', q, \phi s)\right)$:

$$g_s = g_{\bar{s}} - \phi g_i^d = -\frac{p'^2}{2K} - \frac{q^2}{6G} + \frac{\phi s_o}{(1-m)} \cdot \left[1 + \frac{\phi s}{\phi s_o}\right]^{(1-m)} \qquad (4.6)$$

where K is the Bulk modulus, G is the shear modulus and m a shape parameter. In this hyper-elastic formulation, the term related to the trapped energy $g_{s_2}(\alpha)$ is taken equal to 0 and both the generalized stresses and the generalized suction are equal to the true ones $\left(p' = x'_p; q = x'_q; \phi s = \phi x_s\right)$. Under this condition, the hydraulic behaviour is reversible leading to a non-hysteretic retention curve.

From the state equations, the volumetric strain $\left(\varepsilon_p^e\right)$, deviatoric strain $\left(\varepsilon_q^e\right)$ and degree of saturation (S_l) take the form:

$$\varepsilon_p = -\frac{\partial g_s}{\partial p'} = \frac{p'}{K} \quad ; \quad \varepsilon_q = -\frac{\partial g_s}{\partial q} = \frac{q}{3G} \quad ; \quad S_l = \frac{\partial g_s}{\partial \phi s} = \left[1 + \frac{\phi s}{\phi s_o}\right]^{-m} \qquad (4.7)$$

The last term of Eq. 4.7 provides the relationship for the retention curve. It is depicted in Fig. 4.27 for two values of porosity.
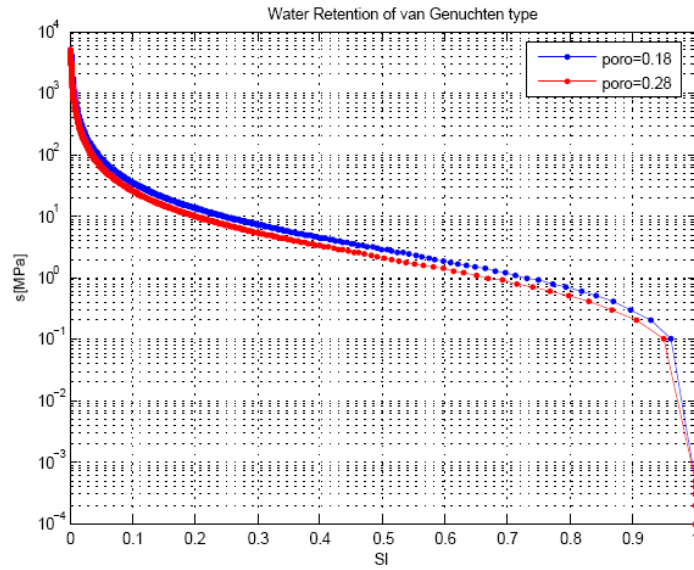
Figure 4.27: Shape of the simplified van Genuchten like Retention Curve

The potential $f_s^g(\varepsilon_{ij}, \phi s) = \sigma'_{ij}\varepsilon_{ij} + g_s(\sigma'_{ij}, \phi s)$ is more suitable for models formulated within the framework of Finite Element coupled computations, because it allows deriving stresses from strains and suction. In the present model, it can be seen to be expressed by:

_____

$$f_s^g = \frac{K}{2} \cdot \varepsilon_p^2 + \frac{3}{2} G \cdot \varepsilon_q^2 + \frac{\phi s_o}{(1-m)} \cdot \left[1 + \frac{\phi s}{\phi s_o}\right]^{(1-m)} \tag{4.8}$$

Leading to the following expression for stresses and degree of saturation:

$$p' = \frac{\partial f_s^g}{\partial \varepsilon_p} = K \cdot \varepsilon_p \quad ; \quad q = \frac{\partial f_s^g}{\partial \varepsilon_q} = 3G \cdot \varepsilon_q \quad ; \quad S_l = \frac{\partial f_s^g}{\partial \phi s} = \left[1 + \frac{\phi s}{\phi s_o}\right]^{-m} \tag{4.9}$$

Thermal effect is introduced through the term of thermal expansion in the Gibbs energy Eq. 4.6. Because the tensile strength of water, which controls menisci formation in partially saturated pores, is sensitive to temperature a thermal dependence is considered for the retention curve through the dependency of the air entry pressure coefficient s_0 on temperature. For the sake of simplicity, elastic stiffness is considered independent of temperature. Then Gibbs free energy reads:

$$g_s = -\frac{p'^2}{2K} - \frac{q^2}{6G} + \frac{\phi s_o(T)}{(1-m)} \cdot \left[1 + \frac{\phi s}{\phi s_o(T)}\right]^{(1-m)} + b_s \cdot (T - T_i)p' \tag{4.10}$$

where T is the temperature, T_i a reference temperature and b_s the volumetric expansion coefficient of the porous medium ($b_s < 0$ following the Soils Mechanics convention). From the corresponding state equations (Table 3.5) the following relationship prevails for the volumetric and deviatoric elastic strains and the degree of saturation:

$$\varepsilon_p = \frac{p'}{K} + 3b_s \cdot (T - T_i) \quad ; \quad \varepsilon_q = \frac{q}{3G} \quad ; \quad S_l = \left[1 + \frac{\phi s}{\phi s_o(T)}\right]^{-m} \tag{4.11}$$

Equation 4.11a reveals that non-isothermal processes in porous media directly influence the volumetric deformation of the media. In fact the skeleton structure shrinks or dilates depending on (T-Ti). For the energy function Eq. 4.10 no thermal effects are produced on deviatoric strain. As well, Helmholtz potential f_s^g is expressed by:

$$f_s^g = \frac{K}{2} \cdot \varepsilon_p^2 + \frac{3}{2} G \cdot \varepsilon_q^2 + \frac{\phi s_o(T)}{(1-m)} \cdot \left[1 + \frac{\phi s}{\phi s_o(T)}\right]^{(1-m)} - Kb_s \cdot (T - T_i)\varepsilon_p \tag{4.12}$$

and the mean and deviatoric effective stresses and degree of saturation read:

$$p' = K(\varepsilon_p - b_s(T - T_i)) \quad ; \quad q = G\varepsilon_q \quad ; \quad S_l = \left[1 + \frac{\phi s}{\phi s_o(T)}\right]^{-m} \tag{4.13}$$

As before, thermal processes influence the volumetric response of the soil. The mean effective pressure is increased or decreased according to cooling or heating processes. Furthermore, the interface energy of the porous skeleton is also affected by the thermal processes and, as a result, the water capillary curve is also influenced, Eq. 4.13.

_____

Table 4.8 summarizes the simplest elastic energy function seen above in order to model the soil response to environmental action.

Table 4.8: Simplest Thermo-hydro-mechanical elastic energy function for environmental actions on partially saturated soils

Energy	Function	State variables
Helmholtz: (linear mechanical elasticity)	$f_s^g = \dfrac{K}{2} \cdot \varepsilon_p^2 + \dfrac{3}{2}G \cdot \varepsilon_q^2 + \dfrac{\phi s_o(T)}{(1-m)}$ $\cdot \left[1 + \dfrac{\phi s}{\phi s_o(T)}\right]^{(1-m)} - Kb_s$ $\cdot (T - T_i)\varepsilon_p$	$p' \quad \left(= \partial f_s^g \big/ \partial \varepsilon_p\right)$ $q \quad \left(= \partial f_s^g \big/ \partial \varepsilon_q\right)$ $S_l \quad \left(= \partial f_s^g \big/ \partial \phi s\right)$
Gibbs: (linear mechanical elasticity)	$g_s = -\dfrac{p'^2}{2K} - \dfrac{q^2}{6G} + \dfrac{\phi s_o(T)}{(1-m)}$ $\cdot \left[1 + \dfrac{\phi s}{\phi s_o(T)}\right]^{(1-m)} + b_s$ $\cdot (T - T_i)p'$	$\varepsilon_p \quad \left(= -\partial g_s \big/ \partial p'\right)$ $\varepsilon_q \quad \left(= -\partial g_s \big/ \partial q\right)$ $S_l \quad \left(= \partial g_s \big/ \partial \phi s\right)$

4.3.1)   Generalization to general stress states

For general stress states other than triaxial states, the Gibbs energy Eq. 4.10 depends on the effective stress tensor:

$$g_s = -\frac{\sigma'_{ii}\sigma'_{jj}}{18K} - \frac{s'_{ij}s'_{ij}}{4G} + \frac{\phi s_o(T)}{(1-m)} \cdot \left[1 + \frac{\phi s}{\phi s_o(T)}\right]^{(1-m)} + \left(b_s \cdot (T - T_i)\right) \cdot \sigma_{kk} \qquad (4.14)$$

in this energy function Eq. 4.14 indicial notation has been used. Then standard procedures in thermomechanics lead to the expression for the strain tensor which takes the following form:

$$\varepsilon_{ij} = -\frac{\partial g_s}{\partial \sigma'_{ij}} = \frac{\sigma'_{kk}}{9K}\delta_{ij} + \frac{s_{ij}}{2G} + b_s(T - T_i) \cdot \delta_{ij}; \quad S_l = \left[1 + \frac{\phi s}{\phi s_o}\right]^{-m} \qquad (4.15)$$

_____

As can be seen, the thermal effects on the soil's strain are only volumetric as the temperature in Eq. 4.15 is only affected by the Kronecker delta. Strain increment $\dot{\varepsilon}_{ij}$ is related to stress $\dot{\sigma}'_{ij}$ and temperature $\dot{T}$ increments by the Maxwell's rule:

$$\dot{\varepsilon}_{ij} = \frac{\partial^2 g_s}{\partial \sigma'_{ij} \partial \sigma'_{kl}} \cdot \dot{\sigma}'_{kl} + \frac{\partial^2 g_s}{\partial \sigma'_{ij} \partial T} \cdot \dot{T} \tag{4.16}$$

Leading in view of Eq. 4.15 to the incremental relationship:

$$\dot{\varepsilon}_{ij} = \left[\frac{\delta_{ij}\delta_{kl}}{9K} + \frac{1}{2G}\left(\delta_{ik}\delta_{jl} - \frac{1}{3}\delta_{kl}\delta_{ij} \right) \right] \cdot \dot{\sigma}'_{kl} - b_s \delta_{ij} \cdot \dot{T} \tag{4.17}$$

Alternatively, stress increment is related to strain and temperature increments through the partial second derivatives of f_s^g potential:

$$f_s^g = \frac{K}{2} \cdot \varepsilon_{ii}\varepsilon_{jj} + G \cdot \varepsilon'_{ij}\varepsilon'_{ji} + \frac{\phi s_o(T)}{(1-m)} \cdot \left[1 + \frac{\phi s}{\phi s_o(T)} \right]^{(1-m)} \tag{4.18}$$
$$- \left(K \cdot b_s \cdot (T - T_i) \right) \cdot \varepsilon_{kk}$$

From Eq. 4.18, the stress tensor is expressed by:

$$\sigma'_{ij} = \frac{\partial f_s}{\partial \varepsilon_{ij}} = K \cdot \varepsilon_{ii}\delta_{ij} + G \cdot \varepsilon'_{ij} - \left(Kb_s \cdot (T - T_i) \right) \cdot \delta_{ij} \tag{4.19}$$

and the increment of stress tensor and degree of saturation are obtained by applying Maxwell's rule:

$$\dot{\sigma}'_{ij} = \frac{\partial^2 f_s}{\partial \varepsilon_{ij} \partial \varepsilon_{ij}} \dot{\varepsilon}_{ij} + \frac{\partial^2 f_s}{\partial \varepsilon_{ij} \partial T} \dot{T}; \quad \dot{S}_l = \frac{-m}{\phi s_o}\left[1 + \frac{\phi s}{\phi s_o} \right]^{-(m+1)} \dot{\phi} s + \frac{\partial^2 f_s}{\partial \phi s \partial T} \dot{T} \tag{4.20}$$

The last equation in view of Eq. 4.18 leads to the following explicit expression for the incremental relationship between $\dot{\sigma}'_{ij}$, $\dot{\varepsilon}_{ij}$ and $\dot{T}$.

$$\dot{\sigma}'_{ij} = \left[K \cdot \delta_{kl}\delta_{ij} + G \cdot \left(\delta_{ik}\delta_{jl} - \frac{1}{3}\delta_{kl}\delta_{ij} \right) \right] \cdot \dot{\varepsilon}_{ij} - Kb_s \delta_{ij} \cdot \dot{T} \tag{4.21}$$

This formulation gives the tangent elastic thermo-hydro-mechanical behaviour of partially saturated porous media, particularized for a simplified non hysteretic van Genuchten-like retention curve.

The present formulation represents one of the simplest thermo-hydro-mechanical coupling. More complex energy formulations will be presented particularly accounting for the dependency of the elastic moduli on pressure and the hysteretic behavior of the capillary curve.

4.4) Hyper-Plastic Models for Suction Hysteresis (WRC)

When a sample of porous material is subjected to a wetting-drying cycle, a hysteresis loop is usually observed and the relationship between suction and degree of saturation becomes non-unique. For example, when suction is progressively increased from a fully saturated state, the saturation degree S_l progressively decreases such that the point (s, S_l) follows the main drying curve "MC_I" shown in Fig. 4.28. If drying is stopped at a given point and imbibition starts, an increase in S_l is observed along a path different to MC_I. Instead, if wetting is performed from a fully dried state, the saturation degree S_l progressively increases and the corresponding point (s, S_l) follows the main wetting curve "MC_D", see Fig. 4.28. Any drainage at this stage produces a decrease of S_l along a path different to the MC_D, call scanning curves, down to the reach of MC_I.
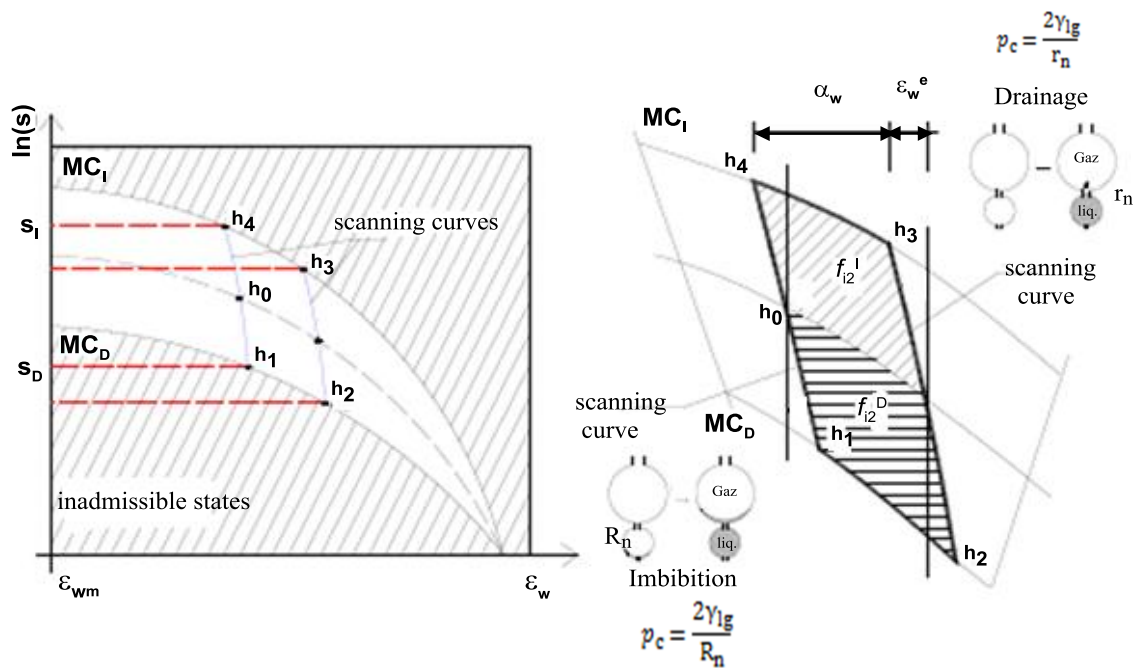
Figure 4.28: Hysteresis Behavior of Water Retention Curve (after Vaunat et al., 2000; Coussy, 2004).

In the last decade, different models have been developed to tackle the hysteresis behavior of soil water retention curve on the basis of the theory of the elasto-plasticity (Vaunat et al., (2000); Wheeler et al., (2003)).

4.4.1) Wheeler et al. Model

Wheeler et al. (2003) proposed to define the retention curve in the plane $S_l - \ln(\phi s)$ and to approximate the smooth curves "MCI" and "MCD" with two straight lines having the same slope λ_w, see Fig. 4.29 but shifted by a given value.

The relationship between degree of saturation and suction along a scanning path is given by the equation:

$$S_l = -\kappa_w \ln\left(\frac{s}{s_0}\right) + S_{l_0} \tag{4.22}$$

κ_w is the slope of the scanning curve. The pair (s_0, S_{l_0}) provides the origin of the scanning path and can be any point along this path. In the present model, it has been chosen to work with point C, located at mid-distance between points A and B, see Fig. 4.29. S_{l_0} is given by the relation between suction and degree of saturation prevailing on the main drying path:

$$S_{l_0} = -\lambda_w \ln\left(\frac{s_0}{s^0}\right) \tag{4.23}$$

where λ_w is the slope of the main drying and wetting curves and s^0 is the half of the intercepts of the main drying and wetting curves with the suction axis.
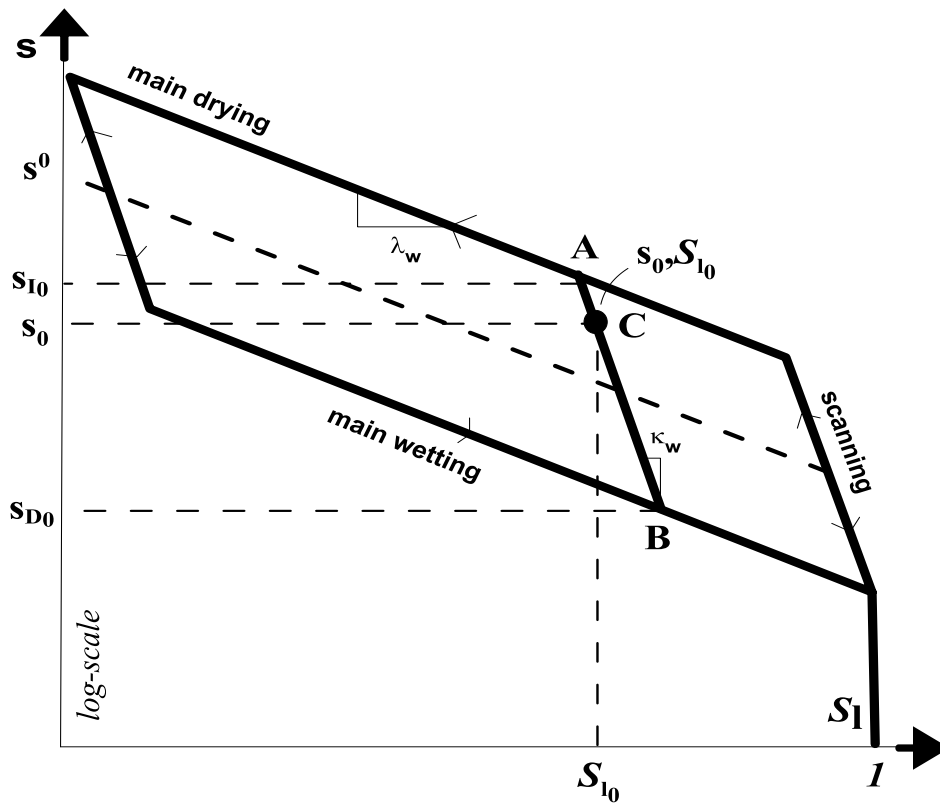
Figure4. 29: Water Retention Curve Hysteresis Wheeler (2003).

155

Equations 4.22 and 4.23 can be reworked as:

$$S_l = -\lambda_w \ln\left(\frac{s_0}{s^0}\right) - \kappa_w \ln\left(\frac{s}{s_0}\right) = -\kappa_w \ln\left(\frac{s}{s^0}\right) \underbrace{-(\lambda_w - \kappa_w)\ln\left(\frac{s_0}{s^0}\right)}_{\alpha_l} \tag{4.24}$$

or equivalently:

$$S_l = -\kappa_w \ln\left(\frac{s}{s^0}\right) + \alpha_l \quad \text{with} \quad \alpha_l = -(\lambda_w - \kappa_w)\ln\left(\frac{s_0}{s^0}\right) \tag{4.25}$$

where α_l is an internal variable representing the irreversible part of the degree of saturation. Equations 4.25 provide the equations to model hysteresis in the retention curve within the elasto-plastic framework. They can alternatively be written as:

$$s = s^0 \exp\left(-\frac{(S_l - \alpha_l)}{\kappa_w}\right) \quad \text{with} \quad s_0 = s^0 \exp\left(\frac{-\alpha_l}{\lambda_w - \kappa_w}\right) \tag{4.26}$$

Such a model can be derived within the hyperporoplastic framework by defining adequate Helmholtz f_i and Gibbs g_i free energy for the gas-liquid interface. According to the Eq. 3.70 they can be composed by two terms: (a) the elastic energies f_{i_1} and g_{i_1}, given by the expressions:

$$\begin{aligned}
f_{i_1}(S_l - \alpha_l) \left(\equiv \int s\, dS_l\right) &= -\kappa_w s^0 \exp\left(-\frac{(S_l - \alpha_l)}{\kappa_w}\right) \\
g_{i_1}(s) \left(\equiv -\int S_l\, ds\right) &= \kappa_w s\left[\ln\left(\frac{s}{\rho_s^0}\right) - 1\right] - s\alpha_l
\end{aligned} \tag{4.27}$$

and (b) the trapped or stored energies:

$$\begin{aligned}
f_{i_2}(\alpha_l) \left(\equiv \int s_0\, d\alpha_l\right) &= -(\lambda_w - \kappa_w)s^0 \exp\left(\frac{-\alpha_l}{\lambda_w - \kappa_w}\right) \\
\tilde{g}_{i_2}(s_0) \left(\equiv -\int \alpha_l\, ds_0\right) &= -(\lambda_w - \kappa_w)s_0\left[\ln\left(\frac{s_0}{s^0}\right) - 1\right]
\end{aligned} \tag{4.28}$$

Then the Gibbs energy function of the gas-liquid interface is given by:

$$g_i(\phi s, \alpha_l) = -\kappa_w \phi s\left[\ln\left(\frac{\phi s}{\rho_s^0}\right) - 1\right] + \phi s\alpha_l + \underbrace{(\lambda_w - \kappa_w)s^0 \exp\left(\frac{-\alpha_l}{\lambda_w - \kappa_w}\right)}_{g_{s2}} \tag{4.29}$$

In this purely hydraulic model, the porosity ϕ is constant. The state equations lead to the expressions for the degree of saturation and the back suction:

$$S_l = \frac{\partial g_i}{\partial \phi s} = -\kappa_w \ln\left(\frac{\phi s}{\rho_s^0}\right) + \alpha_l \tag{4.30}$$

$$\rho_s = -\frac{\partial g_{i2}}{\partial \alpha_l} = s^0 \exp\left(\frac{-\alpha_l}{\lambda_w - \kappa_w}\right)$$

Further derivation of Eq. 4.30 leads to the incremental relationship between, on the one hand, degree of saturation S_l and suction and, on the other hand, back suction ρ_s and internal variable α_l:

$$\dot{S}_l = -\frac{\kappa_w}{s}\dot{s} \tag{4.31}$$

$$\dot{\rho}_s = -\frac{s^0}{\lambda_w - \kappa_w} \exp\left(\frac{-\alpha_l}{\lambda_w - \kappa_w}\right)\dot{\alpha}_l$$

The inverse relation between suction and degree of saturation is alternatively derived from the Helmholtz energy ($f_s(S_l, \alpha_l) = g_s(s, \alpha_l) - \phi s S_l$), valid in the range of admissible values ($S_l \leq 1$) :

$$f_i(S_l, \alpha_l) = \kappa_w \rho_s^0 \exp\left(-\frac{(S_l - \alpha_l)}{\kappa_w}\right) + \underbrace{(\lambda_w - \kappa_w)s^0 \exp\left(\frac{-\alpha_l}{\lambda_w - \kappa_w}\right)}_{f_{s2}} \tag{4.32}$$

From Eq. 4.32 the expressions for the suction and the back suction are derived as:

$$\phi s = -\frac{\partial f_i}{\partial S_l} = \rho_s^0 \exp\left(-\frac{(S_l - \alpha_l)}{\kappa_w}\right) \tag{4.33}$$

$$\rho_s = -\frac{\partial f_{i2}}{\partial \alpha_l} = s^0 \exp\left(\frac{-\alpha_l}{\lambda_w - \kappa_w}\right)$$

Other alternative consists in applying the Legendre transformation ($\tilde{g}_i(s, x_s) = g_i(s, \alpha_l) - x_s \alpha_l$) defined by considering ϕs and generalized suction x_s ($x_s = \phi s - \rho_s$) as independent variables:

$$\tilde{g}_i(\phi s, x_s) = -\kappa_w \phi s\left[\ln\left(\frac{\phi s}{\rho_s^0}\right) - 1\right] + (\lambda_w - \kappa_w)\rho_s\left[\ln\left(\frac{\rho_s}{s^0}\right) - 1\right] \tag{4.34}$$

Derivation of the last equation leads to the expression of the plastic degree of saturation:

$$\alpha_l = -\frac{\partial \tilde{g}_i}{\partial x_s} = -(\lambda_w - \kappa_w)\ln\left(\frac{\rho_s}{s^0}\right) \tag{4.35}$$

The state equation $S_l = {\partial \tilde{g}_i}/{\partial \phi s}$ is valid at any time for any state ($\phi s, S_l$) lying inside the domain limited by the main loop of hysteresis. This domain of reversible saturations at the suction space is defined at each time by two side constraint condition,

$$\phi s_D \le \phi s \le \phi s_I \tag{4.36}$$

where the suction decrease s_D and the suction increase s_I represent the lower and upper limits of the current field of reversibility (hydraulic elastic branch) of the water retention curve. It is then possible to define the hydraulic elastic domain through the scalar function,

$$f^y = (\phi s - \phi s_D)(\phi s - \phi s_I) \tag{4.37}$$

valid in the domain $\left(D_{f^y} = D_{f_D^y} \cap D_{f_I^y}\right)$. At any time, variables $(\phi s, s_D, s_I)$ lie inside the closed set $(\mathfrak{H} = \{(\phi s, s_D, s_I): f^y \le 0\})$. Purely elastic behavior takes place for any pair $(\phi s, S_I)$ at the interior of $\mathfrak{H}$ while plastic loading will take place only when $(\phi s, S_I)$ lies on the boundary of $\mathfrak{H}$.

The more general case to model the behavior of a material is achieved by considering a non homogeneous dissipation function, first-order function of the internal variable rate. In this case, (d_i) is a pseudo-potential and it is not possible to take Legendre transformations on it. Houlsby et.al. (2006) proposed the introduction of a new function (z) "the force potential" to overtake this drawback. In the present study of the retention curve, $\left(z(\dot\alpha_I)\right)$ is a function of material interface skin,

$$z(\dot\alpha_I) = \frac{(\rho_s^2 - \phi^2 s_D s_I)}{4} \cdot \dot\alpha_I^2 \tag{4.38}$$

or in the anecdotal particular case $s_I = 4 s_D$

$$z(\dot\alpha_I) = \frac{\phi^2 s_D s_I}{4} \cdot \dot\alpha_I^2$$

where the back suction ρ_s has been introduced as the mean value of s_D and s_I.

The force potential of the interface skin results to be a homogeneous function as the one seen before for the cam-clay model. However it is a quadratic function of the rates of plastic saturation. Similar functions were used by Ziegler (1977) to model the response of linear viscous materials.

Because $z(\dot\alpha_I)$ acts as a true potential, it is possible to obtain an expression for F^y (the flow potential) analog to the yield function, by applying the following Legendre transformation $(F^y = x_s \dot\alpha_I - z = d_i - z)$. After the transformation, the flow potential can be written in non-dimensional form as:

$$F^y(x_s) = \frac{x_s^2}{\rho_s^2 - \phi^2 s_D s_I} \tag{4.39}$$

or for the particular case $s_I = 4s_D$

$$F^y(x_s) = \frac{x_s^2}{\phi^2 s_D s_I}$$

The quadratic character of the flow potential for the interface skin, recalled the order of this function used to model linear viscous materials (Maugin, 1999). For the particular case $F^y = 1$, the yield surface given by Eq. 4.37 is recovered. It is expressed in the generalized interface space by:

$$f^y(x_s) = x_s^2 - \rho_s^2 + \phi^2 s_D s_I = 0 \tag{4.40}$$

or for the particular case $s_I = 4s_D$

$$f^y(x_s) = x_s^2 - \phi^2 s_D s_I = 0$$

When shifted to the true interface space by invoking the fundamental relation $x_s = \phi s - \rho_s$, Eq. 4.40 becomes:

$$f^y(s, \rho_s) = (\phi s - \rho_s)^2 - \rho_s{}^2 + \phi^2 s_D s_I = 0 \tag{4.41}$$

or for the particular case $s_I = 4s_D$

$$f^y(s, \rho_s) = (\phi s - \rho_s)^2 - \phi^2 s_D s_I = 0$$

Eq. 4.29 (Gibbs potential) and Eq. 4.41 (Force potential) are the two ingredients that define, in a thermo-mechanical consistent way, a hysteretic model for the schematic retention curve proposed by Wheeler et al. (2003). This model has been implemented in an implicit algorithm (see Chapter 5). The response is depicted in Fig. 4.30 in the space degree of saturation – suction (porosity is constant in such a pure hydraulic hyperplastic model). Model parameters are $\kappa_w = 0.02$, $\lambda_w = 0.095$, $s_{D0} = 90$ kPa, $s_{I0} = 700$ kPa and $s_{I0} = 0.5$.
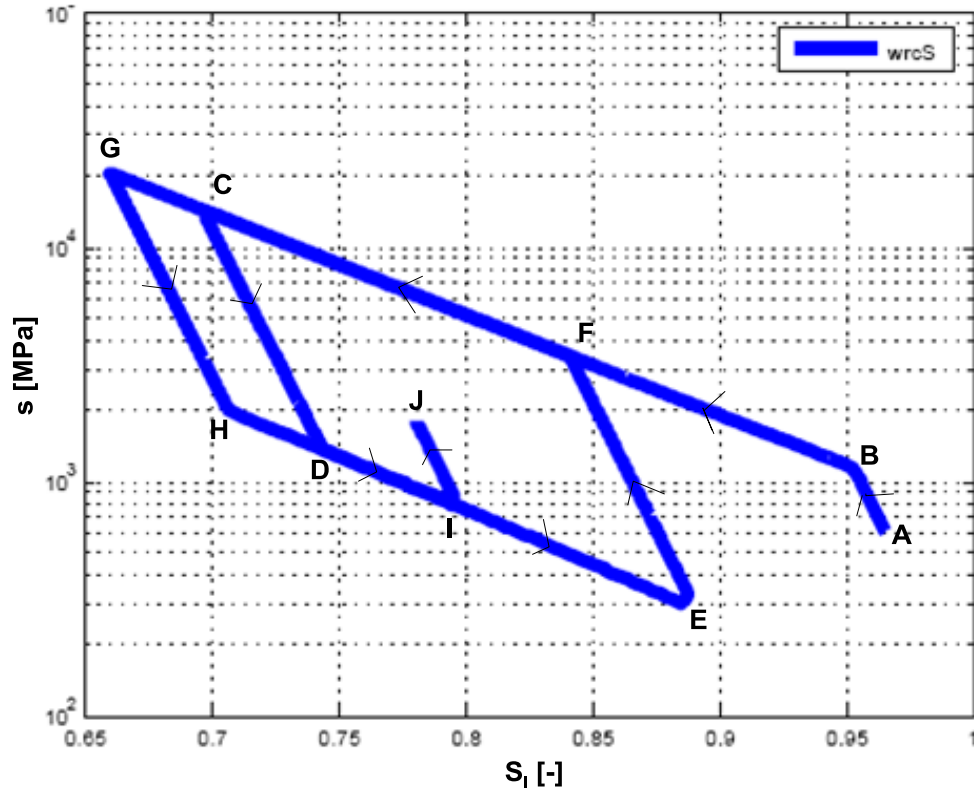
Figure 4.30: Hysteresis Model for WRC following (Wheeler, Sharma, & Buison, 2003))

Figure 4.30 shows an initial state in an elastic branch close to the full saturation of the sample (A). From that state, a drying path is followed firstly over the scanning curve until the main drying curve is reached (B). From that state, irreversible saturation degrees start to develop following the line with slope λ_w until point (C). From this last point a saturation of the sample produces an elastic response following again an scanning curve with slope κ_w until the main wetting curve is reached at point (D). Plastic response is developed from this state, generating irreversible saturation degrees. The drying-wetting cycles continue until point (J) in which the test is finished.

4.4.2)   Simplified van Genuchten like retention curve

A similar hysteretic model can be derived for the simplified van Genuchten-like curve, provided the equations of the main branches of the retention curve are slightly modified in order to introduce the air entry pressure (suction at which the soil starts to desaturate) and accommodate the elastic shift:

$$S_l = -k_w \ln\left(\frac{s}{\rho_s^0}\right) + \underbrace{\left[1 + \frac{s - \phi s_a}{\rho_s^0}\right]^{-m} + k_w \ln\left(\frac{s_o}{\rho_s^0}\right)}_{\alpha_l} \tag{4.42}$$

Following the same procedure as for Wheeler et al. (2003) model, Gibbs free energy of the solid skeleton is expressed by:

$$g_i(\phi s, \alpha_l) = -\kappa_w \phi s \left[\ln\left(\frac{\phi s}{\rho_s^0}\right) - 1\right] + \phi s \alpha_l \underbrace{-\rho_s^0 \left[\frac{m}{m-1} \alpha_l^{*(1-1/m)} - \alpha_l^*\right] - \phi s^a \alpha_l^*}_{g_{i2}} \tag{4.43}$$

where, as for the previous model, ρ_s^0 is defined as the average value of the intercepts of the scanning curve with the main drying (s_D^0) and wetting curves (s_w^0) in the reference configuration and $\alpha_l^* = \alpha_l - k_w \ln\left(\frac{s_o}{\rho_s^0}\right)$. The expressions for the degree of saturation and back suction are:

$$S_l = \frac{\partial g_i}{\partial \phi s} = -\kappa_w \ln\left(\frac{\phi s}{\rho_s^0}\right) + \alpha_l \tag{4.44}$$

$$\rho_s = -\frac{\partial g_{i2}}{\partial \alpha_l} = \rho_s^0 \left(\underbrace{\left(\alpha_l - k_w \ln\left(\frac{s_o}{\rho_s^0}\right)\right)}_{\alpha_l^*}^{(-1/m)} - 1\right) + s^a$$

while the incremental relationships between S_l, s, ρ_s and α_l are obtained from double differentiation of Eq. 4.43:

$$\dot{S}_l = -\frac{\kappa_w}{s} \dot{s} \tag{4.45}$$

$$\dot{\rho}_s = -\frac{\rho_s^0}{m}\left(\alpha_l - k_w \ln\left(\frac{s_o}{\rho_s^0}\right)\right)^{-(1+1/m)} \dot{\alpha}_l$$

The shape of a hysteretic loop from saturated to dry state and *vice-versa* is depicted in Fig. 4.31, together with a scanning path.
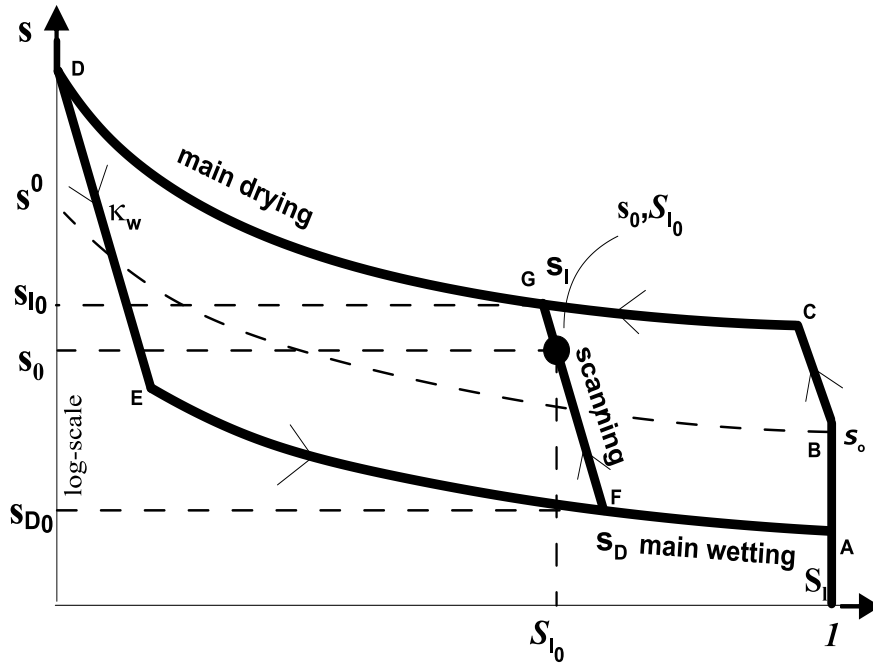
Figure 4.31: Simplified van Genuchten model derived from energy potentials

The simplified van Genuchten's model differs from Wheeler's model in the fact that once the main curves of drying and wetting are reached the developed irreversible saturations follow the path drawn by the simplified van Genuchten law. Starting from a saturation state A, the desaturation starts once the value s_o is reached. Over this point B and under a drying path the response of the model is elastic with the saturation degree following the scanning curve with slope κ_w. This response continues until the main drying curve is reached, in that moment irreversible saturations start to develop. Those irreversible saturations follow a path defined by the simplified van Genuchten law s_I (point D in Fig. 4.31). If from that last point a wetting path is followed the response of the model is elastic following a scanning curve until the main wetting curve is reached. From point E (Fig. 4.31) irreversible saturations develop following the contour defined by the simplified van Genuchten law. The model response follows the same pattern under repeated cycles of wetting and drying.

The relationship between the back suction and the plastic component of the degree of saturation α_l is obtained from the dual energy $\tilde{g}_i(\phi s, x_s) = g_i(s, \alpha_l) - x_s \alpha_l$

$$\tilde{g}_i(\phi s, x_s) = -k_w \phi s \left[\ln \left(\frac{\phi s}{\rho_s^o} \right) - 1 \right] + \frac{\rho_s^o}{1 - m} \left(1 + \frac{\rho_s - s^a}{\rho_s^o} \right)^{1-m} + k_w \rho_s \ln \left(\frac{\phi s_o}{\rho_s^o} \right) \qquad (4.46)$$

where the fundamental relation $(x_s = s - \rho_s)$ has been used. It comes from Eq. 4.46 that α_l is related to ρ_s by the following kinematical hardening law:

$$\alpha_l = -\frac{\partial \tilde{g}_s}{\partial x_s} = \left(1 + \frac{\rho_s - s^a}{\rho_s^o}\right)^{-m} + k_w \ln\left(\frac{\phi s_o}{\rho_s^o}\right) \tag{4.47}$$

Finally, the equation for the scanning path (elastic hydraulic behaviour) can be explicitly derived from the following expression of Helmholtz energy function for the interface skin $f_i(S_l, \alpha_l) = g_i(\phi s, \alpha_l) - \phi s S_l$:

$$f_i(S_l, \alpha_l) = \kappa_w \rho_s^o \exp\left(-\frac{(S_l - \alpha_l)}{\kappa_w}\right) - \rho_s^o \left[\frac{m}{m-1}\alpha_l^{*(1-1/m)} - \alpha_l\right] - \phi s^a \alpha_l^* \tag{4.48}$$

$$\phi s = -\frac{\partial f_i}{\partial S_l} = \rho_s^o \exp\left(-\frac{(S_l - \alpha_l)}{\kappa_w}\right) \tag{4.49}$$

This model has been implemented in an implicit scheme, following techniques presented in Chapter 5 to integrate implicitly hyper-poroplastic laws. Figure 4.32 shows a typical response (in the plane S_l-s) during a drying path followed by a wetting path and several cycles of wetting and drying. The range of suction considered is below 10 MPa, which corresponds to the upper limit of suction values prevailing in soil macro-porosity (where free water exists). Main drying and wetting curves draw typical paths in granular soils, with a sudden decrease in saturation when the air entry value is overcame, a relatively flat shape for degree of saturation above 40% or 50% and a progressive increase to high values of suction for low degree of saturation. Material parameters are: κ_w = 0.021, *m*= 0.8 (for both the main drying and wetting curves), ρ_s^o = 600 kPa (s_{D0} = 109.1kPa and s_{l0} = 1091kPa).

Effect of *m* and s_0 parameters on the shape of drying/wetting cyclic path is depicted in Figs. 4.33 and 4.34. A limitation of the model relies on the constant ratio predicted between s_D and s_I leading to a strong hysteresis loop even at a low degree of saturation. This aspect can be easily tackled by considering different values of *m* for the main drying and wetting curves.

_____
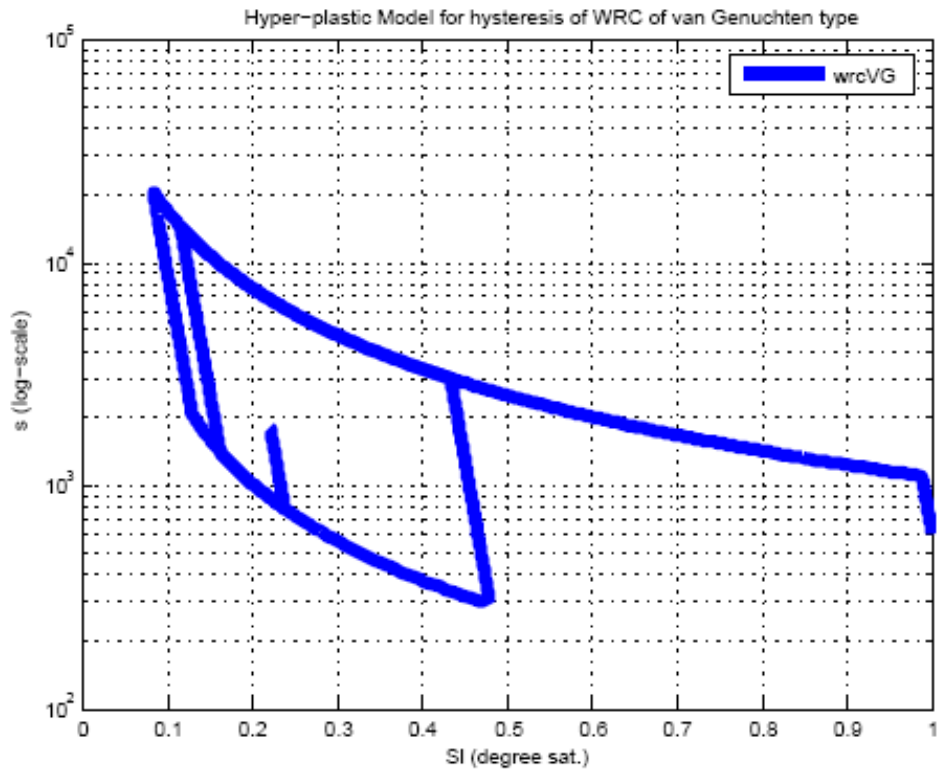
Figure 4.32: Hysteresis Model for WRC of van Genuchten type.
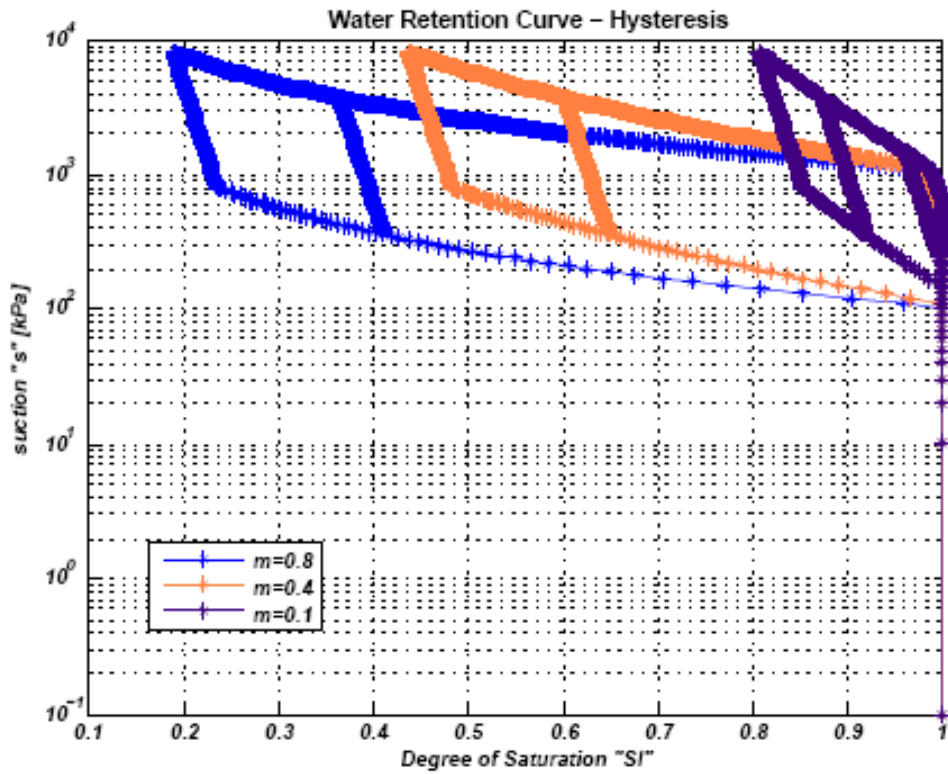
Figure 4.33: Hysteresis Model for Simplified van Genuchten WRC. Sensibility to m parameter.
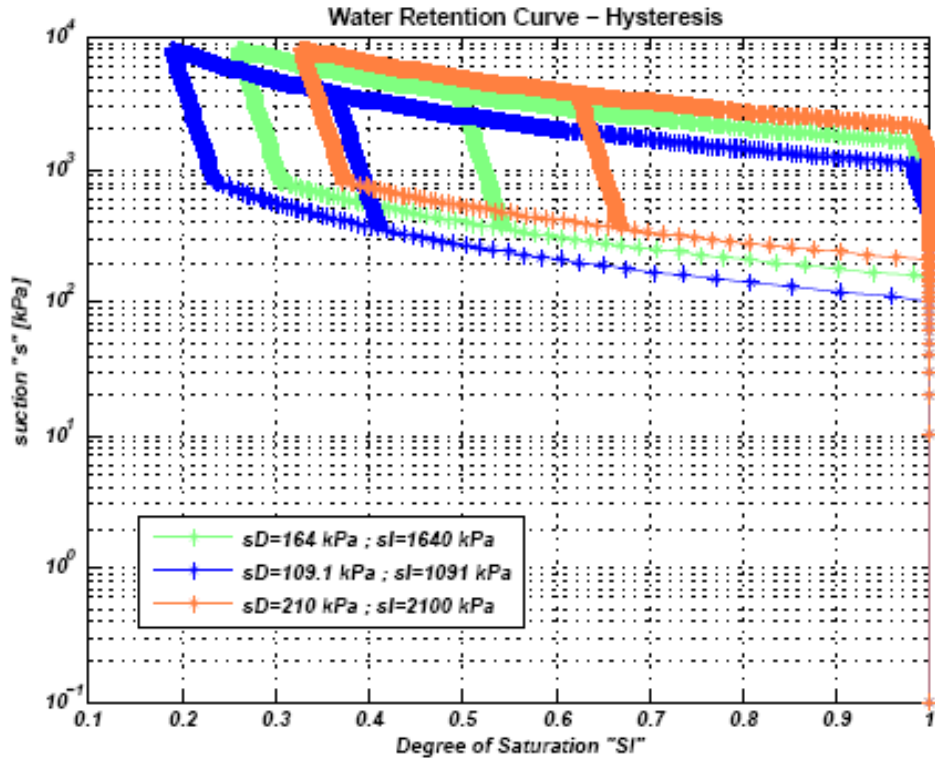
Figure 4.34: Hysteresis Model for Simplified van Genuchten WRC. Sensibility to s0 parameter.

Finally, Table 4.9 summarizes the energy functions describing the behavior of hydraulic skin (WRC) developed along the subsection.

Table 4.9: summary of energy and dissipation functions for the hydraulic interface skin.

	Energy	Dissipation-Yield Function
Wheeler WRC	*Gibbs energy*: $$g_i(\phi s, \alpha_l) = -\kappa_w \phi s \left[\ln\left(\frac{\phi s}{\rho_s^0}\right) - 1 \right] + \phi s \alpha_l$$ $$+ \underbrace{(\lambda_w - \kappa_w)\rho_s^o \exp\left(\frac{-\alpha_l}{\lambda_w - \kappa_w}\right)}_{g_{s2}}$$ *Partial Gibbs energy*: $$\tilde{g}_s(\phi s, x_s) = -\kappa_w \phi s \left[\ln\left(\frac{\phi s}{\rho_s^o}\right) - 1 \right]$$ $$+ (\lambda_w - \kappa_w)\rho_s \left[\ln\left(\frac{\rho_s}{\rho_s^o}\right) - 1 \right]$$ *Helmholtz energy*:	*Force potential*: $$z(\dot{\alpha}_l) = \frac{(\rho_s^2 - \phi^2 s_D s_I)}{4} \cdot \dot{\alpha}_l^2$$

165

	$f_i(S_l, \alpha_l) = \kappa_w \rho_s^o \exp\left(-\frac{(S_l - \alpha_l)}{\kappa_w}\right)$ $+ \underbrace{(\lambda_w - \kappa_w)\rho_s^o \exp\left(\frac{-\alpha_l}{\lambda_w - \kappa_w}\right)}_{f_{s2}}$	
Simplified van Genuchten WRC	*Gibbs energy*: $g_s(\phi s, \alpha_l)$ $= -\kappa_w \phi s\left[\ln\left(\frac{\phi s}{\rho_s^0}\right) - 1\right]$ $+ \phi s\alpha_l \underbrace{-\rho_s^0\left[\frac{m}{m-1}\alpha_l^{(1-1/m)} - \alpha_l\right] - \phi s^a \alpha_l}_{g_{s2}}$ *Partial Gibbs energy*: $\tilde{g}_s(\phi s, x_s) = -\kappa_w \phi s\left[\ln\left(\frac{\phi s}{\phi s_0}\right) - 1\right]$ $- \frac{\rho_s^o}{1-m}\left(1 + \frac{\rho_s - s^a}{\rho_s^o}\right)^{1-m}$ *Helmholtz energy*: $f_s(S_l, \alpha_l) = \kappa_w \phi s_0 \exp\left(-\frac{(S_l - \alpha_l)}{\kappa_w}\right)$ $- \rho_s^o\left[\frac{m}{m-1}\alpha_l^{(1-1/m)} - \alpha_l\right]$ $- \phi s^a \alpha_l$	*Flow potential*: $F^y(x_s) = \frac{x_s^2}{\rho_s^2 - \phi^2 s_D s_I}$

4.5) Unsaturated Soil Models from Hyper-Poroplastic Potentials

Because a saturated medium is a limit case of a three-phase porous medium when the gas phase vanishes, modeling of unsaturated soils has been historically based of an extension of saturated soils model to account, from the mechanical point of view, of the effect of gas-liquid internal pressures and interfaces forces. Within these models, the critical state models have had taken a particular relevance because of their capacity to model collapse phenomena as a result of yielding along the mean stress axis. In this section, several variants of the so-called Barcelona Basic Model, which extends the Modified Cam Clay Model to unsaturated conditions, are reviewed and merged within the hyperplasticity framework.

4.5.1) Formulation of Gallipoli et al.'s model with pure volumetric hardening

The first studied model corresponds to the model developed by Gallipoli et al. (2003). This model is based on an extension of Cam clay conditions through the use of Bishop's effective stresses σ'_{ij} and the introduction of a bonding variable ξ whose value is related to the effect produced by the interface forces on the skeleton particles. The use of the Bishop effective stress makes this model particularly suitable to be studied within the framework developed in Chapter 3. In this section, two different hyperplastic formulations of the model will be developed, leading to different types of hardening: purely volumetric or purely kinematical. It will be seen that both of them provide reliable predictions of stress-strain curves in presence of suction.

In the original paper, the model recovers the simple elastic law considered in Modified Cam clay model, whose limitations have been discussed at the end of Chapter 3. Despite of these limitations and with the aim to present in a first instance a hyperplastic formulation for the original model, this is a simple law that will be considered in the development of the thermodynamic potentials. The model will be further enhanced according to the coupled shear-volumetric elastic law presented at the end of Chapter 3.

According to Chapter 3, a hyperplastic model in three-phase porous media must include terms related to the hydraulic behaviour in the definition of the potentials. In the present section, the simplified van-Genuchten like expression will be considered for modeling the water retention curve.

If the hysteretic response of the retention curve is disregarded then the curves of elastic response "scanning curves" are no longer valid. It result is $f_{i_1} = 0$ and as consequence $S_l^e = 0$ and the degree of saturation is given by the internal saturation variable $S_l = \alpha_1$ or equivalently $S_l = \dfrac{\partial f_{i_2}}{\partial \phi s}$.

Moreover, the simplest hydro-mechanical coupling, corresponding to expression 3.75 is adopted. According to this assumption, the free energy of the solid skeleton in presence of gas-liquid interface sums up the free energy of the interface (weighted by the porosity) to the free energy of the solid skeleton in absence of gas-liquid interfaces. In Gallipoli et al.'s model, the latter is directly given by the Helmholtz (alternatively Gibbs) free energy of Modified Cam Clay model. Considering for the moment that there is no kinematical hardening, then the energies of the solid skeleton read:

$$f_s = \kappa^* p^o \exp\left(\frac{\varepsilon_p}{\kappa^*}\right) + \frac{3G\varepsilon_q^2}{2} + \phi \underbrace{\rho_s^0 \left[\frac{m}{m-1} S_l^{(1-1/m)} - S_l\right]}_{E_i} \tag{4.50}$$

$$g_s = -\kappa^* p' \left[\ln\left(\frac{p'}{p^o}\right) - 1\right] - \frac{q^2}{6G} + \phi \underbrace{\frac{\rho_s^0}{m-1}\left[\left(1 + \frac{\phi s}{\phi \rho_s^0}\right)^{(1-m)}\right]}_{E_i} - \left(p'\alpha_p + q\alpha_q\right) \tag{4.51}$$

from which:

$$p' = p^o \exp\left(\frac{\varepsilon_p}{\kappa^*}\right) \tag{4.52}$$

$$q = 3G\varepsilon_q$$

$$\phi s = \phi \rho_s^0 \left(S_l^{(-1/m)} - 1\right)$$

$$\varepsilon_p = \kappa^* \ln\left(\frac{p'}{p^o}\right)$$

$$\varepsilon_q = \frac{q}{3G}$$

$$S_l = \left(1 + \frac{\phi s}{\phi \rho_s^0}\right)^{-m}$$

Differentiation of equations 4.52 gives rise to the stiffness matrix $C^{fg}(\varepsilon_{ij}, \phi s)$:

$$C^{fg} = \begin{bmatrix} \frac{p^o}{\kappa^*}\exp\left(\frac{\varepsilon_p}{\kappa^*}\right) & 0 & 0 \\ 0 & 3G & 0 \\ 0 & 0 & -\frac{m}{\phi\rho_s^0}\left(1 + \frac{\phi s}{\phi\rho_s^0}\right)^{-(m+1)} \end{bmatrix} \tag{4.53}$$

and the compliance matrix $D^{gs}(\sigma_{ij}, \phi s)$,

$$D^{gs} = \begin{bmatrix} \frac{\kappa^*}{p'} & 0 & 0 \\ 0 & \frac{1}{3G} & 0 \\ 0 & 0 & -\frac{m}{\phi\rho_s^0}\left(1 + \frac{\phi s}{\phi\rho_s^0}\right)^{-(m+1)} \end{bmatrix} \tag{4.54}$$

A more real representation of the behaviour consists in introducing the dependence of the shear modulus on the mean effective stress, as done in section 3.6.1. Following the hydro-

_____

mechanical coupling provided by expression 3.76, the Helmholtz (alternatively the Gibbs) free energy sums up Houlsby et al. (2005)'s proposal for the solid skeleton Eq. 3.96 (alternatively Eq. 3.100) to the Helmholtz (alternatively Gibbs) potential associated to the retention curve:

$$f_s = \kappa^* p^c \exp\left(\frac{\varepsilon_p}{\kappa^*} + \frac{3\varrho\varepsilon_q^{~2}}{2\kappa^*}\right) + \varphi\rho_s^0 \left[\frac{m}{m-1} S_l^{(1-1/m)} - S_l\right] \tag{4.55}$$

$$g_s = -\kappa^* \cdot p' \left[\ln\left(\frac{p'}{p^c}\right) - 1\right] - \frac{q^2}{6\varrho p'} + \varphi \frac{\rho_s^0}{1-m}\left[\left(1 + \frac{\varphi s}{\varphi\rho_s^0}\right)^{(1-m)}\right] \tag{4.56}$$

The expressions for the mean stress, the deviatoric stress and constitutive suction are then (alternatively: volumetric strain, deviatoric strain and degree of saturation):

$$p' = \frac{\partial f_s}{\partial \varepsilon_p} = p^c \exp\left(\frac{\varepsilon_p}{\kappa^*} + \frac{3\varrho\varepsilon_q^{~2}}{2\kappa^*}\right) \tag{4.57}$$

$$q = \frac{\partial f_s}{\partial \varepsilon_q} = 3\varrho p^c \exp\left(\frac{\varepsilon_p}{\kappa^*} + \frac{3\varrho\varepsilon_q^{~2}}{2\kappa^*}\right)\varepsilon_q$$

$$\varphi s = -\frac{\partial f_s}{\partial S_l} = \varphi\rho_s^0\left(S_l^{(-1/m)} - 1\right)$$

$$\varepsilon_p = -\frac{\partial g_s}{\partial p'} = \kappa^* \log\left(\frac{p'}{p^o}\right) - \frac{q^2}{6\varrho p'^2}$$

$$\varepsilon_q = -\frac{\partial g_s}{\partial q} = \frac{q^2}{3\varrho p'}$$

$$S_l = \frac{\partial g_s}{\partial \varphi s} = \left(1 + \frac{\varphi s}{\varphi\rho_s^0}\right)^{-m}$$

From double differentiation of Eq. 4.55 and Eq. 4.56, the stiffness $C^{f_s}(\varepsilon_{ij}, S_l)$ and compliance $D^{g_s}(\sigma'_{ij}, \varphi s)$ matrices read:

$$C^{f_s} = \begin{bmatrix} \dfrac{p'}{\kappa^*} & \dfrac{q}{\kappa^*} & 0 \\[3mm] \dfrac{q}{\kappa^*} & \dfrac{q^2}{p'\kappa^*} + 3\varrho p' & 0 \\[3mm] 0 & 0 & -\dfrac{\varphi\rho_s^0}{m} S_l^{-(1/m+1)} \end{bmatrix} \tag{4.58}$$

$$D^{gs} = \begin{bmatrix} \dfrac{\kappa^*}{p'} + \dfrac{q^2}{3\varrho(p')^3} & -\dfrac{q}{3\varrho(p')^2} & 0 \\[2.5ex] -\dfrac{q}{3\varrho(p')^2} & \dfrac{1}{3\varrho p'} & 0 \\[2.5ex] 0 & 0 & -\dfrac{m}{\phi\rho_s^0}\left(1+\dfrac{\phi s}{\phi\rho_s^0}\right)^{-(m+1)} \end{bmatrix} \tag{4.59}$$

Within the framework of Finite Element formulation of u-p type, it is interesting to be able to compute the secondary variables – stresses and degree of saturation – from the primary variables – strain and suction. The corresponding relationship is provided by derivatives of the cross potential $f_s^g(\varepsilon_{ij}, \phi s)$:

$$f_s^g = \kappa^* p^o \exp\left(\frac{\varepsilon_p}{\kappa^*} + \frac{3\varrho\varepsilon_q{}^2}{2\kappa^*}\right) + \phi \underbrace{\frac{\rho_s^0}{m-1}\left[\left(1+\frac{\phi s}{\phi\rho_s^0}\right)^{(1-m)}\right]}_{E_i} \tag{4.60}$$

Leading to the mixed Hessian matrix:

$$C^{f_s^g} = \begin{bmatrix} \dfrac{p'}{\kappa^*} & \dfrac{q}{\kappa^*} & 0 \\[2.5ex] \dfrac{q}{\kappa^*} & \dfrac{q^2}{p'\kappa^*} + 3\varrho p' & 0 \\[2.5ex] 0 & 0 & -\dfrac{m}{\phi\rho_s^0}\left(1+\dfrac{\phi s}{\phi\rho_s^0}\right)^{-(m+1)} \end{bmatrix} \tag{4.61}$$

$C^{f_s^g}$ can be easily obtained from matrix C^{f_s}, as it is diagonally dominant due to the absence of hydro-mechanical coupling. The interest of using f_s^g to derive the constitutive law to be implemented in a Finite Element program becomes more evident in case of higher coupling.

The modeling of the plastic behavior requires to consider the formulation of the constraint that limits the elastic (admissible) domain. The surface proposed by Gallipoli and co-workers has the same elliptic shape as in the Modified Cam Clay Model, but its size is magnified due to the presence of gas-liquid interface forces which structure the material. To model this effect, the authors introduce a new "bonding" variable (ξ) that quantifies the magnitude of inter-particle bonding due to water menisci. It is defined as the product of the degree of saturation of the gas phase $(1 - S_l)$ multiplied by a function of suction $f_1(s)$:

$$\xi = f_1(s)(1 - S_l) \tag{4.62}$$

The factor $(1 - S_l)$ accounts for the number of water menisci per unit volume of solid fraction and is equal to zero when the soil is saturated $(S_l = 1)$. When the soil becomes

_____

drier and the number of water menisci increase, this factor assumes positive and increasing values. The function $f_1(s)$ accounts for the stabilizing inter-particle force exerted by a single meniscus whose efficiency decreases as the radius of the meniscus becomes smaller. It varies monotonically between 1 and 1.5 for values of suction ranging between zero and infinite respectively.

At the present model the bounding variable is modeled in terms of the effective suction instead of total suction to fulfill with hyperporoplastic framework, thus the bounding variable is redefined as,

$$\xi = f_1(\phi s)\big(1 - f_2(\phi s)\big) \tag{4.63}$$

$$\begin{cases} f_1(\phi s) = 1 + \dfrac{{}^{\phi s}\!/_{\phi s_i}}{f_1 + f_2\,{}^{\phi s}\!/_{\phi s_i}} \\[3mm] f_2(\phi s) = \left(1 + \dfrac{\phi s}{\phi s_0}\right)^{-m}\left(1 - f_2^{\min}\right) + f_2^{\min} \end{cases}$$

where the factors $f_1(\phi s)$ and $[1 - f_2(\phi s)]$ have the same connotations to those of the original model, described above.

Based on the results of isotropic virgin compression tests at constant suction, Gallipoli et al. (2003) studied the changes of the slope of the normal compression line for a range of average skeleton pressure. The study revealed that the normal compression lines at non-zero values of suction are not straight lines in the semi-logarithmic plane $(e - \ln(p'))$ but they are curves with decreasing slope as they approach the saturated line, see Fig. 4.35. Motivated by the test evidence, the authors propose a unique relationship for the proportion $\left({}^e\!/_{e_s}\right)$ and the bonding variable (ξ) at constant suction,

$$\frac{e}{e_s} = 1 - a[1 - \exp(b\xi)] \tag{4.64}$$

where a and b are material parameters. For the model we use the specific volume $(v = 1 + e)$ instead of the void ratio(e), its use is consistent with the bi-logarithmic compressibility law proposed by (Butterfield, 1979) which leads to an analytical formulation tractable to implicit integration. Equation 4.64 is then re-written as,

$$\frac{v}{v_s} = 1 - \frac{a}{\left(\dfrac{1}{e_s} + 1\right)}[1 - \exp(b\xi)] \tag{4.65}$$

The last equation was also used by (Borja R. I., 2004).

According to 4.64, the isotropic yield locus at suction s (denoted p_0) is related to the yield locus in saturated conditions p_0^* by the relationship (see Gallipoli et al., 2003, for further details):

$$\left(\frac{v}{v_s}\lambda^* - \kappa^*\right)\ln p_0 - N\frac{v}{v_s} = (\lambda^* - \kappa^*)\ln p_0^* - N \tag{4.66}$$

where N is the origin of the virgin loading branch in saturated conditions, κ^* and λ^* the slope of the unloading-reloading and virgin branch, respectively, also in saturated conditions.
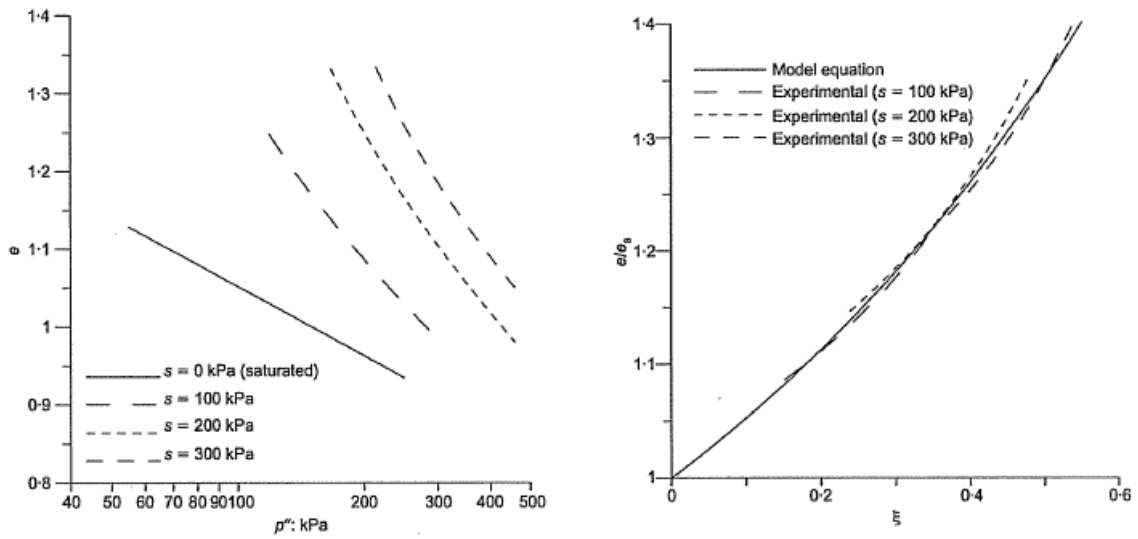
Figure 4.35: (a) Normal compression lines at constant suction in the plane $\left(e - ln(p')\right)$ (data by Sivakumar, 1993), after Gallipoli et. al (2003). (b) Relationship between ratio$\left(e/e_s\right)$ and the bonding factor (ξ) during isotropic virgin loading at constant suction (data by (Sivakumar, 1993), after (Gallipoli, Gens, Sharma, & Vaunat, 2003)).

From Eq. 4.66 and Eq. 3.110 (note that p_0^* is twice the center of the ellipse), the dependency of p_0 on the internal variable α_p and suction s reads:

$$p_0(\alpha_p, s) = z\left(\frac{p^c}{2} \cdot \exp\left(\frac{\alpha_p}{\lambda^* - \kappa^*}\right)\right)^b \tag{4.67}$$

$$z(\xi) = 2^{b(\xi)}\exp\left(\frac{N\left(\frac{v}{v_s} - 1\right)}{\left(\frac{v}{v_s}\lambda^* - \kappa^*\right)}\right)$$

$$b = \frac{\lambda^* - \kappa^*}{\left(\frac{v}{v_s}\lambda^* - \kappa^*\right)}$$

_____

where $\frac{v}{v_s}$ depends on suction. The equation of the yield surface $f^y\big(p', q, \phi s, \alpha_p\big)$ in the true stress space is:

$$f^y = \frac{q^2}{M^2} + p'\left(p' - z\underbrace{\left(\frac{p^c}{2} \cdot \exp\left(\frac{\alpha_p}{\lambda^* - \kappa^*}\right)\right)^b}_{p_0}\right) = 0 \tag{4.68}$$

From the expression of the Gibbs energy, the back stress ρ_{ij} is identically null and the generalized stress x'_{ij} is equal to the true stress σ'_{ij}. The equation for the yield surface reads then:

$$f^y = \frac{x_q'^{\,2}}{M^2} + x'_p\big(x'_p - p_0\big) = 0 \tag{4.69}$$

Leading to the flow rule:

$$\dot{\alpha}_p = \dot{\lambda}\frac{\partial f^y}{\partial x'_p} = \dot{\lambda}\big(2x'_p - p_0\big) \tag{4.70}$$

$$\dot{\alpha}_q = \dot{\lambda}\frac{\partial f^y}{\partial x'_q} = \dot{\lambda}\frac{2x'_q}{M^2}$$

The dissipation is finally obtained by eliminating $\dot{\lambda}$ in Eq. 4.70:

$$
\begin{aligned}
d_s(s, \alpha_p, \dot{\alpha}_p, \dot{\alpha}_q) &= \frac{p_0}{2}\left(\big[\dot{\alpha}_p^2 + M^2\dot{\alpha}_q^2\big]^{1/2} + \dot{\alpha}_p\right) \\
&= \frac{z}{2}\left[p^c\exp\left(\frac{\alpha_p}{\lambda^* - \kappa^*}\right)\right]^b\left(\big[\dot{\alpha}_p^2 + M^2\dot{\alpha}_q^2\big]^{1/2} + \dot{\alpha}_p\right)
\end{aligned}
\tag{4.71}
$$

and the hardening law takes the following form:

$$x'_p = \frac{\partial d_s}{\partial \dot{\alpha}_p} = \frac{p_0}{2}\left(\big[\dot{\alpha}_p^{\,2} + M^2\dot{\alpha}_q^{\,2}\big]^{-1/2}\dot{\alpha}_p + 1\right) \tag{4.72}$$

$$x'_q = \frac{\partial d_s}{\partial \dot{\alpha}_q} = M^2\frac{p_0}{2}\big[\dot{\alpha}_p^{\,2} + M^2\dot{\alpha}_q^{\,2}\big]^{-1/2}\dot{\alpha}_q$$

This model, referred as BBM[1], has been implemented in the framework of the Interior Point Method presented in Chapter 5. Its performance is investigated through a series of tests performed on the Barcelona Harbour Clay, whose parameters are given in Table 4.10.

Table 4.10: Material properties for Barcelona Harbour Clay

$\kappa*$	0.018	p^c	0.01	ϱ	0.09	N	1.1759	M	1
$\lambda*$	0.09	A	0.185	B	0.1419	ρ_s^0	0.4	m	0.6

Figure 4.36 shows the response of the model at constant suction. The curves evidence the classical duality of Modified Cam Clay Model: dilatancy at low confining stress and contractancy at high confining stress. The reach of the yield point at lower deviatoric stress as the pre-consolidation ratio decreases can also be verified.

Figure 4.37 shows the evolution of the deviatoric stress and the volumetric strain with the axial strain for three different values of suction, maintained constant during the tests. In the three tests, the yield surface is reached on the wet-side of the critical state line. Model predicts consistently higher deviatoric stresses and lower contractancy when the suction is higher.

Figure 4.38 depicts the void ratio – mean effective stress curves predicted for three isotropic loading paths performed at distinct prescribed suctions. In the three computations, the yield point is exceeded and loading pursued in the plastic regime. It can be observed in the figure that 1) the yield point increases with the value of the prescribed suction and 2) the virgin loading branches converge towards the saturated line because of the plastic reduction of the void ratio e and, thus, of the ratio v/v_s.

_____
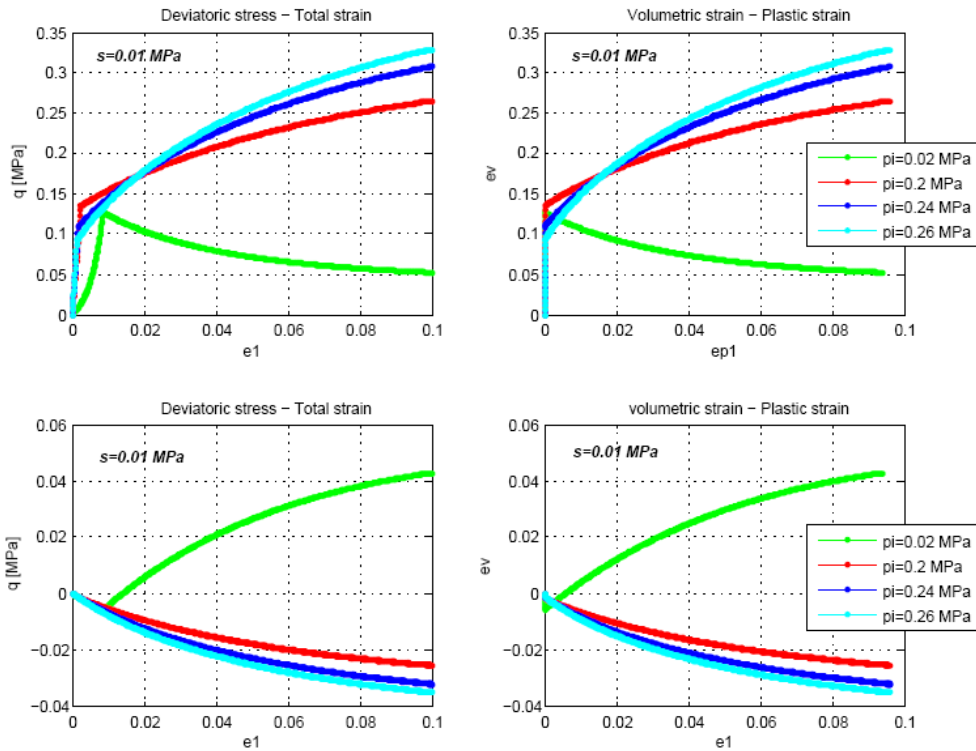
*Figure 4.36: (Gallipoli's model) Conventional Drained Triaxial Test on normally and over-consolidated compressed soil Samples. **BBM**[1] Model at a constant suction of 0.01MPa*
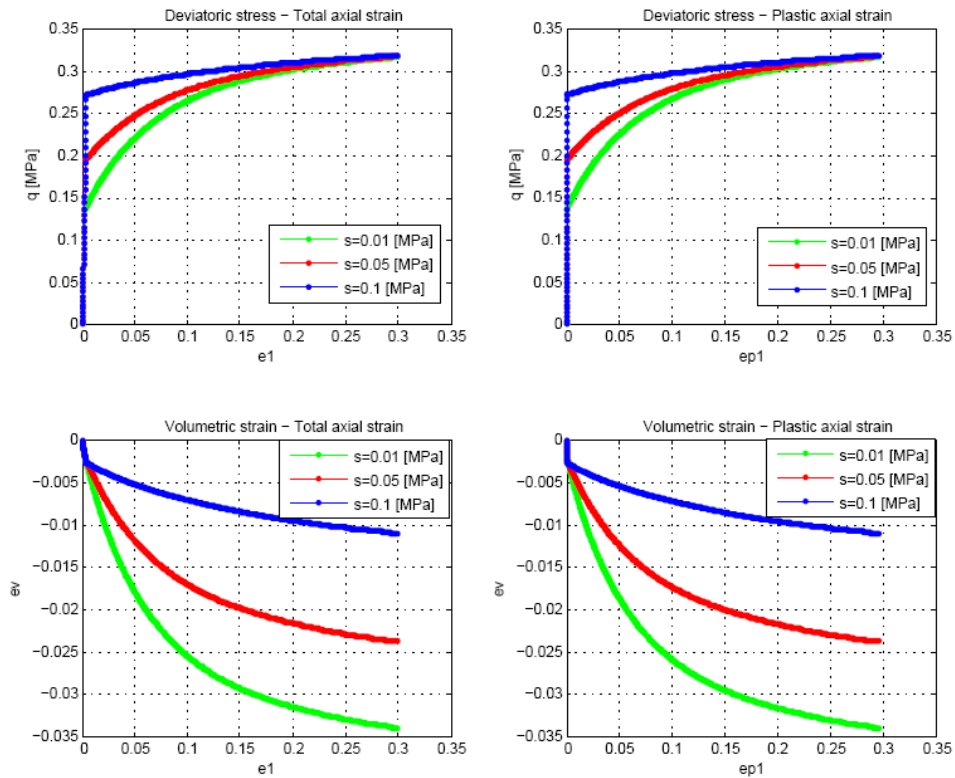
*Figure 4.37: (Gallipoli's model) Conventional Drained Triaxial Test on normally and over-consolidated compressed soil Samples. **BBM**[1] Model at three different suction values (0.01MPa, 0.05MPa, 0.1MPa).*

175
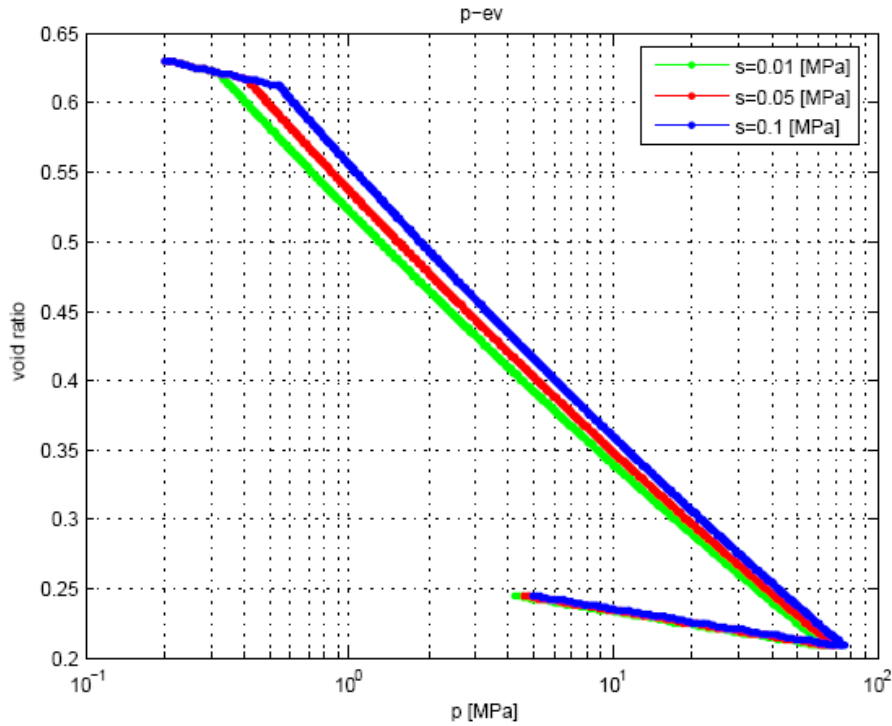
Figure 4.38: (Gallipoli's model) Relation between mean effective stress "p' " and the void ratio "e". Loading-Unloading for BBM[1] model with non-linear elastic modulus. For three different suctions $(0.01\ MPa,\ 0.05\ MPa,\ 0.1\ MPa)$

4.5.2) Formulation of Gallipoli et al.'s model with pure kinematic hardening

Gallipoli et al.'s model can be alternatively modeled within a hyperporoplastic framework by introducing kinematical hardening for the mechanical part. As before the hysteretic response of the retention curve is disregarded and as consequence $f_{i_1} = 0$ and the equality $S_l = \alpha_1$ holds or equivalently $S_l = \left.\frac{\partial f_{i_2}}{\partial \phi s}\right.$. Dependency of WRC on density is moreover considered in this version of the model. In the next subsection 4.5.2.1 this dependency is addressed in concise manner revisiting two well documented proposals Coussy et.al. (2002) and Gallipoli et.al. (2003) and framing them in a hyperplastic scenario. Finally a simpler dependency is proposed for the WRC which will lead to a well posed formulation.

4.5.2.1) Dependency of WRC on soil density

Several dependencies exist to introduce the soil's density dependency on the WRC, Coussy (2002) proposed to set a dependency of the interface energy on soil porosity $f_{i_2} = \phi^{-1/3} f_i^u(S_l)$. More recently, Gallipoli et.al. (2003) proposed to set the air entry on specific

_____

volume $\rho_s^o(v) = \rho_{s_o}^o w_1 (v-1)^{w_2}$. As shown hereinafter energy potentials for both proposals are identical for specific values of w_1 and w_2. According to Coussy's proposal interface energy reads:

$$
\begin{aligned}
f_{i_2} &= \left(\frac{\exp(\varepsilon_p)-1}{1+e}\right)^{2/3} \cdot f_i^u(S_l) \\
&= \rho_s^o \left(\frac{\exp(\varepsilon_p)-1}{1+e}\right)^{2/3} \cdot \left[\frac{m}{m-1}S_l^{1-1/m} - S_l\right]
\end{aligned}
\tag{4.73}
$$

which states the dependency of the WRC on volumetric strain. On the other side, following the Gallipoli's proposal, the interface energy takes the form:

$$
\begin{aligned}
f_{i_2} &= \rho_s^o w_1 \left(\exp(\varepsilon_p)-1\right)^{w_2} \cdot \left[\frac{m}{m-1}S_l^{1-1/m} - S_l\right] \\
&= \rho_s^o \left(\frac{\exp(\varepsilon_p)-1}{1+e}\right)^{2/3} \cdot \left[\frac{m}{m-1}S_l^{1-1/m} - S_l\right]
\end{aligned}
\tag{4.74}
$$

Both expressions coincide for $w_1 = \left(\frac{1}{1+e}\right)^{2/3}$ and $w_2 = \frac{2}{3}$.

Such a dependency can alternatively be expressed in term of the mean stress as:

$$
f_{i_2}^g = \rho_s^o \left(\frac{\exp\left(k^* \ln\left(\frac{p'}{p_o}\right)\right)-1}{1+e}\right)^{2/3} \cdot \left[\frac{m}{m-1}S_l^{1-1/m} - S_l\right]
\tag{4.75}
$$

Or in terms of suction after the transformation $g_{i_2} = \phi s S_l - f_{i_2}^g$

$$
g_{i_2} = \frac{\rho_s^o}{m-1}\left(\frac{\exp\left(k^* \ln\left(\frac{p'}{p_o}\right)\right)-1}{1+e}\right)^{2/3} \cdot \left[1 + \frac{\phi s}{\rho_s^o}\right]^{1-m}
$$

These last two expressions provide expressions for the interface energy with dependency on the soil density. Those proposals lead to layouts of potential function f_{i_2} with complex Legendre transformation, as consequence a simpler expression is proposed to account for such dependency which will lead to a well posed formulation. Let consider the Gibbs energy for the interface skin given by,

$$g_{i_2} = \phi \frac{\rho_s^o \left(\frac{p'}{p_0^s} - \chi^o \right)}{m - 1} \cdot \left(1 + \frac{\phi s}{\phi \rho_s^o} \right)^{1-m} \qquad (4.76)$$

where $\left(\chi^o = \frac{p_i}{p_0^s} - 1 \right)$, p_i is the initial mean stress and p_0^s is a reference mean stress. The magnitude of the reference stress p_0^s defines the sensibility of the capillary curve to mechanical actions. Thus the expression of degree of saturation obtained by differentiation of Eq. 4.6 is:

$$S_l = \left(\frac{p'}{p_0^s} - \chi^o \right) \left(1 + \frac{\phi s}{\rho_s^0} \right)^{-m} \qquad (4.77)$$

Equation 4.77 differs from the simplified van Genuchten law by the term $\left(\frac{p'}{p_o} - \chi^o \right)$

which acts as a shifting parameter of the hydraulic skin due to mechanical actions.

This subsection established the basis to proceed further with the model development accounting for the kinematic hardening formulation. It is clearly noted that in this case the decouple consideration between the solid and the interface phases is not possible and the layout of the Gibbs and Helmholtz energy functions is of the form: (a) $g_s = g_1 - \sigma \alpha + (g_{i2} + g_2)$ and (b) $f_s = (f_1 + f_{i2}) + f_2$.

Considering the energy 4.76, the Gibbs and Helmholtz energy functions for the porous skeleton result, explicitly:

$$g_s = -\kappa^* p' \left[\ln \left(\frac{p'}{p_o} \right) - 1 \right] - \frac{q^2}{6 \varrho p'} - (p' \alpha_p + q \alpha_q) \qquad (4.78)$$

$$+ \underbrace{\phi \frac{\rho_s^0 \left(\frac{p'}{p_0^s} - \chi^o \right)}{m - 1} \left[\left(1 + \frac{\phi s}{\phi \rho_s^0} \right)^{(1-m)} \right]}_{g_{s_2}} + f_2$$

with the trapped energy of the solid skeleton f_2 given by:

$$f_2\left(\equiv \int \frac{p_0}{2}\,d\alpha_p\right) = \int \frac{z}{2}\left(\frac{p^c}{2}\exp\left(\frac{\alpha_p}{\lambda^* - \kappa^*}\right)\right)^b d\alpha_p \tag{4.79}$$

$$= \frac{(\lambda^* - \kappa^*)}{b}\frac{z}{2}\left(\frac{p^c}{2}\exp\left(\frac{\alpha_p}{\lambda^* - \kappa^*}\right)\right)^b = \frac{(\lambda^* - \kappa^*)}{b}\frac{p_0}{2}$$

Note that f_2 is not only function of α_p but also of ϕs (or alternatively S_l as the relationship between both variables is univoque in this model) through parameters z and b. As a consequence, since f_2 and f_{i_2} depend on mechanical and hydraulic variables, the uncoupled assumption is not valid.

The complementary Helmholtz energy function obtained as a Legendre transformation of the Gibbs energy, is:

$$\begin{aligned} f_s^g \quad &= \kappa^* p^o \exp\left(\frac{\varepsilon_p^e - \varepsilon^c(s)}{\kappa^*} + \frac{3\varrho\varepsilon_q^{e2}}{2\kappa^*}\right) + f_2 \tag{4.80} \\ &= \kappa^* p^o \exp\left(\frac{\varepsilon_p^e}{\kappa^*} - \phi\frac{\rho_s^0}{\kappa^* p_0^s(m-1)}\left[\left(1 + \frac{\phi s}{\phi\rho_s^0}\right)^{(1-m)}\right] + \frac{3\varrho\varepsilon_q^{e2}}{2\kappa^*}\right) + f_2 \end{aligned}$$

where the coupled strain $\varepsilon^c(s)$ appears within the exponential function in addition to the volumetric and deviatoric strains. Mechanical state equations provide the expressions for the strains, stresses and generalized stresses:

$$\varepsilon_p = -\frac{\partial g_s}{\partial p} = \underbrace{\kappa^* \ln\left(\frac{p'}{p_o}\right) - \frac{q^2}{6\varrho p'^2}}_{\varepsilon^e} + \alpha_p + \underbrace{\phi\frac{\rho_s^0}{p_0^s(m-1)}\left[\left(1 + \frac{\phi s}{\phi\rho_s^0}\right)^{(1-m)}\right]}_{\varepsilon^c} \tag{4.81}$$

$$\varepsilon_q = -\frac{\partial g_s}{\partial q} = \frac{q'}{3\varrho p'} + \alpha_q$$

$$p' = \frac{\partial f_s}{\partial \varepsilon_p} = p^o\exp\left(\frac{\varepsilon_p^e}{\kappa^*} - \phi\frac{\rho_s^0}{\kappa^* p_o(m-1)}\left[\left(1 + \frac{\phi s}{\phi\rho_s^0}\right)^{(1-m)}\right] + \frac{3\varrho\varepsilon_q^{e2}}{2\kappa^*}\right)$$

$$q' = \frac{\partial f_s}{\partial \varepsilon_q} = p^o\exp\left(\frac{\varepsilon_p^e}{\kappa^*} - \phi\frac{\rho_s^0}{\kappa^* p_o(m-1)}\left[\left(1 + \frac{\phi s}{\phi\rho_s^0}\right)^{(1-m)}\right] + \frac{3\varrho\varepsilon_q^{e2}}{2\kappa^*}\right)3\varrho\varepsilon_q^e$$

$$x_p' = -\frac{\partial g_s}{\partial \alpha_p} = p' - \underbrace{\frac{\partial f_2}{\partial \alpha_p}}_{\rho'} = p' - \underbrace{\frac{z}{2}\left(\frac{p^c}{2}\exp\left(\frac{\alpha_p}{\lambda^* - \kappa^*}\right)\right)^b}_{\rho_p = \frac{p_0}{2}}$$

$$x_q' = -\frac{\partial g_s}{\partial \alpha_q} = q$$

Equations 4.81a and 4.80c state relations for the volumetric strain and mean stress that are different from those derived by Eqs. 4.57a-4.57d. This is due to the assumed dependency of the capillary curve on mechanical variables given by multiplicative ratio $\left(\frac{p'}{p_o} - \chi^o\right)$. As far as the hydraulic part is concerned the degree of saturation is defined as:

$$
\begin{aligned}
S_l &= -\frac{\partial g_s}{\partial \phi s} = \left(\frac{p'}{p_o} - \chi^o\right)\left(1 + \frac{\phi s}{\phi \rho_s^0}\right)^{-m} + \underbrace{\frac{\partial f_2}{\partial \phi s}}_{S_l^c} \\
&= \left(\frac{p'}{p_o} - \chi^o\right)\left(1 + \frac{\phi s}{\phi \rho_s^0}\right)^{-m} - \frac{\lambda^* - \kappa^*}{2}\frac{d\left(\frac{p_0}{b}\right)}{dS_l}
\end{aligned}
\tag{4.82}
$$

where $\left.\frac{\partial\left(\frac{p_0}{b}\right)}{\partial S_l}\right. = \left.\frac{\partial\left(\frac{p_0}{b}\right)}{\partial s}\right.\frac{\partial s}{\partial S_l}$. Equation 4.82 obviously states a relationship between suction and degree of saturation that is different from the water retention curve of the material as a result of the additional term $\left.\frac{(\lambda^* - \kappa^*)}{2}\frac{d\left(\frac{p_0}{b}\right)}{ds}\right.$. This additional terms appear as a consequence of the shift of the whole hydro-mechanical elastic domain driven by both the mechanical kinematical hardening and the hydraulic kinematical hardening.

Due to the new dependencies and couplings coming out of kinematic hardening assumed the following decomposition of strains and degree of saturation for modeling partially saturated soils is possible:

Total strain	ε_{ij}		
elastic + couple (hyd. induced) + plastic recoverable	ε_{ij}^e	ε_{ij}^c	α_{ij}
	Recoverable		
Effective degree of saturation	S_l		
without hysteresis: coupled (mech. induced) + plastic	S_l^c		$S_l \equiv \alpha_l$
with hysteresis:	S_l^e	S_l^c	α_l
elastic + coupled + plastic recoverable	Recoverable		

The model is completed by the definition of the following expression for the dissipation:

$$d_s = \frac{p_0}{2}\sqrt{\dot{\alpha}_p{}^2 + M^2\dot{\alpha}_q{}^2} \tag{4.83}$$

where p_0 is given Eq. 4.67. The hardening law is then expressed as:

$$x'_p = \frac{\partial d_s}{\partial \dot{\alpha}_p} = \frac{p_0}{2}\frac{\dot{\alpha}_p}{\sqrt{\dot{\alpha}_p{}^2 + M^2\dot{\alpha}_q{}^2}} \tag{4.84}$$

$$x'_q = \frac{\partial d_s}{\partial \dot{\alpha}_q} = \frac{p_0}{2}\frac{M^2\dot{\alpha}_q}{\sqrt{\dot{\alpha}_p{}^2 + M^2\dot{\alpha}_q{}^2}}$$

The elimination of $\dot{\alpha}_p$ and $\dot{\alpha}_q$ in Eq. 4.84 provides the expression for the yield surface in the generalized stress space,

$$f^y = x'_p{}^2 + \frac{x'_q{}^2}{M^2} - \left(\underbrace{\frac{z}{2}\left(\frac{p^c}{2}\exp\left(\frac{\alpha_p}{\lambda^* - \kappa^*}\right)\right)^b}_{p_0/2}\right)^2 = 0 \tag{4.85}$$

The flow rule is given by:

$$\dot{\alpha}_p = \frac{\partial f^y}{\partial x'_p}\dot{\lambda} = 2x'_p\dot{\lambda}$$

$$\dot{\alpha}_q = \frac{\partial f^y}{\partial x'_q} = \frac{2x'_q}{M^2}\dot{\lambda} \tag{4.86}$$

and the expression of the yield surface in the true stress space is finally:

$$f^y = \left(p' - \frac{p_0}{2}\right)^2 + \frac{q^2}{M^2} - \left(\frac{p_0}{2}\right)^2 = 0 \tag{4.87}$$

This model, referred as BBM[2], has been implemented in the framework of the Closest Point Projection Method discussed in Chapter 5. Its performance is illustrated on the same set of data as for model BBM[1]. The response on isotropic tests at three different suctions is depicted in Fig. 4.39 while Fig. 4.40 shows the response for the triaxial tests at constant suction and different confining pressures. The response is totally similar to the one obtained with model BBM[1].
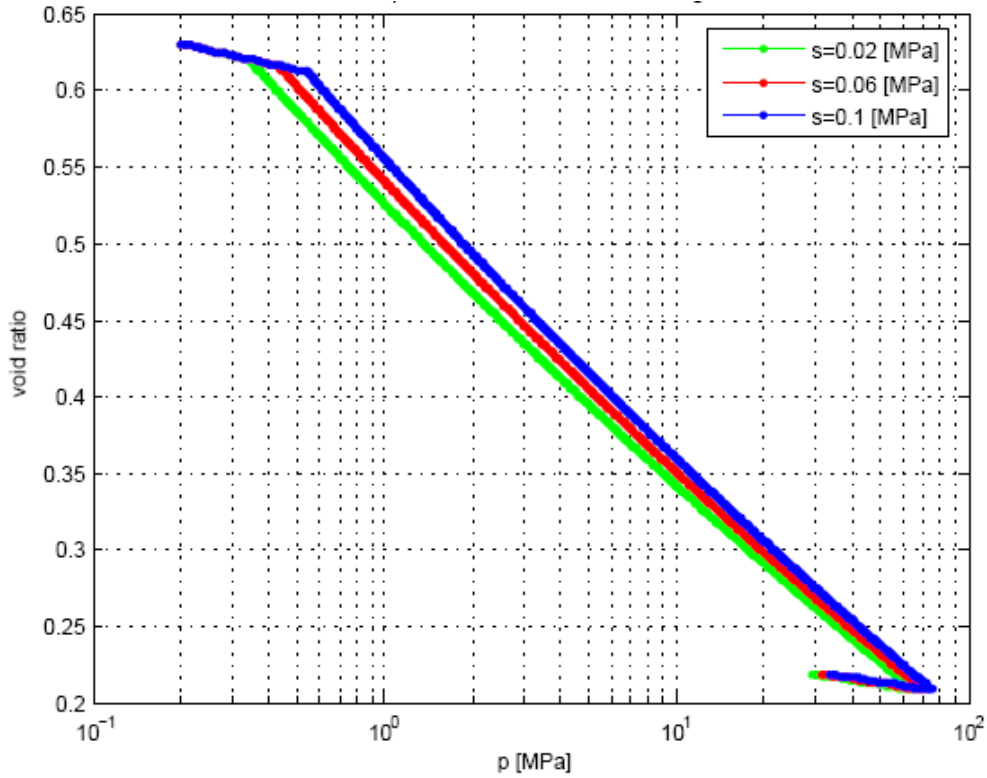
Figure 4.39: (Gallipoli's model) Relation between mean effective stress "p' " and void ratio "e" during an isotropic loading – unloading path modeled using BBM^2 model with non-linear elastic modulus.
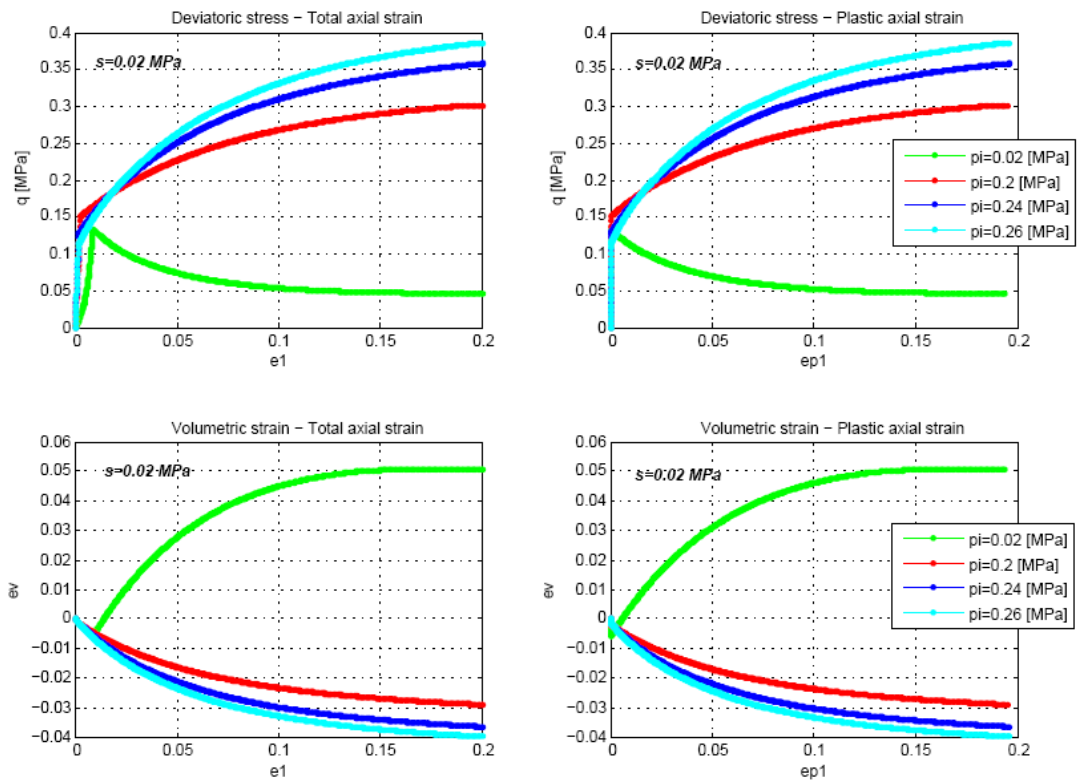
Figure 4.40: (Gallipoli's model) Predicted response of triaxial tests on normally and over-consolidated soils at a constant suction of 0.02MPa using $\textbf{BBM}^2$ Model.

Figures 4.41 and 4.42 show: (a) the variation of mean stress and preconsolidation due to a continuous drying of the sample and (b) the variation of sample saturation due to the exerted triaxial stress path, respectively.

Fig. 4.41c shows a decrease of the preconsolidation pressure as the degree of saturation increases. Moreover, Fig. 4.41a shows an increase of the mean pressure as the degree of saturation increases approaching the stress state to the yield surface.

Furthermore, Fig. 4.42a presents the variations of saturation degree as: (a) the effective mean pressure evolves. In this regard, an increment of saturation is observed until the onset of irreversible strains and (b) the preconsolidation pressure decreases as saturation increases. In this case, the experienced plasticization has a high relevance. It generates a continuous decrease of saturation as hardening increases.
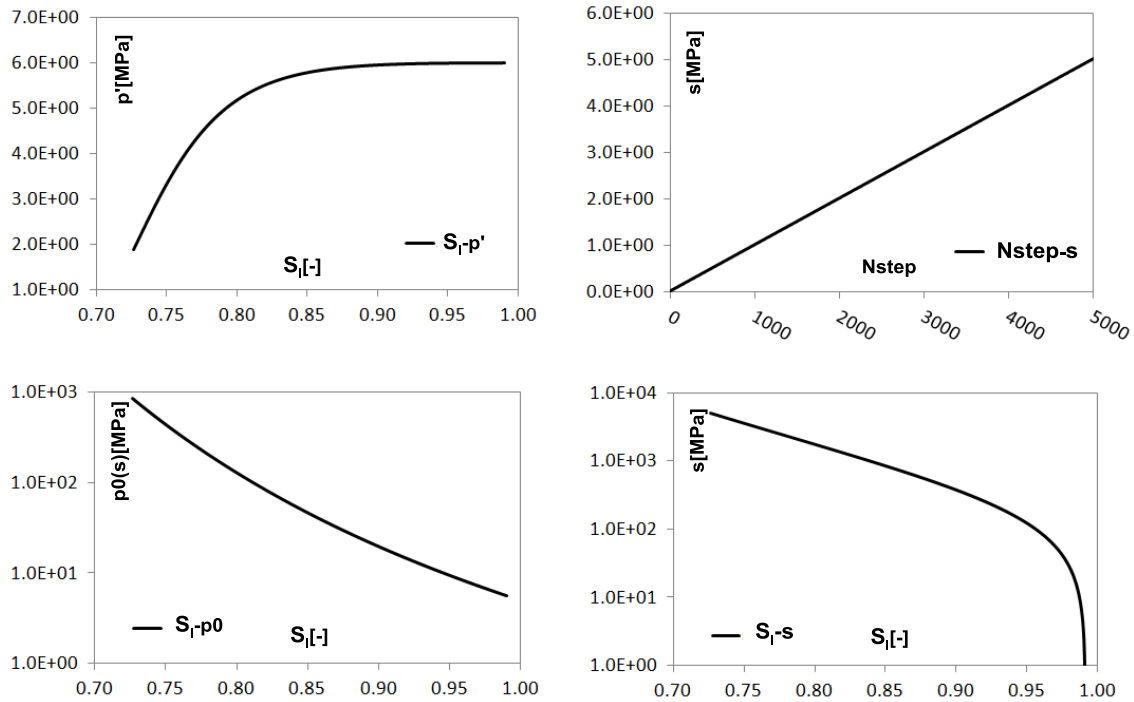
Figure 4.41: (Gallipoli's model) Desaturation test at high pressures. Responses of mean pressure and preconsolidation due to saturation evolution.
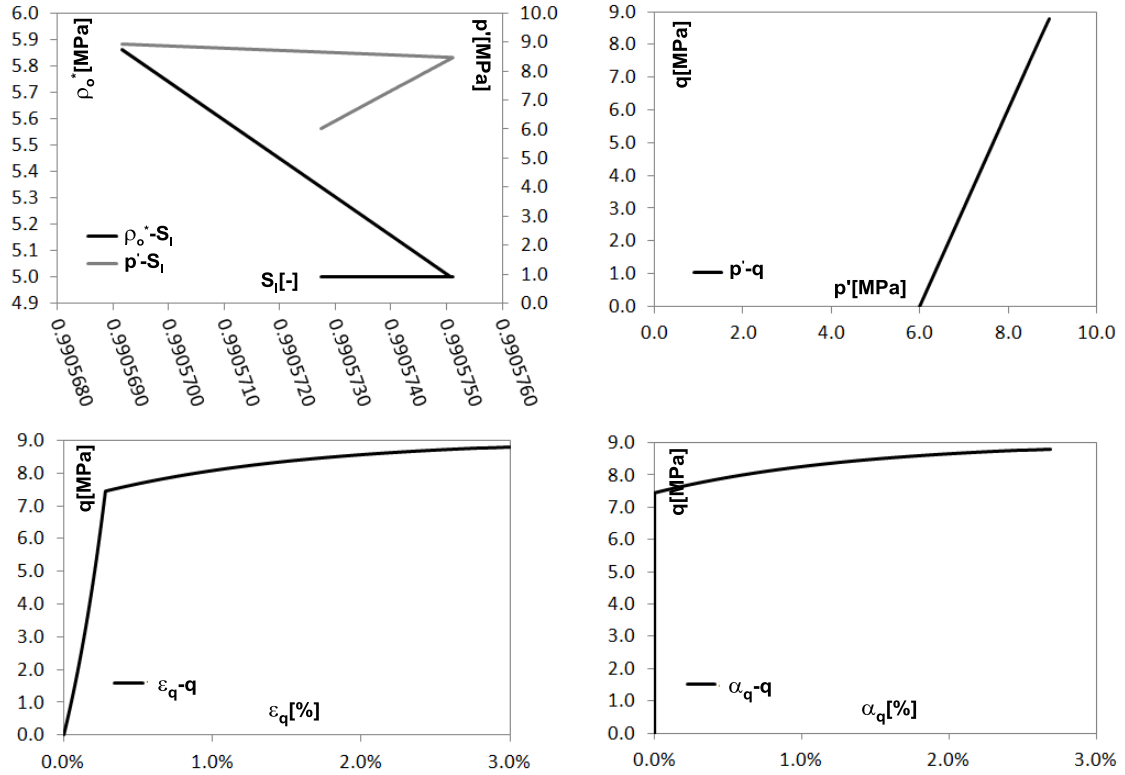
Figure 4.42: (Gallipoli's model) Predicted response of triaxial tests on normally consolidated sample. Variation of saturation degree due to the exerted stress path.

4.5.2.2) A Generalized BBM2 Model

The model BBM[2] can be generalized to capture different shapes of the yield surface in the p'-q plane. This generalization can be obtained by introducing a pressure dependent term as proposed by Collins (2002). Such a generalization give rise to a non-associated flow rule and allows to control the amount of plastic dilatancy $\dot{\alpha}_p / \dot{\alpha}_q$.

If the dissipation function Eq. 4.83 is extended by introducing a pressure dependent term $B(p')$ within the root in the way:

$$d_s = \underbrace{\frac{z}{2}\left(\frac{p^c}{2}\exp\left(\frac{\alpha_p}{\lambda^* - \kappa^*}\right)\right)^b}_{p_0/2} \sqrt{\dot{\alpha}_p{}^2 + M^2 \left(\underbrace{\epsilon + (1-\epsilon)\frac{p'}{\rho}}_{B}\right)^2 \dot{\alpha}_q{}^2} \qquad (4.88)$$

184

where the parameter ϵ quantifies the amount of non-associativity (or shape of the yield surface in the p'-q plane) then, the hardening rules result different to those in Eq. 4.84 by the presence of the new pressure dependent parameter:

$$x'_p = \frac{\partial d_s}{\partial \dot{\alpha}_p} = \frac{p_0}{2} \frac{\dot{\alpha}_p}{\sqrt{\dot{\alpha}_p{}^2 + B^2 M^2 \dot{\alpha}_q{}^2}} \tag{4.89}$$

$$x'_q = \frac{\partial d_s}{\partial \dot{\alpha}_q} = \frac{p_0}{2} \frac{M^2 \dot{\alpha}_q}{\sqrt{\dot{\alpha}_p{}^2 + B^2 M^2 \dot{\alpha}_q{}^2}}$$

and by elimination of the rates of plastic strains between the equations 4.89a and 4.89b the yield function of the generalized BBM^2 model results slightly different to that of Eq. 4.85:

$$f^y = x'_p{}^2 + \frac{x'_q{}^2}{B^2 M^2} - \left(\frac{p_0}{2}\right)^2 = 0 \tag{4.90}$$

Figure 4.43 shows the graph of the yield surface for different values of ϵ.
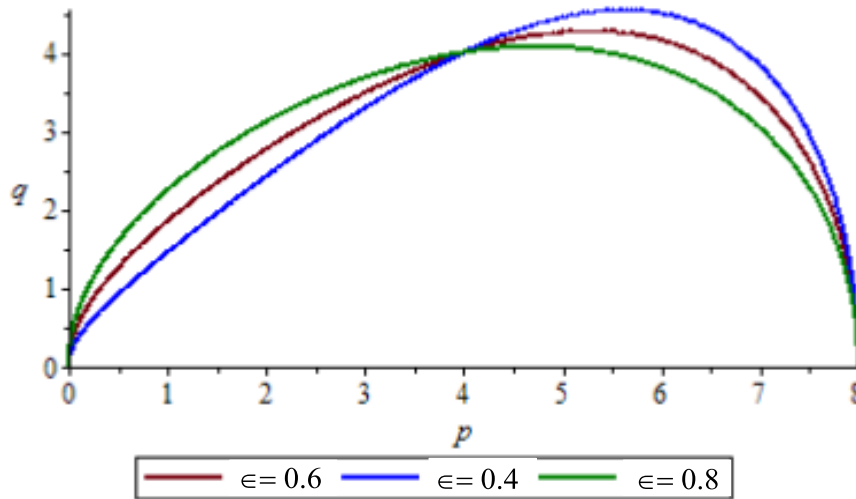
Figure 4.43: Graph of the Generalized BBM2 model for partially saturated soils. Three different values of the material parameter ϵ (Collins (2002)).

Figure 4.44 shows the model response subject to triaxial stress path in a sample under overconsolidated conditions. The response for the two values of ϵ shows a drop of the strength while the parameter ϵ decreases. Furthermore, Figure 4.45 shows a lower

volumetric strain as the parameter ϵ decreases. This happens as a consequence of the change in the plastic flow direction.
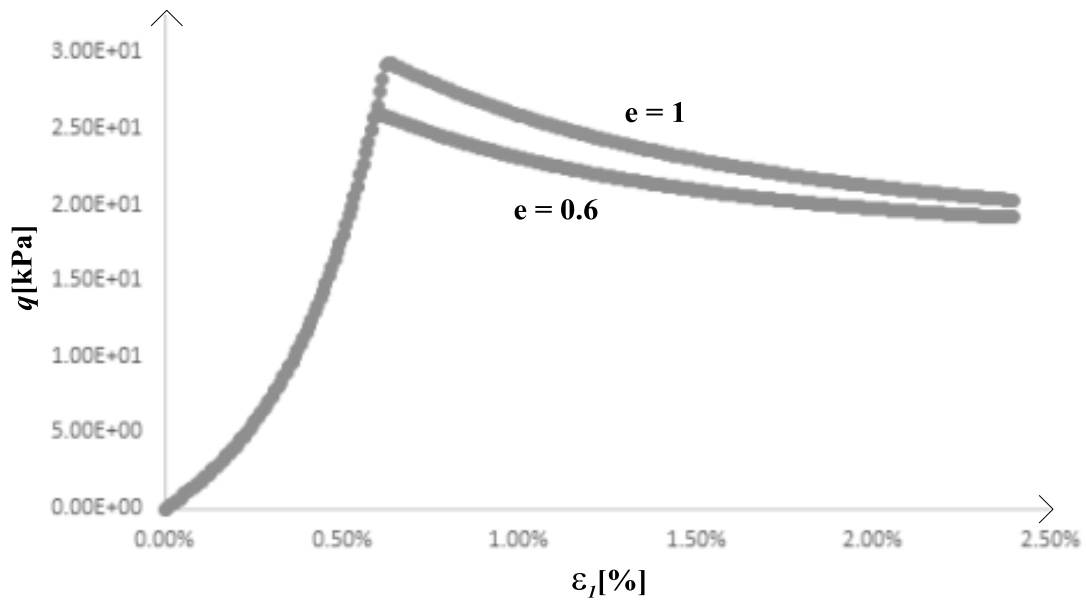
Figure 4.44: Conventional Drained Triaxial Test on an over-consolidated soil Samples. Response of the Generalized BBM2 Model for two values of the material parameter ϵ.
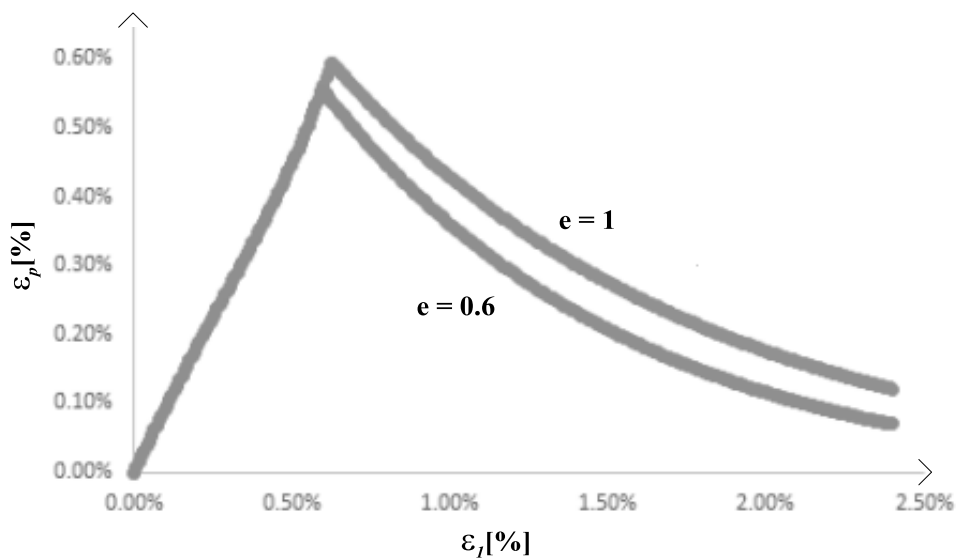
Figure 4.45: Conventional Drained Triaxial Test on an over-consolidated soil Samples. Response of the Generalized BBM2 Model for two values of the material parameter ϵ.

Another way to adapt the Cam-clay surface to fit with experimental observations is to consider a cap surface version of this model. A dissipation function which takes into account this phenomenon is presented in Appendix 1 of this dissertation. The model

_____

accounts for two different dissipation characteristics according to the side with respect to the csl. "wet" or "dry".

4.5.3)   Formulation of Barcelona Basic Model

Other alternative to model the behavior of partially saturated soils is to use the net stresses instead of the effective stress as constitutive stress variable of the mechanical phase. Essentially used for experimental convenience, this variable has been the source of the pioneer model developed by Alonso et al. (1990), today called Barcelona Basic Model (BBM). In this section, a hyperporoplastic formulation is proposed for this historical model, as it is still now widely used in many computations.

According to section 3.5.3, the net stress tensor σ''_{ij} is conjugated to the strain tensor ε_{ij} provided that suction s is conjugated to the hydraulic strain ε_w. A complete coupled hydro-mechanical model requires thus to consider free energy and dissipation functions that depend in the most general case on $(\sigma''_{ij}, \varepsilon_{ij}, \alpha_{ij}, s, \varepsilon_w, \alpha_l)$ and include terms related to soil skeleton and gas-liquid interface. In accordance with Alonso et al.'s model, Modified Cam Clay Model is used for the soil skeleton in absence of interfaces. The effect of suction is introduced by:

1) setting a dependency of the yield point p_0 on suction,
2) considering a resistance to pure traction p_s that depends linearly on suction value ($p_s = k_s\, s$).

The equation of the yield surface is then:

$$f^y = \frac{q^2}{M^2} - (p_0 - p'')(p'' + p_s) = 0 \tag{4.91}$$

As for the previous model, two formulations are presented. The first one sticks to the original Barcelona Basic Model and considers a constant shear modulus. The second one contemplates the enhancement proposed by Houlsby et al. (2005), which allows having a constant Poisson's ratio within a conservative elastic formulation. It is completed by a non-hysteretic van-Genuchten-like retention curve to model the hydraulic skin of the porous skeleton.

In this regard the curves of elastic response "scanning curves" are no longer valid resulting in $f_{i_1} = 0$ and as consequence $\varepsilon_w^e = 0$. Then the hydraulic strain is given by the internal variable $\varepsilon_w = \alpha_1$ or equivalently $\varepsilon_w = \dfrac{\partial f_{i_2}}{\partial s}$, as $s = x_s$.

In a first step both: (a) a consideration of a constant shear modulus G for the elastic mechanical part of the Barcelona Basic Model and (b) a non-dependency of the interface energy on the soil density, lead to the expressions for the Helmholtz $f_{s_1}^g$ and the Gibbs g_{s_1} free energies given by:

$$f_{s_1}^g = \kappa^* p^o \exp\left(\frac{\varepsilon_p}{\kappa^*} - \frac{\kappa_s^*}{\kappa^*} \ln\left(\frac{s + p_{at}}{p_{at}}\right)\right) + \frac{3G\varepsilon_q^2}{2} + \underbrace{\phi \frac{\rho_s^0}{m-1}\left[\left(1 + \frac{s}{\rho_s^0}\right)^{(1-m)}\right]}_{f_{i_2}} \tag{4.92}$$

$$g_{s_1} = -\kappa^*\left[\ln\left(\frac{p"}{p^o}\right) - 1\right] - \kappa_s^* p" \ln\left(\frac{s + p_{at}}{p_{at}}\right) - \frac{q^2}{6G} + \phi \frac{\rho_s^0}{m-1}\left[\left(1 + \frac{s}{\rho_s^0}\right)^{(1-m)}\right] \tag{4.93}$$

where f_s^g is presented here for its compatibility with the u-p Finite Element formulation.

The definition of the following hydro-mechanical strain components and stress components come for the state equations:

$$\varepsilon_p = -\frac{\partial g_s}{\partial p"} = \kappa^* \ln\left(\frac{p"}{p^o}\right) + \kappa_s \ln\left(\frac{s + p_{at}}{p_{at}}\right) \tag{4.94}$$

$$\varepsilon_q = -\frac{\partial g_s}{\partial q} = \frac{q}{3G}$$

$$\varepsilon_w = -\frac{\partial g_s}{\partial s} = \kappa_s \frac{p"}{s + p_{at}} + \phi\left(1 + \frac{s}{\rho_s^0}\right)^{-m}$$

$$p" = \frac{\partial f_s}{\partial \varepsilon_p} = p^o \exp\left(\frac{\varepsilon_p}{\kappa^*} - \frac{\kappa_s^*}{\kappa^*} \ln\left(\frac{s + p_{at}}{p_{at}}\right)\right)$$

$$q = \frac{\partial f_s}{\partial \varepsilon_q} = 3G\varepsilon_q$$

$$\varepsilon_w = \frac{\partial f_s}{\partial \phi s} = \underbrace{p^o \exp\left(\frac{\varepsilon_p}{\kappa^*} - \frac{\kappa_s^*}{\kappa^*} \ln\left(\frac{s + p_{at}}{p_{at}}\right)\right)}_{p"} \frac{\kappa_s}{s + p_{at}} + \phi\left(1 + \frac{s}{\rho_s^0}\right)^{-m}$$

Term $\kappa^* \ln\left(\frac{p"}{p^o}\right)$ represents the volumetric strain due to load changes only while $\kappa_s \ln\left(\frac{s + p_{at}}{p_{at}}\right)$ is the volumetric strain due to changes in suction. Note that this last cross

term imposes a counterpart in the hydraulic response: ε_w must be the sum of two components, one due to the mechanical response of the material $\left(\kappa_s \frac{p"}{s+p_{at}}\right)$ and one due to the hydraulic response $\left(\phi\left(1+\frac{s}{s^o}\right)^{-m}\right)$. Moreover the expression for the net stress within the exponential is composed of two terms: the first term is due to mechanical volumetric strains $\frac{\varepsilon_p}{\kappa^*}$ and the second term considers the change in the net stress due to suction changes $\frac{\kappa_s^*}{\kappa^*}\ln\left(\frac{s+p_{at}}{p_{at}}\right)$.

Moreover, if both (a) the influence of the soil density on the interface energy is considered and (b) in case in which v is constant, the energy functions $f_{s_1}^g$ and g_{s_1} take a slightly different form:

$$f_{s_1}^g = \kappa^* p^o \exp\left(\frac{\varepsilon_p}{\kappa^*} - \phi\frac{\rho_s^0}{\kappa^* p_o^s (m-1)}\left[\left(1+\frac{s}{\rho_s^0}\right)^{(1-m)}\right] + \frac{3\varrho\varepsilon_q}{2\kappa^*}^2 - \frac{\kappa_s^*}{\kappa^*}\ln\left(\frac{s+p_{at}}{p_{at}}\right)\right) \tag{4.95}$$

$$g_{s_1} = -\kappa^*\left[\ln\left(\frac{p"}{p^o}\right) - 1\right] - \kappa_s^* p"\ln\left(\frac{s+p_{at}}{p_{at}}\right) - \frac{q^2}{6\varrho p"} \tag{4.96}$$

$$+ \phi\frac{\rho_s^0\left(\frac{p"}{p_o^s} - \chi^o\right)}{m-1}\left[\left(1+\frac{s}{\rho_s^0}\right)^{(1-m)}\right]$$

then the strain and stress components read:

$$\varepsilon_p = \kappa^*\ln\left(\frac{p"}{p^o}\right) - \frac{q^2}{6\varrho p"^2} + \kappa_s^*\ln\left(\frac{s+p_{at}}{p_{at}}\right) + \underbrace{\phi\frac{\rho_s^0}{p_o^s(m-1)}\left[\left(1+\frac{s}{\rho_s^0}\right)^{(1-m)}\right]}_{\varepsilon^c} \tag{4.97}$$

$$\varepsilon_q = \frac{q}{3\varrho p"}$$

$$\varepsilon_w = \kappa_s^*\frac{p"}{s+p_{at}} + \phi\left(\frac{p"}{p_o^s} - \chi^o\right)\left(1+\frac{s}{\rho_s^0}\right)^{-m}$$

$$p" = p^o\exp\left(\frac{\varepsilon_p - \varepsilon^c(s)}{\kappa^*} + \frac{3\varrho\varepsilon_q^2}{2\kappa^*} - \frac{\kappa_s^*}{\kappa^*}\ln\left(\frac{s+p_{at}}{p_{at}}\right)\right)$$

$$q = 3\varrho p^o\exp\left(\frac{\varepsilon_p - \varepsilon^c(s)}{\kappa^*} + \frac{3\varrho\varepsilon_q^2}{2\kappa^*} - \frac{\kappa_s^*}{\kappa^*}\ln\left(\frac{s+p_{at}}{p_{at}}\right)\right)\varepsilon_q$$

$$\varepsilon_w = \kappa_s\frac{p"}{s+p_{at}} + \phi\left(\frac{p"}{p_o^s} - \chi^o\right)\left(1+\frac{s}{\rho_s^0}\right)^{-m}$$

From expression 4.97 the strains and the stresses result in more complex fashion than those at Eq. 4.94. Double differentiation of Eq. 4.96 provides the hydro-mechanical compliance matrix:

$$(4.98)$$

$$D^{g_s} =$$

$$
\begin{bmatrix}
\dfrac{\kappa^*}{p''} + \dfrac{q^2}{3\varrho(p'')^3} & -\dfrac{q}{3\varrho(p'')^2} & \dfrac{\kappa_s^*}{s + p_{at}} + \dfrac{\phi}{p_o^s}\left(1 + \dfrac{s}{\rho_s^0}\right)^{-m} \\[4mm]
-\dfrac{q}{3\varrho(p'')^2} & \dfrac{1}{3\varrho p''} & 0 \\[4mm]
\dfrac{\kappa_s^*}{s + p_{at}} + \dfrac{\phi}{p_o^s}\left(1 + \dfrac{s}{\rho_s^0}\right)^{-m} & 0 & \dfrac{-\kappa_s^* p''}{(s + p_{at})^2} - \dfrac{m\phi\left(\dfrac{p''}{p_o^s} - \chi^o\right)}{\rho_s^0}\left(1 + \dfrac{s}{\rho_s^0}\right)^{\lambda}
\end{bmatrix}
$$

with $\lambda = -(m + 1)$.

To the opposite of the matrix derived using the effective stress concept Eq. 4.59, the full hydro-mechanical compliance matrix associated with Barcelona Basic Model must have hydro-mechanical coupled terms $\left(\dfrac{\kappa_s^*}{s + p_{at}}\right)$. This fact is in accordance with the proper definition of the effective stress concept that aims at decoupling the hydraulic and the mechanical behaviors.

The formulation of the plastic behavior requires the introduction of a suction-dependent coupled kinematical and volumetric hardening term. Because of the asymmetric increase of preconsolidation pressure p_o and traction strength p_s, both the size and the center of yield function move with suction.

In the framework of hyperplasticity, this feature is introduced by the consideration of a trapped energy term $\left(g_{s_2}\right)$ in the Gibbs energy function. As for Gallipoli et al.'s model, this term is computed as the plastic work done by center the ellipse $g_2 = \int \frac{(p_o - p_s)}{2} d\alpha_p$:

$$g_s = -\kappa^* \left[\ln\left(\frac{p''}{p^o}\right) - 1 \right] - \kappa_s p'' \ln\left(\frac{s + p_{at}}{p_{at}}\right) - \frac{q^2}{6\varrho p''} - \left(p'' \alpha_p + q \alpha_q \right) \tag{4.99}$$

$$+ \phi \underbrace{\frac{s^o \left(\frac{p''}{p_0^s} - \chi^o\right)}{m - 1} \left[\left(1 + \frac{s + p_{at}}{s^o} \right)^{(1-m)} \right]}_{g_{i_2}}$$

$$+ \underbrace{w(s) \frac{(\lambda^* - \kappa^*)}{b(s)} \cdot \left(\frac{p^c}{2} \exp\left(\frac{\alpha_p}{\lambda^* - \kappa^*}\right) \right)^{b(s)} - \frac{p_s}{2} \alpha_p}_{g_2}$$

where $w(s)$ and $b(s)$ are given by the expressions:

$$w = \left(\frac{p^c}{2} \right)^{(1-b)} \tag{4.100}$$

$$b(s) = \frac{\lambda^* - \kappa^*}{\lambda(s) - \kappa^*}$$

and $\lambda(s)$ is the slope of normal compression line at suction (s) (Alonso, 1990). The complementary state equations provide the expressions for the generalized stresses:

$$x_p'' = -\frac{\partial g_s}{\partial \alpha_p} = p'' - \left(\underbrace{\underbrace{w(s) \left(\frac{p^{c_o}}{2} \exp\left(\frac{\alpha_p}{\lambda^* - \kappa^*}\right) \right)^{b(s)}}_{p_0/2} + \frac{p_s}{2}}_{\rho''} \right) \tag{4.101}$$

$$x_q'' = -\frac{\partial g_s}{\partial \alpha_q} = q$$

where $\rho'' = \frac{p_0 + p_s}{2}$ is the shift stress linking the spaces of net stresses: the true net stresses space and the generalized net stresses space. In terms of generalized stresses, the yield function reads:

$$f^y = \frac{x_q''^2}{M^2} + x_p''^2 - \left(\frac{p_0 + p_s}{2} \right)^2 = 0 \tag{4.102}$$

The dissipation function is obtained by applying the singular Legendre transform $d_s = x_p'' \dot{\alpha}_p + x_q'' \dot{\alpha}_q - \gamma f^y$ to Eq. 4.102. Differentiation of f^y with respect to x_p'' and x_q'' lead to the following expressions for the flow rules:

$$0 = \dot{\alpha}_p - 2\gamma x_p'' \tag{4.103}$$

$$0 = M^2 \dot{\alpha}_q - 2\gamma x_q''$$

_____

Using the restriction provided by the yield surface Eq. 4.102, $x_p^{"}$ and $x_q^{"}$ can be eliminated from Eqs. 4.103, leading to:

$$\gamma = \frac{(\dot{\alpha}_p^2 + M^2 \dot{\alpha}_q^2)^{\frac{1}{2}}}{p_0 + p_s} \tag{4.104}$$

and the dissipation finally reads:

$$d_s = x_p^{"} \dot{\alpha}_p + x_q^{"} \dot{\alpha}_q - \gamma f^y = \frac{\dot{\alpha}_p^2 + M^2 \dot{\alpha}_q^2}{2\gamma} = \frac{p_0 + p_s}{2} (\dot{\alpha}_p^2 + M^2 \dot{\alpha}_q^2)^{\frac{1}{2}} \tag{4.105}$$

This formulation presents the advantage of allowing the implementation of this model using modern optimization techniques. Figure 4.46 shows the model response to triaxial tests at three different levels of suction.
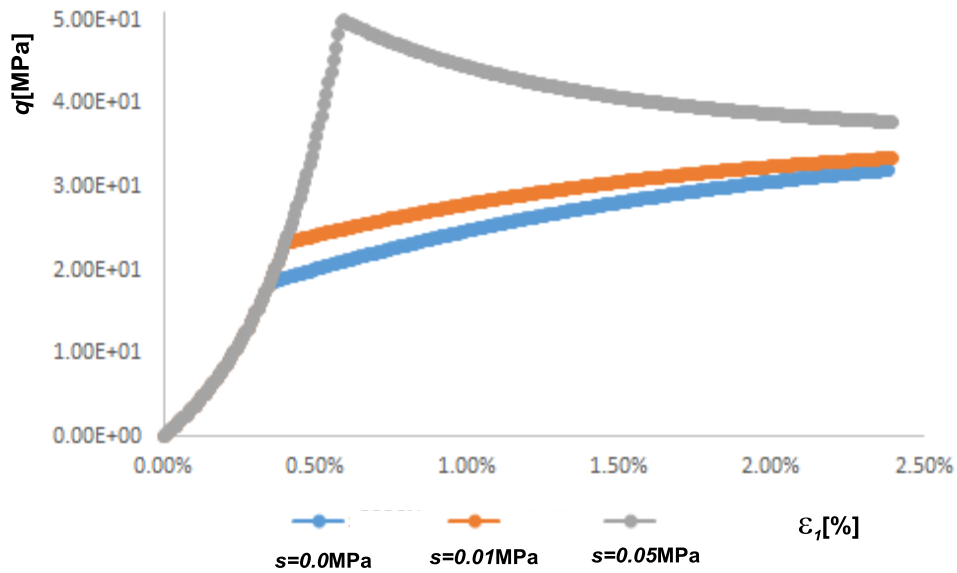
*Figure 4.46: Predicted response of triaxial tests on normally and over-consolidated soils due to different levels of suction, **BBM⁴** Model.*

The corresponding algorithm of integration is described in Chapter 5.

4.5.3.1) BBM formulation in terms of mixed hardening

Alternatively to the pure kinematic hardening formulation of the BBM presented above, a mixed hardening formulation can be adopted in order to develop the model. This formulation will then lead to the same results.

To achieve the mixed hardening formulation it is necessary to observe that p_s can be accommodate within the yield function so it remains working as an isotropic hardening term. Then its presence in the stored energy g_2 disappears. The original expression for the BBM yield locus is given as:

$$f^y = \frac{q^2}{M^2} + (p'' + p_s) \cdot (p'' - p^c)$$

(4.106)

which can be accommodated to give

$$f^y = \frac{q^2}{M^2} + (p'' - \rho'')^2 - \left[\left(\underbrace{w(s) \left(\frac{p^{c_o}}{2} \exp\left(\frac{\alpha_p}{\lambda^* - \kappa^*}\right) \right)^{b(s)}}_{\rho''} \right)^2 - p_s \cdot (p'' - p_s) \right]$$

(4.107)

where the back stress has been defined as $p_0/2$. If the yield function Eq. 4.107 is transferred to the generalized stress space using the fundamental relation $x'' = \sigma'' - \rho''$ is becomes expressed by:

$$f^y = \frac{x_q''^2}{M^2} + x_p''^2 - \left[\left(\frac{p_0}{2}\right)^2 - p_s \cdot (p'' - p_s) \right] = 0$$

(4.108)

Equation 4.108 represents a family of ellipses centered at the origin with mayor semi-axis a=π and minor semi-axis b=Mπ with $\pi = \left(\left(\frac{p_0}{2}\right)^2 - p_s \cdot (p'' - p_s) \right)^{1/2}$. Following the same procedure as before and eliminating the generalized stresses between the equations for the flow rules leads to the expression for the dissipation function:

$$d_s = \left(\left(\frac{p_0}{2}\right)^2 - p_s \cdot (p'' - p_s) \right)^{1/2} \sqrt{(\dot{\alpha}_p^2 + M^2 \dot{\alpha}_q^2)}$$

(4.109)

This expression for the yield function of the BBM model differs from the one presented at Eq. 4.105 in the multiplicative term of the root and it is only due to the assumption of the mixed hardening adopted in the formulation.

It is noted that no additional term is seen at the dissipation for the mixed hardening because in this case the isotropic hardening evolution depends only on hydraulic variable (s). This variable is not conjugated to the rate of plastic strain.

4.5.3.2) Generalized Elasticity for BBM model (Net Stress Space)

In this section a generalization of Gibbs energy and Helmholtz energy is made. These generalizations are based on the energy functions proposed by Houlsby (2005) for the mechanical problem and are extended here to consider partially saturated conditions of soil when the constitutive variables chosen for modeling are $p'' - \varepsilon_p$ and $s - \varepsilon_w$.

The advantage of deriving the elastic behavior from the following functions is the ability to calibrate the amount of non-linear response. The clearest evidence of the non-linearity of the soils elastic strains is the stress-strain relation of the Cam-Clay model. This stress-strain relation defines the isotropic compression line which is generally represented as a straight line at a semi-logarithmic plane: p'(effective mean stress)-e(void ratio). It´s important to highlight that the non-linearity decreases while the soil hardness increases, a commonly observed phenomenon in a brittle material.

The material parameter controlling the amount of non-linearity "*n*" span between 0-1. A value of *n* close to zero gives a minimal non-linearity while a value close to unity provides a non-linearity of cam-clay type.

At first instance a volumetric behavior is addressed by simplicity. Then the extension to consider the deviatoric behavior will be introduced. Consider the Gibbs energy function for the partially saturated medium formulated in terms of net stress,

$$g_s = \frac{-p''^{(2-n)}}{p_o^{1-n} \cdot k(1-n)(2-n)} + \frac{p''}{k(1-n)} - \frac{k_s p''}{(1+\lambda)}\left(\frac{s+p_{at}}{p_{at}}\right)^\lambda + \frac{k_s p''}{(1+\lambda)} - p''\alpha_p \tag{4.110}$$

$$+ \phi \frac{s^o\left(\frac{p''}{p_o^s} - \chi^o\right)}{m-1}\left[\left(1 + \frac{s+p_{at}}{s^o}\right)^{(1-m)}\right]$$

Unlike function Eq. 4.99 where a natural logarithm of suction was considered, in this case the suction is incorporated into the energy function as a polynomial function of degree $(1-n)$. From Eq. 4.110 the expression for the volumetric strain is given by:

$$\varepsilon_p = \frac{p''^{(1-n)}}{p_o^{1-n} \cdot k(1-n)} - \frac{1}{k(1-n)} + \frac{k_s}{(1+\lambda)}\left(\frac{s+p_{at}}{s_0}\right)^\lambda - \frac{k_s}{(1+\lambda)} + \alpha_p \tag{4.111}$$

$$+ \underbrace{\phi\frac{s^o}{p_o^s(m-1)}\left[\left(1 + \frac{s+p_{at}}{s^o}\right)^{(1-m)}\right]}_{\varepsilon^c}$$

This suggest that both the net mean stress and the suction contribute to the expression of the volumetric strain with different polynomial degree. The partial Legendre

transformation leads to the expression of the Helmholtz potential $\left(f_s\left(\varepsilon_p^e, s\right) = g_s(p", s) - p"\varepsilon_p^e\right)$ which is more appropriate for finite element u-p formulations:

$$
f_s = \frac{p_o}{k(2-n)}\Bigg(k(1
$$

$$
-n)\big)^{\frac{2-n}{1-n}}\Bigg(\left(\varepsilon_p^e - \varepsilon^c(s) + \frac{1}{k(1-n)} - \frac{k_s}{(1+\lambda)}\left(\frac{s + p_{at}}{s_o}\right)^\lambda\right.
$$

$$
\left.+ \frac{k_s}{(1+\lambda)}\right)^2\Bigg)^{\frac{2-n}{2-2n}}\Bigg)
$$

(4.112)

In the energy function (Eq. 4.112) the additional suction term of degree (λ) accompanies the volumetric deformation. This fact evidences the degree of coupling between the mechanical and the hydraulic parts when the net stress configuration is chosen for modeling. From the previous expression the mean net stress is expressed as,

$$
p" = p_o\big(k(1-n)\big)^{\frac{1}{1-n}}\left(\varepsilon_p^e - \varepsilon^c(s) + \frac{1}{k(1-n)} - \frac{k_s}{(1+\lambda)}\left(\frac{s + p_{at}}{s_o}\right)^\lambda\right.
$$

$$
\left.+ \frac{k_s}{(1+\lambda)}\right)^{\frac{1}{1-n}}
$$

(4.113)

As in the expression 4.111 a suction dependent term of polynomial character accompanies the volumetric deformation in the computation for the net mean stress.

Finally, the extensions of the Gibbs $g_s(p", q, s)$ and the Helmholtz $f_s\left(\varepsilon_p^e, \varepsilon_q^e, s\right)$ energy functions for the BBM model to consider both the deviatoric behavior and the kinematic hardening are shown below:

$$
g_s = \frac{-\big(k(1-n)(2-n)\big)^{-1}}{p_o^{1-n}}\left(p"^2 + \frac{k(1-n)}{3\varrho}q^2\right)^{\frac{2-n}{2}} + \frac{p"}{k(1-n)}
$$

$$
- \frac{k_s p"}{(1+\lambda)}\left(\frac{s + p_{at}}{s_o}\right)^\lambda + \frac{k_s p"}{(1+\lambda)} - \big(p"\alpha_p + q\alpha_q\big)
$$

$$
+ \phi \underbrace{\frac{s^o\left(\frac{p"}{p_o^s} - \chi^o\right)}{m-1}\left[\left(1 + \frac{s + p_{at}}{s^o}\right)^{(1-m)}\right]}_{g_{i_2}}
$$

$$
+ \underbrace{w(s)\frac{(\lambda^* - \kappa^*)}{b(s)}\cdot\left(\frac{p^c}{2}\exp\left(\frac{\alpha_p}{\lambda^* - \kappa^*}\right)\right)^{b(s)} - \frac{p_s}{2}\alpha_p}_{g_2}
$$

(4.114)

$$f_s = \frac{p_o}{k(2-n)}\left(k(1-n)\right)^{\frac{2-n}{1-n}} \cdot \tag{4.115}$$

$$\left(\left(\varepsilon_p^e - \varepsilon^c(s) + \frac{1}{k(1-n)} - \frac{k_s}{(1+\lambda)}\left(\frac{s+p_{at}}{s_o}\right)^\lambda + \frac{k_s}{(1+\lambda)}\right)^2 + \right.$$

$$\left. \frac{3\varrho(\varepsilon_q - \alpha_q)^2}{k(1-n)}\right)^{\frac{2-n}{2-2n}} + w(s)\frac{(\lambda^* - \kappa^*)}{b(s)}$$

$$\cdot \left(\frac{p^c}{2}\exp\left(\frac{\alpha_p}{\lambda^* - \kappa^*}\right)\right)^{b(s)} - \frac{p_s}{2}\alpha_p$$

The last two terms in energy functions 4.114 and 4.115 correspond to the trapped energy giving rise to the back stress ρ''. From Eqs. 4.114 and 4.115 the expressions for the mechanical and hydraulic strains and the mechanical stresses result:

$$\varepsilon_p = \frac{\left(k(1-n)\right)^{-1}p''}{p_o^{(1-n)}}\left(p''^2 + \frac{k(1-n)}{3\varrho}q^2\right)^{(-n/2)} - \frac{1}{k(1-n)} + \frac{k_s}{(1+\lambda)}\left(\frac{s+p_{at}}{s_0}\right)^\lambda \tag{4.116}$$

$$\qquad - \frac{k_s}{(1+\lambda)} + \alpha_p + \varepsilon^c$$

$$\varepsilon_q = \frac{q}{p_o^{(1-n)}3\varrho}\left(p''^2 + \frac{k(1-n)}{3\varrho}q^2\right)^{(-n/2)} + \alpha_q$$

$$p = p_o(k(1-n))^{\frac{1}{1-n}}\left(\left(\varepsilon_p^e - \varepsilon^c + \frac{1}{k(1-n)} - \frac{k_s}{(1+\lambda)}\left(\frac{s+p_{at}}{s_o}\right)^\lambda + \frac{k_s}{(1+\lambda)}\right)^2 \right.$$

$$\left. + \frac{3\varrho\varepsilon_q^{e\,2}}{k(1-n)}\right)^{\frac{n}{2-2n}}\left(\varepsilon_p^e - \varepsilon^c + \frac{1}{k(1-n)} + \frac{k_s}{(1+\lambda)}\left(\frac{s+p_{at}}{s_o}\right)^\lambda\right)$$

$$q = p_o(k(1-n))^{\frac{1}{1-n}}\left(\left(\varepsilon_p^e - \varepsilon^c + \frac{1}{k(1-n)} - \frac{k_s}{(1+\lambda)}\left(\frac{s+p_{at}}{s_o}\right)^\lambda + \frac{k_s}{(1+\lambda)}\right)^2 \right.$$

$$\left. + \frac{3\varrho\varepsilon_q^{e\,2}}{k(1-n)}\right)^{\frac{n}{2-2n}}3\varrho\varepsilon_q^e$$

$$\varepsilon_w = k_s\lambda\frac{p''}{(1+\lambda)}\frac{(s+p_{at})^{(\lambda-1)}}{s_0^\lambda} + \phi\left(\frac{p''}{p^o} - \chi^o\right)\left(1 + \frac{(s+p_{at})}{s^0}\right)^{-m} + \underset{\varepsilon_w^c}{\frac{\partial f_2}{\partial s}}$$

At the energy functions 4.114 and 4.115 the hysteretic response of the retention curve has been disregarded, as consequence of this assumption $f_{i_1} = 0$ then the equality $S_l = \alpha_l$ is valid $\left(\text{equivalently } S_l = \frac{\partial f_{i_2}}{\partial \phi s}\right)$.

The cross derivatives $\frac{\partial f_{i_2}}{\partial p''}$ and $\frac{\partial f_2}{\partial s}$ due to the store energies appear as a consequence of the shift of the whole hydro-mechanical elastic domain driven by both the mechanical kinematical hardening and the hydraulic kinematical hardening.

4.6) Thermoplastic Soil Model from Hyperplastic Potentials

In this section the non-isothermal response of the soil in addition to the hydro-mechanical one under partially saturated conditions is considered. Before addressing the development of the hyper-Thermoplastic model a review of the thermodynamic equations governing the problem for a three-phase material at non-isothermal conditions is performed. Then the model will be addressed starting by defining the elastic energy and the dissipation energy functions. The last function will lead to introduce a generalization of the Legendre transformation in order to obtain a yield locus for the model. Finally several numerical tests will be performed in order to validate the model performance.

4.6.1) Non-isothermal conditions and Elastic Potentials (Mechanical Part)

The change in internal energy of the soil skeleton E_s is provided by the local form of the first law of thermodynamics Eq. 3.48. In that case Eq. 3.48 was particularized to consider the Bishop effective stress with parameter χ equal to the degree of liquid saturation as constitutive variable.

Furthermore, the existence of a state specific entropy function of the porous medium defined as $\mathfrak{H} = \mathfrak{H}_s + \phi \sum \mathfrak{H}_i^{kl} + \sum \omega_j \mathfrak{H}_j \phi$ leads to the statement of the local form of second law of thermodynamics expressed as in Eq. 3.49. In that expression, the thermal dissipation term $-\frac{q_k T_{,k}}{T}$ plays a central role in non-isothermal conditions and it cannot be neglected in the formulation.

The rate of entropy production within the porous element (the irreversible entropy) defining the dissipation d of the porous medium should again satisfy the inequality,

_____

$$d \quad \equiv \quad T\left(\dot{\mathfrak{H}}_s - \dot{\mathfrak{H}}_{s_r}\right) + \phi T\left(\dot{\mathfrak{H}}_i - \dot{\mathfrak{H}}_{i_r}\right) + \sum_j T\omega_j \phi\left(\dot{\mathfrak{H}}_j - \dot{\mathfrak{H}}_{j_r}\right) \geq 0 \qquad (4.117)$$

$$= \quad T\dot{\mathfrak{H}}_s + \phi T\dot{\mathfrak{H}}_i + \sum_j T\omega_j \phi\dot{\mathfrak{H}}_j + q_{k,k} - \frac{q_k T_{,k}}{T}$$

Then the divergence of the thermal flux in addition to the thermal dissipation $q_{k,k} - \frac{q_k T_{,k}}{T}$ corresponds to the reversible part of entropy in both the bulk phases and the interfaces. This differs from Eq. 3.50 in the presence of thermal dissipation term only.

Now the divergence of the heat flux in the solid skeleton only ($q'_{k,k}$) corresponds to the difference between: (a) the total heat flux in the medium $q_{k,k}$ in addition to the thermal dissipation and (b) the heat flux of the fluid phases $-\sum_j T\omega_j \phi\dot{\mathfrak{H}}_{j_r}$.

Within this scenario, the dissipation of solid skeleton defined as the difference between the dissipation of the whole medium and the dissipation of bulk fluid phases reads:

$$d_s \quad = \quad d - \sum_j T\omega_j \phi\dot{\mathfrak{H}}_j = T\dot{\mathfrak{H}}_s + \phi T\dot{\mathfrak{H}}_i + q'_{k,k} \equiv T\dot{\mathfrak{H}}_{s_i} + \phi T\dot{\mathfrak{H}}_{i_i} \geq 0 \qquad (4.118)$$

$$= \quad T\dot{\mathfrak{H}}_s + \phi T\dot{\mathfrak{H}}_i + \sum_j T\omega_j \phi\dot{\mathfrak{H}}_j + q_{k,k} - \frac{q_k T_{,k}}{T}$$

where unlike in Eq. 3.52 the thermal dissipation term in Eq. 4.118 is present.

Concerning finite element u-p formulation it is more convenient to work with the specific Helmholtz free energy of the porous skeleton dual to the internal energy E_s with respect to entropies $\mathfrak{H}_s$ and $\mathfrak{H}_i : f_s(\varepsilon_{ij}, T) = E_s - T(\mathfrak{H}_s + \phi\mathfrak{H}_i)$. Taking into account Eq. 3.48 the rate of f_s can be expressed as:

$$\dot{f}_s = \sigma'_{ij}\dot{\varepsilon}_{ij} - \phi s\dot{S}_l - T(\dot{\mathfrak{H}}_s + \phi\dot{\mathfrak{H}}_i) - (\mathfrak{H}_s + \phi\mathfrak{H}_i)\dot{T} - q'_{k,k} \qquad (4.119)$$

and finally combining the expression for the divergence of the skeleton heat flux $q'_{k,k}$ and Eq. 4.119 leads to the central result:

$$\dot{f}_s + (\mathfrak{H}_s + \phi\mathfrak{H}_i)\dot{T} + d_s = \sigma'_{ij}\dot{\varepsilon}_{ij} - \phi s\dot{S}_l + \underbrace{\left(-\frac{q_k T_{,k}}{T}\right)}_{d_T} \qquad (4.120)$$

In the framework of hyperplasticity and under non-isothermal conditions again both the free energy function f_s and the dissipation function d_s are required to completely define the constitutive model. Moreover the state equations result to be the same as those summarized in Table 3.5.

Under non-isothermal conditions besides the mechanical strains induced by stress increment, the thermal strains due to temperature changes should be taken into account.

$$d\varepsilon_{pT} = -\beta_T \, dT \tag{4.121}$$

where, β_T is the volumetric thermal expansion coefficient of the solid skeleton. This coefficient increases with the temperature.

As the thermal expansion of the porous medium should consider the influence of the mean pressure magnitude at the soil element with reference to the initial stress, the following law is proposed for the thermal expansion coefficient of the skeleton,

$$d\varepsilon_{pT} = -\left[\left(\frac{p'}{p_o}\right)^{1-n} - 1\right] \cdot \frac{\beta}{3T_m}(T_m - T) \, dT \tag{4.122}$$

where β is the dilation's coefficient of the solid matrix, T_m is a limit temperature below which the pore water does not boil, p_o is a reference initial pressure and n is a material parameter span between 0-1. The proposed incremental law (Eq. 4.122) says that the thermal coefficient decreases as p_o increases.

Based on Houlsby (2005) the general Gibbs energy function for the thermal elastic response is given after integration of Eq. 4.122 by the expression:

$$g_s = \frac{-(1 - \beta_s)}{p_o^{1-n} \cdot k(1 - n)(2 - n)} \cdot \left(p'^2 + \frac{k(1 - n)}{3\varrho}q^2\right)^{\frac{2-n}{2}} + \frac{p'(1 - \beta_s)}{k(1 - n)} \tag{4.123}$$
$$- \left(p'\alpha_p + q\alpha_q\right)$$

where $\beta_s = k(1 - n)\frac{\beta}{3} \cdot (T - T_o)\left(1 - \frac{T - T_o}{2T_m}\right)$, p_o is a reference pressure, ϱ is a dimensionless material parameter and n is a material parameter taking values between 0 and 1 for linear elasticity to Cam-Clay elasticity, respectively. The term β_s considers the non-isothermal response of the porous skeleton. The expressions for the volumetric strain and the deviatoric strain are derived from Eq. 4.123 following regular procedures in thermomechanics (state equations):

$$\varepsilon_p = \frac{p'(1 - \beta_s)}{p_o^{(1-n)}k^*(1 - n)}\left(p'^2 + \frac{k^*(1 - n)}{3\varrho}q^2\right)^{(-n/2)} - \frac{(1 - \beta_s)}{k^*(1 - n)} - \alpha_p \tag{4.124}$$

$$\varepsilon_q = \frac{q(1 - \beta_s)}{p_o^{(1-n)}3\varrho}\left(p'^2 + \frac{k^*(1 - n)}{3\varrho}q^2\right)^{(-n/2)} - \alpha_q$$

From Eq. 4.124, the expressions for the volumetric and the deviatoric strains result in much more complex expressions than those expressions for Cam-Clay elasticity. The complementary energy function $f_s = g_s - (p'\varepsilon_p + q\varepsilon_q)$ results after the Legendre transformation in:

$$f_s = \frac{p_o(1-\beta_s)}{k(2-n)}(k(1-n))^{\frac{2-n}{1-n}}\left(\left(\frac{\varepsilon_p - \alpha_p}{1-\beta_s} + \frac{1}{k(1-n)}\right)^2 + \frac{3\varrho(\varepsilon_q - \alpha_q)^2}{k(1-n)}\right)^{\frac{2-n}{2-2n}} \quad (4.125)$$

leading to the following expressions for the mean and the deviatoric stresses:

$$p' = p_o(k(1-n))^{\frac{1}{1-n}}\left(\left(\frac{\varepsilon_p - \alpha_p}{1-\beta_s} + \frac{1}{k(1-n)}\right)^2 + \frac{3\varrho(\varepsilon_q - \alpha_q)^2}{k(1-n)}\right)^{\frac{n}{2-2n}}. \quad (4.126)$$
$$\left(\frac{\varepsilon_p - \alpha_p}{1-\beta_s} + \frac{1}{k(1-n)}\right)$$

$$q = \frac{p_o}{(1-\beta_s)^{-1}}(k(1-n))^{\frac{n}{1-n}}\left(\left(\frac{\varepsilon_p - \alpha_p}{1-\beta_s} + \frac{1}{k(1-n)}\right)^2 + \frac{3\varrho(\varepsilon_q - \alpha_q)^2}{k(1-n)}\right)^{\frac{n}{2-2n}}$$
$$3\varrho(\varepsilon_q - \alpha_q)$$

Elastic compliance matrix is derived by second differential of Gibbs energy function g_s (Eq. 4.123) while the Stiffness matrix is obtained by second differential of Helmholtz energy f_s (Eq. 4.125).

The model has now to be completed by defining the dissipation energy (eventually yield function) for the thermo-plastic soil skeleton.

4.6.2)   Formulation of Yu's model with pure volumetric thermal-hardening

The layout of the dissipation function to complete the model is based on that proposed by Thurairajah (1948). The proposal established that the dissipation of the porous medium is governed by amount of rate of plastic deviatoric strain developed. Then the rate of work dissipated is given by the expression:

$$d_s = p'\dot{\alpha}_p + q\dot{\alpha}_q = \frac{b}{\ln(r)}Mp'\ln\left(\frac{p'}{p^c(s,T)}\right)|\dot{\alpha}_q| \quad (4.127)$$

where $M = tan\,\phi^c$ is the slope of the critical state line, ϕ^c is the friction angle at the critical state and "r" and "b" are two material parameters. Equation 4.127 says that the dissipated work is proportional to the magnitude of the rate of plastic shear strain. This function results non-smoothed at the origin $\dot{\alpha}_q = 0$ then the way forward to obtain the yield function is to perform a Legendre-Fenchel transformation. It is given by:

$$F^y = sup\left(p'\dot{\alpha}_p + q\dot{\alpha}_q - \frac{b}{ln(r)}Mp'ln\left(\frac{p'}{p^c(s,T)}\right)|\dot{\alpha}_q|\right) \qquad (4.128)$$

where $F^y = \lambda f^y$. Then standard procedure leads to the expression for the deviatoric stress invariant:

$$
\begin{aligned}
q &= -\frac{b}{ln(r)}Mp'ln\left(\frac{p'}{p^c(s,T)}\right)\frac{\dot{\alpha}_q}{\sqrt{\dot{\alpha}_q\dot{\alpha}_q}} \qquad (4.129)\\
&= -\frac{b}{ln(r)}Mp'ln\left(\frac{p^c(s,T)}{p'}\right)
\end{aligned}
$$

Finally the expression for the yield function is obtained from Eq. 4.129 as:

$$F^y = \begin{cases} \dfrac{q}{Mp'} + \dfrac{b}{ln(r)} \cdot ln\left(\dfrac{p'}{p^c(s,T)}\right) & \{(p',q)|F^y \leq 0\} \\[2mm] \\ \infty & \text{otherwise} \end{cases} \qquad (4.130)$$

The yield function Eq. 4.130 corresponds to the original Cam-Clay yield surface with a hardening's pressure sensitive to environmental variables: suction and temperature. Yu *(2006)* proposed a generalization of this surface based on the properties of the exponentials functions. This generalization allows to change the shape of the yield surface at the p-q plane. Such a change can vary from an original cam-clay shape to a cap-model shape, through a modified cam-clay shape.

$$f^y = \left(\frac{q/\varrho(\theta)}{Mp'}\right)^n + \frac{b}{ln(r)} \cdot ln\left(\frac{p'}{p^c(s,T)}\right) \qquad (4.131)$$

where the material parameter b has the effect of diminishing the elastic domain at constant pre-consolidation and n is a material parameter controlling the yield shape. Fig. 4.47 shows the contours of the yield function Eq. 4.131 for different values of the shape parameter.
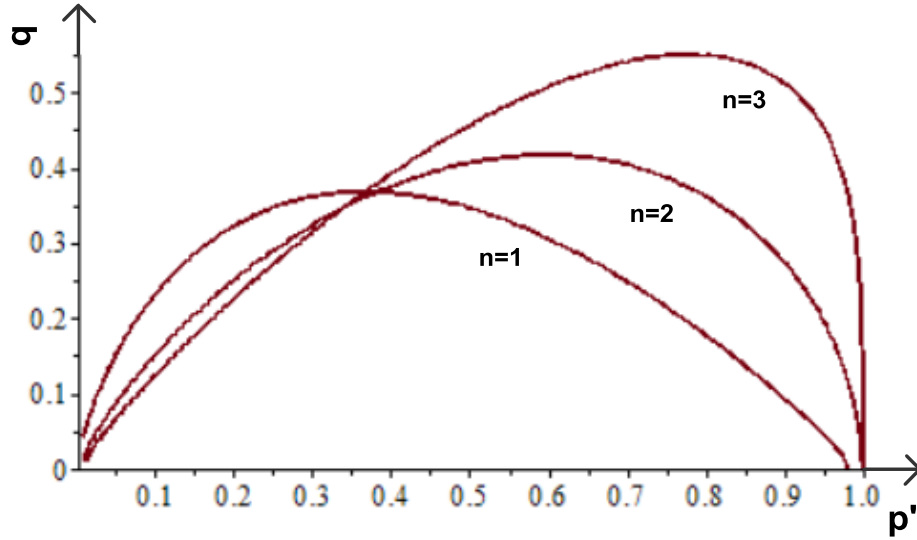
Figure 4.47: Shape of the yield surface for different values of the material parameter "n".

A dependency on the third invariant of the stress tensor has been included in Eq. 4.131. For the model HP-CASM the dependency on the lode angle is introduced through the van Eekelen proposal. This proposal is explicitly written as,

$$\varrho(\theta) \quad = \quad \frac{1}{2^m} \cdot \left(1 + \tilde{\beta}^{\frac{1}{m}} + \left(1 - \tilde{\beta}^{\frac{1}{m}}\right) \cdot [-\sin(3\theta)]\right)^m \tag{4.132}$$

expression 4.132 is valid within the range $\theta = -30°$ (triaxial compression) to $\theta = 30°$ (triaxial extension). Requirements for aspect ratio are given by the two side constraint of ϱ: $\varrho(30°) = \tilde{\beta}$ (triaxial extension state) and $\varrho(-30°) = 1$ (triaxial compression state). Here $\tilde{\beta}$ is given by the term $\tilde{\beta} = \frac{(3-\sin\phi)}{(3+\sin\phi)}$.

Figure 4.48 shows the shape of the yield surface HP-CASM model at the deviatoric plane and for two values of m. It is important to highlight that for m=1, the surface does not preserve the convexity. This fact motivates the study of convexity of the van Eekelen formula with regard to the shape parameter m.
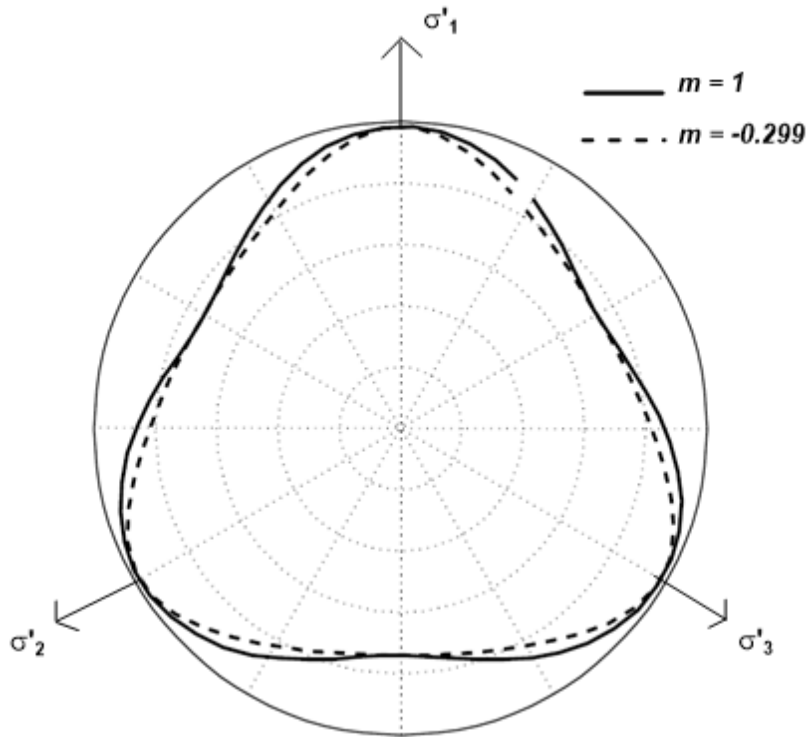
Figure 4.48: BBM5 with Lode Dependency. Plot for two values of m.

In the first instance a view of the contour of the van Eekelen's formula evidence a discontinuity at $m = 0$. This fact motivates to chose values for the shape parameter laying within the interval $[-\infty, 0)$. In a further step, the derivative function $\partial\varrho/\partial m$ shows a change in the growth for values of shape parameter close to zero, Fig. 4.49. Those minimum values match with changes of curvature $\partial^2\varrho/\partial^2 m$ of the van Eekelen's formula and must be avoided since they produce non-convexity of the yield surface.

Minimum values of van Eekelen's shape parameter can be obtained by solving the minimization problem $\begin{cases} \min & \rho(m|\theta, \phi) \\ & m \in [-\infty, 0) \end{cases}$ for constants values of both lode angle and friction angle. Fig. 4.50 shows the minimum values of van Eekelen parameter obtained as solution of the former problem for different values of the Lode's angle (It is recommended to add a safeguard value "-0.1" to those presented at Fig. 4.50).
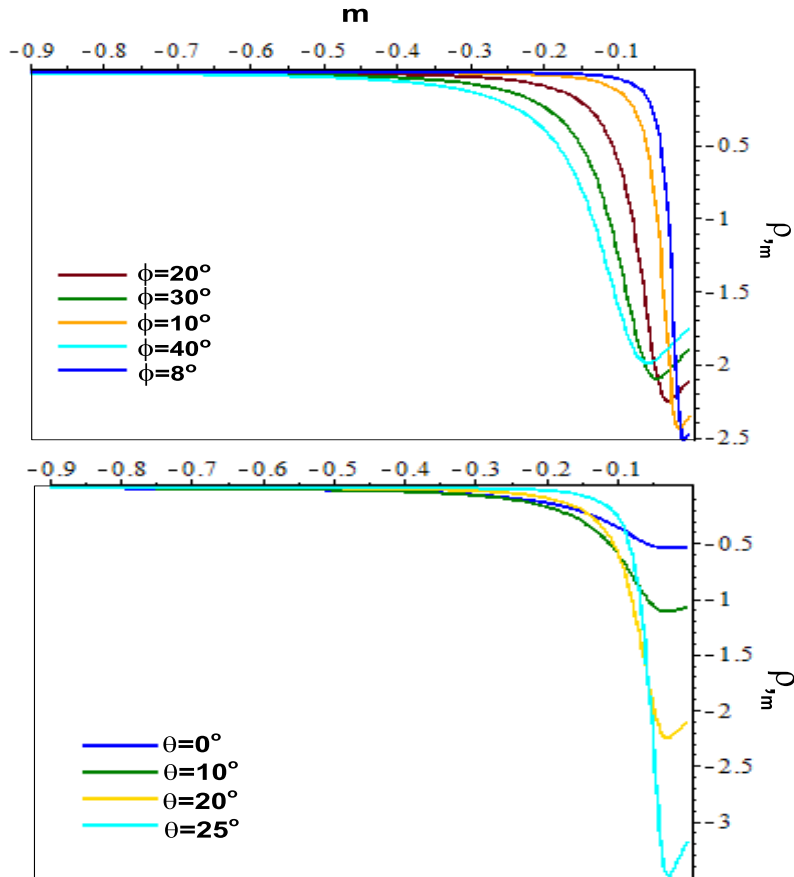
Figure 4.49:Contour of the gradient of van Eekelen's radio for different values of friction and Lode angles.
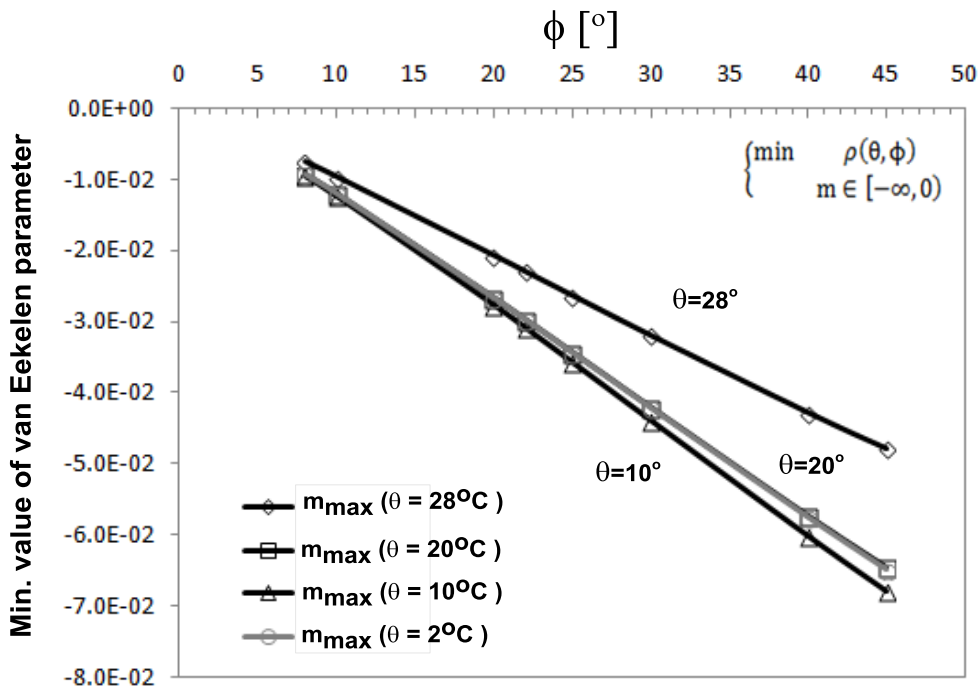
Figure 4.50:Minimum values of van Eekelen's shape parameter to guarantee convexity of the yield function at the deviatoric plane.

Below a frame with contours of the van Eekelen's radio is shown for different values of both: (a) friction angle and (b) shape parameters.
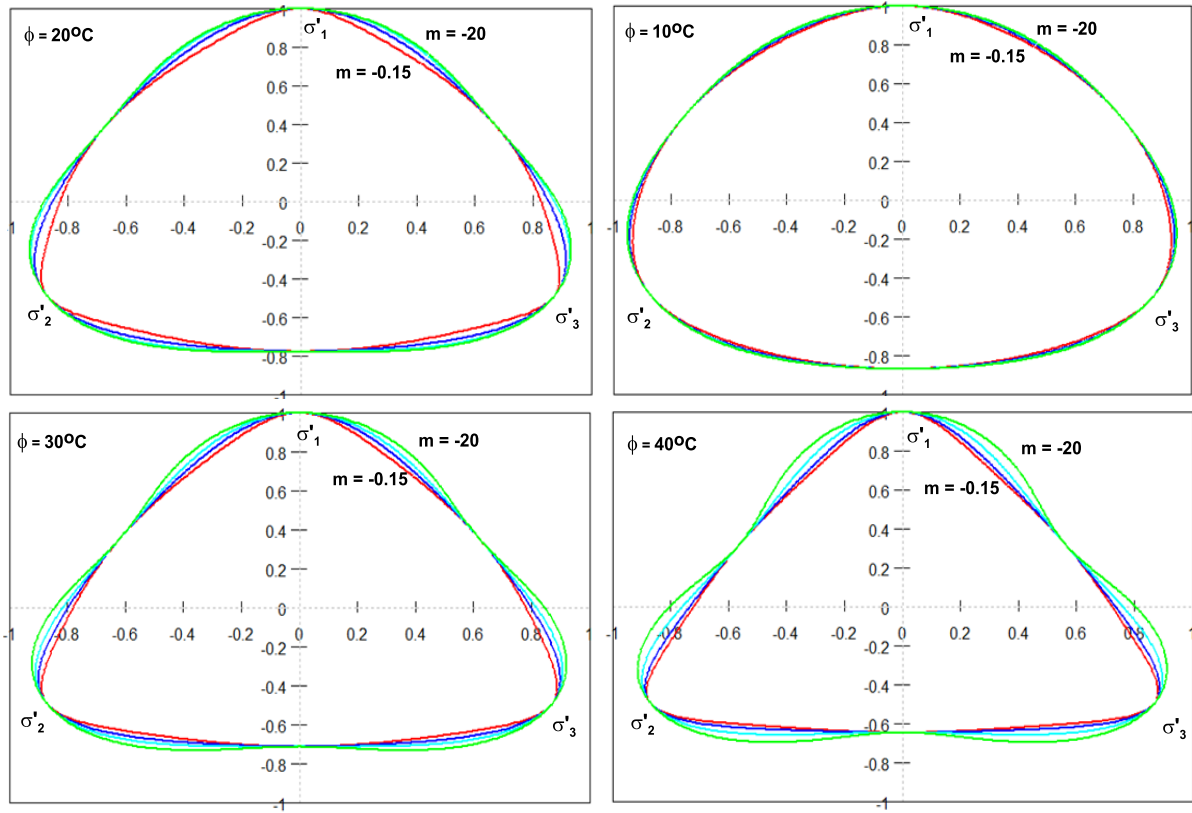
Figure 4.51: Contours of van Eekelen's radio for different friction angles and shape parameter m.

It is noted from Fig. 4.51 that convexity is also lost for very low values of the shape parameter m at high friction angles.

In view of the above, it is concluded that the choice of the shape parameter is highly important to obtain satisfactory results at the time of integration. A typical value assumed by Bardet (1990) is $m = -0.299$. The van Eekelen's shape parameter must range between: (a) maximum values shown at Fig. 4.51 plus a safeguard value of -0.1, and (b) a minimum value of -0.4 (from shape observation).

Model dependency on environmental variables is reflected in the pre-consolidation pressure, p^c is stated as dependent on hydraulic and thermal loading through the expression,

$$p^c(s, T) = \frac{z(\xi)}{2} \left[p_o^c \cdot \exp\left(\frac{\alpha_p}{\lambda^* - k^*}\right) \right]^{b(\xi)} \cdot \left(1 - c_T \log\left(\frac{T + |T_{min}|}{T_o}\right) \right) \qquad (4.133)$$

where $z(\xi)$ and $b(\xi)$ have been defined previously by Eq. 4.67, T_o and T_{min} are the reference and the minimum allowed temperatures, respectively, and c_T is a parameter giving the rate of degradation.

Model performance has been studied shown through modeling a series of conventional tests. Parameters used in the numerical tests correspond to clay material and are summarized in Table 4.11.

Table 4.11: Material properties for Synthetic Clay to evaluate the model performance

κ	0.018	P	0.09	n	0.9	e_o	1.1759	ϕ'	26
λ	0.09	c_T	0.2	b	1	G	0.4	m	-0.229
n_{CASM}	1	N	1.1759	A	0.185	B	0.1419		

Conventional drained triaxial tests on lightly overconsolidated $\left({p^c(\mathrm{s},\mathrm{T})}\big/{p'} < 2 \right)$ and

heavily overconsolidated $\left({p^c(\mathrm{s},\mathrm{T})}\big/{p'} > 2 \right)$ samples are initially performed.

In the first test, the model response is initially elastic; when plastic strains start to develop, the curve $q\!:\!\varepsilon_1$ shows a sharp drop in stiffness, Fig. 4.52a. Magnitude of the plastic strains can be seen at Fig. 4.52b. Similarly the change of the elastic volume is small and a break point is also observable at the end of the elastic response, Fig. 4.52c. In the second test the response remains elastic until the stress state reaches the yield locus at a point lying to the left of the critical pressure. At that point the plastic strain increment vector produces plastic volumetric expansion, Fig. 4.52c. After the initial elastic rise in q and decrease in volume, further plastic shearing is associated with a drop in q and an increase in volume Fig. 4.52.
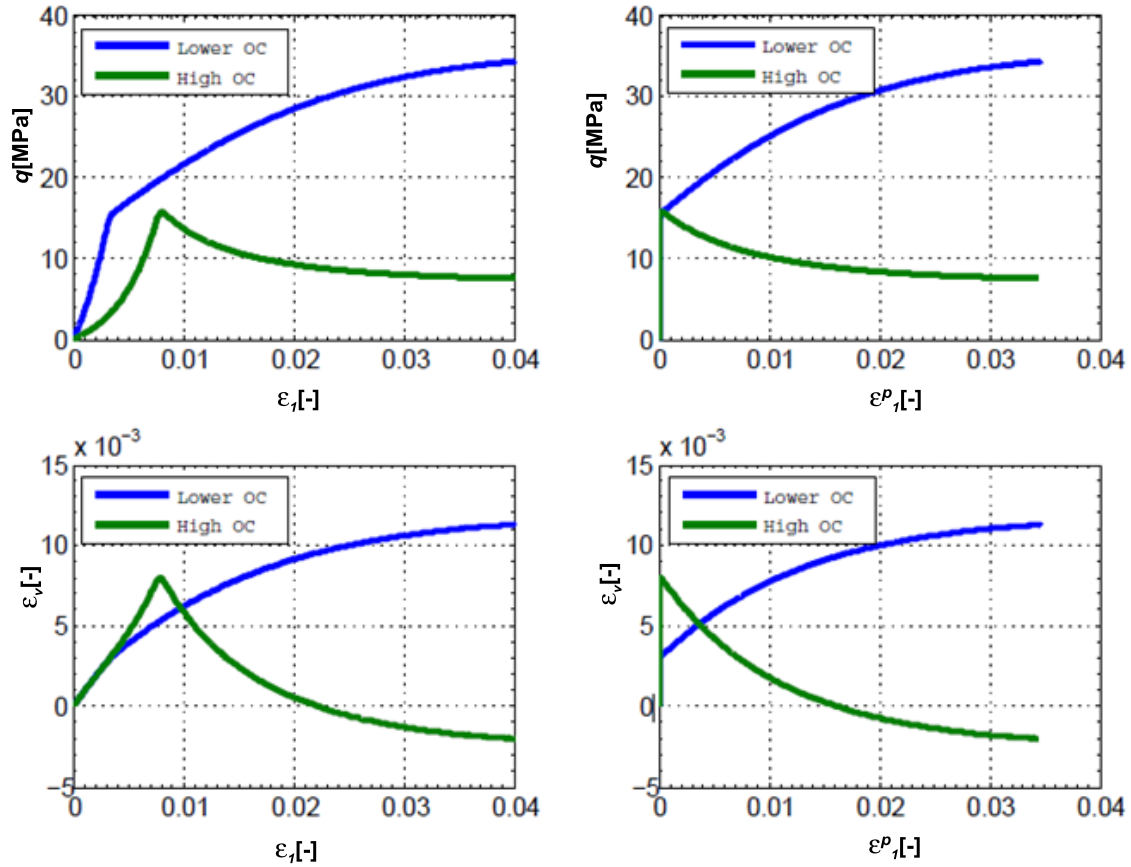
Figure 4.52: Conventional drained triaxial tests on BBM5 model. (a)Deviatoric Stress vs. axial strain for lightly overconsolidated sample and heavily overconsolidated sample. Stress path: A shearing (1:3) load was applied.

Figure 4.53 shows a comparison of the HP-CASM model response under drained triaxial conditions on samples lightly overconsolidated subjected to triaxial compression and triaxial extension stress paths. It is seen in both cases that after the plastic strains start to develop, the curves $q:\varepsilon_1$ show a sharp drop in the stiffness Fig. 4.53. The soil sample resistance to triaxial extension results lower than that observed under compression conditions. At the same time the soil sample under compression conditions needs more time to enter in plastic yielding, Fig. 4.53. Conversely, the developed plastic volumetric strains during yielding are greater in extension due to the lower resistance of the soil to support strains in extension, Fig. 4.53. These behaviors evidence the influence of the third invariant of the stress tensor θ on the HP-CASM model response.
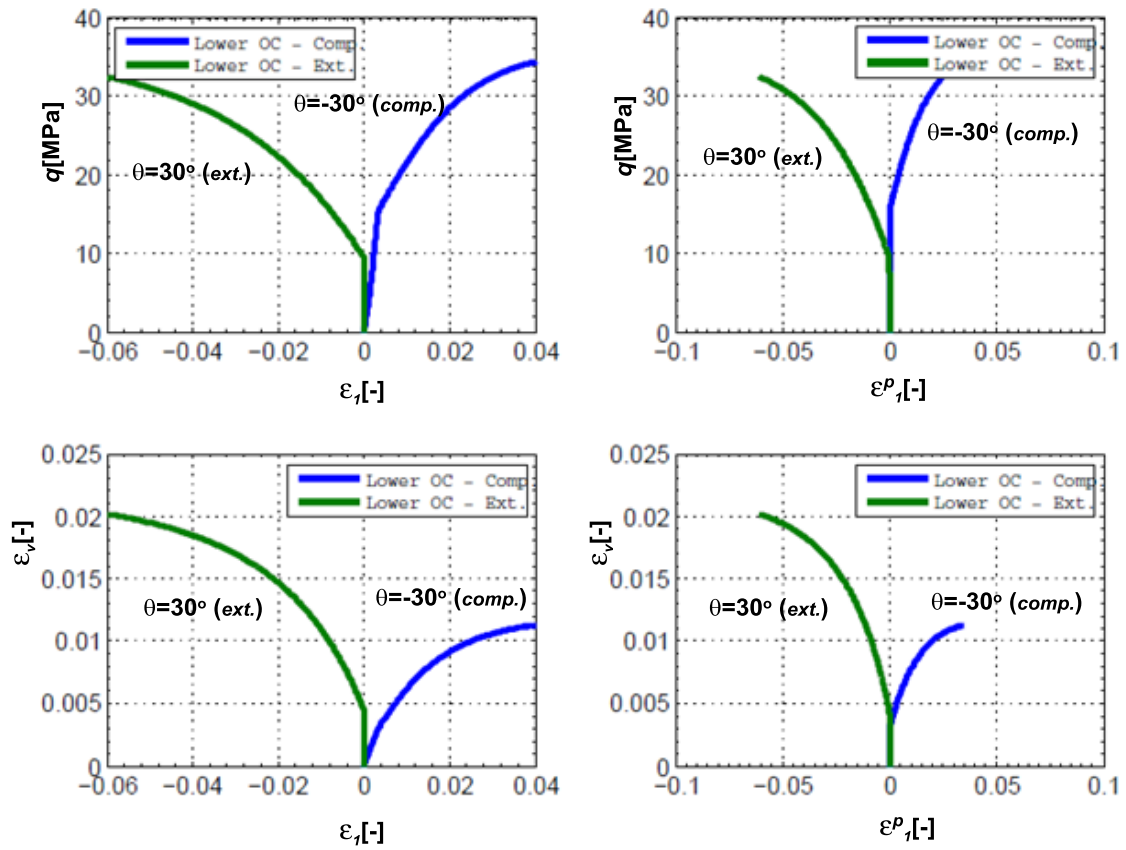
Figure 4.53: Conventional triaxial test on lightly overconsolidated sample: Deviatoric stress vs axial strain.. (a) triaxial compression $\theta = -30^o$. (b) triaxial extension $\theta = 30^o$.Stress path: A shearing (1:3) load was applied.

Figure 4.54 shows a comparison of the HP-CASM model response under drained triaxial conditions on samples heavily overconsolidated subjected to triaxial compression and triaxial extension stress paths. It is seen in both cases that after the plastic strains start to develop, the curves $q: \varepsilon_1$ show a sharp drop in the stiffness, Fig. 4.54. The soil sample resistance to triaxial extension results lower than that observed under compression conditions. At the same time the soil sample under compression conditions needs more time to enter in plastic yielding, Fig. 4.54. These behaviors evidence the influence of the third invariant of the stress tensor θ on the implicit HP-CASM model response.
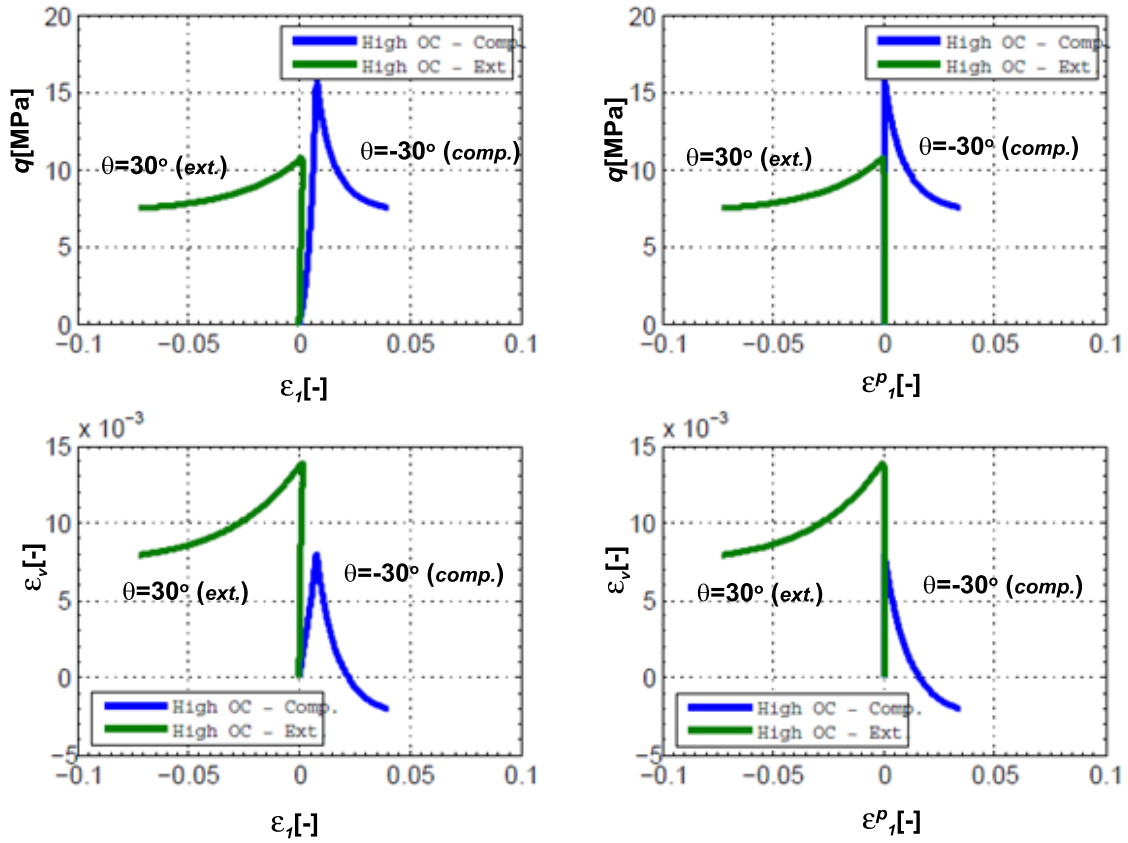
Figure 4.54: Conventional triaxial test on heavily overconsolidated sample: Deviatoric stress vs. axial strain. (a) triaxial compression $\theta = -30^o$. (b) triaxial extension $\theta = 30^o$. Stress path: A shearing (1:3) load was applied.

The following are model tests at different suction and temperature values. Those trials evidence the model performance under environmental variables.

Three different tests involving temperature cycles are considered. The test commenced with the application of an isotropic load from the initial state $p' = 0.04\ MPa$ and up to the final state of $p' = 0.15\ MPa$ (at constant temperature of 25°C). The application of the isotropic load fixed the stress state close to the pre-consolidation pressure of the material. After that, three temperature cycles were carried out within three trails: (a) 25-22-25; (b) 25-70-25; (c) 25-90-25; Fig. 4.55.

Those cycles shift the yield surface according to the mobilized plasticity. This mobilized plasticity is generated by the temperature increase (p'_{c_1} in Fig. 4.55). After those cycles of temperature, the samples were subjected to triaxial compression under drain conditions.

Figure 4.56 indicates that the branch of elastic response during triaxial compression of the sample subjected to the cycle 25-90-25 is higher than the branches of the samples subjected to the temperature cycles of 25-70-25 and 25-22-25 grades. This observation

demonstrates that the sample subjected to the broader scope of temperatures (25-90-25) mobilizes more plasticity than the samples subjected to the narrower scopes of temperature.
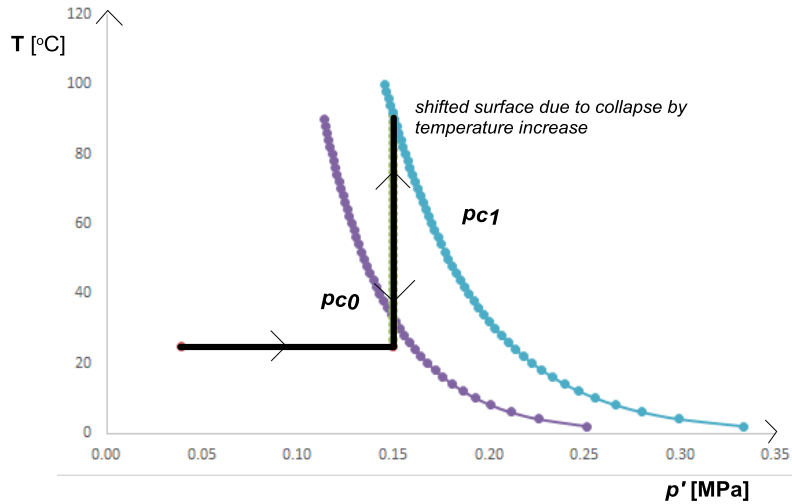
Figure 4.55: Stress-Thermal Path follows in the test on Bangkok Clay.

Figure 4.56 evidences the good ability of the model to capture the behavior observed in the laboratory test. These results show the thermal strengthening of the material once the plasticity is developed by thermal processes.
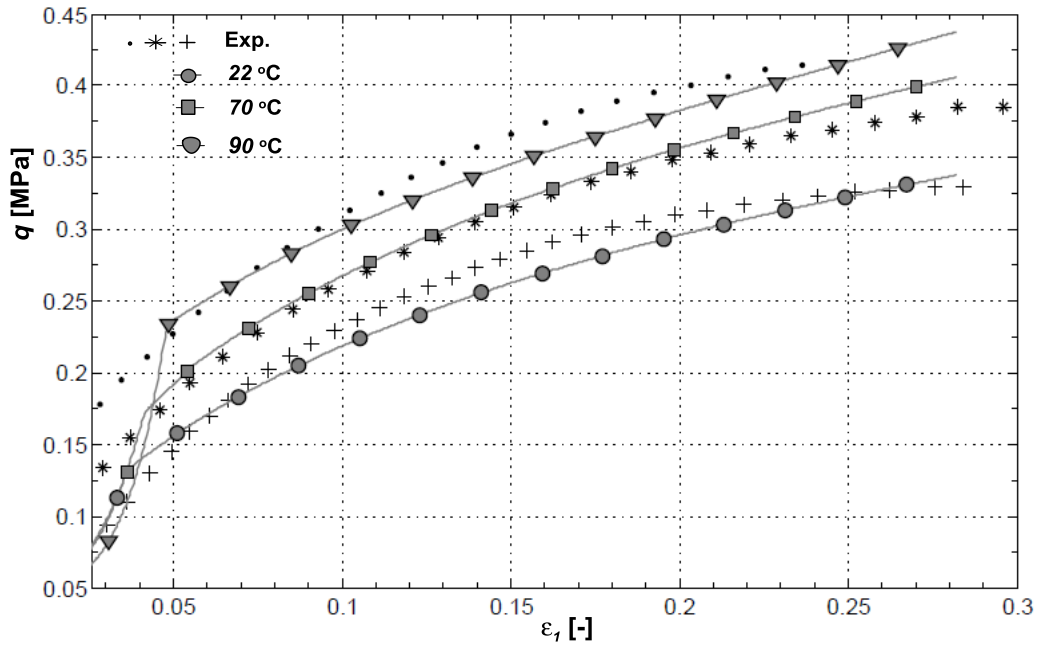
Figure 4.56: Numerical simulations of drained triaxial compression tests on normally consolidated Bangkok Clay. Comparison with experimental results.

To test model response under partially saturated conditions, three conventional drained triaxial tests realized in lightly overconsolidated samples, at three different values of soil moisture are simulated. In all tests, model response is initially elastic, being this response maintained longer at driest states Fig. 4.57. At the onset of plastic yielding, the curve $q: \varepsilon_1$ shows a sharp drop in the stiffness Fig. 4.57. The magnitude of the developed plastic strains can be seen also at Fig. 4.57. In the driest state samples, the change in volume results to be lower than the change in volume at the wettest samples. This fact evidences the increase of resistance of the soil observed at partially saturated samples see Fig. 4.57.
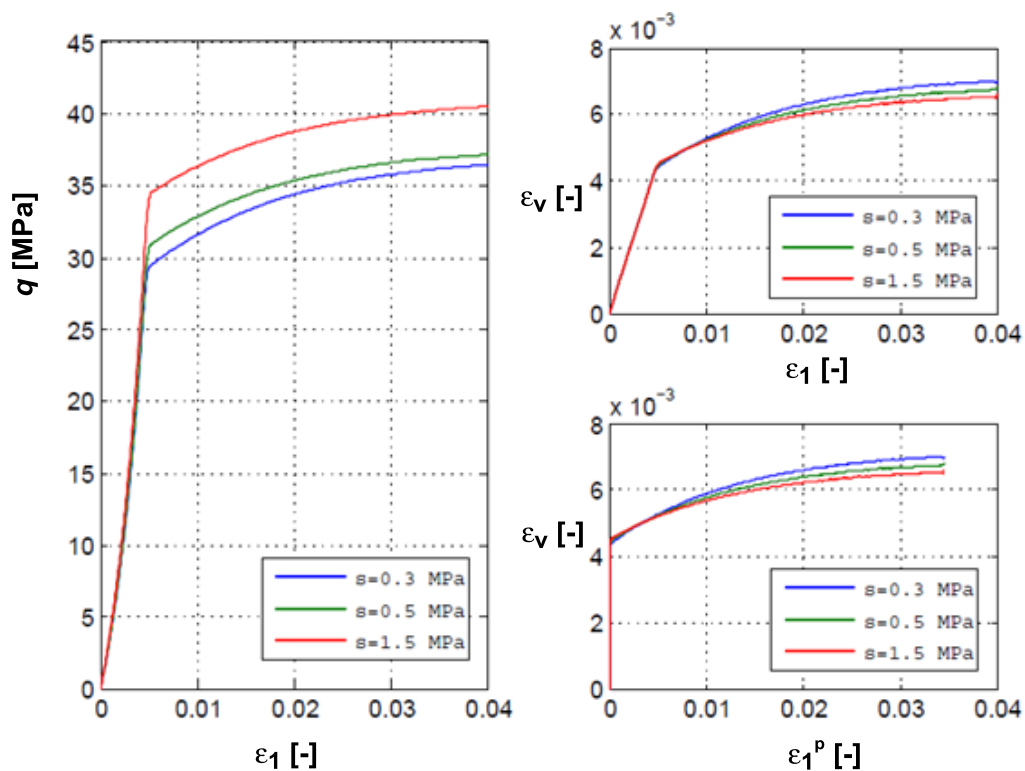
Figure 4.57: Conventional drained triaxial tests on BBM5 model. Samples at three different states of humidity: (a) Deviatoric Stress vs. axial strain, (b) Volumetric strain vs axial strain; (c) Plastic volumetric strain vs axial strain. Stress path: shearing (1:3).

According to the results presented, a good performance of the model HP-CASM is evidenced to capture both: (a) typical response under traditional mechanical stress paths and (b) mechanical response under thermal loadings.

4.7)   Frictional Soil Models for environmental actions

In this last section, two cohesive-frictional models will be reviewed in some detail within the hyper-plastic framework. First, the Drucker-Prager model, already derived from a dissipation potential by Collins & Houlsby (1997) in case of purely frictional materials, will be extended to consider a cohesive component and degradation under temperature changes. Then, the hyperplastic formulation of Matsuoka-Nakai model (Matsuoka & Nakai, 1974) will be described, with special attention devoted to the representation of dilatancy. This model has been chosen because it provided a more realistic shape of the yield locus in the deviatoric plane, close to that of Mohr-Coulomb yield criterion.

4.7.1)   Introduction to friction and dilatancy angles and Historic case

The simplest frictional model considered to capture soil failure is the one based on Coulomb´s pioneering work in 1773. It is depicted in Fig. 4.58 in a Mohr diagram. In this framework, when the soil do not present cohesion, the strength of the soil is defined by the line of angle ϕ' (friction angle). The soil element is considered to experiment failure when the stress state (represented by the Mohr circle in Fig. 4.58) is tangent to the line.
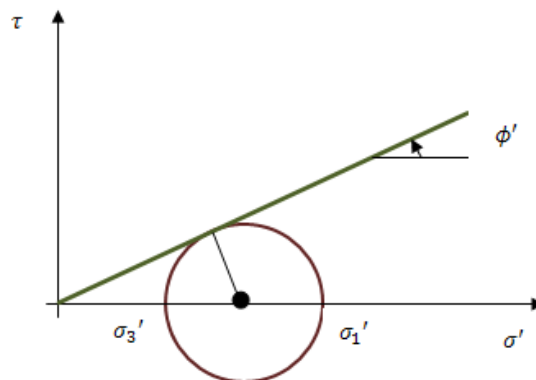
Figure 4.58: The Mohr-Coulomb Failure Criterion

This approach often represents only an oversimplification of the real behaviour of the sample, particularly in dense materials, where a peak is observed in the shear stress-shear strain relationship, followed by a reduction in shear stress at large strain, Fig. 4.59a. If the vertical displacements are furtherly monitored, they will indicate an upward movement of

_____

the upper face of the sample, related to material dilation. It is usually preceded by a small initial compression, Fig. 4.59b.
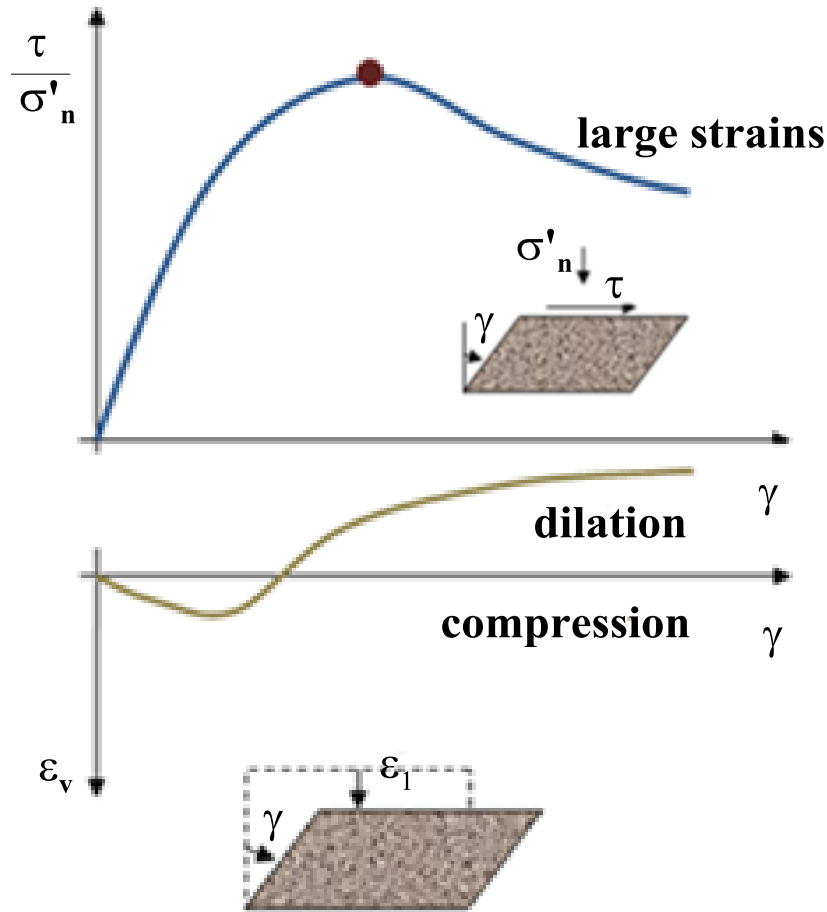
Figure 4.59: (a) Typical shear stress – shear strain curve in simple shear test; (b) Dilation of dense sand in a simple shear test

If shear tests are carried under different normal stress levels, the peak angles reduce with increasing stress. As a result, the peak strength surface is curved in the Mohr-Coulomb diagram, Fig. 4.60.
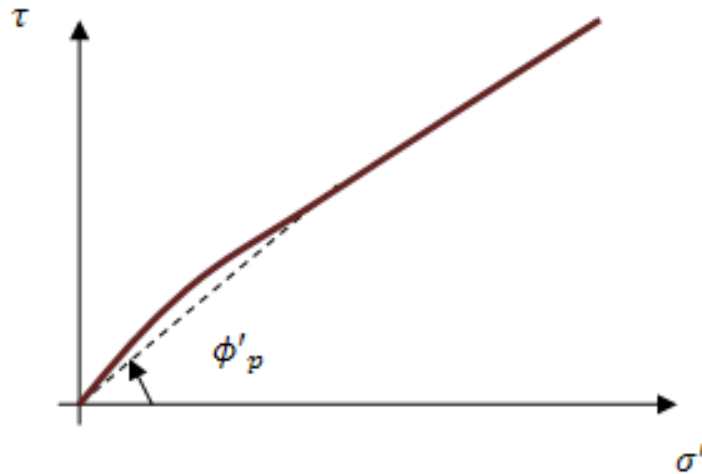
Figure 4.60: Curve peak strength envelope on Mohr's circle plot

All these features: (a) peak and large strain strength, (b) dilation and (c) reduction of peak strength with stress level, are indeed closely connected. Dilation play a key role in the understanding of their interactions.

The angle of friction expresses the ratio of a shear stress to a normal stress, and can be defined in terms of principal stresses, see Fig. 4.61a:

$$\sin(\phi') = \frac{\sigma_1 - \sigma_3}{\sigma_1 + \sigma_3} \tag{4.134}$$

In a similar manner, dilation can be expressed by an angle that expresses the ratio between the volumetric and shear strain rate. In the case of plane strain tests, it can be defined in terms of principal strain rates Fig. 4.61b:

$$\sin(\psi) = \frac{-(\dot{\varepsilon}_1 + \dot{\varepsilon}_3)}{\dot{\varepsilon}_1 - \dot{\varepsilon}_3} \tag{4.135}$$

The sign "minus" arises from the convention used in soil mechanics where compressive stress and strain are taken positive. According to this convention, dilation angle is positive when soil expands.

$$\sin(\phi') = \frac{\sigma_1 - \sigma_3}{\sigma_1 + \sigma_3} \qquad \sin(\psi) = \frac{-(\dot{\varepsilon}_1 + \dot{\varepsilon}_3)}{\dot{\varepsilon}_1 - \dot{\varepsilon}_3}$$
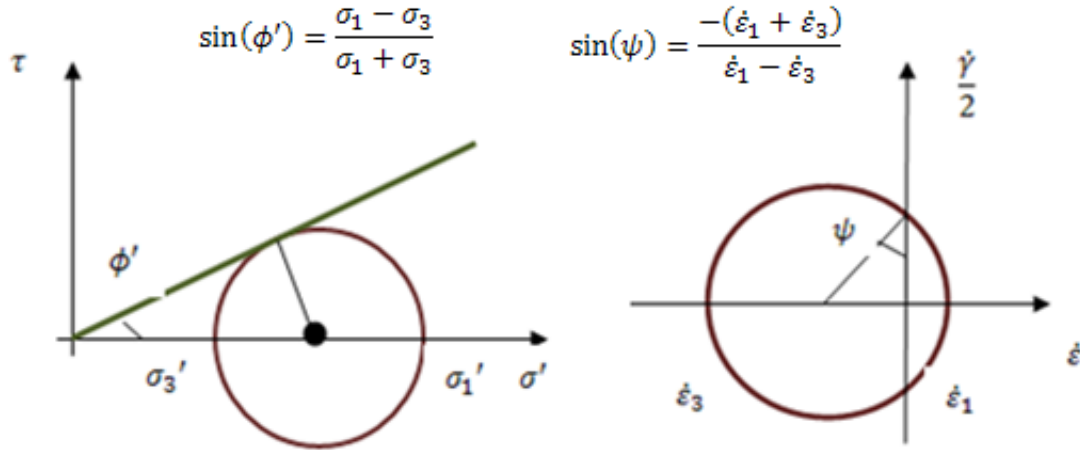
Figure 4.61: Definitions of friction and dilation angles. (a) Friction angle in Mohr diagram; (b) Dilation angle in the Mohr representation of strain rates.

Dilation angle has an important meaning in constitutive modeling as it is associated to the flow rule. Equation 4.135 is however the source of experimental difficulties as it requires to remove the elastic component from the measured strains. In many situations, the elastic stiffness of the material is considered sufficiently high in order to neglect the elastic strains and to assess the ratio between plastic volumetric and shear strains as:

$$\sin(\psi) = \frac{-(\dot{\alpha}_1 + \dot{\alpha}_3)}{\dot{\alpha}_1 - \dot{\alpha}_3} \tag{4.136}$$

A variety of theories have been proposed to explain the relationship between the friction angle and dilation angle. One of the first was the "energy correction" concept introduced by Taylor (1948); nowadays understood as based on the assumption about the "work dissipated" in a frictional soil. According to this framework, the rate of work input to a block during its sliding on a smooth plane is:

$$\dot{W} = \tau\dot{\gamma} \tag{4.137}$$

and will be dissipated internally by friction. This dissipation is then equal to the shear stress computed in a Coulomb fashion ($\sigma'_n \tan \phi'_1$) times the rate of shear strain $\dot{\gamma}$:

$$\dot{W} = \tan(\phi'_1)\,\sigma'_n \dot{\gamma} \tag{4.138}$$

If the sample experiments additionally a change in volume in addition to distortion then the equation for the dissipated work has to include the work exerted by the normal stress:

_____

$$\dot{W} = \sigma'_n \dot{\varepsilon}_v + \tau \dot{\gamma} = \tan(\phi'_1) \, \sigma'_n \dot{\gamma} \qquad (4.139)$$

which can be rearranged into:

$$\tan(\phi') = \tan(\phi'_1) + \tan(\psi) \qquad (4.140)$$

According to Eq. 4.138 the observed (or apparent) angle of friction is the sum of the angle of friction at constant volume and the angle of dilation. This relation will be further used to express non-associated behaviors in the Drucker-Prager and Matsuoka-Nakai models.

As a starting point to derive hyperplastic formulations for cohesive Drucker Prager and generalized Matsuoka-Nakai model, the derivation made by Collins & Houlsby (1997) for Tresca´s model is now recalled. For a stress state such that $\sigma_1 > \sigma_2 > \sigma_3$, Tresca's yield criterion is expressed by:

$$\frac{1}{2}(\sigma_1 - \sigma_3) = b \qquad (4.141)$$

where σ_1 and σ_3 are the maximum and minimum principal stresses and b is the yield stress of material determined from pure shear tests. This model, extensively used to represent failure in metals, has been further generalized for soils by introducing a pressure dependent term. In that case, the yield criterion reads:

$$\frac{|x_1 - x_3|}{a \cdot p + b} = 2 \qquad (4.142)$$

where a and b are material parameters dependent on friction angle ϕ and cohesion c (a(ϕ) and b(c, ϕ)) and x_i the generalized stress components that depend on dissipation function. Collins & Houlsby (1997) propose the following expression for this function:

$$d = (a \cdot p + b) \cdot [|\dot{\alpha}'_1| + |\dot{\alpha}'_2| + |\dot{\alpha}'_3|] \qquad (4.143)$$

where $\dot{\alpha}'_i$ are the principal components of the plastic distortion-rate tensor. From the standard hyperplastic procedure, the principal generalized stresses take the form:

$$x_1 = \frac{\partial d}{\partial \dot{\alpha}'_1} = (a \cdot p + b) \cdot \text{sg}(\dot{\alpha}'_1) \qquad (4.144)$$

$$x_3 = \frac{\partial d}{\partial \dot{\alpha}'_3} = (a \cdot p + b) \cdot \text{sg}(\dot{\alpha}'_3)$$

which provide the following expression for the yield surface:

$$x_1 - x_3 = (a \cdot p + b) \cdot [sg(\dot{\alpha}_1') - sg(\dot{\alpha}_3')] \tag{4.145}$$

where $sg(\dot{\alpha}_i')$ is the signum function of the rate of principal distortion plastic strains.

Figure 4.62 depicts the Extended Tresca's model and the direction of the plastic distortion strain rate vector. If $\dot{\alpha}_1'$ is positive and $\dot{\alpha}_3'$ is negative, the yield stress is equal to $2 \cdot (a \cdot p + b)$ whereas it is equal to $-2 \cdot (a \cdot p + b)$ when $\dot{\alpha}_1'$ is negative and $\dot{\alpha}_3'$ is positive. If either one of these two principal distortion rates is equal to zero then $(x_1 - x_3)$ is undetermined. Finally, $x_1 - x_3 = 0$ if $\dot{\alpha}_1'$ and $\dot{\alpha}_3'$ have the same sign. The latter situation is only possible if $\dot{\alpha}_2' \neq 0$ and is of the opposite sign to $\dot{\alpha}_1'$ and $\dot{\alpha}_3'$.
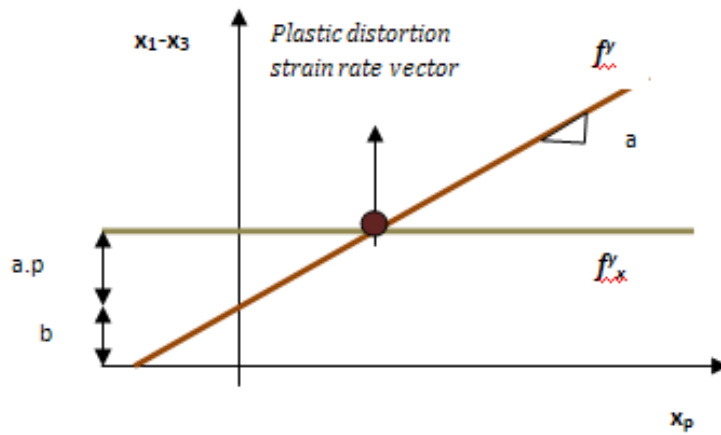
Figure 4.62: Extended Tresca Yield Surface for frictional materials

4.7.2) Drucker-Prager thermo-plastic Model

The Drucker-Prager model (Drucker & Prager, 1952) can be considered as the first attempt to approximate the Coulomb criterion by a simple smooth function. The model neglects the influence of the third invariant J_3 on the cross sectional shape of the failure surface thus providing a circular appearance to surface contour at the deviatoric plane.

The criterion is expressed as a function of the first invariant of the stress tensor $(I_1 = 3p)$ and the second invariant of the deviatoric stress tensor $\left(J_2 \left(\equiv J = \sqrt{J_2}\right)\right)$ as given by Eq. A3.1 $(f^y = J - Mp - a = 0)$. Material parameters M and a are related to the friction angle and the cohesion of the soil, Eq. A3.2.

In this section, a hyperplastic version of Drucker Prager model is developed following Houlsby (2000). It introduces two additional features: (a) traction resistance by

considering a cohesive component of the porous medium and (b) thermal degradation by explicit dependency of the yield surface on temperature.

Cohesion is introduced in the model by considering a modified expression of the dissipation function proposed by Collins & Houlsby (1997) for the pure frictional Drucker-Prager model. This modification appears as an additional term dependent on the soil cohesion. Furthermore the challenge to make the yield criterion dependent on thermal degradation is accomplished by introducing a multiplicative temperature dependent term.

Then the dissipation function reads:

$$d = r_c \left[N \frac{\sigma_{kk}}{3} + b \right] \sqrt{\frac{2}{3} \dot{\alpha}'_{ij} \dot{\alpha}'_{ij}}$$

(4.146)

where $N = \sqrt{3}M$ is a friction dependent parameter, $b = \sqrt{3}a$ is cohesion dependent parameter and r_c is a weighting factor that degrades as temperature increases. From the literature a possible variation for the weighting factor r_c is given by a linear law: $r_c = r_{c^0} - k_t(T - T_o)$ where r_{c^0} is the value of the thermal degradation parameter r_c at $T = T_o$ and k_T gives the rate of degradation.

Standard procedures in hyperplasticity lead to the expression for the generalized deviatoric stress x'_{ij} as:

$$x'_{ij} = \frac{\partial d}{\partial \dot{\alpha}_{ij}} = x_{ij} - \delta_{ij} x_{kk} = \sqrt{2} \left(M \frac{\sigma_{kk}}{3} + a \right) \cdot \frac{\dot{\alpha}'_{ij}}{\sqrt{\dot{\alpha}'_{ij} \dot{\alpha}'_{ij}}}$$

(4.147)

It can be verified from Eq. 4.147 that the internal plastic strains α'_{ij} satisfy Drucker-Prager's flow rule. The dilatant behavior of the material (consequently the non-associativity of the plastic flow) is introduced by considering an additional constraint through the technique of Lagrange multipliers (Collins & Houlsby, (1997). The constraint reads:

$$c = \dot{\alpha}_{ii} + B \cdot r_c \sqrt{\frac{2}{3} \dot{\alpha}'_{ij} \dot{\alpha}'_{ij}} = 0$$

(4.148)

where B is a material parameter function of the dilatancy angle Eq. A3.6. The constraint equation 4.148 gives a dilatancy relation for the plastic flow.

The same procedure followed in appendix A3 leads to the expression for the extended dissipation function d' as:

_____

$$d' = d + \Lambda c = r_c \left(\frac{N\sigma_{kk} + 3(b + \Lambda B)}{3} \right) \cdot \sqrt{\frac{2}{3} \dot{\alpha}'_{ij} \dot{\alpha}'_{ij}} + \Lambda \cdot \dot{\alpha}_{ii} \tag{4.149}$$

Then the expressions for the generalized deviatoric and volumetric stresses are derived from Eq. 4.149 as:

$$x_{kk} = 3\Lambda \tag{4.150}$$

$$x'_{ij} = r_c \left[\frac{N\sigma_{kk} + Bx_{kk}}{3} + b \right] \sqrt{\frac{2}{3}} \frac{\dot{\alpha}'_{ij}}{\sqrt{\dot{\alpha}'_{ij} \dot{\alpha}'_{ij}}}$$

Then computation of the yield function is obtained by elimination of the plastic strain rates at Eq. 4.150 leading to:

$$\frac{1}{r_c} \cdot \sqrt{\frac{3}{2} x'_{ij} x'_{ij}} - \left(\frac{N\sigma_{kk} + Bx_{kk}}{3} \right) - b = 0 \tag{4.151}$$

Or

$$f^{yx} = \frac{J}{r_c} - Cx_p - Mp - a = 0 \tag{4.152}$$

where $C = B \cdot (3)^{-1/2}$ and the term Mp plays a role of an apparent cohesion. Eq. 4.152 provides a yield surface identical to that considered in conventional plasticity when $M' = C + M$ and the plastic flow becomes associated.

The yield surface and plastic potential for the extended Drucker-Prager thermo-plastic model is plotted in Fig. 4.63.
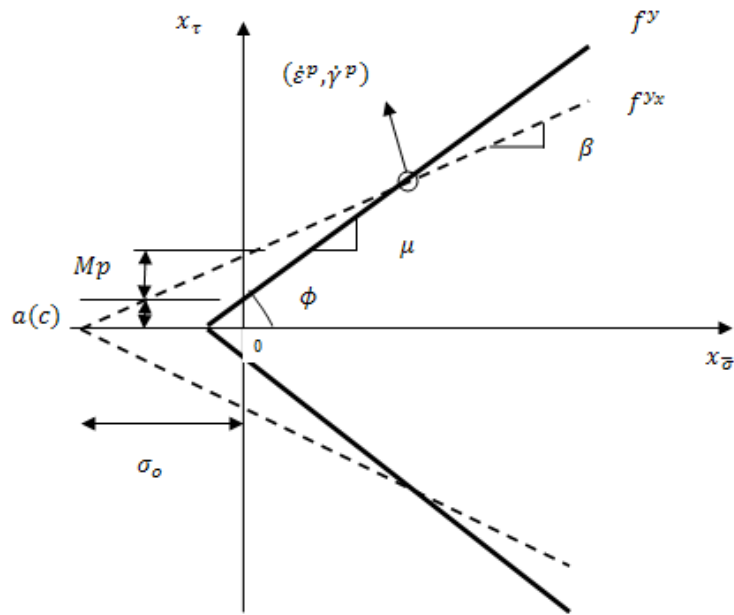
Figure 4.63: Drucker-Prager Yield Surface and Plastic Potential for frictional Plasticity (meridian plane). $\boldsymbol{M = \mu}$; $\boldsymbol{C = \beta}$.

Figure 4.64 shows in the meridian plane the admissible elastic domain enclosed by a Drucker-Prager yield surface for three different reference temperatures. Domain expands when temperature decreases and shrinks when it increases. In absence of kinematical hardening, a hyperplastic model can be easily completed by adding to the dissipation function a thermo-mechanical free energy potential with thermal dependency.
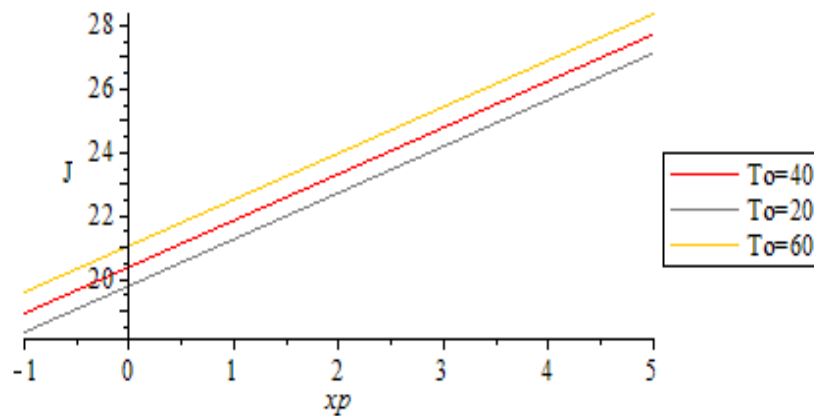
Figure 4.64: Modified Drucker-Prager Model considering loss of resistance with Temperature

_____

4.7.2.1) Smoothing the surface at the apex

A numerical issue in the implementation of Drucker-Prager model relies on the existence of a singularity in the flow rule at the apex $J = 0$. A solution to that problem is to smooth the yield criterion close to the singularity point. Several procedures exist already in the literature to perform this smoothing. Following the rounded hyperbolic technique proposed by Abbo et al. (2011) the equation 4.151 can be re-written as:

$$\left(\left(\frac{J}{r_c} \right)^2 + \vartheta^2 \right)^{1/2} - Cx_p - Mp - a = 0 \qquad (4.153)$$

where ϑ is the target distance between the apex of the non-smooth and smooth functions. Figure 4.65 compares the shape of the hyperbolic surface with that of the non-smooth DP criterion. Parameters used for the smoothing are given in Table 4.12.

Table 4.12: Parameters for the Hyperbolic Rounded of Drucker-Prager Model

$a(c)$ [MPa]	M	B	ϑ [MPa]
0.06	0.5	0.3	0.1
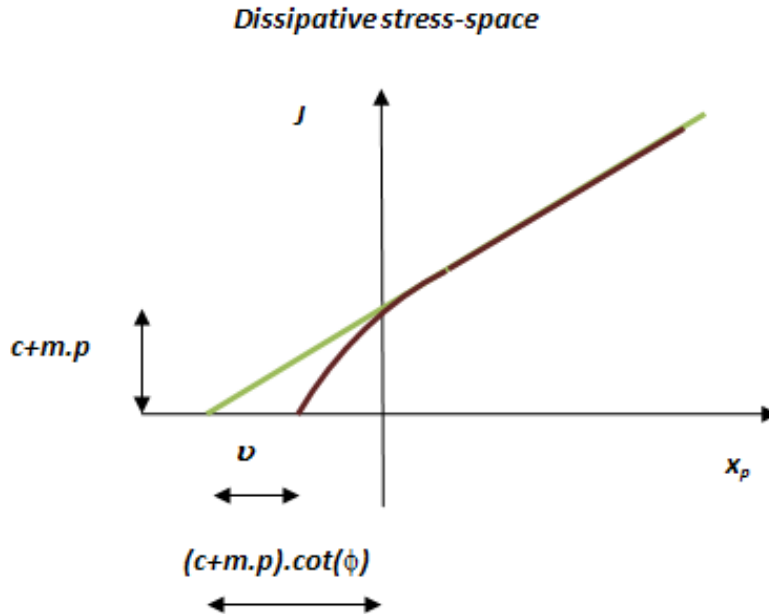
Figure 4.65: Drucker-Prager Yield Surface with Rounded Hyperbolic at the apex (at the Dissipative stress space)

Below an alternative and general method is proposed for the smoothing. It is based on a mathematical procedure proposed by Bendito et al. (2007) and later applied by Gesto et al. (2011) to approximate non smooth yield surfaces. It allows computing the equation of the smoothed surface as the sum of the equations of each single surface, provided they are appropriately normalized. For example, in the case of the Drucker-Prager model it is possible to obtain a smoothed surface at the apex by summing up the equations of the yield criteria in compression and in extension with previous normalization. The method consists in applying an exponential to each of the expression for compression and extension surfaces leading to:

$$\tilde{f}^y = \exp\left[a_1 \cdot \left(\frac{J}{r_c} + (C + M)p + a\right)\right] + \exp\left[a_1 \cdot \left(\frac{-J}{r_c} + (C + M)p + a\right)\right] = 1 \qquad (4.154)$$

Coefficient a_1 defines the amount of smoothing and is calibrated to reach a required tolerance between the non-smooth and smooth functions. Figure 4.66 shows the performance of the method for two different values of the coefficient a_1: 6 and 160 respectively. The smooth surface gets closer and closer to the non-smooth one as a_1 takes lower and lower values.
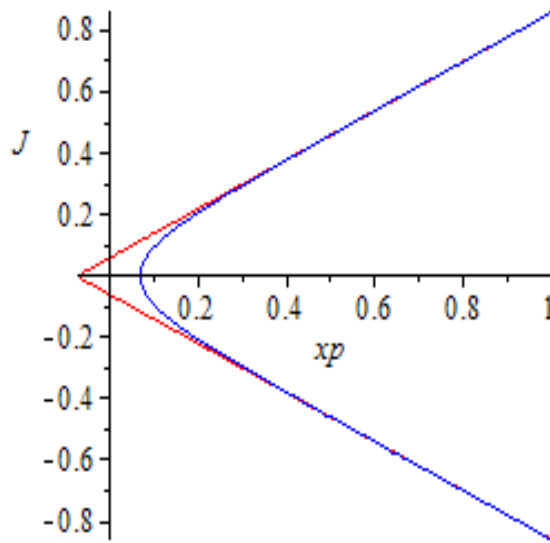
Figure 4.66: Smoothed Drucker-Prager yield surface at the dissipative stress space: (a-red) $\boldsymbol{a_1 = 6}$ and (b-blue)
$\boldsymbol{a_1 = 160}$

The integration of the frictional/cohesive and temperature dependent model has been performed through two algorithms based respectively on the Closest Point Projection and Interior Point methods. They are described in detail in Chapter 5. Here, some results at the level of Gauss point are presented, not with the objective of testing the integration algorithm, but to verify model equations. Parameters used in the tests at Gauss point level

_____

are given in Table 4.13. The hyperbolic smoothing is used in this particular case. Convergence is considered when the norm of the residue is less than 10^{-8}.

Table 4.13: Parameters for Modified Extended Drucker-Prager Model

E (MPa)	ϑ (MPa)	ν	T_0 (^{o}C)	ϕ (^{o})	$r_c{}^0$	ψ (^{o})	k_T ($^{o-1}$)
31000	0.01	0.2	20	24	1	14	1.561 10^{-3}

Fig. 4.67 and 4.68 show the stress paths obtained during triaxial compressions, as provided by both the CPPM and IPM algorithm. Both paths end on the yield criterion of the material defined by the friction angle and a null cohesion.

Fig. 4.69 depicts the stress path obtained during a triaxial compression at constant volume. Because of the dilatancy, the path follows the yield criterion as the mean stress increases, which provides a good check of the shape of the yield criterion. The difference between the initial and smoothed DP criteria can be observed in the figure.

The tests are repeated in the case of a cohesive materials Fig. 4.70 and temperature dependent yield criterion Fig. 4.71. Stress paths end again correctly on the yield surface. Stress-strain curves with and without elasticity are shown in Figure 4.72.
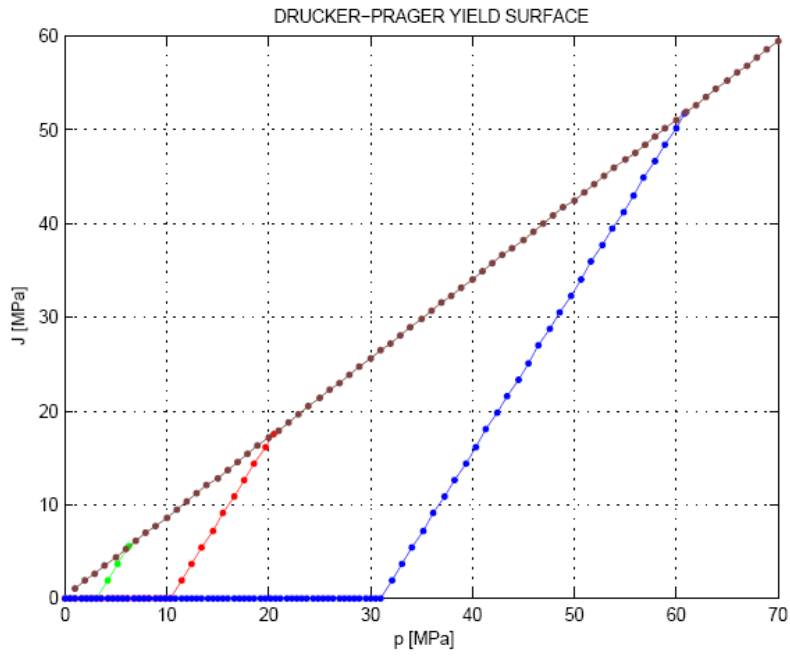
Figure 4.67: Drucker-Prager yield surface verification of criterion (at Gauss Point level) "c=0". Integrated with a Closest-Point-Projection Algorithm (No temperature effects)
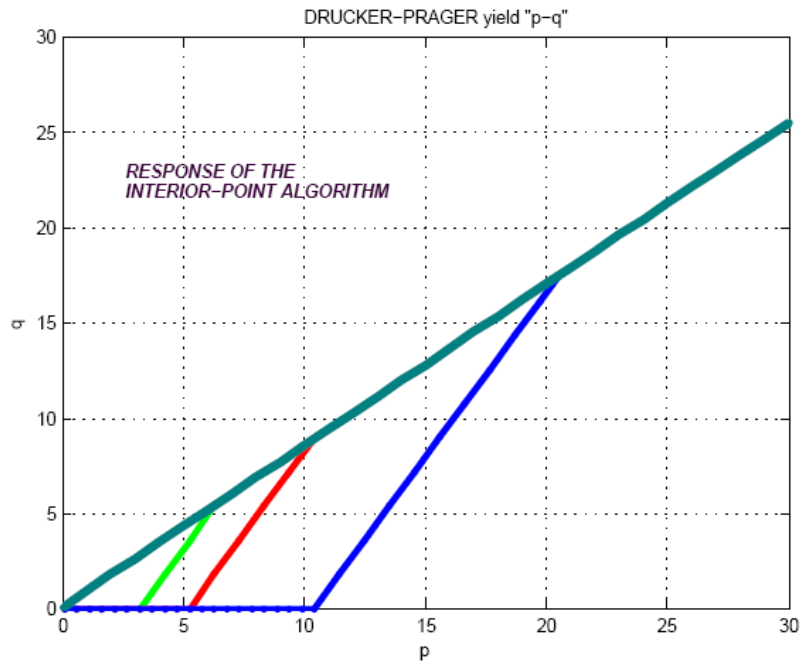
Figure 4.68: Drucker-Prager Yield Surface, verification of criterion (at Gauss Point level) "c=0". Integrated with an Interior-Point Algorithm
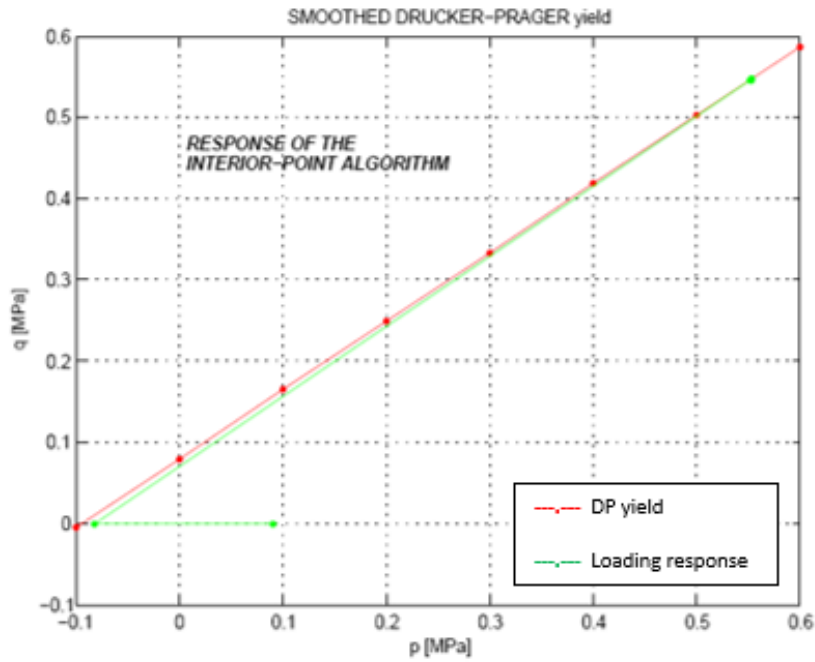
Figure 4.69: Smooth Drucker-Prager Yield Surface, verification of criterion (at Gauss Point level) "c = 0",
integrated with an Interior-Point Algorithm. (a-red) Non-smooth DP-yield function, (b-green) Smooth DP-yield
function.
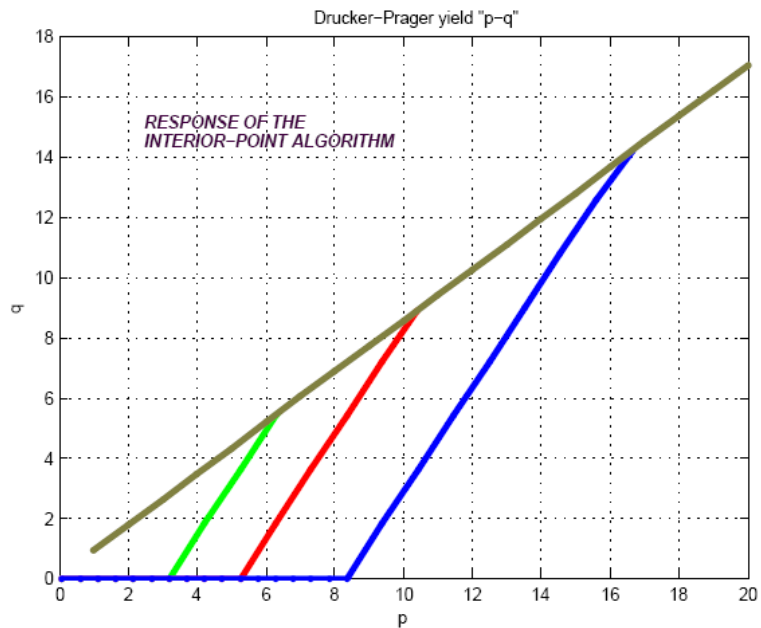
Figure 4:70: Drucker-Prager Yield Surface, verification of criterion (at Gauss Point level) "c=0.01 MPa", integrated
with an Interior-Point Algorithm
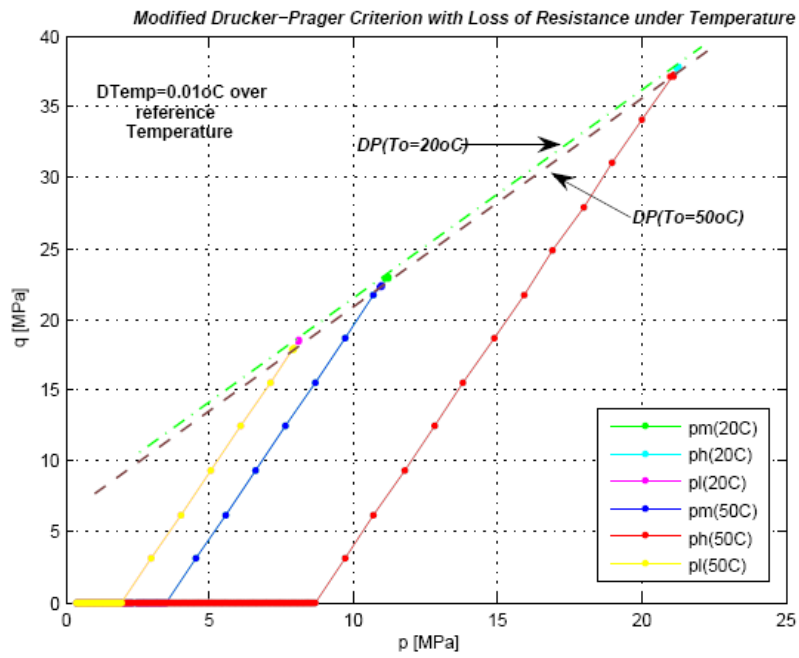
Figure 4.71: Drucker-Prager Yield Surface, verification of criterion. For two initial values of temperatures T_i=20ºC and T_i=50ºC; Reference Temperature T_0=20ºC; $r_c^o = 1$; $k_T = 1.561\ 10^{-3}\ ^{\circ-1}$ Integrated with an Interior-Point Algorithm
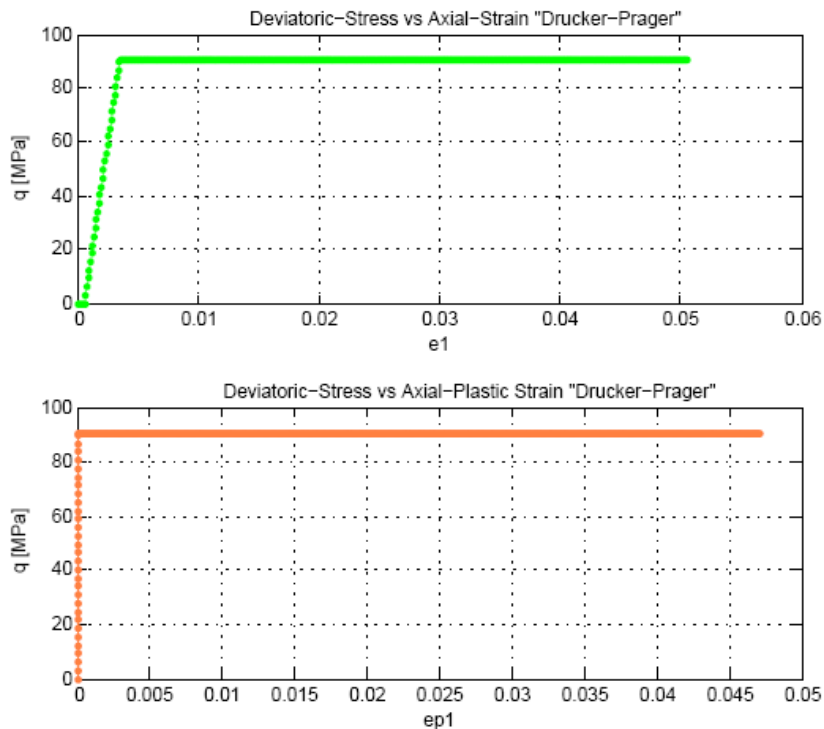
Figure 4.72: Deviatoric Stress – Axial Strain for elastic-plastic and perfectly plastic Drucker-Prager Model. Response provided by the Interior-Point Algorithm.

4.7.3)   Generalized Matsuoka-Nakai Model

In this subsection a new insight into pressure-dependent dissipation functions is made within the framework of frictional plasticity. It is recalled that such a pressure-dependency results in a non-associated flow of plastic strains.

In this regard the Matsuoka-Nakai yield criterion (Matsuoka & Nakai, (1974)) provides a smooth approximation of Mohr-Coulomb model by the expression A3.12 and its contour at the deviatoric plane is depicted at Fig. 4.73.
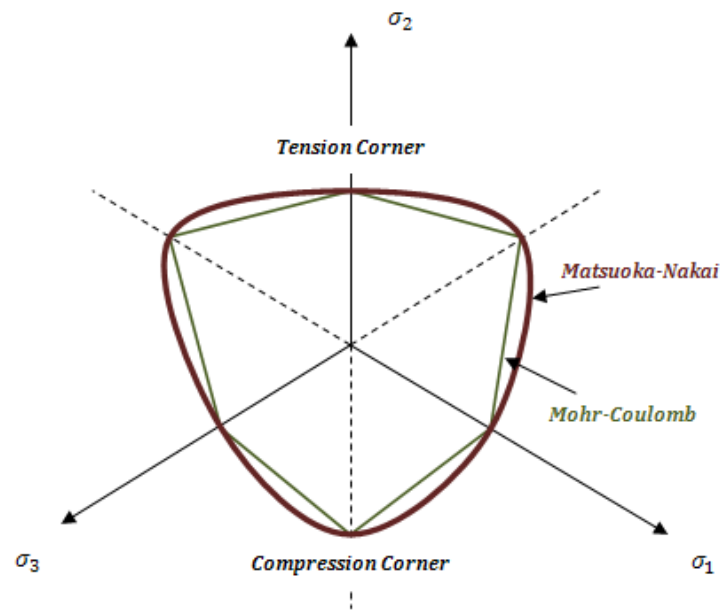
Figure 4.73: Shape of Mohr-Coulomb and Matsuoka-Nakai yield criterion in the deviatoric plane.

Figure 4.73 clearly shows the smoothed shape of the yield surface at the deviatoric plane giving rise to an adequate scenario for the numerical integration.

A detailed procedure of Legendre transformation which in this case is not direct was presented by Houlsby (1986) and reproduced at appendix A3.2 in order to obtain a dissipation function for the model. Furthermore Houlsby (1986) proposed a generalization of this criterion, such that it encloses both Tresca (for cohesive materials) and Matsuoka & Nakai (for pure frictional materials) criteria such that the expression for the yield function results in a more complex form shown at Eq. A3.20.

As with surface A3.17 following the same procedure of transformation except that in this case $\bar{\sigma}_i$ is restated to ($\bar{\sigma}_i = c + \mu\sigma_i$) a dissipation function for the extended version of the model was proposed Eq. A3.21.

An enhanced expression is now proposed for Matsuoka-Nakai-Houlsby yield criterion in order to accommodate yield functions that are curved in the meridian plane Fig. 4.74.
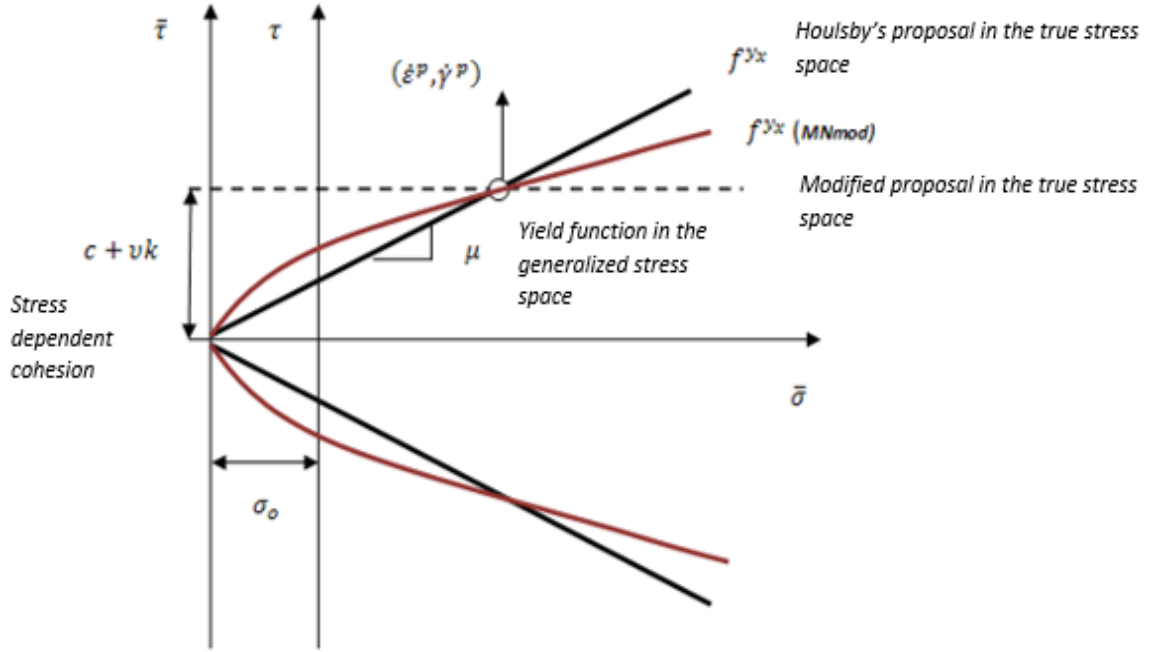
Figure 4.74: Original and Modified Matsuoka-Nakai Models in the Meridian plane.

The curvature is introduced through a pressure-dependent term in the dissipation function and is controlled by material parameter m. To this end the enhanced yield function reads:

$$d = \sqrt{\frac{8}{9}\left(\frac{c + \mu p_a}{3c + \mu(\sigma_1 + \sigma_2 + \sigma_3)}\right)^m \begin{bmatrix} (c + \mu\sigma_1)(c + \mu\sigma_2)(\dot{\alpha}_1 - \dot{\alpha}_2)^2 + \\ (c + \mu\sigma_2)(c + \mu\sigma_3)(\dot{\alpha}_2 - \dot{\alpha}_3)^2 + \\ (c + \mu\sigma_3)(c + \mu\sigma_1)(\dot{\alpha}_3 - \dot{\alpha}_1)^2 \end{bmatrix}} \tag{4.155}$$

where p_a is a reference pressure. Using the same Legendre transformation procedure described at the appendix A3 in addition to the zero plastic dilation condition $C = \dot{\alpha}_1 + \dot{\alpha}_2 + \dot{\alpha}_3 = 0$ and noting that ($\bar{\sigma}_i = c + \mu\sigma_i$) the yield surface at the true stress space is expressed as:

$$k_1^2\bar{\sigma}_1 + k_2^2\bar{\sigma}_2 + k_3^2\bar{\sigma}_3 - 8\bar{\sigma}_1\bar{\sigma}_2\bar{\sigma}_3 \left(\frac{c + \mu p_a}{3c + \mu(\sigma_1 + \sigma_2 + \sigma_3)}\right)^m \tag{4.156}$$

$$-\frac{(k_1\bar{\sigma}_1 + k_2\bar{\sigma}_2 + k_3\bar{\sigma}_3)^2}{3c + \mu(\sigma_1 + \sigma_2 + \sigma_3)} = 0$$

If the last term in Eq. 4.156 vanishes then the yield surface can be rewritten as:

$$\frac{(x_1 - x_2)^2}{(c + \mu\sigma_1)(c + \mu\sigma_2)} + \frac{(x_2 - x_3)^2}{(c + \mu\sigma_2)(c + \mu\sigma_3)} + \frac{(x_3 - x_1)^2}{(c + \mu\sigma_3)(c + \mu\sigma_1)} \tag{4.157}$$

$$= 8\left(\frac{c + \mu p_a}{3c + \mu(\sigma_1 + \sigma_2 + \sigma_3)}\right)^m$$

In terms of the generalized principal stresses. Figure 4.74 above depicts the shape of the yield surface and the direction of plastic flow vector as result of the imposed constraint condition $C = \dot{\alpha}_1 + \dot{\alpha}_2 + \dot{\alpha}_3 = 0$.

For $m = 0$, the generalized Matsuoka-Nakai criterion proposed by Houlsby (1986) is recovered.

4.7.3.1) Non zero plastic dilation condition

The last enhancement consists in introducing a variable dilatancy in the model. Until now the zero plastic dilation condition has been imposed through the constraint $C = 0$. The strict requirement for the yield surface at the dissipative stress space f^{y_x} is that the current stress point should lay on f^{y_x}.

This is accomplished by modifying the expression of the yield surface in the generalized stress space, according to the equation:

$$\frac{(x_1 - x_2)^2}{((c + \nu k) + \beta x_1)((c + \nu k) + \beta x_2)} + \frac{(x_2 - x_3)^2}{((c + \nu k) + \beta x_2)((c + \nu k) + \beta x_3)} \tag{4.158}$$

$$+ \frac{(x_3 - x_1)^2}{((c + \nu k) + \beta x_3)((c + \nu k) + \beta x_1)} = 8$$

where β is the dilatancy coefficient and $\nu = \mu - \beta$. k is computed to respect the yield condition (the current stress point must lay on the yield surface) and can be seen as a solution of an algebraic equation of order 3:

$$k^3 + \frac{1}{v}(3c + \beta I_1) \cdot k^2 + \left(\frac{1}{v^2}(3c^3 + 2c\beta I_1 + \beta^2 I_2) + \frac{3}{4v^2}J_2\right) \cdot k \tag{4.159}$$

$$+ \frac{\beta}{8v^3}(9I_3 - I_1 I_2) + \frac{\beta}{8v^3}J_2 + \frac{1}{v^3}(c^3 + c^2\beta I_1 + c\beta^2 I_2 + \beta^3 I_3) = 0$$

k depends thus on the current stresses, the effective cohesion and the dilatancy coefficient. Finally the term (vk) plays the role of an apparent cohesion which adds to c in order to fulfill the f^{yx} condition.

Figure 4.75 shows the shape of the yield surface in the meridian plane in the true and generalized stress space.
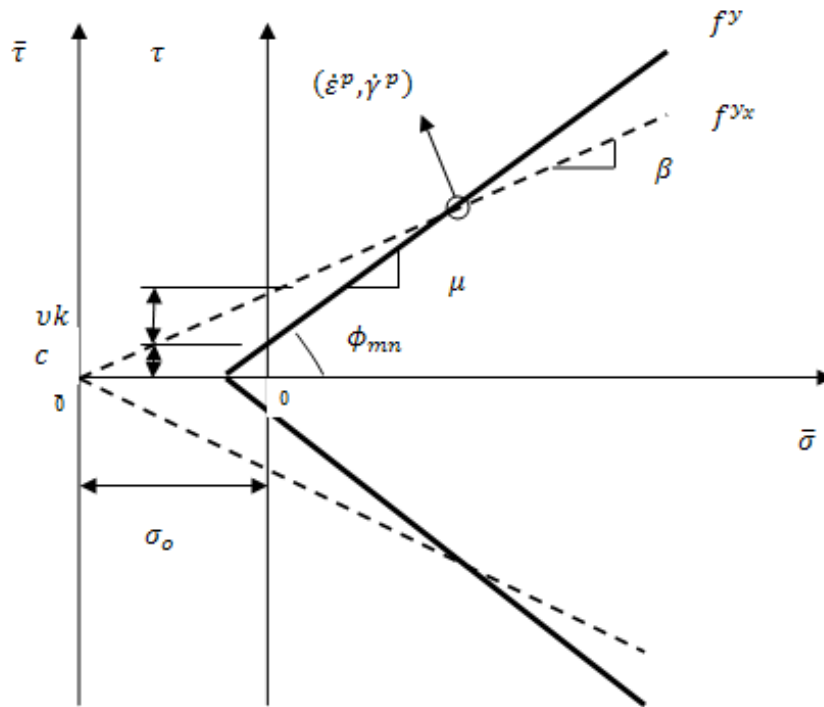
Figure 4.75: Yield surface in the true and generalized stress Meridan planes for the Modified Matsuoka-Nakai Model with variable dilatancy.

The model has been verified through a series of triaxial tests. The integration of the model is performed through an algorithm of interior-point built within the framework of the mathematical optimization.

The tests were performed considering a linear elastic response of the material controlled by the Young's modulus and the Poisson's ratio. Convergence is reached when the norm of the residue is less than 10^{-8}. Table 4.14 summarized the parameters used in the numerical simulation.

Table 4.14: Parameters used in Matsuoka-Nakai model simulations

E (MPa)	ν	ϕ	c (MPa)
100	0.2	21	0.108

Results are shown for several confining pressures, a straight yield criterion (*m = 0*) and two limit values of dilatancy: null and full dilatancy. As expected, stress paths end on the yield surface. When no dilatancy is considered, the response is perfectly plastic. For full dilatancy, the stress-strain relationship experiments a further increase as the result of increase in $\dot{\alpha}_p$.

Figures 4.76-4.77 show standard plots of conventional triaxial test for the Extended Matsuoka-Nakai Model (zero dilatancy) while Figures 4.78-4.79 show the responses of the triaxial tests for the Original Matsuoka-Nakai Model (full dilatancy - associate plasticity).
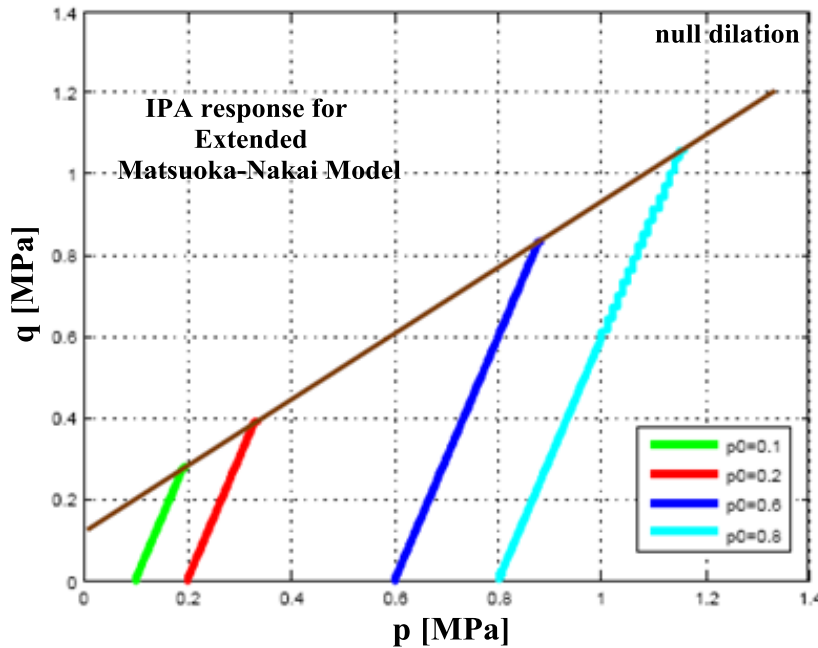
Figure 4.76: Extended (Zero dilatancy) Matsuoka-Nakai Model Response for Three Different Confining Pressures (Meridian Plane), with $\boldsymbol{m = 0}$.
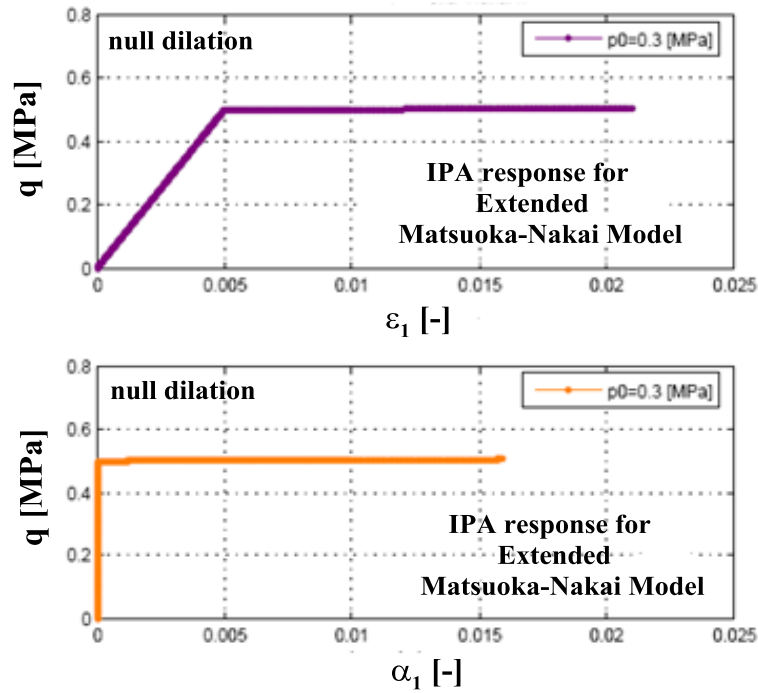
Figure 4.77: Standard Plots: Results of Conventional Triaxial Test for the Extended Matsuoka-Nakai Model. (a) Axial Strain vs. Deviatoric Stress; (b) Axial Plastic Strain vs. Deviatoric Stress.
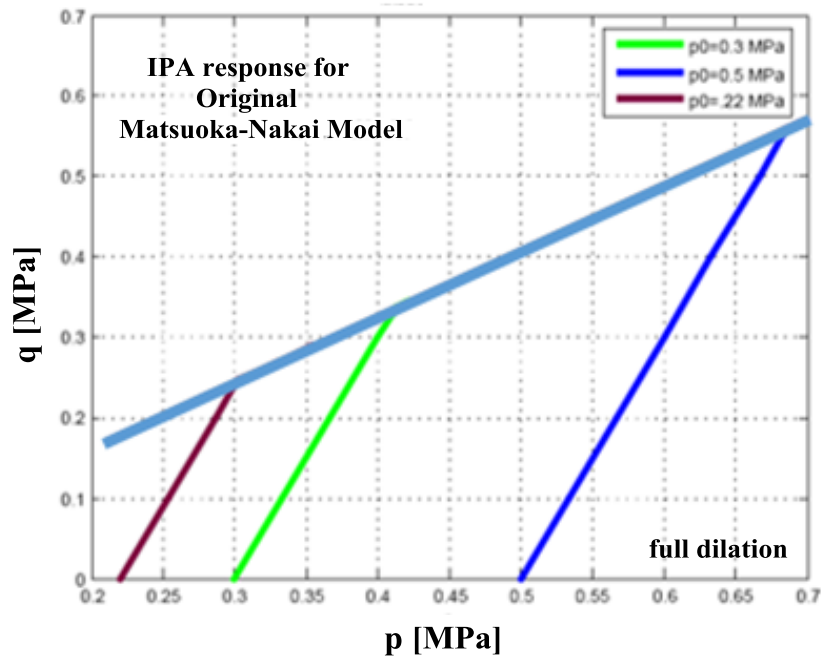
Figure 4.78: Original (full dilatancy) Matsuoka-Nakai Model Response for Three Different Confining Pressures (Meridian Plane) with $m = 0$. Integrated with an Interior-Point algorithm.

_____
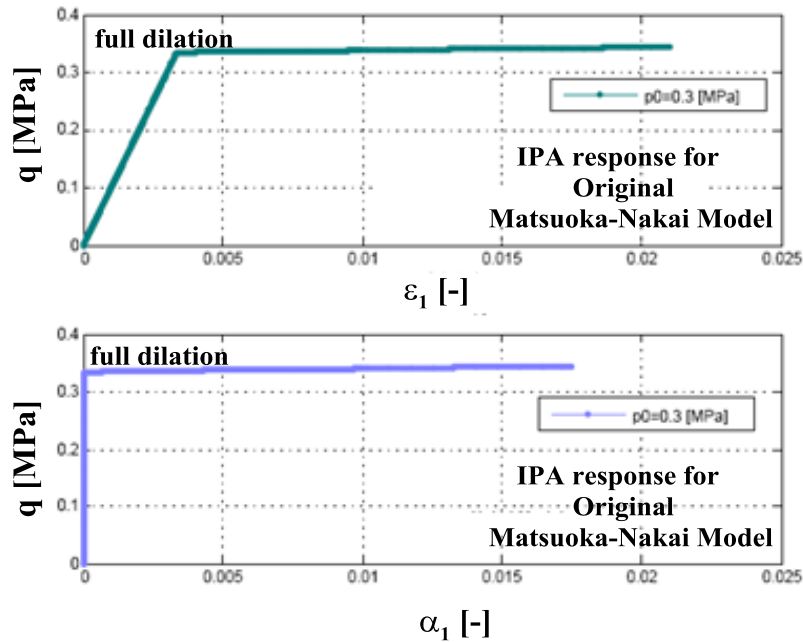
Figure 4.79: Standard Plots of Results of Conventional Triaxial Test for the Original Matsuoka-Nakai Model. (a)
Axial Strain vs. Deviatoric Stress; (b) Axial Plastic Strain vs. Deviatoric Stress.

4.8)   Summary Tables

This section summarizes the main energy and dissipation functions developed throughout the chapter for modeling the studied constitutive laws. Table 4.15 summarizes the energies and dissipation for modeling BBM1, BBM2 and generalized BBM2 models. Table 4.16 summarizes the energies and dissipation functions for modeling the Barcelona Basic Model - BBM, while Table 4.17 summarizes the generalized energies that could be used for modeling BBM. Table 4.18 summarizes the energies and dissipation functions for modeling the HP-CASM model. Finally, Table 4.19 summarizes the energies and dissipation functions for modeling both the Drucker-Prager and Matsuoka-Nakai models.

Table 4.15: Summary of Energy and Dissipation functions for modeling of BBM1 and BBM2 models

Model	Energy	Dissipation - Yield Function
Gallipoli et. al. Isotropic Hardening BBM1	Helmholtz Energy: $$f_s = \kappa^* p^c \exp\left(\frac{\varepsilon_p}{\kappa^*} + \frac{3\varrho\varepsilon_q{}^2}{2\kappa^*}\right)$$ $$+ \rho_s^0\left[\frac{m}{m-1}S_l{}^{(1-1/m)} - S_l\right]$$ Gibbs Energy: $$g_s = -\kappa^* \cdot p'\left[\ln\left(\frac{p'}{p^c}\right) - 1\right] - \frac{q^2}{6\varrho p'}$$ $$+ \frac{\phi\rho_s^0}{1-m}\left[\left(1 + \frac{\phi s}{\phi\rho_s^0}\right)^{(1-m)}\right]$$ With: $$f_2 = 0$$	$$d_s = \frac{z}{2}\left[p^c\exp\left(\frac{\alpha_p}{\lambda^* - \kappa^*}\right)\right]^b \cdot$$ $$\left(\sqrt{\dot{\alpha}_p^2 + M^2\dot{\alpha}_q^2} + \dot{\alpha}_p\right)$$
Gallipoli et. al. Kinematic Hardening BBM2	Helmholtz Energy: $$f_s = \kappa^* p^c \exp\left(\frac{\varepsilon_p^e}{\kappa^*}\right.$$ $$- \frac{\phi\rho_s^0}{\kappa^* p_0^s(m-1)}\left[\left(1\right.\right.$$ $$\left.\left.+ \frac{\phi s}{\phi\rho_s^0}\right)^{(1-m)}\right] + \frac{3\varrho\varepsilon_q^{e\,2}}{2\kappa^*}\right) + f_2$$ Gibbs Energy: $$g_s = -\kappa^* p'\left[\ln\left(\frac{p'}{p^c}\right) - 1\right] - \frac{q^2}{6\varrho p'}$$ $$- (p'\alpha_p + q\alpha_q)$$ $$+ \phi\frac{\rho_s^0\left(\frac{p'}{p^c} - \chi^o\right)}{m-1}\left[\left(1\right.\right.$$ $$\left.\left.+ \frac{\phi s}{\phi\rho_s^0}\right)^{(1-m)}\right] + f_2$$ With: $$f_2 = \frac{(\lambda^* - \kappa^*)}{b}\frac{z}{2}\left(\frac{p^c}{2}\exp\left(\frac{\alpha_p}{\lambda^* - \kappa^*}\right)\right)^b$$	$$d_s = \frac{z}{2}\left[p^c\exp\left(\frac{\alpha_p}{\lambda^* - \kappa^*}\right)\right]^b \cdot$$ $$\sqrt{\dot{\alpha}_p^2 + M^2\dot{\alpha}_q^2}$$ With: $$B = 0$$ Generalized BBM2: $$d_s = \frac{z}{2}\left[p^c\exp\left(\frac{\alpha_p}{\lambda^* - \kappa^*}\right)\right]^b \cdot$$ $$\sqrt{\dot{\alpha}_p^2 + M^2 B^2\dot{\alpha}_q^2}$$ With: $$B = \epsilon + (1-\epsilon)\frac{p'}{\rho}$$

Table 4.16: Summary of Energy and Dissipation functions for modeling of BBM model

Model	Energy	Dissipation - Yield Function
Alonso et. al. Kinematic Hardening (Mixed Hardening) BBM	Partial Helmholtz energy: $$f_s^g = \kappa^* p^o \exp\left(\frac{\varepsilon_p}{\kappa^*}\right.$$ $$-\frac{\phi \rho_s^0}{\kappa^* p_0^s (m-1)}\left[\left(1+\frac{s}{\rho_s^0}\right)^{(1-m)}\right] + \frac{3\varrho\varepsilon_q{}^2}{2\kappa^*}$$ $$\left.-\frac{\kappa_s^*}{\kappa^*}\ln\left(\frac{s+p_{at}}{p_{at}}\right)\right) + f_2$$ Gibbs energy: $$g_s = -\kappa^*\left[\ln\left(\frac{p''}{p^o}\right) - 1\right] - \kappa_s p'' \ln\left(\frac{s+p_{at}}{p_{at}}\right)$$ $$-\frac{q^2}{6\varrho p''} - (p''\alpha_p + q\alpha_q)$$ $$+\phi\frac{s^o\left(\frac{p''}{p^o} - \chi^o\right)}{m-1}\left[\left(1+\frac{s+p_{at}}{s^o}\right)^{(1-m)}\right] + f_2$$ with: $$f_2 = w(s)\frac{(\lambda^* - \kappa^*)}{b(s)}$$ $$\cdot\left(\frac{p^c}{2}\exp\left(\frac{\alpha_p}{\lambda^* - \kappa^*}\right)\right)^{b(s)}$$ $$-\frac{p_s}{2}\alpha_p$$	Kinematic Hardening: $$d_s = \left(w\left(\frac{p^c}{2}\exp\left(\frac{\alpha_p}{\lambda^* - \kappa^*}\right)\right)^b \right.$$ $$\left.+\frac{p_s}{2}\right)\cdot\sqrt{\dot\alpha_p^2 + M^2\dot\alpha_q^2}$$ Mixed Hardening (hydraulic) : $$d_s = \left(\left(\frac{p_0}{2}\right)^2 - p_s\cdot(p'' - p_s)\right)$$ $$\cdot\sqrt{\dot\alpha_p^2 + M^2\dot\alpha_q^2}$$ With: $$\frac{p_0}{2} = w\left(\frac{p^{c_o}}{2}\exp\left(\frac{\alpha_p}{\lambda^* - \kappa^*}\right)\right)^b$$

Table 4.17: Summary of Generalized Energy functions for modeling of BBM model

Model	Energy
Alonso et. al. Kinematic Hardening (Mixed Hardening) BBM	**Generalized Potentials** Helmholtz energy: $$f_s = \frac{p_o}{k(2-n)}\Big(k(1-n)\Big)^{\frac{2-n}{1-n}}\left(\left(\varepsilon_p^e - \varepsilon^c(s) + \frac{1}{k(1-n)} - \frac{k_s}{(1+\lambda)}\left(\frac{s+p_{at}}{s_o}\right)^{\lambda} + \frac{k_s}{(1+\lambda)}\right)^2 + \frac{3\varrho\varepsilon_q^{e\,2}}{k(1-n)}\right)^{\frac{2-n}{2-2n}} + \underbrace{f_{i_2} + f_2}_{f_{s_2}}$$ Gibbs energy: $$g_s = \frac{-1}{p_o^{\,1-n} \cdot k(1-n)(2-n)} \cdot \left(p''^2 + \frac{k(1-n)}{3\varrho}q^2\right)^{\frac{2-n}{2}} + \frac{p''}{k(1-n)} - \frac{k_s p''}{(1+\lambda)}\left(\frac{s+p_{at}}{s_0}\right)^{\lambda} + \frac{k_s p''}{(1+\lambda)} - \left(p''\alpha_p + q\alpha_q\right) + \underbrace{f_{i_2} + f_2}_{f_{s_2}}$$ With: $$f_{s_2} = \phi \underbrace{\frac{\rho_s^o \left(\frac{p''}{p_0^s} - \chi^o\right)}{m-1}\left[\left(1 + \frac{s+p_{at}}{\rho_s^o}\right)^{(1-m)}\right]}_{f_{i_2}} + \underbrace{w(s)\frac{(\lambda^* - \kappa^*)}{b(s)} \cdot \left(\frac{p^c}{2}\exp\left(\frac{\alpha_p}{\lambda^* - \kappa^*}\right)\right)^{b(s)} - \frac{p_s}{2}}_{f_2}$$

Table 4.18: Summary of Energy and Dissipation functions for modeling of HP-CASM model

Model	Energy	Dissipation - Yield Function
Yu et.al. Isotropic Hardening HP-CASM	Helmholtz energy: $$f_s = \frac{p_o(1 - \beta_s)}{k(2 - n)}\Big(k(1 - n)\big)^{\frac{2-n}{1-n}}\Big(\Big(\frac{\varepsilon_p^e}{1 - \beta_s} + \frac{1}{k(1 - n)}\Big)^2 + \frac{3\varrho\varepsilon_q^{e\,2}}{k(1 - n)}\Big)^{\frac{2-n}{2-2n}}$$ Gibbs energy: $$g_s = \frac{-(1 - \beta_s)}{p_o{}^{1-n} \cdot k(1 - n)(2 - n)} \cdot \Big(p'^2 + \frac{k(1 - n)}{3\varrho}q^2\Big)^{\frac{2-n}{2}} + \frac{p'(1 - \beta_s)}{k(1 - n)} - \big(p'\alpha_p + q\alpha_q\big)$$	$$d_s = \frac{b}{\ln(r)}Mp' \cdot \ln\Big(\frac{p'}{p^c(s, T)}\Big)|\dot{\alpha}_q|$$ With: $$p^c = \frac{z}{2}\Big[p_o^c \cdot \exp\Big(\frac{\alpha_p}{\lambda^* - k^*}\Big)\Big]^b \cdot \Big(1 - c_T\log\Big(\frac{T + |T_{min}|}{T_o}\Big)\Big)$$

Table 4.19: Summary of Energy and Dissipation functions for modeling of Drucker-Prager and Matsuoka-Nakai models

Model	Energy	Dissipation - Yield Function
Drucker-Prager	Partial Helmholtz energy: f_s^g $= \dfrac{K}{2} \cdot \varepsilon_p^2 + \dfrac{3}{2} G \cdot \varepsilon_q^2 + \dfrac{\phi s_o(T)}{(1-m)}$ $\cdot \left[1 + \dfrac{\phi s}{\phi s_o(T)} \right]^{(1-m)} - K b_s$ $\cdot (T - T_i)\varepsilon_p$	Dissipation: $d' = d + \Lambda c = r_c \left(\dfrac{N\sigma_{kk} + 3(b + \Lambda B)}{3} \right)$ $\cdot \sqrt{\dfrac{2}{3} \dot{\alpha}'_{ij} \dot{\alpha}'_{ij}} + \Lambda \cdot \dot{\alpha}_{ii}$ Yield: $\left(\left(\dfrac{J}{r_c} \right)^2 + \vartheta^2 \right)^{1/2} - C x_p - M p - a = 0$
Matsuoka-Nakai	Gibbs energy: g_s $= -\dfrac{p'^2}{2K} - \dfrac{q^2}{6G} + \dfrac{\phi s_o(T)}{(1-m)}$ $\cdot \left[1 + \dfrac{\phi s}{\phi s_o(T)} \right]^{(1-m)} + b_s$ $\cdot (T - T_i)p'$	Dissipation: $d = \sqrt{\dfrac{8}{9} \left(\dfrac{c + \mu p_a}{3c + \mu(\sigma_1 + \sigma_2 + \sigma_3)} \right)^m} \cdot$ $\begin{bmatrix} (c + \mu\sigma_1)(c + \mu\sigma_2)(\dot{\alpha}_1 - \dot{\alpha}_2)^2 + \\ (c + \mu\sigma_2)(c + \mu\sigma_3)(\dot{\alpha}_2 - \dot{\alpha}_3)^2 + \\ (c + \mu\sigma_3)(c + \mu\sigma_1)(\dot{\alpha}_3 - \dot{\alpha}_1)^2 \end{bmatrix}^{\frac{1}{2}}$ Yield: $\dfrac{(x_1 - x_2)^2}{(c + \mu\sigma_1)(c + \mu\sigma_2)}$ $+ \dfrac{(x_2 - x_3)^2}{(c + \mu\sigma_2)(c + \mu\sigma_3)}$ $+ \dfrac{(x_3 - x_1)^2}{(c + \mu\sigma_3)(c + \mu\sigma_1)}$ $= 8 \left(\dfrac{c + \mu p_a}{3c + \mu(\sigma_1 + \sigma_2 + \sigma_3)} \right)^m$

4.9)   Conclusions

Along this chapter, the hyperporoplasticity framework for hydro-mechanical and thermo-mechanical modeling of multiphase media has been applied to several constitutive models that appear to be of importance in practical problems of soil-atmosphere interactions. They are:

- Water retention with and without hysteresis,
- Thermo-hydro-mechanical elastic law,
- BBM-like models,
- HP-CASM model,
- Drucker-Prager and Matsuoka-Nakai yield criterion with linear elasticity (or also perfectly plastic).

A simplified van Genuchten law has been proposed. This simplified law admits a closed-form integration and therefore the construction of an energy potential for the air-liquid interface. Hysteresis of the retention model has been addressed proposing a proper energy function g_i (or f_i) and a force potential.

Dissipation functions for BBM-like models, formulated in both net stress and effective stress, have been presented and their performances shown at Gauss point level.

Dissipation function for a hyperplastic-CASM model has been proposed. In this case the hardening parameter has been provided with a thermal dependency in addition to suction.

Generalized elastic potentials proposed by Houlsby (2005) have been extended to consider: (a) suction due to partially saturation of porous media, (b) thermal strains due to temperature changes and (c) water retention dependence on mean stress by an adequate interface energy. The obtained dependencies and couplings at the proposed potentials has led to an extended partition of both strains and degree of saturation, beyond the classical elastic and plastic partition.

Drucker-Prager model, derived within the framework of hyperplasticity, has been adapted to consider thermal strength degradation. The presented model has also been smoothed at the apex to avoid the lack of definition of the plastic flow vector at that point.

_____

All the models appear to fit well in this framework. The obtained formulations present the advantage of being susceptible to implementation in optimization algorithms with good performance. The development and implementation work is described in the next chapter.

CHAPTER 5

NUMERICAL IMPLEMENTATION: IMPLICIT ALGORITHMS FOR TWO-PHASE AND THREE-PHASE MEDIA

5.1) Introduction

As shown in the previous chapter, the numerical analysis of soil behavior requires the consideration of elasto-plastic models that are non-standard in computational mechanics. Particularly, the presence of friction as the fundamental dissipative energy mechanism makes most of the models used in this field to be non-associated in character. These facts have promoted deep studies on numerical techniques to integrate the former relations in a reliable and robust way. In this perspective, the hyper-poroplasticity framework developed in the previous chapter proves to provide sound basis for reliable integration methods as the constitutive relationship is completely derived from potentials (Gibbs and Helmholtz free energies, dissipation function) which allow using algorithms based on convex mathematical programming techniques.

Such techniques are based on theoretical concepts developed within two branches of mathematics: (a) convex analysis and (b) numerical methods for unconstrained and constrained optimization. Their goal is to minimize or maximize a real value function by choosing systematically the values of real variables from an allowed set (feasible set). In

the present work, the dependent variables correspond to stress increments while the independent ones are deformation increments.

Two different approaches will be explored. The first one follows similar procedures to those exposed in Simo & Hughes (1998), and is based on the classical return mapping algorithm. The second approach corresponds to primal-dual interior-point methods (Wright, (1992); Wright, (1997); Forsgren et al., (2002); Krabbenhoft et al., (2007)). The latter has been selected for its performance to resolve saddle-point problems (Benzi et al., (2005)), which is the case in constrained optimization plasticity problems. Both procedures enable the development of generic computer routines, which allow to process the integration of hyper-poroplastic constitutive laws in a quite automatic way. More specifically, the present study focuses, on the one hand, on the formulation of the solution of local discrete equations at a quadrature point by the closest-point projection method and the interior-point method and, on the other hand, on the development of the corresponding algorithms to solve the resulting nonlinear system of algebraic equations. This approach contemplates an implicit scheme in the discretization of the equations and differs in that sense from the explicit methods proposed by Einav et al. (2003) to integrate hyperplastic models.

The chapter is organized as follows. In the first section, notation and terminology used along the chapter is presented. Then, a review of the bases of mathematical programming in convex analysis is presented with special attention devoted to both Newton's method and modified Newton's method in order to get a global convergence algorithm. Thirdly, the governing equations and the variational structure of a hyper-poroplastic biphasic medium is addressed and the consistent tangent operator is obtained for this medium. Fourthly, implicit algorithms based on the "closest-point-projection" and "interior-point" methods are described and confronted in terms of the convergence results to check the performance of the algorithms. Fifthly, the governing equations and the variational structure for: (a) hydraulic (retention curve), (b) mechanical (stress-strain relationship) models in unsaturated media and (c) mechanical cohesive-frictional models are tackled and the consistent tangent operator derived. Finally, the observed advantages of the proposed interior-point algorithm are commented and the general conclusions presented.

5.2) Notation and Terminology

P_u	Unconstraint optimization problem
x	Vector of driven variables $\left(\text{optimal point } (x^*)\right)$
∇	Gradient operator
$r(x)$	Vector of residuals
$J(x)$	Jacobian matrix of residual vector
$d(x)$	Vector of feasible advance direction
$m(x)$	Merit function for Global Newton convergence
β	Line search Goldstein parameter
$\bar{\alpha}$	Line search parameter (step size)
f^y	Yield function (Constraint function)
E	Poro-elastic Domain (Compact Set)
$\mathcal{L}$	Lagrangian function
$\Delta\gamma$	Discrete Plastic multiplier
$(\blacksquare)^{trial}$	Algorithmic vector (variables) at trial state
$(\blacksquare)^n$	Algorithmic vector (variables) at beginning of current step
$(\blacksquare)^{n+1}$	Algorithmic vector (variables) at the end of current step
μ	Duality gap variable
z	Slack variables
ε^e	Elastic strain tensor
α	Plastic strain tensor
σ'	Effective stress tensor
ρ'	Effective shift stress tensor
x'	Generalized stress tensor
σ''	Net stress tensor
ρ''	Net back stress tensor
x''	Net generalized stress tensor
S_l	Degree of saturation
α_l	Plastic degree of saturation
s	Matrix suction
ρ_s	Back suction
f_s	Specific Helmholtz energy function of the skeleton (objective function)
g_s	Specific Gibbs energy function of the skeleton (objective function)
g_i	Gibbs energy function of the interface gas-liquid (objective function)

5.3) Mathematical Optimization Theory Basis

In this section, a brief summary of the main principles supporting the variational study and the development of algorithms are presented. Firstly, some fundamental theorems on optimization theory are exposed without deep insight into their demonstrations, which are referring to the cited bibliography. Secondly some properties of the Newton's methods are commented, like its local convergence characteristic and an extension to get global convergence property.

5.3.1) Unconstraint optimization theory: "Hyperelasticity"

From a general point of view, the problem of finding a solution to an unconstrained problem is usually expressed in the form:

$$\text{P}_\text{u} \quad \begin{cases} \min & f_\text{s}(\text{x}) : \text{R}^\text{n} \to \text{R} \\ \text{x} \in \text{R}^\text{n} \end{cases} \tag{5.1}$$

where x is the vector of driven variables and f_s is the Helmholtz energy function of the skeleton (objective function in mathematical optimization theory).

The first question that arises in the study of the problem 5.1 is whether a solution exists. The main result that can be used to address this issue is the Weierstrass theorem, which together with the feasible direction of advance, allow deriving the First Order Necessary Condition to achieve a minimum (Luenberger, (1984)).

Box 5.1: Optimality Conditions 1.

First Order Necessary Condition:

      Let (E) be a subset of (E^n) and let $(f_s \in \text{C}^1)$ be a function on(E). If (x^*) is a relative minimum point of (f_s) over (E) then for any $(d \in \text{E})$ that is a feasible direction at(x^*) , we have$(\nabla f_\text{s}(x^*) \cdot \text{d} \geq 0)$.

According to this condition, if the objective point of f_s has been reached at x^* then the directional derivative $\nabla f_\text{s}(\text{x}^*) \cdot \text{d}$ of the gradient of the objective function in the direction d would result positive $|\nabla f_\text{s}(\text{x}^*)| > 0$ or zero $|\nabla f_\text{s}(x^*)| = 0$ which means horizontal tangent, then x^* is the solution sought.

Additional conditions to achieve a minimum are derived considering higher order approximations defined in terms of the Hessian matrix $\nabla^2 f_\text{s}$ of the functionf_s, which leads to the Second Order Condition (Luenberger, (1984)).

Box 5.2: Optimality Conditions 2.

Second Order Sufficient Condition:

Let (E) be a subset of (E^n) and let $(f_s \in C^2)$ be a function on(E). If (x^*) is a relative minimum point of (f_s) over (E), then for any $(d \in E)$ that is a feasible direction at(x^*) , we have:

a) $\nabla f_s(x^*) \cdot d \geq 0$

b) if $\nabla f_s(x^*) \cdot d = 0 \;\; \rightarrow \;\; d \cdot [\nabla^2 f_s(x^*)] \cdot d \geq 0$

In view of the convexity assumption of the energy function f_s, the second order condition states that once the directional derivative of $\nabla f_s(x^*)$ in the direction d vanishes, the positive definition of the Hessian matrix is verified $(d \cdot [\nabla^2 f_s(x^*)] \cdot d \geq 0)$ and the function f_s reaches a minimum value at the pair $(x^*, f_s(x^*))$.

Accordingly, convex strain energy functions (alternatively stress energy functions) allow to built algorithms with global convergence properties. The definition of a convex function is provided in the next box and illustrated in Fig. 5.80.

Box 5.3: Convexity Definition.

Convexity of a Function:

A function (f_s) defined on a convex set (E) is said to be convex if, for every $((x_1, x_2) \text{ in E})$ and every $(0 \leq \alpha \leq 1)$ there holds

$$f_s(\alpha x_1 + (1 - \alpha)x_2) \leq \alpha f_s(x_1) + (1 - \alpha)f_s(x_2)$$

If for every $(0 < \alpha < 1)$ and $(x_1 \neq x_2)$, there holds

$$f_s(\alpha x_1 + (1 - \alpha)x_2) < \alpha f_s(x_1) + (1 - \alpha)f_s(x_2)$$

then (f_s) is said to be strictly convex.

Definition at Box 5.3 is illustrated at Fig. 5.80.
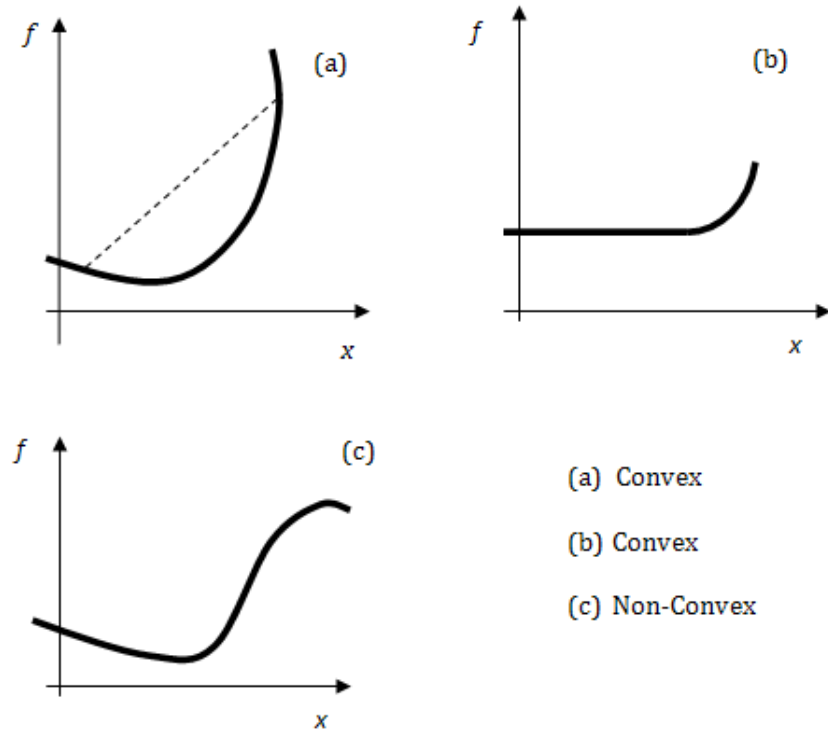
Figure 5.80: Convex and Non-Convex functions, after (Luenberger, 1984).

Verification of convexity by both methods, the first derivative or the second derivative, is usually carried out within optimization algorithms.

The last one is a mapping **A** between an initial state x_0 in a space E (input of the algorithm) to a new state x in the same space (output of the algorithm) (Luenberger, 1984). The new point is obtained iteratively within the algorithm **A** after repeated application of the sequence:

$$x_{k+1} = \mathbf{A}(x_k) \tag{5.2}$$

If, for the arbitrary starting state x_o , the algorithm **A** guarantees to generate a sequence of states converging to a solution then this algorithm is said to be "globally convergent". Many of the most important algorithms for solving non-linear programming problems are not globally convergent in their purest form. An example is the well-known Newton's method that may occasionally generate sequences that either do not converge at all or converge to states that are not solutions of the problem. In fact, the Newton's method can be guaranteed to converge to a solution of r(x) = 0 if the initial state is located close enough to the final solution state.

The solution of a system of nonlinear equations can be formulated as:

$$\begin{cases} \text{given} & : \quad r(x) \ : \ R^n \to R^n \\ \text{find} & : \quad x^* \in R^n \ | \ r(x) = 0 \end{cases} \tag{5.3}$$

If $r(x)$ is assumed to be continuously differentiable, the Newton's method is derived by taking a Taylor series approximation to $r(x)$ around the current iteration x_k. $r(x_c + d)$ is approximated as:

$$r(x_c + d) = r(x_c) + \int_{x_c}^{x_c+d} J(z) \, dz \tag{5.4}$$

where the integral is approximated by a linear term $(J(x_c) \cdot d)$ to get the affine approximation to $r(x)$:

$$r_c(x_c + d) = r(x_c) + J(x_c) \cdot d \tag{5.5}$$

Next, for the current Newton iteration, d is computed such that $r_c(x_c + d) = 0$:

$$J(x_c) \cdot d = -r(x_c) \tag{5.6}$$

$$x^+ = x_c + d$$

Since x^+ is not expected to be equal to the solution x^* but only the best estimate for the current Newton iteration, the sequence (in the sense of Eq. 5.2) 5.4 to 5.6 is iteratively repeated from the starting guess x_0.

Box 5.4: Newton's Method.

Newton's Method for system of nonlinear equations:

      Given $(r : R^n \to R^n)$ continuously differentiable and $(x_0 \in R^n)$: at each iteration (k) solve:

$$J(x_k) \cdot d_k = -r(x_k)$$

$$x_{k+1} = x_k + d_k$$

The basic idea while building a successfully nonlinear algorithm consists in combining a globally convergent strategy with a fast local convergent strategy in a way that the final result has the benefits of both. Such an improvement is performed by appealing special devices to guarantee global convergence.

The global convergent properties of the algorithm will be obtained by: (a) limiting the magnitude of the step $(\alpha \cdot d)$ in the descent direction (Line-Search method), (b) changing the descent direction to a different one from Newton direction $((J' = J + \tilde{\alpha}I)$ Trust-Region method).

This magnitude is obtained imposing upper and lower limits "**LC**" to the ratio: magnitude of the decrease in the objective function $f(x^+) - f(x_0)$ to the given step size $x^+ - x_0$. The

global convergence theorem establishes the formal technical conditions for which convergence is guaranteed.

Global Convergent Theorem:

Let (**A**) be an algorithm on ($\mathbb{N}$), and suppose that given (x_o) the sequence ($\{x_k\}_k^\infty$) is generated satisfying: $\qquad\qquad\qquad x_{k+1} \in \mathbf{A}(x_k)$

Let a solution set (E $\subset$ $\mathbb{N}$) be given and suppose:

    a)   All points are contained in a compact set (M $\subset$ E) $\big($(M) is bounded and closed$\big)$

    b)   There is a continuous function (m) on ($\mathbb{N}$) such that:

          I.   If (x $\notin$ M) $\rightarrow$ $\big(m(y) < m(x)\big)$ $\forall$ $\big(y \in \mathbf{A}(x)\big)$

          II.   If (x $\in$ M) $\rightarrow$ $\big(m(y) \leq m(x)\big)$ $\forall$ $\big(y \in \mathbf{A}(x)\big)$

          III.   The mapping (**A**) is closed at points outside (E)

According to this theorem, when a point of the sequence x does not belong to the compact set $\mathcal{M}$ the descent function m results unbounded below and the minimum is impossible to be reached.

Conversely, if x does belong to the compact set $\mathcal{M}$ the former function is bounded and the minimum "solution-point" exists.

5.3.1.1) Line-Search global convergence

The line-search method is based on the idea that, given any direction d_k such that ($\nabla f_s \cdot d_k < 0$) and satisfying limit conditions "**LC**", an $\alpha_k > 0$ exist. The algorithm **A** is globally convergent with sequence $\big(x_{k+1} \in \mathbf{A}(\alpha_k, x_k)\big)$ obeying at each iteration "**LC**" and the rule ($\nabla f_s \cdot (x_{k+1} - x_k) < 0$).

Close to the minimum $f_s(x^*)$, Newton's steps satisfy the same conditions "**LC**" and($\alpha_k \cong$ 1). Box 5.6 summarizes the basic idea of "Line-search" method.

Line-Search scheme:

    Given a descent direction (d) a step is taken which yields an acceptable (x_{k+1});

        At iteration (k):

            1.   Compute (d_k)

            2.   Set $x_{k+1} = x_k + \alpha_k d_k$ for some (α_k) making (x_{k+1}) acceptable

The procedure is to try the full step length first $\alpha_o = 1$ and if it fails to satisfy the "**LC**" conditions to backtrack in a systematic way along the direction(d_k). The global method is usually achieved by considering the unconstrained minimization problem over the norm function $\left(m = \frac{1}{2}r(x)^T \cdot r(x)\right)$

$$\min_{x \in R^n} \quad m(x) : R^n \to R \tag{5.7}$$

also called merit function. We must be sure that each step decreases the value of m, that is $m(x_{k+1}) \equiv m(x_k + \alpha_k d_k) \leq m(x_k)$. One of the most useful inexact line-search conditions "Goldstein Conditions (**GC**)" stipulates that α should give sufficient decrease in the objective function (upper limit) while preserving α from being too small (lower limit). Eq. 5.8 summarizes "Goldstein Conditions" for the determination of the line-search parameter:

$$m(x_k) + (1 - \beta)\alpha_k \nabla m_k^T d_k \leq m(x_k + \alpha_k d_k) \leq m(x_k) + \beta\alpha_k \nabla m_k^T d_k \tag{5.8}$$

where $\beta \in \left(0, \frac{1}{2}\right)$ is an algorithmic parameter. The above restrictions have a geometrical interpretation shown in Fig. 5.81.
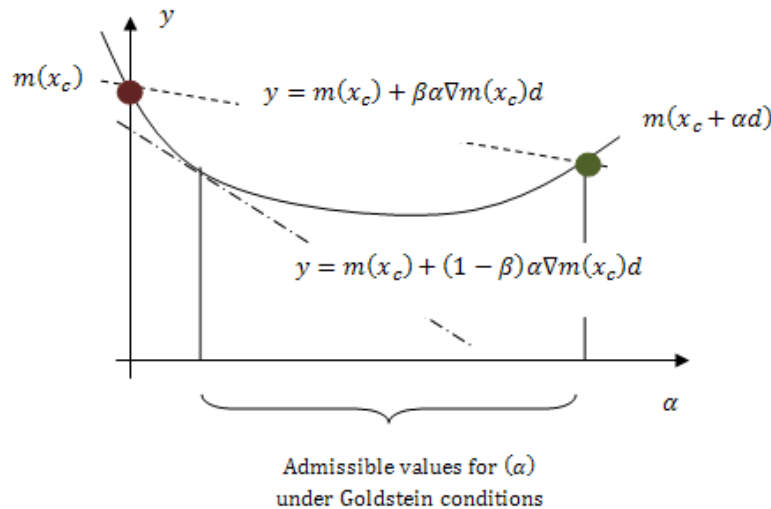
Figure 5.81: Permissible values of ($\boldsymbol{\alpha}$)under Goldstein Conditions, eq. (5.8).

The backtrack procedure used in the search of the α parameter which provides an acceptable value of x_{k+1} is usually performed through "quadratic" or "cubic" models. The latter is strongly recommended for highly nonlinear problems. In any case, the first backtrack iteration will be of quadratic type. The resulting framework is given in Box 5.7.

Box 5.7: Backtracking search.

Backtracking Line-Search framework:

$\quad$ Given $\left(\beta \in \left(0, {}^{1}\!/_{2}\right)\right)$ and

$\quad \alpha = 1$

$\quad$ While $\left[m(x_k + \alpha_k d_k) > m(x_k) + \beta \alpha_k \nabla m_k^T d_k\right]$

$\qquad \alpha_k = \rho_l \cdot \alpha_k$ $\quad$ with (ρ_l) given by the backtrack model procedure

$\quad x_{k+1} = x_k + \alpha_k d_k$

5.3.1.2) Trust-Region global convergence

The second option to provide global convergence properties to a Newton's base algorithm is the Trust-region method. Unlike the previous method, the Trust-region method swings the search direction between steepest descent and Newton descent directions looking for the adequate next state until x^+ is reached.

The swing of the search direction is given by changing the diagonal terms of the Jacobian matrix J(x), such that:

$$J'(x) = J(x) + \tilde{\alpha} I \qquad\qquad (5.9)$$

with

$$J'(x, \tilde{\alpha}) \cdot d = -r(x) \quad \text{and} \quad \|d(\tilde{\alpha})\| = \delta$$

The solution states that x^+ from 5.9 which solves $r_c(x_c + d) = 0$ is an acceptable next stage only if δ is a good step bound. Therefore a complete step of trust-region algorithm will have the form:

Box 5.8: Trust Region concept.

Trust-Region:

Given the energy function f_s such that $f_s \colon R^n \to R$, $\delta > 0$, $x_c \in R^n$, $J_{(x)} \in R^{n \times n}$ symmetric and positive definite:

While $r_k\left(x_k + d(\tilde{\alpha})\right) \neq 0$

$\qquad \tilde{\alpha}_j = \tilde{\alpha}_{j-1} - \dfrac{\|d_k\|}{\delta} \dfrac{\|d(\tilde{\alpha})\| - \delta}{\nabla(\|d(\tilde{\alpha})\| - \delta)}$

$\qquad d(\tilde{\alpha}) = -\left(J_j^k + \tilde{\alpha}_j I\right)^{-1} \cdot r_k$

$\qquad$ decide if x_j^{k+1} is acceptable and compute δ_j^{k+1} with a backtrack model (*Box 5.7*)

end

The advance direction $d(\tilde{\alpha})$ is the Newton's direction while $\tilde{\alpha} \cong 0$ and approaches the steepest descent direction as $\tilde{\alpha} \gg 0$.

5.3.2) Constraint optimization theory: "Hyperporoplasticity"

If the admissible state solutions of the minimization problem Eq. 5.1 are restricted to lay in a closed space (namely x^* must satisfy a number of constraints), the general formulation for a nonlinear constrained optimization problem is expressed as:

$$P \begin{cases} \min \quad f_s(x) \\ x \in R^n \\ \text{sub. to:} \quad f_i^y(x) \le 0 \end{cases} \tag{5.10}$$

where, for the problems considered in this dissertation, f_s is a smooth energy real-value function on subset E and f^y is the limiting yield function.

In this context, f_s is called the objective function while f^y is the inequality constraint. Accordingly, the feasible set E is defined to be the set of points x that satisfy the constraint condition $\left(E = \{ x(\sigma, \alpha) \mid f_i^y(\sigma, \alpha) \le 0 \} \right)$ and corresponds to the elastic domain in a plasticity environment.

If the limiting functions f_i^y are assumed to be continuous of C^1, then the envelope surface defined by those functions results to be smooth. This envelope surface has associated two remarkable geometric elements: (a) a point designated as "Regular Point" (Fig. 5.82) and (b) a plane referred as "Tangent Plane" (Fig. 5.83).
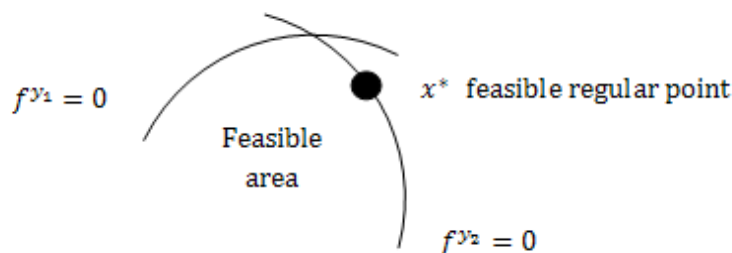
Figure 5.82: Active constraints and Regular point

Regular Point:

      A point (x^*) satisfying the constraints $\left(f_i^y = 0\right)$ is said to be regular point of the constraints if the gradient vectors $\left(\nabla f_i^y(x^*)\right)$ are linearly independent.

At the regular point on the smooth surface, it is possible to characterize a plane tangent to the surface in terms of the gradients of the yield surfaces, Fig. 5.83.

Tangent Plane:

      At a regular point (x^*) of the surface defined by $\left(f_i^y = 0\right)$, the tangent plane is given by the set :

$$M = \left\{d \mid \nabla f_i^y(x^*) \cdot d = 0\right\}$$
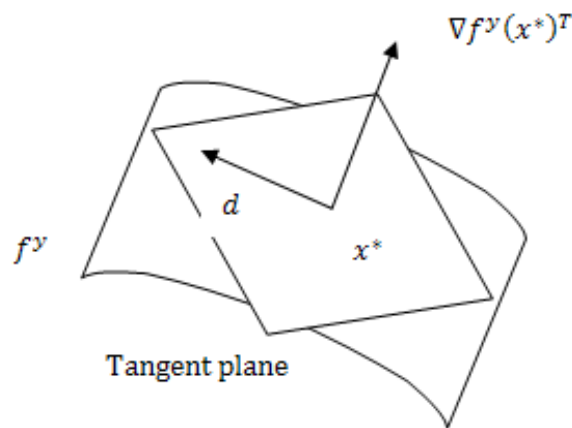
Figure 5.83: Tangent plane at the feasible point(x^*).

The definition of those geometrical elements establishes the bases to verify the first order (necessary) and the second order (sufficient) conditions in the search of the solution state (optimal point).

Lemma Orthogonality:

      Let (x^*) be a regular point of the constraints $\left(f_i^y = 0\right)$ and a local minimum or maximum point of (f_s) subject to these constraints. Then all $(d \in E)$ satisfying,

$$\nabla f_i^y(x^*) \cdot d = 0$$

    must also satisfy,

$$\nabla f_s(x^*) \cdot d = 0$$

The above lemma establishes the orthogonality between ∇f_s and the tangent plane Fig. 5.84.
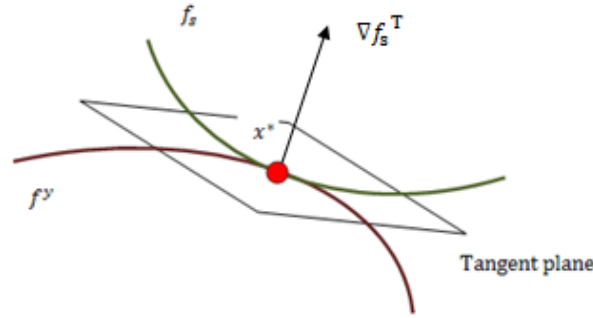
Figure 5.84: Orthogonality between the energy function's gradient $\boldsymbol{\nabla f}_s$ and the Tangent plane.

It also concludes that ∇f_s is a linear combination of the gradients of the constraints ∇f_i^y at the regular feasible point x^*. This fact allows to introduce the theory of Lagrange multipliers, such that,

$$\nabla f_s + \sum_{i=1}^{n} \gamma_i \nabla f_i^y = 0 \tag{5.11}$$

Equation 5.11 represents the Euler equations for the constraint problem.

In the next paragraphs both the necessary and the sufficient conditions for the solution of the constrained optimization problem Eq. 5.10 are introduced in a similar way as for the unconstrained case (First Necessary and Second Sufficient Conditions).

The Lagrange functional associated with the constraint problem 5.10 and in view of 5.11 is expressed as:

$$\mathcal{L}(x, \gamma) = f_s(x) + \sum_{i=1}^{n} \gamma_i f_i^y(x) \tag{5.12}$$

where γ_i is the Lagrange multiplier associated to the constraint f_i^y. This multiplier plays the role of plastic multiplier within the elasto-plastic framework.

The linear independence of the constraints f_i^y allows to state the first optimality condition which concerns the gradient's properties of both the objective and the constraint functions.

First Order Necessary Conditions " Karush-Kuhn-Tucker (KKT)*"*:

Suppose that (x^*) is a local solution of (5.10) and the linear independence of the constraints hold at(x^*). Then there is a Lagrange multiplier vector (γ^*), with components (γ_i^*), such that the following conditions are satisfied at (x^*, γ^*):

$$
\begin{aligned}
\nabla f_s(x^*) + \sum_{i=1}^{n} \gamma_i^* \nabla f_i^y(x^*) &= 0 \\
f_i^y(x^*) &\leq 0 \quad \forall\, i \in \partial E \\
\gamma_i^* &> 0 \quad \forall\, i \in \partial E \\
\gamma_i^* \cdot f_i^y &= 0 \quad \forall\, i \in \partial E
\end{aligned}
$$

(5.13)

where the first line of last system coincides with $\nabla_x \mathcal{L}(x, \gamma)$. Equations 5.13 are often known as the Karush-Kuhn-Tucker (KKT) conditions for the solution of the nonlinear program.

Those conditions have a more intuitive and geometric interpretation as a saddle point form:

Saddle Point form of KKT *conditions*:

For the consistent convex program (5.10), (x^*) is the solution if and only if $\exists$ a (γ^*) such that:

$$\mathcal{L}(x^*, \gamma) \leq \mathcal{L}(x^*, \gamma^*) \leq \mathcal{L}(x, \gamma^*)$$

For $(\gamma^* \geq 0)$ and $\left(\gamma_i^* f_i^y(x^*) = 0\right)\ \forall\ i$.

Then, the solution of the program (P) (Eq. 5.10) is:

$$
P = \begin{array}{c} \mathbf{inf} \\ x \in E \end{array} \left\{ f_s(x) + \sum_{i=1}^{n} \gamma_i f_i^y(x) \right\}
$$

(5.14)

The second order conditions involve the second derivative term in the Taylor expansion of both f_s and f_i^y and refer to the curvature of the Lagrange functional for the candidate direction d $(\in M_1)$. The subset M_1 is the set of descent directions of those active limiting yield functions $M_1 = \left\{ d \mid \nabla f_i^y \cdot d = 0\, , \forall\, i \in I \text{ with } \gamma_i^* > 0 \right\}$.

This second condition is established in two instances: (a) The evaluation of the Hessian matrix of the Lagrange functional $\mathcal{L}(x^*, \gamma^*)$ at the local minimum x^* results in:

$d \cdot \nabla^2 \mathcal{L} \cdot d \geq 0$, Box 5.14 and (b) Given a regular point and the positive definition of the matrix $\nabla^2_{xx}\mathcal{L}(x^*, \gamma^*)$ it is shown that x^* is a local minimum.

Second Order Necessary Conditions (a):

      Suppose that (x^*) is a local solution of Eq. 5.8 and that the linear independence of the constraint is satisfied. Let (γ_i^*) be a Lagrange multiplier vector such that the KKT conditions are satisfied and by virtue of M_1 definition, then:

$$d^T \cdot \nabla^2_{xx}\mathcal{L}(x^*, \gamma^*) \cdot d \geq 0 \; \forall \, d \in M_1 \tag{5.15}$$

On the contrary, the second instance assumes that x^* is a local optimum and deduces properties of f_s and f^y.

Second Order Sufficient Conditions (b):

      Suppose that for a feasible point $(x^* \in R^n)$ there is a Lagrange multiplier vector (γ^*) such that the KKT conditions are satisfied. Suppose also that

$$d \, \nabla^2_{xx}\mathcal{L}(x^*, \gamma^*) \, d > 0 \;\; \forall \, d \in M_1$$

      Then (x^*) is a strict local minimum of (f_s) subjected to (f_i^y).

The last conditions established the positive semi-definite property of the Hessian matrix $\nabla^2_{xx}\mathcal{L}(x, \gamma)$ of the Lagrangian on the set M_1.

$$\nabla^2_{xx}\mathcal{L}(x, \gamma) = \nabla^2_{xx}f_s(x) + \sum_{i \in I} \gamma_i \, \nabla^2_{xx}f_i^y(x) \tag{5.16}$$

Both Eq. 5.13 (alternatively 5.14) and Eq. 5.16 define the algorithmic residual vector and the algorithmic Jacobian matrix:

$$r(x) = \left\{ \begin{array}{c} \nabla_x\mathcal{L}(x, \gamma) \\ f_i^y(x) \end{array} \right\} \tag{5.17}$$

$$J(x) = \begin{pmatrix} \nabla^2_{xx}\mathcal{L}(x, \gamma) & \nabla^2_{x\gamma}\mathcal{L}(x, \gamma) \\ \nabla^2_{x\gamma}\mathcal{L}(x, \gamma) & 0 \end{pmatrix}$$

They will be used further at the pseudo-code instance of the implicit algorithms and particularized for each addressed constitutive model.

5.3.2.1) Particularization to an Interior-Point environment

If program given by Eq. 5.10 is re-written in the standard form by introducing additional positive variables, it reads:

$$P_i \quad \begin{cases} \min & f_s(x) \\ x \in \mathbb{R}^n \\ \text{sub. to:} & f_i^y(x) + z_i = 0 \end{cases} \tag{5.18}$$

where z_i is the slack positive variable corresponding to constraint f_i^y. The Lagrange functional associated to this variational problem Eq. 5.18 is:

$$\mathcal{L}(x,\gamma) = f_s(x) + \sum_{i=1}^{n} \gamma_i \cdot \left(f_i^y(x) + z_i\right) + \mu \cdot \sum_{i=1}^{n} \log(z_i) \tag{5.19}$$

where μ is the positive duality parameter which measures the distance to the optimum of program P_i and is given by the mean value:

$$\mu = \frac{1}{n} \cdot \sum_{i=1}^{n} \gamma_i z_i \tag{5.20}$$

where n is the number of active constraints.

The Karush-Kuhn-Tucker conditions (KKT) associated with the program Eq. 5.18 are obtained by minimization of the Lagrange functional Eq. 5.19 and read:

$$\begin{aligned}
\nabla f_s(x^*) + \sum_{i=1}^{n} \gamma_i^* \nabla f_i^y(x^*) &= 0 \\
f_i^y(x^*) + z_i^* &= 0 \quad \forall\, i \in I \\
\sum_{i=1}^{n} \gamma_i^* z_i^* - \mu &= 0 \\
(\gamma_i^*, z_i^*) &> 0 \quad \forall\, i \in I \\
\gamma_i^* z_i^* &= 0 \quad \forall\, i \notin I
\end{aligned} \tag{5.21}$$

It should be noticed that, in this case, the unilateral constraint of positivity of both γ_i and z_i is required. Then, the solution of the program P_i (Eq. 5.18) is found as the infimum of the Lagrange functional:

$$P_i = \inf_{x \in E} \left\{ f_s(x) + \sum_{i=1}^{n} \gamma_i\left[f_i^y(x) + z_i\right] + \mu \cdot \sum_{i=1}^{n} \log(z_i) \right\}$$

From Eq. 5.21, the residual vector of the Euler equations considering a unique yield function is expressed in general as:

$$r(x) = \begin{Bmatrix} \nabla_x \mathcal{L}(x,\gamma) \\ f^y(x) - z \\ \gamma z - \mu \end{Bmatrix} \tag{5.22}$$

Comparing the last expression with Eq. 5.17a, the presence of a new linear term in the last component of the residual vector can be observed. Then the Jacobian matrix of the last vector $r(x)$ is expressed in a general form as:

$$J(x) = \begin{pmatrix} \nabla^2_{xx}\mathcal{L}(x,\gamma) & \nabla^2_{x\gamma}\mathcal{L}(x,\gamma) & 0 \\ \nabla^2_{x\gamma}\mathcal{L}(x,\gamma) & 0 & I \\ 0 & z & \gamma \end{pmatrix} \tag{5.23}$$

The system formed by the Eqs. 5.22 and 5.23 represents the unreduced system form of the interior point method. By eliminating d_z (the last component of the unreduced system) a system of the same dimension to CPPM, called the augmented system, is obtained. It looks like:

$$\begin{pmatrix} \nabla^2_{xx}\mathcal{L}(x,\gamma) & \nabla^2_{x\gamma}\mathcal{L}(x,\gamma) \\ \\ \nabla^2_{x\gamma}\mathcal{L}(x,\gamma) & \dfrac{z}{\gamma} \end{pmatrix} \begin{Bmatrix} d_x \\ d_\gamma \end{Bmatrix} = -\begin{Bmatrix} r_x \\ r_\gamma - \dfrac{r_z}{\gamma} \end{Bmatrix} \tag{5.24}$$

where the updated rule for the slack variable is directly given by the ratio μ/γ.

The bases for the mathematical analysis of constraint optimization leading to the resolution of nonlinear problems have been reviewed in this section and they will be used recurrently throughout the rest of the chapter.

5.4) Integration and Algorithms for Modified Cam-Clay Model

The propositions, lemmas and theorems reviewed above form the bases that underpin the construction of the variational forms and implicit algorithms developed hereinafter for the integration of hyper-poroplastic models: (a) closest point projection "CPPM" and (b) interior point method "IPM".

The section is organized as follows: First, a variational form of the governing equations for the Cam-Clay model is presented. The Lagrange functional giving rise to the variational form of the model is proposed. Then the vector of residuals of unbalanced strains (alternatively stresses) and the Jacobian matrix of such residuals are obtained. Secondly, the Lagrange functional of the equivalent equality constraint problem leading to the residual vector of the interior-point algorithm for the Cam-clay model is presented. Thirdly, the implicit algorithms for both the closest-point and interior-point to integrate the former variational equations are developed and presented in modular form. The performance of both CPPM and IPM algorithms is shown through different tests at Gauss

point level. Finally, the consistent tangent operator for the hyperplastic Cam-Clay model is developed.

5.4.1) Stress Point algorithms

In this subsection, the local continuum equations governing the problem of hyper-poroplasticity in a biphasic medium and its numerical approximation using both the closest-point projection scheme and the interior-point scheme are described. An introduction of the continuum equations is first presented, followed by the discrete closest-point projection approximation and the extension to the interior-point. Then a variational structure is derived for hyperplastic mechanical models by minimizing the energy functions f_s and g_s under the constraint $f^y = 0$.

Due to the assumption of infinitesimal deformations, the strains ε ($\equiv \nabla^s u$) of the porous skeleton are assumed to be decomposed additively into an elastic and a plastic components $\varepsilon = \varepsilon^e + \alpha$. Noting σ as the stress tensor and ρ as the shift stress tensor (characterizing the kinematical hardening of the material), the non-incremental hyperplastic constitutive relationships take the form:

$$\sigma = \frac{\partial f_s(\varepsilon, \alpha)}{\partial \varepsilon} \quad ; \quad \rho = \frac{\partial f_{s_2}(\alpha)}{\partial \alpha} \tag{5.25}$$

where $f_s(\varepsilon, \alpha)$ is the Helmholtz energy function of the porous skeleton defined in chapter 4 and $f_{s2}(\varepsilon, \alpha)$ the trapped part of this energy. As well, the evolution equations for the plastic internal variables α and ρ read:

$$\dot{\alpha} = \gamma \frac{\partial f^y(x)}{\partial x} \quad ; \quad \dot{\rho} = \gamma \frac{\partial^2 g_{s_2}(\alpha)}{\partial \alpha \, \partial \alpha} \frac{\partial f^y(x)}{\partial x} \tag{5.26}$$

where f^y is the yield surface, γ the scalar plastic multiplier and $\partial f^y(x)/\partial x$ the general flow vector. In this context, the plastic multiplier is determined by the classical Kuhn-Tucker complementary conditions:

$$\gamma \geq 0 \; ; \; f^y(x) \leq 0 \; ; \; \gamma f^y(x) = 0 \tag{5.27}$$

in addition to the consistency condition:

$$\gamma \dot{f}^y(x) = 0 \tag{5.28}$$

Equation 5.27 characterizes the loading-unloading conditions with Eq. 5.28 defining the persistency of the plastic state during plastic flow. The flow rule given by Eq. 5.26a can be alternatively written using the additive decomposition of strains:

$$\dot{\varepsilon}^e = \dot{\varepsilon} - \gamma \frac{\partial f^y(x)}{\partial x} \tag{5.29}$$

Equations 5.27, 5.28 and 5.29 define the strain-driven structure of the problem. It consists in determining, for a given increment of the total strain, the corresponding increments of stress σ, plastic internal variable α and the shift stress ρ. The enforcement of the consistency condition Eq. 5.28 combined with the governing equations 5.25 to 5.27 allows stating the expression for the plastic multiplier:

$$\gamma = \frac{1}{h} \frac{\partial f^y}{\partial x} \frac{\partial x}{\partial \sigma} \frac{\partial^2 f_s}{\partial \varepsilon \partial \varepsilon} \dot{\varepsilon} \tag{5.30}$$

where $h = \nabla f^{yT} \nabla^2 f_s \nabla f^y$ is the hardening modulus. The constitutive relations described above require to be integrated in time, usually in a strain-driven structure.

In this discrete scheme, stresses and internal variables are known at time t_n and updated at time t_{n+1} according to the strain increment $\Delta \varepsilon_{n+1}$ applied during time interval $\Delta t = t_{n+1} - t_n$. Thus, at time t_{n+1}, total strains are equal to:

$$\varepsilon_{n+1} = \varepsilon_n + \Delta \varepsilon_{n+1} \tag{5.31}$$

while stresses σ_{n+1}, plastic internal variable α_{n+1} and shift stresses ρ_{n+1} have to be computed. To this purpose, a common strategy is to use a backward-Euler approximation of the governing equations:

$$
\begin{aligned}
-\alpha_{n+1} + \alpha_n + \Delta\gamma \frac{\partial f^y(x_{n+1})}{\partial x} &= 0 \\
-\rho_{n+1} + \rho_n + \Delta\gamma \frac{\partial^2 g_{s_2}}{\partial \alpha \partial \alpha} \frac{\partial f^y(x_{n+1})}{\partial x} &= 0
\end{aligned}
\tag{5.32}
$$

where $\Delta\gamma$ must satisfy the loading-unloading conditions:

$$\Delta\gamma \geq 0 \; ; \; f^y_{n+1} \leq 0 \; ; \; \Delta\gamma \cdot f^y_{n+1} = 0 \tag{5.33}$$

The updated stress tensor is given by the relation, Eq. 5.25a:

$$\sigma_{n+1} = \frac{\partial f_s(\varepsilon_{n+1}, \alpha_{n+1})}{\partial \varepsilon} \tag{5.34}$$

The numerical solution of the algebraic system of equations defined by Eqs. 5.32 to 5.34 is accomplished following a predictor-corrector strategy. A common consideration for the predictor is the introduction of the elastic trial state computed by freezing the internal variables at time t_n:

$$\alpha_{n+1}^{trial} = \alpha_n \tag{5.35}$$

and updating the stress values:

$$\sigma_{n+1}^{\text{trial}} = \frac{\partial f_s\left(\varepsilon_{n+1}, \alpha_{n+1}^{\text{trial}}\right)}{\partial \varepsilon} \quad ; \quad \rho_{n+1}^{\text{trial}} = \frac{\partial f_{s_2}\left(\alpha_{n+1}^{\text{trial}}\right)}{\partial \alpha} \tag{5.36}$$

Note that the freezing of internal variables implies that $\rho_{n+1}^{\text{trial}} = \rho_n$. However, to respect the strain driven structure of the algorithm, it is preferred to perform the elastic trial over all stress variables. Check of loading-unloading conditions is then performed on the basis of the elastic trial:

$$\text{If} \quad \left(f_{n+1}^{y\,\text{trial}}\left(\sigma_{n+1}^{\text{trial}}, \rho_{n+1}^{\text{trial}}\right) \leq 0 \right) \quad \text{then} \quad (\blacksquare)_{n+1} = (\blacksquare)_{n+1}^{\text{trial}} \tag{5.37}$$

the elastic trial state is taken as the final solution. If not, a new solution is looked for (leading to the so-called plastic corrector step) where $\Delta\gamma > 0$:

$$\varepsilon_{n+1}^e = \varepsilon_{n+1} - \alpha_{n+1} \tag{5.38}$$
$$\varepsilon_{n+1}^{e\,\text{trial}} = \varepsilon_{n+1} - \alpha_n$$

The system of equations 5.32 can be re-written equivalently in terms of the elastic strains ε_{n+1}^e and the elastic trial strains $\varepsilon_{n+1}^{e\,\text{trial}}$ as:

$$\varepsilon_{n+1}^e - \varepsilon_{n+1}^{e\,\text{trial}} + \Delta\gamma \frac{\partial f^y(x_{n+1})}{\partial x} \quad = \quad 0 \tag{5.39}$$
$$-\rho_{n+1} + \rho_{n+1}^{\text{trial}} + \Delta\gamma \frac{\partial^2 g_{s_2}}{\partial \alpha\,\partial \alpha} \frac{\partial f^y(x_{n+1})}{\partial x} \quad = \quad 0$$

The set of nonlinear equations 5.39 is solved using a Newton-like iterative strategy (like the one used in unconstraint theory).

Despite the discrete form of the constitutive equations, both (CPPM) and (IPM) algorithms can be properly understood by finding the existence of a variational structure behind the specific forms of the general evolution equations.

The algorithms proposed hereinafter take advantage of this variational structure and the characteristics of the energy functions presented in the previous chapter. Firstly, they can be recognized as being convex of their arguments, according to the definition at Box 5.3. Furthermore, they are twice differentiable with positive definite Hessian matrix $\nabla^2 f_s$. Also, as one of the main characteristic of hyper-poroplasticity, the evolution laws are associated in the dissipative stress space:

$$\varepsilon = -\frac{\partial g_s(\sigma, \alpha)}{\partial \sigma} = -\frac{\partial \bar{g}_s(\sigma, x)}{\partial \sigma} \tag{5.40}$$

$$\sigma = \frac{\partial f_s(\varepsilon, \alpha)}{\partial \varepsilon} = \frac{\partial \bar{f}_s(\varepsilon, x)}{\partial \varepsilon}$$

$$x = \frac{\partial g_s(\sigma, \alpha)}{\partial \alpha}$$

$$\alpha = \frac{\partial \bar{g}_s(\sigma, x)}{\partial x}$$

where functions $\bar{f}_s$ and $\bar{g}_s$ are Legendre transform of Helmholtz and Gibbs free energies with respect to internal variables:

$$\bar{f}_s(\sigma, \bar{x}) = \min_{(\varepsilon, \alpha) \in E} \{-g_s(\sigma, \alpha) - (\sigma\varepsilon + \bar{x}\alpha)\} \tag{5.41}$$

$$\bar{g}_s(\sigma, \bar{x}) = \min_{(\varepsilon, \alpha) \in E} \{f_s(\varepsilon, \alpha) - (\sigma\varepsilon + \bar{x}\alpha)\}$$

and the orthogonality condition $\bar{x} = x$ is implicitly considered in equations 5.40. From results in convex analysis, it comes out that:

$$\nabla^2 \bar{g}_s(\sigma, x) = \left(\nabla^2 f_s(\varepsilon, \alpha)\right)^{-1} \tag{5.42}$$

Provided the convexity properties of the energy functions, the formulation of the minimization problem is then:

$$\boxed{\begin{aligned} &\text{Find } (\varepsilon_{n+1}, x_{n+1}) \in E \text{ such that} \\ &\qquad \bar{f}_s(\varepsilon_{n+1}, x_{n+1}) = \min_{(\sigma, \alpha) \in E} \{-g_s(\sigma, \alpha) - (\sigma\varepsilon_{n+1} + x_{n+1}^{\text{trial}}\alpha)\} \end{aligned}} \tag{5.43}$$

which can be alternatively expressed as the inequality mathematical program:

$$\text{CPPM} \begin{cases} \min & -g_s(\sigma, \alpha) - (\sigma\varepsilon_{n+1} + x_{n+1}^{\text{trial}}\alpha) \\ (\sigma, \alpha) \\ \text{sub. to} & f^y(x) \le 0 \end{cases} \tag{5.44}$$

Now, from standard arguments in constraint optimization, the Lagrange functional associated to the variational problem 5.44 is given by the expression:

$$\mathcal{L}^{\bar{g}}(\sigma, x, \Delta\gamma) = -g_s(\sigma, \alpha) - (\sigma\varepsilon_{n+1} + x_{n+1}^{\text{trial}}\alpha) + \Delta\gamma \cdot f^y(x) \tag{5.45}$$

The application of the necessary first order optimality conditions on Eq. 5.45 leads to the Kuhn-Tucker restrictions.

By using Eq. 5.41, the state equations 5.40 and the fundamental relationship $\rho_{n+1}^{\text{trial}} = \sigma_{n+1}^{\text{trial}} - x_{n+1}^{\text{trial}}$, these restrictions are expressed as:

$$\varepsilon_{n+1}^e - \varepsilon_{n+1}^{e\,\text{trial}} + \Delta\gamma \frac{\partial f_{n+1}^y(x)}{\partial x}\frac{\partial x}{\partial \sigma} \quad = \quad 0 \tag{5.46}$$

$$-\rho_{n+1} + \rho_{n+1}^{\text{trial}} + \Delta\gamma \frac{\partial f_{n+1}^y(x)}{\partial x}\frac{\partial x}{\partial \rho}\frac{\partial^2 g_{s_2}}{\partial\alpha\,\partial\alpha} \quad = \quad 0$$

$$f_{n+1}^y(x) \quad = \quad 0$$

$$\Delta\gamma \quad \geq \quad 0$$

Then the residual vector used in the algorithm (primal − dual CPPM) reads:

$$r(x) = \begin{cases} \varepsilon_{n+1}^e - \varepsilon_{n+1}^{e\,\text{trial}} + \Delta\gamma \dfrac{\partial f_{n+1}^y(x)}{\partial x}\dfrac{\partial x}{\partial \sigma} \\[2mm] -\rho_{n+1} + \rho_{n+1}^{\text{trial}} + \Delta\gamma \dfrac{\partial f_{n+1}^y(x)}{\partial x}\dfrac{\partial x}{\partial \rho}\dfrac{\partial^2 g_{s_2}}{\partial\alpha\,\partial\alpha} \\[2mm] f_{n+1}^y(x) \end{cases} \tag{5.47}$$

and the Jacobian matrix of the residual vector giving rise to the computation of advance direction to search the optimal point (solution state) is given by:

$$J(x) = \begin{bmatrix} I + \Delta\gamma \dfrac{\partial^2 f^y}{\partial x\,\partial x}\left(\dfrac{\partial x}{\partial\sigma}\right)^2\dfrac{\partial^2 f_s}{\partial\varepsilon\,\partial\varepsilon} & \Delta\gamma\dfrac{\partial^2 f^y}{\partial x\,\partial x}\dfrac{\partial x}{\partial\sigma}\dfrac{\partial x}{\partial\rho} & \dfrac{\partial f^y}{\partial x}\dfrac{\partial x}{\partial\sigma} \\[3mm] \Delta\gamma\dfrac{\partial^2 f^y}{\partial x\,\partial x}\dfrac{\partial x}{\partial\rho}\dfrac{\partial x}{\partial\sigma}\dfrac{\partial^2 g_{s_2}}{\partial\alpha\,\partial\alpha}\dfrac{\partial^2 f_s}{\partial\varepsilon\,\partial\varepsilon} & -I + \Delta\gamma\dfrac{\partial^2 f^y}{\partial x\,\partial x}\left(\dfrac{\partial x}{\partial\rho}\right)^2\dfrac{\partial^2 g_{s_2}}{\partial\alpha\,\partial\alpha} & \dfrac{\partial f^y}{\partial x}\dfrac{\partial x}{\partial\rho}\dfrac{\partial^2 g_{s_2}}{\partial\alpha\,\partial\alpha} \\[3mm] \dfrac{\partial f^y}{\partial x}\dfrac{\partial x}{\partial\sigma}\dfrac{\partial^2 f_s}{\partial\varepsilon\,\partial\varepsilon} & \dfrac{\partial f^y}{\partial x}\dfrac{\partial x}{\partial\rho} & 0 \end{bmatrix} \tag{5.48}$$

Eq. 5.48 provides the Jacobian to be used in the primal-dual CPPM algorithm.

Before proceeding further it is noted that the last matrix is also obtained by double differentiation of the Lagrange functional 5.45 called the Hessian matrix $\nabla_{xx}^2 \mathcal{L}(x)$:

$$\nabla^2 \mathcal{L}^{g_s} = \begin{pmatrix} \dfrac{\partial^2 g_s}{\partial\sigma\,\partial\sigma} & \left(\dfrac{\partial^2 g_s}{\partial\sigma\,\partial\alpha} - 1\right) \\[3mm] \left(\dfrac{\partial^2 g_s}{\partial\alpha\,\partial\sigma} - 1\right) & -\dfrac{\partial^2 g_s}{\partial\alpha\,\partial\alpha} \end{pmatrix} \tag{5.49}$$

$$+ \Delta\gamma \begin{pmatrix} \dfrac{\partial^2 f^y}{\partial x\,\partial x}\left(\dfrac{\partial x}{\partial\sigma}\right)^2 & \dfrac{\partial^2 f^y}{\partial x\,\partial x}\dfrac{\partial x}{\partial\sigma}\dfrac{\partial x}{\partial\rho}\dfrac{\partial^2 g_s}{\partial\alpha\,\partial\alpha} \\[3mm] \dfrac{\partial^2 f^y}{\partial x\,\partial x}\dfrac{\partial x}{\partial\sigma}\dfrac{\partial x}{\partial\rho}\dfrac{\partial^2 g_s}{\partial\alpha\,\partial\alpha} & \dfrac{\partial^2 f^y}{\partial x\,\partial x}\left(\dfrac{\partial x}{\partial\rho}\right)^2\dfrac{\partial^2 g_s}{\partial\alpha\,\partial\alpha}\dfrac{\partial^2 g_s}{\partial\alpha\,\partial\alpha} \end{pmatrix}$$

Multiplying $\nabla^2 \mathcal{L}^{g_s}$ by the Hessian matrix of Helmholtz free energy:

$$\nabla_{\varepsilon\varepsilon}^2 H = \begin{pmatrix} \dfrac{\partial^2 f_s}{\partial\varepsilon\,\partial\varepsilon} & 0 \\[3mm] 0 & \dfrac{\partial^2 f_s}{\partial\varepsilon\,\partial\varepsilon} \end{pmatrix} \tag{5.50}$$

leads to the matrix form:

$$\nabla^2_{\varepsilon\varepsilon} H \nabla^2 \mathcal{L}^{g_s} = \begin{pmatrix} I & 0 \\ 0 & -I \end{pmatrix} + \Delta\gamma \begin{pmatrix} \dfrac{\partial^2 f^y}{\partial x \partial x} \left(\dfrac{\partial x}{\partial \sigma}\right)^2 \dfrac{\partial^2 f_s}{\partial \varepsilon \partial \varepsilon} & \dfrac{\partial^2 f^y}{\partial x \partial x} \dfrac{\partial x}{\partial \sigma} \dfrac{\partial x}{\partial \rho} \\ \dfrac{\partial^2 f^y}{\partial x \partial x} \dfrac{\partial x}{\partial \sigma} \dfrac{\partial x}{\partial \rho} \dfrac{\partial^2 g_s}{\partial \alpha \partial \alpha} \dfrac{\partial^2 f_s}{\partial \varepsilon \partial \varepsilon} & \dfrac{\partial^2 f^y}{\partial x \partial x} \left(\dfrac{\partial x}{\partial \rho}\right)^2 \dfrac{\partial^2 g_s}{\partial \alpha \partial \alpha} \end{pmatrix} \quad (5.51)$$

The last matrix is also an Hessian matrix that coincides with the upper sub-matrix of the Jacobian at Eq. 5.51.

On the other hand the constraint program Eq. 5.44 can be re-written in the standard form of equality constraint by introducing the slack variable z:

$$\text{IPM} \quad \begin{cases} \min \limits_{(\sigma,\alpha)} & -g_s(\sigma,\alpha) - \left(\sigma\varepsilon_{n+1} + x^{trial}_{n+1}\alpha\right) + \mu \cdot \log(z) \\ \text{sub. to} & f^y(x) + z = 0 \end{cases} \quad (5.52)$$

On this occasion the Lagrange functional of the equality constraint program 5.52 is given by:

$$\mathcal{L}^{\bar{g}}(\sigma, x, \Delta\gamma) = -g_s(\sigma,\alpha) - \left(\sigma\varepsilon^{trial}_{n+1} + x^{trial}_{n+1}\alpha\right) + \Delta\gamma[f^y + z] + \mu \cdot \log(z) \quad (5.53)$$

Using Eq. 5.41, the state equations 5.40 and the fundamental relation $\rho^{trial}_{n+1} = \sigma^{trial}_{n+1} - x^{trial}_{n+1}$, the imposition of the necessary first order optimality conditions to the Lagrangian 5.53 leads to the following extension of Kuhn-Tucker restrictions:

$$\begin{aligned} \varepsilon^e_{n+1} - \varepsilon^{e\,trial}_{n+1} + \Delta\gamma \dfrac{\partial f^y_{n+1}(x)}{\partial x} \dfrac{\partial x}{\partial \sigma} &= 0 \\ -\rho_{n+1} + \rho^{trial}_{n+1} + \Delta\gamma \dfrac{\partial f^y_{n+1}(x)}{\partial x} \dfrac{\partial x}{\partial \rho} \dfrac{\partial^2 g_{s_2}}{\partial \alpha \partial \alpha} &= 0 \\ f^y_{n+1}(x) + z &= 0 \\ \Delta\gamma - \dfrac{\mu}{z} &= 0 \\ (\Delta\gamma, z) &\geq 0 \end{aligned} \qquad (5.54)$$

where in this case the positive character of both the discrete plastic multiplier $\Delta\gamma$ and the slack variable z should be preserved.

Primal-dual interior-point methods generate iterates $x^{(k)}$ that strictly satisfy the bounds given by Eq. 5.54e, that is $\Delta\gamma^{(k)} > 0$ and $z^{(k)} > 0$. This method modifies the basic Newton procedure in two important ways: (a) it deviates the search direction toward the interior of the nonnegative octant $(\Delta\gamma, z)$ allowing moving further along the feasible direction before one of the components $(\Delta\gamma, z)$ becomes negative (this property is indeed the origin of the term interior-point); (b) it prevents the variables $(\Delta\gamma, z)$ from moving too close to

the boundary of the nonnegative octant. This last condition is controlled by the duality measure variable $\mu = {}^{1}/_{n} \cdot \sum \Delta\gamma_i z_i$.

From the first optimality KKT conditions 5.54 the residual vector used in the algorithm (primal − dual IPM) is derived as:

$$
r(x) = \begin{Bmatrix} \varepsilon_{n+1}^e - \varepsilon_{n+1}^{e\,\text{trial}} + \Delta\gamma \dfrac{\partial f_{n+1}^y(x)}{\partial x} \dfrac{\partial x}{\partial \sigma} \\[2mm] -\rho_{n+1} + \rho_{n+1}^{\text{trial}} + \Delta\gamma \dfrac{\partial f_{n+1}^y(x)}{\partial x} \dfrac{\partial x}{\partial \rho} \dfrac{\partial^2 g_{s_2}}{\partial \alpha\,\partial \alpha} \\[2mm] f_{n+1}^y(x) + z \\[2mm] \Delta\gamma \cdot z - \mu \end{Bmatrix} \tag{5.55}
$$

where the Jacobian matrix of $r(x)$ is:

$$
J(x) \tag{5.56}
$$

$$
= \begin{bmatrix} I + \Delta\gamma \dfrac{\partial^2 f^y}{\partial x\,\partial x}\left(\dfrac{\partial x}{\partial \sigma}\right)^2 \dfrac{\partial^2 f_s}{\partial \varepsilon\,\partial \varepsilon} & \Delta\gamma \dfrac{\partial^2 f^y}{\partial x\,\partial x}\dfrac{\partial x}{\partial \sigma}\dfrac{\partial x}{\partial \rho} & \dfrac{\partial f^y}{\partial x}\dfrac{\partial x}{\partial \sigma} & 0 \\[3mm] \Delta\gamma \dfrac{\partial^2 f^y}{\partial x\,\partial x}\dfrac{\partial x}{\partial \rho}\dfrac{\partial x}{\partial \sigma}\dfrac{\partial^2 g_{s_2}}{\partial \alpha\,\partial \alpha}\dfrac{\partial^2 f_s}{\partial \varepsilon\,\partial \varepsilon} & -I + \Delta\gamma \dfrac{\partial^2 f^y}{\partial x\,\partial x}\left(\dfrac{\partial x}{\partial \rho}\right)^2 \dfrac{\partial^2 g_{s_2}}{\partial \alpha\,\partial \alpha} & \dfrac{\partial f^y}{\partial x}\dfrac{\partial x}{\partial \rho}\dfrac{\partial^2 g_{s_2}}{\partial \alpha\,\partial \alpha} & 0 \\[3mm] \dfrac{\partial f^y}{\partial x}\dfrac{\partial x}{\partial \sigma}\dfrac{\partial^2 f_s}{\partial \varepsilon\,\partial \varepsilon} & \dfrac{\partial f^y}{\partial x}\dfrac{\partial x}{\partial \rho} & 0 & 1 \\[3mm] 0 & 0 & z & \Delta\gamma \end{bmatrix}
$$

Both $r(x)$ and $J(x)$ is used to compute the advance direction to search for the solution state in the primal-dual IPM algorithm described below.

Before concluding this sub-section, other alternative formulations of Lagrange functionals are shown. They are built based on the energy functions $(g_s, f_s, \bar{g}_s, \bar{f}_s)$ used to derive the model. They are summarized in Table 5.20.

Table 5.20: Possible Lagrangian Formulations from Energy functions

Energy function	$\mathcal{L}$ − function	$(g_s$ or $\bar{g}_s)$ − function
$f^y(x) = 0$ $f_s(\varepsilon, \alpha)$	$\mathcal{L}^{\bar{g}}(\sigma, x, \Delta\gamma)$	$\bar{g}_s(\sigma, x) - (\sigma\varepsilon + x\alpha) + \Delta\gamma(f^y(x) + z)$ $+ \mu \cdot \log(z)$
$\bar{f}_s(\varepsilon, x)$	$\mathcal{L}^{g}(\sigma, \alpha, \Delta\gamma)$	$g_s(\sigma, \alpha) - (\sigma\varepsilon + x\alpha) + \Delta\gamma(f^y(x) + z)$ $+ \mu \cdot \log(z)$
Energy function		$(f_s$ or $\bar{f}_s)$ − function

$f^y(x) = 0$		
$g_s(\sigma, \alpha)$	$\mathcal{L}^{\bar{f}}(\varepsilon, x, \Delta\gamma)$	$\bar{f}_s(\varepsilon, x) - (\sigma\varepsilon + x\alpha) + \Delta\gamma(f^y(x) + z)$ $+ \mu \cdot \log(z)$
$\bar{g}_s(\sigma, x)$	$\mathcal{L}^f(\varepsilon, \alpha, \Delta\gamma)$	$\bar{f}_s(\varepsilon, \alpha) - (\sigma\varepsilon + x\alpha) + \Delta\gamma(f^y(x) + z)$ $+ \mu \cdot \log(z)$

Imposition of the first order optimality conditions on those Lagrange functionals lead to different forms for the Karush-Kuhn-Tucker (KKT) conditions. They are summarized in Table 5.21.

Table5.21: Karush-Kuhn-Tucker conditions for alternative Lagrangian formulations

$\mathcal{L}$ − function	$(g_s \text{ or } \bar{g}_s)$ − KKT conditions
$\mathcal{L}^{\bar{g}}(\sigma, x, \Delta\gamma)$	$\varepsilon^e_{n+1} - \varepsilon^{e\,trial}_{n+1} + \Delta\gamma \dfrac{\partial f^y_{n+1}(x)}{\partial x}\dfrac{\partial x}{\partial\sigma} \quad = \quad 0$ $\alpha_{n+1} - \alpha^{trial}_{n+1} + \Delta\gamma \dfrac{\partial f^y_{n+1}(x)}{\partial x} \quad = \quad 0$ $f^y_{n+1}(x) + z \quad = \quad 0$ $\Delta\gamma - \dfrac{\mu}{z} \quad = \quad 0$ $(\Delta\gamma, z) \quad \geq \quad 0$
$\mathcal{L}^g(\sigma, \alpha, \Delta\gamma)$	$\varepsilon^e_{n+1} - \varepsilon^{e\,trial}_{n+1} + \Delta\gamma \dfrac{\partial f^y_{n+1}(x)}{\partial x}\dfrac{\partial x}{\partial\sigma} \quad = \quad 0$ $-\rho_{n+1} + \rho^{trial}_{n+1} + \Delta\gamma \dfrac{\partial f^y_{n+1}(x)}{\partial x}\dfrac{\partial x}{\partial\rho}\dfrac{\partial^2 g_{s_2}}{\partial\alpha\,\partial\alpha} \quad = \quad 0$ $f^y_{n+1}(x) + z \quad = \quad 0$ $\Delta\gamma - \dfrac{\mu}{z} \quad = \quad 0$ $(\Delta\gamma, z) \quad \geq \quad 0$
$\mathcal{L}$ − function	$(f_s \text{ or } \bar{f}_s)$ − KKT conditions
$\mathcal{L}^{\bar{f}}(\varepsilon, x, \Delta\gamma)$	$\sigma_{n+1} - \sigma^{trial}_{n+1} + \Delta\gamma \dfrac{\partial f^y_{n+1}(x)}{\partial x}\dfrac{\partial x}{\partial\sigma}\dfrac{\partial^2 f_s}{\partial\varepsilon\,\partial\varepsilon} \quad = \quad 0$ $-\rho_{n+1} + \rho^{trial}_{n+1} + \Delta\gamma \dfrac{\partial f^y_{n+1}(x)}{\partial x}\dfrac{\partial x}{\partial\rho}\dfrac{\partial^2 g_{s_2}}{\partial\alpha\,\partial\alpha} \quad = \quad 0$ $f^y_{n+1}(x) + z \quad = \quad 0$ $\Delta\gamma - \dfrac{\mu}{z} \quad = \quad 0$ $(\Delta\gamma, z) \quad \geq \quad 0$

$\mathcal{L}^f(\varepsilon, \alpha, \Delta\gamma)$	$\sigma_{n+1} - \sigma_{n+1}^{\text{trial}} + \Delta\gamma \dfrac{\partial f_{n+1}^y(x)}{\partial x} \dfrac{\partial x}{\partial \sigma} \dfrac{\partial^2 f_s}{\partial \varepsilon \, \partial \varepsilon} \quad = \quad 0$ $\alpha_{n+1} - \alpha_{n+1}^{\text{trial}} + \Delta\gamma \dfrac{\partial f_{n+1}^y(x)}{\partial x} \quad = \quad 0$ $f_{n+1}^y(x) + z \quad = \quad 0$ $\Delta\gamma - \dfrac{\mu}{z} \quad = \quad 0$ $(\Delta\gamma, z) \quad \geq \quad 0$

5.4.2) Implicit Algorithms for Hyperplastic Cam-Clay Model

This sub-section concerns the implicit algorithms used in order to integrate the above presented Cam-Clay model. In this regard, the propositions, lemmas and theorems revised above in addition to the variational forms developed in the last sub-section form the bases that underpin the construction of such implicit algorithms: (a) closest point projection "CPPM" and (b) interior point method "IPM".

Those algorithms will be therefore used for the integration of hyper-poroplastic models developed at the former chapter and whose variational structures will be addressed below.

5.4.2.1) Globally Convergent - Closest point projection algorithm "CPPM"

This type of integration is widely used in mechanics and geo-mechanics environments. Simo & Hughes (1987, 1988) showed that the algorithmic problem defined by 5.44 (or in a more general form Eq. 5.10) in addition to a unilateral constraint condition, reduces to the standard problem of finding the closest distance (in the energy norm) of a state-point (elastic trial) to a convex set (elastic domain).

The algorithm is geometrically interpreted as projection of the trial state onto the boundary of the admissible space ∂E. In the stress space, the solution stress tensor σ_{n+1} results to be the closest projection (point) onto the yield surface f^y of the trial stress $\sigma_{n+1}^{\text{trial}}$. Box 5.16 summarizes the mathematical expressions leading to the geometrical interpretation of the closest-point algorithm for the perfect plastic case starting with the Lagrange functional Eq. 5.12.

Box 5.16: Geometrical Interpretation of closest-point projection algorithm.

CCPM algorithm Geometrical's Interpretation:

Lagrange functional for perfect plastic case:

$$\mathcal{L}^{f_s} = f_s(\varepsilon_{n+1} - \alpha_{n+1}) - \sigma_{n+1}^{\text{trial}}\varepsilon + \Delta\gamma \cdot f^y\left(\frac{\partial f_s(\alpha_{n+1})}{\partial\alpha}\right)$$

then the corresponding Kuhn-Tucker optimality conditions read:

$$\frac{\partial\mathcal{L}^{f_s}}{\partial\varepsilon_{n+1}^e} = \sigma_{n+1} - \sigma_{n+1}^{\text{trial}} + \Delta\gamma\frac{\partial f^y}{\partial x}\frac{\partial x}{\partial\sigma}\frac{\partial^2 f_s}{\partial\varepsilon\,\partial\varepsilon} = 0$$

$$\frac{\partial\mathcal{L}^{f_s}}{\partial\Delta\gamma} = \Delta\gamma f^y\left(\frac{\partial f_s(\alpha_{n+1})}{\partial\alpha}\right) = 0$$

$$\Delta\gamma \geq 0$$

Finally, it comes out that:

$$\sigma_{n+1} = \sigma_{n+1}^{\text{trial}} - \Delta\gamma\frac{\partial f^y}{\partial x}\frac{\partial x}{\partial\sigma}\frac{\partial^2 f_s}{\partial\varepsilon\,\partial\varepsilon} \quad = \mathbf{arg}\left[\begin{array}{c}\min\\ \sigma \in E\end{array}\left\{\left\|\sigma_{n+1}^{\text{trial}} - \sigma\right\|_{F_s}\right\}\right]$$

where E is the closure of the elastic domain and $\|\sigma\|_{F_s}$ *the energy norm.* Fig. 5.85
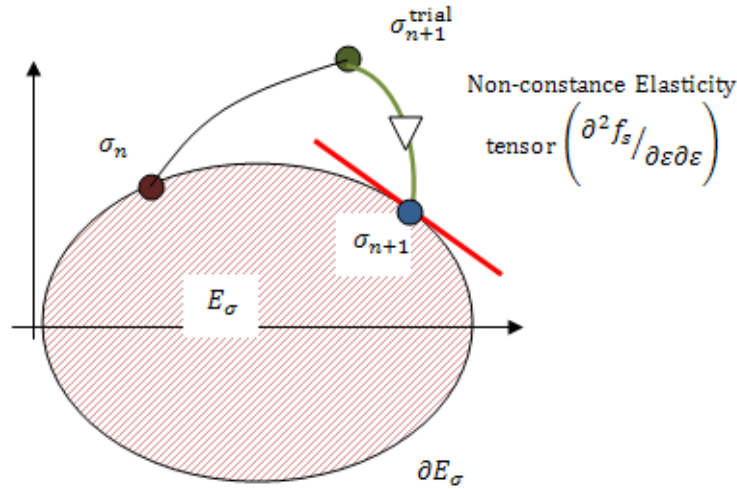
Figure 5.85: Geometric Illustration of the concept of closest point projection.

The return mapping algorithm solving the system of nonlinear equations 5.47 (or generically 5.13) takes pure Newton steps or damped steps (through the line-search parameter α) towards the optimum $r(x^*) = 0$.

A general "primal-dual CPPM" algorithm to solve the nonlinear problem satisfying strictly the condition $\Delta\gamma \geq 0$ at each iteration is summarized in the following boxes.

*Box 5.17: A General pseudo-code for **primal-dual CPPM***

1) Input data (according to the addressed problem):

   i.e. BMM1- $\left(\varepsilon_{n+1}, \varepsilon_{n+1}^{e\,trial}, s_{n+1}, \alpha_{n+1}^{trial}\right)$ with $\left(\sigma_{n+1}^{trial}, \rho_{n+1}^{trial}, S_{l_{n+1}}\right)$ and $\left(f_{n+1}^{y\,trial}\right)$

2) Initialize (set k = 0): $\left(\gamma^{(0)} = 0\right)$

   $\left(x^{(0)}\right)$ and $\left(r^{(0)}(x)\right)$ (according to the addressed problem, Eq.5.14)

3) Check overall convergence: $\left\|r^{(k)}(x)\right\| \leq itol$

4) Compute the Jacobian matrix $\left(J^{(k)}\right)$ (according to the addressed problem, Eq.5.18) with the quantities evaluated at $\left(x^{(k)}\right)$

5) Attempt a modified Newton step:

   $\left(x^{(k+1)}, r^{(k+1)}\right) =$**Newton-step** $\left(x^{(k)}, x^{(0)}, r^{(k)}, J^{(k)}\right)$

6) Set (k ← k + 1) and go to 3

7) $\left(x_{n+1} = x_n^{k+1}\right)$

8) Return $\left(\sigma_{n+1} = \sigma(x_{n+1})\right)$

Then the **Newton-step** is taken as coded in Box 5.18.

*Box 5.18: **Newton-step** $\left(x^{(k)}, x^{(0)}, r^{(k)}, J^{(k)}\right)$ algorithm*

1) Compute the feasible advance direction $\left(d^{(k)}\right)$:

If $\left(\Delta\gamma > 0 \text{ .and. } \nabla m_{\Delta\gamma} \leq 0\right)$ then

   1.a) $d^{(k)} = -\left(J^{(k)}\right)^{-1} r^{(k)}$ and   faux = true   else,

   1.b) $d^{(k)} = -D^{(k)}\left(J^{(k)}\right)^T r^{(k)}$ and   faux = false

   with $\left(D^{(k)}\right)$ as propose by (Perez-Foguet & Armero, 2002) $\Big($the

descent direction is penalized due to $(\Delta\gamma < 0)\Big)$.

2) Line search scheme:

   $\left(x^{(k)}(\alpha), r^{(k)}(\alpha)\right) =$ **Line-search** $\left(x^{(k)}, x^{(0)}, r^{(k)}, J^{(k)}, d^{(k)}\right)$

3) Return with $\left(x^{(k)}(\alpha), r^{(k)}(\alpha)\right)$

and the step size along the Newton's direction is given by the **Line-search** algorithm is coded in Box 5.19.

*Box 5.19: **Line-search** $\left(x^{(k)}, x^{(0)}, r^{(k)}, J^{(k)}, d^{(k)}\right)$ algorithm*

1) Input data: $x^{(k)}, x^{(0)}, r^{(k)}, J^{(k)}, d^{(k)}$

2) Initialize: set $(j = 0)$; $\left(\alpha_{(0)}^{(k)} = 1\right)$; and for $\left(m^{(k)} = \dfrac{1}{2}\left(r^{(k)}\right)^{T} \cdot r^{(k)}\right)$ give

$$m'^{(k)} = \begin{cases} -2m^{(k)} & \text{faux} = \text{true} \\ r^{(k)}J^{(k)}d^{(k)} & \text{faux} = \text{false} \end{cases}$$

3) Update residuals $\left(r_{(j)}^{(k+1)}\right)$, merit function $\left(m_{(j)}^{(k+1)}\right)$:

$$x_{(j)}^{(k+1)} = \langle x^{(k)} + \alpha_{(j)}^{(k)} d^{(k)} \rangle_{(\Delta \gamma)}$$

$$r_{(j)}^{(k+1)} = r\left(x_{(j)}^{(k+1)}\right)$$

$$m_{(j)}^{(k+1)} = \frac{1}{2}\left(\left(r_{(j)}^{(k+1)}\right)^{T} \cdot r_{(j)}^{(k+1)}\right)$$

4) Compute upper limit of Goldstein condition:

If $\left(\text{faux .and. } \left(x^{(k)} + \alpha_{(j)}^{(k)} d^{(k)}\right)_{(\Delta \gamma)} > 0\right)$ then

    4.a) $\text{uplim} = \left(1 - 2\beta\alpha_{(j)}^{(k)}\right) m^{(k)}$ else

    4.b) $\text{uplim} = m^{(k)} + \beta r^{(k)}J^{(k)} \cdot \left(x_{(j)}^{(k+1)} - x^{(k)}\right)$ see (Bertsekas, 1986).

5) Check Goldstein conditions:

  If $\left(m_{(j)}^{(k+1)}\right) \leq \text{uplim}$: $\left(x^{(k+1)}, r^{(k+1)}\right) \leftarrow \left(x_{(j)}^{(k+1)}, r_{(j)}^{(k+1)}\right)$ exit.

  If $(j = j_{max})$ notify, set: $\left(x^{(k+1)}, r^{(k+1)}\right) \leftarrow \left(x_{(j)}^{(k+1)}, r_{(j)}^{(k+1)}\right)$ exit.

6) Compute the new value of line-search parameter:

Cubic backtrack interpolation with first quadratic attempt,

$$\alpha_{(j+1)}^{(k)} = \max\left\{\eta \cdot \alpha_{(j)}^{(k)}, \frac{-\left(\alpha_{(j)}^{(k)}\right)^{2} m'^{k}}{2\left(m_{(j)}^{(k+1)} - m_{(j)}^{(k)} - \alpha_{(j)}^{(k)} m'^{k}\right)}\right\}$$

7) Set $(j \leftarrow j + 1)$ and go to 3.

The performance of the algorithm "primal-dual CPPM" is shown below through a series of tests for models studied in chapter 4.

5.4.2.2) Globally Convergent Interior-Point algorithm "IPM"

The interior point method dates back to the eighties when Karmarkar (1984) presented a new algorithm with efficiency of polynomial complexity which unseated the Simplex method for solving linear programming problems. The method presented a high correlation with penalty algorithms which uses barrier functions. Although it has

_____

developed and spread widely in the study of linear programming and semi-definite programming, the evolution regarding nonlinear convex programming has been more measured.

Before addressing the insights of the interior point algorithm, an update rule for the duality Gap variable of the interior-point method is proposed. It results in a key point of the algorithm's parameterization.

5.4.2.2.1) Update rule for Duality Gap variable ($\boldsymbol{\mu}$)

In this subsection a strategy for finding an update solution for the duality gap variable is discussed. Considering the scalar equation,

$$m(\mu) = -\alpha + \frac{\mu}{\beta} \tag{5.57}$$

with two free parameters α and β. It is reasonable to choose those parameters to satisfy the two conditions $m(\mu) = 0 \equiv r_z(\mu) = -\gamma + {}^{\mu}/z$ and

$$m'(\mu) = \frac{1}{\beta} \rightarrow \beta = \frac{1}{r_z{}'(\mu)} \tag{5.58}$$

Equation 5.58 gives an expression for parameter β. Combining Eq. 5.57 and Eq. 5.58 leads to an expression for the free parameter α:

$$\alpha = \mu \cdot r_z{}'(\mu) - r_z(\mu) \tag{5.59}$$

now replacing the expressions for the free parameters into the definition of the duality variable ($\mu = \alpha\beta \equiv \gamma z$) leads to,

$$\mu^{m+1} = \mu^m - \frac{r_z(\mu)}{r_z{}'(\mu)} \tag{5.60}$$

the expression for updating the duality gap variable will give a continuous reduction as we approach the solution and a continuous increment if we are far from it. Therefore, the update of the slack variable will be given directly by the ratio ${}^{\mu}/\gamma$.

Again the interior-point return mapping solving the system of nonlinear discrete equations 5.55 takes pure Newton steps or damped steps (through the line-search parameter α) towards the optimum. A general "primal-dual IPM" algorithm to solve the nonlinear problem satisfying strictly the condition $(\Delta\gamma, z) \geq 0$ at each iteration is summarized at the boxes 5.20-5.22.

1) Input data (according to the addressed problem):

   i.e. BMM1- $\left(\varepsilon_{n+1}, \varepsilon_{n+1}^{e^{trial}}, s_{n+1}, \alpha_{n+1}^{trial}\right)$ with $\left(\sigma_{n+1}^{trial}, \rho_{n+1}^{trial}, S_{l_{n+1}}\right)$ and $\left(f_{n+1}^{y^{trial}}\right)$

2) Initialize (set $m=0$): $\left(\gamma^{(0)} = 0\right)$, $\left(z^{(0)} = 0\right)$,

3) Check barrier convergence $\mu \le \mu_{TOL}$

4) Initialize (set k = 0): $\left(x^{(0)} = x^{(m)}\right)$, $\left(\mu = \mu^{(m)}\right)$, $\left(r^{(0)} = r^{(m)}\right)$,

5) Check overall convergence: $\left\|r_{\mu}^{(k)}(x)\right\| \le itol$

6) Compute the Jacobian matrix $\left(J^{(k)}\right)$ (according to the addressed problem) with the quantities evaluated at $\left(x^{(k)}\right)$

7) Attempt a modified Newton step:

   $$\left(x^{(k+1)}, r_{\mu}^{(k+1)}\right) = \textbf{Newton-step}\ \left(x^{(k)}, x^{(0)}, r_{\mu}^{(k)}, J^{(k)}\right)$$

8) Set (k ← k + 1) and go to 5

9) $\left(x_{m+1} = x_m^{k+1}\right)$

10) $\mu^{m+1} = \mu^m - \left.r_z(\mu)\middle/r_z{}'(\mu)\right.$ and go to 3

11) $\left(x_{n+1} = x_n^{m+1}\right)$

12) Return $\left(\sigma_{n+1} = \sigma(x_{n+1})\right)$

Then the **Newton-step** is taken as coded in Box5.21.

1) Compute the feasible advance direction $\left(d^{(k)}\right)$:

If $\left(\left(\Delta\gamma > 0\ .and.\ \nabla m_{\Delta\gamma} \le 0\right) .and.\ (z > 0\ .and.\ \nabla m_z \le 0)\right)$ then

   1.a) $d^{(k)} = -\left(J^{(k)}\right)^{-1} r^{(k)}$ and   faux = true else,

   1.b) $d^{(k)} = -D^{(k)}\left(J^{(k)}\right)^T r^{(k)}$ and   faux = false

       with $\left(D^{(k)}\right)$ as propose by (Perez-Foguet & Armero, 2002)$\left(\text{the}\right.$

descent direction is penalized due to $\left.\left((\Delta\gamma, z) < 0\right)\right)$.

2) Line search scheme:

   $$\left(x^{(k)}(\alpha), r_{\mu}^{(k)}(\alpha)\right) = \textbf{Line-search}\ \left(x^{(k)}, x^{(0)}, r_{\mu}^{(k)}, J^{(k)}, d^{(k)}\right)$$

3) Return with $\left(x^{(k)}(\alpha), r_{\mu}^{(k)}(\alpha)\right)$

and the step size along the Newton's direction is given by the **Line-search** algorithm is coded in Box 5.22.

*Box 5.22: **Line-search** $\left(x^{(k)}, x^{(0)}, r_\mu^{(k)}(\alpha), J^{(k)}, d^{(k)}\right)$ algorithm*

---

1) Input data: $x^{(k)}, x^{(0)}, r_\mu^{(k)}(\alpha), J^{(k)}, d^{(k)}$

2) Initialize: set $(j = 0)$; $\left(\alpha_{(0)}^{(k)} = 1\right)$; and for $\left(m^{(k)} = \frac{1}{2}\left(r^{(k)}\right)^T \cdot r^{(k)}\right)$ give

$$m'^{(k)} = \begin{cases} -2m^{(k)} & \text{faux = \color{green}{true}} \\ r^{(k)}J^{(k)}d^{(k)} & \text{faux = \color{red}{false}} \end{cases}$$

3) Update residuals $\left(r_{(j)}^{(k+1)}\right)$ and merit function $\left(m_{(j)}^{(k+1)}\right)$:

$$x_{(j)}^{(k+1)} = \langle x^{(k)} + \alpha_{(j)}^{(k)}d^{(k)}\rangle_{(\Delta\gamma,z)}$$

$$z_j^{k+1} = \frac{\mu_{(j)}^{(m)}}{\Delta\gamma_j^{k+1}}$$

$$r_{(j)}^{(k+1)} = r\left(x_{(j)}^{(k+1)}\right)$$

$$m_{(j)}^{(k+1)} = \frac{1}{2}\left(\left(r_{(j)}^{(k+1)}\right)^T \cdot r_{(j)}^{(k+1)}\right)$$

4) Compute upper limit of Goldstein condition:

If $\left(\text{faux .and. } \left(x^{(k)} + \alpha_{(j)}^{(k)}d^{(k)}\right)_{(\Delta\gamma,z)} > 0\right)$ then

    4.a) $\text{uplim} = \left(1 - 2\beta\alpha_{(j)}^{(k)}\right)m^{(k)}$ else

    4.b) $\text{uplim} = m^{(k)} + \beta r^{(k)}J^{(k)} \cdot \left(x_{(j)}^{(k+1)} - x^{(k)}\right)$ see (Bertsekas, 1986)

  Check Goldstein conditions:

  If $\left(m_{(j)}^{(k+1)}\right) \leq \text{uplim} : \left(x^{(k+1)}, r^{(k+1)}\right) \leftarrow \left(x_{(j)}^{(k+1)}, r_{(j)}^{(k+1)}\right)$ exit.

  If $(j = j_{max})$ notify, set: $\left(x^{(k+1)}, r^{(k+1)}\right) \leftarrow \left(x_{(j)}^{(k+1)}, r_{(j)}^{(k+1)}\right)$ exit.

5) Compute the new value of line-search parameter:

  Cubic backtrack interpolation with first quadratic attempt,

$$\alpha_{(j+1)}^{(k)} = \max\left\{\eta \cdot \alpha_{(j)}^{(k)}, \frac{-\left(\alpha_{(j)}^{(k)}\right)^2 m'^k}{2\left(m_{(j)}^{(k+1)} - m_{(j)}^{(k)} - \alpha_{(j)}^{(k)}m'^k\right)}\right\}$$

6) Set $(j \leftarrow j + 1)$ and go to 3.

The performance of the algorithm "primal-dual IPM" is illustrated below through a series of tests for models studied in chapter 4.

Modified Cam Clay Model has been implemented in both primal-dual CPPM and primal-dual IPM algorithm. Typical responses of the model have been presented in chapter 4 and only algorithm performance is illustrated in this chapter. Figures 5.86 and 5.87 show convergence results obtained from both algorithms, when the slack variable is equal to zero. As expected, they exhibit exactly the same convergence pattern, which provides a validation of the numerical implementation of the algorithms.
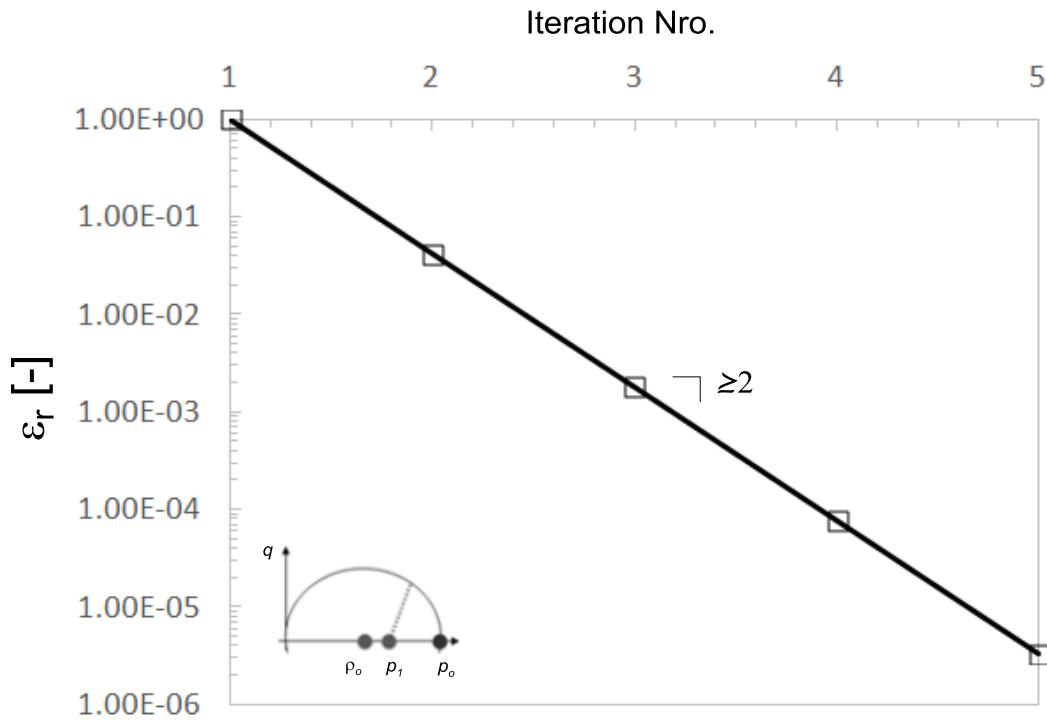
Figure 5.86: Convergence results with the primal-dual CPPM and primal-dual IPM with slack variable equal to 0. Model is tested on the contractant part of the yield surface.
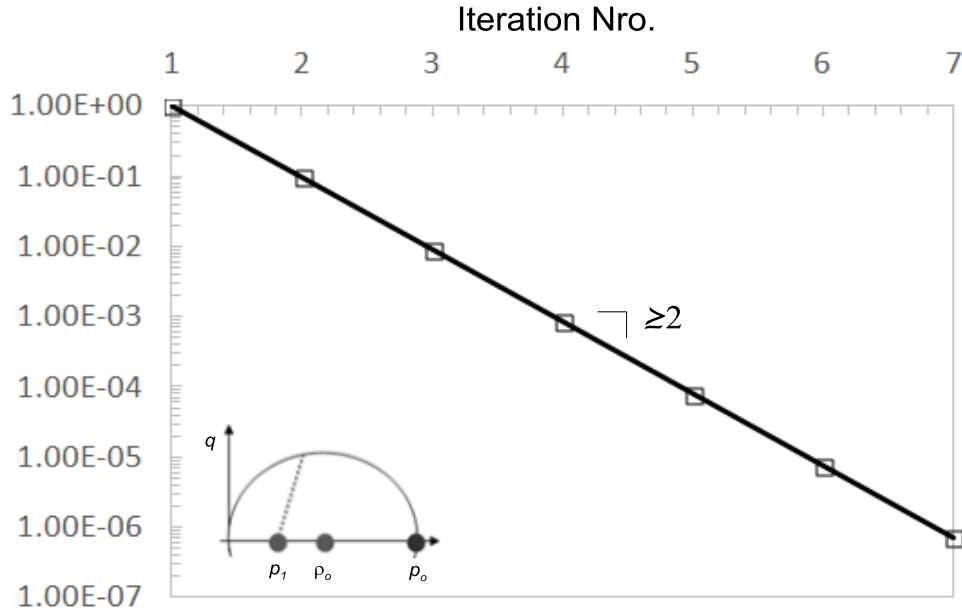
Figure 5.87: Convergence results with the primal-dual CPPM and primal-dual IPM with slack variable equal to 0. Model is tested on the dilatant part of the yield surface.

5.4.3) Consistent Tangent Operator for Hyperplastic Models

The advantage of the proposed algorithms lies in the fact that they can be linearized in a closed form (Simo & Hughes, 1998). This fact leads to the notion of "Consistent Tangent modulus" instead of the "Continuum Elasto-Plastic Tangent modulus". The former is obtained by enforcing the consistency condition on the discrete algorithmic problem, whereas the last notion results from the classical consistency condition of the continuum problem. Next, the procedure followed by Simo & Hughes (1998) is used to derive the algorithmic tangent modulus.

Differentiating the stress-strain relation $\sigma(\varepsilon, \alpha)$ and the algorithmic translation $\rho(\alpha)$, in addition to the flow rule $\dot{\alpha}$ leads to the discrete forms:

$$d\sigma_{n+1} = E : \left[d\varepsilon_{n+1} - d\Delta\gamma_{n+1} \frac{\partial f^y_{n+1}}{\partial x} \right] \tag{5.61}$$

$$d\rho_{n+1} = d\Delta\gamma_{n+1} \frac{\partial^2 g_{2n+1}}{\partial\alpha\,\partial\alpha} \frac{\partial f^y_{n+1}}{\partial x} + \Delta\gamma_{n+1} \frac{\partial^2 g_{2n+1}}{\partial\alpha\,\partial\alpha} \frac{\partial^2 f^y_{n+1}}{\partial x\,\partial x} \frac{\partial x}{\partial\sigma} d\sigma_{n+1}$$

$$d\alpha_{n+1} = d\Delta\gamma_{n+1} \frac{\partial f^y_{n+1}}{\partial x} + \Delta\gamma_{n+1} \frac{\partial^2 f^y_{n+1}}{\partial x\,\partial x} \frac{\partial x}{\partial\sigma} d\sigma_{n+1}$$

where the algorithmic modulus is defined as:

$$E_{n+1} = \left[\frac{\partial^2 g_{n+1}}{\partial \sigma \, \partial \sigma} + \Delta \gamma_{n+1} \frac{\partial^2 f_{n+1}^y}{\partial x \, \partial x} \frac{\partial x}{\partial \sigma}\right]^{-1} \tag{5.62}$$

Additionally, differentiation of the discrete consistency condition $f^y(x) = 0$ gives:

$$\frac{\partial f_{n+1}^y}{\partial x}(d\sigma_{n+1} - d\rho_{n+1}) = 0 \tag{5.63}$$

Equations 5.61 and 5.63 provides the following expression for the incremental plastic multiplier:

$$d\Delta \gamma_{n+1} = \frac{\frac{\partial f_{n+1}^y}{\partial x} \overline{E}_{n+1} d\varepsilon}{H_{n+1} + \left(\nabla^T f_{n+1}^y \overline{C}_{n+1} \nabla f_{n+1}^y\right)} \tag{5.64}$$

where algorithmic moduli $(\overline{E})$ and (H) are given by:

$$\overline{E}_{n+1} = E_{n+1} - \Delta \gamma_{n+1} \frac{\partial^2 g_{2n+1}}{\partial \alpha \, \partial \alpha} \frac{\partial^2 f_{n+1}^y}{\partial x \, \partial x} \frac{\partial x}{\partial \sigma} E_{n+1} \tag{5.65}$$

$$H_{n+1} = -\Delta \gamma \frac{\partial f_{n+1}^y}{\partial x} \frac{\partial^2 g_{2n+1}}{\partial \alpha \, \partial \alpha} \frac{\partial^2 f_{n+1}^y}{\partial x \, \partial x} \frac{\partial x}{\partial \sigma} E_{n+1} \frac{\partial f_{n+1}^y}{\partial x}$$

and $\overline{C}_{n+1}$ and ∇f_{n+1}^y are a compact notation of the following matrix:

$$\overline{C}_{n+1} = \begin{pmatrix} E_{n+1} & 0 \\ 0 & \dfrac{\partial^2 g_{2n+1}}{\partial \alpha \, \partial \alpha} \end{pmatrix} \quad ; \quad \nabla f_{n+1}^y = \begin{pmatrix} \dfrac{\partial f_{n+1}^y}{\partial x} \\ \dfrac{\partial f_{n+1}^y}{\partial x} \end{pmatrix} \tag{5.66}$$

Finally, the substitution of Eq. 5.64 in Eq. 5.61a leads to the expression for the algorithmic elasto-plastic tangent modulus:

$$\left(\frac{d\sigma}{d\varepsilon}\right)_{n+1} = \left[E_{n+1} - \frac{E_{n+1} \frac{\partial f_{n+1}^y}{\partial x} \otimes \frac{\partial f_{n+1}^y}{\partial x} \overline{E}_{n+1}}{H_{n+1} + \left(\nabla^T f_{n+1}^y \overline{C}_{n+1} \nabla f_{n+1}^y\right)}\right] \tag{5.67}$$

for the hyper-poroplastic MCC model.

The tangent modulus obtained in this way, consistent with CPPM and IPM algorithms, is valid for the models developed in terms of Bishop effective stress. As well, the model formulated in terms of net stress BBM will require modifying this tangent operator to introduce suction as a new variable.

5.5) Variational Forms for Unsaturated and Frictional Soils Models

This section describes the numerical implementation of the local continuum equations governing the problem of hyper-poroplasticity in a three-phase medium by CPPM and IPM schemes.

In the first sub-section, a variational structure is proposed to integrate an hysteretic hydraulic response of the model on the basis of the minimization of energy functions g_s and f_s under the constraint provided by the yield surface f^y. The development of the algorithms to perform this integration follows intentionally the same format as for the Modified Cam Clay Model in order to highlight the strong parallelism between mechanical and hydraulic formulations.

The rest of sub-sections address the variational structure for the hydro-mechanical models developed in chapter 4. In all the cases, the local continuum equations are first briefly described followed by their discrete forms and its variational structures. Then the performance analysis of both the CPPM and the IPM algorithms through different tests at Gauss point level is presented. Finally, the observed advantages of the proposed interior-point algorithm are commented.

5.5.1) Integration of hyperplastic retention curve for suction hysteresis

As for the strains, the degree of saturation S_l may be decomposed additively into an elastic and plastic component : $S_l = S_l^e + \alpha_l$. From the hyperplastic state equations, they are related to the gradient of Gibbs function $g_s(s, \alpha_l) = g_{s1}(s, \alpha_l) + g_{s2}(\alpha_l)$ (see sections 4.3 and 4.4) with respect to suction and back suction:

$$S_l = -\frac{\partial g_s(s, \alpha_l)}{\partial s} + \alpha_l$$

$$\rho_s = \frac{\partial g_{s_2}(\alpha_l)}{\partial \alpha_l}$$

(5.68)

The definition of the model is completed by introducing the evolution equations for the internal variables α_l and ρ_s:

$$\dot{\alpha}_l = -\gamma \frac{\partial f^y}{\partial x_s}$$

(5.69)

$$\dot{\rho}_s = \gamma \frac{\partial^2 g_{s_2}}{\partial \alpha_l \partial \alpha_l} \frac{\partial f^y}{\partial x_s}$$

where γ is the plastic multiplier and $\partial f_i^y / \partial x_s$ the flow vector. The plastic multiplier is determined by applying the classical Kuhn-Tucker complementary conditions:

$$\gamma \geq 0 \; ; \; f^y \leq 0 \; ; \; \gamma f^y = 0 \tag{5.70}$$

and the consistency condition:

$$\gamma \dot{f}^y = 0 \tag{5.71}$$

Using the additive decomposition of the degree of saturation and the flow rule, the elastic increment of S_l reads:

$$\dot{S}_l^e = \dot{S}_l - \gamma \frac{\partial f^y}{\partial x_s} \tag{5.72}$$

Equations 5.69 to 5.71 define the structure of the problem driven by the degree of saturation. The enforcement of the consistency condition Eq. 5.70 allows to express the plastic multiplier γ as:

$$\gamma = \frac{1}{h} \frac{\partial f^y}{\partial x_s} \frac{\partial x_s}{\partial s} \frac{\partial^2 f_s}{\partial S_l \partial S_l} \dot{S}_l \tag{5.73}$$

where h is the hardening modulus given by $h = \nabla f_i^{y^T} \nabla^2 f_i \nabla f_i^y$.

To integrate the model over a discrete suction increment in time interval $\Delta t = t_{n+1} - t_n$, the hardening laws are linearized according to:

$$\begin{aligned}
\alpha_{l_{n+1}} - \alpha_{l_n} + \Delta\gamma \frac{\partial f^y(x_{s_{n+1}})}{\partial x_s} &= 0 \\
\rho_{s_{n+1}} - \rho_{s_n} + \Delta\gamma \frac{\partial^2 g_s}{\partial \alpha_l \partial \alpha_l} \frac{\partial f^y(x_{s_{n+1}})}{\partial x} &= 0
\end{aligned} \tag{5.74}$$

where $\Delta\gamma$ is the discrete increment of plastic multiplier. $\Delta\gamma$ must satisfy the loading-unloading conditions:

$$\Delta\gamma \geq 0 \; ; \; f_{i_{n+1}}^y \leq 0 \; ; \; \Delta\gamma f_{i_{n+1}}^y = 0 \tag{5.75}$$

In a first step, an elastic trial $S_{l_{n+1}}^{e\,trial}$ is computed for the degree of saturation at time t_{n+1}:

$$\begin{aligned}
s_{n+1} &= s_n + \Delta s_{n+1} \\
S_l^{trial}{}_{n+1} &= S_{l_n} + \Delta S_{l_{n+1}}
\end{aligned} \tag{5.76}$$

The numerical solution of the system of equations 5.74 together with Eqs. 5.75-5.76 is accomplished following a predictor-corrector strategy. To this end the elastic trial state is defined by taking the value at t_n of the internal variable α_l:

$$\alpha_{l_{n+1}}^{trial} = \alpha_{l_n} \tag{5.77}$$

and computing accordingly the back suction and elastic part of degree of saturation:

$$\rho_{s_{n+1}}^{trial} = \left.\frac{\partial g_{s_2}}{\partial \alpha_l}\right|_{\alpha_{l_{n+1}}^{trial}} \tag{5.78}$$

$$S_{l_{n+1}}^{e^{trial}} = S_{l_n}^e - \left.\frac{\partial^2 g_s}{\partial s\,\partial s}\right|_{s_n,\rho_{s_n}} \Delta s_{n+1}$$

The admissibility of the elastic trial is checked from the condition:

$$\text{If }\ \left(f_{i_{n+1}}^{y^{trial}}\left(s_{n+1},\rho_{s_{n+1}}^{trial}\right) \le 0\right)\ \ \text{then } (\blacksquare)_{n+1} = (\blacksquare)_{n+1}^{trial} \tag{5.79}$$

If the trial guess is not admissible, a solution with $\Delta\gamma > 0$ is looked for, leading to the plastic corrector step, with:

$$S_{l_{n+1}}^e = S_{l_{n+1}} - \alpha_{l_{n+1}} \tag{5.80}$$

$$S_{l_{n+1}}^{e^{trial}} = S_{l_{n+1}} - \alpha_{l_n}$$

and:

$$-S_{l_{n+1}}^e + S_{l_{n+1}}^{e^{trial}} + \Delta\gamma\frac{\partial f^y\left(x_{s_{n+1}}\right)}{\partial x_s} \quad = \quad 0 \tag{5.81}$$

$$\rho_{s_{n+1}} - \rho_{s_{n+1}}^{trial} + \Delta\gamma\frac{\partial^2 g_{i_2}}{\partial\alpha_l\,\partial\alpha_l}\frac{\partial f^y\left(x_{s_{n+1}}\right)}{\partial x_s} \quad = \quad 0$$

The set of nonlinear equations 5.81 is solved using a Newton-like iterative strategy (like the one exposed in unconstrained optimization theory). The existence of a variational structure underlying the CPPM and IPM methods relies on the specific forms of the general evolution equations, governed themselves by the expressions of the energy functions.

Such functions studied at chapter 4 can be classified as belonging to the set of "generalized convexity" functions. In particular, Gibbs energy function g_s defined in section 4.4 falls within the definition of a pseudo-convex function: $(s_1 - s_2)\nabla g_i(s_2) \ge 0$ implies$\left(g_i(s_1) \ge g_i(s_2)\right)$ (Avriel, (1976)) while the yield function f^y belongs to the family of the strictly convex functions.

Then the optimization problem considered, consists in minimizing the Helmholtz free energy expressed in terms of degree of saturation and generalized suction $\bar{f}_s(S_l, \bar{x}_s)$. It is computed as a Legendre transformation of Gibbs energy $g_s(s, \alpha_l)$:

$$\bar{f}_s(S_l, \bar{x}_s) = \min_{(s, \alpha_l) \in E} \{g_s(s, \alpha_l) - (sS_l + \bar{x}_s\alpha_l)\} \tag{5.82}$$

where $\bar{x}_s$ is derived from the state equation $\partial g_s(s, \alpha_l)/\partial\alpha_l$. Using the orthogonality rule $(\bar{x}_s = x_s)$ the minimization program reads:

$$\boxed{\begin{array}{c} \text{Find } \left(S_{l_{n+1}}, x_{s_{n+1}}\right) \in E \text{ such that} \\ \bar{f}_i\left(S_{l_{n+1}}, x_{s_{n+1}}\right) = \min_{(s, \alpha_l) \in E} \left\{g_i(s, \alpha_l) - \left(sS_{l_{n+1}}^{e^{trial}} + x_{s_{n+1}}^{trial}\alpha_l\right)\right\} \end{array}} \tag{5.83}$$

It can be expressed alternatively as the inequality mathematical program:

$$\text{CPPM} \begin{cases} \min & g_s(s, \alpha_l) - \left(sS_{l_{n+1}}^{e^{trial}} + x_{s_{n+1}}^{trial}\alpha_l\right) \\ (s, \alpha_l) & \\ \text{sub. to} & f^y(x_s) \leq 0 \end{cases} \tag{5.84}$$

Now, from standard arguments in constraint optimization the Lagrange functional associated to the variational problem 5.84 is:

$$\mathcal{L}^g(s, \alpha_l, \Delta\gamma) = g_s(s, \alpha_l) - \left(sS_{l_{n+1}}^{e^{trial}} + x_{s_{n+1}}^{trial}\alpha_l\right) + \Delta\gamma f^y(x_s) \tag{5.85}$$

The application of the first order optimality conditions at Eq. 5.84 leads to the Kuhn-Tucker restrictions. By using: (a) Eq. 5.80, (b) the state equations $S_l = \partial g_s(s, \alpha_l)/\partial s$ and $x_s = \partial g_s(s, \alpha_l)/\partial\alpha_l$ and (c) the fundamental relation $\rho_{s_{n+1}}^{trial} = s_{n+1} - x_{s_{n+1}}^{trial}$, the last restrictions are expressed by the discrete system:

$$\begin{array}{rcl} -S_{l_{n+1}}^e + S_{l_{n+1}}^{e^{trial}} + \Delta\gamma\dfrac{\partial f^y\left(x_{s_{n+1}}\right)}{\partial x_s}\dfrac{\partial x_s}{\partial s} & = & 0 \\[4mm] \rho_{s_{n+1}} - \rho_{s_{n+1}}^{trial} + \Delta\gamma\dfrac{\partial f^y\left(x_{s_{n+1}}\right)}{\partial x_s}\dfrac{\partial x_s}{\partial\rho_s}\dfrac{\partial^2 g_{s_2}}{\partial\alpha_l\,\partial\alpha_l} & = & 0 \\[4mm] f^y\left(x_{s_{n+1}}\right) & \leq & 0 \\[2mm] \Delta\gamma & \geq & 0 \end{array} \tag{5.86}$$

The residual vector coming out from Eq. 5.86 reads:

$$r(x) = \begin{cases} -S_{l_{n+1}}^e + S_{l_{n+1}}^{e^{trial}} + \Delta\gamma\dfrac{\partial f_{n+1}^y(x_s)}{\partial x}\dfrac{\partial x}{\partial\sigma} \\[4mm] \rho_{s_{n+1}} - \rho_{s_{n+1}}^{trial} + \Delta\gamma\dfrac{\partial f_{n+1}^y(x_s)}{\partial x}\dfrac{\partial x}{\partial\rho}\dfrac{\partial^2 g_{s_2}}{\partial\alpha\,\partial\alpha} \\[4mm] f_{n+1}^y(x_s) \end{cases} \tag{5.87}$$

and the Jacobian matrix takes the form:

$$J(x) = \begin{bmatrix} -1 + \Delta\gamma \dfrac{\partial^2 f^y}{\partial x_s \partial x_s} \dfrac{\partial^2 f_s}{\partial S_l \partial S_l} & \Delta\gamma \dfrac{\partial^2 f^y}{\partial x_s \partial x_s} \dfrac{\partial x_s}{\partial s} \dfrac{\partial x_s}{\partial \rho_s} & \dfrac{\partial f^y}{\partial x_s} \dfrac{\partial x_s}{\partial s} \\[2em] \Delta\gamma \dfrac{\partial^2 f^y}{\partial x_s \partial x_s} \dfrac{\partial x_s}{\partial \rho_s} \dfrac{\partial x_s}{\partial s} \dfrac{\partial^2 g_{s_2}}{\partial \alpha_l \partial \alpha_l} \dfrac{\partial^2 f_s}{\partial S_l \partial S_l} & 1 + \Delta\gamma \dfrac{\partial^2 f^y}{\partial x_s \partial x_s} \dfrac{\partial^2 g_{s_2}}{\partial \alpha_l \partial \alpha_l} & \dfrac{\partial f^y}{\partial x_s} \dfrac{\partial x_s}{\partial \rho_s} \dfrac{\partial^2 g_{s_2}}{\partial \alpha_l \partial \alpha_l} \\[2em] \dfrac{\partial f^y}{\partial x_s} \dfrac{\partial x_s}{\partial s} \dfrac{\partial^2 f_s}{\partial S_l \partial S_l} & \dfrac{\partial f^y}{\partial x_s} \dfrac{\partial x_s}{\partial \rho_s} & 0 \end{bmatrix} \quad (5.88)$$

Both the residual vector 5.87 and the Jacobian matrix 5.88 are used in the CPPM algorithm to compute the advance direction to search for the solution state (the optimal point). Another possibility is to rewrite the constraint program 5.84 into the standard form of equality constraint by introducing the slack variable z:

$$\text{IPM} \quad \begin{cases} \min\limits_{(s,\alpha_l)} & g_s(s,\alpha_l) - \left(sS_{l_{n+1}}^{etrial} + x_{s_{n+1}}^{trial}\alpha_l \right) + \mu \cdot \log(z) \\ \text{sub. to} & f^y(x_s) + z = 0 \end{cases} \quad (5.89)$$

In this formulation, the Lagrange functional associated with the equality constraint program 5.89 is given by:

$$\mathcal{L}^g(s,\alpha_l,\Delta\gamma) = g_s(s,\alpha_l) - \left(sS_{l_{n+1}}^{etrial} + x_{s_{n+1}}^{trial}\alpha_l \right) + \Delta\gamma[f^y(x_s) + z] + \mu \cdot \log(z) \quad (5.90)$$

which by virtue of the first order optimality conditions leads to the Kuhn-Tucker restrictions:

$$\begin{aligned} -S_{l_{n+1}}^e + S_{l_{n+1}}^{etrial} + \Delta\gamma \dfrac{\partial f^y\left(x_{s_{n+1}}\right)}{\partial x_s} \dfrac{\partial x_s}{\partial s} &= 0 \\ \rho_{s_{n+1}} - \rho_{s_{n+1}}^{trial} + \Delta\gamma \dfrac{\partial f^y\left(x_{s_{n+1}}\right)}{\partial x_s} \dfrac{\partial x_s}{\partial \rho_s} \dfrac{\partial^2 g_{s_2}}{\partial \alpha_l \partial \alpha_l} &= 0 \\ f^y\left(x_{s_{n+1}}\right) + z &= 0 \\ \Delta\gamma - \dfrac{\mu}{z} &= 0 \\ (\Delta\gamma, z) &\geq 0 \end{aligned} \quad (5.91)$$

Then the residual vector used in the IPM algorithm reads:

$$r(x) = \begin{Bmatrix} -S_{l_{n+1}}^e + S_{l_{n+1}}^{etrial} + \Delta\gamma \dfrac{\partial f_{n+1}^y(x_s)}{\partial x} \dfrac{\partial x}{\partial \sigma} \\[1.5em] \rho_{s_{n+1}} - \rho_{s_{n+1}}^{trial} + \Delta\gamma \dfrac{\partial f_{n+1}^y(x_s)}{\partial x} \dfrac{\partial x}{\partial \rho} \dfrac{\partial^2 g_{s_2}}{\partial \alpha \partial \alpha} \\[1.5em] f_{n+1}^y(x_s) + z \\[0.5em] \Delta\gamma \cdot z - \mu \end{Bmatrix} \quad (5.92)$$

and the Jacobian matrix takes the form:

$$J(x) \tag{5.93}$$

$$= \Delta\gamma \begin{bmatrix} -1 + \Delta\gamma \dfrac{\partial^2 f^y}{\partial x_s\, \partial x_s} \dfrac{\partial^2 f_s}{\partial S_l\, \partial S_l} & \Delta\gamma \dfrac{\partial^2 f^y}{\partial x_s\, \partial x_s} \dfrac{\partial x_s}{\partial s} \dfrac{\partial x_s}{\partial \rho_s} & \dfrac{\partial f^y}{\partial x_s} \dfrac{\partial x_s}{\partial s} & 0 \\[2.5ex] \Delta\gamma \dfrac{\partial^2 f^y}{\partial x_s\, \partial x_s} \dfrac{\partial x_s}{\partial \rho_s} \dfrac{\partial x_s}{\partial s} \dfrac{\partial^2 g_{s_2}}{\partial \alpha_l\, \partial \alpha_l} \dfrac{\partial^2 f_s}{\partial S_l\, \partial S_l} & 1 + \Delta\gamma \dfrac{\partial^2 f_i^y}{\partial x_s\, \partial x_s} \dfrac{\partial^2 g_{i_2}}{\partial \alpha_l\, \partial \alpha_l} & \dfrac{\partial f_i^y}{\partial x_s} \dfrac{\partial x_s}{\partial \rho_s} \dfrac{\partial^2 g_{i_2}}{\partial \alpha_l\, \partial \alpha_l} & 0 \\[2.5ex] \dfrac{\partial f^y}{\partial x_s} \dfrac{\partial x_s}{\partial s} \dfrac{\partial^2 f_s}{\partial S_l\, \partial S_l} & \dfrac{\partial f^y}{\partial x_s} \dfrac{\partial x_s}{\partial \rho_s} & 0 & 1 \\[2.5ex] 0 & 0 & z & \Delta\gamma \end{bmatrix}$$

Figure 5.88 shows geometric and numerical convergence properties of the implemented integration scheme.

Fig. 5.88a shows the return processes for a suction-increase step and a suction-decrease step. Both the back suction and the generalized suction are depicted in this figure. Fig. 5.88b shows the convergence rate of Wheeler's wrc hyperplastic model for two different loading steps. The speed of convergence is slightly higher than 2.
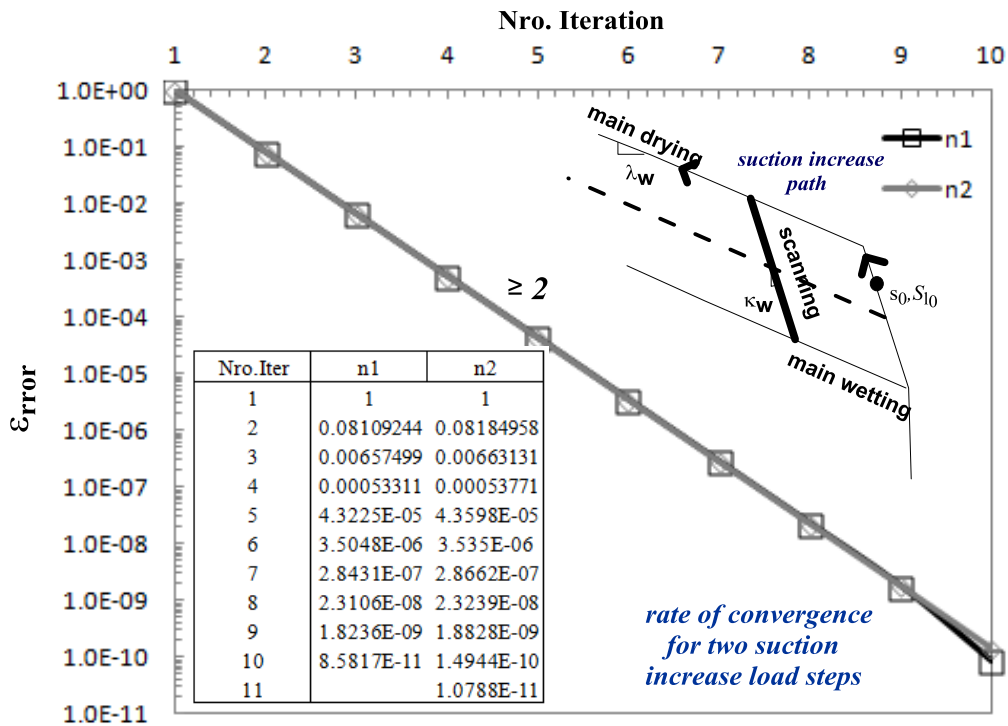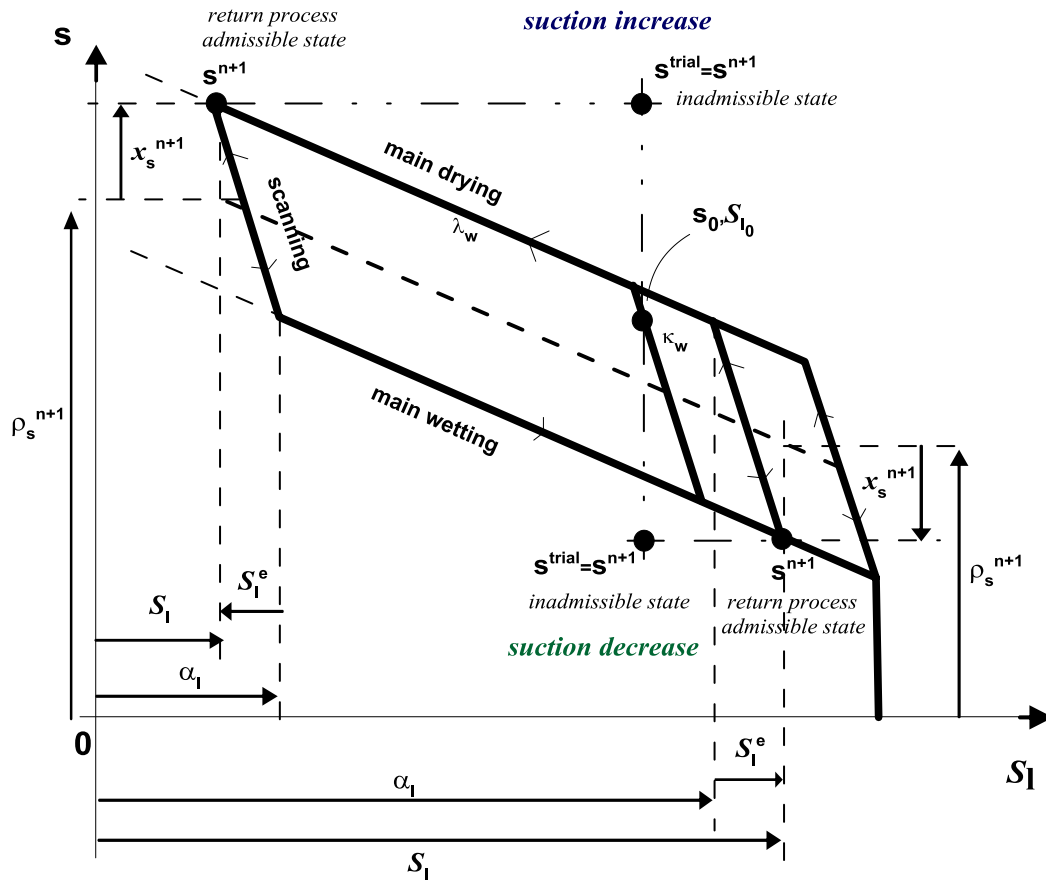
Figure 5.88: WRC integration: (a)Return processes for suction increase and suction decrease. (b)Convergence results with the primal-dual IPM with slack variable $\mu^0 = 0$, convergence model is tested against a suction increase path.

5.5.2) Integration of Gallipoli's et al. model - pure isotropic hardening BBM1

In this sub-section the local continuum equations governing the problem of hyper-poroplasticity in a three-phase medium ("the solid matrix + the interface skin"= the porous skeleton) and its numerical approximation using both the closest-point projection and the interior-point scheme are described. As before, for the biphasic medium, infinitesimal deformations are considered in the three-phase medium. Then the strains ε identified as $(\nabla^s u)$ are assumed to be decomposed additively as $(\varepsilon = \varepsilon^e + \alpha)$, sum of the elastic and plastic strain components.

Let (σ') be the effective Bishop Stress tensor and $(\rho' = 0)$ the effective shift stress tensor that characterizes the hardening of the material. Assuming a reversible behavior of the capillary curve, the non-incremental constitutive relationships for the **BBM1** model (pure isotropic hardening) take the form,

$$\sigma' = \frac{\partial f_s^g(\varepsilon, \alpha, \phi s)}{\partial \varepsilon} \tag{5.94}$$

$$S_l = \frac{\partial f_s^g(\varepsilon, \alpha, \phi s)}{\partial \phi s}$$

where $f_s(\varepsilon, \alpha, \phi s)$ is the Helmholtz energy function of the porous skeleton defined at chapter 4 of the present dissertation. Because the component of stored energy $f_{s_2} = 0$ is null then ρ' vanishes and all the generated plastic work is dissipated. In addition, the evolution equation for the plastic internal variable (α) reads,

$$\dot{\alpha} = \gamma \frac{\partial f^y(\sigma', \alpha, \phi s)}{\partial \sigma'} \tag{5.95}$$

where, (γ) is the scalar plastic multiplier and $\left(\frac{\partial f^y(\sigma', \alpha, \phi s)}{\partial \sigma'} \right)$ is the general flow vector. In this context the plastic multiplier is determined by the classical Kuhn-Tucker complementary conditions,

$$\gamma \geq 0 \; ; \; f^y(\sigma', \alpha, \phi s) \leq 0 \; ; \; \gamma \cdot f^y(\sigma', \alpha, \phi s) = 0 \tag{5.96}$$

which leads to the consistency condition,

$$\gamma \cdot \dot{f}^y(\sigma', \alpha, \phi s) = 0 \tag{5.97}$$

Equation 5.96 characterizes the loading-unloading conditions with Eq. 5.97 defining the persistency of the plastic state during plastic flow.

It is important to notice that the flow rule 5.95 can be written, using the additive decomposition of strains, in the equivalent form,

$$\dot{\varepsilon}^e = \dot{\varepsilon} - \gamma \frac{\partial f^y(\sigma', \alpha, \phi s)}{\partial \sigma'} \tag{5.98}$$

Equations 5.96 to 5.98 define the strain-driven structure of the problem. It is, for a given increment of the total strain the last set of equations determine the increments of stress (σ) and plastic internal variable(α).

The constitutive relation described above is integrated over time in a strain-driven structure. In this framework the stresses and internal variables are updated from their known values at certain time for a given strain increment in time ($\Delta t = t_{n+1} - t_n$). In such a scheme all the variables are known at (t_n) and updated at time (t_{n+1}) according to the strain increment ($\Delta \varepsilon_{n+1}$) and to the suction increment (Δs_{n+1}), leading to,

$$\varepsilon_{n+1} = \varepsilon_n + \Delta \varepsilon_{n+1} \tag{5.99}$$
$$s_{n+1} = s_n + \Delta s_{n+1}$$

while the stresses (σ_{n+1}) and the updated plastic internal variable (α_{n+1}) have to be computed. To this purpose the backward-Euler approximation of the governing equations is used,

$$-\alpha_{n+1} + \alpha_n + \Delta \gamma \frac{\partial f^y(\sigma'_{n+1}, \alpha_{n+1}, \phi s_{n+1})}{\partial \sigma'} = 0 \tag{5.100}$$

where the plastic multiplier ($\Delta \gamma$) must satisfy the loading-unloading conditions:

$$\Delta \gamma \geq 0 \; ; \; f^y_{n+1} \leq 0 \; ; \; \Delta \gamma \cdot f^y_{n+1} = 0 \tag{5.101}$$

The updated stress tensor and degree of saturation are given by the state equations 5.94 leading to the discrete form:

$$\sigma'_{n+1} = \frac{\partial f^g_s(\varepsilon_{n+1}, \alpha_{n+1}, \phi s_{n+1})}{\partial \varepsilon} \tag{5.102}$$

$$S_{l_{n+1}} = \frac{\partial f^g_s(\varepsilon_{n+1}, \alpha_{n+1}, \phi s_{n+1})}{\partial \phi s}$$

The numerical solution of the algebraic system of equations defined by Eqs. 5.100 to 5.102 is accomplished following a predictor-corrector strategy. The predictor step is conducted introducing the trial state defined by the known values at (t_n),

$$\alpha^{trial}_{n+1} = \alpha_n \tag{5.103}$$

and the corresponding stress values,

$$\sigma_{n+1}'^{\text{trial}} = \frac{\partial f_s\left(\varepsilon_{n+1}, \alpha_{n+1}^{\text{trial}}, \phi s_{n+1}\right)}{\partial \varepsilon} \tag{5.104}$$

and in this environment the loading-unloading conditions are checked:

$$\text{If } \left(f_{n+1}^{\text{y trial}}\left(\sigma_{n+1}'^{\text{trial}}, \alpha_{n+1}^{\text{trial}}, \phi s_{n+1}\right) \le 0\right) \quad \text{then } (\blacksquare)_{n+1} = (\blacksquare)_{n+1}^{\text{trial}} \tag{5.105}$$

then the trial state is taken as the final solution.

If not, a new solution with $(\Delta\gamma > 0)$ is being looked for, leading to the so-called plastic corrector step. Noting that,

$$\varepsilon_{n+1}^e = \varepsilon_{n+1} - \alpha_{n+1} \tag{5.106}$$
$$\varepsilon_{n+1}^{e \text{ trial}} = \varepsilon_{n+1} - \alpha_n$$

The equation 5.100 can be re-written equivalently in terms of the elastic strains (ε_{n+1}^e) and the elastic trial strains $\left(\varepsilon_{n+1}^{e \text{ trial}}\right)$ as,

$$\varepsilon_{n+1}^e - \varepsilon_{n+1}^{e \text{ trial}} + \Delta\gamma \frac{\partial f^y(\sigma_{n+1}', \alpha_{n+1}, \phi s_{n+1})}{\partial \sigma'} = 0 \tag{5.107}$$

The nonlinear equation 5.107 is solved using a Newton-like iterative strategy. Despite the discrete version of the constitutive equations describing a triphasic model, the algorithms (CPPM) and (IPM) are properly understood by finding the existence of a variational structure of the general evolution equations.

The energy functions developed in the former chapter for the Gallipoli's model **BBM1** present convex characteristics with respect to its arguments according to definition at Box 5.3 and are twice differentiable with positive definite Hessian matrix $\nabla^2 f_s$, as well. Under these properties the complementary Gibbs free energy function $g_s(\sigma', \alpha, \phi s)$ is introduced as a Legendre transformation of the Helmholtz free energy $f_s^g(\varepsilon, \alpha, \phi s)$ it is,

$$g_s(\sigma', \alpha, \phi s) = \min_{(\sigma') \in E} \left\{f_s^g(\varepsilon, \alpha, \phi s) - \sigma'\varepsilon\right\} \tag{5.108}$$

here the strain tensor (ε) is derived from the state equation,

$$\varepsilon = -\frac{\partial g_s(\sigma', \alpha, \phi s)}{\partial \sigma'} \tag{5.109}$$

and $\nabla^2 g_s = (\nabla^2 f_s)^{-1}$. Under the convexity properties of the energy functions and the yield surface describing the **BBM1** model, the formulation of the minimization problem is then:

| Find $(\varepsilon_{n+1}) \in E$ such that | (5.110) |

$$f_s^g(\varepsilon_{n+1}, \alpha_{n+1}, \phi s_{n+1}) = \min_{(\sigma') \in E} \{-g_s(\sigma', \alpha, \phi s) - (\sigma' \varepsilon_{n+1})\}$$

Which can be alternatively expressed as the inequality mathematical program:

$$\text{CPPM} \begin{cases} \min_{(\sigma')} & -g_s(\sigma', \alpha, \phi s) - (\sigma' \varepsilon_{n+1}) \\ \text{sub. to} & f^y(\sigma', \alpha, \phi s) \leq 0 \end{cases} \tag{5.111}$$

Now from standard arguments in constraint optimization the Lagrange functional associated to the variational problem 5.111 is,

$$\mathcal{L}^g(\sigma', \alpha, \phi s, \Delta\gamma) = -g_s(\sigma', \alpha, \phi s) - \sigma' \varepsilon_{n+1} + \Delta\gamma \cdot f^y(\sigma', \alpha, \phi s) \tag{5.112}$$

The application of the necessary first order optimality conditions to 5.112 leads to the Kuhn-Tucker restrictions. By using 5.106 and the state equation 5.109, these restrictions can be expressed as:

$$\begin{aligned} \varepsilon_{n+1}^e - \varepsilon_{n+1}^{e\,trial} + \Delta\gamma \frac{\partial f^y(\sigma'_{n+1}, \alpha_{n+1}, \phi s_{n+1})}{\partial \sigma'} &= 0 \\ f_{n+1}^y(\sigma', \alpha, \phi s) &= 0 \\ \Delta\gamma &\geq 0 \end{aligned} \tag{5.113}$$

From the first optimality KKT conditions 5.113 the residual vector of unbalance strains is:

$$r(x) = \begin{cases} \varepsilon_{n+1}^e - \varepsilon_{n+1}^{e\,trial} + \Delta\gamma \frac{\partial f_{n+1}^y}{\partial \sigma'} \\ f_{n+1}^y \end{cases} \tag{5.114}$$

and the Jacobian matrix of the residual vector used to compute the advance direction to search for the solution state (optimal point) is given by:

$$J(x) = \begin{bmatrix} I + \Delta\gamma \left(\dfrac{\partial^2 f^y}{\partial \sigma' \partial \sigma'} \dfrac{\partial^2 f_s}{\partial \varepsilon \partial \varepsilon} + \dfrac{\partial^2 f^y}{\partial \sigma' \partial \alpha} \dfrac{\partial \alpha}{\partial \varepsilon^e} \right) & \dfrac{\partial f^y}{\partial \sigma'} \\ \dfrac{\partial f^y}{\partial \sigma'} \dfrac{\partial^2 f_s}{\partial \varepsilon \partial \varepsilon} + \dfrac{\partial f^y}{\partial \alpha} \dfrac{\partial \alpha}{\partial \varepsilon^e} & 0 \end{bmatrix} \tag{5.115}$$

Both the residual vector 5.114 and the Jacobian matrix 5.115 are used in the algorithm primal-dual CPPM developed above.

If the constraint program 5.111 is re-written in the standard form of equality constraint by introducing the slack variables (z) then:

$$\text{IPM} \begin{cases} \min & -g_s(\sigma', \alpha, \phi s) - \sigma' \varepsilon_{n+1} + \mu \cdot \log(z) \\ (\sigma') & \\ \text{sub. to} & f^y(\sigma', \alpha, \phi s) + z = 0 \end{cases} \qquad (5.116)$$

In this case the Lagrange functional is expressed as:

$$\mathcal{L}^g(\sigma', \alpha, \phi s, \Delta\gamma) = -g_s(\sigma', \alpha, \phi s) - \sigma' \varepsilon_{n+1}^{trial} + \Delta\gamma[f^y + z] + \mu \cdot \log(z) \qquad (5.117)$$

which again presents an additional term with respect to 5.112. In this scenario an extended form of the Kuhn-Tucker restrictions is obtained:

$$\begin{aligned} \varepsilon_{n+1}^e - \varepsilon_{n+1}^{e\,trial} + \Delta\gamma \frac{\partial f^y(\sigma'_{n+1}, \alpha_{n+1}, \phi s_{n+1})}{\partial \sigma'} &= 0 \\ f_{n+1}^y(\sigma') + z &= 0 \\ \Delta\gamma - \frac{\mu}{z} &= 0 \\ (\Delta\gamma, z) &\geq 0 \end{aligned} \qquad (5.118)$$

and as before the residual vector of unbalance strains and the Jacobian matrix of this residual are:

$$r(x) = \begin{cases} \varepsilon_{n+1}^e - \varepsilon_{n+1}^{e\,trial} + \Delta\gamma \dfrac{\partial f^y(\sigma'_{n+1}, \alpha_{n+1}, \phi s_{n+1})}{\partial \sigma'} \\ f_{n+1}^y(\sigma') + z \\ \Delta\gamma \cdot z - \mu \end{cases} \qquad (5.119)$$

$$J(x) = \begin{bmatrix} I + \Delta\gamma\left(\dfrac{\partial^2 f^y}{\partial \sigma' \partial \sigma'}\dfrac{\partial^2 f_s}{\partial \varepsilon \partial \varepsilon} + \dfrac{\partial^2 f^y}{\partial \sigma' \partial \alpha}\dfrac{\partial \alpha}{\partial \varepsilon^e}\right) & \dfrac{\partial f^y}{\partial \sigma'} & 0 \\ \dfrac{\partial f^y}{\partial \sigma'}\dfrac{\partial^2 f_s}{\partial \varepsilon \partial \varepsilon} + \dfrac{\partial f^y}{\partial \alpha}\dfrac{\partial \alpha}{\partial \varepsilon^e} & 0 & 1 \\ 0 & z & \Delta\gamma \end{bmatrix} \qquad (5.120)$$

Both algorithmic elements are essential to compute the advance direction searching for the solution state (the optimal point). So they are used at the algorithm primal-dual IPM described above.

Figures 5.89 to 5.90 show the convergence results obtained from both the (primal − dual CPPM) and the (primal − dual IPM) algorithms when the model BBM1 is integrated.

Figure 5.89 shows the convergence properties of the model BBM1 under saturated and isothermal conditions.
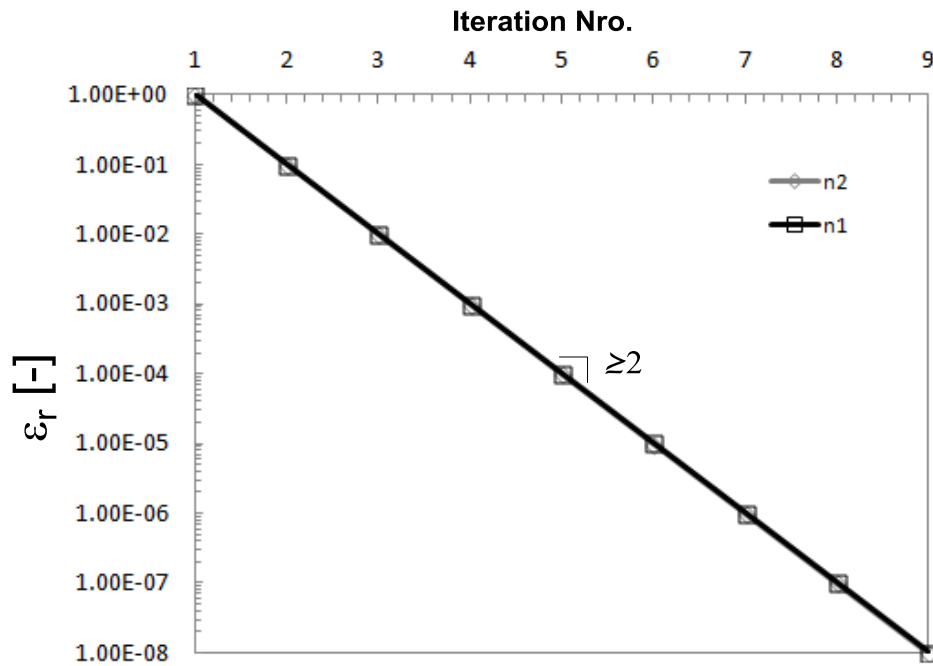
Figure 5.89: Convergence Results with the primal-dual CPPM and primal-dual IPM ($\mu = 0$). Both show the same results for the same starting trial state($s^0 = 0.0MPa$).

The slope of the straight line results lightly higher than 2 (2.298). Table 5.22 summarizes the convergence properties of the BBM1 model for two different loading steps.

Table 5.22: Table of convergence for the model BBM1 for two loading steps

N-iter	$\frac{\|r\|}{\|r^0\|}$ (n1)	$\frac{\|r\|}{\|r^0\|}$ (n2)
1	1	1
2	0.09926911	0.09915203
3	0.00996116	0.00993808
4	0.00100146	0.000998
5	0.0001007	0.00010024
6	1.0126E-05	1.0068E-05
7	1.0182E-06	1.0113E-06
8	1.0239E-07	1.0157E-07
9	1.0296E-08	1.0202E-08

Figure 5.90 shows the convergence properties of the algorithm integrating BBM1 model under two different states of partial saturation.

288
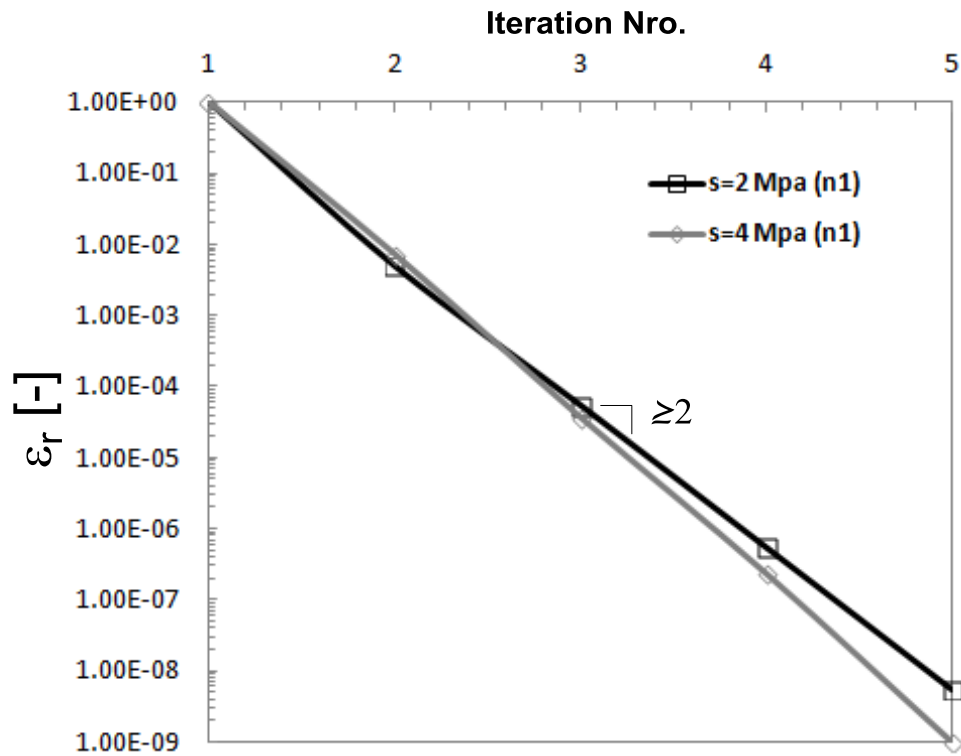
Figure 5.90: Convergence Results of the primal-dual CPPM for two different suction states; a) $\left(s_a^0 = 2MPa\right)$ and b) $\left(s_b^0 = 4MPa\right)$.

The slope of the straight line which is higher than 2 (≈ 3) shows the convergence properties of the BBM1 model for two different suctions. Fig. 5.91 shows the convergence properties of the algorithm integrating BBM1 model at a state of partial saturation for two different loading conditions.
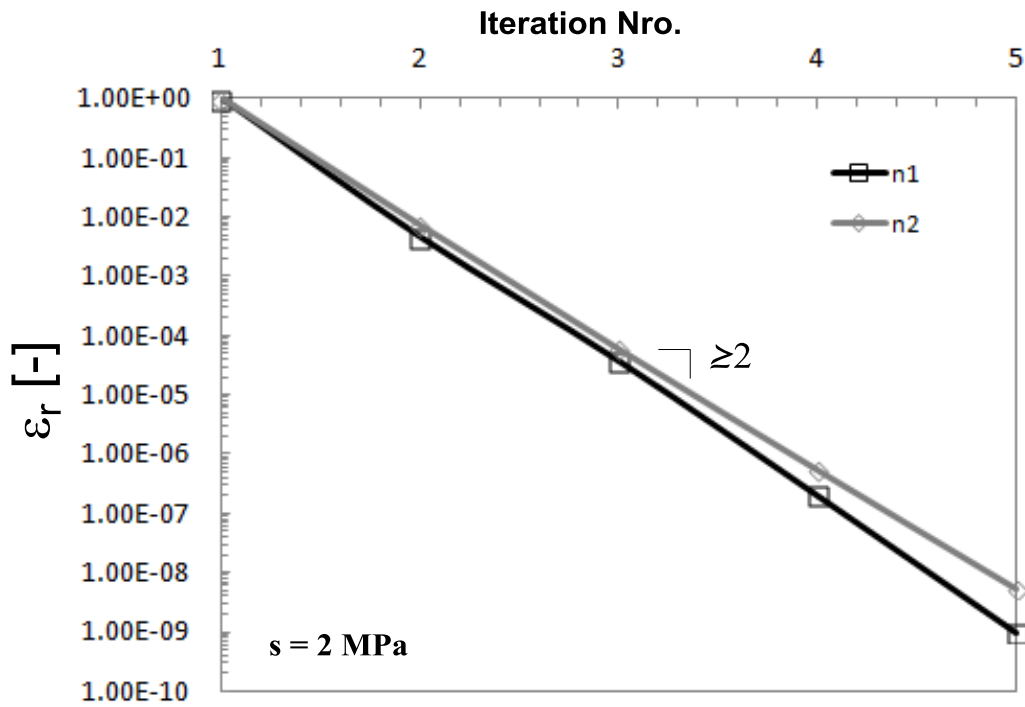
Figure 5.91: Convergence Results of the primal-dual CPPM for two different loading steps at a suction of 2MPa.

The slope of the straight line results lightly higher than 2 (≈ 3). Fig. 5.92 shows the convergence properties of the algorithm integrating BBM1 model at a state of partial saturation for two different thermal conditions.
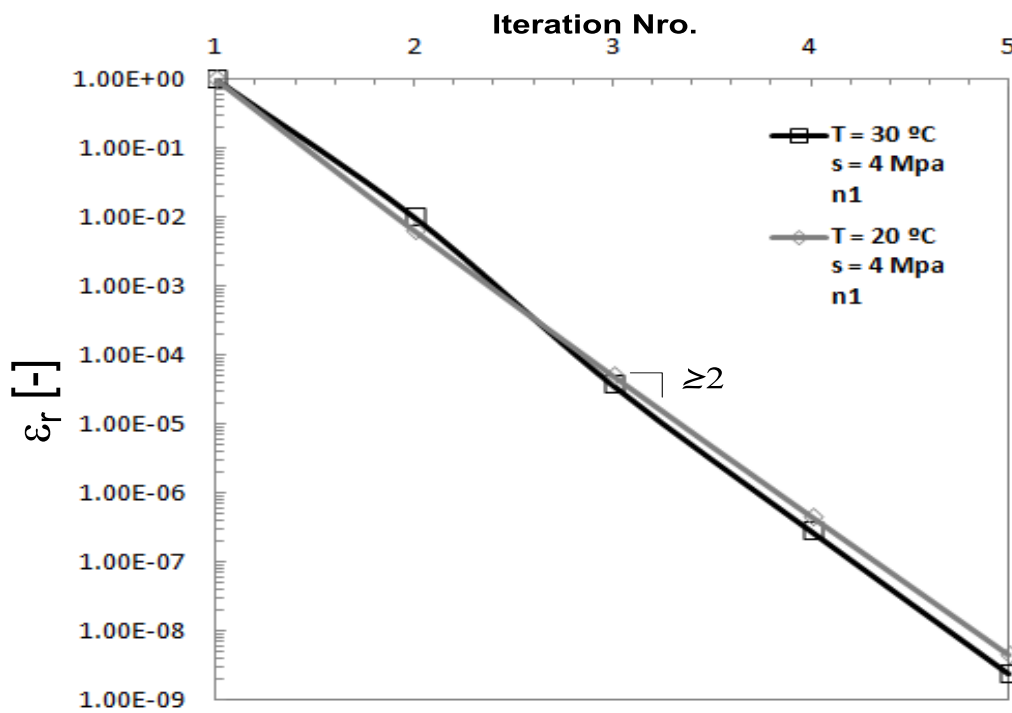
Figure 5.92: Convergence Results of the primal-dual CPPM for two different Temperatures and under non-isothermal conditions s=4MPa.

The slope of the straight line which is higher than 2 (≈ 3) shows the convergence properties of the BBM1 model for the two different temperatures and under non-saturated conditions.

5.5.3) Integration of Gallipoli's et al. model - pure kinematic hardening BBM2

The derivation of Gallipoli's model within a hyper-poroplastic approach, assuming that the hardening developed during plastic flow is purely kinematic **BBM2**, is defined by the non-incremental constitutive relations:

$$\sigma' = \frac{\partial f_s^g(\varepsilon, \alpha, \phi s)}{\partial \varepsilon} \tag{5.121}$$

$$\rho' = \frac{\partial f_{s_2}^g(\alpha)}{\partial \alpha}$$

$$S_l = \frac{\partial f_s^g(\varepsilon, \alpha, \phi s)}{\partial \phi s}$$

where $f_s^g(\varepsilon, \alpha, \phi s)$ is the energy function of the porous skeleton defined at chapter 4 and $f_{s_2}^g(\alpha, \phi s)$ is the trapped part of this energy. Unlike the last model, in this case $f_{s_2}^g \neq 0$ and as consequence not all the plastic work is dissipated but a part is stored, $L_s^p = \dot{f}_{s_2}^g + d_s$.

As well, the evolution equation for the plastic internal variables (α) and (ρ') read,

$$\dot{\alpha} = \gamma \frac{\partial f^y(x')}{\partial x'} \tag{5.122}$$

$$\dot{\rho}' = \gamma \frac{\partial^2 g_{s_2}(\alpha)}{\partial \alpha \, \partial \alpha} \frac{\partial f^y(x')}{\partial x'}$$

where, (γ) is the scalar plastic multiplier and $\left(\frac{\partial f^y(x')}{\partial x'} \right)$ is the general flow vector. In this context the plastic multiplier is determined by the classical Kuhn-Tucker complementary conditions and the consistency condition (5.96-5.97). Alternatively the flow rule Eq. 5.122 can be written, using the additive decomposition of strains, in the equivalent form,

$$\dot{\varepsilon}^e = \dot{\varepsilon} - \gamma \frac{\partial f^y(x')}{\partial x'} \tag{5.123}$$

Equations 5.96-5. 97 and 5.122-5.123 define the strain-suction-driven structure of the problem. In the same manner as for the BBM1 model but now the shift stress (ρ') should be determined as well.

The time integration of the constitutive relations described above is made in a strain-driven structure, as before with the BBM1 model. Thus at time t_{n+1} the total strain and suction are $\varepsilon_{n+1} = \varepsilon_n + \Delta\varepsilon_{n+1}$ and $s_{n+1} = s_n + \Delta s_{n+1}$, respectively.

The objective is to compute the stress σ'_{n+1}, the degree of saturation $S_{l_{n+1}}$, the update plastic internal variable α_{n+1} and the shift stress ρ'_{n+1} at the current time. To this purpose the backward-Euler approximation of the governing equations is used:

$$-\alpha_{n+1} + \alpha_n + \Delta\gamma \frac{\partial f^y(x'_{n+1})}{\partial x'} \quad = \quad 0 \tag{5.124}$$

$$-\rho'_{n+1} + \rho'_n + \Delta\gamma \frac{\partial^2 g_{s_2}}{\partial\alpha\,\partial\alpha} \frac{\partial f^y(x'_{n+1})}{\partial x'} \quad = \quad 0$$

For the discrete plastic multiplier $\Delta\gamma$ satisfying the loading-unloading conditions 5.101. As before, the updated stress tensor and the degree of saturation are given by the relations

$$\sigma'_{n+1} = \frac{\partial f^g_s{}_{n+1}}{\partial\varepsilon} \text{ and } S_{l_{n+1}} = \frac{\partial f^g_s{}_{n+1}}{\partial\phi s}.$$

The numerical solution of the algebraic system of equations 5.124 together with the KKT conditions 5.101 is accomplished following a predictor-corrector strategy as before with the BBM1 model, but now for **BBM2** the trial state is defined by one additional equation corresponding to the shift stress:

$$\alpha_{n+1}^{\text{trial}} = \alpha_n \tag{5.125}$$

$$\sigma'^{\text{trial}}_{n+1} = \frac{\partial f^g_s\left(\varepsilon_{n+1}, \alpha_{n+1}^{\text{trial}}, \phi s_{n+1}\right)}{\partial\varepsilon}$$

$$\rho'^{\text{trial}}_{n+1} = \frac{\partial f^g_{s_2}\left(\alpha_{n+1}^{\text{trial}}\right)}{\partial\alpha}$$

Note that $\left(\rho'^{\text{trial}}_{n+1} = \rho'_n\right)$ due to the second term of the energy function $\left(f^g_{s_2}\right)$. Afterwards the loading-unloading conditions are verified, taking the trial state as the final solution if $f^{y\,\text{trial}}_{n+1} < 0$, otherwise a plastic corrector step is performed ($\Delta\gamma > 0$) in the same manner as done for the Cam Clay model (equations 5.38 and 5.39).

The set of nonlinear equations 5.124 re-expressed in terms of the elastic strains $\varepsilon^e_{n+1} = \varepsilon_{n+1} - \alpha_{n+1}$ is solved using a Newton-like iterative strategy (like that in unconstraint theory).

The variational forms of the discrete equations developed above allow to properly understand both (CPPM) and (IPM) algorithms for the integration of **BBM2** model.

Provided the convexity properties of the energy functions describing the (**BBM2**) model the formulation of minimization problem is then:

$$
\boxed{
\begin{aligned}
&\text{Find} \quad (\varepsilon_{n+1}, x'_{n+1}) \in E \;\; \text{such that} \\
&\bar{f}_s^{g}(\varepsilon_{n+1}, x'_{n+1}, \phi s_{n+1}) = \min_{(\sigma', \alpha) \in E} \left\{ -g_s(\sigma, \alpha, \phi s) - \left(\sigma' \varepsilon_{n+1} + x'^{\text{trial}}_{n+1} \alpha \right) \right\}
\end{aligned}
}
\qquad (5.126)
$$

which can be expressed alternatively as the inequality mathematical program,

$$
\text{CPPM} \begin{cases} \min_{(\sigma', \alpha)} & -g_s(\sigma', \alpha, \phi s) - \left(\sigma' \varepsilon_{n+1} + x'^{\text{trial}}_{n+1} \alpha \right) \\ \text{sub. to} & f^y(x') \leq 0 \end{cases}
\qquad (5.127)
$$

Both problems 5.126 and 5.127 are similar to that formulated for the Cam Clay model for a constant value of suction. The Lagrange functional associated to the variational problem 5.127 is:

$$
\mathcal{L}^{\bar{g}}(\sigma', x', \phi s, \Delta\gamma) = -g_s(\sigma', \alpha, \phi s) - \left(\sigma' \varepsilon_{n+1} + x'^{\text{trial}}_{n+1} \alpha \right) + \Delta\gamma \cdot f^y(x')
\qquad (5.128)
$$

The application of the necessary first order optimality conditions on 5.128 leads to the Kuhn-Tucker restrictions which results in the similar system to that of Eq. 5.46. This restrictions system results to be identical to the discrete equations 5.124 which emphasizes the variational structure of the discrete equations for the model **BBM2**.

The residual vector as well as the Jacobian matrix used to compute the advance direction towards the solution state (optimal point) are identical to the expressions 5.47 and 5.48 for a given suction value. Then they are used in the algorithm (primal − dual CPPM).

The constraint program 5.127 can be re-written in the standard form of equality constraint by introducing the slack variables(z),

$$
\text{IPM} \begin{cases} \min_{(\sigma, \alpha)} & -g_s(\sigma', \alpha, \phi s) - \left(\sigma' \varepsilon_{n+1} + x'^{\text{trial}}_{n+1} \alpha \right) + \mu \cdot \log(z) \\ \text{sub. to} & f^y(x') + z = 0 \end{cases}
\qquad (5.129)
$$

Then the Lagrange functional associated to the equality constraint program 5.129 is:

$$\mathcal{L}^{\bar{g}}(\sigma', x', \phi s, \Delta\gamma) = \quad -g_s(\sigma', \alpha, \phi s) - \left(\sigma' \varepsilon_{n+1}^{\text{trial}} + x_{n+1}'^{\text{trial}} \alpha\right) + \Delta\gamma[f^y + z] \qquad (5.130)$$
$$+ \mu \cdot \log(z)$$

In virtue of: (a) the complementarity of the energy functions, (b) the state functions derived at chapter 4 and (c) the fundamental relation $\left(\rho_{n+1}'^{\text{trial}} = \sigma_{n+1}'^{\text{trial}} - x_{n+1}'^{\text{trial}}\right)$, the imposition of the first order optimality conditions to 5.130 leads to the extended Kuhn-Tucker restrictions which result to be identical to those of Eq.5.54 for a given value of suction.

The residual vector as well as the Jacobian matrix used to compute the advance direction towards the optimal point are identical to those given by the expressions 5.55 and 5.56 for a given value of suction. They are further used in the algorithm (primal − dual IPM). The following Boxes summarize the model: (a) General equations, (b) Discrete approximation and (c) Variational Forms.

Box 5.23: Continuum Governing Equations for BBM2 model

CONTINUUM FORM

Continuum constitutive equations for BBM2 model:

$$\sigma' = \frac{\partial f_s^g(\varepsilon, \alpha, \phi s)}{\partial \varepsilon}; \quad \rho' = \frac{\partial f_{s_2}^g(\alpha)}{\partial \alpha}; \quad S_l = \frac{\partial f_s^g(\varepsilon, \alpha, \phi s)}{\partial \phi s}$$

$$\dot{\alpha} = \gamma \frac{\partial f^y(x')}{\partial x'} \quad ; \quad \dot{\rho} = \gamma \frac{\partial^2 g_{s_2}(\alpha)}{\partial \alpha \partial \alpha} \frac{\partial f^y(x')}{\partial x'}$$

Strain driven problem:

$$\gamma \geq 0 \; ; \; f^y(x') \leq 0 \; ; \; \gamma \cdot f^y(x') = 0$$

$$\gamma \cdot \dot{f}^y(x') = 0$$

$$\dot{\varepsilon}^e = \dot{\varepsilon} - \gamma \frac{\partial f^y(x')}{\partial x'}$$

Enforcement of consistency leads to:

$$\gamma = \frac{1}{h} \frac{\partial f^y}{\partial x} \frac{\partial x}{\partial \sigma} \frac{\partial^2 f_s}{\partial \varepsilon \partial \varepsilon} \dot{\varepsilon}$$

Box 5.24: Discrete Equations Backward-Euler approximation for BBM2 model

DISCRETE FORM

Increment $\Delta\varepsilon_{n+1}$ and Δs_{n+1} during time interval $\Delta t = t_{n+1} - t_n$, leads to:

$$\varepsilon_{n+1} = \varepsilon_n + \Delta\varepsilon_{n+1}$$

$$s_{n+1} = s_n + \Delta s_{n+1}$$

Backward-Euler discrete system of the equations for MCC model:

$$-\alpha_{n+1} + \alpha_n + \Delta\gamma\frac{\partial f^y(x'_{n+1})}{\partial x'} \quad = \quad 0$$

$$-\rho'_{n+1} + \rho'_n + \Delta\gamma\frac{\partial^2 g_{s_2}}{\partial\alpha\,\partial\alpha}\frac{\partial f^y(x'_{n+1})}{\partial x'} \quad = \quad 0$$

$$\Delta\gamma \geq 0 \; ; \; f^y_{n+1} \leq 0 \; ; \; \Delta\gamma \cdot f^y_{n+1} = 0$$

$$\sigma_{n+1} = \frac{\partial f^g_s(\varepsilon_{n+1}, \alpha_{n+1}, \phi s_{n+1})}{\partial\varepsilon}; \quad S_{l_{n+1}} = \frac{\partial f^g_s(\varepsilon_{n+1}, \alpha_{n+1}, \phi s_{n+1})}{\partial\phi s}$$

predictor-corrector strategy:

$$\alpha^{trial}_{n+1} = \alpha_n \quad ; \quad \rho'^{trial}_{n+1} = \frac{\partial f^g_{s_2}(\alpha^{trial}_{n+1})}{\partial\alpha}$$

$$\sigma'^{trial}_{n+1} = \frac{\partial f^g_s(\varepsilon_{n+1}, \alpha^{trial}_{n+1}, \phi s_{n+1})}{\partial\varepsilon}$$

Check of loading-unloading conditions:

$$\left(f^{y\,trial}_{n+1}\left(\sigma'^{trial}_{n+1}, \rho^{trial}_{n+1}, \phi s_{n+1}\right) \leq 0\right) \quad \text{then } (\blacksquare)_{n+1} = (\blacksquare)^{trial}_{n+1}$$

Plastic corrector:

$$\varepsilon^e_{n+1} - \varepsilon^{e\,trial}_{n+1} + \Delta\gamma\frac{\partial f^y(x'_{n+1})}{\partial x'} \quad = \quad 0$$

$$-\rho'_{n+1} + \rho'_n + \Delta\gamma\frac{\partial^2 g_{s_2}}{\partial\alpha\,\partial\alpha}\frac{\partial f^y(x'_{n+1})}{\partial x'} \quad = \quad 0$$

with:

$$\varepsilon^e_{n+1} = \varepsilon_{n+1} - \alpha_{n+1} \quad ; \quad \varepsilon^{e\,trial}_{n+1} = \varepsilon_{n+1} - \alpha_n$$

Box 5.25: Variational Form for the Inequality constraint BBM2 model

<div style="border:1px solid">

VARIATIONAL FORM (inequality const.)

Variational Form BBM2 model:

$$\text{CPPM} \begin{cases} \min & -g_s(\sigma', \alpha, \phi s) - \left(\sigma'\varepsilon_{n+1} + x_{n+1}'^{\text{trial}}\alpha\right) \\ (\sigma', \alpha) \\ \text{sub. to} & f^y(x') \leq 0 \end{cases}$$

Lagrange functional associated:

$$\mathcal{L}^{\bar{g}}(\sigma', x', \phi s, \Delta\gamma) = -g_s(\sigma', \alpha, \phi s) - \left(\sigma'\varepsilon_{n+1} + x_{n+1}'^{\text{trial}}\alpha\right) + \Delta\gamma \cdot f^y(x')$$

KKT conditions:

$$\begin{array}{rcl} \varepsilon_{n+1}^e - \varepsilon_{n+1}^{e\,\text{trial}} + \Delta\gamma\dfrac{\partial f^y(x')}{\partial x'} & = & 0 \\[2mm] -\rho'_{n+1} + \rho_{n+1}'^{\text{trial}} + \Delta\gamma\dfrac{\partial f_{n+1}^y(x')}{\partial x'}\dfrac{\partial x'}{\partial \rho'}\dfrac{\partial^2 g_{s_2}}{\partial\alpha\,\partial\alpha} & = & 0 \\[2mm] f_{n+1}^y(x') & = & 0 \\[2mm] \Delta\gamma & \geq & 0 \end{array}$$

where:

$$\rho_{n+1}'^{\text{trial}} = \sigma_{n+1}'^{\text{trial}} - x_{n+1}'^{\text{trial}}$$

Residual vector:

$$r(x) = \begin{Bmatrix} \varepsilon_{n+1}^e - \varepsilon_{n+1}^{e\,\text{trial}} + \Delta\gamma\dfrac{\partial f_{n+1}^y(x')}{\partial x'}\dfrac{\partial x'}{\partial \sigma'} \\[3mm] -\rho'_{n+1} + \rho_{n+1}'^{\text{trial}} + \Delta\gamma\dfrac{\partial f_{n+1}^y(x')}{\partial x'}\dfrac{\partial x'}{\partial \rho'}\dfrac{\partial^2 g_{s_2}}{\partial\alpha\,\partial\alpha} \\[3mm] f_{n+1}^y(x') \end{Bmatrix}$$

Jacobian Matrix: $J = \nabla r(x)$

</div>

Box 5.26: Variational Form for the Equality constraint BBM2 model

<div style="border:1px solid">

VARIATIONAL FORM (equality const.)

Variational Form BBM2 model:

$$\text{IPM} \begin{cases} \min & -g_s(\sigma', \alpha, \phi s) - \left(\sigma'\varepsilon_{n+1} + x_{n+1}'^{\text{trial}}\alpha\right) + \mu \cdot \log(z) \\ (\sigma, \alpha) \\ \text{sub. to} & f^y(x') + z = 0 \end{cases}$$

Lagrange functional associated:

$$\mathcal{L}^{\bar{g}}(\sigma', x', \phi s, \Delta\gamma) = -g_s(\sigma', \alpha, \phi s) - \left(\sigma'\varepsilon_{n+1}^{\text{trial}} + x_{n+1}'^{\text{trial}}\alpha\right) + \Delta\gamma[f^y + z] + \mu \cdot \log(z)$$

KKT conditions:

</div>

$$\varepsilon_{n+1}^e - \varepsilon_{n+1}^{e\,trial} + \Delta\gamma \frac{\partial f^y(x'_{n+1})}{\partial x'} = 0$$

$$-\rho'_{n+1} + \rho'^{trial}_{n+1} + \Delta\gamma \frac{\partial f^y_{n+1}(x')}{\partial x'} \frac{\partial x'}{\partial \rho'} \frac{\partial^2 g_{s_2}}{\partial\alpha\,\partial\alpha} = 0$$

$$f^y_{n+1}(x') + z = 0$$

$$\Delta\gamma - \frac{\mu}{z} = 0$$

$$(\Delta\gamma, z) \geq 0$$

where:

$$\rho'^{trial}_{n+1} = \sigma'^{trial}_{n+1} - x'^{trial}_{n+1}$$

Residual vector:

$$r(x) = \left\{ \begin{array}{c} \varepsilon_{n+1}^e - \varepsilon_{n+1}^{e\,trial} + \Delta\gamma \dfrac{\partial f^y_{n+1}(x')}{\partial x'} \dfrac{\partial x'}{\partial \sigma'} \\[2mm] -\rho'_{n+1} + \rho'^{trial}_{n+1} + \Delta\gamma \dfrac{\partial f^y_{n+1}(x')}{\partial x'} \dfrac{\partial x'}{\partial \rho'} \dfrac{\partial^2 g_{s_2}}{\partial\alpha\,\partial\alpha} \\[2mm] f^y_{n+1}(x') + z \\[1mm] \Delta\gamma \cdot z - \mu \end{array} \right\}$$

Jacobian Matrix: $J = \nabla r(x)$

Figures 5.93-5.94 show the convergence results obtained with the algorithm $primal-dual$ CPPM.

Specifically, Fig. 5.93 shows the convergence speed of the algorithm while it integrates the BBM2 model and it is shown for two different loading steps under saturated and isothermal conditions.
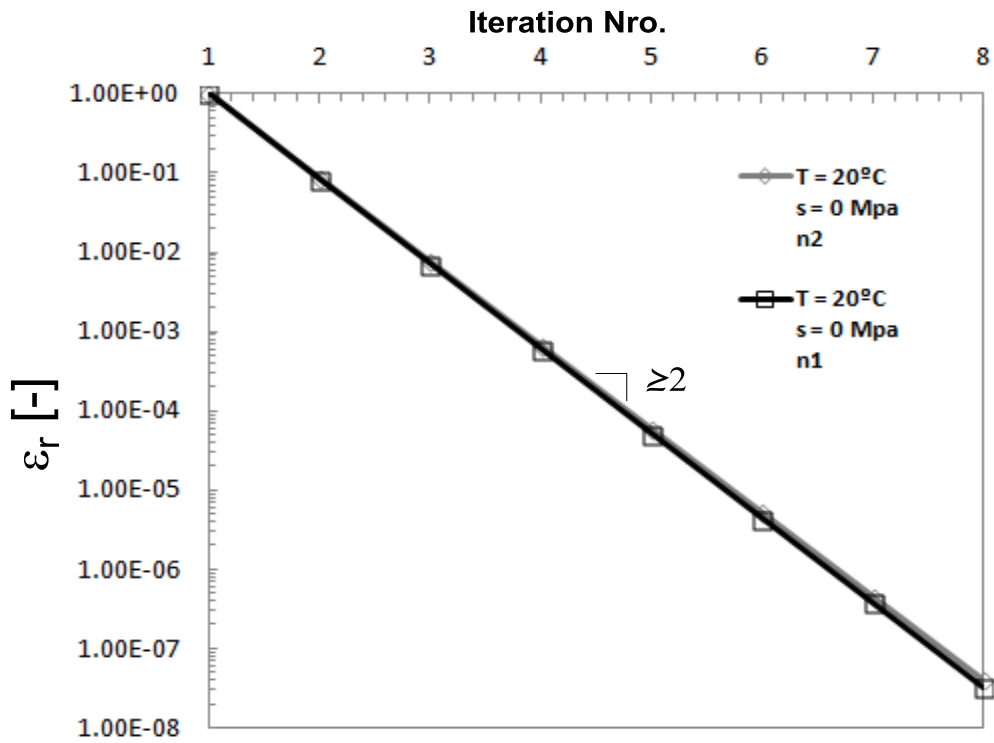
Figure 5.93: Convergence Results of the primal-dual CPPM for two different loading steps under isothermal and saturated conditions.

The slope of the straight line results lightly higher than 2 (2.4). Table 5.23 summarizes the convergence properties of the BBM2 model for two different loading steps.

Table 5.23: Table of convergence for the model BBM2 for two loading steps

N-iter	$\frac{\|r\|}{\|r^0\|}$ $(n1)$	$\frac{\|r\|}{\|r^0\|}$ $(n2)$
1	1	1
2	0.08269406	0.08574449
3	0.0070833	0.00761982
4	0.000603	0.0006723
5	5.1382E-05	5.9397E-05
6	4.3777E-06	5.2465E-06
7	3.7298E-07	4.6344E-07
8	3.1778E-08	4.0937E-08

Figure 5.94 shows the convergence speed of the algorithm while it integrates the BBM2 model and it is shown for two different suctions states under isothermal conditions.
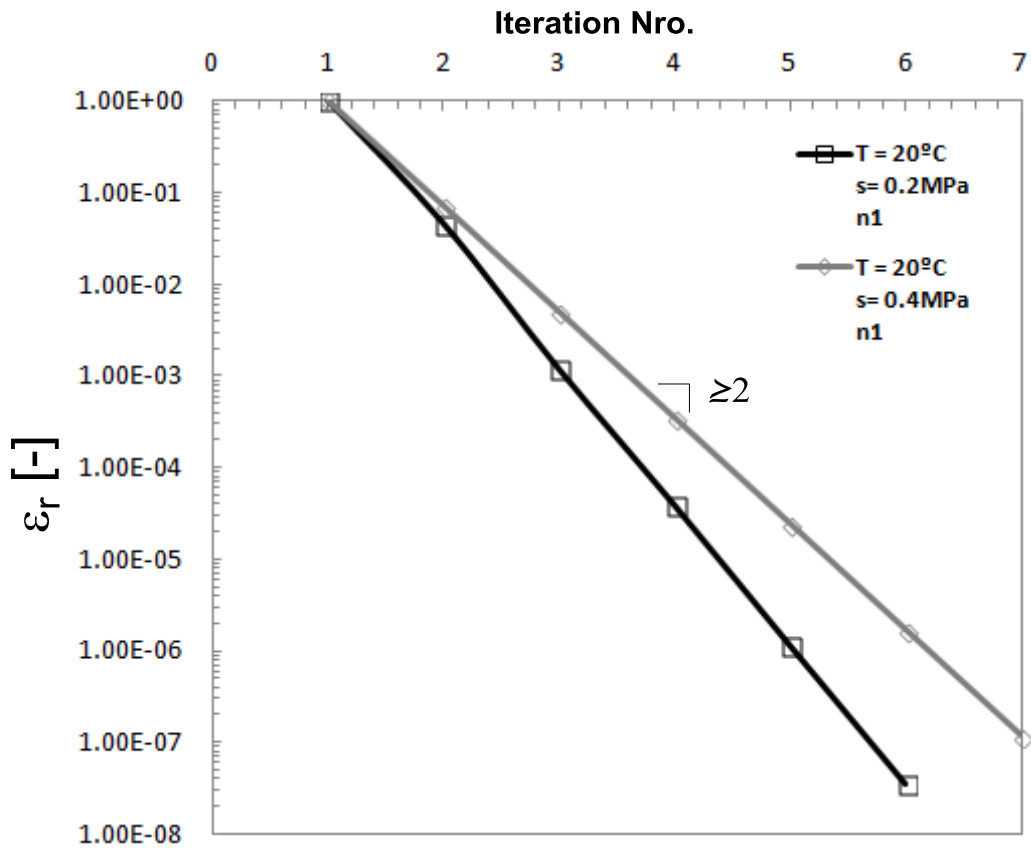
Figure 5.94: Convergence Results of the primal-dual CPPM for two different suction states; a) $\left(s_a^0 = \boldsymbol{0.2MPa}\right)$ *and b)* $\left(s_b^0 = \boldsymbol{0.4MPa}\right)$.

The slopes of the straight lines range between 2.6-3. In any case they result higher than two. Table 5.24 summarizes the convergence properties of the BBM2 model for two different suctions.

Table 5.24: Table of convergence for the model BBM2 for two suctions.

N-iter	$\dfrac{\|r\|}{\|r^0\|}$ $(s = 0.2\text{MPa})$	$\dfrac{\|r\|}{\|r^0\|}$ $(s = 0.4\text{MPa})$
1	1	1
2	0.04562536	0.07122715
3	0.00118364	0.00494266
4	3.8678E-05	0.0003433
5	1.1396E-06	2.3841E-05
6	3.5119E-08	1.6557E-06
7		1.1498E-07

5.5.3.1) Convergence performance of Generalized BBM2 model

The following is a convergence analysis of the generalized BBM2 model. Different values of the scalar parameter ϵ have been tested to analyses its sensibility to the speed of convergence. Partially saturated conditions and non-isothermal conditions have also been considered.

Figure 5.95 shows the speed of convergence of the generalized BBM2 model for different values of ϵ.
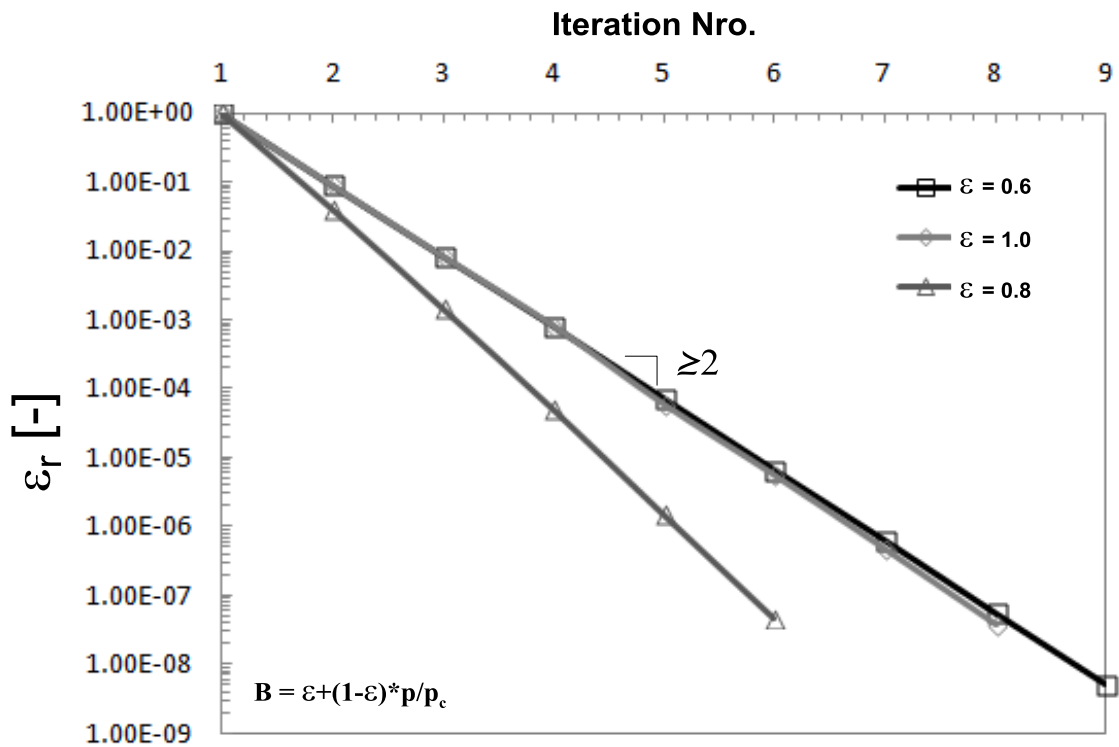
Figure 5.95: Convergence speed of the Generalized BBM2 model. Convergence for three different values of e.

The slope of the straight lines range between 2.46 to 3.00. All the registered slopes results greater than two. A similar convergence response is observed under partially saturated conditions.

Figure 5.96 shows the convergence speed of the BBM2 model under partially saturated conditions for two values of ε.
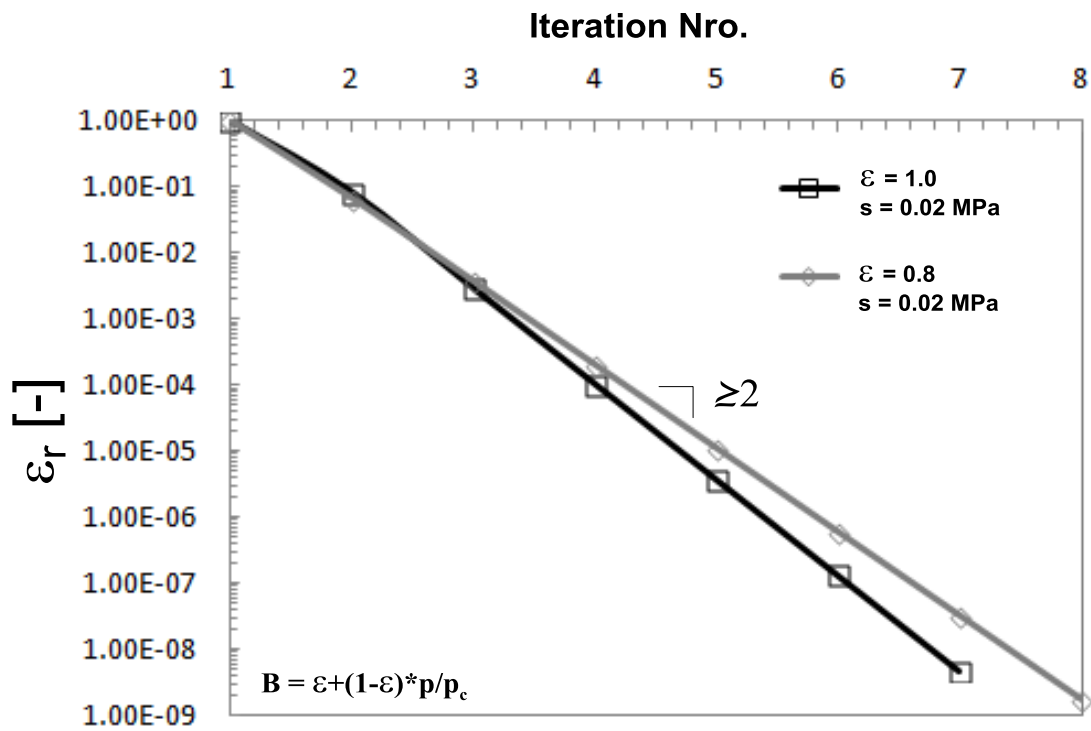
Figure 5.96: Convergence speed of the Generalized BBM2 model. Convergence for two different values of e and under partially saturated condition.

The slope of the straight lines results lightly higher than two and range between 2.8-3.0. The Table 5.25 shows the convergence speed of the generalized BBM2 model under partially saturated conditions.

Table 5.25: Convergence speed of the Generalized BBM2 model under partially saturated conditions

N-iter	$\frac{\|r\|}{\|r^0\|}\left(\begin{array}{c}\epsilon = 1.0 \\ s = 0.02\text{MPa}\end{array}\right)$	$\frac{\|r\|}{\|r^0\|}\left(\begin{array}{c}\epsilon = 0.8 \\ s = 0.02\text{MPa}\end{array}\right)$
1	1	1
2	0.08358383	0.06707397
3	0.00294887	0.00372466
4	0.00010539	0.00020207
5	3.7564E-06	1.0936E-05
6	1.3389E-07	5.917E-07
7	4.7734E-09	3.2014E-08
8		1.7313E-09

Figure 5.97 shows the speed of convergence of the model BBM2 under non-isothermal conditions and different values of the parameter ϵ.
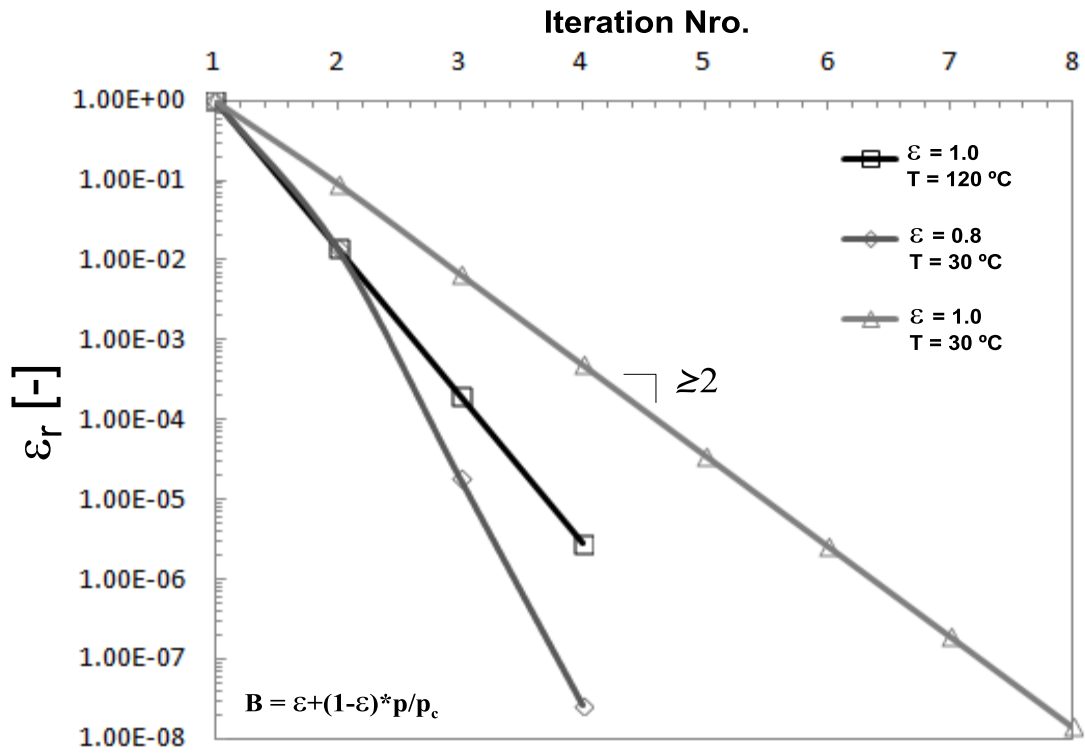
Figure 5.97: Convergence speed of the Generalized BBM2 model. Convergence for two different values of e and under non-isothermal condition.

The slope of the straight lines results higher than two as happens in the previous cases. The registered slopes range between 2.6-3.0. Table 5.26 summarize the convergence speed for non-isothermal conditions.

Table 5.26: Convergence speed of the Generalized BBM2 model under non-isothermal conditions

N-iter	$\frac{\|r\|}{\|r^0\|}\left(\begin{array}{l}\epsilon = 1.0 \\ T = 120°C\end{array}\right)$	$\frac{\|r\|}{\|r^0\|}\left(\begin{array}{l}\epsilon = 0.8 \\ T = 30°C\end{array}\right)$	$\frac{\|r\|}{\|r^0\|}\left(\begin{array}{l}\epsilon = 1.0 \\ T = 30°C\end{array}\right)$
1	1	1	1
2	0.01395902	0.01392713	0.09209213
3	0.00019499	1.8149E-05	0.00670839
4	2.7238E-06	2.6168E-08	0.00049153
5			3.598E-05
6			2.6339E-06
7			1.9282E-07
8			1.4114E-08

5.5.4) Integration of Barcelona Basic Model BBM

A stress-point algorithm for the integration of models of BBM type was addressed by Vaunat et. al (2000), however the proposed integration scheme was performed in incremental form which represents a main difference with the procedure adopted in this thesis.

The derivation of the Barcelona Basic Model **BBM**, formulated in terms of the net stress as conjugate variable of the strain tensor $(\sigma'' - \varepsilon)$ and the hydraulic strain as conjugate variable of suction$(s - \varepsilon_w)$, within a hyper-poroplastic approach is defined by the non-incremental constitutive relations

$$\sigma'' = \frac{\partial f_s^g(\varepsilon, \alpha, s)}{\partial \varepsilon} \tag{5.131}$$

$$\rho'' = \frac{\partial f_{s_2}^g(\alpha)}{\partial \alpha}$$

$$\varepsilon_w = \frac{\partial f_s^g(\varepsilon, \alpha, s)}{\partial s}$$

where $f_s^g(\varepsilon, \alpha, s)$ is the energy function of the porous skeleton defined at chapter 4 and $f_{s_2}^g(\alpha)$ is the trapped part of this energy. The evolution equations for the plastic internal variables α and ρ'' read,

$$\dot{\alpha} = \gamma \frac{\partial f^y(x'')}{\partial x''} \tag{5.132}$$

$$\dot{\rho}'' = \gamma \frac{\partial^2 g_{s_2}(\alpha)}{\partial \alpha \, \partial \alpha} \frac{\partial f^y(x'')}{\partial x''}$$

where, (γ) is the scalar plastic multiplier and $\left(\frac{\partial f^y(x'')}{\partial x''} \right)$ is the general flow vector. In this context the plastic multiplier is determined by the classical Kuhn-Tucker complementary conditions $\gamma \geq 0$; $f^y(x'') \leq 0$; $\gamma f^y(x'') = 0$ and the consistency condition $\gamma \dot{f}^y(x'') = 0$ which in addition to the flow rule 5.132a expressed in terms of the elastic strain define the strain-suction-driven structure of the problem.

The time integration is performed following a strain-suction-driven structure in the same manner as with the previous models. The process ends with the backward-Euler approximation of the governing equations:

$$-\alpha_{n+1} + \alpha_n + \Delta\gamma \frac{\partial f_{n+1}^y}{\partial x"} \frac{\partial x"}{\partial \sigma"} \quad = \quad 0 \tag{5.133}$$

$$-\rho_{n+1}^{"} + \rho_n^{"} + \Delta\gamma \frac{\partial f_{n+1}^y(x")}{\partial x"} \frac{\partial x"}{\partial \rho"} \frac{\partial^2 g_{s_2}}{\partial \alpha\, \partial \alpha} \quad = \quad 0$$

with the discrete plastic multiplier $(\Delta\gamma)$ satisfying the loading-unloading conditions $\Delta\gamma \geq 0$; $f_{n+1}^y \leq 0$; $\Delta\gamma f_{n+1}^y = 0$. The updated stress tensor and the hydraulic strain are given by the relations:

$$\sigma_{n+1}^{"} = \frac{\partial f_s^g(\varepsilon_{n+1}, \alpha_{n+1}, s_{n+1})}{\partial \varepsilon} \tag{5.134}$$

$$\varepsilon_{w_{n+1}} = \frac{\partial f_s^g(\varepsilon_{n+1}, \alpha_{n+1}, s_{n+1})}{\partial s}$$

The variational forms of the discrete equations developed above allow to properly understand both (CPPM) and (IPM) algorithms for the integration of **BBM** model.

Provided the convexity properties of the energy functions describing the Barcelona Basic Model, the formulation of minimization problem is the following:

$$\boxed{\begin{aligned} &\text{Find } \left(\varepsilon_{n+1}, x_{n+1}^{"}\right) \in E \text{ such that} \\ &\bar{f}_s^g\left(\varepsilon_{n+1}, x_{n+1}^{"}, s_{n+1}\right) = \min_{(\sigma", \alpha) \in E} \left\{-g_s(\sigma", \alpha, s) - \left(\sigma"\varepsilon_{n+1} + x_{n+1}^{"trial}\alpha\right)\right\} \end{aligned}} \tag{5.135}$$

which can be expressed alternatively as the inequality mathematical program,

$$\text{CPPM} \begin{cases} \min_{(\sigma", \alpha)} & -g_s(\sigma", \alpha, s) - \left(\sigma"\varepsilon_{n+1} + x_{n+1}^{"trial}\alpha\right) \\ \text{sub. to} & f^y(x") \leq 0 \end{cases} \tag{5.136}$$

Both problems 5.135 and 5.136 are similar to that formulated for the Cam Clay model for a given value of suction. The Lagrange functional associated to the variational problem 5.136 is,

$$\mathcal{L}^{\bar{g}}(\sigma", x", s, \Delta\gamma) = -g_s(\sigma", \alpha, s) - \left(\sigma"\varepsilon_{n+1} + x_{n+1}^{"trial}\alpha\right) + \Delta\gamma \cdot f^y(x") \tag{5.137}$$

The application of the necessary first order optimality conditions to 5.137 leads to the Kuhn-Tucker restrictions which results in an identical system to the one given by Eq. 5.46 for a given value of suction.

The residual vector as well as the Jacobian matrix used to compute the advance direction towards the solution state (optimal point) are identical to the expressions 5.47 and 5.48 for a given value of suction.

If the Gibbs energy function $\bar{g}_s(\sigma", x", s)$ is used at Eq. 5.137 a slightly different form of the first optimality KKT conditions is obtained, where the second equation of the system is given in terms of the plastic internal variables (α) instead of the back net stress ($\rho"$). Thus the residual vector used in the algorithm (primal $-$ dual CPPM) results,

$$r(x) = \begin{Bmatrix} \varepsilon^e_{n+1} - \varepsilon^{e\,trial}_{n+1} + \Delta\gamma \dfrac{\partial f^y_{n+1}}{\partial x"} \dfrac{\partial x"}{\partial \sigma"} \\[2ex] -\alpha_{n+1} + \alpha^{trial}_{n+1} + \Delta\gamma \dfrac{\partial f^y_{n+1}}{\partial x"} \\[2ex] f^y_{n+1}(x") \end{Bmatrix} \qquad (5.138)$$

and the Jacobian matrix of the residual vector used to compute the advance direction to search the optimal point is:

$$J(x) = \begin{bmatrix} 1 + \Delta\gamma \dfrac{\partial^2 f^y}{\partial x" \partial x"} \dfrac{\partial^2 f_s}{\partial \varepsilon \partial \varepsilon} & \Delta\gamma \dfrac{\partial^2 f^y}{\partial x" \partial x"} \dfrac{\partial x"}{\partial \rho"} \dfrac{\partial g_{s_2}}{\partial \alpha \partial \alpha} & \dfrac{\partial f^y}{\partial x"} \\[3ex] \Delta\gamma \dfrac{\partial^2 f^y}{\partial x" \partial x"} \dfrac{\partial^2 f_s}{\partial \varepsilon \partial \varepsilon} & -1 + \Delta\gamma \dfrac{\partial^2 f^y}{\partial x" \partial x"} \dfrac{\partial x"}{\partial \rho"} \dfrac{\partial^2 g_{s_2}}{\partial \alpha \partial \alpha} & \dfrac{\partial f^y}{\partial x"} \\[3ex] \dfrac{\partial f^y}{\partial x"} \dfrac{\partial^2 f_s}{\partial \varepsilon \partial \varepsilon} & \dfrac{\partial f^y}{\partial x"} \dfrac{\partial x"}{\partial \rho"} \dfrac{\partial^2 g_{s_2}}{\partial \alpha \partial \alpha} & 0 \end{bmatrix} \qquad (5.139)$$

If the constraint program 5.136 is re-written in the standard form of equality constraint leads to the minimization problem:

$$\text{IPM} \begin{cases} \min_{(\sigma", x")} & -\bar{g}_s(\sigma", x", s) - \left(\sigma"\varepsilon_{n+1} + x^{"trial}_{n+1}\alpha\right) \\ \text{sub. to} & f^y(x") + z = 0 \end{cases} \qquad (5.140)$$

On this occasion the Lagrange functional of the equality constraint program 5.140 is given by:

$$\begin{aligned} \mathcal{L}^{\bar{g}}(\sigma", \alpha, s, \Delta\gamma) = \;&-\bar{g}_s(\sigma", x", s) - \left(\sigma"\varepsilon_{n+1} + x^{"trial}_{n+1}\alpha\right) + \Delta\gamma \cdot [f^y(x") + z] \\ &+\mu \cdot \log(z) \end{aligned} \qquad (5.141)$$

In virtue of: (a) the complementarity of the energy functions, (b) the state functions derived at chapter 4 and (c) the fundamental relation $\left(\rho''^{\text{trial}}_{n+1} = \sigma''^{\text{trial}}_{n+1} - x''^{\text{trial}}_{n+1}\right)$, the imposition of the first order optimality conditions leads to the following extension of Kuhn-Tucker restrictions:

$$
\begin{aligned}
\varepsilon^e_{n+1} - \varepsilon^{e\,\text{trial}}_{n+1} + \Delta\gamma \frac{\partial f^y_{n+1}}{\partial x''}\frac{\partial x''}{\partial \sigma''} &= 0 \\
-\alpha_{n+1} + \alpha^{\text{trial}}_{n+1} + \Delta\gamma \frac{\partial f^y_{n+1}}{\partial x''} &= 0 \\
f^y_{n+1}(x'') + z &= 0 \\
\Delta\gamma - \frac{\mu}{z} &= 0 \\
(\Delta\gamma, z) &\geq 0
\end{aligned}
\tag{5.142}
$$

again the positive character of both the discrete plastic multiplier $\Delta\gamma$ and the slack variable z should be preserved. From the KKT restrictions the residual vector used in the algorithm $(\text{primal} - \text{dual IPM})$ is derived as:

$$
r(x) = \left\{
\begin{array}{c}
\varepsilon^e_{n+1} - \varepsilon^{e\,\text{trial}}_{n+1} + \Delta\gamma \dfrac{\partial f^y_{n+1}}{\partial x''}\dfrac{\partial x''}{\partial \sigma''} \\[2mm]
-\alpha_{n+1} + \alpha^{\text{trial}}_{n+1} + \Delta\gamma \dfrac{\partial f^y_{n+1}}{\partial x''} \\[2mm]
f^y_{n+1}(x'') + z \\[2mm]
\Delta\gamma \cdot z - \mu
\end{array}
\right\}
\tag{5.143}
$$

finally the Jacobian matrix of $r(x)$ is:

$$
J(x) = \begin{bmatrix}
1 + \Delta\gamma \dfrac{\partial^2 f^y}{\partial x'' \partial x''}\dfrac{\partial^2 f_s}{\partial \varepsilon \partial \varepsilon} & \Delta\gamma \dfrac{\partial^2 f^y}{\partial x'' \partial x''}\dfrac{\partial x''}{\partial \rho''}\dfrac{\partial g_{s_2}}{\partial \alpha \partial \alpha} & \dfrac{\partial f^y}{\partial x''} & 0 \\[3mm]
\Delta\gamma \dfrac{\partial^2 f^y}{\partial x'' \partial x''}\dfrac{\partial^2 f_s}{\partial \varepsilon \partial \varepsilon} & -1 + \Delta\gamma \dfrac{\partial^2 f^y}{\partial x'' \partial x''}\dfrac{\partial x''}{\partial \rho''}\dfrac{\partial^2 g_{s_2}}{\partial \alpha \partial \alpha} & \dfrac{\partial f^y}{\partial x''} & 0 \\[3mm]
\dfrac{\partial f^y}{\partial x''}\dfrac{\partial^2 f_s}{\partial \varepsilon \partial \varepsilon} & \dfrac{\partial f^y}{\partial x''}\dfrac{\partial x''}{\partial \rho''}\dfrac{\partial^2 g_{s_2}}{\partial \alpha \partial \alpha} & 0 & 1 \\[3mm]
0 & 0 & z & \Delta\gamma
\end{bmatrix}
\tag{5.144}
$$

The last two algorithmic elements $r(x)$ and $J(x)$ are used in the globally convergent algorithm of interior-point to compute the advance direction towards the solution state.

The following Boxes summarize the model: (a) General equations, (b) Discrete approximation and (c) Variational Forms.

Box 5.27: Continuum Governing Equations for BBM model

CONTINUUM FORM

Continuum constitutive equations for BBM model:

$$\sigma^{"} = \frac{\partial f_s^g(\varepsilon, \alpha, s)}{\partial \varepsilon}; \quad \rho^{"} = \frac{\partial f_{s_2}^g(\alpha)}{\partial \alpha}; \quad \varepsilon_w = \frac{\partial f_s^g(\varepsilon, \alpha, s)}{\partial s}$$

$$\dot{\alpha} = \gamma \frac{\partial f^y(x^{"})}{\partial x^{"}} \quad ; \quad \dot{\rho} = \gamma \frac{\partial^2 g_{s_2}(\alpha)}{\partial \alpha \, \partial \alpha} \frac{\partial f^y(x^{"})}{\partial x^{"}}$$

Strain driven problem:

$$\gamma \geq 0 \; ; \; f^y(x^{"}) \leq 0 \; ; \; \gamma \cdot f^y(x^{"}) = 0$$

$$\gamma \cdot \dot{f}^y(x') = 0$$

$$\dot{\varepsilon}^e = \dot{\varepsilon} - \gamma \frac{\partial f^y(x^{"})}{\partial x^{"}}$$

Enforcement of consistency leads to:

$$\gamma = \frac{1}{h} \frac{\partial f^y}{\partial x^{"}} \frac{\partial x^{"}}{\partial \sigma} \frac{\partial^2 f_s}{\partial \varepsilon \, \partial \varepsilon} \dot{\varepsilon}$$

Box 5.28: Discrete Equations Backward-Euler approximation for BBM model

---

DISCRETE FORM

Increment $\Delta\varepsilon_{n+1}$ and Δs_{n+1} during time interval $\Delta t = t_{n+1} - t_n$, leads to:

$$\varepsilon_{n+1} = \varepsilon_n + \Delta\varepsilon_{n+1}$$

$$s_{n+1} = s_n + \Delta s_{n+1}$$

Backward-Euler discrete system of the equations for MCC model:

$$-\alpha_{n+1} + \alpha_n + \Delta\gamma \frac{\partial f^y(x_{n+1}^{"})}{\partial x^{"}} \quad = \quad 0$$

$$-\rho_{n+1}^{"} + \rho_n^{"} + \Delta\gamma \frac{\partial^2 g_{s_2}}{\partial \alpha \, \partial \alpha} \frac{\partial f^y(x_{n+1}^{"})}{\partial x^{"}} \quad = \quad 0$$

$$\Delta\gamma \geq 0 \; ; \; f_{n+1}^y \leq 0 \; ; \; \Delta\gamma \cdot f_{n+1}^y = 0$$

$$\sigma_{n+1}^{"} = \frac{\partial f_s^g(\varepsilon_{n+1}, \alpha_{n+1}, s_{n+1})}{\partial \varepsilon}; \quad \varepsilon_{w_{n+1}} = \frac{\partial f_s^g(\varepsilon_{n+1}, \alpha_{n+1}, s_{n+1})}{\partial \phi s}$$

predictor-corrector strategy:

$$\alpha_{n+1}^{trial} = \alpha_n \quad ; \quad \rho_{n+1}^{"trial} = \frac{\partial f_{s_2}^g(\alpha_{n+1}^{trial})}{\partial \alpha}$$

$$\sigma_{n+1}^{"trial} = \frac{\partial f_s^g(\varepsilon_{n+1}, \alpha_{n+1}^{trial}, s_{n+1})}{\partial \varepsilon}$$

Check of loading-unloading conditions:

$$\left(f_{n+1}^{y\,trial}\left(\sigma_{n+1}^{"trial}, \rho_{n+1}^{"trial}, s_{n+1}\right) \leq 0\right) \quad \text{then} \; (\blacksquare)_{n+1} = (\blacksquare)_{n+1}^{trial}$$

plastic corrector:

$$\varepsilon_{n+1}^e - \varepsilon_{n+1}^{e\,trial} + \Delta\gamma \frac{\partial f_{n+1}^y}{\partial x''} \quad = \quad 0$$

$$-\alpha_{n+1} + \alpha_{n+1}^{trial} + \Delta\gamma \frac{\partial f_{n+1}^y}{\partial x''} \quad = \quad 0$$

with:

$$\varepsilon_{n+1}^e = \varepsilon_{n+1} - \alpha_{n+1} \quad ; \quad \varepsilon_{n+1}^{e\,trial} = \varepsilon_{n+1} - \alpha_n$$

Box 5.29: Variational Form for Inequality constraint BBM model

VARIATIONAL FORM (inequality const.)

Variational Form BBM model:

$$\text{CPPM} \begin{cases} \min & -\bar{g}_s(\sigma'', x'', s) - \left(\sigma''\varepsilon_{n+1} + x_{n+1}^{''trial}\alpha\right) \\ (\sigma'', x'') & \\ \text{sub. to} & f^y(x'') \leq 0 \end{cases}$$

Lagrange functional associated:

$$\mathcal{L}^{\bar{g}}(\sigma'', \alpha, s, \Delta\gamma) = -g_s(\sigma'', x'', s) - \left(\sigma''\varepsilon_{n+1} + x_{n+1}^{''trial}\alpha\right) + \Delta\gamma \cdot f^y(x'')$$

KKT conditions:

$$\varepsilon_{n+1}^e - \varepsilon_{n+1}^{e\,trial} + \Delta\gamma \frac{\partial f^y(x'')}{\partial x''} \quad = \quad 0$$

$$-\alpha_{n+1} + \alpha_{n+1}^{trial} + \Delta\gamma \frac{\partial f_{n+1}^y}{\partial x''} \quad = \quad 0$$

$$f_{n+1}^y(x'') \quad = \quad 0$$

$$\Delta\gamma \quad \geq \quad 0$$

where:

$$\rho_{n+1}^{''trial} = \sigma_{n+1}^{''trial} - x_{n+1}^{''trial}$$

Residual vector:

$$r(x) = \begin{cases} \varepsilon_{n+1}^e - \varepsilon_{n+1}^{e\,trial} + \Delta\gamma \frac{\partial f_{n+1}^y(x)}{\partial x}\frac{\partial x}{\partial \sigma} \\ -\alpha_{n+1} + \alpha_{n+1}^{trial} + \Delta\gamma \frac{\partial f_{n+1}^y}{\partial x''} \\ f_{n+1}^y(x'') \end{cases}$$

Jacobian Matrix: $\quad J = \nabla r(x)$

Box 5.30: Variational Form for the Equality constraint BBM model

---

<div align="center">

VARIATIONAL FORM (equality const.)

</div>

Variational Form BBM model:

$$
\text{IPM} \begin{cases} \min\limits_{(\sigma'',x'')} & -\bar{g}_s(\sigma'',x'',s) - \left(\sigma''\varepsilon_{n+1} + x_{n+1}^{''trial}\alpha\right) \\ \text{sub. to} & f^y(x'') + z = 0 \end{cases}
$$

Lagrange functional associated:

$$
\mathcal{L}^{\bar{g}}(\sigma'',\alpha,s,\Delta\gamma) = \ -\bar{g}_s(\sigma'',x'',s) - \left(\sigma''\varepsilon_{n+1} + x_{n+1}^{''trial}\alpha\right) + \Delta\gamma \cdot [f^y(x'') + z]
$$
$$
+\mu \cdot \log(z)
$$

KKT conditions:

$$
\varepsilon_{n+1}^e - \varepsilon_{n+1}^{e\,trial} + \Delta\gamma\frac{\partial f_{n+1}^y}{\partial x''}\frac{\partial x''}{\partial \sigma''} \ = \ 0
$$
$$
-\alpha_{n+1} + \alpha_{n+1}^{trial} + \Delta\gamma\frac{\partial f_{n+1}^y}{\partial x''} \ = \ 0
$$
$$
f_{n+1}^y(x'') + z \ = \ 0
$$
$$
\Delta\gamma - \frac{\mu}{z} \ = \ 0
$$
$$
(\Delta\gamma, z) \ \geq \ 0
$$

where:

$$
\rho_{n+1}^{''trial} = \sigma_{n+1}^{''trial} - x_{n+1}^{''trial}
$$

Residual vector:

$$
r(x) = \ \begin{cases} \varepsilon_{n+1}^e - \varepsilon_{n+1}^{e\,trial} + \Delta\gamma\dfrac{\partial f_{n+1}^y}{\partial x''}\dfrac{\partial x''}{\partial \sigma''} \\[2mm] -\alpha_{n+1} + \alpha_{n+1}^{trial} + \Delta\gamma\dfrac{\partial f_{n+1}^y}{\partial x''} \\[2mm] f_{n+1}^y(x'') + z \\ \Delta\gamma \cdot z - \mu \end{cases}
$$

Jacobian Matrix: $\quad J = \nabla r(x)$

Figure 5.98 shows the convergence results obtained with the algorithm primal $-$ dual CPPM. The convergence speed of the algorithm for the BBM integration is shown for three different suctions. It slope of convergence rate results lightly higher than 2 (= 2.07).
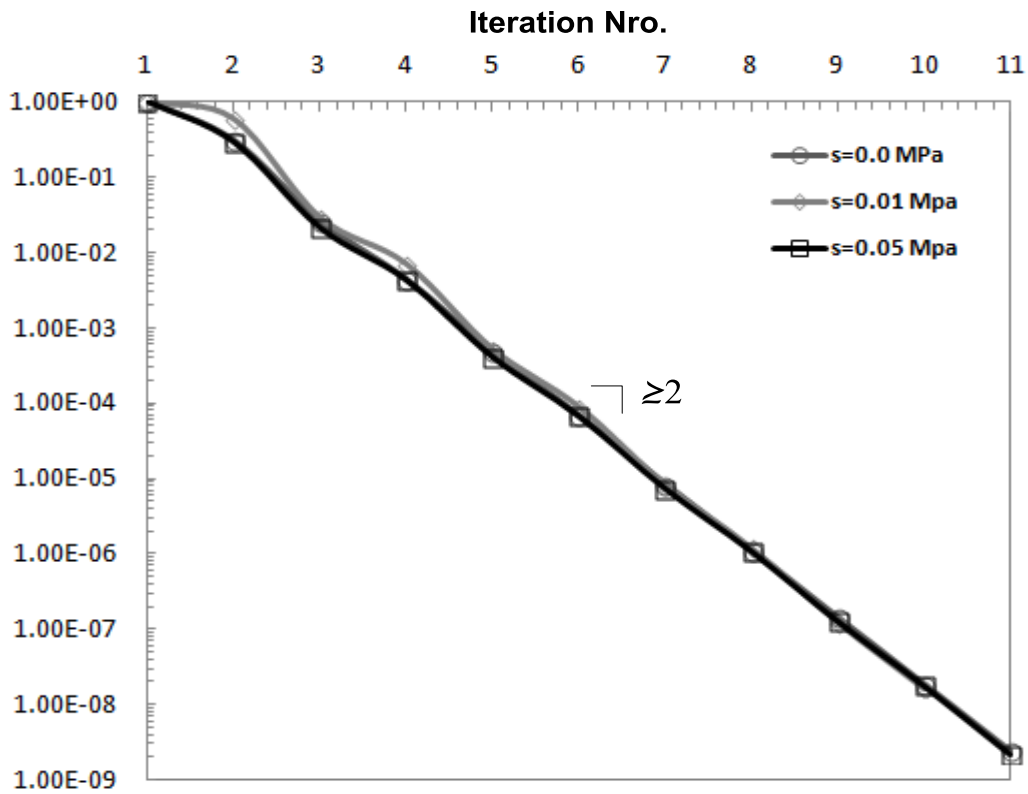
Figure 5.98: Convergence Results of the primal-dual CPPM algorithm for three different suction states; a)
($s_1 = \mathbf{0.0MPa}$), b) ($s_2 = 0.01\mathbf{MPa}$) and ($s_3 = 0.05\mathbf{MPa}$).

Table 5.27 summarizes the convergence properties of the BBM model for the three
different suctions.

Table 5.27: Table of Convergence of the model BBM4 for three different suctions.

N-iter	$\frac{\|r\|}{\|r^0\|}(s = 0.0 \text{ MPa})$	$\frac{\|r\|}{\|r^0\|}(s = 0.01 \text{ MPa})$	$\frac{\|r\|}{\|r^0\|}(s = 0.05 \text{ MPa})$
1	1	1	1
2	0.30855229	0.60048421	0.29196928
3	0.02598482	0.02945251	0.02132521
4	0.00440247	0.0071395	0.0043271
5	0.00048775	0.00052972	0.000411
6	6.8973E-05	9.0549E-05	6.7562E-05
7	8.4334E-06	8.3353E-06	7.3868E-06
8	1.1226E-06	1.1994E-06	1.0879E-06
9	1.421E-07	1.2405E-07	1.2847E-07
10	1.8526E-08	1.6319E-08	1.7842E-08
11	2.3737E-09		2.1974E-09

5.5.4.1) Consistent Tangent Operator for the hyperporoplastic model BBM

One of the advantages of the proposed algorithms lies in the fact that they can be linearized in closed form (Simo & Hughes, 1998). This fact leads to the notion of "Consistent Tangent modulus" as opposite to the "Continuum Elasto-Plastic Tangent modulus". The former is obtained by enforcing the consistency condition on the discrete algorithmic problem, whereas the last notion results from the classical consistency condition of the continuum problem. Next, the procedure followed by Simo (1998) is used to derive the algorithmic tangent modulus. Differentiating the stress-strain relation $\left(\sigma''(\varepsilon, \alpha, s)\right)$, the algorithmic translation $\left(\rho''(\alpha, s)\right)$ and the flow rule $(\dot{\alpha})$ leads to:

$$d\sigma_{n+1} = E:\left\{\left(d\varepsilon_{n+1} - d\Delta\gamma_{n+1}\frac{\partial f^y_{n+1}}{\partial x}\right) + \frac{\partial^2 g_{n+1}}{\partial\sigma\,\partial\sigma}\frac{\partial^2 f_{n+1}}{\partial\varepsilon\,\partial s}ds_{n+1}\right\} \tag{5.145}$$

$$d\rho_{n+1} = d\Delta\gamma_{n+1}\frac{\partial^2 g_{2_{n+1}}}{\partial\alpha\,\partial\alpha}\frac{\partial f^y_{n+1}}{\partial x} + \Delta\gamma_{n+1}\frac{\partial^2 g_{2_{n+1}}}{\partial\alpha\,\partial\alpha}\frac{\partial^2 f^y_{n+1}}{\partial x\,\partial x}\frac{\partial x}{\partial\sigma}d\sigma_{n+1}$$
$$+ \frac{\partial^2 g_{2_{n+1}}}{\partial\alpha\,\partial s}ds_{n+1}$$

$$d\alpha_{n+1} = d\Delta\gamma_{n+1}\frac{\partial f^y_{n+1}}{\partial x} + \Delta\gamma_{n+1}\frac{\partial^2 f^y_{n+1}}{\partial x\,\partial x}\frac{\partial x}{\partial\sigma}d\sigma_{n+1}$$

where the algorithmic modulus is defined as,

$$E_{n+1} = \left[\frac{\partial^2 g_{n+1}}{\partial\sigma\,\partial\sigma} + \Delta\gamma_{n+1}\frac{\partial^2 f^y_{n+1}}{\partial x\,\partial x}\frac{\partial x}{\partial\sigma}\right]^{-1} \tag{5.146}$$

On the other hand differentiating the discrete consistency condition $f^y(x) = 0$ leads to,

$$\frac{\partial f^y_{n+1}}{\partial x}(d\sigma_{n+1} - d\rho_{n+1}) + \frac{\partial f^y_{n+1}}{\partial s}ds_{n+1} = 0 \tag{5.147}$$

From Eqs.5.145 and 5.147 the incremental plastic multiplier is obtained, resulting

$$d\Delta\gamma_{n+1} = \frac{\frac{\partial f^y_{n+1}}{\partial x}\overline{E}_{n+1}d\varepsilon}{H_{n+1} + \left(\nabla^T f^y_{n+1}\overline{C}_{n+1}\nabla f^y_{n+1}\right)} + \frac{\frac{\partial f^y_{n+1}}{\partial x}\overline{E}_{n+1}\frac{\partial^2 g_{n+1}}{\partial\sigma\,\partial\sigma}\frac{\partial^2 f_{n+1}}{\partial\varepsilon\,\partial s}ds}{H_{n+1} + \left(\nabla^T f^y_{n+1}\overline{C}_{n+1}\nabla f^y_{n+1}\right)} \tag{5.148}$$

where the algorithmic moduli $(\overline{E})$ and (H) are given by

$$\overline{E}_{n+1} = E_{n+1} - \Delta\gamma_{n+1}\frac{\partial^2 g_{2_{n+1}}}{\partial\alpha\,\partial\alpha}\frac{\partial^2 f^y_{n+1}}{\partial x\,\partial x}E_{n+1} \tag{5.149}$$

$$H_{n+1} = -\Delta\gamma \frac{\partial f_{n+1}^y}{\partial x} \frac{\partial^2 g_{2_{n+1}}}{\partial\alpha\,\partial\alpha} \frac{\partial^2 f_{n+1}^y}{\partial x\,\partial x} \frac{\partial x}{\partial\sigma} E_{n+1} \frac{\partial f_{n+1}^y}{\partial x}$$

and the compact notation has been used at 5.148,

$$\bar{C}_{n+1} = \begin{pmatrix} E_{n+1} & 0 \\ 0 & \dfrac{\partial^2 g_{2_{n+1}}}{\partial\alpha\,\partial\alpha} \end{pmatrix} \quad ; \quad \nabla f_{n+1}^y = \begin{pmatrix} \dfrac{\partial f_{n+1}^y}{\partial x} \\ \dfrac{\partial f_{n+1}^y}{\partial x} \end{pmatrix} \tag{5.150}$$

Finally, the substitution of the Eq. 5.148 in the Eq. 5.145a and after manipulation leads to the expression for the algorithmic elasto-plastic tangent modulus for the **BBM** model (formulated in terms of the net stress),

$$d\sigma_{n+1} = \left[E_{n+1} - \frac{E_{n+1} \dfrac{\partial f_{n+1}^y}{\partial x} \otimes \dfrac{\partial f_{n+1}^y}{\partial x} \bar{E}_{n+1}}{H_{n+1} + \left(\nabla^T f_{n+1}^y \bar{C}_{n+1} \nabla f_{n+1}^y\right)} \right] d\varepsilon_{n+1} \tag{5.151}$$

$$+ \left[W_{n+1} - \frac{E_{n+1} \dfrac{\partial f_{n+1}^y}{\partial x} \otimes \dfrac{\partial f_{n+1}^y}{\partial x} \bar{E}_{n+1} W_{n+1}}{H_{n+1} + \left(\nabla^T f_{n+1}^y \bar{C}_{n+1} \nabla f_{n+1}^y\right)} \right] ds_{n+1}$$

where $\left(W_{n+1} = \dfrac{\partial^2 g_{n+1}}{\partial\sigma\,\partial\sigma} \Big/ \dfrac{\partial^2 f_{n+1}}{\partial\varepsilon\,\partial s} \right)$ has been introduce for simplicity.

5.5.5)   Integration of Yu's hyperporoplastic model for non-isothermal conditions HP-CASM

In this sub-section the scheme of integration adopted for the model HP-CASM is summarized. Due to the identical structure of integration with the one proposed for the BBM1 model, the process of integration is not detailed.

In this case, two differential elements should be considered: (a) the new layout of the yield function and its dependence on the third invariant of the stress tensor J_3 and (b) the temperature dependency of the hardening law.

The following Boxes summarize the model: (a) General equations, (b) Discrete approximation and (c) Variational Forms.

<div style="border:1px solid black">

CONTINUUM FORM

Continuum constitutive equations for BBM3 model:

$$\sigma' = \frac{\partial f_s^g(\varepsilon, \alpha, \phi s, T)}{\partial \varepsilon} \quad ; \quad S_l = \frac{\partial f_s^g(\varepsilon, \alpha, \phi s)}{\partial \phi s}$$

$$\dot{\alpha} = \gamma \frac{\partial f^y(\sigma', \alpha, \phi s, T)}{\partial \sigma'} \quad ; \quad \rho = \dot{\rho} = 0$$

Strain driven problem:

$$\gamma \geq 0 \; ; \; f^y(\sigma', \alpha, \phi s, T) \leq 0 \; ; \; \gamma \cdot f^y(\sigma', \alpha, \phi s, T) = 0$$

$$\gamma \cdot \dot{f}^y(\sigma', \alpha, \phi s, T) = 0$$

$$\dot{\varepsilon}^e = \dot{\varepsilon} - \gamma \frac{\partial f^y(\sigma', \alpha, \phi s, T)}{\partial \sigma'}$$

Enforcement of consistency leads to:

$$\gamma = \frac{1}{h} \frac{\partial f^y}{\partial \sigma} \frac{\partial^2 f_s}{\partial \varepsilon \partial \varepsilon} \dot{\varepsilon}$$

</div>

<div style="border:1px solid black">

DISCRETE FORM

Increment $\Delta\varepsilon_{n+1}$, ΔT_{n+1} and Δs_{n+1} during time interval $\Delta t = t_{n+1} - t_n$, leads to:

$$\varepsilon_{n+1} = \varepsilon_n + \Delta\varepsilon_{n+1}$$

$$s_{n+1} = s_n + \Delta s_{n+1}$$

$$T_{n+1} = T_n + \Delta T_{n+1}$$

Backward-Euler discrete system of the equations for MCC model:

$$-\alpha_{n+1} + \alpha_n + \Delta\gamma \frac{\partial f^y(\sigma'_{n+1}, \alpha_{n+1}, \phi s_{n+1}, T)}{\partial \sigma'} \quad = \quad 0$$

$$\Delta\gamma \geq 0 \; ; \; f_{n+1}^y \leq 0 \; ; \; \Delta\gamma \cdot f_{n+1}^y = 0$$

$$\sigma_{n+1} = \frac{\partial f_s^g(\varepsilon_{n+1}, \alpha_{n+1}, \phi s_{n+1}, T_{n+1})}{\partial \varepsilon}; \quad S_{l_{n+1}} = \frac{\partial f_s^g(\varepsilon_{n+1}, \alpha_{n+1}, \phi s_{n+1}, T_{n+1})}{\partial \phi s}$$

predictor-corrector strategy:

$$\alpha_{n+1}^{trial} = \alpha_n \quad ; \quad \rho_{n+1}^{trial} = 0$$

$$\sigma_{n+1}'^{trial} = \frac{\partial f_s^g(\varepsilon_{n+1}, \alpha_{n+1}^{trial}, \phi s_{n+1}, T_{n+1})}{\partial \varepsilon}$$

Check of loading-unloading conditions:

$$\left(f_{n+1}^{y\,trial}\left(\sigma_{n+1}'^{trial}, \alpha_{n+1}^{trial}, \phi s_{n+1}, T_{n+1}\right) \leq 0\right) \quad \text{then} \quad (\blacksquare)_{n+1} = (\blacksquare)_{n+1}^{trial}$$

</div>

313

plastic corrector:

$$\varepsilon_{n+1}^{e} - \varepsilon_{n+1}^{e\,trial} + \Delta\gamma \frac{\partial f^{y}(\sigma'_{n+1}, \alpha_{n+1}, \phi s_{n+1}, T_{n+1})}{\partial \sigma'} \quad = \quad 0$$

with:

$$\varepsilon_{n+1}^{e} = \varepsilon_{n+1} - \alpha_{n+1} \quad ; \quad \varepsilon_{n+1}^{e\,trial} = \varepsilon_{n+1} - \alpha_{n}$$

Box 5.33:Variational Form for Inequality constraint HP-CASM model

VARIATIONAL FORM (inequality const.)

Variational Form BBM3 model:

$$\text{CPPM} \quad \begin{cases} \min & -g_{s}(\sigma', \alpha, \phi s, T) - (\sigma'\varepsilon_{n+1}) \\ (\sigma') & \\ \text{sub. to} & f^{y}(\sigma', \alpha, \phi s, T) \leq 0 \end{cases}$$

Lagrange functional associated:

$$\mathcal{L}^{g}(\sigma', \alpha, \phi s, T, \Delta\gamma) = -g_{s}(\sigma', \alpha, \phi s, T) - \sigma'\varepsilon_{n+1} + \Delta\gamma \cdot f^{y}(\sigma', \alpha, \phi s, T)$$

KKT conditions:

$$\varepsilon_{n+1}^{e} - \varepsilon_{n+1}^{e\,trial} + \Delta\gamma \frac{\partial f^{y}(\sigma'_{n+1}, \alpha_{n+1}, \phi s_{n+1}, T_{n+1})}{\partial \sigma'} \quad = \quad 0$$

$$f_{n+1}^{y}(\sigma', \alpha, \phi s, T) \quad = \quad 0$$

$$\Delta\gamma \quad \geq \quad 0$$

Residual vector:

$$r(x) = \quad \left\{ \begin{array}{c} \varepsilon_{n+1}^{e} - \varepsilon_{n+1}^{e\,trial} + \Delta\gamma \dfrac{\partial f_{n+1}^{y}}{\partial \sigma'} \\ f_{n+1}^{y} \end{array} \right\}$$

Jacobian Matrix: $\quad J = \nabla r(x)$

$$J(x) = \begin{bmatrix} I + \Delta\gamma \left(\dfrac{\partial^{2}f^{y}}{\partial\sigma'\,\partial\sigma'} \dfrac{\partial^{2}f_{s}}{\partial\varepsilon\,\partial\varepsilon} + \dfrac{\partial^{2}f^{y}}{\partial\sigma'\,\partial\alpha} \dfrac{\partial\alpha}{\partial\varepsilon^{e}} \right) & \dfrac{\partial f^{y}}{\partial\sigma'} \\ \dfrac{\partial f^{y}}{\partial\sigma'} \dfrac{\partial^{2}f_{s}}{\partial\varepsilon\,\partial\varepsilon} + \dfrac{\partial f^{y}}{\partial\alpha} \dfrac{\partial\alpha}{\partial\varepsilon^{e}} & 0 \end{bmatrix}$$

VARIATIONAL FORM (equality const.)

Variational Form BBM3 model:

$$\text{IPM} \begin{cases} \min \quad -g_s(\sigma', \alpha, \phi s, T) - \sigma' \varepsilon_{n+1} + \mu \cdot \log(z) \\ (\sigma') \\ \text{sub. to} \qquad f^y(\sigma', \alpha, \phi s, T) + z = 0 \end{cases}$$

Lagrange functional associated:

$$\mathcal{L}^g(\sigma', \alpha, \phi s, T, \Delta\gamma) = -g_s(\sigma', \alpha, \phi s, T) - \sigma' \varepsilon_{n+1}^{\text{trial}} + \Delta\gamma[f^y + z] + \mu \cdot \log(z)$$

KKT conditions:

$$\varepsilon_{n+1}^e - \varepsilon_{n+1}^{e \, \text{trial}} + \Delta\gamma \frac{\partial f^y(\sigma'_{n+1}, \alpha_{n+1}, \phi s_{n+1}, T_{n+1})}{\partial \sigma'} \quad = \quad 0$$

$$f_{n+1}^y + z \qquad\qquad = \quad 0$$

$$\Delta\gamma - \frac{\mu}{z} \qquad\qquad = \quad 0$$

$$(\Delta\gamma, z) \qquad\qquad \geq \quad 0$$

Residual vector:

$$r(x) = \begin{cases} \varepsilon_{n+1}^e - \varepsilon_{n+1}^{e \, \text{trial}} + \Delta\gamma \dfrac{\partial f^y(\sigma'_{n+1}, \alpha_{n+1}, \phi s_{n+1}, T_{n+1})}{\partial \sigma'} \\ f_{n+1}^y + z \\ \Delta\gamma \cdot z - \mu \end{cases}$$

Jacobian Matrix: $\quad J = \nabla r(x)$

$$J(x) = \begin{bmatrix} I + \Delta\gamma \left(\dfrac{\partial^2 f^y}{\partial \sigma' \partial \sigma'} \dfrac{\partial^2 f_s}{\partial \varepsilon \partial \varepsilon} + \dfrac{\partial^2 f^y}{\partial \sigma' \partial \alpha} \dfrac{\partial \alpha}{\partial \varepsilon^e} \right) & \dfrac{\partial f^y}{\partial \sigma'} & 0 \\ \dfrac{\partial f^y}{\partial \sigma'} \dfrac{\partial^2 f_s}{\partial \varepsilon \partial \varepsilon} + \dfrac{\partial f^y}{\partial \alpha} \dfrac{\partial \alpha}{\partial \varepsilon^e} & 0 & 1 \\ 0 & z & \Delta\gamma \end{bmatrix}$$

Figure 5.99 shows the convergence speed of the model integration for two different loading steps.
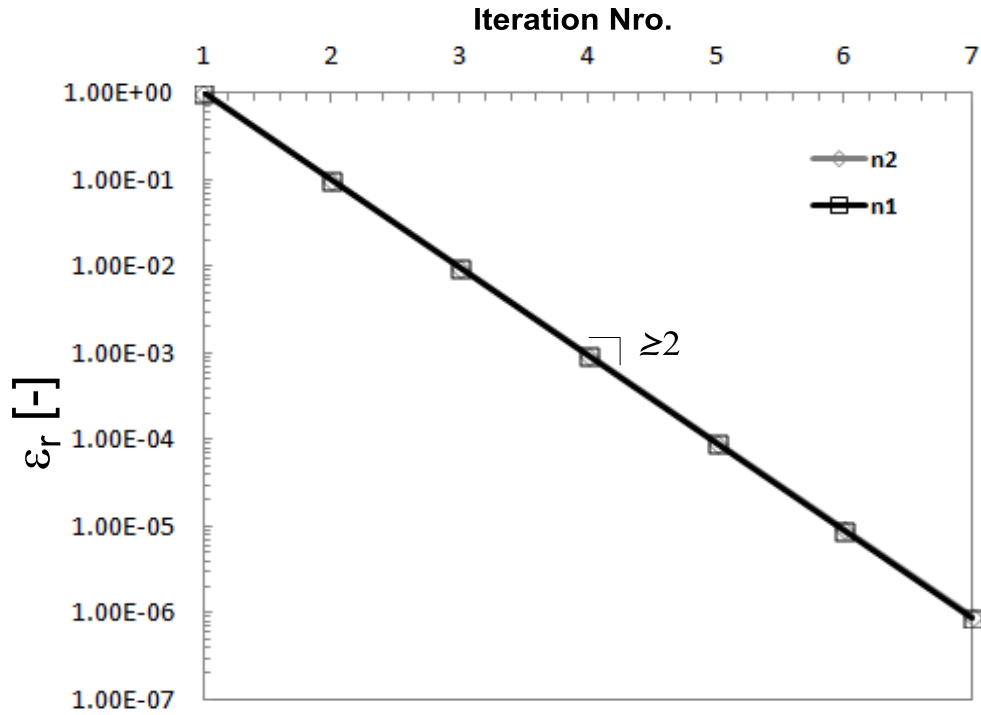
Figure 5.99: Convergence results of the primal-dual CPPM algorithm for two different loading steps. The slope results lightly higher than 2. For the selected value of the duality gap $\mu = 1e - 10$ the rate of convergence of both IPM and CPPM coincide.

The slope of the straight line results lightly higher than 2, precisely 2.321. Table 5.28 presents the values of the residual norm for two different load steps.

Table 5.28: Convergence properties of the HP-CASM model. Convergence speed for two different loading steps.

N-iter	$\frac{\|r\|}{\|r^0\|}$ (n1)	$\frac{\|r\|}{\|r^0\|}$ (n2)
1	1	1
2	0.098196763	0.098537465
3	0.009637009	0.009704331
4	0.00094589	0.000955835
5	9.28399E-05	9.41448E-05
6	9.11233E-06	9.27279E-06
7	8.94385E-07	9.13322E-07

Figures 5.100 and 5.101 show the rate of convergence of the HP-CASM model under three different dry states and three different thermal states.
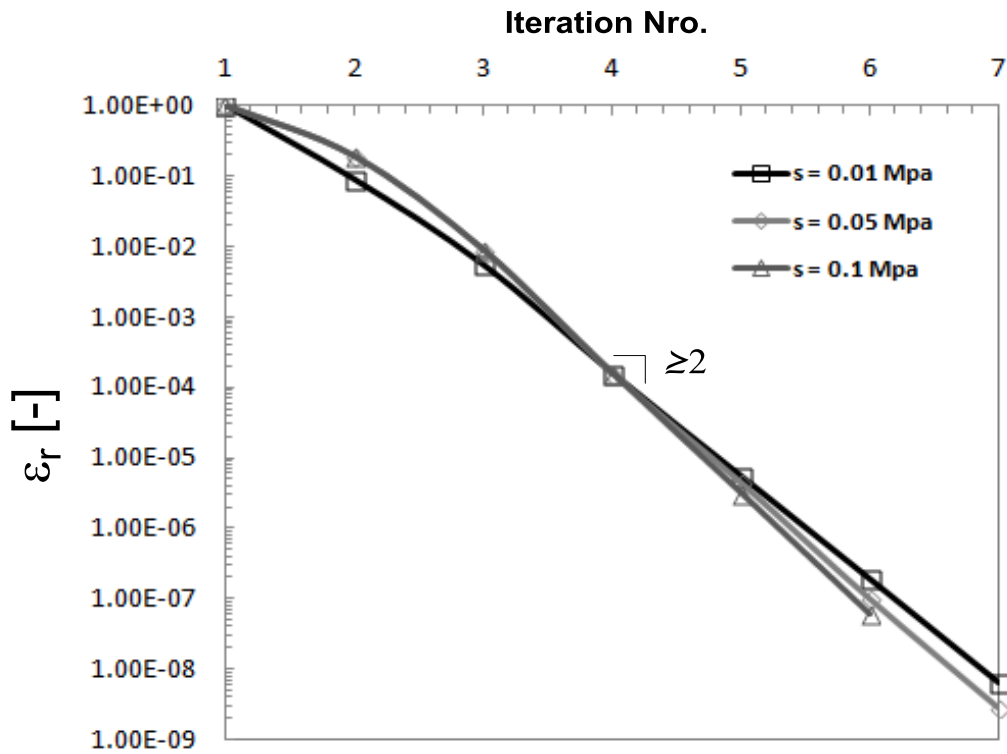
Figure 5.100: Convergence results of the primal-dual CPPM algorithm for three different suctions. The slope results lightly higher than 2. For the selected value of the duality gap $\mu = 1e - 10$ the rate of convergence of both IPM and CPPM coincide.
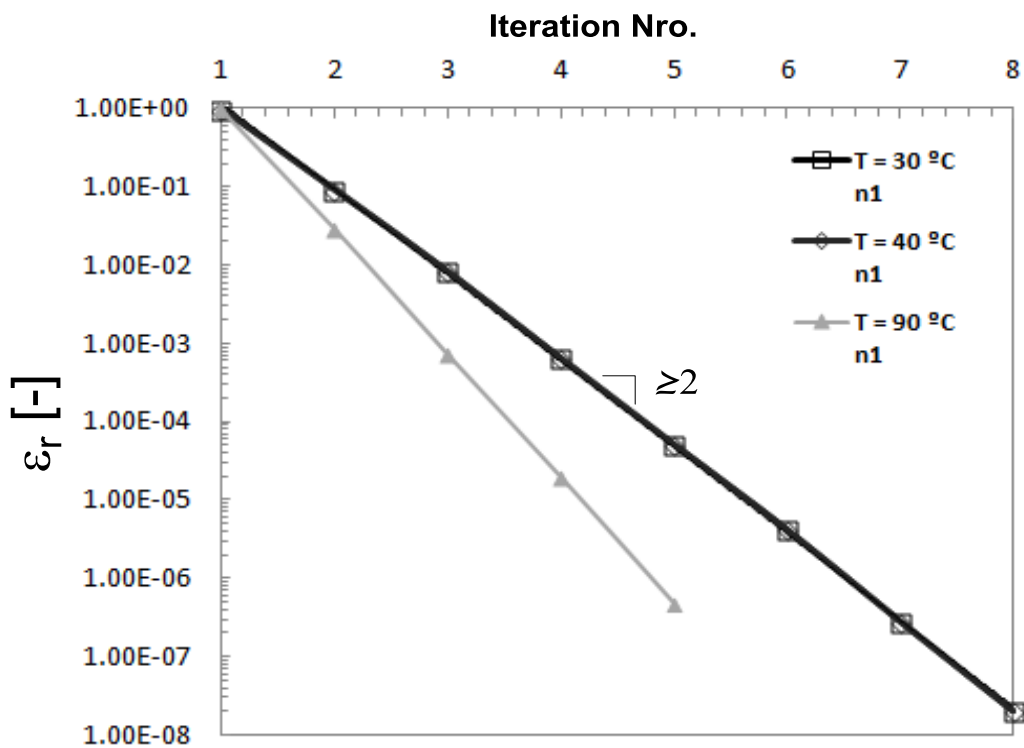
Figure 5.101: Convergence results of the primal-dual CPPM algorithm for three different temperatures. The slope results lightly higher than 2. For the selected value of the duality gap $\mu = 1e - 10$ the rate of convergence of both IPM and CPPM coincide.

For the partially saturated case the slope of the straight lines results lightly higher than two, around≈ 2.6. For the non-isothermal tests the slope of the straight lines results higher than two in all the cases.

5.5.6) Integration of Smoothed cohesive-frictional Drucker-Prager Model DP

In a hyper-poroplastic approach, and under the assumption of infinitesimal deformations, the non-incremental constitutive relations are derive from the energy functions of the porous skeleton presented at the former chapter as:

$$\sigma' = \frac{\partial f_s^g(\varepsilon, \alpha, \phi s, T)}{\partial \varepsilon} \tag{5.152}$$

$$S_l = \frac{\partial f_s^g(\varepsilon, \alpha, \phi s, T)}{\partial \phi s}$$

where $f_s^g(\varepsilon, \alpha, \phi s, T)$ has been defined in chapter 4. Also the evolution equation for the plastic internal variables (α) reads:

$$\dot{\alpha} = \gamma \frac{\partial f^y(x')}{\partial x'} \tag{5.153}$$

where, (γ) is the scalar plastic multiplier and $\left(\frac{\partial f^y(x')}{\partial x'} \right)$ is the general flow vector.

In this context the plastic multiplier is determined by the classical Kuhn-Tucker complementary conditions $\gamma \geq 0$; $f^y(x'') \leq 0$; $\gamma f^y(x'') = 0$ and the consistency condition $\gamma \dot{f}^y(x'') = 0$. These last two equations characterize the loading-unloading conditions and the persistency of the plastic state during plastic flow, respectively.

Those last condition together with the flow rule 5.153 expressed in terms of the elastic strains define the strain-suction-Temperature-driven structure of the problem. It is, for a given increment of total strain, suction and temperature the last set of equations determines the increments of stress σ', degree of saturation S_l, temperature T and plastic internal variable α.

The enforcement of the consistency condition allows arriving at the expression for the plastic multiplier γ.

The time integration of the above constitutive relations is performed in a strain-suction-temperature driven structure. In this scheme the stresses, suction, temperature and

internal variables known at t_n are updated to t_{n+1} according to the strain $(\Delta\varepsilon_{n+1})$, suction (Δs_{n+1}) and temperature (ΔT_{n+1}) increments applied during time interval $(\Delta t = t_{n+1} - t_n)$. Thus at time t_{n+1} total strains, suction and temperature are:

$$\varepsilon_{n+1} = \varepsilon_n + \Delta\varepsilon_{n+1} \tag{5.154}$$

$$s_{n+1} = s_n + \Delta s_{n+1}$$

$$T_{n+1} = T_n + \Delta T_{n+1}$$

while the stresses σ'_{n+1} and plastic internal variables α_{n+1} have to be computed.

To this purpose a backward-Euler approximation of the governing equation is used,

$$-\alpha_{n+1} + \alpha_n + \Delta\gamma\frac{\partial f^y(x'_{n+1})}{\partial x'} = 0 \tag{5.155}$$

with the discrete plastic multiplier $(\Delta\gamma)$ satisfying the loading-unloading conditions. The updated stress tensor is given by the relation:

$$\sigma_{n+1} = \frac{\partial f_s^g(\varepsilon_{n+1}, \alpha_{n+1}, \phi s_{n+1}, T_{n+1})}{\partial\varepsilon} \tag{5.156}$$

The numerical solution of the algebraic system of equations 5.155 expressed in terms of the elastic strain together with the discrete KKT conditions and Eq. 5.156 is accomplished following a predictor-corrector strategy. The predictor is given by the trial state defined by the known values at t_n:

$$\alpha_{n+1}^{trial} = \alpha_n \tag{5.157}$$

$$\sigma_{n+1}^{trial} = \frac{\partial f_s^g(\varepsilon_{n+1}, \alpha_{n+1}^{trial}, \phi s_{n+1}, T_{n+1})}{\partial\varepsilon}$$

Afterwards the loading-unloading conditions are verified, taking the trial state as the final solution when $f_{n+1}^{y^{trial}} < 0$, otherwise a plastic corrector step is performed $(\Delta\gamma > 0)$ in the same manner as done for the BBM1 model. The set of discrete nonlinear equations identical to the set at Eq. 5.107 is solved using a Newton-like iterative strategy.

The algorithms CPPM and IPM are properly understood by finding the existence of a variational structure of the general evolution equations.

Due to: (a) the convexity of the energy functions proposed to derive the **DP** model with respect to its arguments, (b) the twice differentiability with positive definite Hessian matrix $\nabla^2 f_s$ and (c) the associativity of the plastic flow in the dissipative space (hyper-poroplasticity), the solution state is obtained as the argument of the minimization problem:

Find $(\varepsilon_{n+1}) \in E$ such that $\qquad$ (5.158)

$$f_s^g(\varepsilon_{n+1}, \alpha_{n+1}, \phi s_{n+1}, T_{n+1}) = \min_{(\sigma') \in E} \{-g_s(\sigma', \alpha, \phi s, T) - (\sigma' \varepsilon_{n+1})\}$$

which, can be expressed alternatively as the inequality mathematical program,

$$\text{CPPM} \begin{cases} \min & -g_s(\sigma', \alpha, \phi s, T) - (\sigma' \varepsilon_{n+1}) \\ (\sigma') \\ \text{sub. to} & f^y(x') \leq 0 \end{cases} \qquad (5.159)$$

For this program the Lagrange functional associated is:

$$\mathcal{L}^g(\sigma', \alpha, \phi s, T, \Delta\gamma) = -g_s(\sigma', \alpha, \phi s, T) - (\sigma' \varepsilon_{n+1}) + \Delta\gamma \cdot f^y(x') \qquad (5.160)$$

The application of the necessary first order optimality conditions to 5.160 leads to the Kuhn-Tucker restrictions which results in an identical system of Eq. 5.113 for given values of suction and temperature.

Both the residual vector and the Jacobian matrix used to compute the advance direction towards the optimal point at CPPM algorithm are given by the expressions 5.114 and 5.115, respectively.

The constraint program Eq. 5.159 can be re-written in the standard form of equality constraint by introducing the slack variables (z):

$$\text{IPM} \begin{cases} \min & -g_s(\sigma', \alpha, \phi s, T) - (\sigma' \varepsilon_{n+1}) + \mu \cdot \log(z) \\ (\sigma') \\ \text{sub. to} & f^y(x') + z = 0 \end{cases} \qquad (5.161)$$

with an associated Lagrange functional given by:

$$\mathcal{L}^g(\sigma', \alpha, \phi s, T, \Delta\gamma) = \begin{aligned}[t] &-g_s(\sigma', \alpha, \phi s, T) - (\sigma' \varepsilon_{n+1}) + \Delta\gamma \cdot [f^y(x') + z] \\ &+ \mu \cdot \log(z) \end{aligned} \qquad (5.162)$$

In virtue of: (a) the complementarity of the energy functions and (b) the state functions derived in chapter 4, the imposition of the first order optimality conditions leads to the extended Kuhn-Tucker restrictions identical to those in Eq. 5.118. Moreover, both the residual vector and the Jacobian matrix are identical to those given by the expressions 5.119 and 5.120, respectively.

The following Boxes summarize the model: (a) General equations, (b) Discrete approximation and (c) Variational Forms.

Box 5.35: Continuum Governing equations for DP model

CONTINUUM FORM

Continuum constitutive equations for DP model:

$$\sigma' = \frac{\partial f_s^g(\varepsilon, \alpha, \phi s, T)}{\partial \varepsilon} \quad ; \quad S_l = \frac{\partial f_s^g(\varepsilon, \alpha, \phi s)}{\partial \phi s}$$

$$\dot{\alpha} = \gamma \frac{\partial f^y(\sigma', \alpha, \phi s, T)}{\partial \sigma'} \quad ; \quad \rho = \dot{\rho} = 0$$

Strain driven problem:

$$\gamma \geq 0 \ ; \ f^y(\sigma', \alpha, \phi s, T) \leq 0 \ ; \ \gamma \cdot f^y(\sigma', \alpha, \phi s, T) = 0$$

with $c = c(\phi s)$.

$$\gamma \cdot \dot{f}^y(\sigma', \alpha, \phi s, T) = 0$$

$$\dot{\varepsilon}^e = \dot{\varepsilon} - \gamma \frac{\partial f^y(\sigma', \alpha, \phi s, T)}{\partial \sigma'}$$

Enforcement of consistency leads to:

$$\gamma = \frac{1}{h} \frac{\partial f^y}{\partial \sigma} \frac{\partial^2 f_s}{\partial \varepsilon \partial \varepsilon} \dot{\varepsilon}$$

Box 5.36:Discrete Equations Backward - Euler approximation for DP model

---

DISCRETE FORM

Increment $\Delta \varepsilon_{n+1}$, ΔT_{n+1} and Δs_{n+1} during time interval $\Delta t = t_{n+1} - t_n$, leads to:

$$\varepsilon_{n+1} = \varepsilon_n + \Delta \varepsilon_{n+1}$$

$$s_{n+1} = s_n + \Delta s_{n+1}$$

$$T_{n+1} = T_n + \Delta T_{n+1}$$

Backward-Euler discrete system of the equations for MCC model:

$$-\alpha_{n+1} + \alpha_n + \Delta \gamma \frac{\partial f^y(\sigma'_{n+1}, \alpha_{n+1}, \phi s_{n+1}, T)}{\partial \sigma'} \quad = \quad 0$$

$$\Delta \gamma \geq 0 \ ; \ f_{n+1}^y \leq 0 \ ; \ \Delta \gamma \cdot f_{n+1}^y = 0$$

$$\sigma_{n+1} = \frac{\partial f_s^g(\varepsilon_{n+1}, \alpha_{n+1}, \phi s_{n+1}, T_{n+1})}{\partial \varepsilon}; \quad S_{l_{n+1}} = \frac{\partial f_s^g(\varepsilon_{n+1}, \alpha_{n+1}, \phi s_{n+1}, T_{n+1})}{\partial \phi s}$$

predictor-corrector strategy:

$$\alpha_{n+1}^{trial} = \alpha_n \quad ; \quad \rho_{n+1}^{trial} = 0$$

$$\sigma_{n+1}'^{trial} = \frac{\partial f_s^g(\varepsilon_{n+1}, \alpha_{n+1}^{trial}, \phi s_{n+1}, T_{n+1})}{\partial \varepsilon}$$

Check of loading-unloading conditions:

$$\left(f_{n+1}^{y\ trial}\left(\sigma_{n+1}'^{trial},\alpha_{n+1}^{trial},\phi s_{n+1},T_{n+1}\right)\leq 0\right)\quad then\ (\blacksquare)_{n+1}=(\blacksquare)_{n+1}^{trial}$$

with $c = c(\phi s)$.

plastic corrector:

$$\varepsilon_{n+1}^e-\varepsilon_{n+1}^{e\ trial}+\Delta\gamma\frac{\partial f^y(\sigma_{n+1}',\alpha_{n+1},\phi s_{n+1},T_{n+1})}{\partial\sigma'}\ =\ 0$$

with:

$$\varepsilon_{n+1}^e=\varepsilon_{n+1}-\alpha_{n+1}\quad ;\quad\varepsilon_{n+1}^{e\ trial}=\varepsilon_{n+1}-\alpha_n$$

Box 5.37:*Variational Form for Inequality constraint DP model*

<div align="center">

VARIATIONAL FORM (inequality const.)
</div>

Variational Form BBM3 model:

$$\text{CPPM}\quad\begin{cases}\min & -g_s(\sigma',\alpha,\phi s,T)-(\sigma'\varepsilon_{n+1})\\(\sigma')\\\text{sub. to} & f^y(\sigma',\alpha,\phi s,T)\leq 0\end{cases}$$

with $c = c(\phi s)$.

Lagrange functional associated:

$$\mathcal{L}^g(\sigma',\alpha,\phi s,T,\Delta\gamma)=-g_s(\sigma',\alpha,\phi s,T)-\sigma'\varepsilon_{n+1}+\Delta\gamma\cdot f^y(\sigma',\alpha,\phi s,T)$$

KKT conditions:

$$\varepsilon_{n+1}^e-\varepsilon_{n+1}^{e\ trial}+\Delta\gamma\frac{\partial f^y(\sigma_{n+1}',\alpha_{n+1},\phi s_{n+1},T_{n+1})}{\partial\sigma'}\ =\ 0$$
$$f_{n+1}^y(\sigma',\alpha,\phi s,T)\ =\ 0$$
$$\Delta\gamma\ \geq\ 0$$

Residual vector:

$$r(x)=\ \begin{Bmatrix}\varepsilon_{n+1}^e-\varepsilon_{n+1}^{e\ trial}+\Delta\gamma\dfrac{\partial f_{n+1}^y}{\partial\sigma'}\\ f_{n+1}^y\end{Bmatrix}$$

Jacobian Matrix: $J=\nabla r(x)$

$$J(x)=\begin{bmatrix}I+\Delta\gamma\left(\dfrac{\partial^2 f^y}{\partial\sigma'\partial\sigma'}\dfrac{\partial^2 f_s}{\partial\varepsilon\partial\varepsilon}+\dfrac{\partial^2 f^y}{\partial\sigma'\partial\alpha}\dfrac{\partial\alpha}{\partial\varepsilon^e}\right) & \dfrac{\partial f^y}{\partial\sigma'}\\[2ex]\dfrac{\partial f^y}{\partial\sigma'}\dfrac{\partial^2 f_s}{\partial\varepsilon\partial\varepsilon}+\dfrac{\partial f^y}{\partial\alpha}\dfrac{\partial\alpha}{\partial\varepsilon^e} & 0\end{bmatrix}$$

Box 5.38: Variational Form for Equality constraint DP model

VARIATIONAL FORM (equality const.)

Variational Form BBM3 model:

$$
\text{IPM} \begin{cases} \min_{(\sigma')} & -g_s(\sigma', \alpha, \phi s, T) - \sigma' \varepsilon_{n+1} + \mu \cdot \log(z) \\ \text{sub. to} & f^y(\sigma', \alpha, \phi s, T) + z = 0 \end{cases}
$$

with $c = c(\phi s)$.

Lagrange functional associated:

$$
\mathcal{L}^g(\sigma', \alpha, \phi s, T, \Delta\gamma) = -g_s(\sigma', \alpha, \phi s, T) - \sigma' \varepsilon_{n+1}^{\text{trial}} + \Delta\gamma[f^y + z] + \mu \cdot \log(z)
$$

KKT conditions:

$$
\begin{aligned}
\varepsilon_{n+1}^e - \varepsilon_{n+1}^{e\,\text{trial}} + \Delta\gamma \frac{\partial f^y(\sigma'_{n+1}, \alpha_{n+1}, \phi s_{n+1}, T_{n+1})}{\partial\sigma'} &= 0 \\
f_{n+1}^y + z &= 0 \\
\Delta\gamma - \frac{\mu}{z} &= 0 \\
(\Delta\gamma, z) &\geq 0
\end{aligned}
$$

Residual vector:

$$
r(x) = \begin{Bmatrix} \varepsilon_{n+1}^e - \varepsilon_{n+1}^{e\,\text{trial}} + \Delta\gamma \dfrac{\partial f^y(\sigma'_{n+1}, \alpha_{n+1}, \phi s_{n+1}, T_{n+1})}{\partial\sigma'} \\ f_{n+1}^y + z \\ \Delta\gamma \cdot z - \mu \end{Bmatrix}
$$

Jacobian Matrix: $\quad J = \nabla r(x)$

$$
J(x) = \begin{bmatrix} I + \Delta\gamma \left(\dfrac{\partial^2 f^y}{\partial\sigma'\,\partial\sigma'} \dfrac{\partial^2 f_s}{\partial\varepsilon\,\partial\varepsilon} + \dfrac{\partial^2 f^y}{\partial\sigma'\,\partial\alpha} \dfrac{\partial\alpha}{\partial\varepsilon^e} \right) & \dfrac{\partial f^y}{\partial\sigma'} & 0 \\ \dfrac{\partial f^y}{\partial\sigma'} \dfrac{\partial^2 f_s}{\partial\varepsilon\,\partial\varepsilon} + \dfrac{\partial f^y}{\partial\alpha} \dfrac{\partial\alpha}{\partial\varepsilon^e} & 0 & 1 \\ 0 & z & \Delta\gamma \end{bmatrix}
$$

Figures 5.102 and 5.103 show convergence results obtained with the algorithms CPPM and IPM, respectively. Particularly, Fig. 5.102 presents the convergence of the model integration for two different loading steps and under both saturated and isothermal conditions. The slope of the straight line results lightly higher than 2 (2.688).
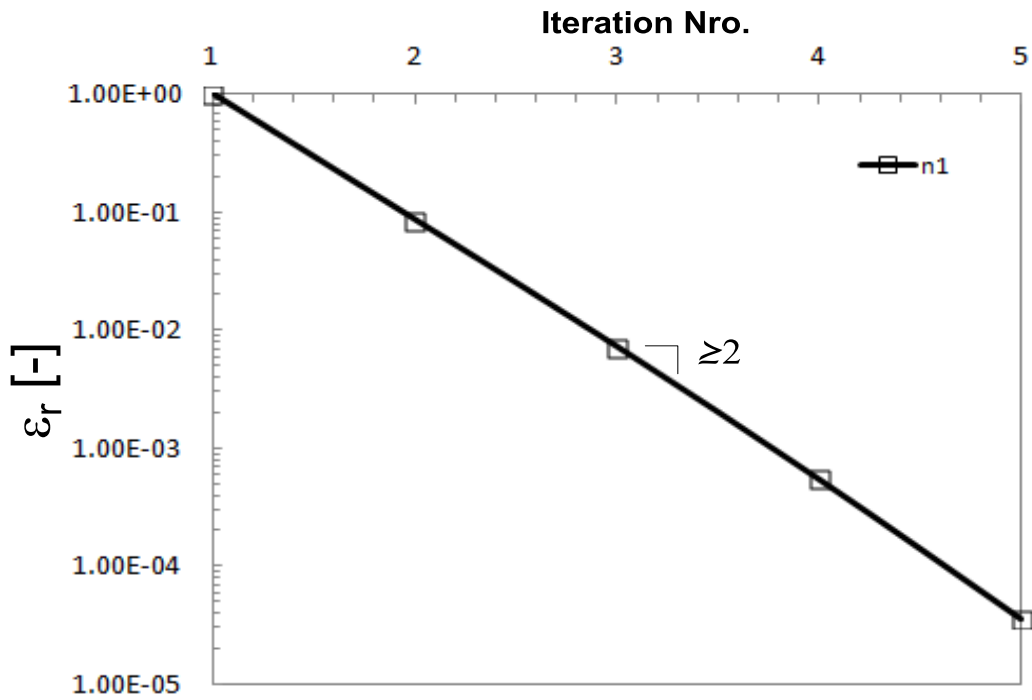
Figure 5.102: Convergence Results with the primal-dual CPPM and primal-dual IPM. Both show similar convergence properties for the same starting trial state and $\mu = 1e - 30$.

Figure 5.103 shows the model convergence under non-isothermal conditions. The model response in terms of convergence was tested for two different values of temperature.
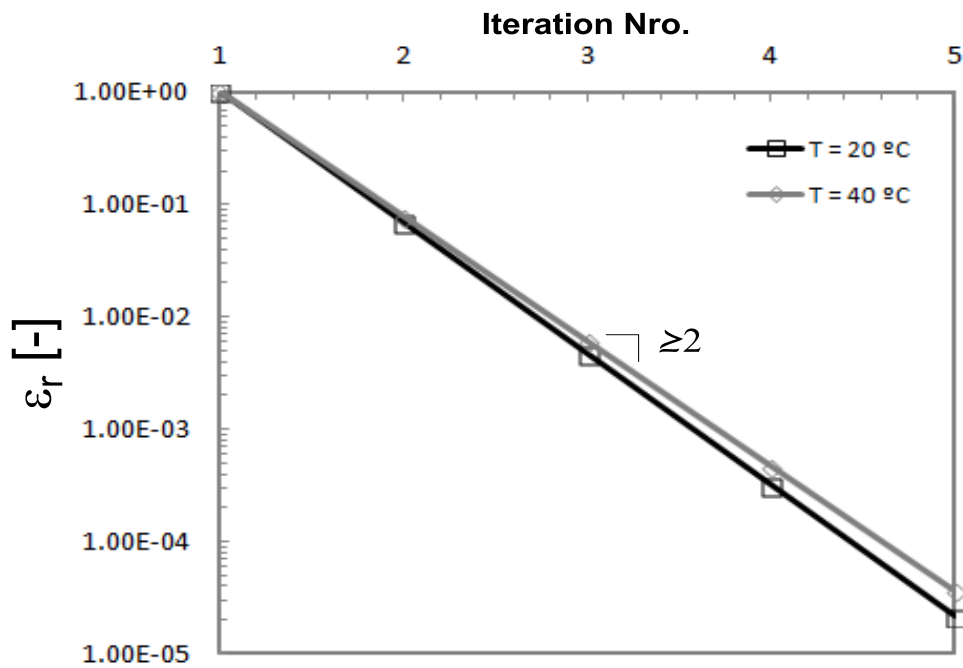
Figure 5.103: Convergence Results of the primal-dual CPPM for two different states of Temperature; a) $\left(T_a^0 = 20°C\right)$ and b)$\left(T_b^0 = 40°C\right)$. Both the CPPM and the IPM for a duality gap = 1e-10 have already the same properties of convergence.

The slopes of the straight lines results lightly higher than two. They are 2.688 for the test carried out at $T = 20°C$ and 2.556 for the test carried out at $T = 40°C$. Table 5.29 summarizes the convergence properties of the model for the two tests.

Table 5.29: Convergence speed of the DP model for two different temperatures.

N-iter	$\frac{\|r\|}{\|r^0\|}$ (*T20*)	$\frac{\|r\|}{\|r^0\|}$ (*T40*)
1	1	1
2	0.068079492	0.077695863
3	0.004629023	0.006028747
4	0.000314721	0.000467748
5	2.13973E-05	3.62906E-05

5.5.7) Integration of Matsuoka-Nakai Model - Principal Stress Space

The dependency of the Matsuoka-Nakai model on the three stress invariants I_1, I_2 and I_3 makes convenient to address the model integration in the plane of the principal stresses. This fact will allow to interpret the stress trajectories in an easier way.

Under the assumption of infinitesimal strains, the non-incremental constitutive relationships take the form:

$$\sigma' = \frac{\partial f_s^g(\varepsilon, \alpha, \phi s)}{\partial \varepsilon} \tag{5.163}$$

$$S_l = \frac{\partial f_s^g(\varepsilon, \alpha, \phi s)}{\partial \phi s}$$

for the Helmholtz energy function of the porous skeleton $f_s^g(\varepsilon, \alpha, \phi s)$ defined in chapter 4. As well, the evolution equation for the plastic internal variable α reads,

$$\dot{\alpha} = \gamma \frac{\partial f^y\big(I_1(x'), I_2(x'), I_3(x')\big)}{\partial x'} \tag{5.164}$$

where, (γ) is the scalar plastic multiplier and $\left(\partial f^y(x')\big/_{\partial x'}\right)$ is the general flow vector and $\big(I_1(x'), I_2(x'), I_3(x')\big)$ are the first, second and third invariants of the generalized stress tensor(x'). In this context the plastic multiplier is determined by the classical Kuhn-Tucker complementary conditions $\gamma \geq 0; f^y \leq 0; \gamma f^y = 0$ and the consistency condition $\gamma \dot{f}^y = 0$.

Those conditions together with Eq. 5.164 characterize the loading-unloading conditions and the persistency of the plastic state during plastic flow.

Moreover the expression of the flow rule in terms of the elastic strains $\dot{\varepsilon}^e = \dot{\varepsilon} + \dot{\alpha}$ in addition to the KKT conditions define the strain-driven structure of the problem, while enforcement of the consistency condition eq. 5.31 allows stating the expression for the plastic multiplier γ:

$$\gamma = \frac{1}{h} \frac{\partial f^y\big(I_1(x'), I_2(x'), I_3(x')\big)}{\partial x'} \frac{\partial x'}{\partial \sigma'} \frac{\partial^2 f_s^g}{\partial \varepsilon \, \partial \varepsilon} \dot{\varepsilon} \qquad (5.165)$$

Here (h) is the hardening modulus given by $\left(h = \nabla f^{yT} \nabla^2 f_s \nabla f^y\right)$.

The time integration of the above constitutive relations is performed in a strain-suction driven structure as done for the Drucker-Pager model. The objective is to obtain the updated stresses (σ'_{n+1}). To this purpose the backward-Euler approximation of the governing equations is used,

$$-\alpha_{n+1} + \alpha_n + \Delta\gamma \frac{\partial f^y(x'_{n+1})}{\partial x'} = 0 \qquad (5.166)$$

However due to the three invariant dependency of the model, it is highly convenient to represent it in the principal stress space.

So now the goal is to present the discrete equations in terms of its principal components (σ_i) and (ε_i) using the spectral decomposition and later find a variational structure of these equations to give a proper interpretation to the integration algorithm CPPM.

The stress-point algorithm appropriate for three-invariant MN plastic model must explicitly take into account the rotation of principal stress axes. To this end the linearization of the stresses for the non-rotating principal stresses results in an unique form of the tangent operator while the linearization of the spin part (rotation of the principal axis) can be carried out through two options; (a) "eigenvector linearization approach" (Simo & Hughes, 1998) or (b) "eigenbases linearization approach" (Borja, Sama, & Sanz, 2003). The first option has been used at the present dissertation to compute the principal axis rotation as result of the return mapping.

The numerical solution of 5.166 obeying the KKT conditions is accomplished following a predictor corrector strategy. The predictor step is given by the trial state defined by the known values at t_n,

$$\alpha_{n+1}^{trial} = \alpha_n \tag{5.167}$$

$$\sigma_{n+1}^{trial} = \frac{\partial f_s^g\left(\varepsilon_{n+1}, \alpha_{n+1}^{trial}, \phi s_{n+1}\right)}{\partial \varepsilon}$$

Check of loading-unloading conditions is then performed on the basis of the trial state:

$$\text{If } \left(f_{n+1}^{y\,trial}\left(I_1\left(\sigma_{n+1}'^{trial}\right), I_2\left(\sigma_{n+1}'^{trial}\right), I_3\left(\sigma_{n+1}'^{trial}\right)\right) \le 0\right) \quad \text{then } (\blacksquare)_{n+1} = (\blacksquare)_{n+1}^{trial} \tag{5.168}$$

the trial state is taken as the final solution. If not, a new solution is being looked for (leading to the so-called plastic corrector step) where $\Delta\gamma > 0$:

$$\varepsilon_{n+1}^e = \varepsilon_{n+1} - \alpha_{n+1} \tag{5.169}$$

$$\varepsilon_{n+1}^{e\,trial} = \varepsilon_{n+1} - \alpha_n$$

Equation 5.166 can be re-written equivalently in terms of the elastic strains (ε_{n+1}^e) and the elastic trial strains $\left(\varepsilon_{n+1}^{e\,trial}\right)$ as,

$$\varepsilon_{n+1}^e - \varepsilon_{n+1}^{e\,trial} + \Delta\gamma\frac{\partial f^y(x_{n+1}')}{\partial x'} = 0 \tag{5.170}$$

and in terms of principal strains results in the system:

$$\begin{aligned}
\varepsilon_{1_{n+1}}^e - \varepsilon_{1_{n+1}}^{e\,trial} + \Delta\gamma \cdot \frac{\partial f_{n+1}^y}{\partial x_{1_{n+1}}}\frac{\partial x_1}{\partial \sigma_1} &= 0 \\
\varepsilon_{2_{n+1}}^e - \varepsilon_{2_{n+1}}^{e\,trial} + \Delta\gamma \cdot \frac{\partial f_{n+1}^y}{\partial x_{2_{n+1}}}\frac{\partial x_2}{\partial \sigma_2} &= 0 \\
\varepsilon_{3_{n+1}}^e - \varepsilon_{3_{n+1}}^{e\,trial} + \Delta\gamma \cdot \frac{\partial f_{n+1}^y}{\partial x_{3_{n+1}}}\frac{\partial x_3}{\partial \sigma_3} &= 0
\end{aligned} \tag{5.171}$$

The set of nonlinear equations 5.171 is solved using a Newton-like iterative strategy.

On the other hand due to the convexity properties of the energy functions and the yield surface (MN), described in chapter 4 the solution state can be find by minimization of the problem:

$$\boxed{\begin{aligned}
&\text{Find } (\varepsilon_{n+1}) \in E \text{ such that} \\
&\quad f_s^g(\varepsilon_{n+1}, \alpha_{n+1}, \phi s_{n+1}) = \min_{(\sigma') \in E} \{-g_s(\sigma', \alpha, \phi s) - (\sigma'\varepsilon_{n+1})\}
\end{aligned}} \tag{5.172}$$

this can be expressed alternatively as the inequality mathematical program,

$$\text{CPPM} \begin{cases} \min\limits_{(\sigma')} & -g_s(\sigma', \alpha, \phi s) - (\sigma'\varepsilon_{n+1}) \\ \text{sub. to} & f^y(x') \le 0 \end{cases} \tag{5.173}$$

Now, from standard arguments in constraint optimization the Lagrange functional associated to the variational problem 5.172 is:

$$\mathcal{L}^g(\sigma', \alpha, \phi s, \Delta\gamma) = -g_s(\sigma', \alpha, \phi s) - (\sigma'\varepsilon_{n+1}) + \Delta\gamma \cdot f^y(x') \qquad (5.174)$$

The application of the necessary first order optimality conditions to 5.174 leads to the Kuhn-Tucker restrictions which in terms of the principal strains read:

$$(5.175)$$

$$
\begin{aligned}
\varepsilon^e_{1_{n+1}} - \varepsilon^{e\,\text{trial}}_{1_{n+1}} + \Delta\gamma \cdot \frac{\partial f^y_{n+1}}{\partial x_{1_{n+1}}} \frac{\partial x_1}{\partial \sigma_1} &= 0 \\[2mm]
\varepsilon^e_{2_{n+1}} - \varepsilon^{e\,\text{trial}}_{2_{n+1}} + \Delta\gamma \cdot \frac{\partial f^y_{n+1}}{\partial x_{2_{n+1}}} \frac{\partial x_2}{\partial \sigma_2} &= 0 \\[2mm]
\varepsilon^e_{3_{n+1}} - \varepsilon^{e\,\text{trial}}_{3_{n+1}} + \Delta\gamma \cdot \frac{\partial f^y_{n+1}}{\partial x_{3_{n+1}}} \frac{\partial x_3}{\partial \sigma_3} &= 0 \\[2mm]
f^y_{n+1}(x'_1, x'_2, x'_3) &= 0 \\[2mm]
\Delta\gamma &\geq 0
\end{aligned}
$$

where $\left(\varepsilon^e_a = \sum_{b=1}^{3} D^{gs}_{ab}\, \sigma_b\right)$. From the first optimality KKT conditions 5.175 the residual vector used in the algorithm CPPM is obtained as:

$$(5.176)$$

$$
r(x) = \left\{
\begin{aligned}
&\varepsilon^e_{1_{n+1}} - \varepsilon^{e\,\text{trial}}_{1_{n+1}} + \Delta\gamma \cdot \frac{\partial f^y_{n+1}}{\partial x_{1_{n+1}}} \frac{\partial x_1}{\partial \sigma_1} \\[2mm]
&\varepsilon^e_{2_{n+1}} - \varepsilon^{e\,\text{trial}}_{2_{n+1}} + \Delta\gamma \cdot \frac{\partial f^y_{n+1}}{\partial x_{2_{n+1}}} \frac{\partial x_2}{\partial \sigma_2} \\[2mm]
&\varepsilon^e_{3_{n+1}} - \varepsilon^{e\,\text{trial}}_{3_{n+1}} + \Delta\gamma \cdot \frac{\partial f^y_{n+1}}{\partial x_{3_{n+1}}} \frac{\partial x_3}{\partial \sigma_3} \\[2mm]
&\qquad\qquad f^y_{n+1}(x'_1, x'_2, x'_3)
\end{aligned}
\right.
$$

and the Jacobian matrix of the residual vector used to compute the advance direction to search for the solution state (the optimal point), results:

$$J(x) \qquad\qquad\qquad\qquad\qquad\qquad\qquad\qquad\qquad\qquad\qquad\qquad (5.177)$$

$$
= \begin{bmatrix}
D^{gs}_{11} + \Delta\gamma \dfrac{\partial f^y}{\partial x_1 \partial x_1}\dfrac{\partial x_1}{\partial \sigma_1} & D^{gs}_{12} + \Delta\gamma \dfrac{\partial f^y}{\partial x_1 \partial x_2}\dfrac{\partial x_2}{\partial \sigma_2} & D^{gs}_{13} + \Delta\gamma \dfrac{\partial f^y}{\partial x_1 \partial x_3}\dfrac{\partial x_3}{\partial \sigma_3} & \dfrac{\partial f^y}{\partial x_1}\dfrac{\partial x_1}{\partial \sigma_1} \\[4mm]
D^{gs}_{21} + \Delta\gamma \dfrac{\partial f^y}{\partial x_2 \partial x_1}\dfrac{\partial x_1}{\partial \sigma_1} & D^{gs}_{22} + \Delta\gamma \dfrac{\partial f^y}{\partial x_2 \partial x_2} & D^{gs}_{23} + \Delta\gamma \dfrac{\partial f^y}{\partial x_2 \partial x_3} & \dfrac{\partial f^y}{\partial x_2}\dfrac{\partial x_2}{\partial \sigma_2} \\[4mm]
D^{gs}_{31} + \Delta\gamma \dfrac{\partial f^y}{\partial x_3 \partial x_1}\dfrac{\partial x_1}{\partial \sigma_1} & D^{gs}_{32} + \Delta\gamma \dfrac{\partial f^y}{\partial x_3 \partial x_2} & D^{gs}_{33} + \Delta\gamma \dfrac{\partial f^y}{\partial x_3 \partial x_3} & \dfrac{\partial f^y}{\partial x_3}\dfrac{\partial x_3}{\partial \sigma_3} \\[4mm]
\dfrac{\partial f^y}{\partial x_1}\dfrac{\partial x_1}{\partial \sigma_1} & \dfrac{\partial f^y}{\partial x_2}\dfrac{\partial x_2}{\partial \sigma_2} & \dfrac{\partial f^y}{\partial x_3}\dfrac{\partial x_3}{\partial \sigma_3} & 0
\end{bmatrix}
$$

with D^{gs}_{ab} being the elastic moduli given by:

$$D_{ab}^{gs} = \frac{3K+G}{9KG} \cdot \begin{bmatrix} 1 & -\dfrac{3K-2G}{2(3K+G)} & -\dfrac{3K-2G}{2(3K+G)} \\[2mm] -\dfrac{3K-2G}{2(3K+G)} & 1 & -\dfrac{3K-2G}{2(3K+G)} \\[2mm] -\dfrac{3K-2G}{2(3K+G)} & -\dfrac{3K-2G}{2(3K+G)} & 1 \end{bmatrix} \qquad (5.178)$$

Then a Pseudo-code of the CPPM algorithm is presented. On this occasion it incorporates the determination of the variables values at the principal directions before its entrance in return loop.

Box 5.39: CPPM Pseudo-code for the MN model's integration

1) $\varepsilon_{n+1} = \varepsilon_n + \Delta\varepsilon_n$; $\left(\varepsilon_{n+1}^{etrial}\right)$; $\sigma_{n+1}^{trial} = \sigma\left(\varepsilon_{n+1}^{etrial}\right)$; s_{n+1}, α_{n+1}^{trial}

2) Compute the principal stress components $\left(\sigma_a^{trial}\right)$

3) Evaluate the yield surface $\left(f^y\left(\sigma_1^{trial}, \sigma_2^{trial}, \sigma_3^{trial}\right)\right)$

4) If $\left(f^y\left(\sigma_1^{trial}, \sigma_2^{trial}, \sigma_3^{trial}\right) \leq 0\right)$ then $\left(\sigma_{n+1} \leftarrow \sigma_{n+1}^{trial}\right)$

5) Else "Return Mapping" Initialize (set $k = 0$): $\left(\gamma^{(0)} = 0\right)$

   $\left(x^{(0)}\right)$ and $\left(r^{(0)}(x)\right)$ (according to the addressed problem, eq. (164))

5.1) Check overall convergence: $\quad \left\|r^{(k)}(x)\right\| \leq$ itol

5.2) Compute the Jacobian matrix $\left(J^{(k)}\right)$ Eq.5.141

   with quantities evaluated at $\left(x^{(k)}\right)$

5.3) Attempt a modified Newton step:
   $$\left(x^{(k+1)}, r^{(k+1)}\right) = \textbf{Newton-step}\ \left(x^{(k)}, x^{(0)}, r^{(k)}, J^{(k)}\right)$$

5.4) Set $(k \leftarrow k + 1)$ and go to 3

6) $\left(x_{n+1} = x_n^{k+1}\right)$

7) Return $\left(\sigma_{n+1} = \sigma(x_{n+1})\right)$

Figure 5.104 shows the convergence results obtained with the algorithm (primal − dual CPPM) when MN model is integrated.
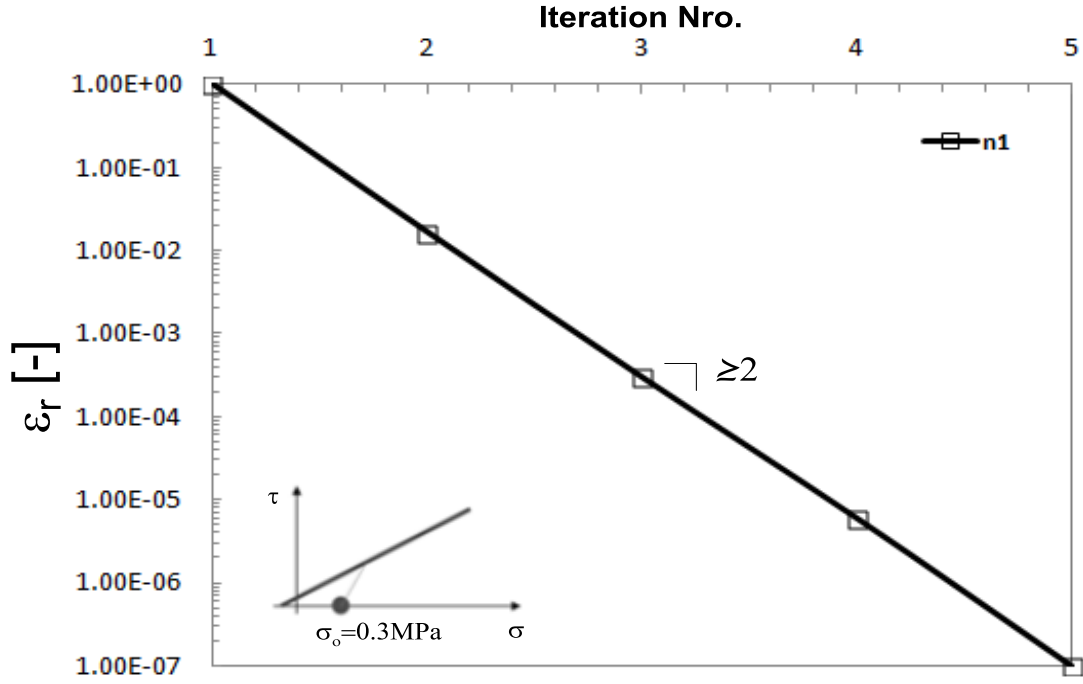
Figure 5.104: Convergence Results with the primal-dual CPPM for the Matsuoka-Nakai model at principal stress space.

5.5.7.1) Tangent Operator for Hyper-Poroplastic MN - Model

The tangent operator defined by the instantaneous variation of stresses with respect to the strains $\left(c = {d\sigma}/{d\varepsilon}\right)$ can be obtained by considering first the expression for the principal stress tensor(σ_a),

$$\sigma_a = \sigma_a^{trial} - \Delta\lambda \sum_{b=1}^{3} C_{ab}^{f_s} \frac{\partial f^y}{\partial x_b} \frac{\partial x_b}{\partial \sigma_b} \tag{5.179}$$

Differentiation of equation 5.179 allows to obtain the expression for the plastic multiplier$(\Delta\gamma)$,

$$\Delta\gamma = \frac{1}{H} \sum_{a=1}^{3} \sum_{b=1}^{b} \frac{\partial f^y}{\partial x_a} \frac{\partial x_a}{\partial \sigma_a} C_{ab}^{f_s} \dot{\varepsilon}_a \tag{5.180}$$

from equations 5.179 and 5.180 the elasto-plastic tangent moduli (ignoring the rotation of the principal stress) is obtained as:

$$C_{ab} = C_{ab}^{f_s} - \frac{1}{H} \sum_{i=1}^{3} \sum_{j=1}^{3} C_{ai}^{f_s} \frac{\partial f^y}{\partial x_i} \otimes \frac{\partial f^y}{\partial x_j} C_{jb}^{f_s} \tag{5.181}$$

Alternatively (C_{ab}) can be computed from the Jacobian matrix 5.177 penalizing the rows and column in excess as:

$$C_{ab} = (I_{n3} \quad 0) \cdot J(x)^{-1} \cdot \begin{pmatrix} I_{n3} \\ 0 \end{pmatrix} \tag{5.182}$$

Finally, the tangent fourth-order tensor reflecting the change in the orientation of the spectral directions, is given by Borja (2003),

$$\mathbb{C} = \sum_{a=1}^{3} \sum_{b=1}^{3} C_{ab} \, m^a \otimes m^b + \frac{1}{2} \sum_{a=1}^{3} \sum_{\substack{b=1 \\ b \neq a}}^{3} \left(\frac{\sigma_b - \sigma_a}{\varepsilon_b^e - \varepsilon_a^e} \right) \cdot \left(m^{ab} \otimes m^{ab} + m^{ab} \otimes m^{ba} \right) \tag{5.183}$$

The first term of $(\mathbb{C})$ is a function of the constitutive response and the algorithm is used to track this response, whereas the second term is a function of the rotation of the principal directions alone and not of the specific plasticity model used.

5.6) Interior-Point algorithm advantages and benefits

This subsection addresses the benefits of the interior-point algorithm over the classical closest-point algorithm. Until now, similarities of both algorithms have been referred.

In cases where the stress points are very far from the allowable space, the last algorithm fails to converge. The distance between the stress points and the yield surface is large enough to make the global CPP algorithm impossible to reach a satisfactory optimal point, Fig. 5.105.

However, the interior-point algorithm has the necessary flexibility to achieve the optimum even in cases of difficult convergence as the one set at Fig. 5.105. In fact the algorithm provides progressive and partial KKTµ solutions characterized by positive values of the duality variable $\mu > 0$. Those values form a decreasing series until the final solution is reached characterized by $\mu = 0$. This property confers to the algorithm with a significative robustness.

Then the algorithm is able to reach solution states (optimal points) even when the stress trials are far from the allowable space and therefore far from the Newton's convergence zone.
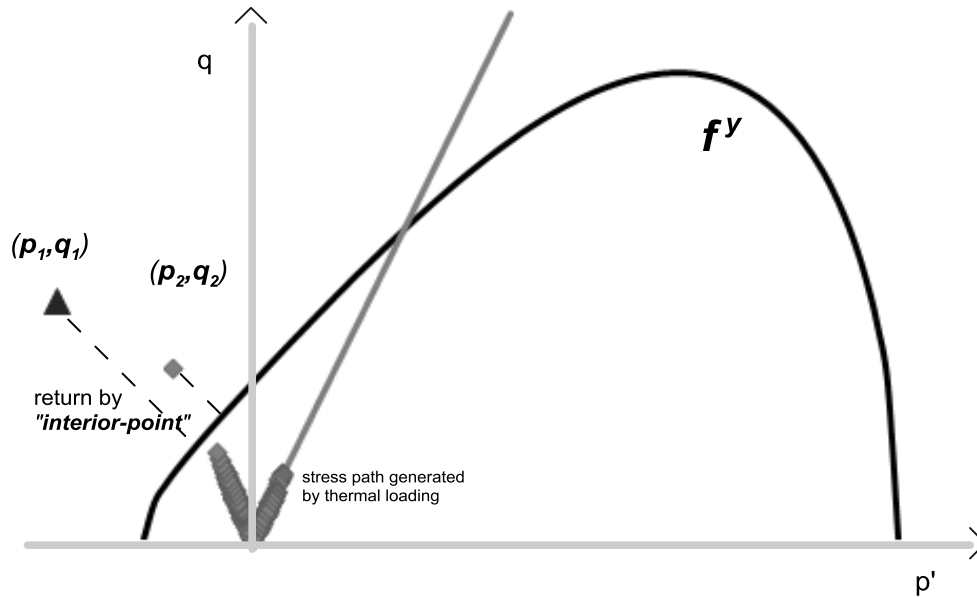
Figure 5.105: Distance between the points(1- 2) and the yield surface is large enough that the CPPM fail to reach the optimal point. However the interior-point algorithm IPM, allows a progressive approach to the optimal point (solution) by solving the KKT$_\mu$ conditions.

Box 5.40 recovers the Pseudo-code of the interior-point algorithm shown above to an easier comprehension of the main loop.

Box 5.40: Pseudo-code for primal-dual interior point method for integration of hyper-poroplasticity.

1) Input data x_{n+1}^{trial}, $f_{n+1}^{y\,\text{trial}}$

2) Initialize (set m=0): $\left(\gamma^{(0)} = 0\right), \left(z^{(0)} = 0\right),$

3) **barrier loop**: check barrier convergence $\mu \leq \mu_{TOL}$

4) Initialize (set $k = 0$): $\left(x^{(0)} = x^{(m)}\right), \left(\mu = \mu^{(m)}\right), \left(r^{(0)} = r^{(m)}\right),$

5) **Newton loop**: Check overall convergence: $\left\| r_\mu^{(k)}(x) \right\| \leq$ itol

6) Attempt Newton step: $\left(x^{(k+1)}, r_\mu^{(k+1)}\right) =$**Newton-step** $\left(x^{(k)}, x^{(0)}, r_\mu^{(k)}, J^{(k)}\right)$

7) Set $(k \leftarrow k + 1)$ and **go to 5**

8) $\left(x_{m+1} = x_m^{k+1}\right)$

9) $\mu^{m+1} = \mu^m - {r_z(\mu)}\big/{r_z{}'(\mu)}$ and **go to 3**

10) $(x_{n+1} = x_n^{m+1})$

Figure 5.106 shows the graph of the central-path obtained by the progressive solution of the partial KKTµ conditions when a shear stress path in extension is followed. This stress path is similar to the one observed at the analyzed case La Roque Gageac in chapter 7. Fig. 5.106 shows a progressive decrease (from a peak) of the slack variable z. Furthermore a progressive increase of the plastic multiplier Δγ is evidenced.
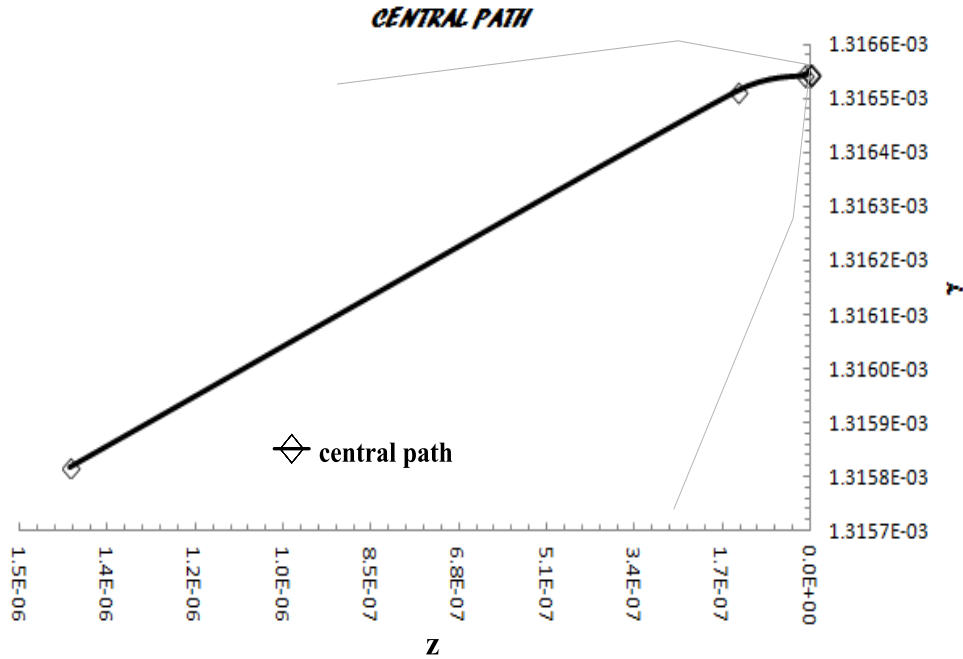
*Figure 5.106: Central-path of the progressive solution of KKTµ conditions, for a shear stress path in extension. A progressive decrease of the slack variable **z** is observed as well as the continuous increment of the plastic multiplier Δγ (amount of plasticity).*

Finally, Fig. 5.107 shows the rate of decrease of the duality gap variable while the number of barrier loops progresses.
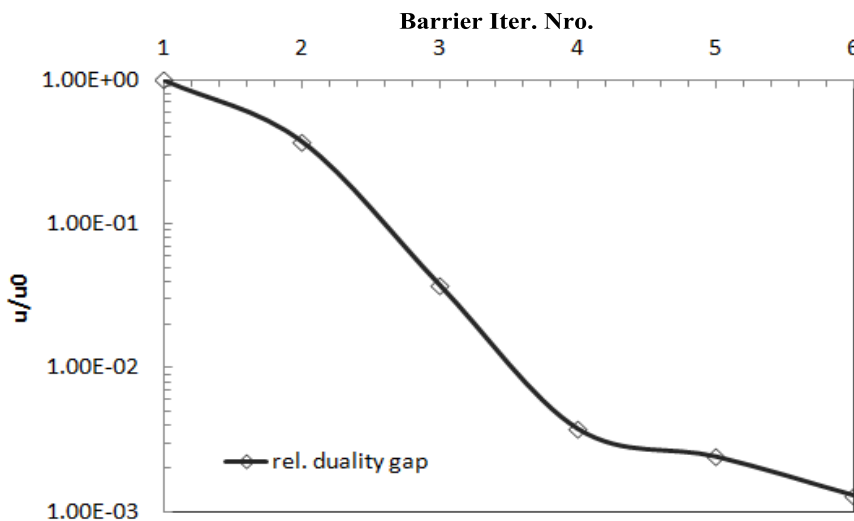
Figure 5.107: Rate of decrease of the duality gap variable with the number of barrier loops.

5.7) Conclusions

The study of the integration of the constitutive models developed in the previous chapters has been addressed along the chapter 5. The proper integration of the constitutive laws is a key point of the constitutive modeling.

One of the advantages of the elasto-plastic models being derived from the thermo-mechanical principles is that both, internal and dissipation energy functions, are known. Those functions include all the information on the models. Having those functions allows to integrate the constitutive laws through mathematical programming tools. The minimization of the functionals defined by the sum of the internal energy function and the dissipation function provides with proper variational structures. These structures allow to determine the optimal points (solution states) which are the solution to the return plastic mapping where the stress state lies on the yield surface. The study and development of two types of integration algorithm has been carried out:

   a) Return mapping by the closest-point projection
   b) Return mapping by the interior-point method

An additional method to control the step-size of the correction is included in both algorithms:

   c) Line-search method

Both algorithms have shown to have a lot in common. They have also presented very mild difference in convergence properties. In favor of the interior-point algorithm, its versatility should be noted in terms of parameterization options, leading to catch the optimal point even when the starting trial point is considerably far from the admissible region. It is a vast and open subject for further exploration.

CHAPTER 6

THERMO-HYDRAULIC MODELLING OF AN EXPERIMENTAL FALLOW FIELD

6.1) Introduction

Chapters 6, 7 and 8 deal with numerical modeling of geotechnical cases, concerning the interaction between the soil and the atmosphere.

Particularly, chapter 6 addresses the TH modeling of the soil-vegetation-atmosphere interaction in an experimental crop field instrumented to record the evolutions of water content and temperature in the upper soil layer. The study aims to predict temperature and humidity conditions in soils with similar characteristics under comparable climatic conditions to those prevailing in the region of Midi-Pyrénées, France.

Chapter 7, addresses the THM numerical modeling of a shallow foundation under atmospheric actions. The study aims to quantify differential settlements as a result of different wetting and temperature states changing at the topsoil.

Chapter 8, addresses the TM modeling of a cliff located in the south of France under the action of atmospheric radiation and atmospheric temperature. The study aims to predict displacements in the massif as well as an evaluation of the massif stability.

_____

The modeling of the experimental field considered in this chapter has been carried out to validate the boundary condition soil-vegetation-atmosphere presented in chapter 2. It will emphasize the decisive influence of transpiration flux on water variations in the soil.

The experimental field studied is located at "Le Fauga" Midi-Pyrénées- France, see Fig. 6.108.
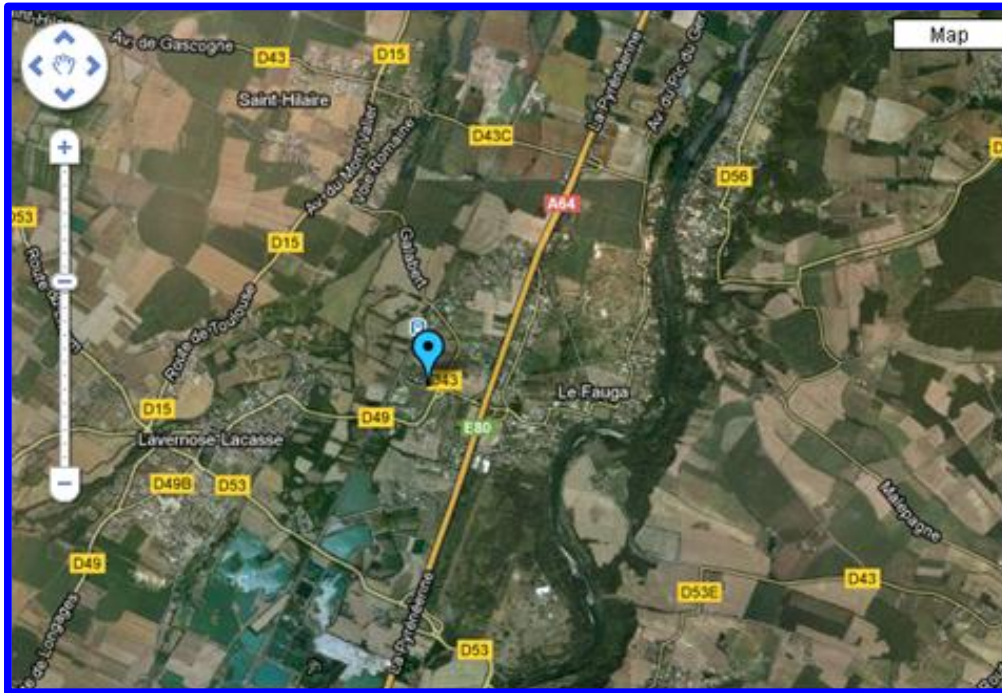
Figure 6.108: Satellite map of Le Fauga site (43° 24' 0" -North, 1° 17' 0" –East).

It is an experimental fallow field of the National Institute of French Meteorology (METEO FRANCE). This well instrumented field provides with high frequency measurements of atmosphere and soil variables.

The chapter is organized as follows, firstly notation and terminology used is presented. Secondly, the case and field characterization are addressed. Thirdly, equations governing the problem are stated. Fourthly, material properties of the upper soil layer at Le Fauga are presented. Fifthly, geometry-mesh and initial and boundary conditions assumed in the numerical model are shown. Finally, the results of the numerical model are exposed.

_____

6.2) Notation and Terminology

θ_l^w	apparent mass of liquid water
θ_g^w	apparent mass of vapor
S_l	Liquid degree of saturation
S_g	Gas degree of saturation
ϕ	Porosity
ρ_s	Unit mass of solid skeleton
ρ_l	Liquid density
ρ_g	Gas density
E_s	Specific energy of porous skeleton
E_l	Specific energy of liquid phase
E_g	Specific energy of gas phase
j_l^w	Net flow of liquid water
j_g^w	Net flow of vapor
j_{E_s}	Net flow of energy in the porous skeleton
j_{E_l}	Net flow of energy in the liquid phase
j_{E_g}	Net flow of energy in the gas phase
i_c	Conductive heat flux

6.3) Case statement and Field characterization

The atmospheric variables used for modeling the experimental field Le Fauga were registered at a weather station installed on the site for this purpose. Among others, precipitation, air temperature and air humidity (at 2m elevation), wind speed and direction (at 10 m elevation), atmospheric pressure and incoming solar radiation are registered. Figure 6.109 shows the variations of temperature, relative humidity and precipitation, registered at the site during the period between the years 2005 to 2007. The highest temperatures are registered in accordance with summer seasons. Those peaks coincide with the minimum values of relative humidity. Besides they appear outdated in relation to the highest precipitation.

In addition to the typical meteorological devices, two radiancemeters were installed in July 2003 to measure the incoming atmosphere radiation (R_g) and the upward luminance at a 40° incidence angle over the fallow field. These two radiancemeters allow the daily determination of the "surface reflectances" at five frequencies from the visible to the near infrared and the thermal infrared.
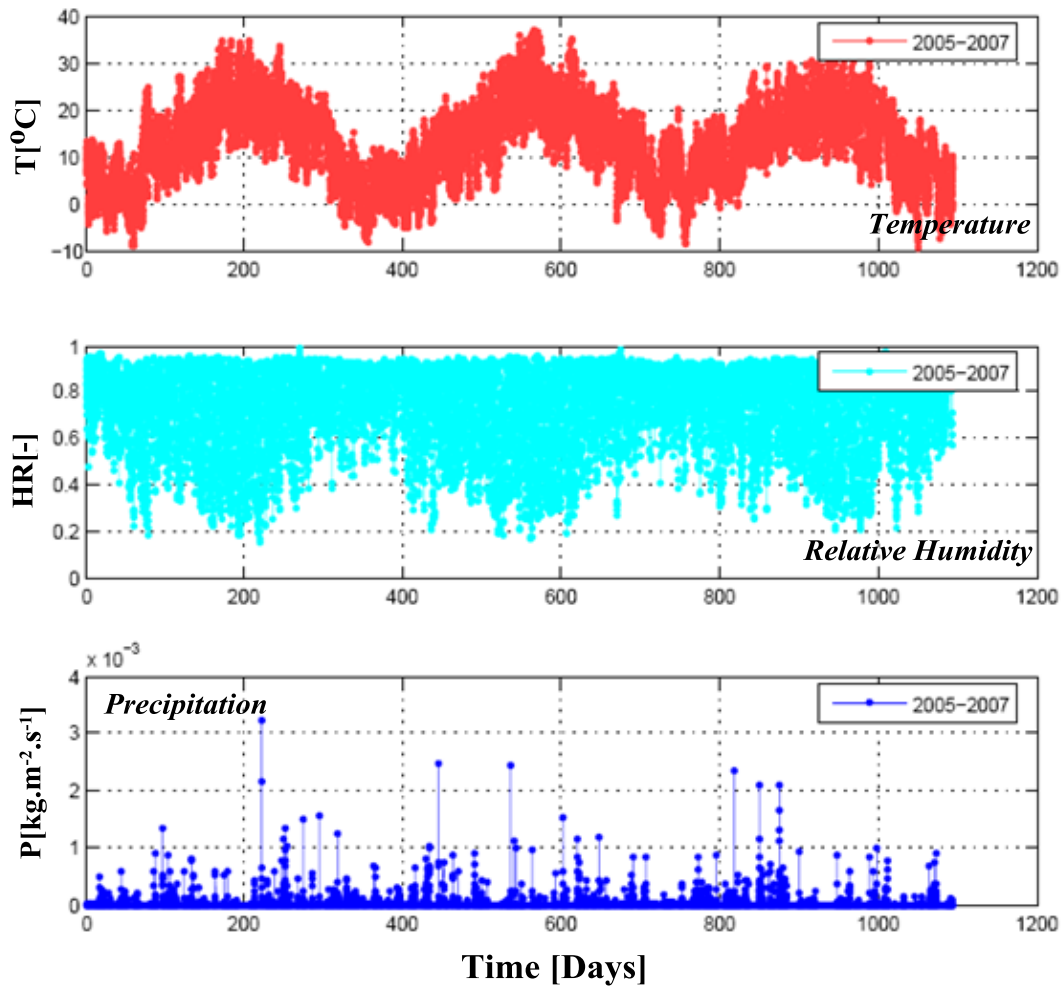
Figure 6.109: Temperature(T[°C]), Relative Humidity(HR) and Precipitation$\left(P\left[\dfrac{k_g}{m^2 s} \right] \right)$ measures with a

$(30\ min)$ *frequency at the site "Le Fauga".*

The surface reflectances permit the computation of vegetation indexes such as the NDVI (Normalized Vegetation Difference Index), which is shown to be related to the LAI. The roughness of the soil underneath the natural grass is found to be stable for the experiment duration. The roughness height was estimated to be a constant value of 20.0mm. Fig. 6.110 shows the cycles of Leaf Area Index during years 2005 to 2007.
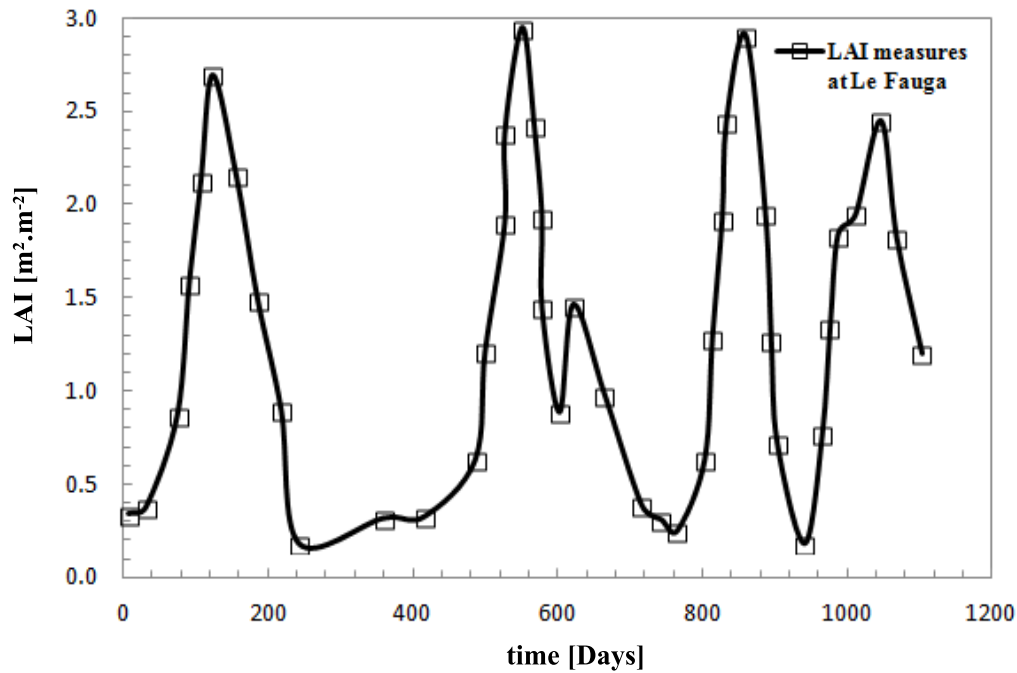
Figure 6.110: Cycles of Leaf Area Index (LAI) measured at "Le Fauga" site during years 2005, 2006 and 2007.

At ground level, land surface fluxes (sensible and latent heat fluxes) and vegetation characteristics (height, biomass, dry matter, water content and LAI) were measured. Samples of area ($25x25cm^2$) were randomly chosen in the fallow zone next to the LEWIS radiometer field, in order to measure vegetation mass and water content using a fresh and dry weighing method. Those quantities as well as the LAI measurements were frequently taken during spring, summer and fall, while sparser measurements were taken in winter when vegetation activity is slower.

6.4) Material Properties

Regarding the material characterization, only the upper soil layer was of interest in the present study. It is the layer where the main fluctuations take place. The grading curve of the upper soil layer shown in Fig. 6.111 shows a well-graded material.

_____
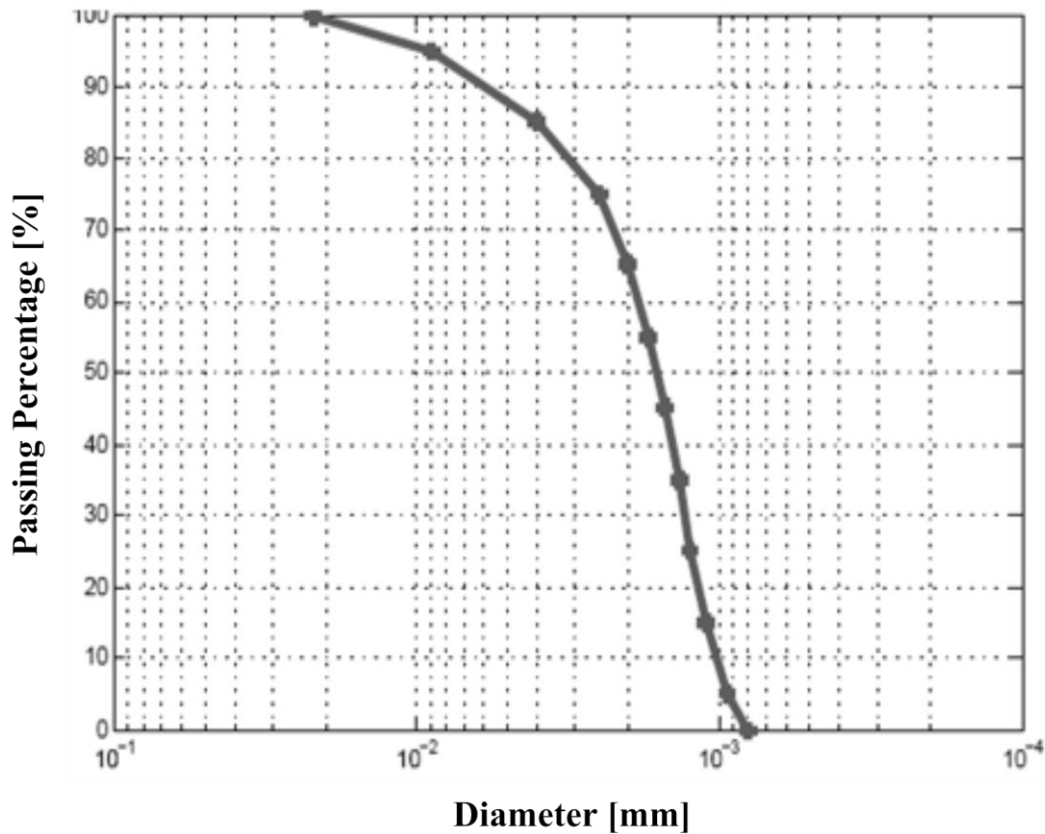
Figure 6.111: Grading curve of the upper soil layer at "Le Fauga" site.

It contains fractions of clay between 15.6% and 16.6% , silt between 47.2% and 47.4% and sand between 36.0% and 37.2%.

Table 6.30 gives a detailed profile of clay, silt and sand percentages present at the analyzed layer. Between 0.5m and 2m the soil becomes more sandy. Below 2m, a layer of gravel extends to the depth of 4.6m, roof of the underlying marl formation. Water table is found at 3.4 m depth.

Table 6.30: Upper Soil Layer characterization at "Le Fauga"

	Clay (Fallow area) [%]	Silt [%]	Sand [%]
5 cm	15.6	47.2	37.2
20 cm	15.4	45.9	38.7
40 cm	26	45.6	28.4
60 cm	28.4	44.4	27.2
80 cm	28.7	43.6	27.7

The capillary curve of the material was determined at the Laboratory of Soil Mechanics of the Geotechnical Engineering Department at Barcelona-TECH in samples of reconstituted material at two different dry densities (16 and 17 kN/m³). Experimental data has been fitted with:

a) the classical expression of van Genuchten (labelled vG in Fig. 6.112):

$$S_e = \left(1 + \left(\frac{p_g - p_l}{p_o}\right)^{1/_{1-\lambda}}\right)^{-\lambda} \tag{6.1}$$

with $p_o = 0.1$ and $\lambda = 0.3$.

b) a modified expression of van Genuchten (labelled svG in Fig. 6.112) :

$$S_e = \left(1 + \left(\frac{p_g - p_l}{p_o}\right)\right)^{-\lambda} \tag{6.2}$$

with $p_o = 0.3$ and $\lambda = 0.6$.

Figure 6.112 shows a comparison between experimental the data and the analytical expressions.
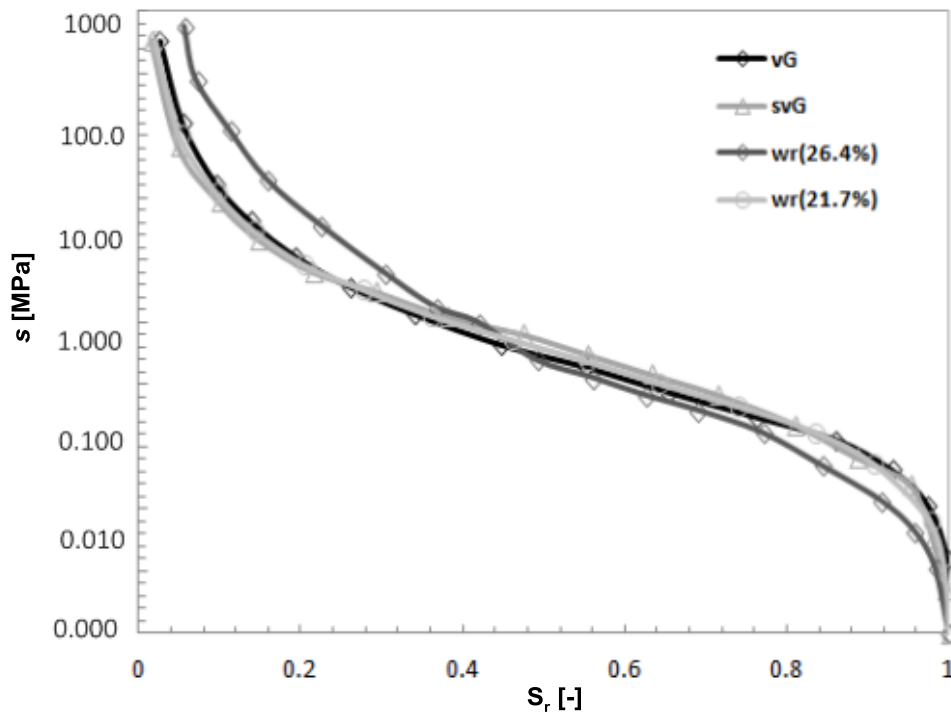
Figure 6.112: Capillary Curve for the porous material at the zone of study at "Le Fauga".

_____

Regarding the in situ measurements at the experimental field, soil moisture profiles were automatically performed using impedance sensors (ML2 Theta-probes1) with a period of 30 min. Duplicated sensors were installed at the following depths: 0–6 cm (×4), 10 cm (×3), 20 cm (×3), 30 cm (×2), 40 cm (×2), 50 cm (×2), 60 cm (×2), 70 cm, 80 cm, 90 cm, in order to improve sampling close to soil layer surface where higher levels of spatial and temporal variability of soil moisture are observed.

Soil temperatures were measured at 1, 5, 20, 50 and 90 cm by thermistor probes.

6.5) Modeling of Experimental Field Le Fauga

6.5.1) Equations solved

The numerical problem is addressed by solving the equations of water mass balance and energy balance. It is noted that the gas phase is neglected in this case assuming that the variations of gas pressure are negligible in comparison to water pressure variations (infinite mobile gas).

The mass balance of water is mathematically given by the equation:

$$\frac{\partial}{\partial t}\left(\theta_l^w S_l \phi + \theta_g^w S_g \phi\right) + \nabla \cdot \left(j_l^w + j_g^w\right) + (f^w) = 0 \tag{6.3}$$

where θ_l^w and θ_g^w are the apparent mass of liquid water and vapor in the liquid and gas phases respectively and, j_l^w and j_g^w are the advective and diffusive fluxes of water defined in appendix 1.

Energy balance is mathematically expressed by the equation:

$$\frac{\partial}{\partial t}\left(E_s \rho_s \cdot (1 - \phi) + E_l \rho_l S_l \phi + E_g \rho_g S_g \phi\right) + \nabla \cdot \left(i_c + j_{E_s} + j_{E_l} + j_{E_g}\right) + \left(f^Q\right) = 0 \tag{6.4}$$

where E_s, E_l and E_g are the specific energies of porous skeleton, liquid and gas phases respectively, i_c is the heat flux vector of the porous medium and j_{E_s}, j_{E_l} and $j_{E_{gl}}$ are the energy fluxes of the porous skeleton, the liquid phase and the gas phase, respectively.

Both equations are discretized by a finite element scheme and solved simultaneously by using the finite element code Code_Bright, Olivella et.al. (1996).

6.5.2)   Geometry, Mesh, Initial and Boundary conditions

Geometry and mesh used in the finite element model are sketched in Fig. 6.113. These consist of a homogeneous soil column formed by two layers of 1m depth each one. Water pressure, gas pressure and temperature are prescribed at the bottom of the column and the Soil-Vegetation-Atmosphere boundary condition imposed on the top (soil surface). Specifically, the vegetation boundary condition is applied in the area of roots depth (1m).
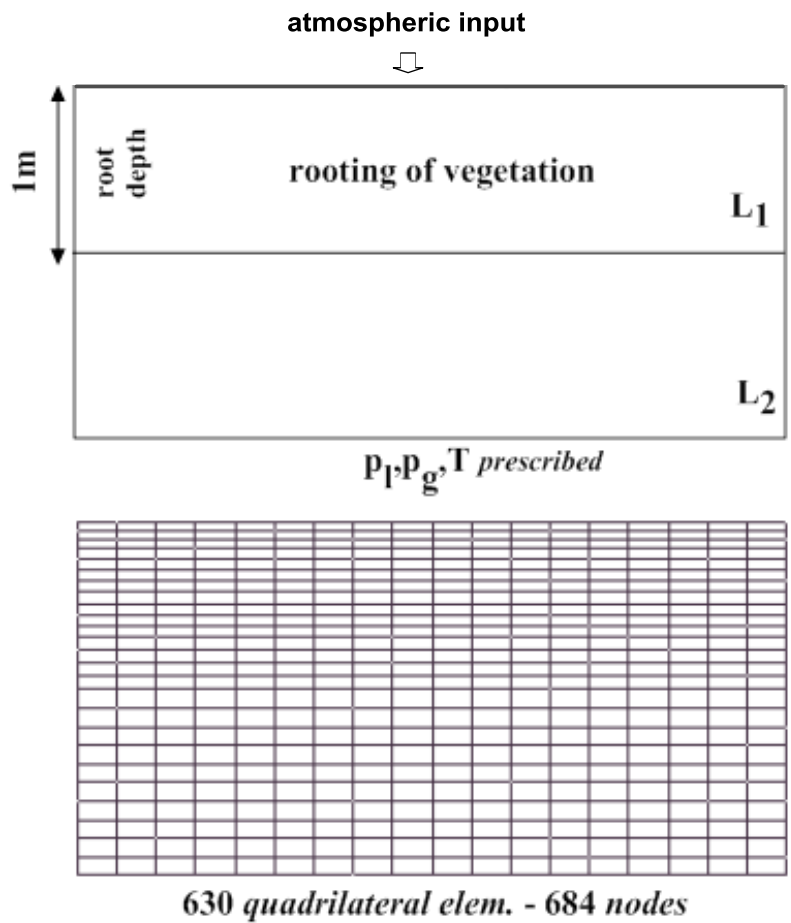
Figure 6.113: Soil Column Used to Model Atmospheric and Vegetation Boundary Conditions at Le Fauga site.

343

The mesh used in the modeling is composed of 630 quadrilateral elements and 684 nodes. It is densified in the root zone where water uptake is significant.

Table 6.31 summarizes the initial and boundary conditions assumed in the simulation as well as the time interval duration.

Table 6.31: Summary of initial and boundary conditions for modeling the experimental field Le Fauga

Interval	Time [days]	Initial and Boundary Conditions
1	0-1095	$\phi^0 = 0.4$ $p_{l_U}^0 = -0.086$ MPa , $p_{l_D}^0 = -0.067$ MPa $p_g^0 = 0.1$ MPa $T^0 = 10\,°C$ *Lower boundary*: $p_g = 0.1$ MPa $p_l = -0.067$ MPa $T = 10\,°C$ *Upper boundary*: Atmospheric load (*root_atm.dat*)

6.5.3)   Soil and Vegetation Cover Parameters

Table 6.32 presents the parameters of the soil, the atmosphere and the vegetation on top of the soil column, used in the numerical simulation.

The quantities of vegetation fraction, wet and dry albedo, roughness length, screen high, limit global radiation, minimum and maximum stomatal surface resistances, root density, degree of saturation at wilting point, field capacity and anaerobiosis point are specified.

Table 6.32: Parameter of Soil-Vegetation-Atmosphere boundary condition.

Veg	$z_0[m]$	$z_a[m]$	$r_{g_{lim}}\left[W/m^2\right]$	$r_{s_{min}}[S/m]$	$r_{s_{max}}[S/m]$	$\rho_{g_{atm}}\left[kg/m^3\right]$
0.85	0.02	10	80	40	5000	1.2
S_l^w	S_l^{fc}	S_l^a	f_ρ^r	$f_4^c[1/K]$	$A_{l_d}[-]$	$A_{l_s}[-]$
0.22	0.78	0.98	1	0.0016	0.2	0.2

_____

Material parameters used for: (a)Darcy's law, (b)Retention curve, (c) Relative permeability, (d) Fick's law and (e) Fourier's law to model the soil layers L_1 and L_2 are summarize in the Tables 6.33 and 6.34 respectively.

Table 6.33: Parameters of constitutive equations for the root zone (L1).

Retention Curve (van Genuchten)		Intrinsic Permeability (Darcy's law)		Liq. Phase Rel. Permeability (van Genuchten type)	
$S_r = \left[1 + \left(\frac{p_g - p_l}{p_o}\right)^{1/1-\lambda}\right]^{-\lambda}$		$\boldsymbol{q}_\alpha = -\frac{\mathbf{k}k_{r\alpha}}{\mu_\alpha} \cdot (\nabla p_\alpha - \rho_\alpha \mathbf{g})$		$k_{rl} = \sqrt{S_r}\left[1 - \left(1 - S_r^{1/\lambda}\right)^{\lambda}\right]^2$	
p_0 [MPa]	0.10	$k\ [m^2]$	1.00E-15	λ	0.3
λ	0.30	5cm	0.42		
Srl	0.00	ϕ 10cm	0.38		
Sls	1.00	80cm	0.32		
Diffusive Flux of vapor (Fick's law)		Conductive flux of Heat (Fourier's law)		Liquid Phase Property (Density)	
$\mathbf{i}_\alpha^i = -\left(\tau\phi\rho_\alpha S_\alpha D_m^i \mathbf{I}\right)\nabla\omega_\alpha^i$		$\mathbf{i}_c = -\lambda\nabla T$		$\boldsymbol{\rho}_l = \boldsymbol{\rho}_{l_0}\exp\left(\begin{array}{c}\beta(p_l - p_{l_0}) + \\ \alpha T + \gamma\omega_l^h\end{array}\right)$	
$D\left[m^2 P_a/_{sK^n}\right]$	5.90E–06	λsat	0.5	$\rho_{l_0}\left[^{kg}/_{m^3}\right]$	1002.6
τ	1	λdry	1	$\beta[^1/_{MPa}]$	4.50E-04
N	2.3			$\alpha[^1/_{°C}]$	-3.40E-04
				γ	0.6923

Table 6.34: Parameters of constitutive equations for the lower soil layer (L2).

Retention Curve (van Genuchten)		Intrinsic Permeability (Darcy's law)		Liq. Phase Rel. Permeability (van Genuchten type)	
p_0 [MPa]	0.10	$k\ [m^2]$	1.00E-16	λ	0.3
λ	0.30				
Srl	0.00	ϕ	0.32		
Sls	1.00				
Diffusive Flux of vapor (Fick's law)		Conductive flux of Heat (Fourier's law)		Liquid Phase Property (Density)	
$D\left[m^2 P_a/_{sK^n}\right]$	5.90E–06	λsat	0.5	$\rho_{l_0}\left[^{kg}/_{m^3}\right]$	1002.6
τ	1	λdry	1	$\beta[^1/_{MPa}]$	4.50E-04

N	2.3			$\alpha[1/_{°C}]$	-3.40E-04
				γ	0.6923

6.5.4) Modeling results

Figures 6.114, 6.115, 6.116 and 6.117 show the comparison between numerical results and measurements performed at different depths in the silt layer during the period 2005-2007. They include:

a) water contents (Figs. 6.114-6.115) as measured by the thetaprobes,

b) temperatures (Fig. 6.116) as measured by the termistors

c) evaporation fluxes (Fig. 6.117) as deduced in the field from water budget.

Figure 6.114: Comparison between numerical results and water content measured during years 2005 to 2007 at the first 30cm depths within the silt layers

_____
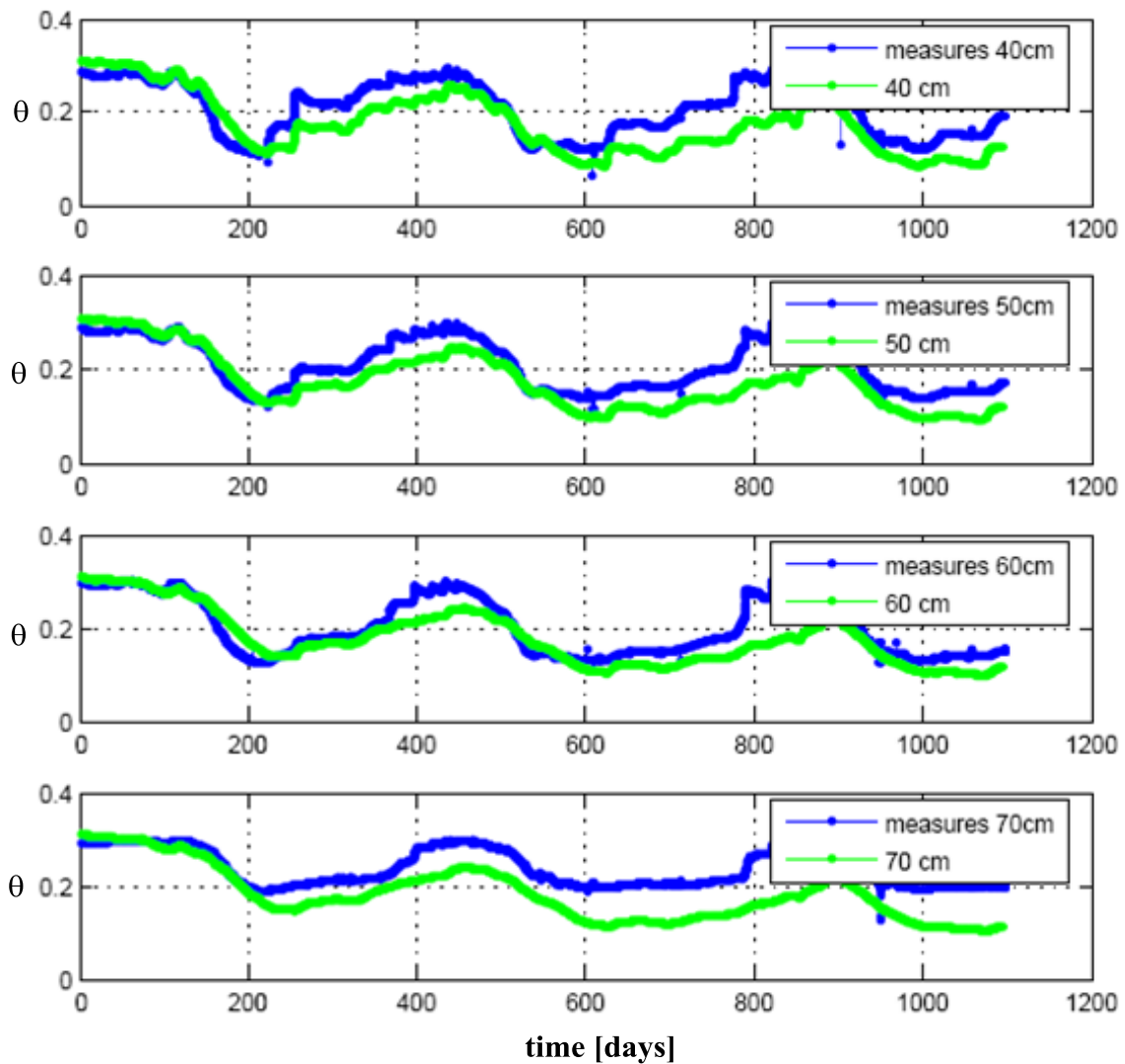
Figure 6.115: Comparison between numerical results and water content measured during years 2005 to 2007 between the depths 30cm and 70cm within the silt layers

The comparison between the results obtained with the numerical model and the in situ measurements regarding water contents, show a good agreement between them. Figures 6.114 and 6.115 show the high relevance of daily variations of water content at the upper soil layers. This relevance decreases as the depth increases. At the same time the temporal scale gradually increases with depth from daily scale to seasonal temporal scale.

This response explains the high influence of the evaporation flux E_v on the soil layer close to the surface. Moreover, as depth increases the transpiration flux E_T gains relevance over the evaporation one.
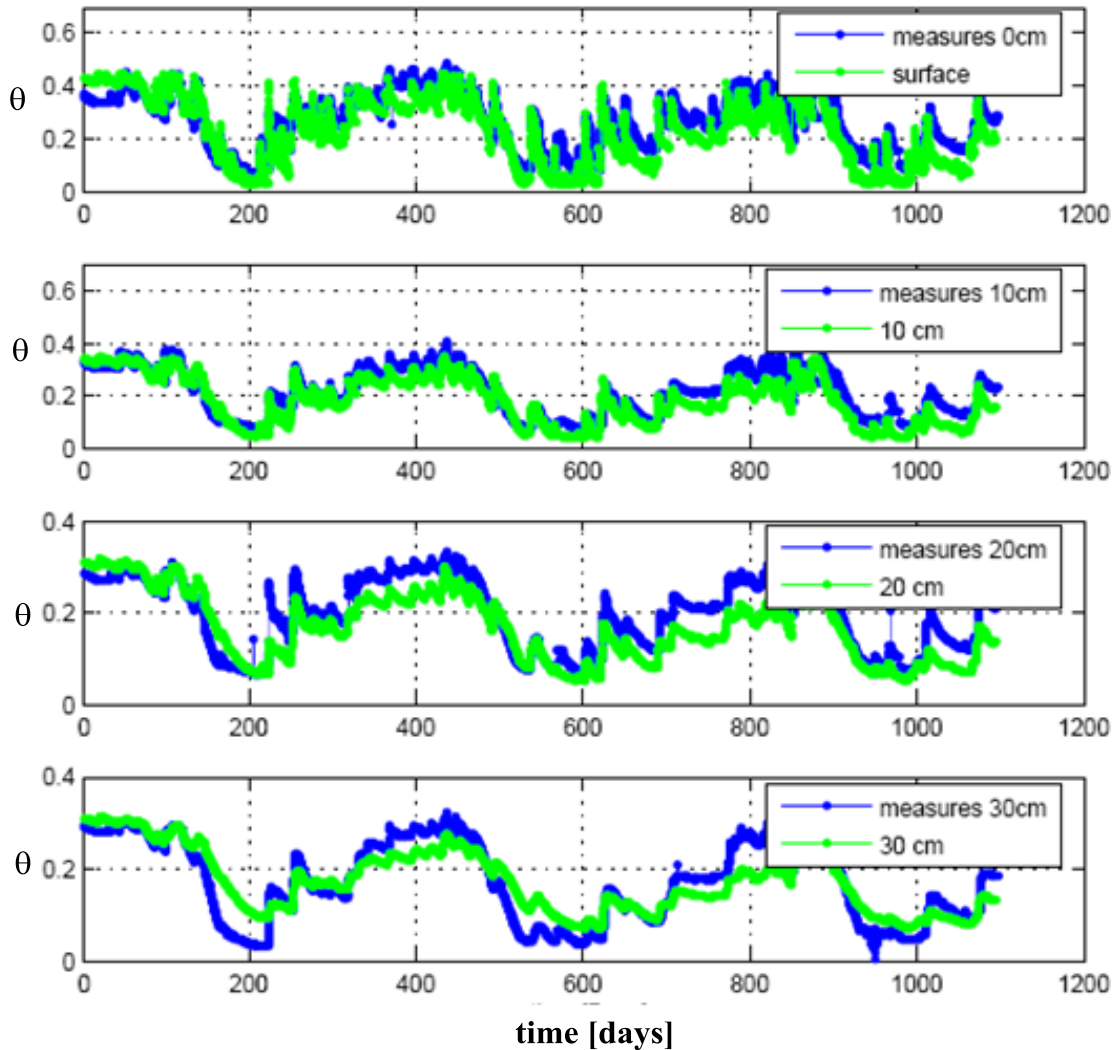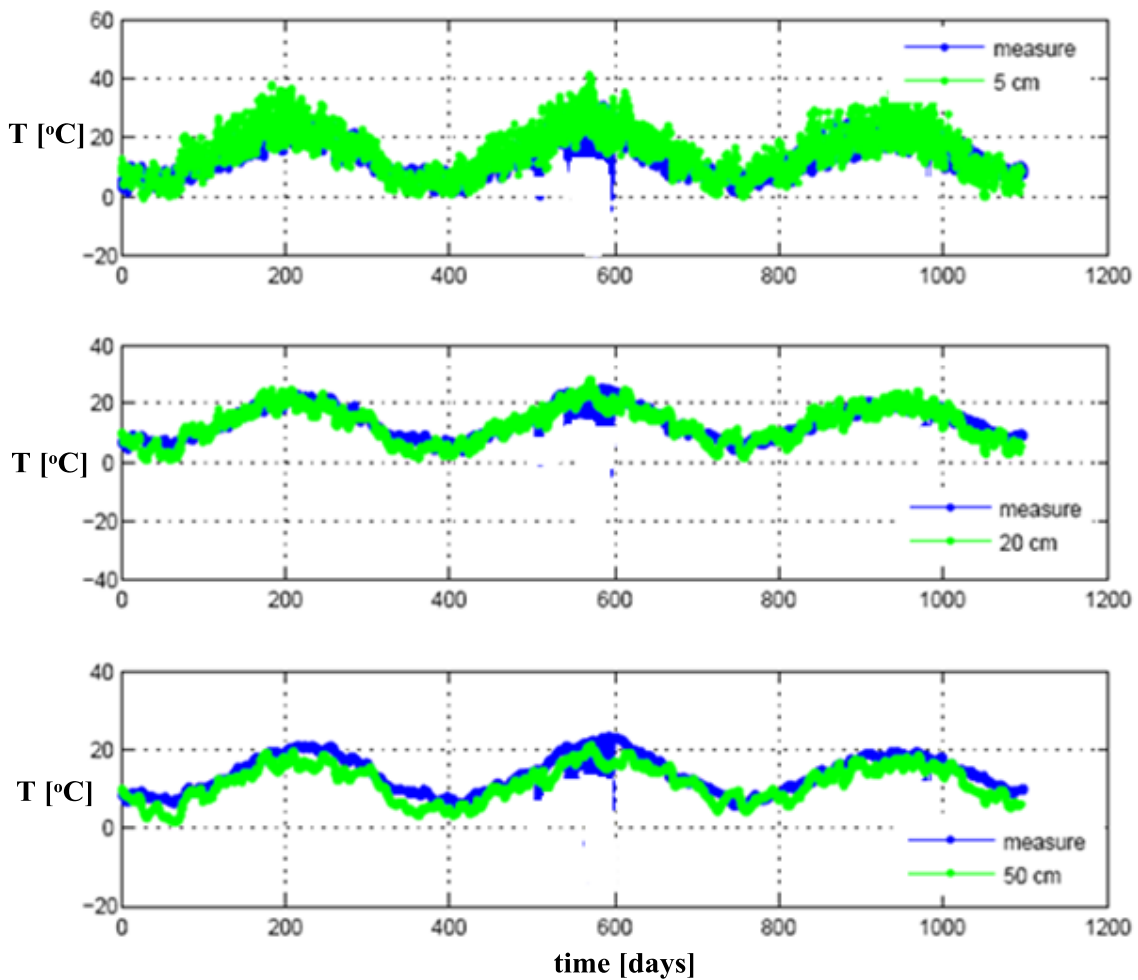
Figure 6.116: Comparison between numerical results and temperatures measured during years 2005 to 2007 at five depths within the silt layer.

Similarly, temperature evolutions registered in situ compared with those obtained from the numerical model show a good correlation. Again the higher influence of the evaporation flux is observed at the soil layers located closer to the surface.

In view of these positive results, it can be said that the atmospheric-vegetation boundary condition presented in chapter 2 has been validated and can give the desired response if a special attention is being paid to the parameterization of both vegetation type and upper soil layer.

Finally, Fig. 6.117 confirms the proper performance of the atmospheric-vegetation model through comparison of both the evapo-transpiration fluxes obtained in the field by water budget and those given by the numerical model.
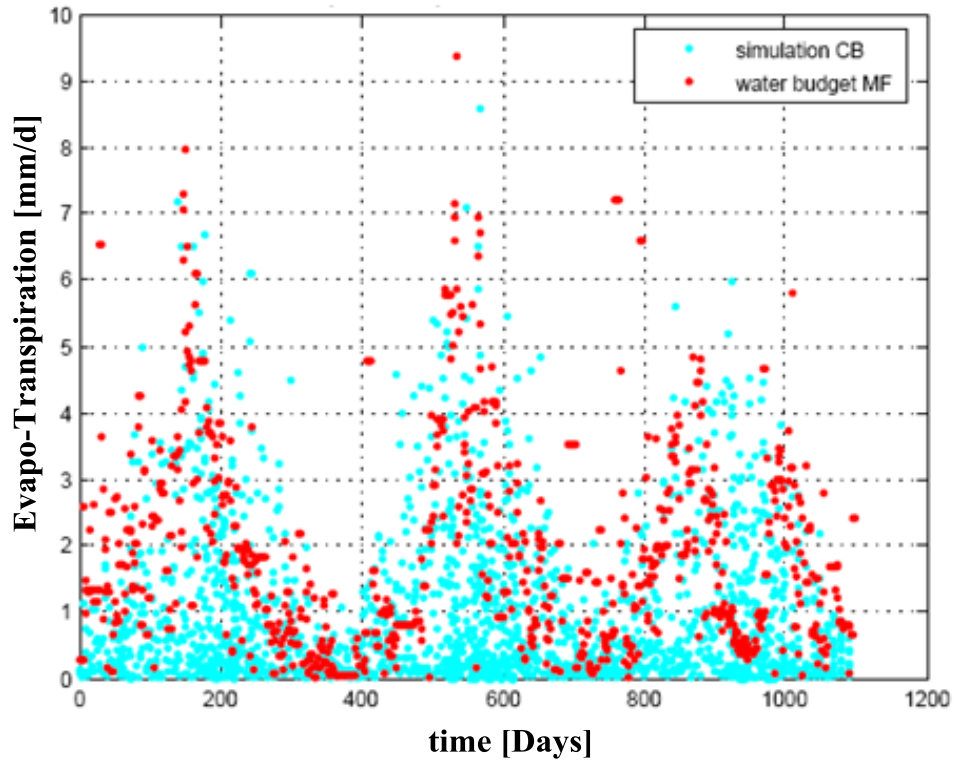
Figure 6.117: Comparison between numerical results and evapo-transpiration fluxes estimated in the field from water budget.

It is observed that the higher magnitudes of both evaporation and transpiration fluxes are observed at times corresponding to summer season ($200 \equiv 21\text{Jun} - 05$, $565 \equiv 21\text{jun} - 06$, $930 \equiv 21\text{jun} - 07$).

Then a series of isochrones corresponding to the main variables describing the model responses are presented. Isochrones of maximum and minimum values are confronted. The firsts two frames, Fig. 6.118 and Fig. 6.119, show the degree of saturation and temperatures distributions along the model profile. While the last frame Fig. 6.120 gives a global view of the model response. Liquid pressures and vapor concentrations are also presented.

Consecutively, the corresponding profiles of degree of saturation and temperatures along the model profile (Figs. 6.121-6.122) as well as a frame of profiles offering the global view of the model response (Fig. 6.123) are presented.

349
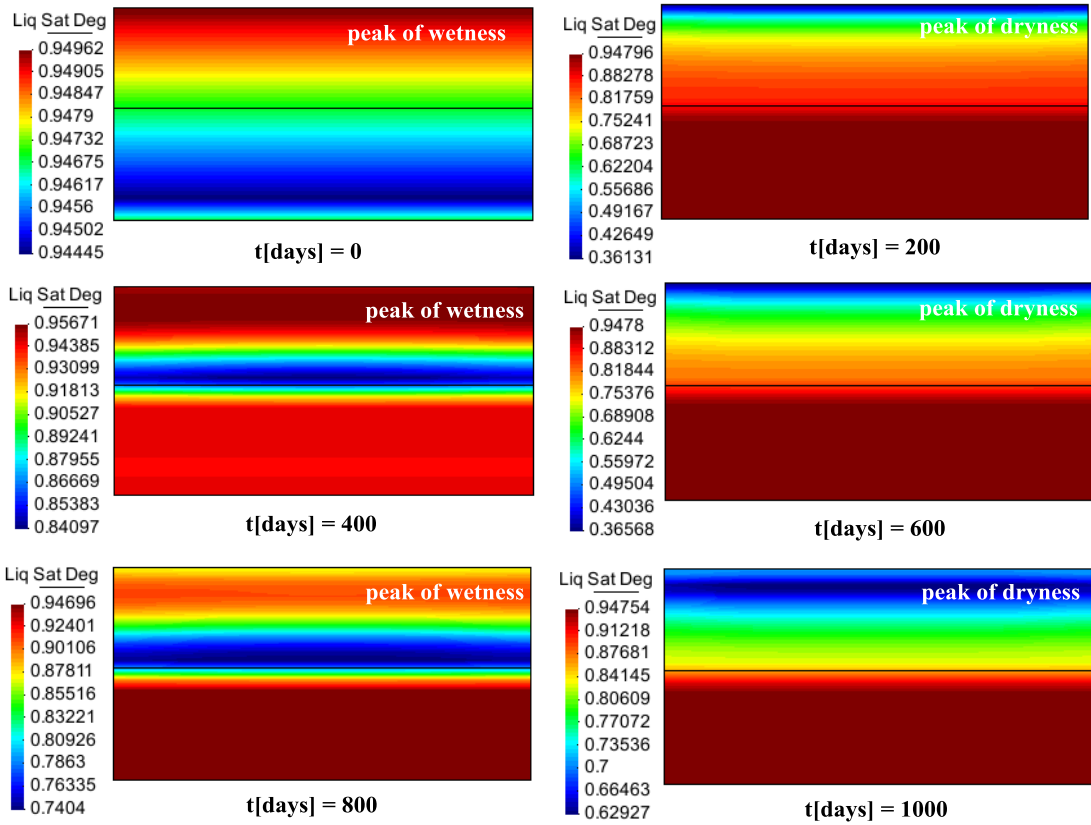
Figure 6.118: Contours of liquid saturation at different times for the experimental field Le Fauga
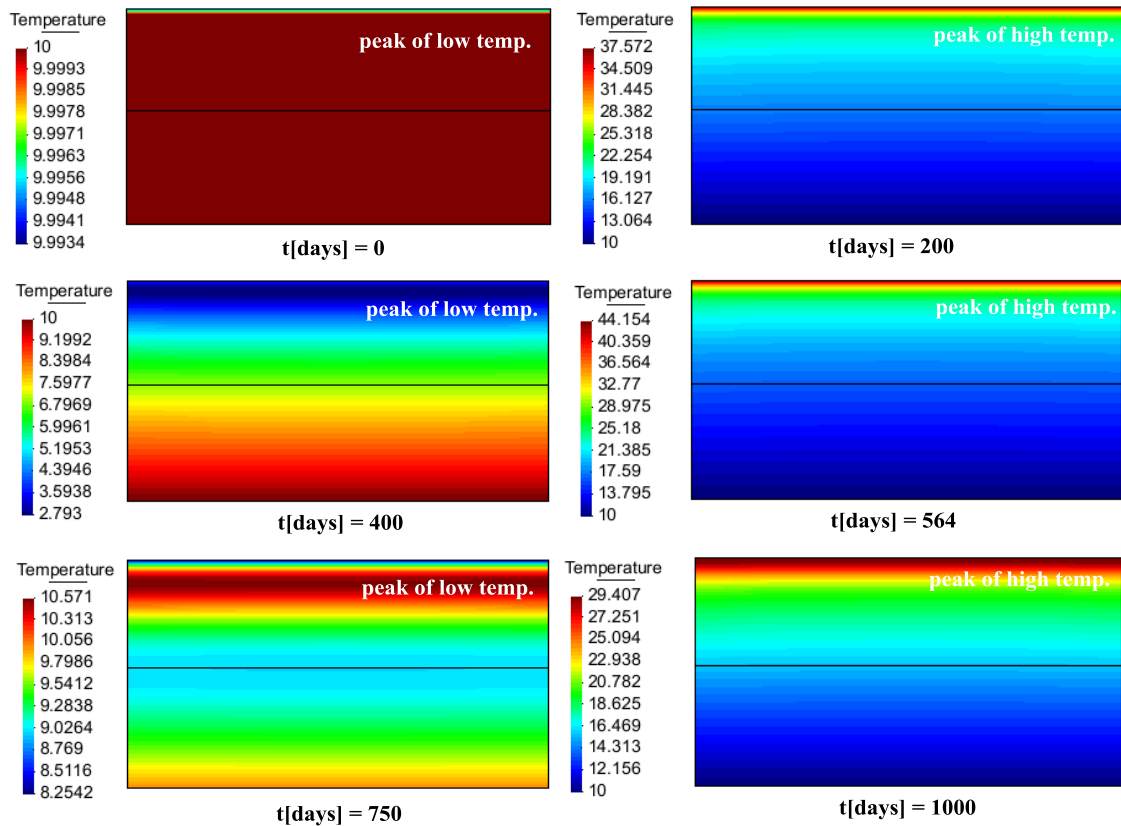
Figure 6.119: Contours of temperature at different times for the experimental field Le Fauga
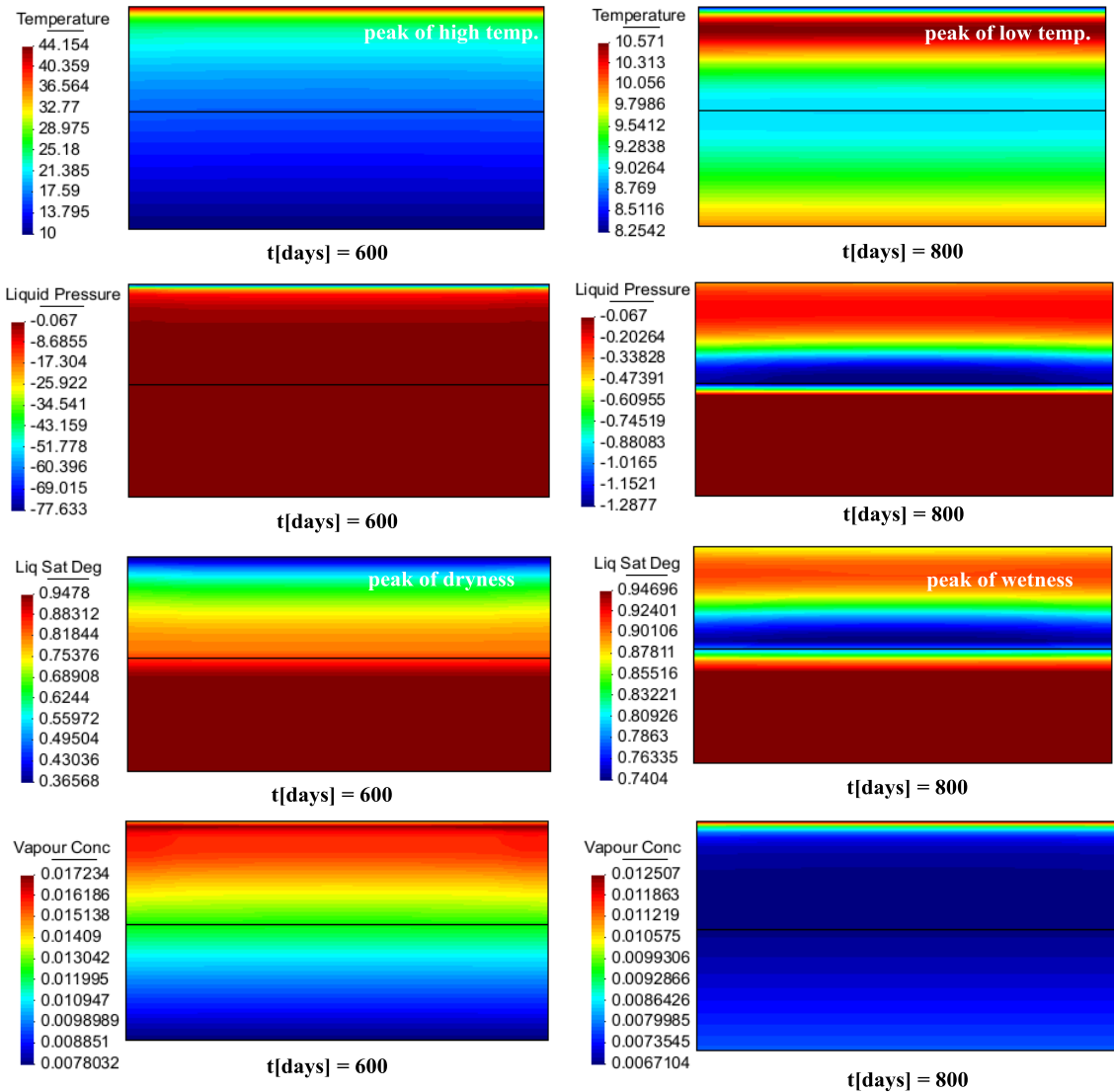
Figure 6.120: Contours of temperature ,liquid pressure, saturation degree and vapor concentration at different times for the experimental field Le Fauga

Isochrones of liquid saturation at Fig. 6.118, reveal the strong effect that evaporation and transpiration fluxes have on topsoil in summer seasons. In winter seasons upper layers appear to be more saturated than down layers, evidencing that during winter the precipitation has a higher effect in comparison to the effect of temperature.

Conclusions about isochrones of temperature Fig. 6.119 indicate that the layer in direct contact with the atmosphere exhibits maximum and minimum values of temperature in coincidence with summer and winter seasons. Isochrones of Fig. 6.120 confirm the observed responses.

Below, Fig. 6.121 presents profiles of saturation degree obtained in the soil column at different times under the atmospheric actions. Fig. 6.122 shows profiles of temperature obtained at the soil column under the atmospheric actions.
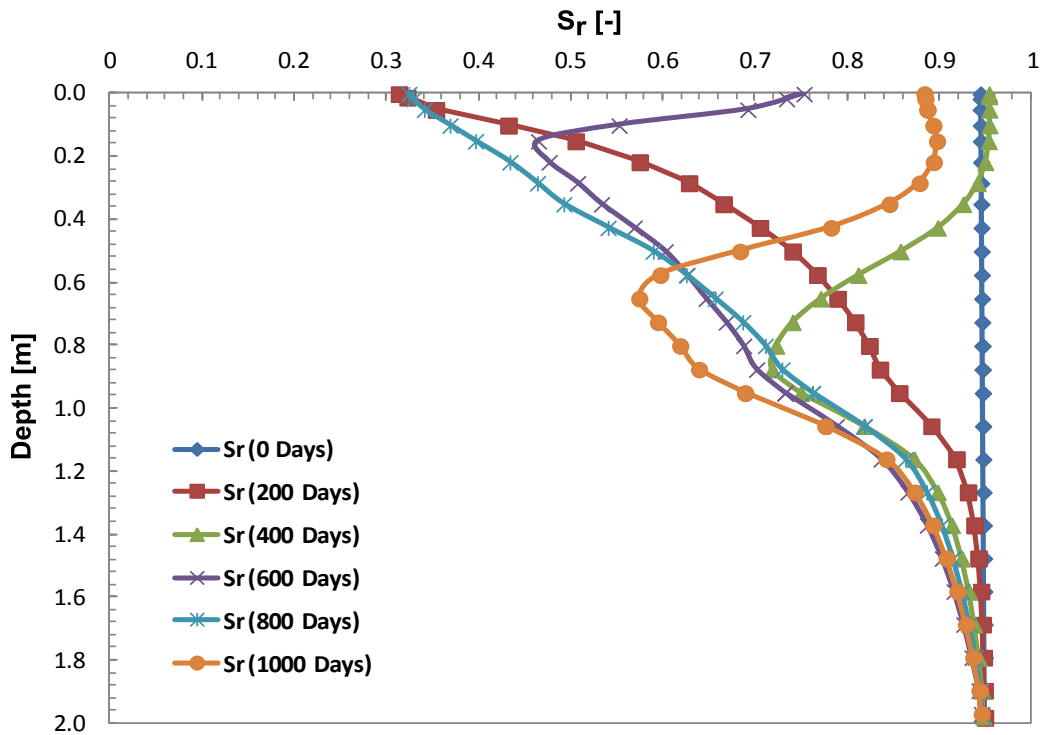
Figure 6.121: Profiles of saturation degree at different times of the model response.
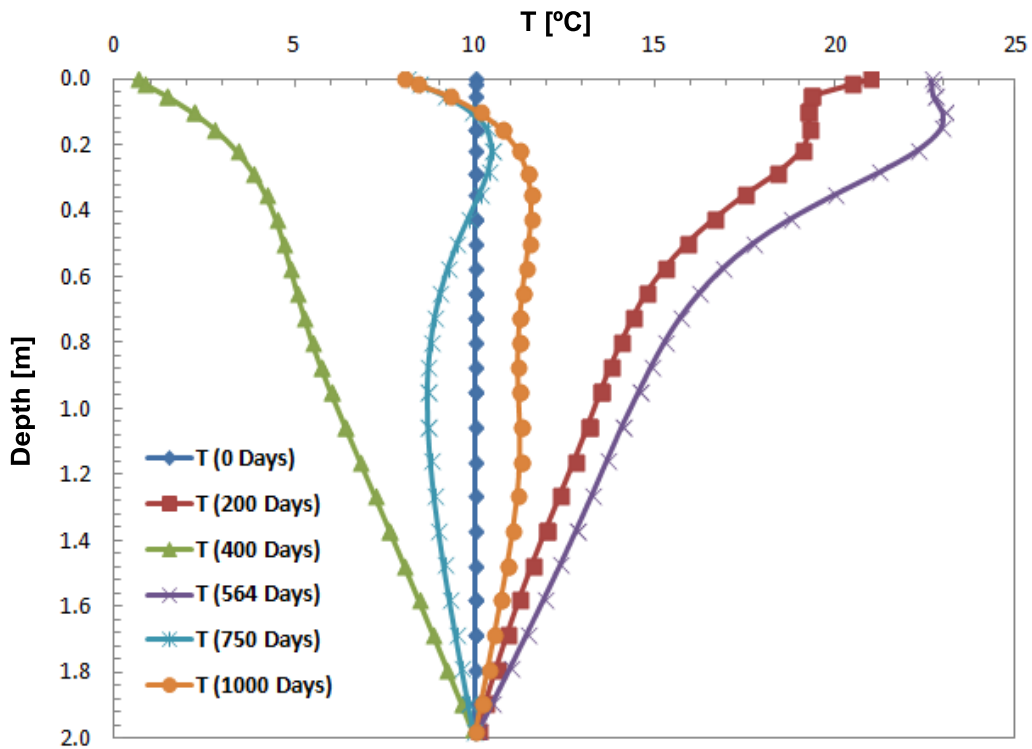
Figure 6.122: Profiles of temperature at different times of the model response.

Profiles of saturation (Fig. 6121) obtained in summer seasons show a continuous decrease up to the soil surface, reaching values around 30% of saturation. Profiles of saturation, out of summer seasons, show a bell-shaped with deeper peaks of minimum saturation as closer to colder stages they are pictured.

Profiles of temperature (Fig. 6.122) have an easier interpretation as continuous decreasing profiles of temperature are obtained in winter seasons while continuous increasing profiles of temperature are obtained in summer seasons.

Fig. 6.123 offers a set of profiles of temperature, degree of saturation, liquid pressure and vapor concentration obtained at the soil column at different times of response under atmospheric actions.
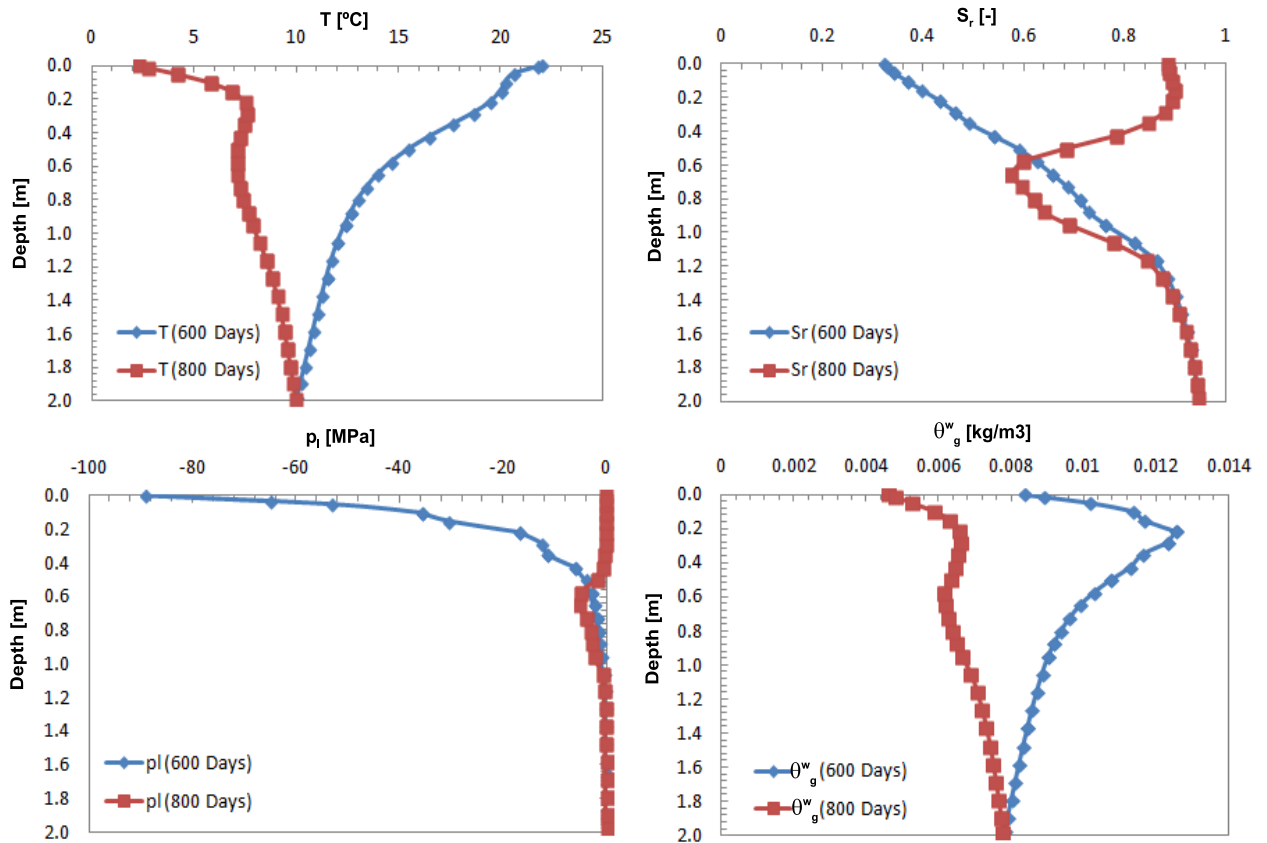
Figure 6.123: Set of profiles of temperature, degree of saturation, liquid pressure and vapor concentration at two different times of the run.

The observed response in the profiles confirms the commented behaviors.

_____

Fig. 6.124 shows the water fluxes directions at two periods of full saturation of the soil column. The water is not allowed to enter in the medium but drains along the soil surface.

t[days] = 400   t[days] = 800
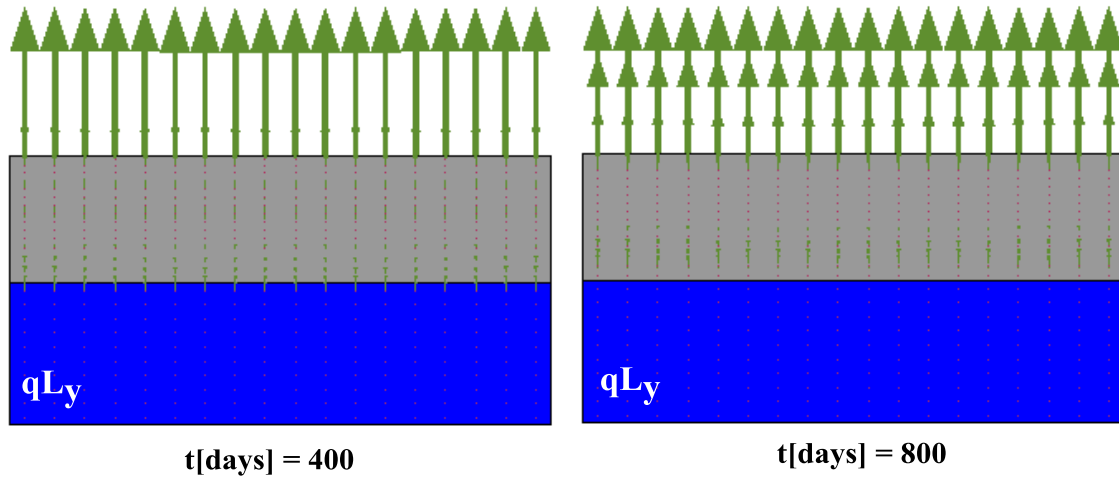
Figure 6.124:Vectors of water flows at two times of the model saturation.

Finally, it is interesting to present from the obtained numerical results two profiles of water content at extreme conditions of: (a) dry season and (b) wet season, Fig. 6.125.
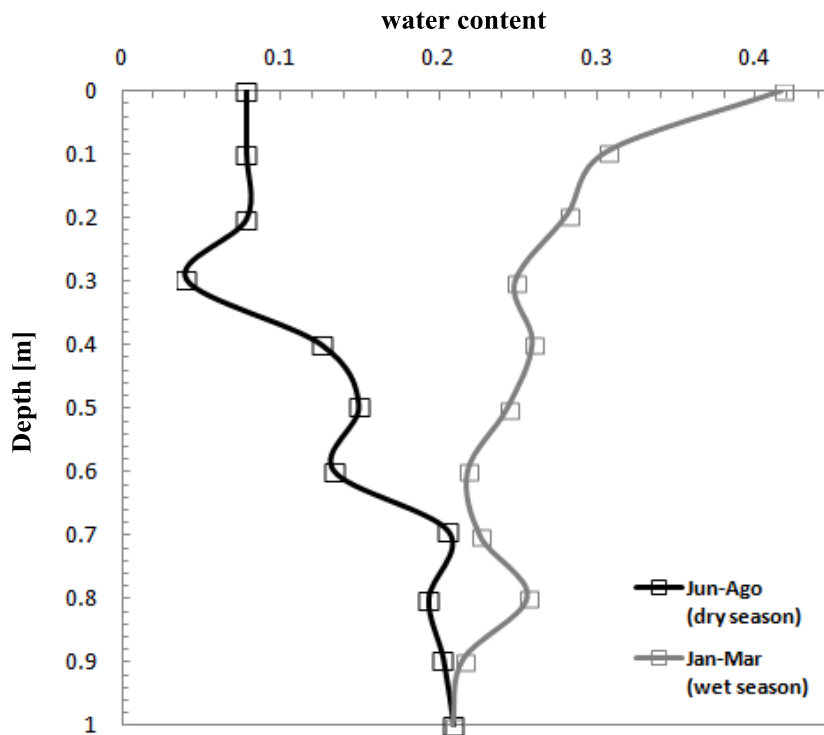
Figure 6.125: Seasonal changes of water content at Le Fauga site.

_____

From Fig. 6.125, it can be observed that for the studied case the active zone (sensible to atmospheric actions) reaches 90cm depths. The volumetric water content at ground surface ranges from 10 % in the dry season to 40 % in the wet season and this difference decreases with depth.

6.6) Conclusions

Climate actions on the ground surface shown to have a great influence on the topsoil layer. The obtained results highlight the action of the transpiration flow over the evaporation flow in the summertime. In winter time the direct evaporation from the soil surface plays the main role.

The modelling of the experimental field Le Fauga has allowed to validate the soil-vegetation-atmosphere boundary condition presented in chapter 2.

This boundary condition allows to determine extreme conditions in the topsoil layer due to its interaction with the atmosphere. For example the formation of surface cracks due to desiccation observed in fine soils.

<div align="right">

CHAPTER 7

</div>

RESPONSE OF A FOUNDATION ON A COLLAPSIBLE LAYER UNDER ATMOSPHERIC ACTIONS

7.1) Introduction

In the present chapter a geotechnical problem is studied using constitutive models developed in chapter 4 and implemented following the algorithms described in chapter 5. It corresponds to the case of a circular foundation loaded by a vertical centered force and relying on an unsaturated collapsible layer.

The case computes and quantifies the deformations and settlements induced by saturation of an unsaturated soil layer and compute the bearing capacity of the foundation located at the top left side of the model. The soil column is assumed to be homogeneous.

Prediction of settlements induced by wetting in collapsible soils has been of interest in a series of studies, one of the most relevant being Pereira Barreto town, Brazil, see Gens (2010). Thus, when exceptional water condition's exists which rise the water level to elevations never reached before a collapse of the soil may occur leading to unacceptable settlements.

In fact, in partially saturated conditions, a soil mass can swell or shrink when it experiences a "wetting path". The volume change will be a function of: the initial void ratio(e^0), the water content (θ^w) and the initial stresses (σ^0) (Gens (1995), Alonso et al. (1990)).

This collapse depends on the following factors: (a) suction and dry densities after compaction, (b) vertical stress applied during the inundation, (c) intrinsic properties of the soil such as plasticity index, (d) stress anisotropy during the inundation and (e) water content increase (the settlement increases non-linearly with suction decrease).

The case studied corresponds to a strictly academic case which has been however simulated in a centrifuge. Thus, model can be validated by comparing with measurements obtained. After being validated, model has been used to simulate the same foundation subjected to an atmospheric load, typical of the central part of Catalonia in order to gain further insight into the response of the soil below the foundation.

The centrifuge model has been constructed at a length scale of $\left(1/50\right)$ and tested under a centripetal acceleration equivalent to 50 gravities. Acceleration is provided by rotating the model at an angular rotation ω in a box attached to an arm of radio r such that $-\omega^2 \cdot r = 50g$, see Fig. 7.126.
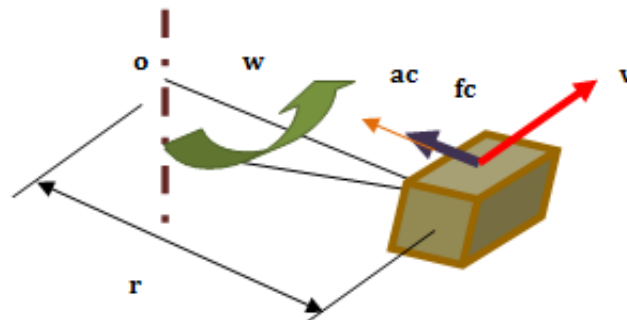
Figure 7.126: Diagram of centrifuge model test

According to dimensional analysis the following scaling relations are used between model and prototype,

Variable	Relation	Scale
Acceleration	$\dfrac{a_m}{a_p}$	N
Length	$\dfrac{l_m}{l_p}$	$\dfrac{1}{N}$
Time (diffusion processes)	$\dfrac{t_m}{t_p}$	$\dfrac{1}{N^2}$
Stress	$\dfrac{\sigma_m}{\sigma_p}$	1

They provide the scaling relations to simulate the prototype of a foundation of 3m diameter relaying in a collapsible layer of 15m depth.

The test consists in two main stages: (a) First, a water pressure is applied at the model base and (b) Second, a loading is applied at the model top under a displacement rate of $0.12\ ^{mm}/_{min}$.

The chapter is organized as follows: first notation and terminology used along the chapter is presented; then the characterization of the material used in the experiment and the tests themselves are described in detail. Afterwards the modeling stages previously presented (watering and loading) are studied and validated respectively by comparison of both the numerical model results and the experimental data. The laboratory tests has been realized within the program of research "Mechanics of unsaturated soil for engineering" MUSE.

7.2)   Notation and Terminology

a_m	Acceleration of the model
a_p	Acceleration at prototype scale
l_m	Length at model's scale
l_p	Length at prototype 's scale
t_m	Time at model's scale
t_p	Time at prototype's scale
γ_s	Saturated unit weight

w_p	Plastic limit
w_l	Liquid limit
I_p	Plastic index
γ_d	Dry unit weight
W	Water content
E	Void ratio
S_r	Degree of saturation
σ_v	Vertical stress
p_w	Pore water pressure
p_o^*	pre-consolidation pressure
ϕ	Porosity
k_{ii}	Intrinsic permeability
k	Slope of unloading-reloading line
λ	Slope of normal compression line
x_p'	Effective generalized mean stress
x_q'	Effective generalized deviatoric stress
α_p	Volumetric plastic strain
$\dot{\alpha}_p$	Volumetric plastic strain rate
$\dot{\alpha}_q$	Deviatoric plastic strain rate
ξ_c	Shape factor for bearing capacity
N_c	Bearing capacity coefficient
ξ_γ	Shape factor for bearing capacity
N_γ	Bearing capacity coefficient
B_γ	Foundation dimension
q_{ult}	Bearing capacity

7.3) Material Characterization

The tested material named "Jossigny silt" has been extracted from a layer of alluvial silt located at Jossigny (east of Paris, France) and further studied by Vicol (1990), Cui (1993) and Casini (2008). In those studies both saturated and partially saturated conditions were conducted: physical, hydraulic and mechanical properties has been determined with particular focus on the unsaturated response of the soil.

Physical properties of the Jossigny silt has been obtained by conventional laboratory tests, summarized at Table 7.35.

$\gamma_s[kN/m^3]$	$w_p(\%)$	$w_l(\%)$	$I_p(\%)$	Clay Fraction (%)
26.4	17	32.3	15.3	25

In order to analyze the occurrence of possible large foundation settlements during wetting of the soil layer, it was of interest to prepare the sample at a low density. In this perspective the optimal compaction density of the material was studied by performing a series of oedometer tests statically compacted at different dry densities and initial water contents (Casini, 2008), see Table 7.36.

Test Nro.	$\gamma_{d_0}\left(kN/m^3\right)$	$W_0(\%)$	e_0	$S_{r_0}(\%)$
1	12.4	12.8	1.1	30.1
2	13.3	12.8	1.0	34.5
3	14.2	12.8	0.9	39.4
4	14.5	12.4	0.8	40.1
5	15.0	13.5	0.8	47.0
6	15.9	13.4	0.7	53.4
7	16.0	15.6	0.7	55.0
8	16.6	11.4	0.6	68.6
9	16.5	15.6	0.6	70.0
10	17.0	13.5	0.6	64.5
11	14.5	12.4	0.8	40.2

The applied stress-suction paths were selected in order to reproduce the conditions of prevalence in the centrifuge: An increase of vertical stress up to 200 kPa was first applied followed by decrease of suction down to 0 MPa, Casini (2008). The compressibility curves of those oedometer tests are shown in Fig. 7.127. The tests T1-T5 show that the reduction in volume induced by saturation is lower in samples with lower compaction void ratio. The test T11 loaded up to 100kPa evidences that the collapse was much lower in this case that in the rest of the tests (load up to 200kPa).
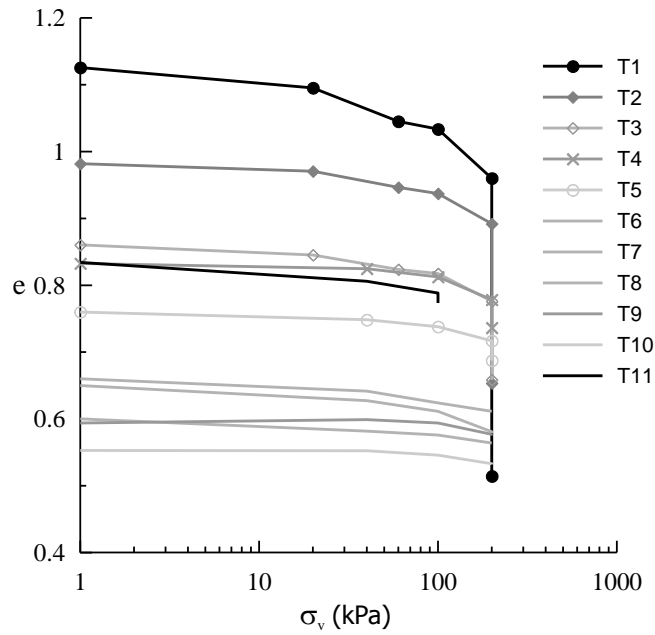
Figure 7.127: Oedometer wetting tests at various initial void ratios and vertical stresses (after Casini et. al., 2013).

Axial strains acquired by saturation of the sample allow to obtain optimum dry density value for the soil sample, favoring collapse. Those strains plotted versus the compaction dry unit weight Fig. 7.128 led to the conclusion of preparing the material sample at a dry unit weight of $\gamma_d = 14.5 \, ^{kN}/_{m^3}$ and a water content of w = 13%,. These properties are associated with a collapse strain equal to 2.5%.
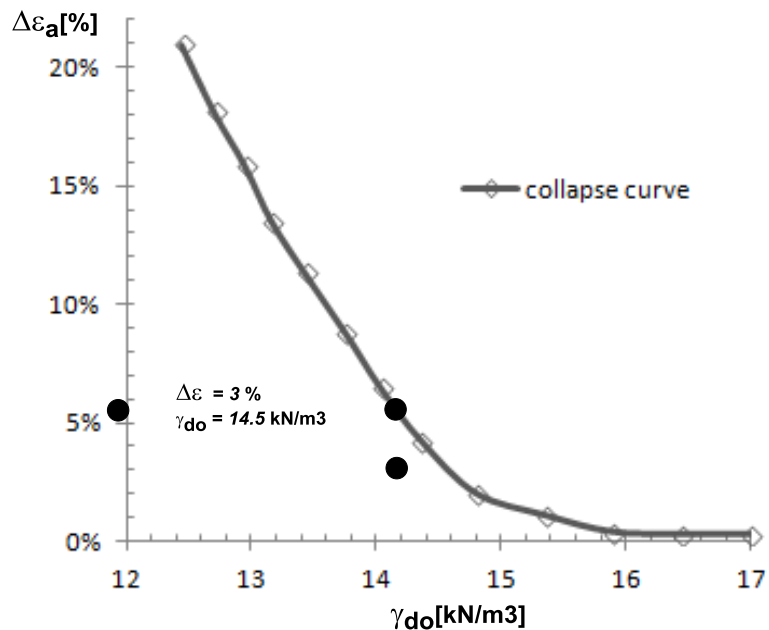
Figure 7.128: Collapse axial strain upon saturation versus compaction dry unit weight (after Casini et. al., 2008)

_____

Soil water retention curve has been also obtained in a suction controlled oedometer test with a sample prepared at a void ratio $e = 0.82$ and a degree of saturation $S_r = 0.42$ and loaded at constant vertical stress $\sigma_v - p_a = 20\,kPa$. The suction was controlled by changing pore water pressure p_l in the range between $200\,kPa$ and $390\,kPa$. The experimental data shown in Fig. 7.129 reveals the existence of hysteresis in the soil water retention curve. The drying branch is plotted in dash line. The value of suction at a degree of saturation of 95% is slightly lower than 10kPa.
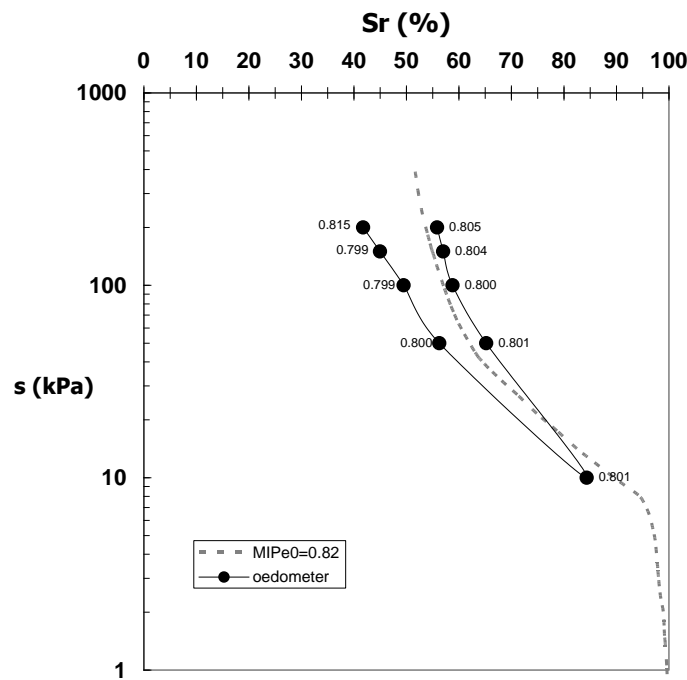
Figure 7.129: Soil water retention curve obtained with oedometer and Mercury intrusion porosimetry tests (after Casini et. al. 2008)

Additionally, the material presents an intrinsic permeability of $k_{ii} = 2.85 \times 10^{-14}\,m^2$. Finally, a diagram of isotropic compression built from several oedometer tests performed at different suctions (Casini, 2008) allowed to quantify both the slope of the isotropic compression line and the slope of the normal compression line.

7.4) Experimental Program

Two specimens were tested for the feasibility of the centrifuge trial (Casini, 2008). The test performed on the "sample F1" aimed at setting up the procedure of saturation at 1g. The objective of the test performed on "sample F2" was to investigate the response of the suction measurement during the centrifugation. Several measurement devices were

installed at different heights to register the degree of saturation at each point. Samples were prepared at a compaction state of dry density of $\gamma_d = 14.5 \, {}^{kN}/_{m^3}$ and a water content of $w = 13\%$. Properties of the centrifuged specimen F2 are summarized in Table 7.37.

Table 7.37: Post-compaction properties of the Samples (after Casini et. al. 2013)

Sample	$w(\%)$	$\gamma_{d_0} \left({}^{kN}/_{m^3} \right)$	$\sigma_{v_c}(kPa)$
F-2	16.8	14.1	65

The sample was placed in a cylindrical container of 300 mm in diameter and 300 mm height, Fig. 7.130. It includes 5 high-capacity tensiometers, 4 LVDTs and a system to impose water pressure at the bottom of the sample. Five tensiometers were installed on the lateral side of the container. Three of them, provided by ENPC-CERMES (labeled ENPC) (Chiu, Cui, Delage, De Laure, & Haza, 2005), (Muñoz, De Gennaro, & Delaure, 2008) were installed along one vertical profile. The two remaining tensiometers were provided by Durham University (labeled DU) (Lourenço, Gallipoli, Toll, Evans, & Medero, 2006) and installed along the diametrically opposed vertical profile. The tensiometers were first saturated in a pressurized cell at 2.0 MPa. Afterwards, the porous stone was covered by a thin layer of saturated paste of Jossigny silt in order to ensure contact with the soil. Four LVDTs allowed the measurement of the vertical displacements u_y at the top of the sample. These LVDTs were positioned at a distance of about 10 cm from the center of the sample.

_____
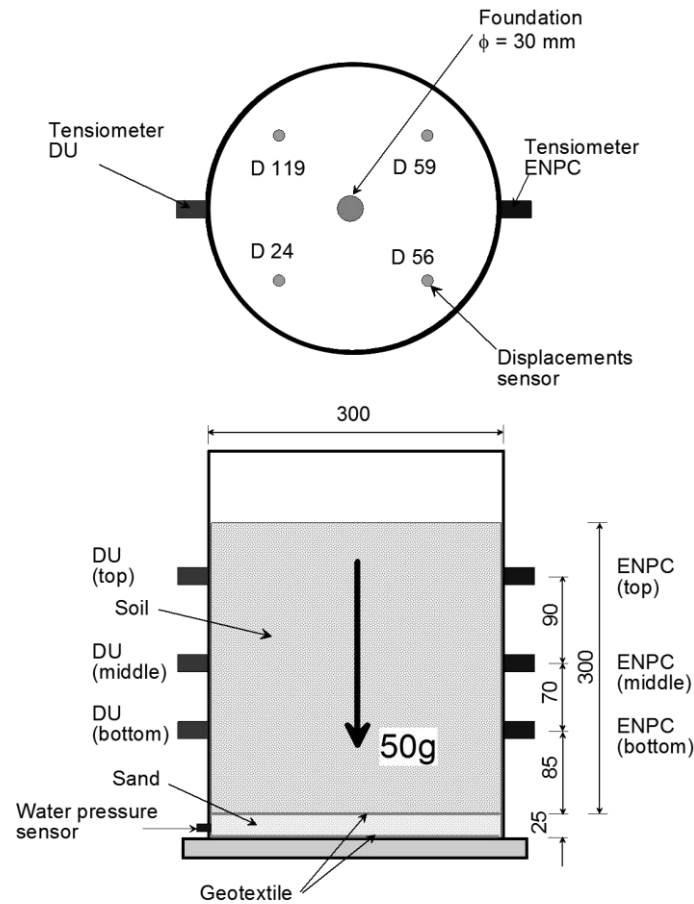
Figure 7.130: Scheme of the samples. Top: Top view of the samples with a circular foundation and displacements transducers (LVDT). Bottom: Vertical section of the samples with the HCTs diametrically opposed (after Casini 2008)

The "test F2", consists of six stages: (1) a period of equilibration of the tensiometers at 1g, (2) the beginning of the centrifugation with the corresponding increase in gravity, (3) the connection of the base of the sample with the water reservoir (in order to maintain a water level at the bottom of the silt layer and afterwards to let the suction profile to balance), (4) the saturation of the sample at 50g (by raising the water level up to the ground surface), (5) the realization of a penetration test at 50g (under this saturated conditions) and (6) the stop of centrifugation with the corresponding decrease in gravity.

7.4.1)   Measures from experimental tests

Figure 7.131 shows the evolution of the water pressures versus the imposed acceleration, in the following stages: acceleration and deceleration. Fig. 7.132 shows the evolutions of both the displacements and pore water pressures registered throughout the entire Test F2.

Response of the tensiometers during acceleration and deceleration is shown in Fig. 7.131. The upper plot shows the evolution of the pore pressures measured in one of the tensiometer sets (CERMES) during the acceleration stage. Initial pore pressures are negative, corresponding to the suctions set up during compaction. There is a slight response of tensiometers during the acceleration stage from 1g to 50g (7 minutes duration) probably due to the reaction of the measurement devices.

It is noteworthy that, at the end of the acceleration suction values are very similar to the initial values indicating that suction forces are not affected by gravitational forces Gens (2010). At longer term, there are changes in pore pressures corresponding to the consolidation process associated with the new stress state in the specimen.

 The observations are confirmed by measurements during the deceleration stage from 50g to 1g, As Fig. 7.131b shows, pore pressure readings do not react to the change of centrifuge acceleration, indicating again the insensitivity of matrix suction to gravitational forces.
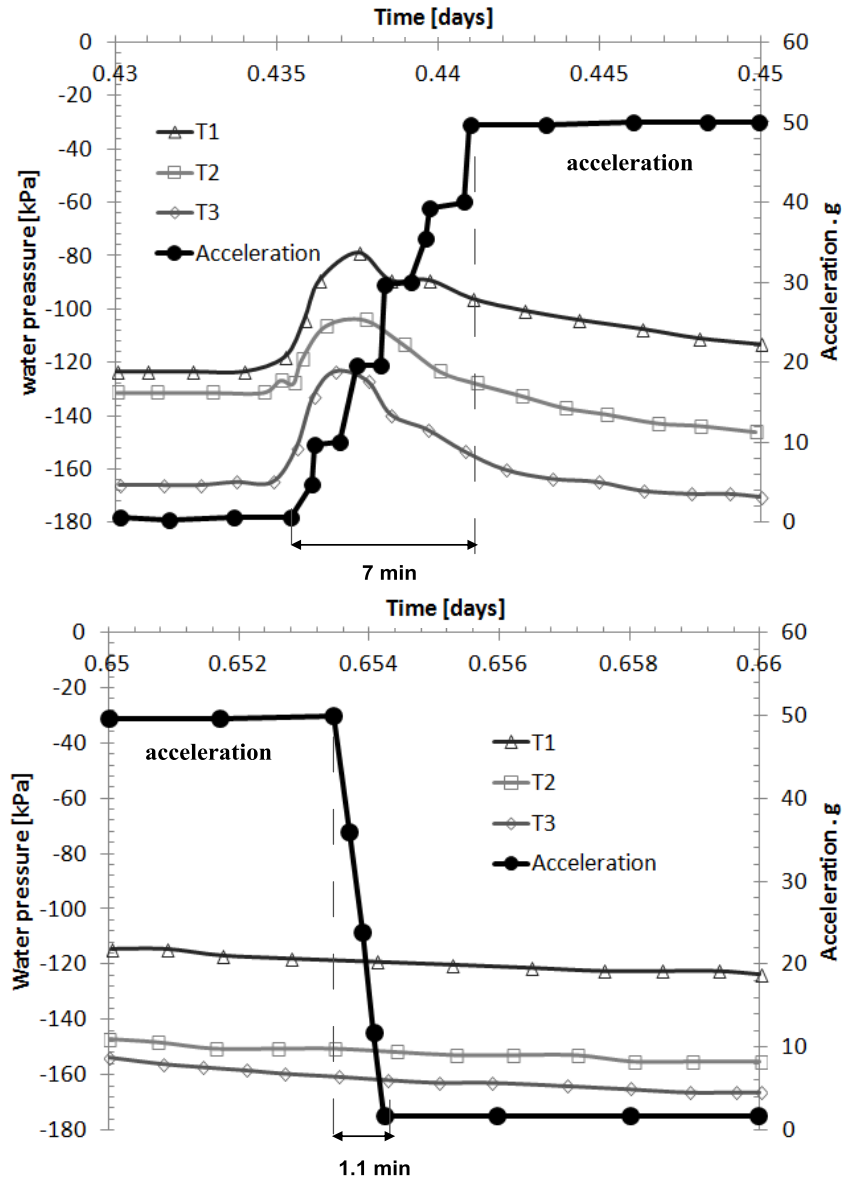
Figure 7.131: Evolution of pore pressures in the centrifuge test on Jossigny silt: (a) acceleration stage, (b) deceleration stage. (After Gens 2010)

Evolution of the pore water pressure p_l [kPa], vertical displacement u_y [mm] and acceleration are shown in Fig. 7.132 for the entire test.
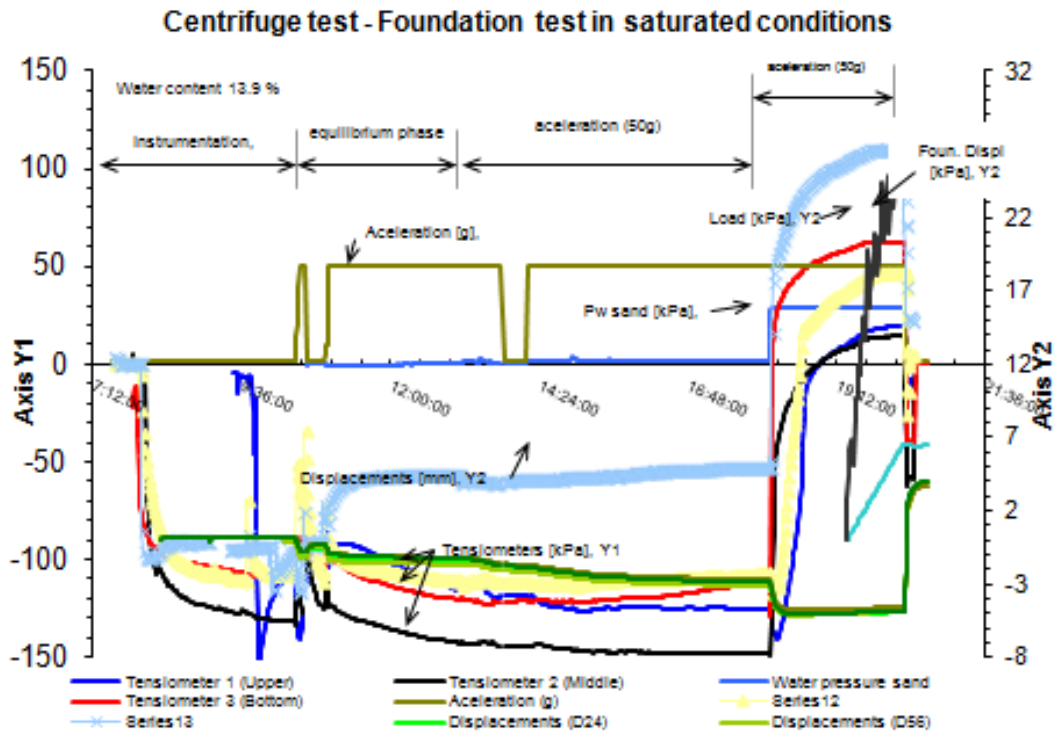
Figure 7.132: Evolution of pore pressures and vertical displacements in the centrifuge test on Jossigny silt. (After Casini 2008).

At the beginning of the test before the centrifugation, the DU tensiometers equilibrate quickly with the initial value of suction in the compacted material. At the same time ENPC tensiometers experiment a slightly slower suction increase. At the end of this equilibration period at 1g, all the tensiometers indicate almost the same value of suction, corresponding to the value of suction prevailing in the sample just after compaction. At beginning of the centrifugation, all the tensiometers exhibit a sudden increase in water pressure, followed by a progressive return to the values registered before the centrifugation. This effect can also be understood as an undrained process followed by a consolidation. This undrained process is governed by the rapid increase in total stress caused by the gravity increases. After connection with water reservoir, the water pressure measurements evolve progressively towards new values of suction governed by the hydrostatic profile that developed above the water level at 50g. Further increase is observed in the measurements once the water level is raised up in the sample and the material become nearly saturated.

Regarding the registered displacements, it is noted that once centrifugation was started a sudden problem caused the total deceleration of the rotation's arm. In that moment LVDT's registered a sudden deformation of the sample which at the time of restart of the test was not completely recovered, leaving a remaining and permanent deformation. From

367

this moment and during the centrifuge period the devices registered a remarkable displacement at the stage of watering from the sample's base 0.15MPa. This watering produces the collapse of the sample as the water front rise up to the sample's top, Fig. 7.132.

7.5) Modelling of F2 Test

The test has been modeled by FEM hydro-mechanical formulation including the generalized BBM2 model and the simplified van Genuchten retention curve described at chapter 4.

7.5.1) Equations solved

The numerical problem is addressed by solving the equations of water mass balance and stress equilibrium. It is noted that the gas phase is neglected in this case assuming that the variations of gas pressure are negligible in comparison to water pressure variations. The mass balance of water is mathematically given by the equation:

$$\frac{\partial}{\partial t}\left(\theta_l^w S_l \phi + \theta_g^w S_g \phi\right) + \nabla \cdot \left(j_l^w + j_g^w\right) + (f^w) = 0 \qquad (7.1)$$

where θ_l^w and θ_g^w are the apparent mass of liquid water and vapor in the liquid and gas phases respectively and, j_l^w and j_g^w are the advective and diffusive fluxes of water defined in chapter 2. The stress equilibrium is mathematically express by the equation:

$$\frac{\partial \sigma_{ij}}{\partial x_j} + \rho \cdot (1 + \phi\omega_l)g_j = 0 \qquad (7.2)$$

where $\rho = \rho_s(1 - \phi)$ is the dry density and $\omega_l = {\rho_l}/{\rho}$.

Both equations are discretized in a finite element fashion and solved simultaneously by using the finite element code Code_Bright, Olivella et.al. (1996).

7.5.2)   Geometry, Mesh, Initial and Boundary conditions

The model used to simulate centrifuge test of the shallow foundation is an axisymmetric piece of sizes 0.15m width and 0.30m high, Fig. 7.133. The mesh of the model consists of 450 rectangular elements (with linear interpolation).
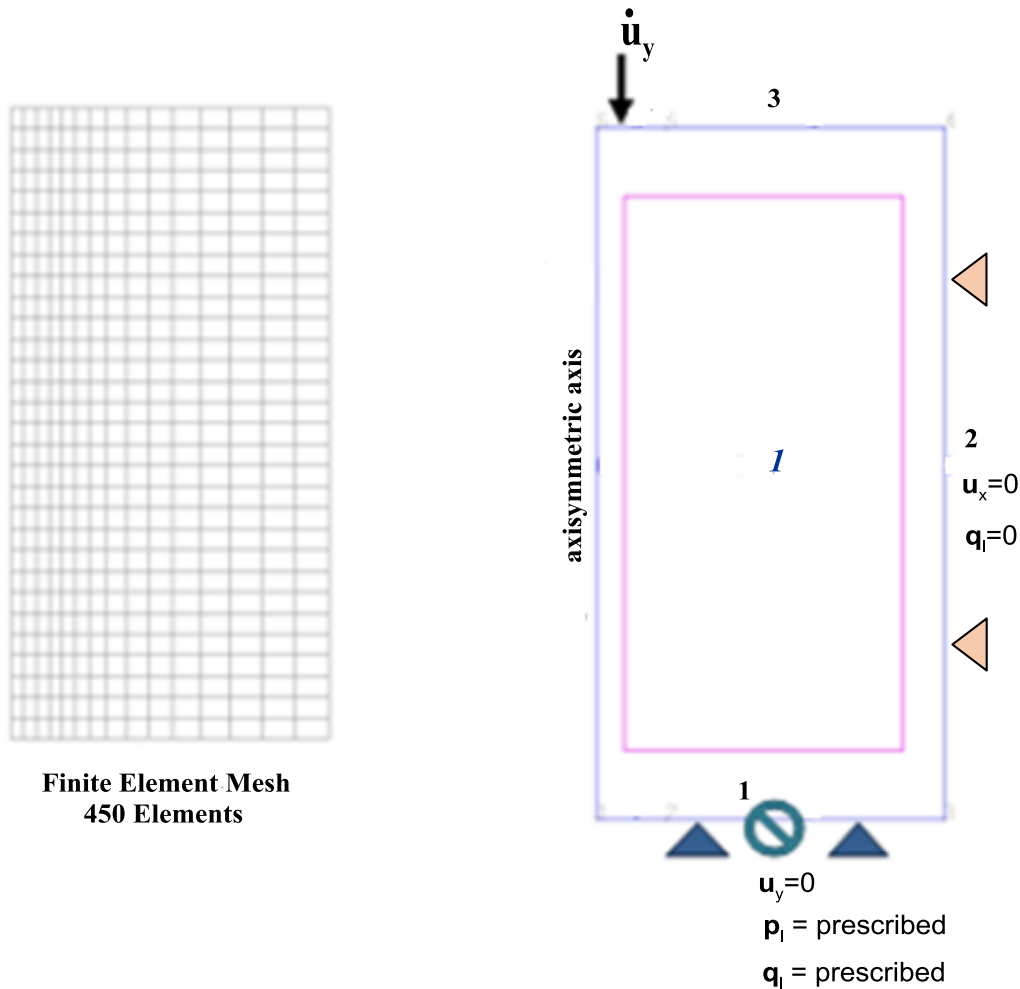
Figure 7.133: Model Geometry, mesh and both mechanical and hydraulic boundary conditions.

The tests is composed of three time intervals: (a) Equilibrium stage at 50g with impervious condition at the bottom boundary of the sample, (b) Saturation stage by water pressure applied at the base and (c) Load stage coming from the foundation.

As for the hydraulic intervals, a null water flux is applied in the bottom and lateral boundaries as conditions. Then at the saturation stage (during centrifugation) the null water flux is maintained for the lateral boundary while a liquid pressure $p_l = 0.15$MPa is applied in the bottom boundary of the sample.

As for the mechanical condition, both null vertical displacements and horizontal displacements are imposed in the bottom and in the lateral boundaries respectively. Then at the loading stage a rate of vertical displacement is applied in the foundation site.

Table 7.38 summarizes the time intervals considered in the simulation together with the corresponding conditions initial and boundary.

Table 7.38: Intervals, Initial and Boundary conditions considered at the centrifuge simulation.

Interval	Time [hs.]	Initial and Boundary Conditions	
1	0-7.6	Initial conditions: $\sigma_x^0 = \sigma_y^0 = 0.01\,\text{MPa}$ $\phi^0 = 0.4583$ $p_l^0 = -0.1\,\text{MPa}$ (suction corresponding to compaction condition)	
		Lower boundary(1): $u_y = 0$ $q_l = 0$	*Lateral boundary(2)*: $u_x = 0$ $q_l = 0$
2	7.6-9	*Lower boundary(1)*: $u_y = 0$ $p_l = 0.15\,\text{MPa}$	
3	9-11.82	*Lower boundary(1)*: $u_y = 0$ $p_l = 0.15\,\text{MPa}$	*Upper left boundary(5)*: $\dot{u}_y = 0.12\ ^{\text{mm}}/_{\text{min}}$

The initial conditions adopted in the simulation correspond to that assumed at the laboratory test. A constant initial water pressure corresponding to a water content of 13% is applied to the sample, an initial volumetric stress state of magnitude 0.01MPa is considered, a pre-consolidation pressure at saturated conditions of about $p_0^* = 0.07$ is provided and an initial porosity of $\phi = 0.46$ is assumed to the medium.

7.5.3)   Material Parameters

In this section, material parameters used in the numerical model are presented. The simplified van Genuchten retention curve presented in chapter 4 has been calibrated based on the laboratory data at hand.

Figure 7.134 presents the contour of the simplified van Genuchten retention curve used in the model and its comparison with the experimental retention curves. The material parameters describing the water retention shape are $P_0 = 0.013$ MPa and $\lambda = 0.52$.
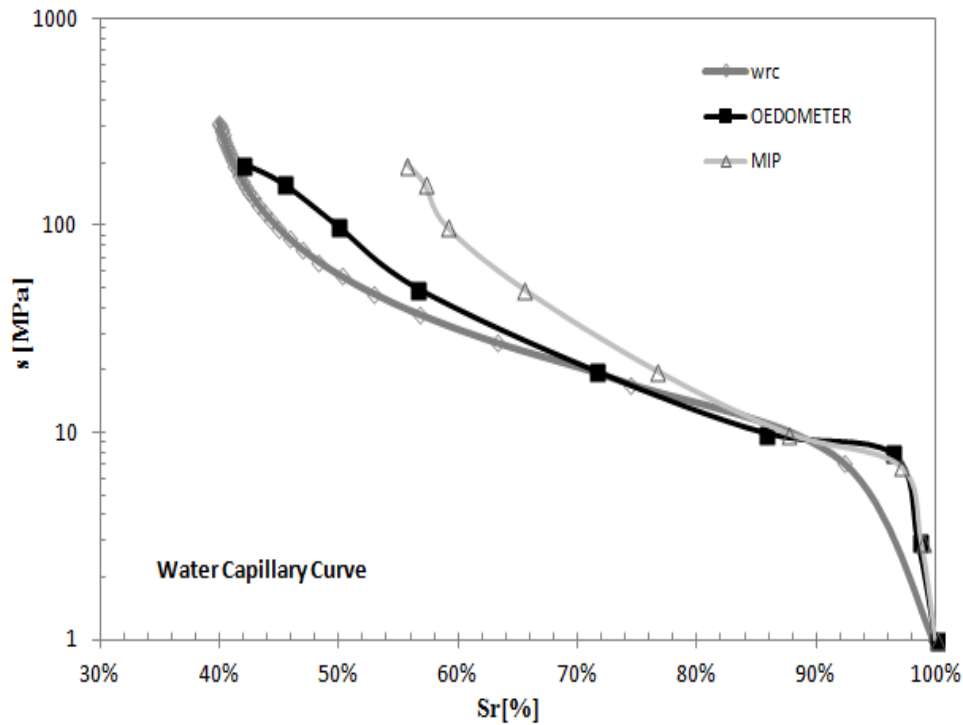
Figure 7.134: Water retention used at the numerical simulation.

As for the mechanical model, the generalized-BBM2 model described in chapter 4 has been used. This model has been chosen because of its ability to deform the yield surface's shape, which allows for a progressive transition from BBM to mixed shear-cap model depending on the value of ϵ:

$$d_s = w(p_o^*)^b \left[\dot{\alpha}_p{}^2 + M^2 \left(\epsilon + (1 - \epsilon) \frac{p'}{w(p_o^*)^b} \right)^2 \dot{\alpha}_q{}^2 \right]^{1/2} \tag{7.3}$$

where a shape parameter $\epsilon = 1$ reproduce the dissipation function (mechanism) of the critical state model BBM2 for partially saturated porous media.

371

During the watering stage, wetting induced collapse has been modeled with $\epsilon = 1$. Then at the loading stage, foundation displacements and stresses have been modeled with a shape parameter $\epsilon = 0.5$ in order to consider a shear failure criterion closer to the Drucker-Prager one. Fig. 7.135 sketches the yield surfaces in addition to stress points at stages of wetting collapse and foundation load for two different sections.
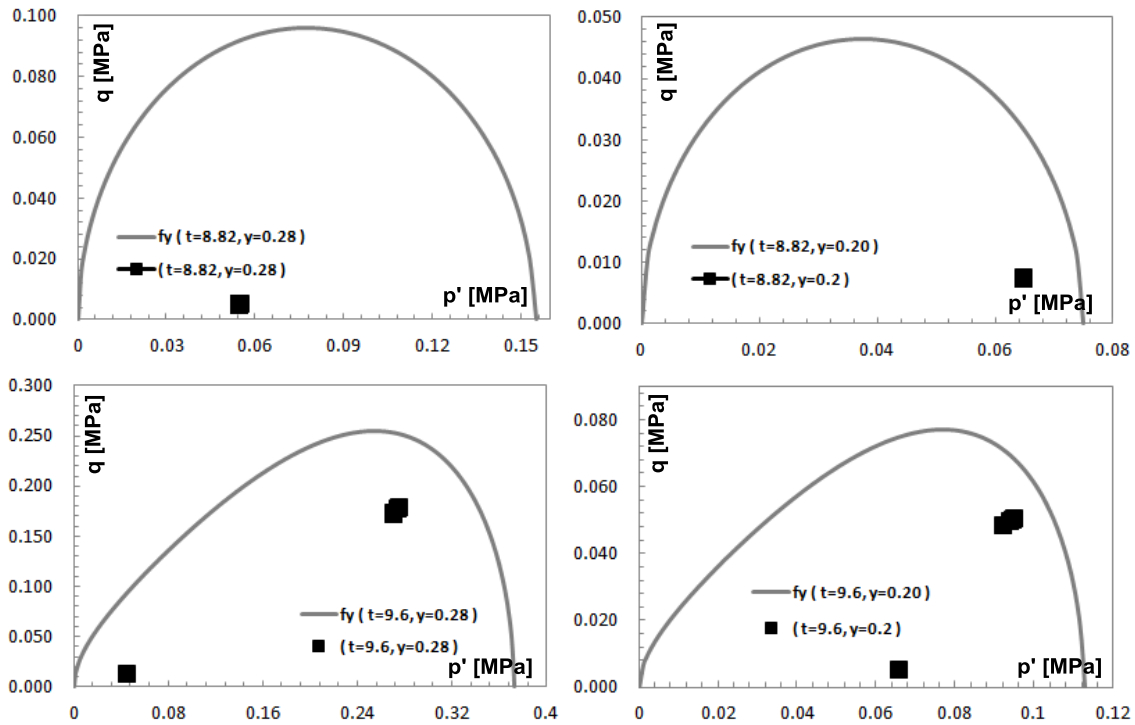
Figure 7.135: Yield surfaces and stress points at stages of: (a) wetting collapse and (b) foundation's loading and for two sections at different depth.

Insights into the stress paths, yielding processes and yield surface states are presented below in subsection of loading phase results.

Mechanical law has been calibrated to reproduce the collapse shown by the test. Values $\kappa = 0.005$ for the slope of isotropic compression line and $\lambda = 0.07$ for the slope of normal compression line has been obtained.

The numerical integration of the mechanical model has been performed with algorithm of Interior-Point class, which gives a return mapping technique at Gauss point level. An initial duality gap parameter $\mu^0 = 1E - 9$ has been assumed. The maximum number of Newton iteration allowed is 30 together with a maximum of 5 reductions of the line-search parameter. A viscosity parameter of about $\eta = 0.09$ is used at the stage 2 to facilitate the

_____

convergence. A tolerance in the error norm of the residual vector ($||\mathbf{r}(\mathbf{x})||$) of ($\epsilon = 1e - 8$) is selected.

Figure 7.136 shows the shape of the dependency of isotropic yield function in the plane $(s - p_0^*)$.

Figure 7.136: Yield Locus Calibration (BBM2)

Table 7.39 summarizes the parameters used for the hyperporoplastic model together with the parameters used in the interior-point algorithm to integrate the mechanical constitutive law.
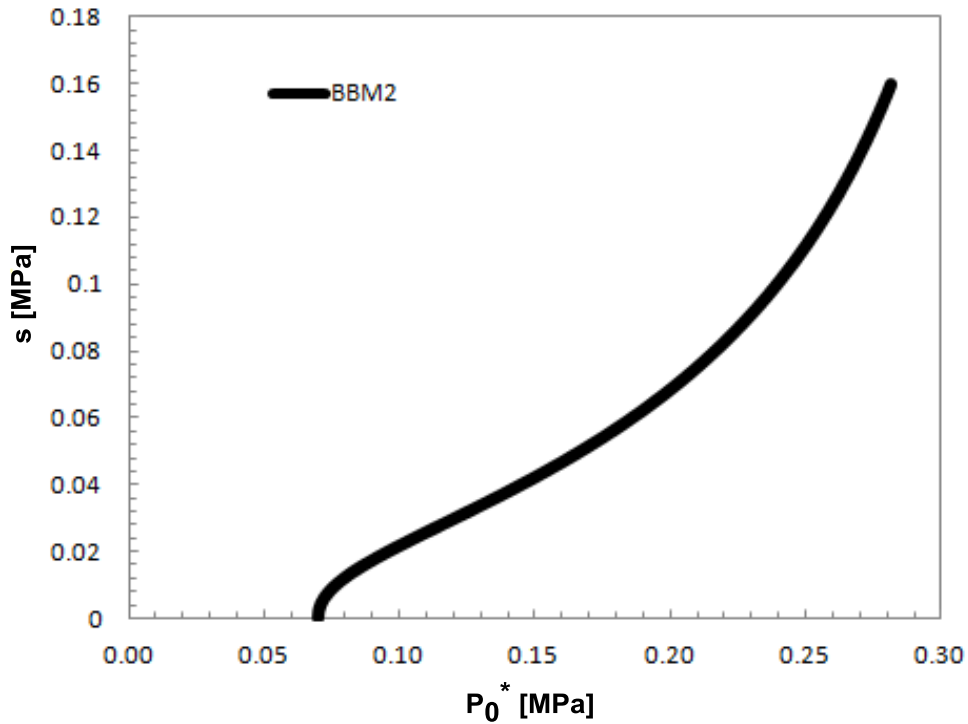
Table 7.39: Mechanical Material parameters used in the numerical model

MECHANICAL DATA		
hyperporoplastic model		
Elastic Parameters		Gibbs energy:
κ	0.005	
ν	0.3	$g_s = \dfrac{1}{p_o^{1-n} \cdot k(1-n)(2-n)}$
n	0.9	$\cdot \left(p'^2 \right.$
Plastic Parameters		
p_0^* [MPa]	0.07	$+ \left. \dfrac{k(1-n)}{3\varrho} q^2 \right)^{\frac{2-n}{2}}$
ϕ [°]	31	
N	1.65	$- \dfrac{p'}{k(1-n)}$
λ	0.07	$- (p'\alpha_p + q\alpha_q)$
a	0.0048	
b	3.4	
ξ_1, ξ_2	10, 3	
p_{at}	1E-10	Yield function:
Shape Parameters		
$\epsilon[-]$: (wetting stage)	1.0	$f^y = x_p'^2 + \dfrac{x_q'^2}{M^2 B(\epsilon)^2}$
$\epsilon[-]$: (loading stage)	0.5	
Integration Parameters		$- w(\xi)^2 \cdot \left(\dfrac{p_c^*}{2}\right)^{2b(\xi)}$
Algorithm index	3 (interior point algorithm)	
Newton tol.	1E-6	
Line_search param. 1	1E-2	
Line_search param. 2	0.1	
Max. iter. barrier	1	
Max. iter. Newton	30	
Max. Line_search iter.	5	

Finally, Table 7.40 summarizes the hydraulic and phase parameters used in the numerical model of the shallow foundation.

Table 7.40: Hydraulic and Phase parameters used in the numerical model

HYDRAULIC DATA		
Retention Curve (simpl. van Genuchten)		
p_0[MPa]	0.013	$S_r = \left(1 + \dfrac{s}{p_0}\right)^{-\lambda}$
λ	0.52	
Intrinsic Permeability		

$k_{ii}[m^2]$	2.85E-14	$k = k_0 \dfrac{\phi^3}{(1-\phi)^2} \dfrac{(1-\phi_0)^2}{\phi_0{}^3}$
ϕ_0	0.4583	
Liquid Phase Rel. Permeability (Power law)		
λ	3	$k_{rl} = AS_r{}^\lambda$
PHASE DATA		
Solid Phase (Density)		
$\rho_s \left[k_g m^{-3}\right]$	2700	

7.5.4)   Modeling Results

In this section the results obtained from the numerical model are presented and validated in comparison with the measurements from centrifuge test. The section is organized as follows: firstly, the wetting stage is addressed analyzing the liquid pressure profiles and evolutions exerted by the sample. Then the displacement produced as a result of the wetting is displayed and analyzed. Secondly, the loading stage is addressed by analyzing the results of the foundation's load application. Finally, isochors and vectors of primary-governing and dependent variables are presented (displacement, hardening, plastic multiplier, liquid saturation, porosity, shear strain, plastic shear strain, water flux).

7.5.4.1)   Modelling results of the wetting stage

Numerical model is validated contrasting both the liquid pressures registered at the measuring devices installed in the sample and the liquid pressures obtained from the simulation.

Firstly, Fig. 7.137 contrasts the evolution of both: (a) liquid pressures registered at the measuring devices installed in the sample and (b) the results from the simulation. They show a good agreement between the measurements and the model computations.
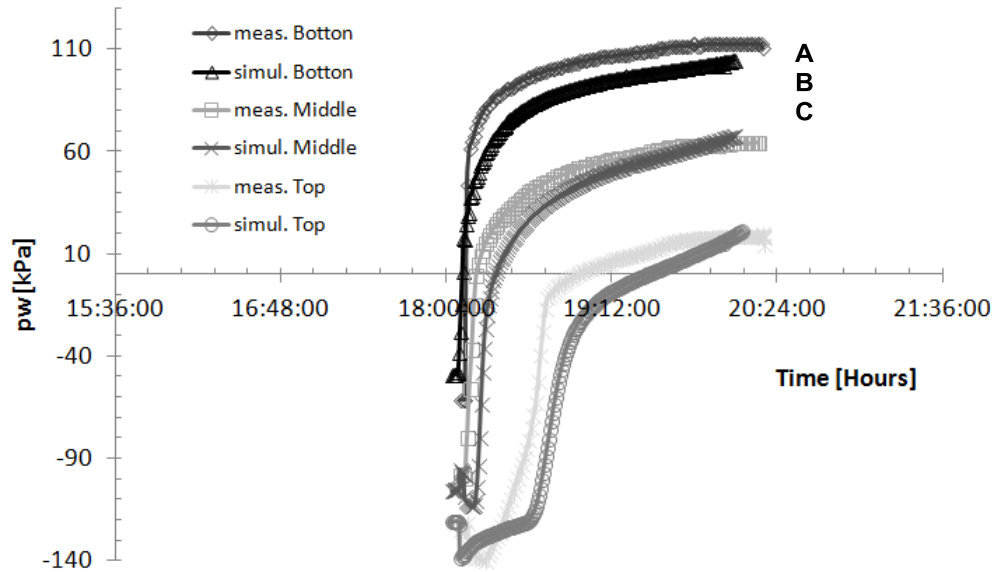
Figure 7.137: Comparison between the Liquid pressures measures at the laboratory and the response of the numerical model. Collection of water pressures' jump at the three depths: (a) Bottom (0.085m) , (b) Middle (0.155m) and (c) Top (0.245m).

At time of connection with water, the water pressures along the sample start to increase. Liquid pressure increases at each horizontal section in accordance with the arrival of the wetting front. At all depth, a jump of liquid pressure of about 0.15 MPa (equivalent to the imposition at the sample base) is observed.

Secondly, in line with the model validation, Fig. 7.138 shows isochrones of saturation degree and porosity obtained through the numerical simulation at three different times: (a) initial time $t = 0$ hs, (b) onset of centrifugation $t = 7.6$ hs. and (c) end of wetting $t = 8.82$ hs. Moreover, Fig. 7.139 shows profiles of liquid pressures in the sample at the same times: (a) initial time, (b) onset of centrifugation and (c) end of wetting, again obtained through the numerical simulation and its comparison with the corresponding measures from the tensiometers at the centrifuge laboratory test.

Fig. 7.138 shows that as the saturation front progresses from below, a continuous collapse of the sample is produced and in consequence a densification of the material is observed. Regarding the liquid pressure profiles, Fig. 7.139 clearly shows its evolution at the end of each phase. The graph shows a good agreement between the profiles measures at the tensiometers and the liquid pressure profiles obtained with the numerical model, except for the upper layer which remains partially saturated. They indicate that water pressures have reached a state close to equilibrium at time of foundation loading.
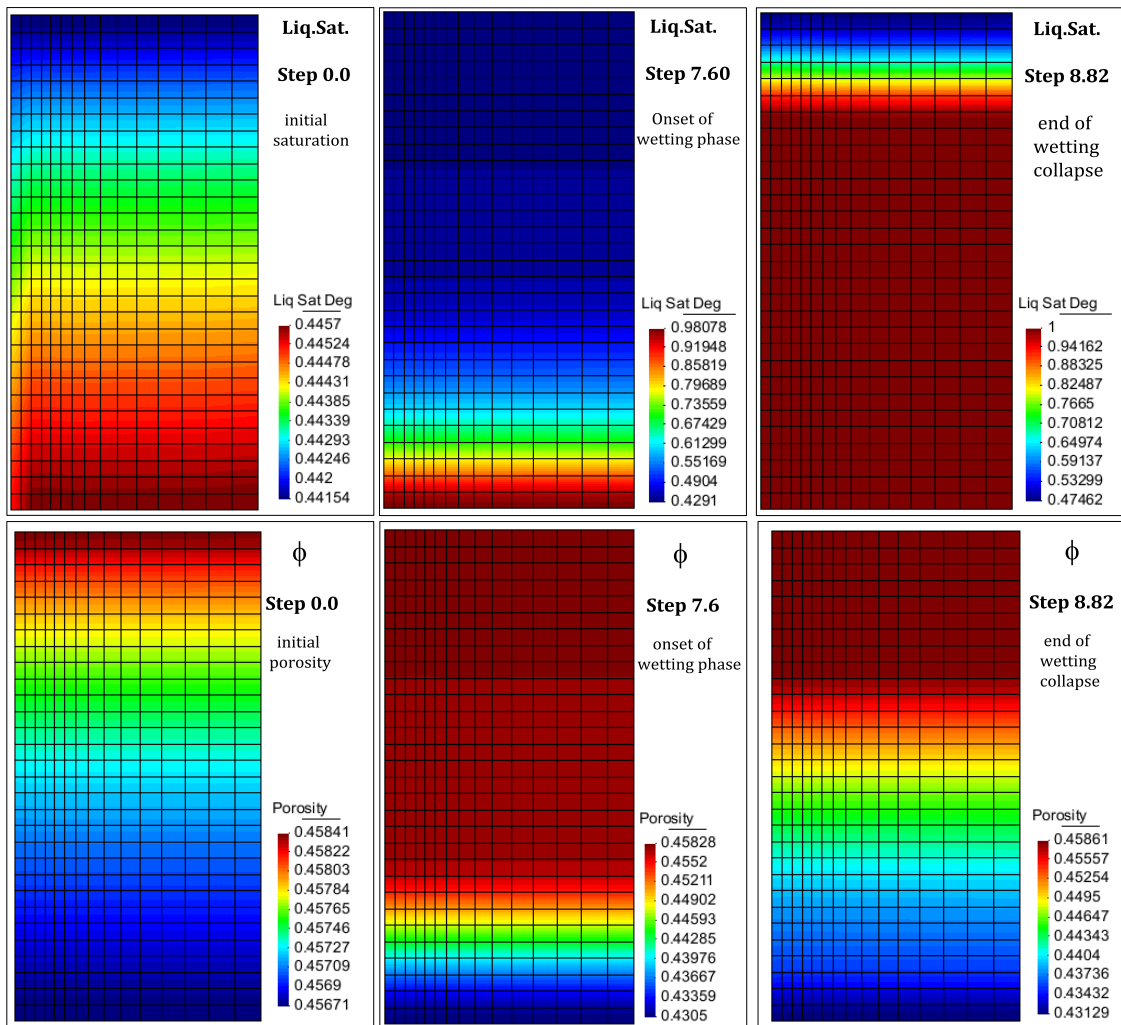
Figure 7.138: Isochrones of: (a) Liq. Saturation and (b) Porosity at three different times of the simulation, the initial state (1g), the onset of wetting process (50g) and the end of wetting collapse (50g).
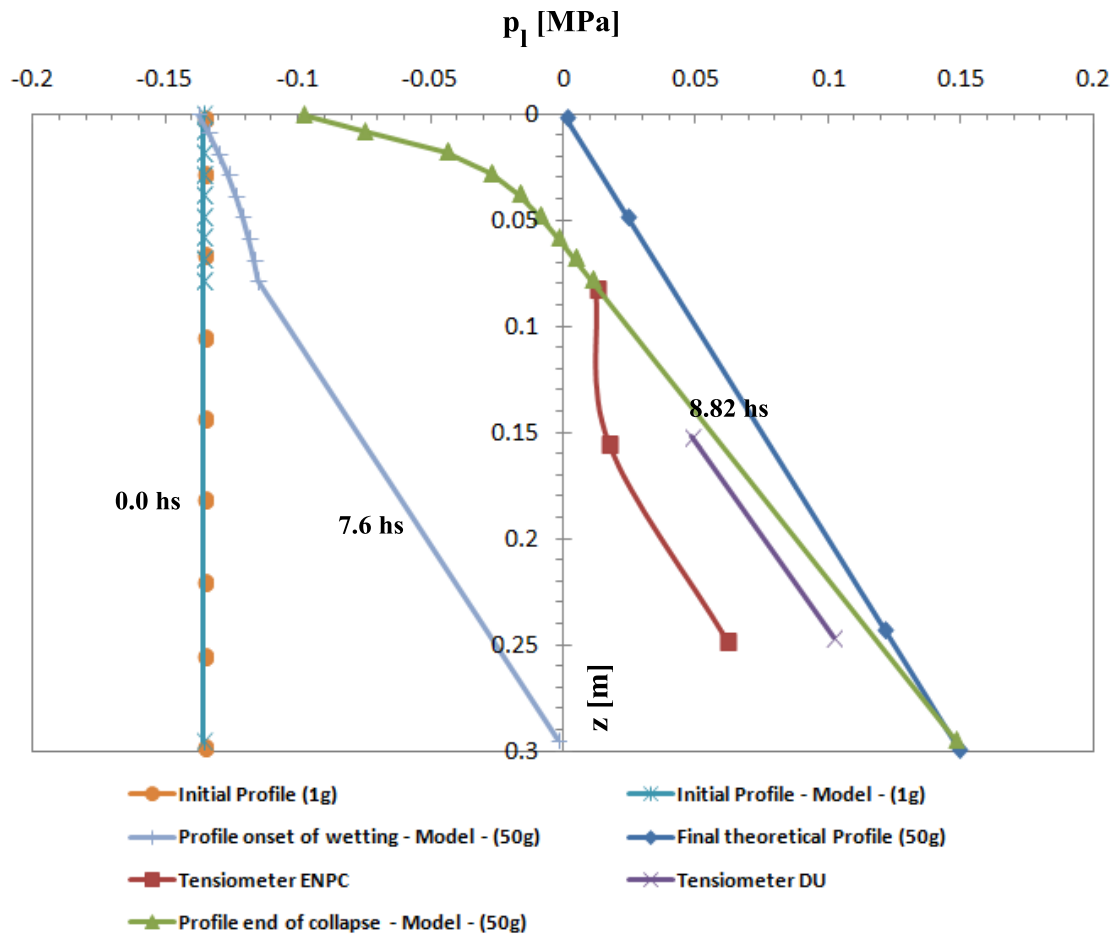
Figure.7.139: Liquid pressure profiles at different times of the simulation: the initial state (1g), the onset of wetting process (50g) and the end of wetting collapse (50g) and its comparison with the experiment measures.

Continuing with the model validation, regarding the displacements induced by wetting "collapse", Fig. 7.140 presents a comparison between the registered vertical displacements and those obtained from the numerical model. Both graphs present a good agreement between them. It is noted that a first settlement takes place during the equilibrium stage. The magnitude of those displacements reaches 3mm. From that moment the water pressure is applied at the model base producing the wetting collapse. This phenomenon leads the observed vertical displacements up to 5mm. A small difference between both settlements is observed. This fact might be due to the remaining unsaturated upper layer in the model.
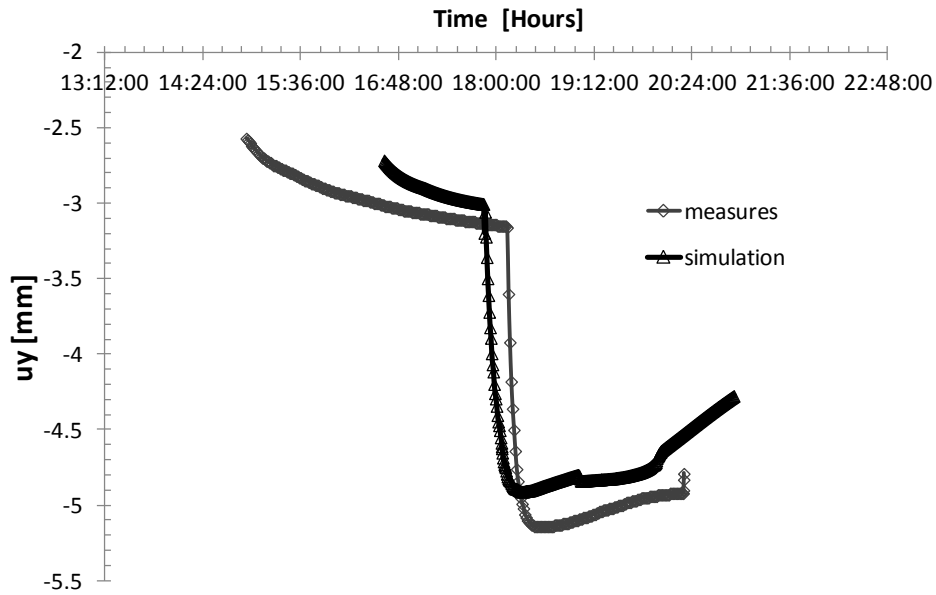
Figure 7.140: Comparison between the vertical displacements measures at the laboratory and that obtained from the numerical model.

Figure 7.141 shows isochrones of vertical displacements exerted at the sample during centrifugation (50g) at two different times: (a) onset of wetting phase and (b) end of wetting collapse. From the onset of wetting phase at $t = 7.6\ hs$ a continuous collapse of the sample until its full saturation is produced. The observed settlements are uniform and reach a magnitude of 5mm.

The evolution of displacements continues in the next stage once the foundation load is applied. This displacements are studied in the next subsection where the results of the loading stage are addressed.
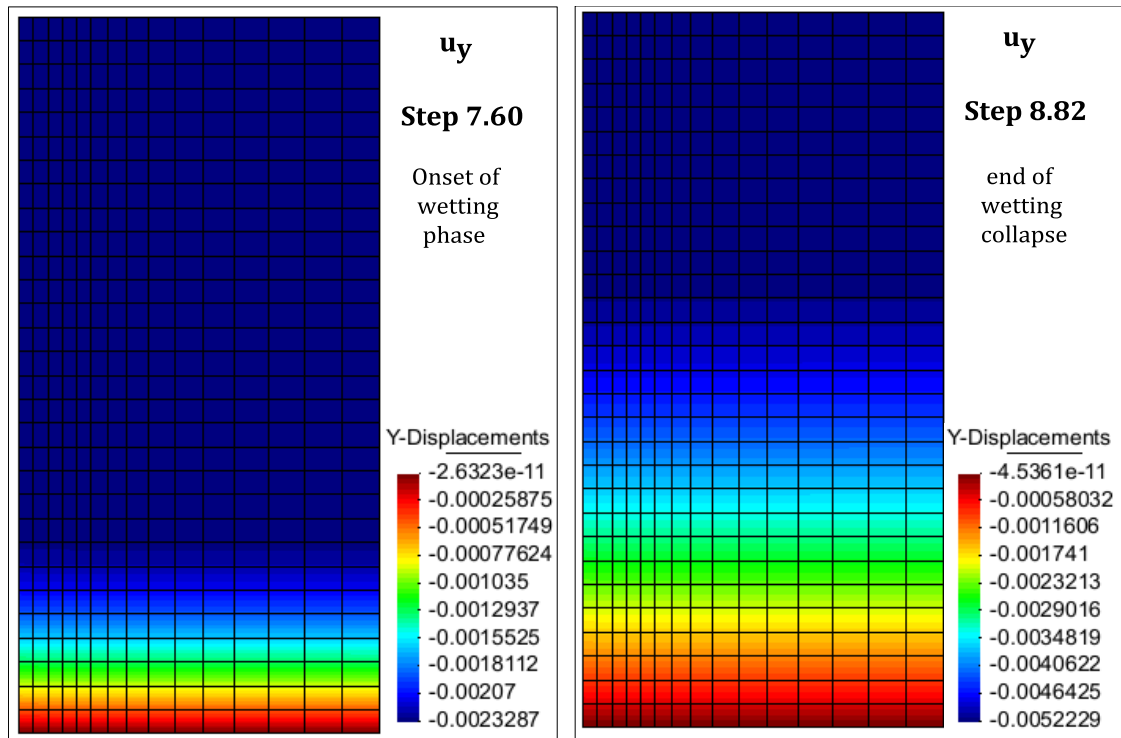
Figure 7.141: Isochrones of vertical displacement at two times of: (a) onset of wetting phase (50g) and (b) end of wetting collapse (50g).

Further insights into the collapse process are provided by isochrones of hardening of the yielding points (p_0^*) and plastic multiplier (γ_p), Figs. 7.142 and 7.143.
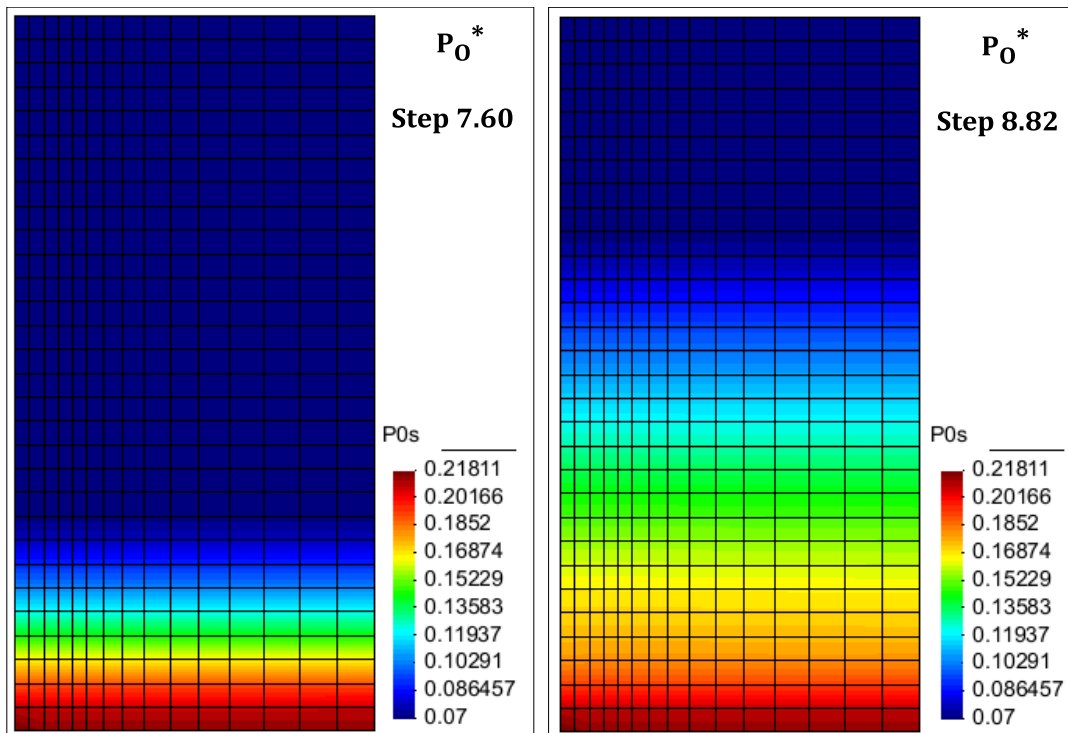
Figure 7.142: Isochrones of hardening parameter at the times of: (a) onset of wetting stage t=7.6hs. (50g) and (b) end of wetting collapse t=8.82hs. (50g).
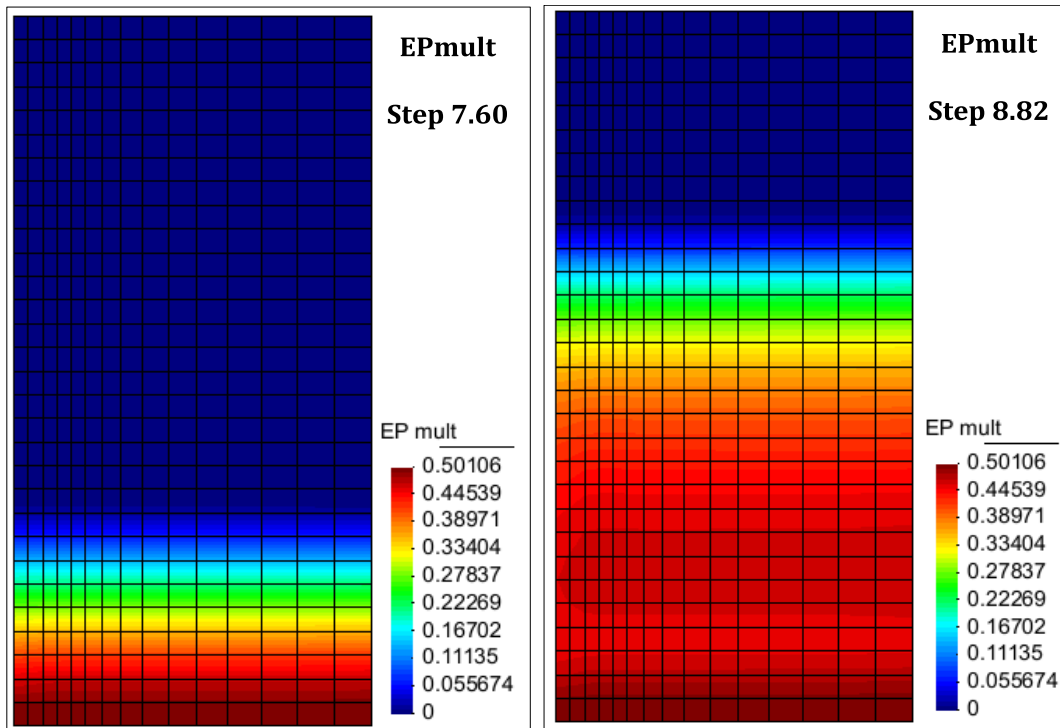
Figure 7.143: Isochrones of Plastic multiplier at the times of: (a) onset of wetting stage t=7.6hs. (50g) and (b) end of wetting collapse t=8.82hs. (50g).

The corresponding stress-suction paths are drawn in Figures 7.144 and 7.145 in three points at different heights of the sample. The upper point, at low stress level does not experiment collapse and remains in elastic regime. The lower point, at the highest stress level, reaches the LC yield limit at early time and starts to collapse at a suction equal to 0.007 MPa.

As consequence, the stress path starts to follow the plastic line. After saturation, water pressure keeps increasing at point A and the effective stress path goes back in the elastic zone while point B starts collapsing.
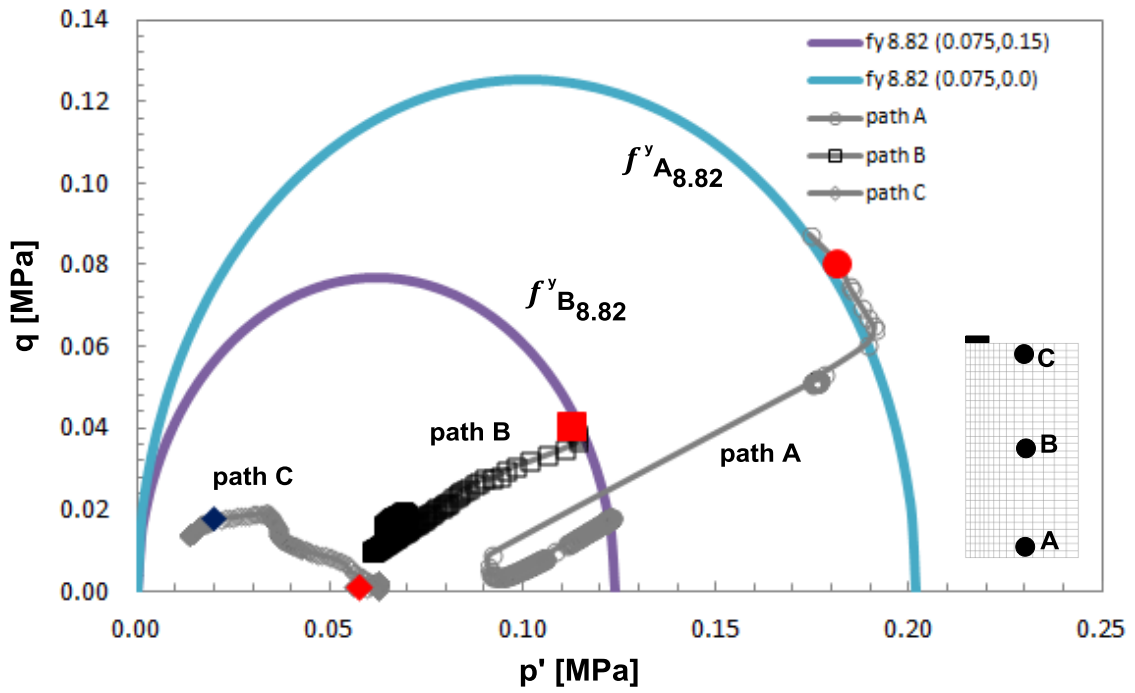
Figure 7.144: Stress paths for three points at different heights of the sample with the corresponding yield surfaces BBM2 at the end of the collapse stage.
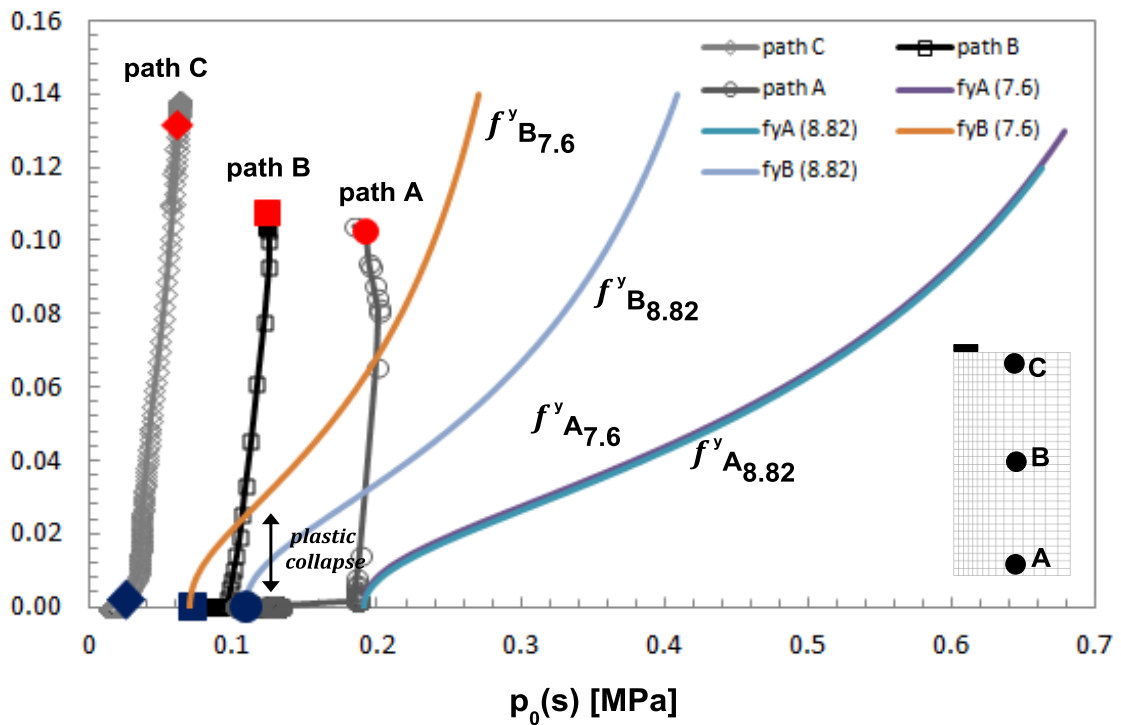
Figure 7.145: Mean stress-Suction paths for three points at different heights of the sample with the corresponding LC yield limits.

7.5.4.2) Modeling results of the loading stage

Following with the numerical model validation, in this sub-section the displacements obtained as consequence of the foundation's load application are addressed. Figure 7.146 shows the load-displacement curve obtained as consequence of the foundation's action. An increase of f (load/foundation area) can be noticed while displacements increase. This increment stops later to give rise to a slow and smooth decrease. The graphs f(load/foundation area)- displacement show a good agreement between the measures and the model results.
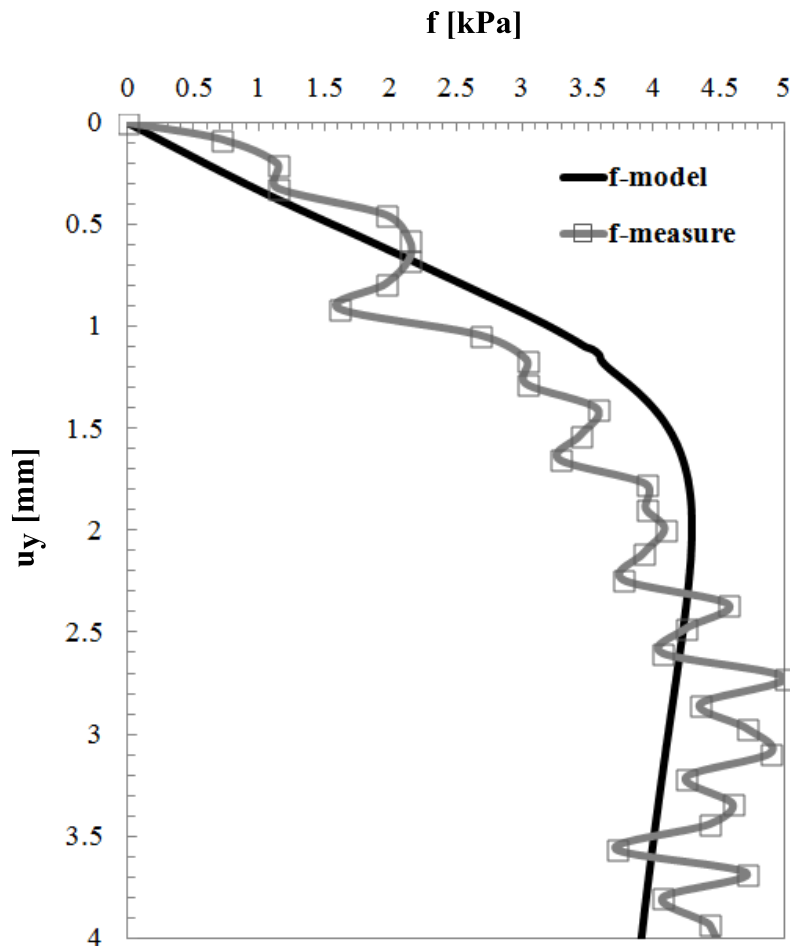
Figure 7.146: Load-Displacement curve due to foundation action. Comparison between the measures and the model results.

Below, Fig. 7.147 shows isochrones of both: (a) vertical displacements and (b) porosity, obtained during the loading stage at three different times of the applied total load.

Unlike the observations on porosity variations during the wetting stage, in the loading stage variations concentrate in the zone under the foundation. A densification of the material is produced just under the foundation while the soil at the footing edge expands continuously until a land lift is produced.
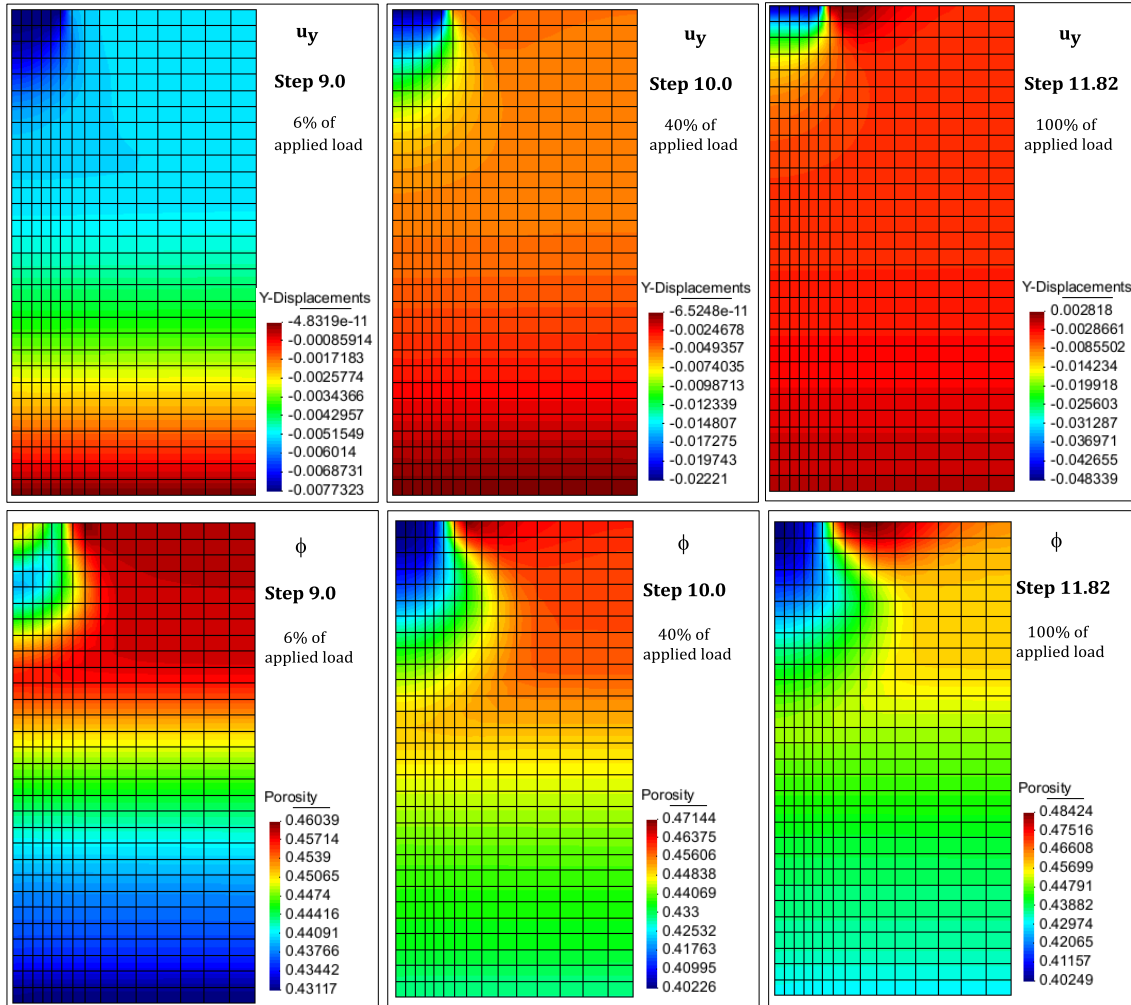
Figure 7.147: Isochrones of vertical displacements and porosity in the loading stage at three different times of the total applied load.

Once the foundation action starts through the displacement rate application, a concentration of stresses and strains can be observed at the upper left side of the model. The zone of influence extends to about $1.5 \cdot d$ (d is the diameter of the foundation). Figure 7.148 shows isochrones of plastic multiplier and deviatoric stress invariant developed at the zone of influence, under the load. Isochrones of porosity and shear strains are also presented. The figure shows an image of the failure mechanics at time of

14% of the total applied load (t=9.23), which corresponds to a load value equivalent to $^{f_{peak}}/_{2.5}$ in the load-displacement curve.
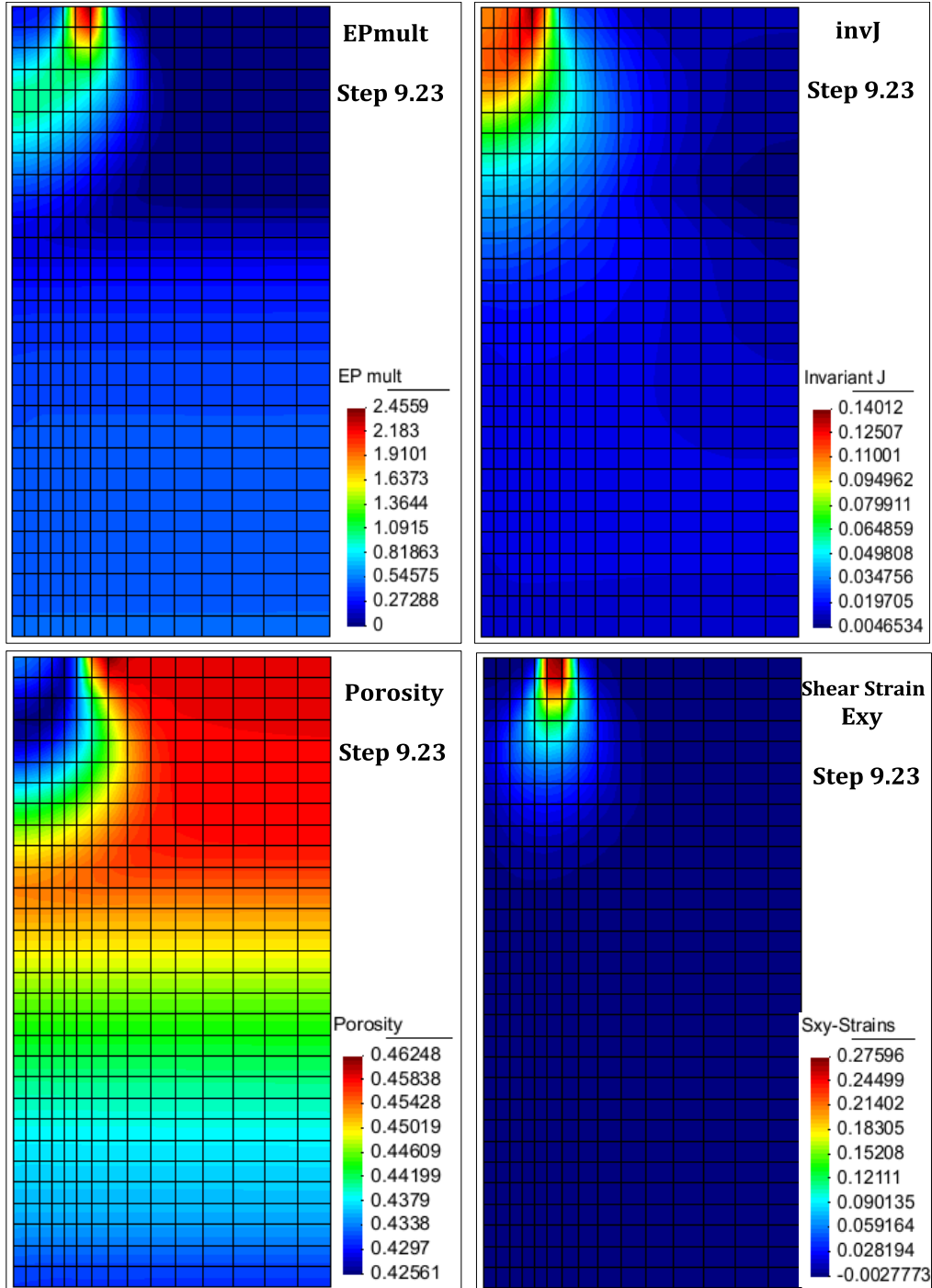
Figure 7.148: Contours of plastic multiplier and Second (Deviatoric) invariant of stresses at a time step after the foundation load application. Contours of porosity in the sample after the foundation load application.

Isochrones of porosity evidence a decrease of porosity matching with concentrations of shear strains and plastic flow, in the same zone.

The development of a localized plastic zone is evident. It is localized below the foundation and indicates that the failure mode in this case is of punching type.

This mode is accompanied by development of plastic shear strain on the outer side foundation as load increases. As load evolves the magnitude of plastic shear strain increases at the foundation boundary but the plastic shear strain at the central zone remains essentially constant, see Fig. 7.149.
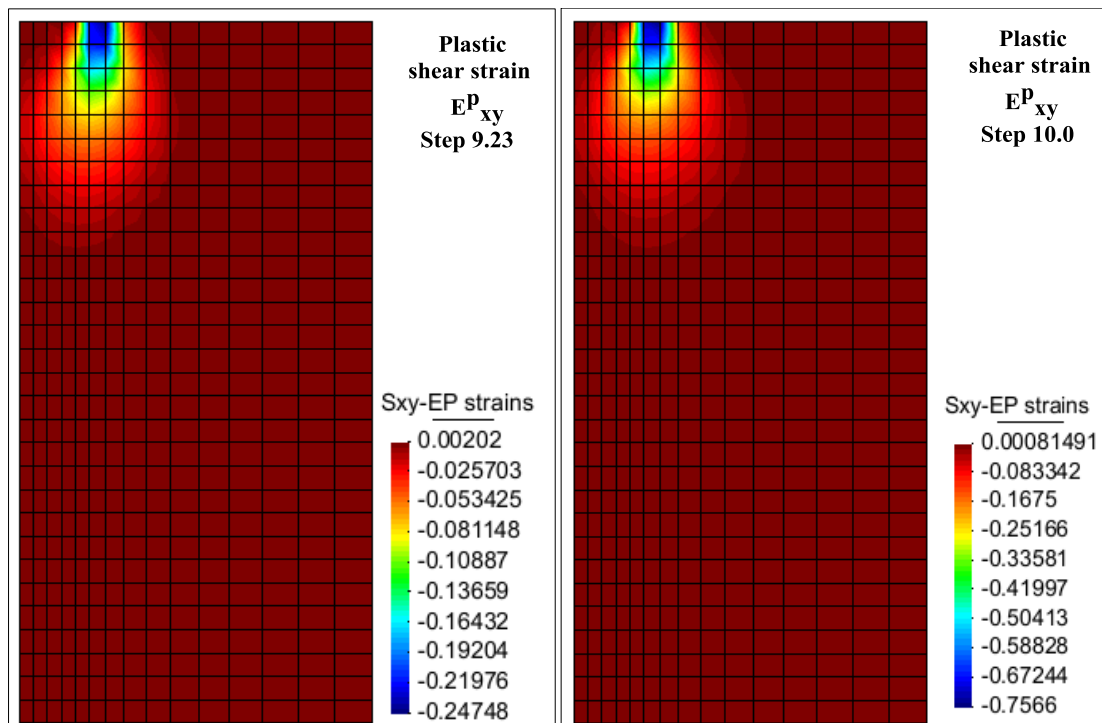
Figure 7.149: Contours of plastic shear strains at two different times after the application of the load's foundation.

Fig. 7.150 shows vectors of displacements, water flux and plastic strains. It evidences a concentration of vertical displacement below the foundation, accompanied by upward movement of the ground water towards the soil surface. Vectors of plastic strains at principal directions are produced in planes at 45° with respect to the plane of principal shear plastic strains. This supports once again the type of failure mode.
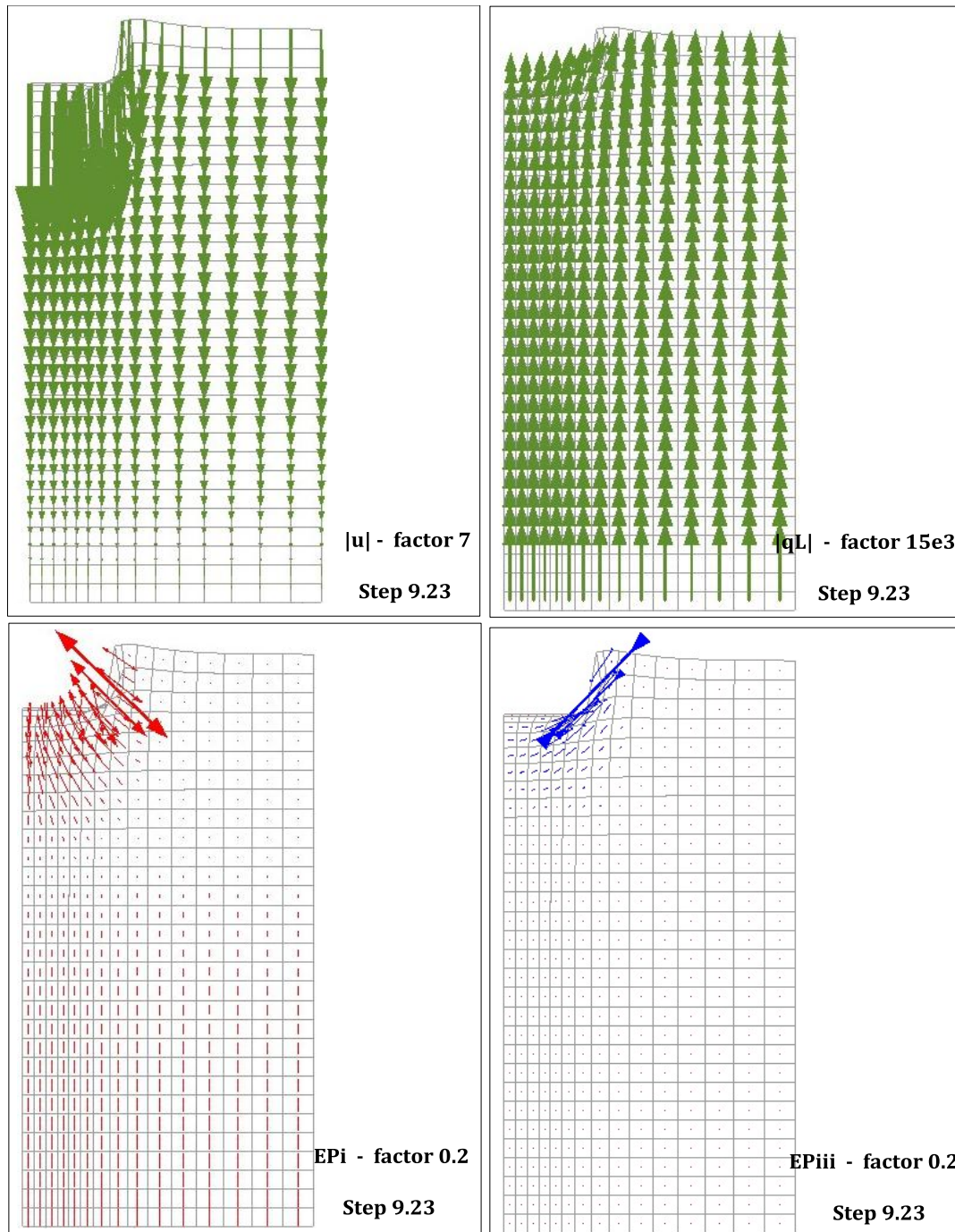
Figure 7.150: Vectors of displacements, Plastic strains and liquid flux on deformed section of the soil. The vectors are shown at the time step 9.23.

Figure 7.151 shows vectors of displacement exerted at the model at different times of the applied load. The overall mechanical response at loading stage is better understand with isochores of porosity and plastic shear strain attached to the vectors of displacements.

387
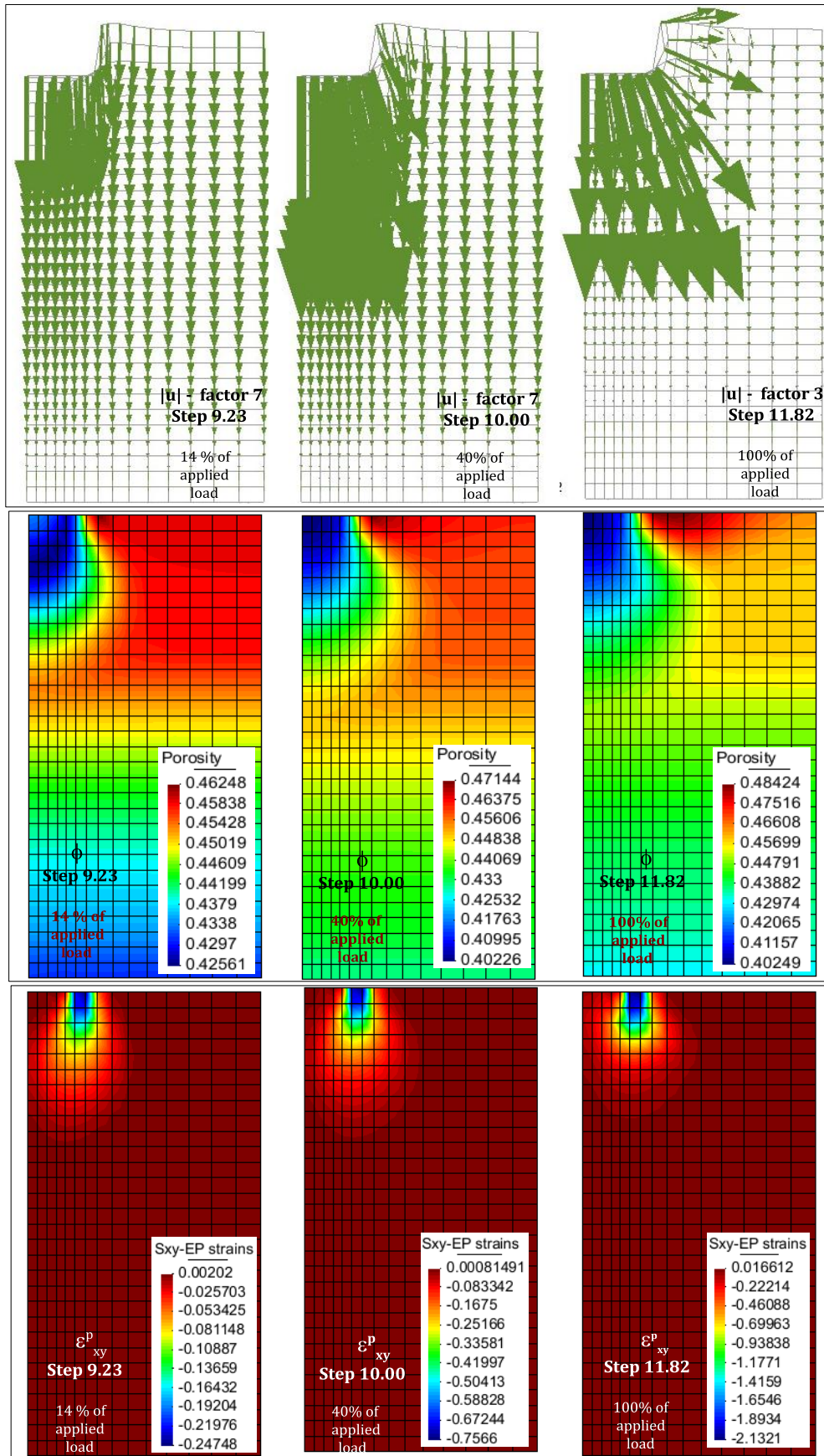
Figure 7.151:Vectors of displacement, isochores of porosity and plastic shear strain at different times of the applied load: (a) 14% of total load, (b) 40%of total load and (c) 100% of total load.

388

Figure 7.152 illustrates the vertical and horizontal components of displacement vectors exerted in the sample during the loading stage.
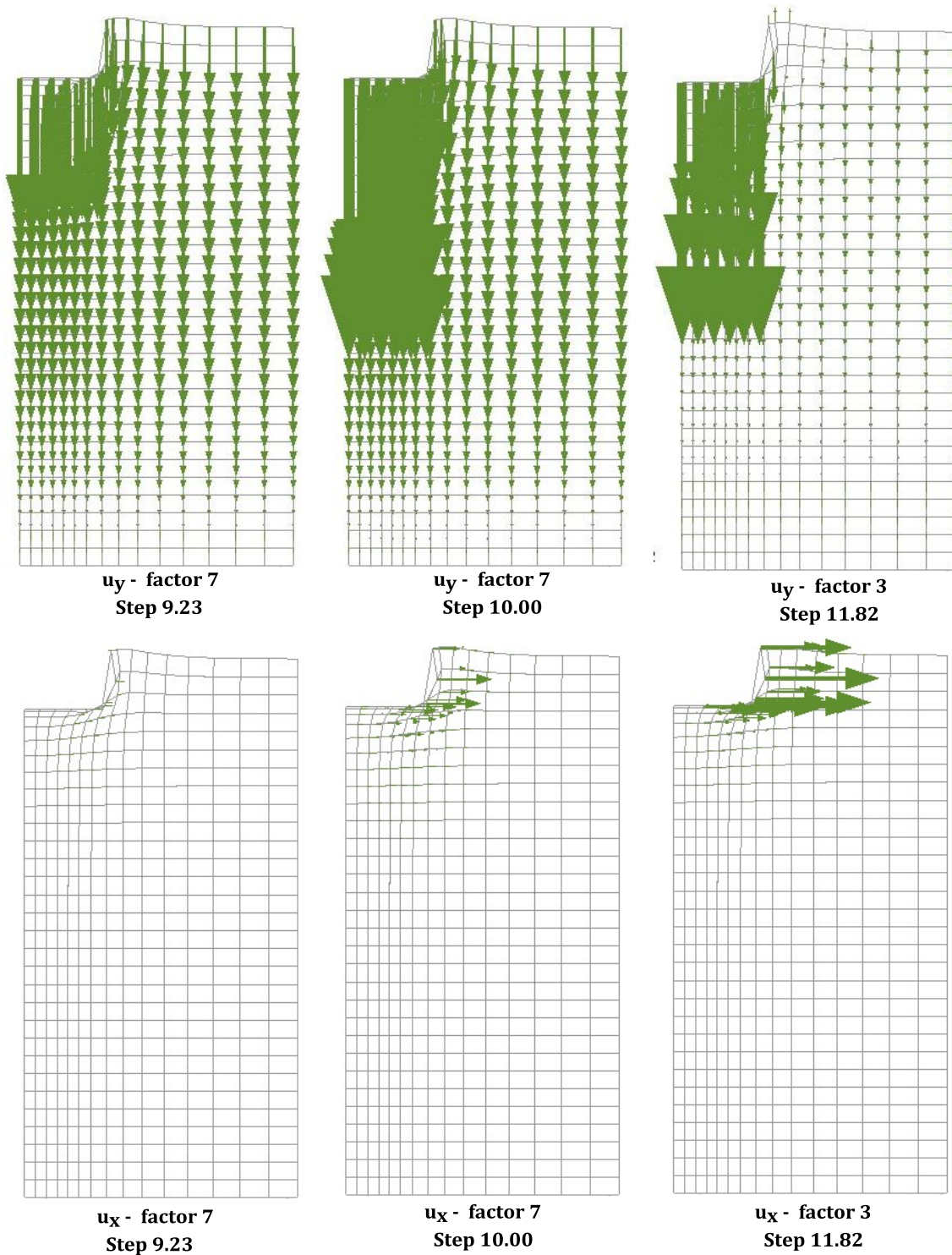
Figure 7.152: Vectors of vertical and horizontal displacements at different times of the centrifuge test.

The components of vertical and horizontal displacements at 100% of the applied load evidence clearly the land lift around the foundation's boundary.

Figure 7.153 shows vectors of liquid flux at different times of the centrifuge test.
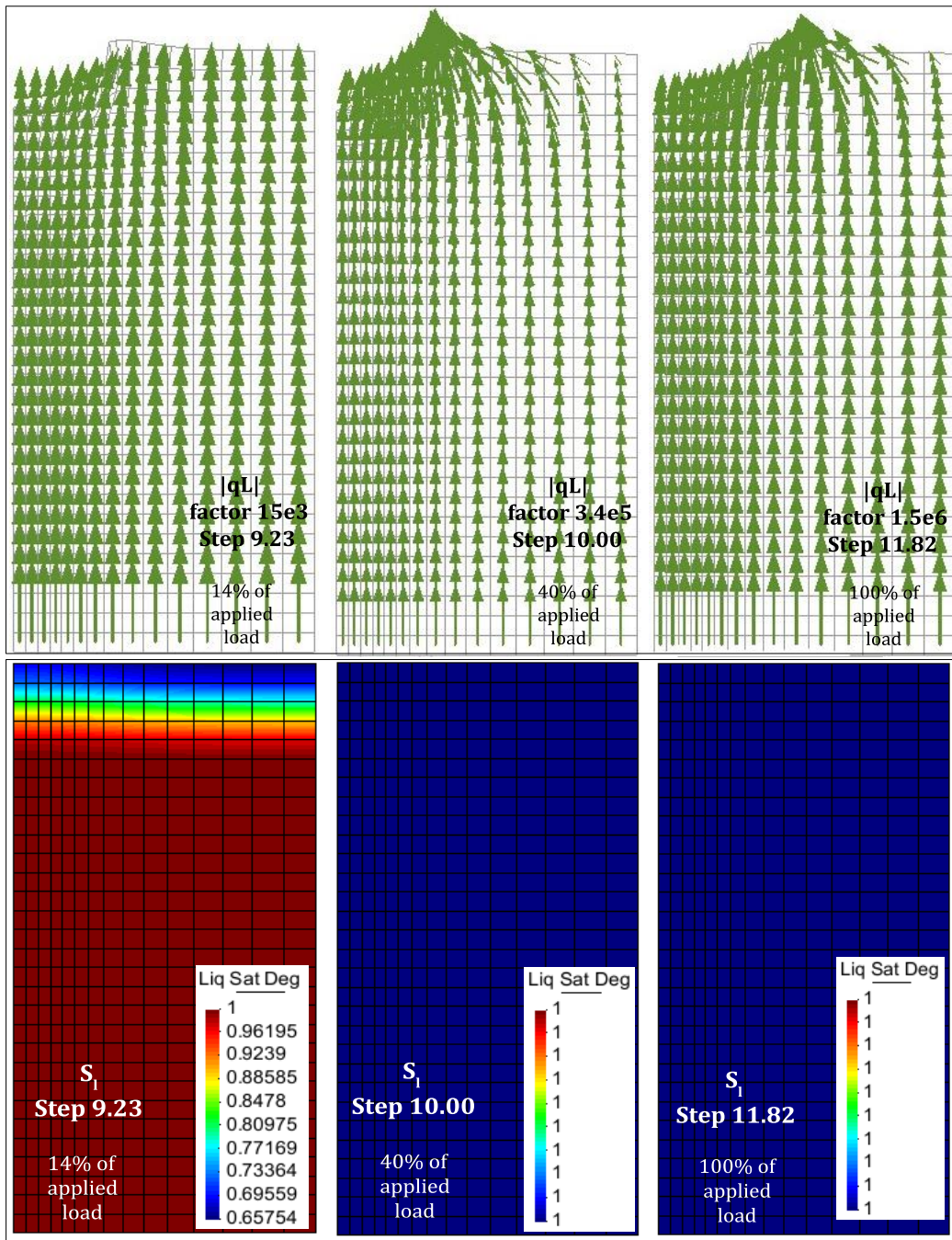
Figure 7.153: Vectors of liquid flux and isochores of saturation at different times of the applied load.

Vertical displacements, along a horizontal profile at a top layer of the soil column, are presented in Fig. 7.154. An analysis of the stress-paths followed is also presented. Stress paths exerted at different points under the foundation are shown due to the relevance they have in the model results.

Figure 7.154 presents profiles of vertical displacement at different time steps. The moments at which the pore water pressure is applied at the sample base, collapse initiation and application of foundation load are marked in the figure. At the time step 11 a land lift is clearly observed next to the footing edge.
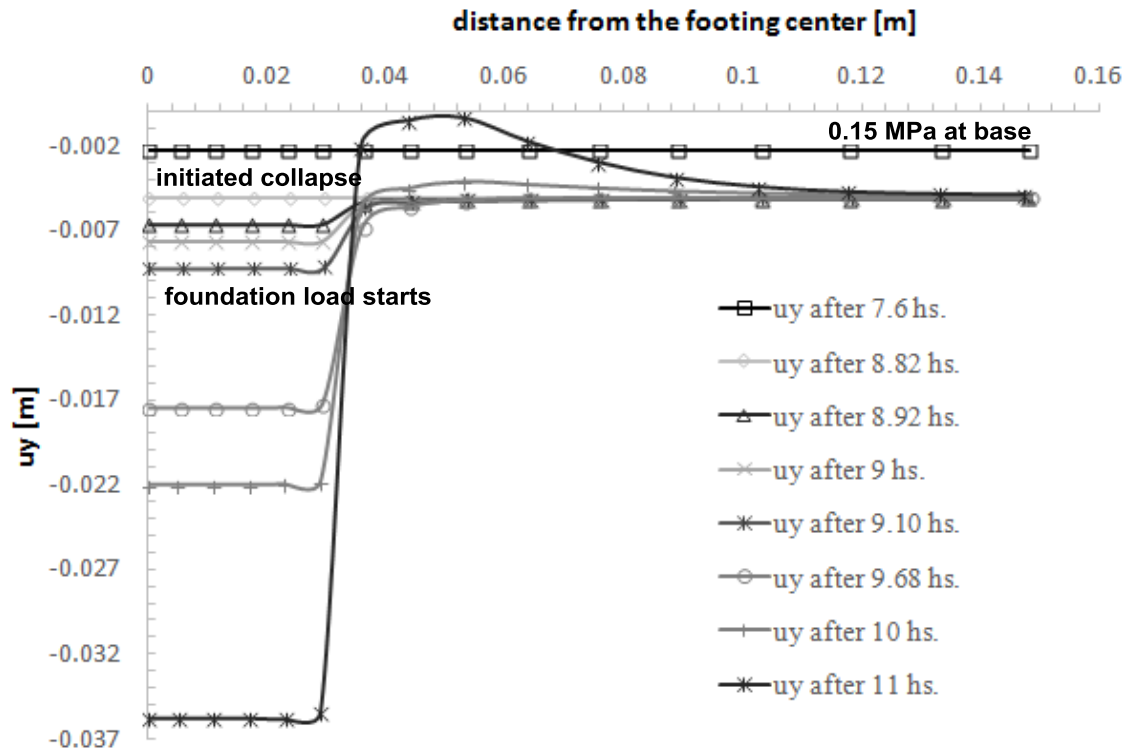
Figure 7.154: Profile of vertical displacements at a horizontal line just under the soil surface. A soil lift is observed next to the footing edge at time step 11.

Settlements below the foundation reach a value of 3.7cm at 100% of the applied load (4.5kPa) while soil surface experiences a lift close to the foundation. This pattern is typical of the punch-type failure generally associated to the response of loose material such as the one considered here $\gamma_d = 14 \, ^{kN}/_{m^3}$.

Figure 7.155 shows the stress paths completed by the model at different points in the vicinity of the foundation. Point P3, which is outside the influence zone, experiences small changes in shear and remains close to the original stress point.

Points P1,P2 and P4 which are located in the area of the load influence, experience a significant increase of the deviator as the stress evolves toward the critical state line.

The punching failure is thus the result of an initial contracting behavior followed by a small dilatancy in the last stage of loading which brings material to the critical state.
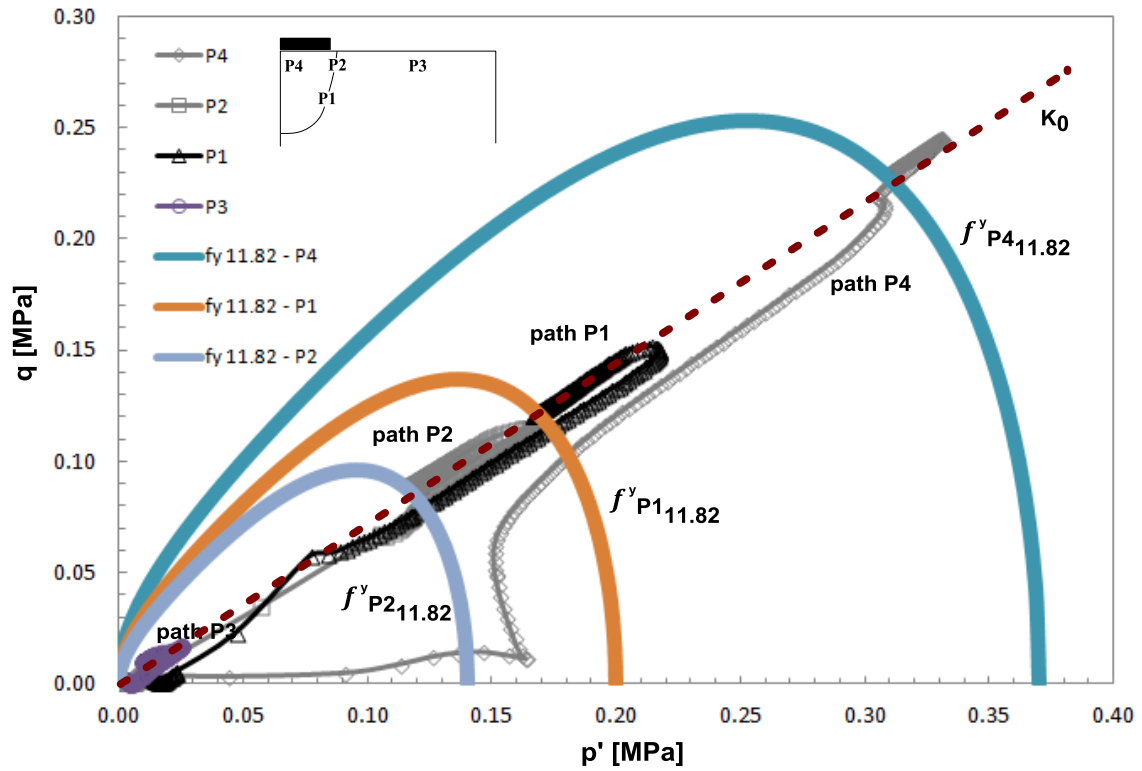
Figure 7.155: Computed stress path for four points in the vicinity of the foundation.

The corresponding shear strain - deviatoric stress curve is plotted in Fig. 7.156. A slight peak in the stress-strain is observed as a result of the late contracting behavior. The slight softening observed explains that no clear shear band develops in the failure mode.
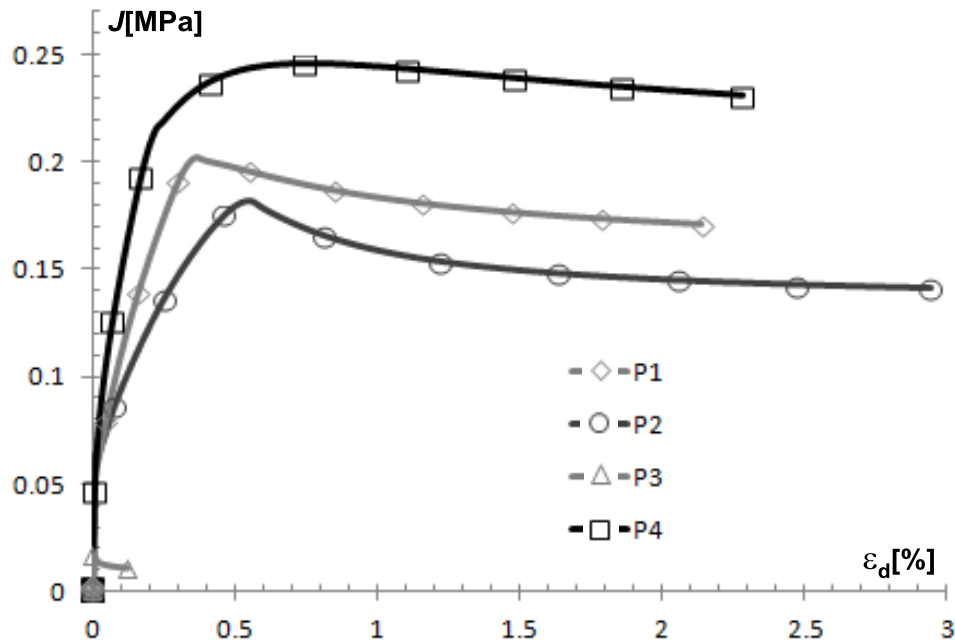
Figure 7.156: Deviatoric stress vs. Deviatoric strain, responses at four different points around the foundation.

7.5.5) Bearing Capacity

The bearing capacity of the shallow foundation can be evaluated following Terzaghi's proposal,

$$q_{\text{ult}} = \underbrace{\xi_c \cdot c(s) \cdot N_c}_{q_c} + q' \cdot Nq + \xi_\gamma \cdot \gamma \cdot \text{B} \cdot N_\gamma \tag{7.6}$$

where the shape factors for circular foundations take the values $\xi_c = 1.3$ and $\xi_\gamma = 0.3$, q' is the surcharge load, B is the radio of the foundation and γ is the specific weight of the porous medium. The cohesion *c(s)* is assumed to depend on the suction. This introduces a direct influence of the partially saturated condition on the bearing capacity of the foundation. The relation assumed is that presented by Alonso et. al. (2010),

$$c(s) = c_o + (S_r)^k \cdot s \tag{7.7}$$

where, (c_o) is the saturated cohesion, (S_r) is the degree of saturation, (s) is the suction and (k) is a material parameter. Thus, according to Potts (2001), it is possible to obtain the bearing capacity factors from numerical simulations where cohesion and soil weight are cancelled separately.

393

From equation 7.6 three cases are necessary for the determination of the bearing capacity factors by finite element method. These cases are the following:

a) weightless soil without surcharge for the determination of "Nc"
b) weightless and cohesionless soil for the determination of "Nq"
c) cohesionless soil without surcharge for the determination of "Nγ"

For the problem at hand only the cases (a) and (c) would be necessary to address due to the absence of surcharge load. Considering a weightless soil without surcharge the determination of the bearing capacity factor is obtained as $\left(N_c = \frac{q_{ult}}{\xi_c \cdot c} \right)$. Moreover, a closed-form exists to determine this capacity factor which in the case of a centered and vertical load on a circular foundation is given by:

$$N_c = \cot(\phi) \cdot \left[\exp(\pi \cdot \tan(\phi)) \cdot \tan^2 \left(\frac{\pi}{4} + \frac{\phi}{2} \right) - 1 \right] \qquad (7.8)$$

N_c is found to be equal to 34.98 using a friction angle of $\phi = 31.83°$.

N_c has been assessed by performing a new finite element simulation where the weight of the soil is cancelled at the beginning of the loading phase. Weight decrease has been done gradually to avoid numerical problems. Figure 7.157 shows the contour of the mobilized bearing capacity factor N_c. Assuming, for the new case as presented by Potts (2001) q_{ult} is the load of first yield, the computed bearing capacity factor for the weightless case is very close to the analytical value $N_c = 34.984$.

_____
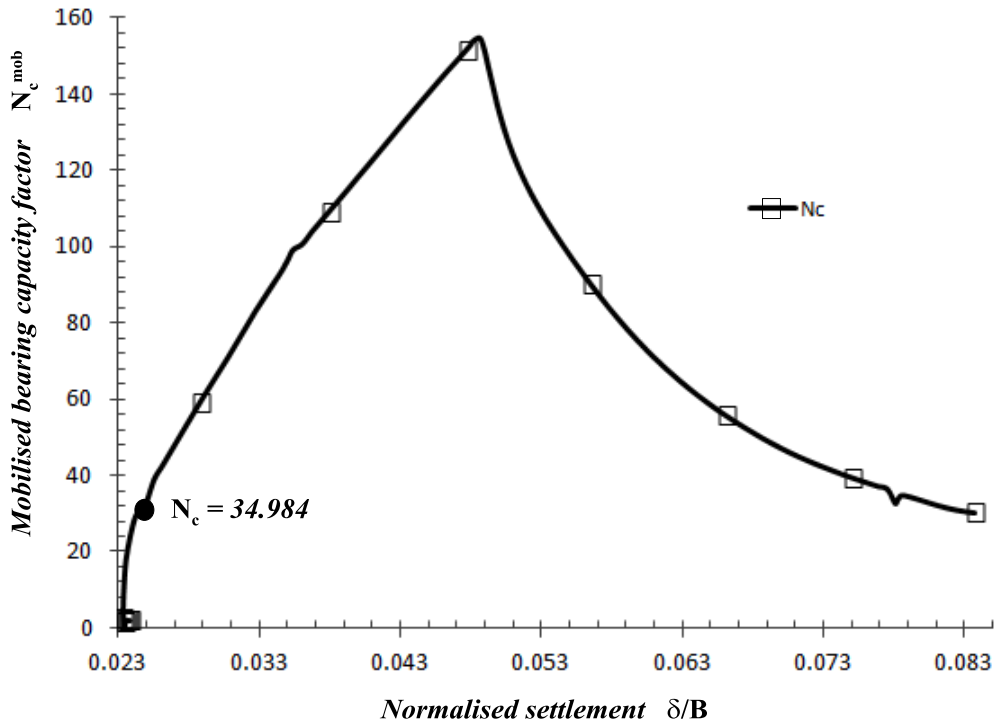
Figure 7.157: Mobilised bearing capacity factor vs Normalised settlement. Result from the numerical FEM model.

For the sake of illustration Fig. 7.158 shows a comparison of the plots $J - \varepsilon_q$ for both the simulation considering the self-weight and the simulations ignoring the self-weight.
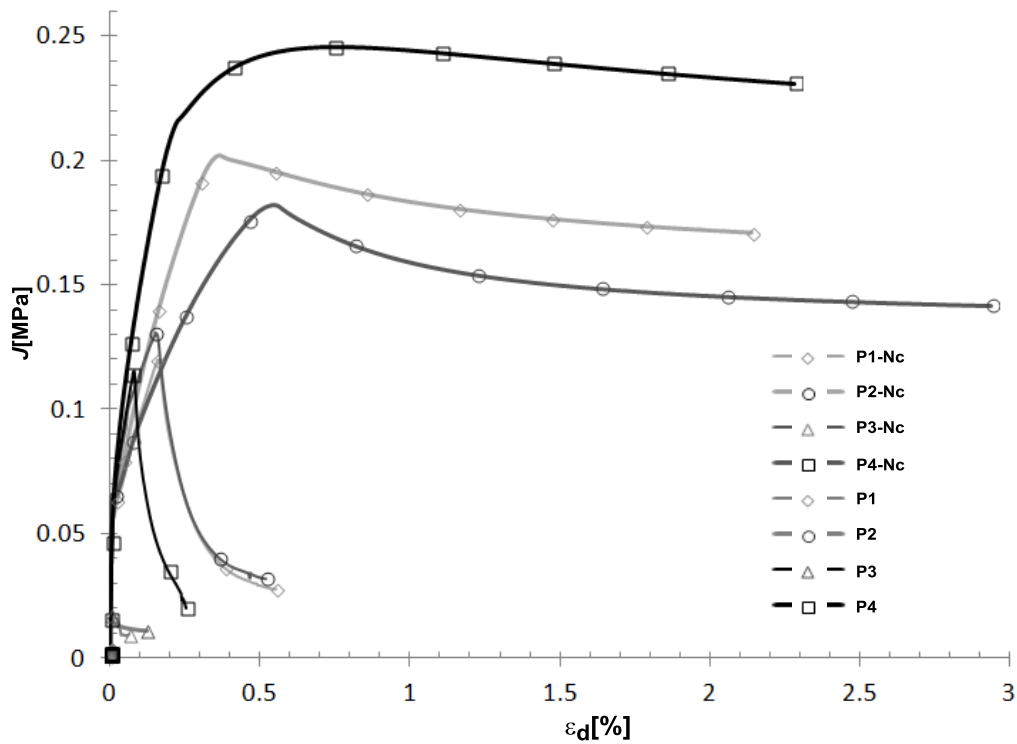
Figure 7.158: Deviatoric stress vs. Deviatoric strain, responses at four different points. Considering and ignoring the self-weight.

Determination of the bearing capacity factor N_γ can be then achieved by subtracting the results obtained in the weightless case from the full case. From Eq. 7.6 and under the previous considerations, N_γ can be determined as $\left(N_\gamma = \dfrac{(q_{ult} - q_c)}{\xi_\gamma \gamma B} \right)$. Figure 7.159 shows the computed mobilized bearing capacity factor N_γ obtained with the numerical computation.
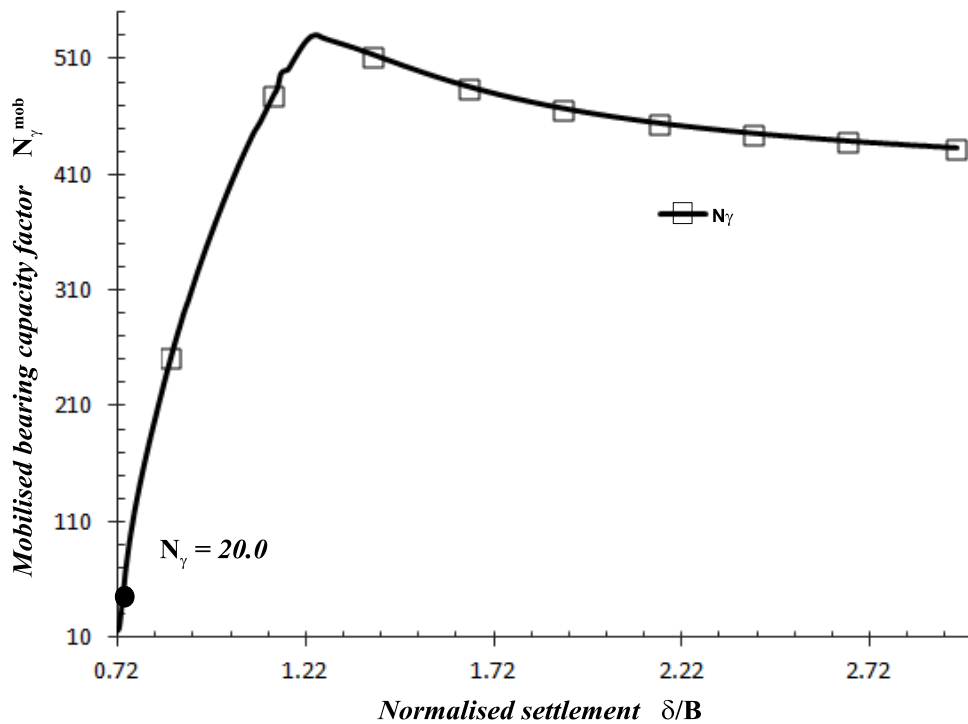
Figure 7.159: Mobilised bearing capacity factor vs. Normalised settlement. Result from the numerical FEM model.

with the same assumption as for N_c, N_γ is estimated as the point of first yield. The bearing capacity factor results to be $N_\gamma = 20$.

Finally, Fig. 7.160 presents the computed mobilized q as the average value of those obtained at points below the foundation, as a launch of settlement. Assuming again that q_{ult} is the value of the mobilized bearing capacity at first yield, a value of 0.06MPa is found.

_____
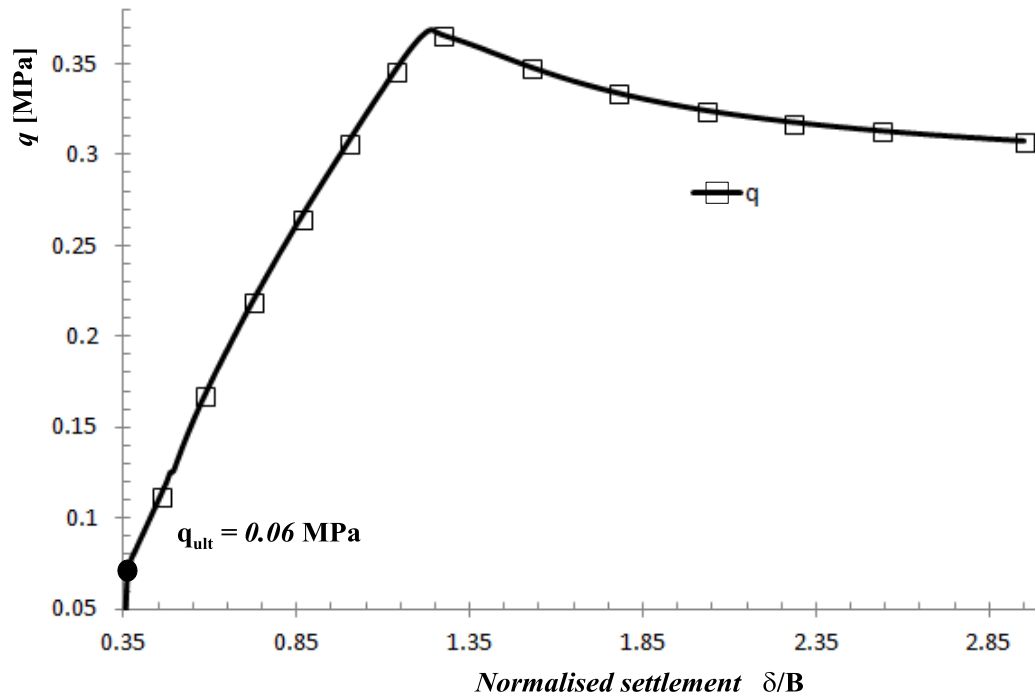
Figure 7.160: Mobilised deviatoric stress vs. Normalised settlement.

The previous study provided a value for the bearing capacity of the foundation equal to $q_{ult} = \sqrt{3}J \cong 0.06$ MPa. The same result can be obtained using Eq. 7.6, superposing the cohesion contribution and the self-weight contribution, and using the computed bearing capacity factors, Table 7.41.

Table 7.41: Bearing Capacity factors obtained from the finite element model.

N_c	N_γ
34.98	20

It can be concluded that the centrifuge test for the collapse of a shallow foundation has been conveniently simulated using the hyperporoplastic model BBM2 and the interior-point algorithm presented in chapters 4 and 5, respectively.

The model has the ability to reproduce the collapse by wetting of the sample as well as the soil response after the load application and provides value of bearing capacity comparable with the classical formula. It evidences moreover that failure pattern is closer to a punching failure rather than a shear band failure.

Further the effect of lode angle on the critical state has been addressed. The influence of the third invariant affects the shape of the yield surface BBM2 in the deviatoric plane, changing from (1) Drucker Prager shape (no Lode) to (2) smoothed Mohr Coulomb by van Eekelen proposal.

The influence is shown by comparing both: (a) the vertical strain / vertical stress curve and (b) the deviatoric stress / deviatoric strain curve, Fig. 7.161. The followed stress path shows a compressive response and keeps following this trend. As consequence negligible differences are given by the Lode consideration.
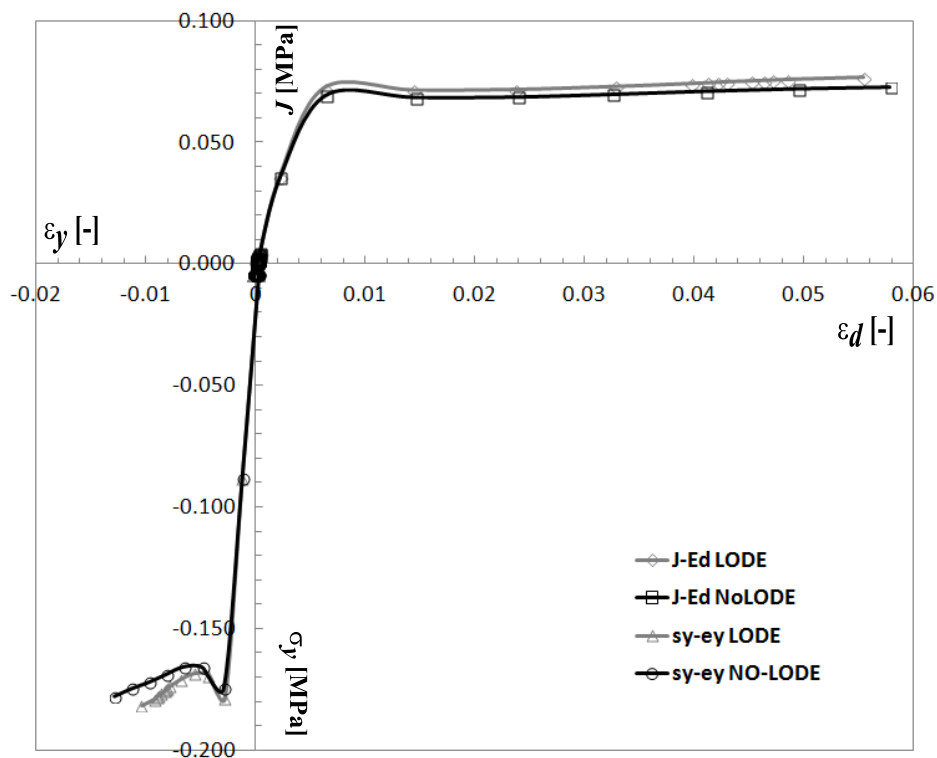
Figure 7.161: Comparison at the centrifuge model's response for both load angle influence and without its influence at the hyper-plastic model.

Figures 7.162 and 7.163 show isochrones of plastic multiplier and deviatoric strain at the time of a 3% of the applied load. The similarity of both isochrones values confirms the negligible influence of the Lode angle in this case, due to the stress path exerted by the sample under the applied loads at (a) wetting stage and (b) loading stage.
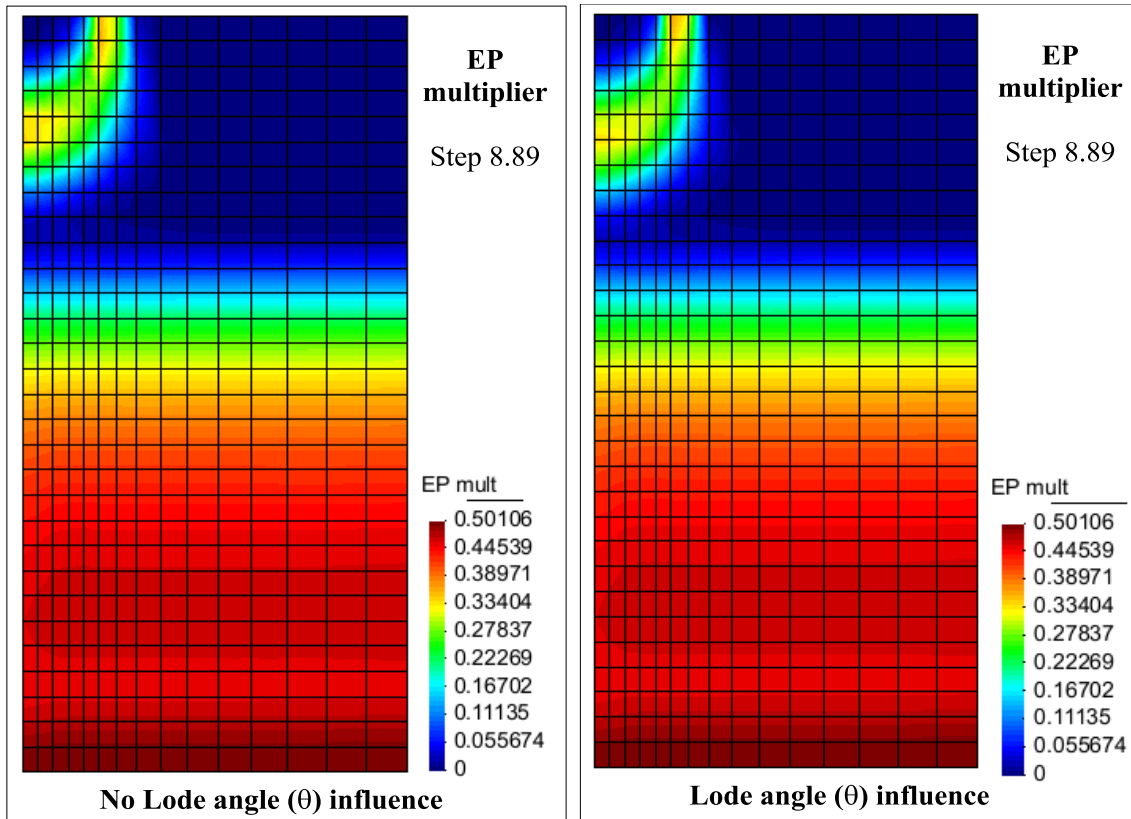
Figure 7.162: Influence of the Lode Angle in the Model Response. Contours of plastic multiplier at time step 8.89.
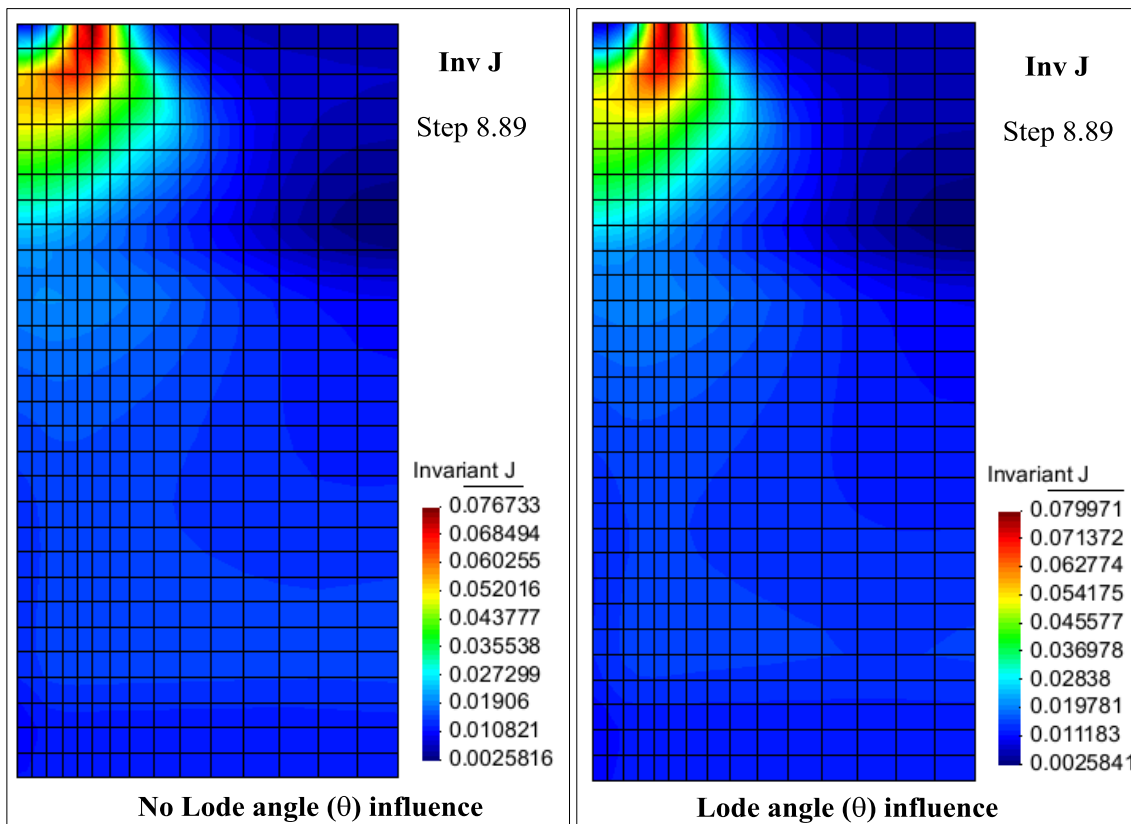
Figure 7.163: Influence of the Lode Angle in the Model. Contours of deviatoric invariant at time step 8.89.

7.6)   Field Bearing Capacity

In this subsection, the field bearing capacity is evaluated by bringing the foundation up to the failure under real atmospheric conditions. To this end, a typical meteorological record from the central part of Catalonia has been used.

The study has been performed at *prototype* scale to avoid scaling of the atmospheric quantities. The initial configuration is a scaled configuration of the centrifuge model at the end of the wetting collapse stage and before the loading stage. The numerical bearing capacity test has been carried out on the soil after two years of atmospheric "climatic" load to represent real conditions.

7.6.1)   Equations solved

The numerical problem is addressed by solving the equations of water mass balance and stress equilibrium stated in subsection 7.5.1, in addition to the equation of energy balance, given by:

$$\frac{\partial}{\partial t}\left(E_s\rho_s \cdot (1-\phi) + E_l\rho_l S_l\phi + E_g\rho_g S_g\phi\right) + \nabla \cdot \left(i_c + j_{E_s} + j_{E_l} + j_{E_g}\right) + \left(f^Q\right) = 0 \quad (7.9)$$

where E_s, E_l and E_g are the specific energies of porous skeleton, liquid and gas phases respectively, i_c is the heat flux vector of the porous medium and j_{E_s}, j_{E_l} and $j_{E_{gl}}$ are the energy fluxes of the porous skeleton, the liquid phase and the gas phase, respectively.

It is noted that gas pressure is considered constant in the problem (infinite mobile gas). The three equations are discretized by a finite element scheme and solved simultaneously by using the finite element code Code_Bright, Olivella et.al. (1996).

7.6.2)   Geometry, Mesh, Initial and Boundary conditions
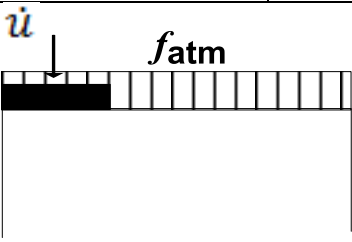
The model is an axisymmetric slice of 0.15m width and 0.30m high, see Table 7.42. The mesh of the model consists of 450 quadrilateral elements (with linear interpolation) and 496 nodes.

Model is composed by two intervals: one for equilibrating temperature and water pressure under the application of atmospheric load and other for application of the

foundation up to failure. During this period the atmospheric load is also acting at the soil surface.

The following boundary conditions have been applied during the test: (a) null water flux and thermal flux at the lateral boundaries and (b) liquid pressure and temperature at the bottom boundary. As for the mechanical condition, both null vertical displacements and horizontal displacements have been imposed at bottom and lateral boundaries, respectively. A rate of vertical displacement has been applied at a part of the top boundary corresponding with the foundation.

Table 7.42: Boundary conditions, Load configuration, Geometry and Mesh used in the modeling.

	Interval	Boundary Conditions	
Interval and Boundary Conditions	**1** Foundation load 0-20 [days]	*Lower boundary*: $u_y = 0$ $p_l = 0.15\,\text{MPa}$ $T = 15.4\,°\text{C}$	*On top of foundation*: $\dot{u}_y = 0.0048\ {}^{\text{mm}}/_{\text{min}}$ atmospheric load *On free soil surface*: atmospheric load (root_atm.dat)
Load Configuration			
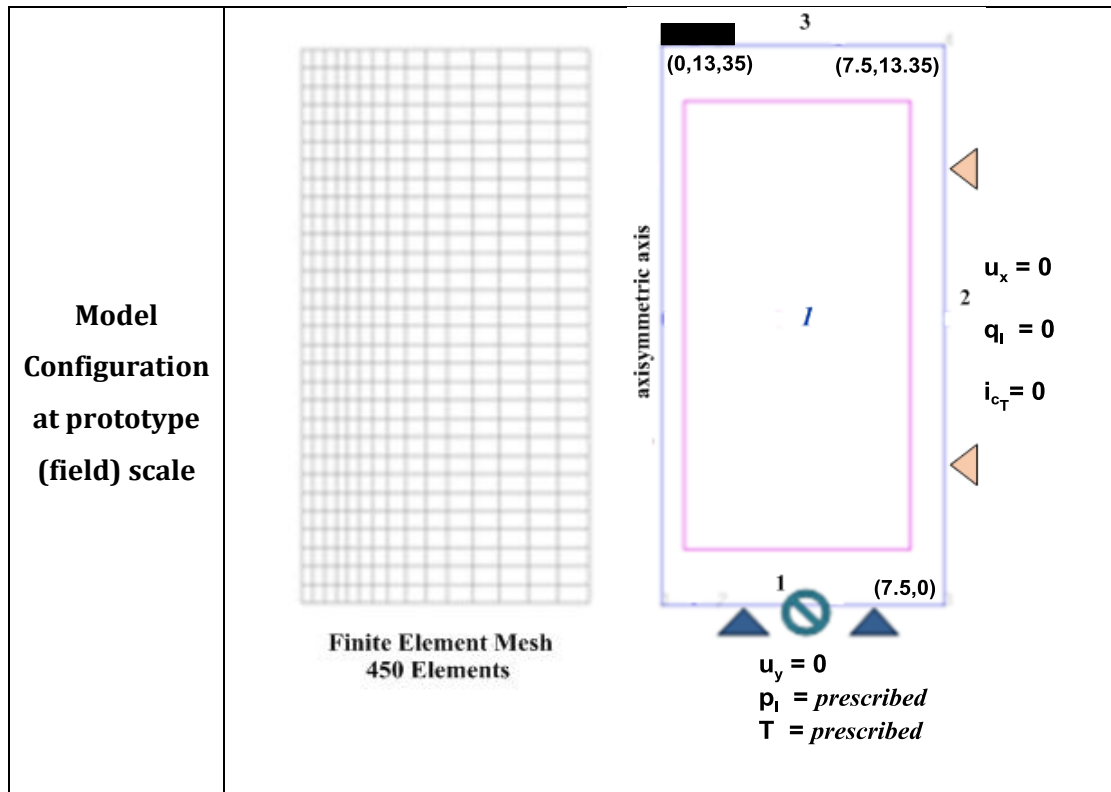
Before application of foundation load, the system has been left equilibrated under the application of the atmospheric condition in order to reach stationary conditions. Initial conditions are those obtained from the centrifuge Test F2-(scaled model) at the time step 8.82hs., which corresponds to the time just before the foundation load application. Fig. 7.164 shows a profile of the initial values considered for the thermo-hydro-mechanical variables.
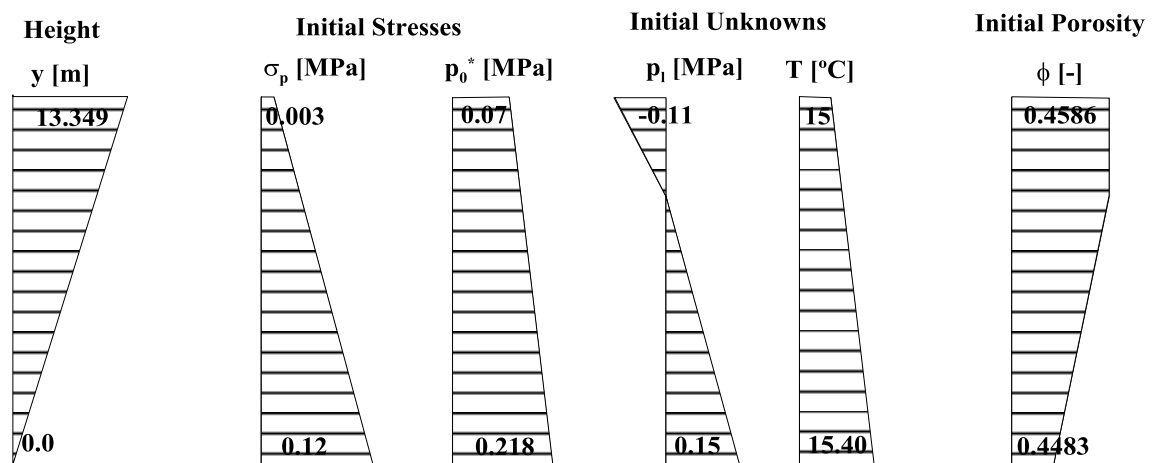
Figure 7.164: Profile of initial values of geotechnical variables for the prototype model.

Foundation is considered permeable and flexible which may corresponds to the limit case of a "deficient" construction practice (poor water-cement ratio, no compaction and bad curing).

7.6.3) Material Parameters

The material parameters used in the modeling are those summarized in Tables 7.43 and 7.44.

Table 7.43: Mechanical material parameters used in the numerical model

MECHANICAL DATA		
hyper-thermoplastic model		
Elastic Parameters		
κ	0.005	
ν	0.3	$g_s = \dfrac{\left(1 - \beta_s(\alpha_T)\right)}{p_o^{1-n} \cdot k(1-n)(2-n)}$
n	0.9	
		$\cdot \left(p'^2 \right.$
Thermal Parameters		
$\alpha_T \left[\dfrac{1}{°C}\right]$	3e-6	
T_0 [°C]	$\equiv T_{initial}$ at the corresponding point	$+ \left. \dfrac{k(1-n)}{3\varrho} q^2 \right)^{\frac{2-n}{2}}$
Plastic Parameters		$- \dfrac{p'\left(1 - \beta_s(\alpha_T)\right)}{k(1-n)}$
p_0^* [MPa]	0.07	$- \left(p'\alpha_p + q\alpha_q \right)$
ϕ [°]	31	
N	1.65	
λ	0.07	
a	0.0048	
b	3.4	
ξ_1, ξ_2	10, 3	$f^y = x_p'^2 + \dfrac{x_q'^2}{M^2 B(\epsilon)^2}$
p_{at}	1E-10	
$c_T \left[\dfrac{1}{°C}\right]$	2.46e-3	$- w(\xi)^2 \cdot \left(\dfrac{p_c^*}{2}\right)^{2b(\xi)} \left(1 \right.$
η [−]	1e-3	
Shape Parameters		
ϵ[−]	0.5	$\left. - c_T \ln\left(\dfrac{T}{T_o}\right)\right)$
Integration Parameters		
Algorithm index	3 (interior point algorithm)	
Newton tolerance	1E-6	
Line_search param. 1	1E-2	
Line_search param. 2	0.1	
Max. iter. barrier	1	
Max. iter. Newton	30	
Max. Line_search iter.	5	

_____

Table 7.44: Hydraulic and Thermal parameters used in the numerical model

HYDRAULIC AND THERMAL DATA		
Retention Curve (simpl. van Genuchten)		
$p_0 [MPa]$	0.013	
λ	0.52	$S_r = \left(1 + \dfrac{s}{p_0}\right)^{-\lambda}$
S_{rl}	0.38	
Intrinsic Permeability (Kozeny's model)		
$k_{ii} [m^2]$	2.85E-14	
ϕ_0	0.4583	$k = k_0 \dfrac{\phi^3}{(1-\phi)^2} \dfrac{(1-\phi_0)^2}{\phi_0^3}$
Liquid Phase Rel. Permeability (van Genuchten law)		
λ	0.52	$k_{rl} = \sqrt{S_r}\left(1 + \dfrac{s}{p_0}\right)^{-\lambda}$
Diffusive flux of Vapor (Fick's law)		
$D \left[\dfrac{m^2 P_a}{s K^n}\right]$	5.9E-10	
N	2.3	$i_\alpha^i = -(\tau \phi \rho_\alpha S_\alpha D(T)I)\nabla\omega_\alpha^i$
τ_0	1.0	
Conductive Flux of Heat (Fourier's law)		
$\lambda_{dry} [WmK^{-1}]$	1.48	
$\lambda_{sat} [WmK^{-1}]$	2.0	$\boldsymbol{i}_c = -\lambda\nabla T$
PHASE DATA		
Solid Phase (Density)		
$C_s [Jk_g^{-1}K^{-1}]$	1000	
$\alpha_T \left[\dfrac{1}{°C}\right]$	3e-6	
$\rho_s [k_g m^{-3}]$	2700	

7.6.4)   Modeling Results

Figures 7.165a, 7.165b and 7.165c show the evolution of temperature, liquid pressure and horizontal stress under the action of the atmospheric load at the pre-load stage.

Figures 7.161d, 7.161e and 7.161f show the profile of liquid pressure and horizontal stress before the start of the foundation load and Fig. 7.161g show profiles of temperature computed under the atmospheric load at the pre-load stage. The evolution of horizontal stress evidences an increase of deviatoric stress due to deformations related to the soil atmosphere condition which leads to a different stress state at the beginning of the load with respect to the centrifuge stress state at this time.
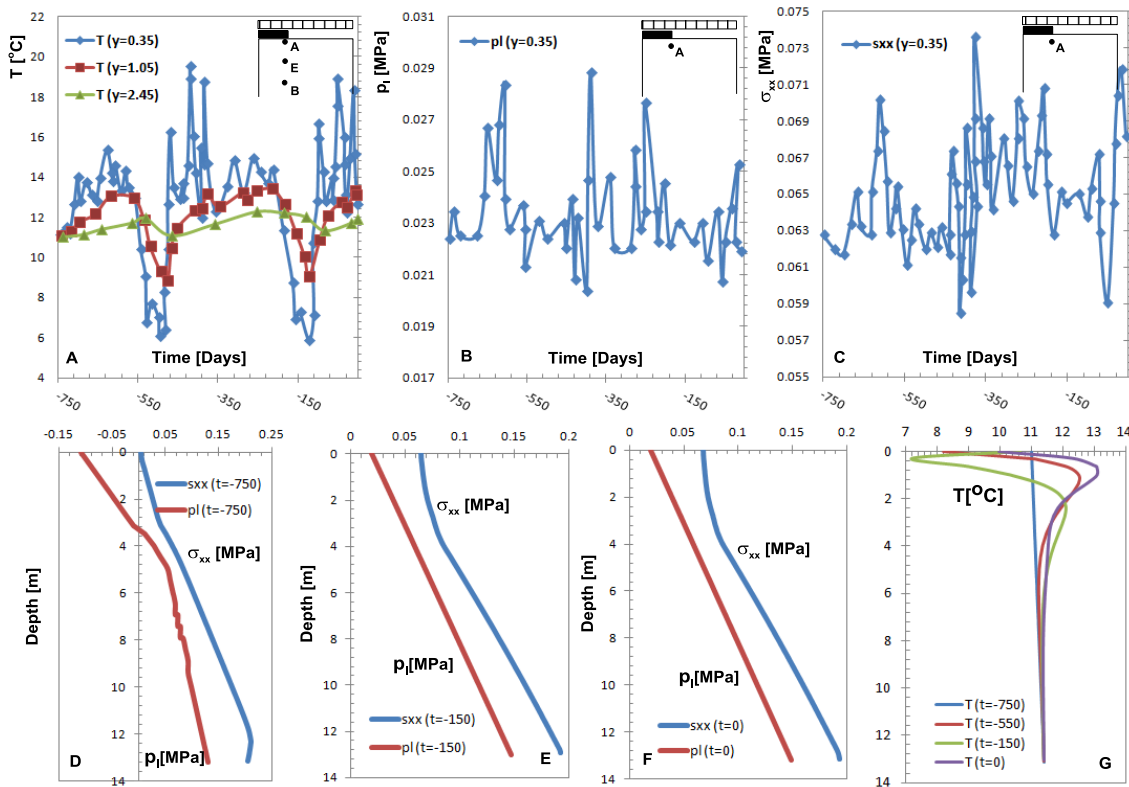
Figure 7.165: Evolutions of Temperature, liquid pressure and horizontal stress at the pre-load stage. Profiles of liquid pressure, horizontal stress and temperature in different times at the pre-load stage.

Displacements are presented along two profiles located at horizontal coordinate *x*=0.6m and horizontal coordinate *x*=1.5m, Fig. 7.166.
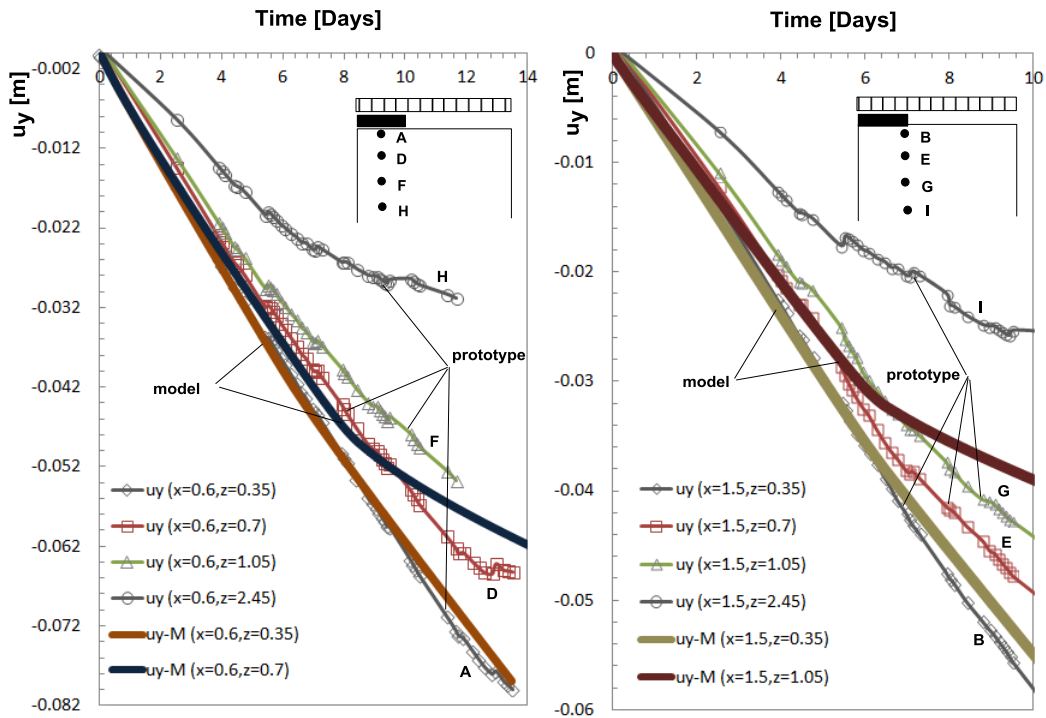
Figure 7.166: (A) Evolution of displacements at three points centered under the foundation, after the foundation load application. (B) Evolution of displacements at three corner points under the foundation, after the foundation load application.

Figure 7.166 evidences that the responses obtained for the prototype and the model at points z=0.35m and z=0.7m present discrepancies. It will be shown that the different responses are due to the different initial states of stress existing between the model and the prototype at time of foundation loading.

They particularly show that displacements at the prototype and the model tend to stabilize at a certain time coinciding with the fact of having reached the maximum (failure) load.

Figure 7.167a shows the load-displacement curve obtained at the prototype (field scale) and its comparison with the corresponding curve obtained at the model "Test-F2". The same discrepancy can be observed between the prototype and the model.

Figure 7.167b shows profiles of vertical displacements taken at different times during foundation load and computed at a horizontal section near the column surface. Those profiles are compared with the corresponding profiles obtained at the model "Test-F2".

An important soil surface lift can be observed close to the foundation in the prototype modeling which is inexistent in the model. This fact will also be further explained by

material dilatancy due to a different initial stress state and saturation condition at time of loading.
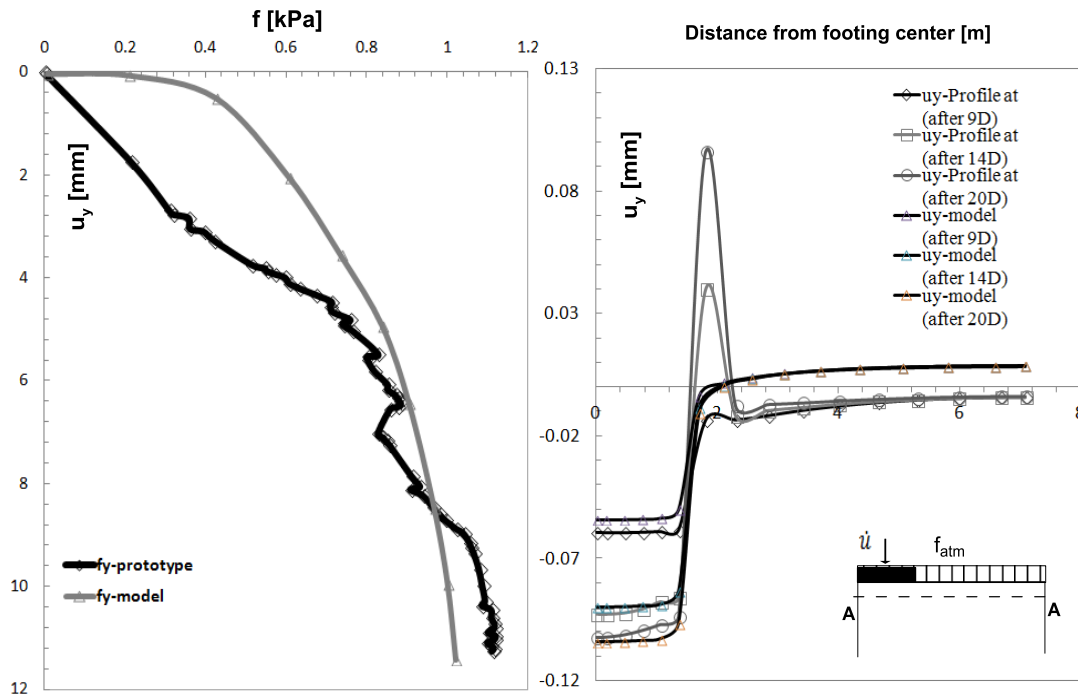
Figure 7.167: Load displacement curve due to foundation action in addition to the atmospheric load at the column surface. Comparison between both the centrifuge model (without atmospheric load) and the prototype responses.

The load-displacement curve for the prototype and the Test F2 evidence a good concordance although the prototype exhibit a lower stiffness in the early stage of loading. This is due to different initial stress state and saturation conditions between the prototype and the model at the time of foundation load initiation.

Fig. 7.168 presents a comparison between deviatoric strain / deviatoric stress curves in three different points under the foundation obtained for the prototype and the Test F2.
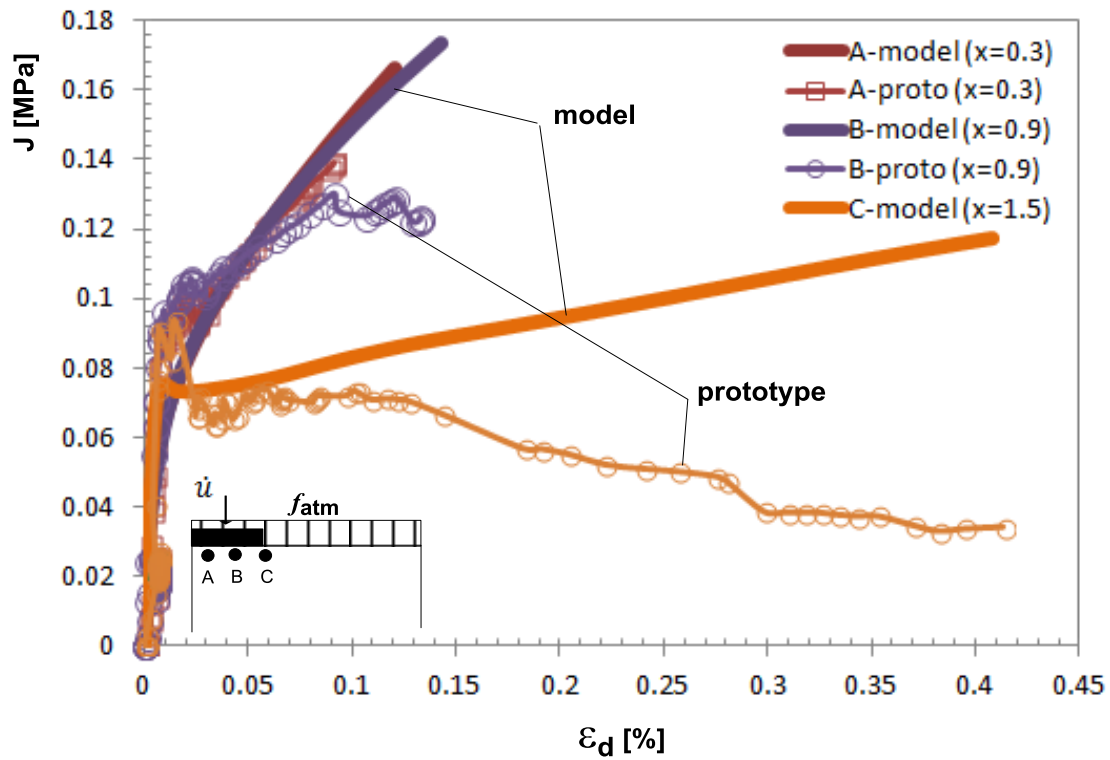
Figure 7.168: Deviatoric stress vs. Deviatoric strain responses at three different points of the upper soil layer of the Silty column, for both: (a) the prototype (field scale) and (b) the Test F2 (laboratory scale).

A good concordance is observed in the curves for low values of deviatoric strains. However softening is observed for strain values below 0.1% in the prototype while it occurs later in the model, see Fig. 7.156. Such a response is emphasized at point c in the foundation boundary.

Fig. 7.169 shows curves deviatoric strain / deviatoric stress at different points of the soil under the foundation.
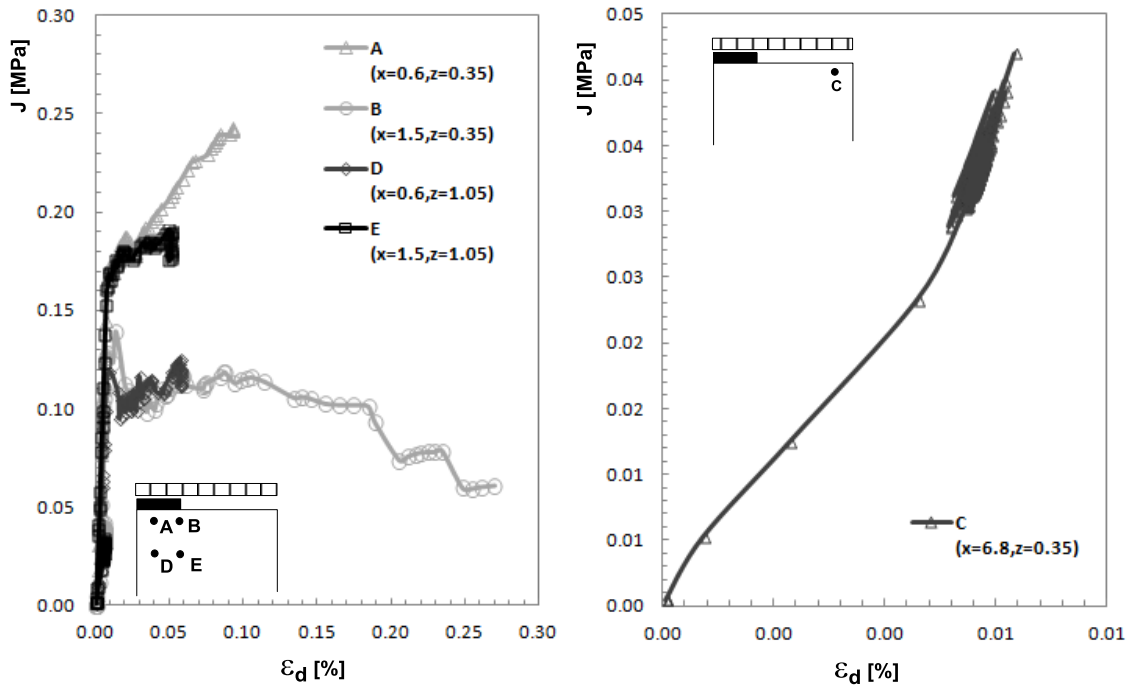
Figure 7.169: (A) Deviatoric stress vs. Deviatoric strain responses at three different points of the upper soil layer of the Silty column. (B) Deviatoric stress vs. Deviatoric strain responses at four different points under the shallow foundation.

In all cases an initial elastic branch is observed followed by a plastic branch evidenced by the sudden increase of strain rate with respect to the stress variations. Points B and D soften earlier than points A and E due to the higher shear stresses observed in those points.

Fig. 7.170 shows stress paths obtained at different points located close to the surface and surrounding the foundation, the corresponding yield surfaces at the end of the loading process are also shown.
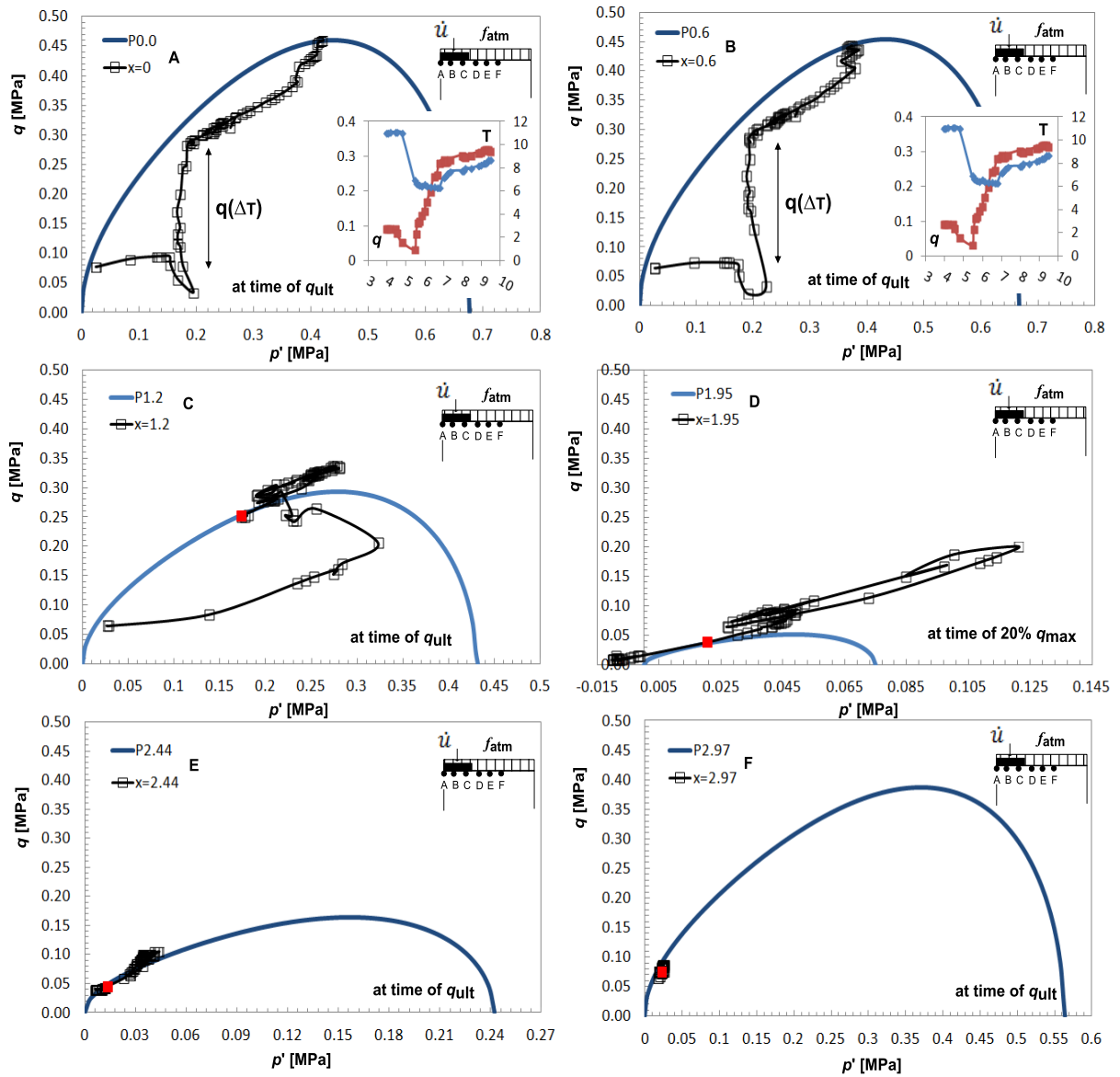
Figure 7.170: Stress path followed at different points located under and next to the foundation's load action.

The points located below the foundation: A, B and C, experience higher level of stress and reach the yield surface near the critical state but always at the dilatant side. At those points a perturbation of the stress-path is observable as consequence of a marked decrease of temperature as foundation load progresses.

The higher softening responses occur in the zone of soil next to the footing edge, points D and E. This zone experiences high shear stresses. As we move away from the area of foundation influence the stress level decreases and stress states reach the yield surface at values of $p' \approx 0.01 MPa$.

Figures 7.171 to 7.179 show isochrones of several thermo-hydro-mechanical variables.

Fig. 7.171 presents isochrones of liquid pressure, temperature, vertical displacements and hardening parameter P_{0_s} experimented by the soil column at 9, 14 and 20 days after the foundation load onset.
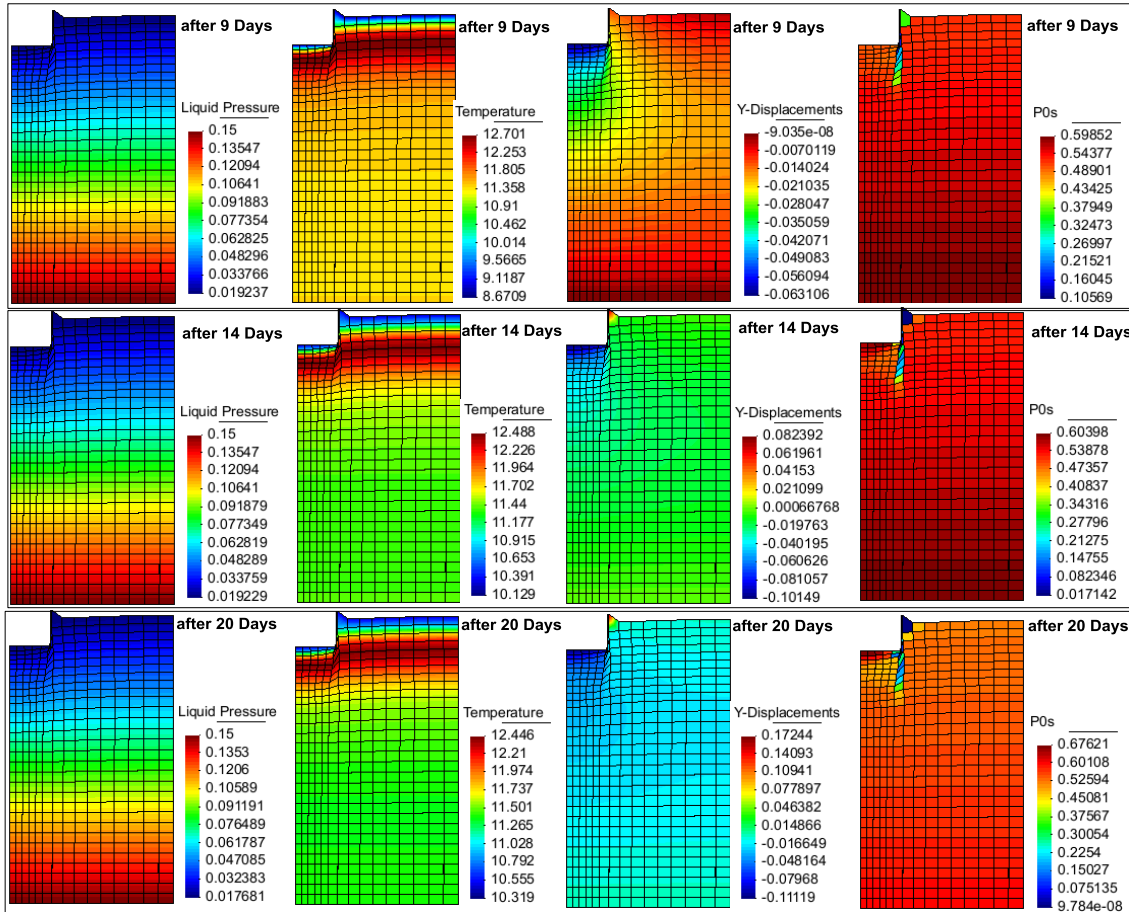
Figure 7.171: Contours of environmental variables, vertical displacements and hardening parameter P_0^* after the foundation's load application. (a) after 9 days of load's application, (b) after 14 days of load's application and (c) after 20 days of load's application.

It can be observed that changes of liquid pressure and temperature are relatively low during the loading process. Thus the process can be analyzed from a mechanical point of view. Leading to consider the bearing capacity obtained by the model as representative of the silty soil in its initial thermo-hydro-mechanical state.

Fig. 7.172 shows the distribution of volumetric strain and mean stress. It evidences a concentration of stress in the zone located below the foundation. This is confirmed by pattern of deviatoric strain and deviatoric stress shown in Fig. 7.173, which shows the development of a near vertical narrow shear band below the corner of the foundation. As

_____

shown in Fig. 7.174 and 7.175 which depict isochrones of plastic strain, plastic multiplier and hardening parameter p0s, the shear bands delimit a plastic zone essentially located below the foundation, indicating a punch-like failure type mechanism.

Fig. 7.172 shows isochrones of volumetric strain, mean stress and liquid pressure exerted in the soil column at 9, 14 and 20 days after the foundation load onset.
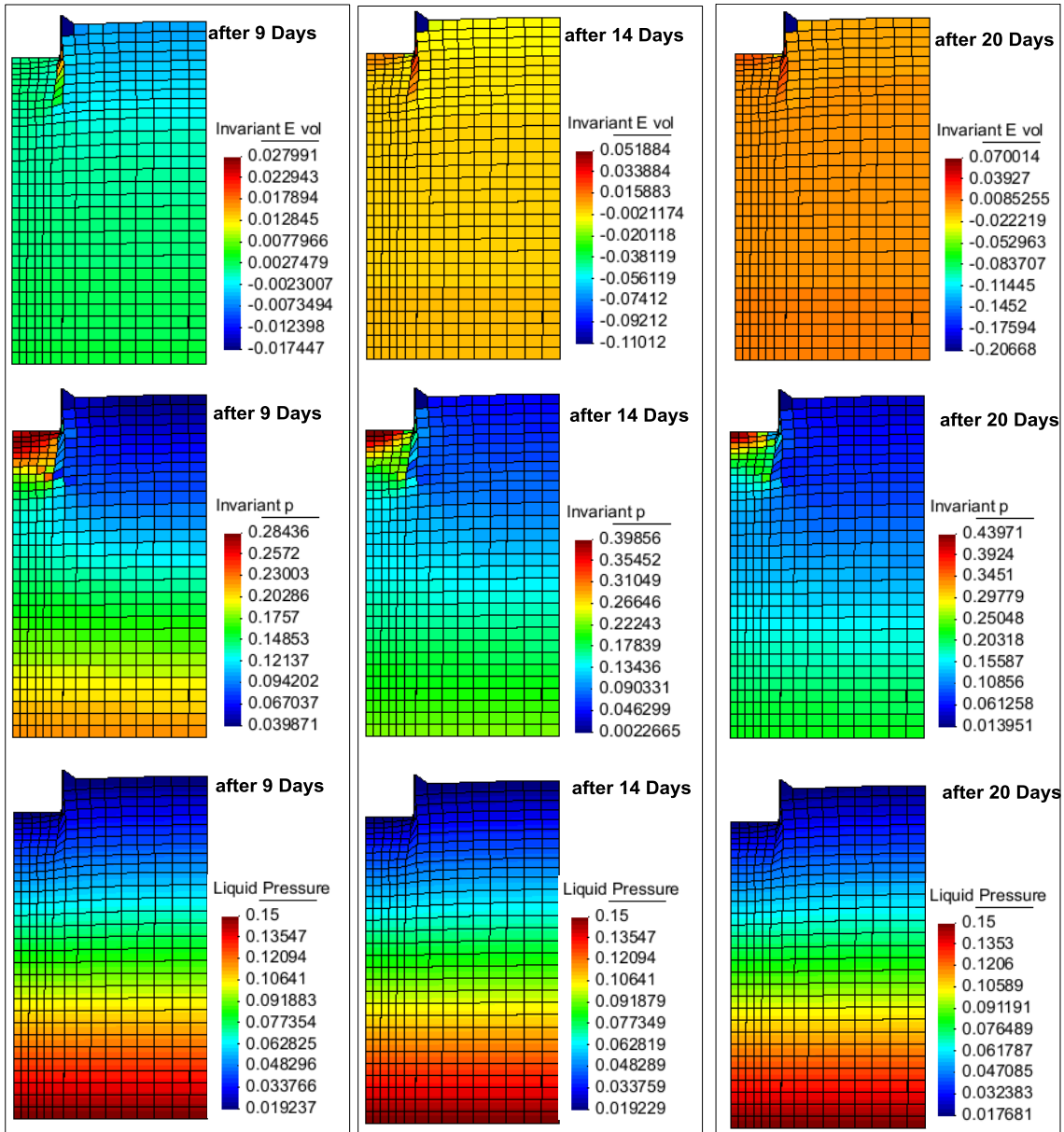
Figure 7.172: Contours of mean strain invariant, mean stress invariants and liquid pressure at three different times after the foundation's load application. (a) after 9 days of load's application, (b) after 14 days of load's application and (c) after 20 days of load's application.

They appear to be only slightly affected by the atmospheric fluxes acting at the soil surface. This fact evidences the quick dissipation on pore-pressure perturbations due to

atmospheric input in presence of a bottom boundary condition that maintains ground water level on surface.

Fig. 7.173 shows isochrones of deviatoric strains, deviatoric stress and porosity experimented by the soil column at 9, 14 and 20 days after the foundation load onset.
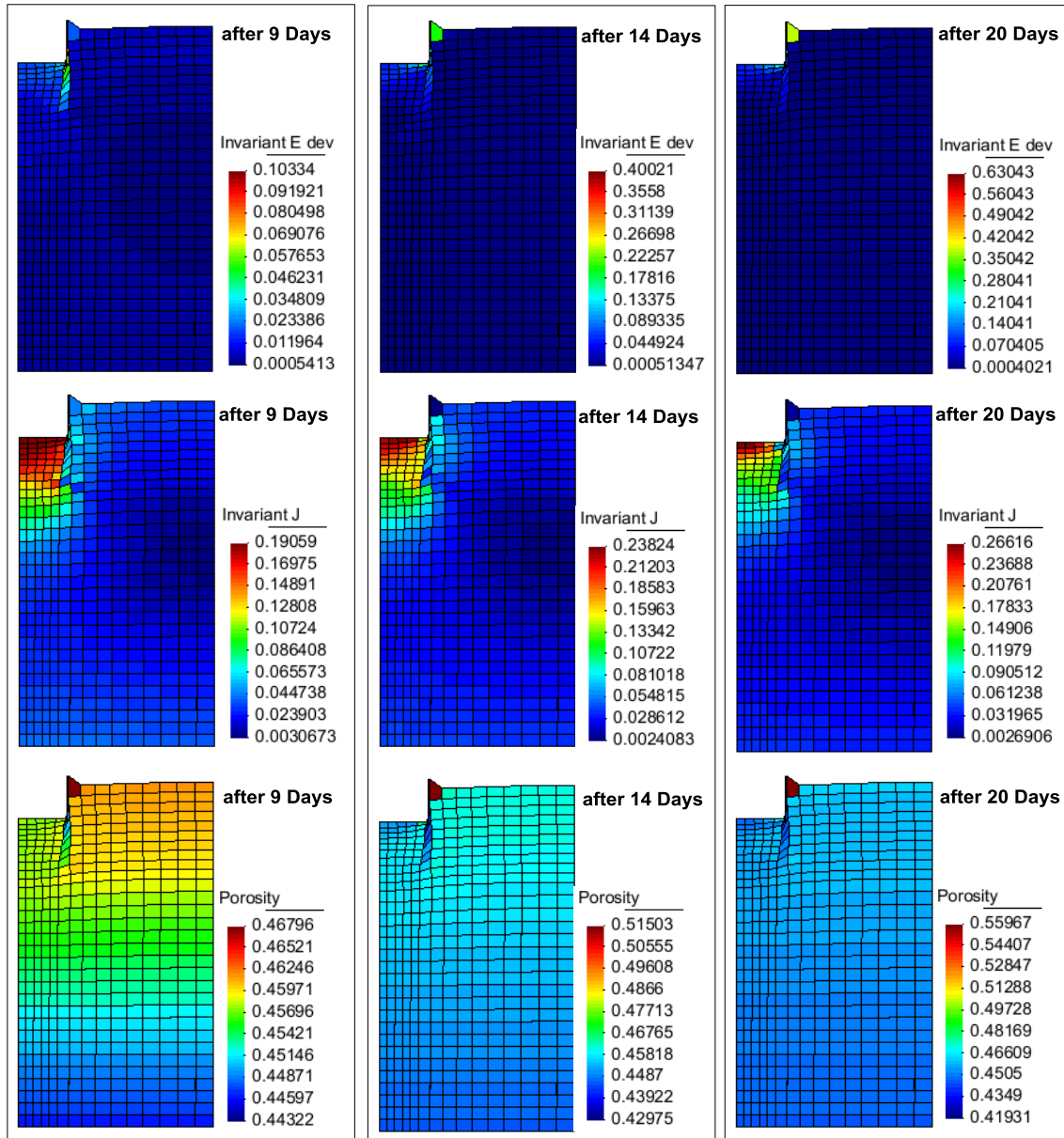
Figure 7.173: Contours of deviatoric strain invariant, deviatoric stress invariants and porosity at three different times after the foundation's load application. (a) after 9 days of load's application, (b) after 14 days of load's application and (c) after 20 days of load's application.

Fig. 7.174 shows isochrones of horizontal, vertical and shear plastic strains obtained in the soil column at 9, 14 and 20 days after foundation load onset.
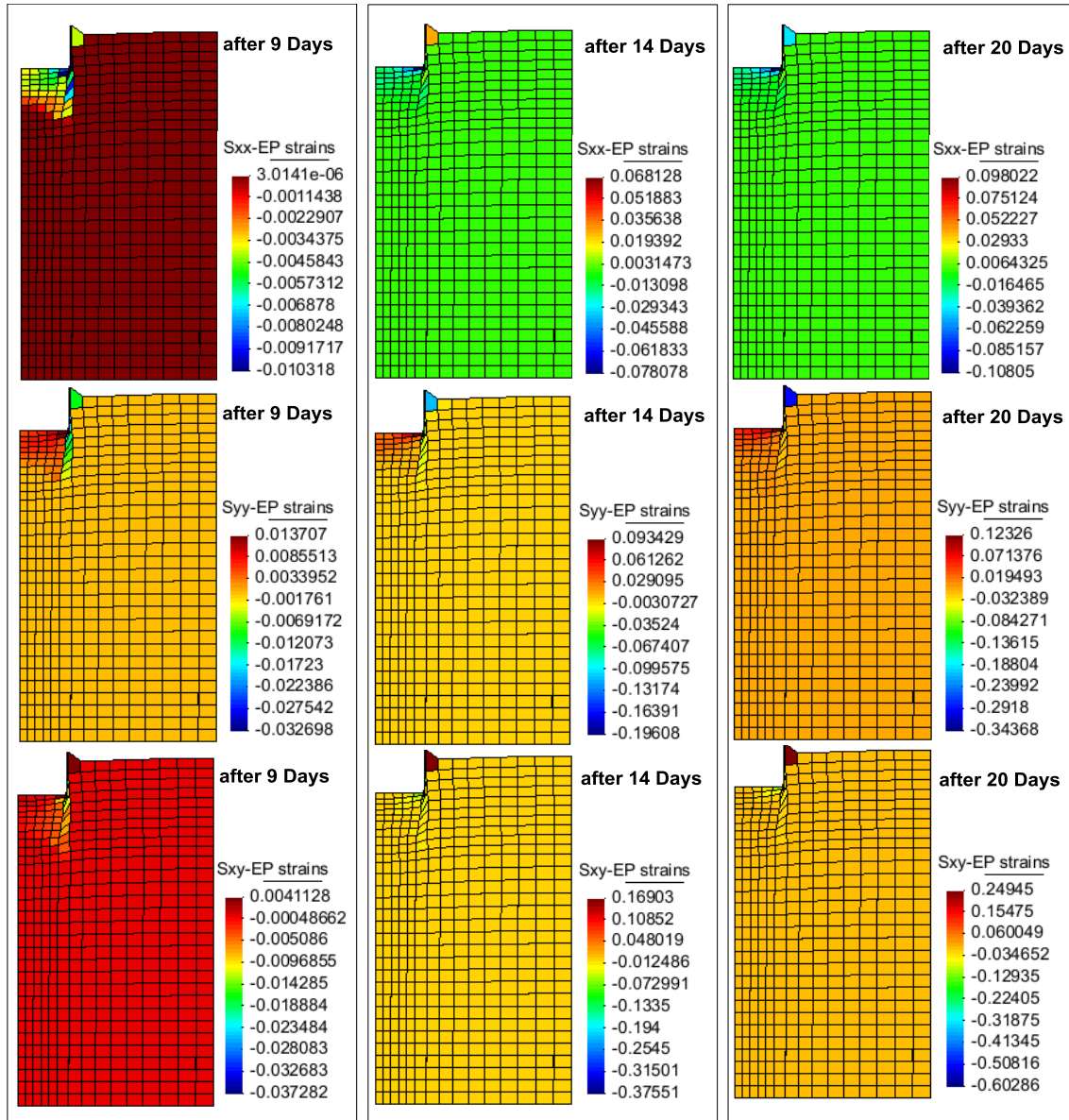
Figure 7.174: Contours of plastic strains ε_{xx}^p, ε_{yy}^p and ε_{xy}^p at three different times after the foundation's load application. (a) after 9 days of load's application, (b) after 14 days of load's application and (c) after 20 days of load's application.

Fig. 7.175 shows isochrones of plastic multiplier and hardening parameter exerted in the soil column at three different times after the onset of foundation load application.
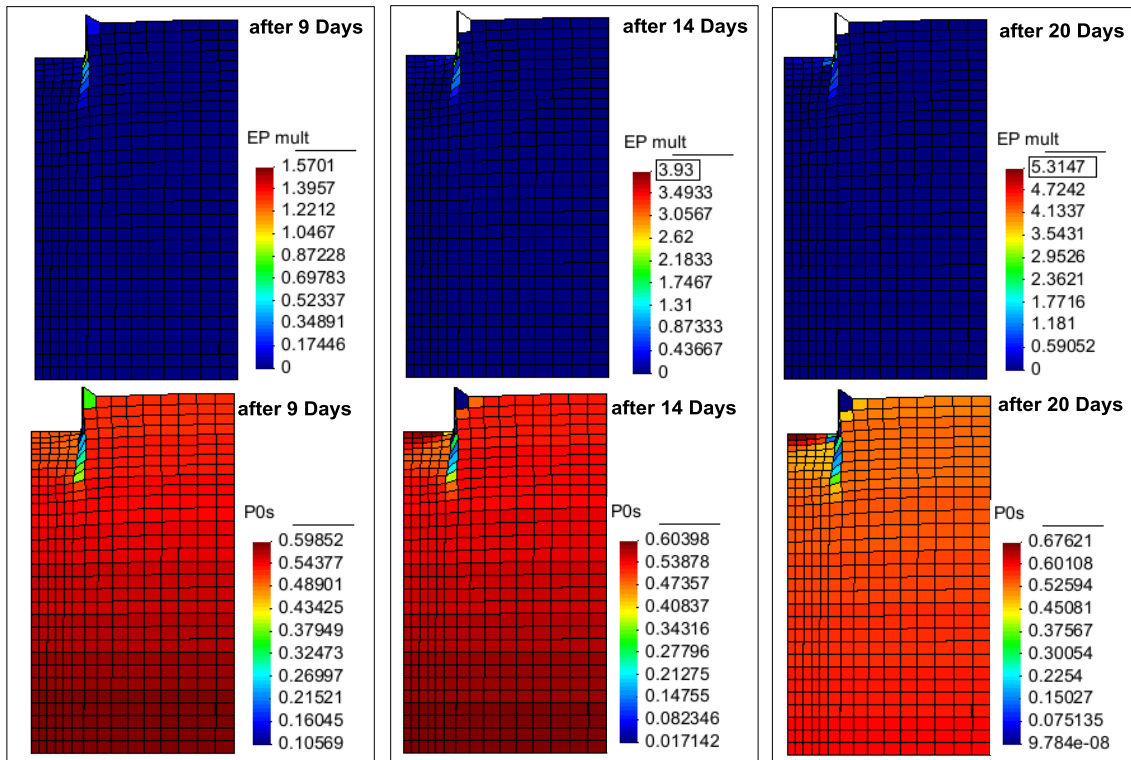
Figure 7.175: Contours of plastic multiplier and hardening parameter P_0^* after the foundation's load application. (a) after 9 days of load's application, (b) after 14 days of load's application and (c) after 20 days of load's application.

Figs. 7.176 to 7.178, show the pattern of strain and stress corresponding with the mechanism discussed above. Isochrones are taken after: (a) 9 days, (b) 14 days and (c) 20 days after load initiation.
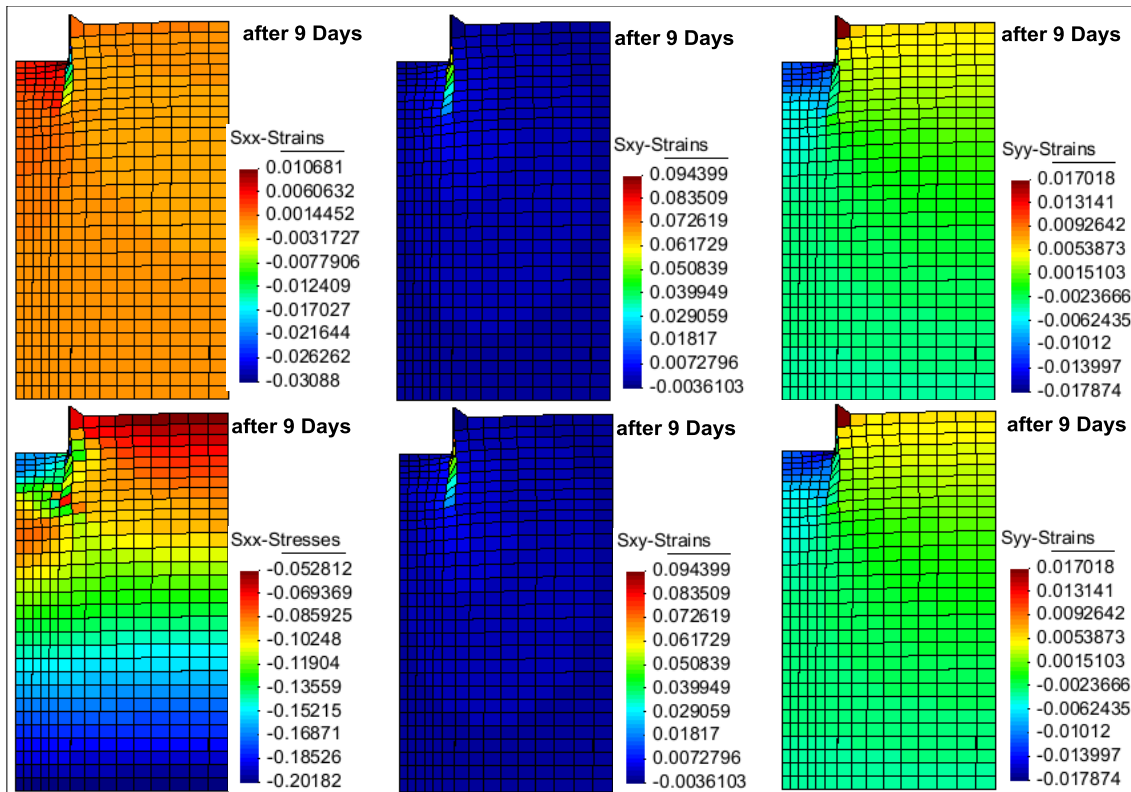
Figure 7.176: Contours of strains and stresses after 9 days of foundation's load application.
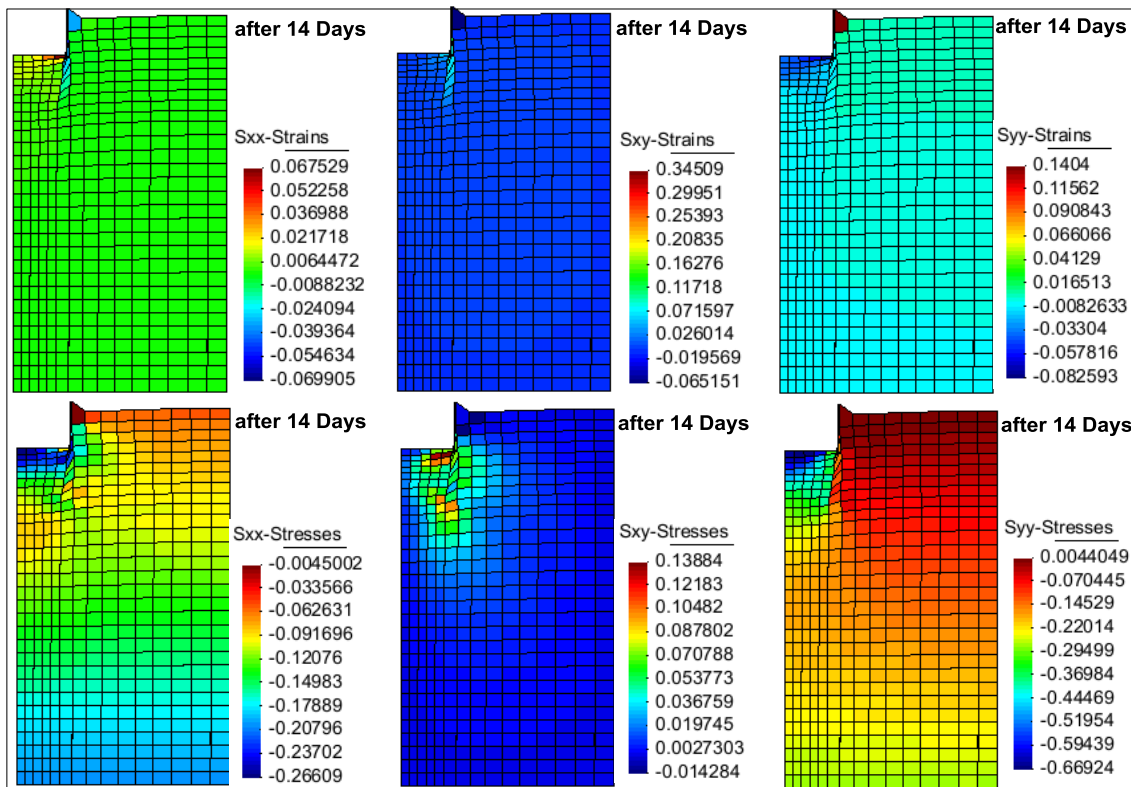
Figure 7.177: Contours of strains and stresses after 14 days of foundation's load application.
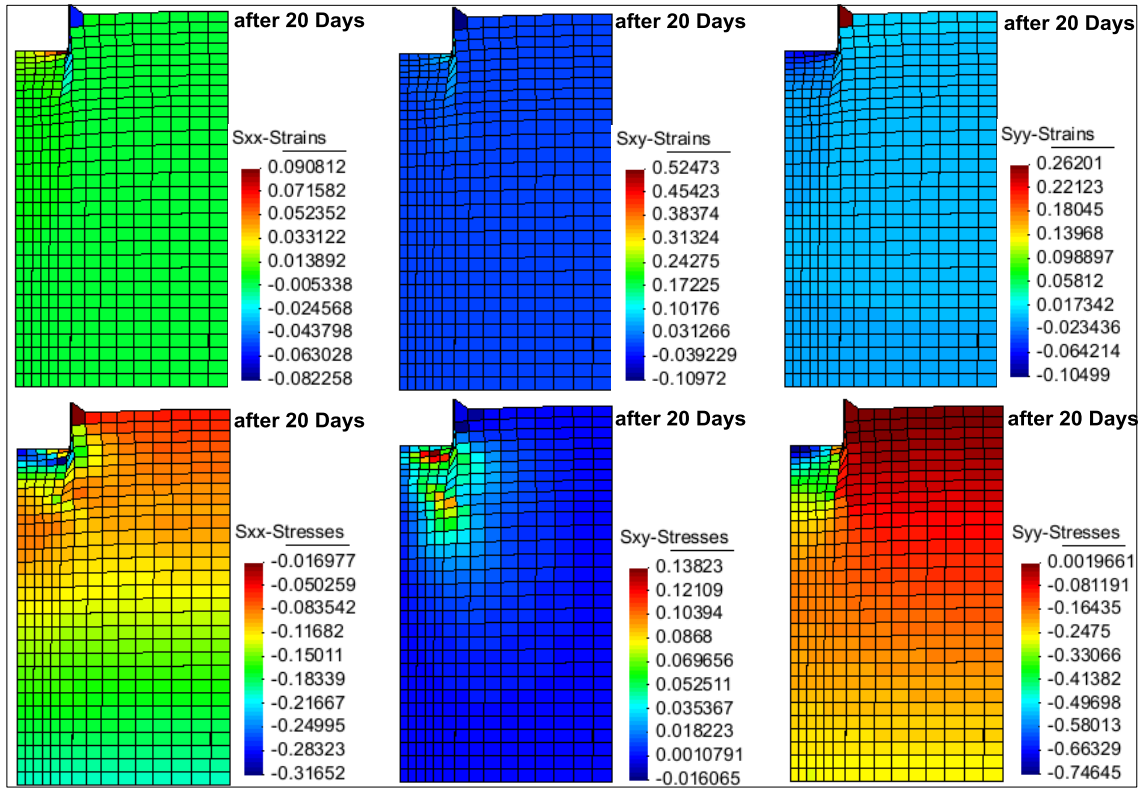
Figure 7.178: Contours of strains and stresses after 20 days of foundation's load application.

Fig. 7.179 shows isochrones of displacements: (a) norm, (b) horizontal and (c) vertical computed in the soil column.
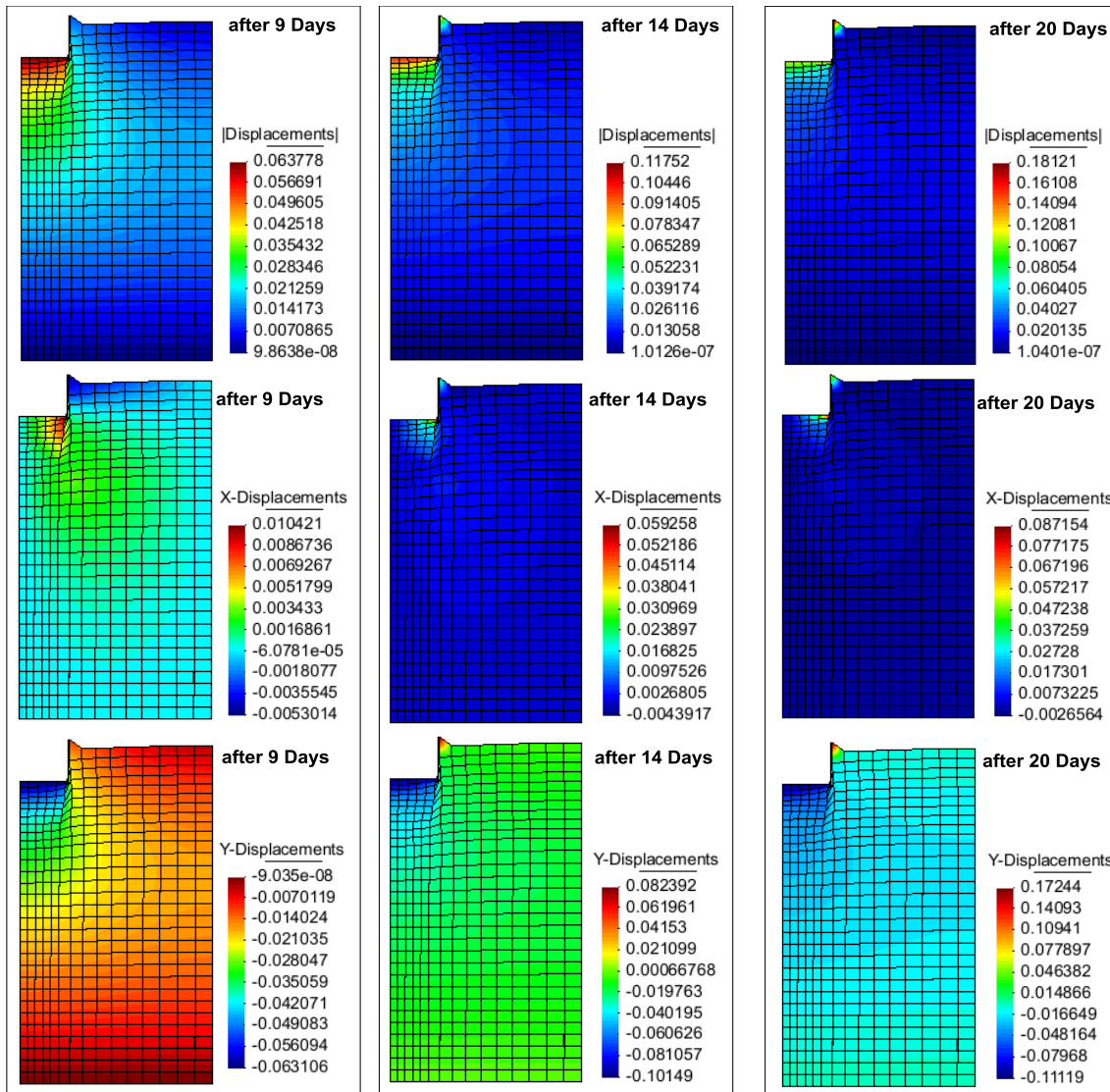
Figure 7.179: Overall picture of:(a) displacements' norm, (b) horizontal displ. and (c) vertical displ. through contours at three different times after the load application.

The isochrones evidence a settlement of about 6cm below the foundation and a soil surface uplift almost vertical in the zone close to the foundation. This zone also exhibits a concentration of shearing.

Fig. 7.180 presents vectors of principal plastic strains, liquid and thermal fluxes and displacements obtained in the soil column at the end of the foundation load application. Magnitude and direction of vectors confirm a collapse mechanism located under the foundation that results in a punching type of failure mechanism.
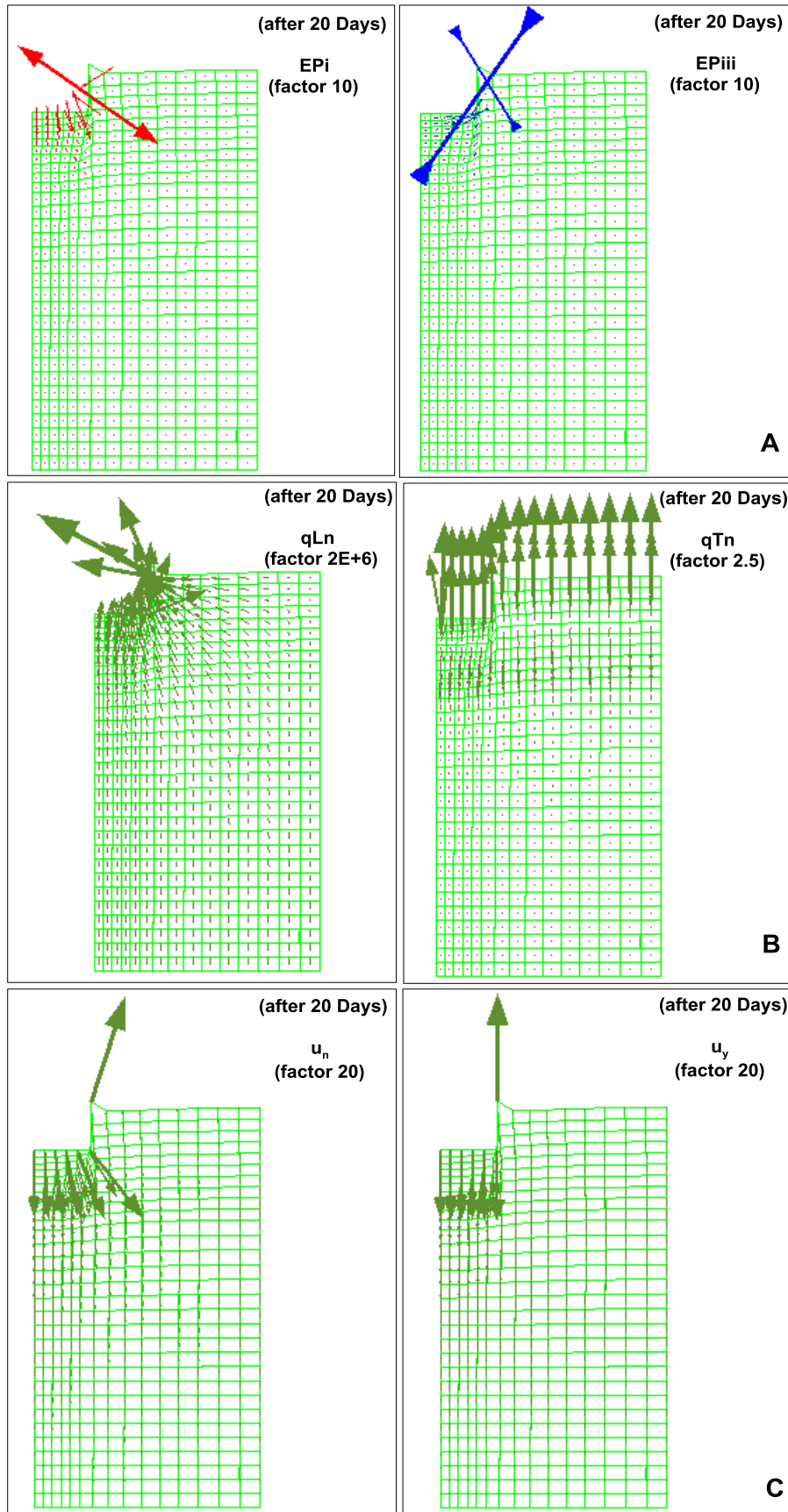
Figure 7.180: (a) Vectors of the principal plastic strains, (b) Vectors of liquid and heat fluxes and (c) Vectors of norm and vertical displacements, exerted at the soil column 20 days after the foundation's load application.

Fig. 7.181 shows evolutions of porosities at different points located at a zone surrounding the shallow foundation.
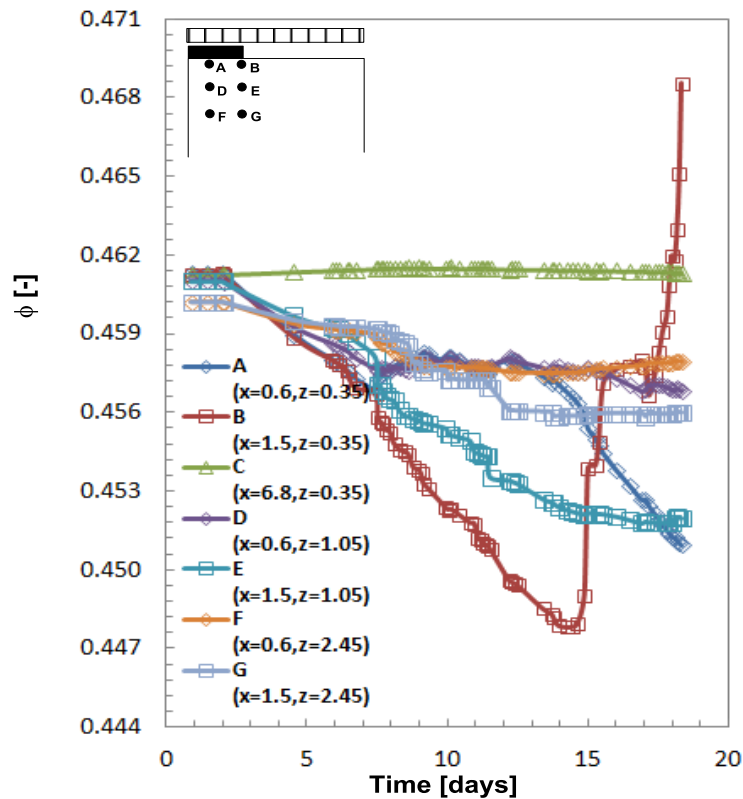
Figure 7.181: Evolutions of porosities at different points located at a zone surrounding the shallow foundation.

It is interesting to note the sudden increase in porosity during shear loading below the corner of the foundation.

7.7)   Study of the foundation's response under atmospheric actions

This case addresses the study of the slice foundation subjected to the atmospheric load. The foundation is considered impervious and the atmospheric load is consequently applied only at the site not occupied by the foundation.

The foundation is carried to a service load equal to one third of maximum bearing capacity $q_{serv} = \frac{1}{3} q_{max}$.

7.7.1)   Equations Solved

The equations solved in this case are the same solved for the problem at section 7.6: (a) mass balance of water (Eq. 7.1), (c) stress equilibrium (Eq. 7.2) and (c) energy balance (Eq. 7.9).

7.7.2)   Geometry, Mesh, Initial and Boundary conditions

Geometry corresponds to a slice of 7.5m width and 13.35m high. Spatial discretization consists of 450 quadrilateral elements (with linear interpolation) and 496 nodes.

The tests is composed by four time intervals defined by: (a) from -750d-0d: application of atmospheric condition in the unloaded soil, (b) from 0d-4d: application of the foundation load until q_{serv} , during this period the atmospheric load is acting at the soil surface, (c) from 4d-54d: application of the atmospheric load only and (d) from 54d-250d: change of prescribed liquid pressure at column under the atmospheric load.

During the entire test: (a) a null water flux and thermal flux have been applied in lateral boundary as conditions, (b) both a liquid pressure and a temperature have been prescribed at the bottom boundary and (c) atmospheric condition in the soil surface at the site not occupied by the foundation, a bare ground free of vegetation has been considered in this surface. As for the mechanical conditions, both null vertical and horizontal displacements have been imposed at bottom and lateral boundaries, respectively. A vertical displacement rate of $0.0048\,^{mm}/_{min}$ has been applied until the limit service load in the foundation has been reached.

Table 7.45 summarizes the parameters of the atmosphere condition.

Table 7.45: Table of atmospheric constants used in the simulation.

Latitude	0.7571
t_{autumn} (s)	0
t_{noon} (s)	0
H_{main}^{rough} (m)	4.00E-04
H_{stable}^{layer} (m)	3.00E-02
$\emptyset_{factor}$ (kg/m3)	1.00E+00
ρ_g^{atm} (kg/m3)	1.2
$albedo_{dry}$	0.2
$albedo_{wet}$	0.2
γ_g	1.00E+06
γ_l	-1.00E+06
$rain_{factor}$	1
rad_{factor}	1
$evap_{factor}$	1
$veg_{fraction}$	0

Time evolution of temperature, relative humidity, precipitation and wind velocity are plotted in Fig. 7.182.

The atmospheric file used for the computation has been filtered with respect to the original file in order to reduce the number of data lines and consequently in order to relieve the computational cost (smaller number of data-lines to read) and the storage requirements. Moreover, the record of temperatures has been corrected in order to avoid values lower than zero which could carry to problems of soil freezing, issue out of the dissertation scope.
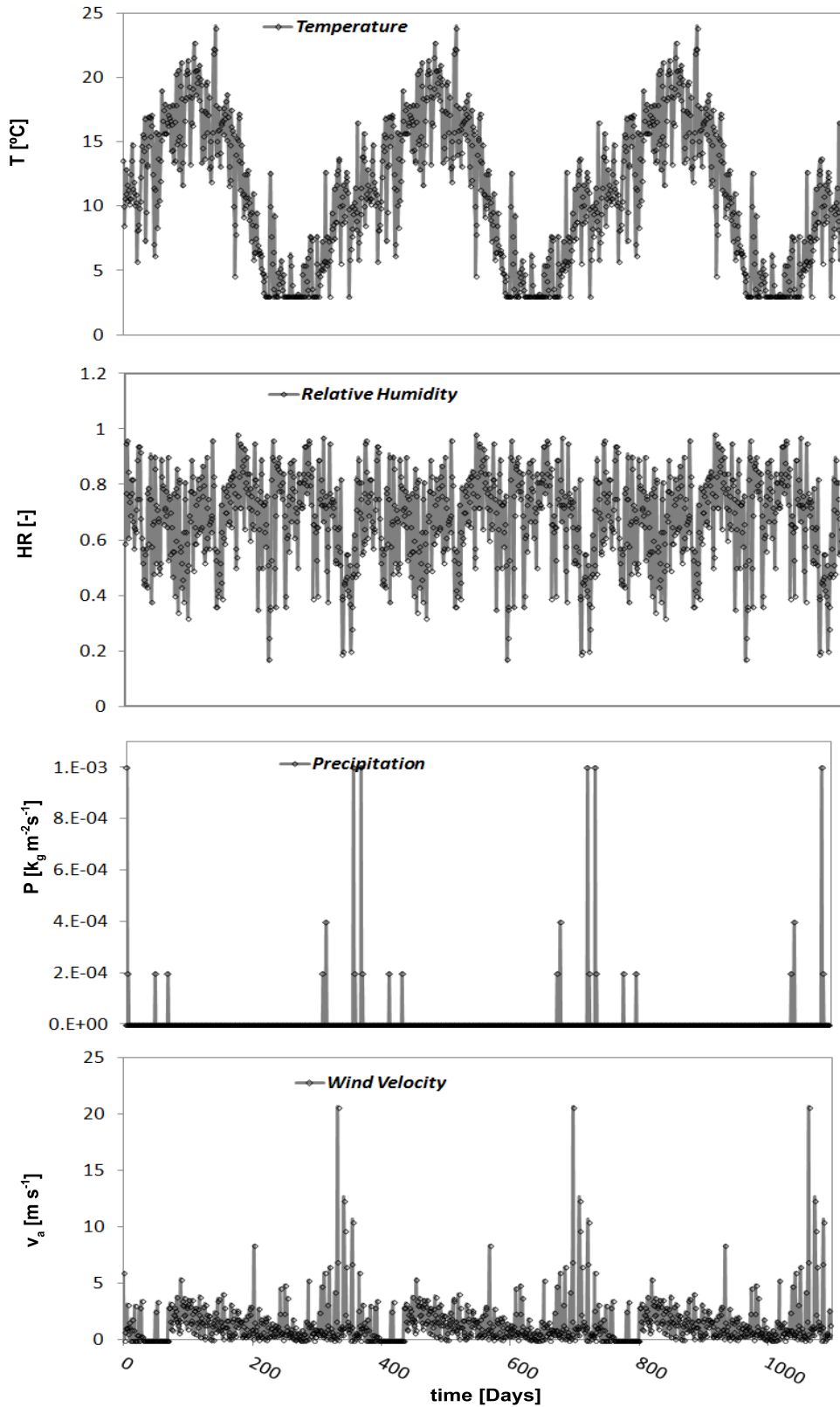
Figure 7.182: Atmospheric load applied at the soil surface of the silty column (root_atm.dat).

Table 7.46 summarizes the conditions, geometry, mesh and boundary conditions adopted for the modeled case.

Table 7.46: Conditions, Load configuration, Geometry and Mesh used in the modeling.

	Interval	Boundary Conditions	
Interval and Boundary Conditions	**1** Foundation load 0-4 [days]	*Lower boundary(1)*: $u_y = 0$ $p_l = 0.15\,\text{MPa}$ $T = 15.4\,°C$	*On top of foundation*: $\dot{u}_y = 0.0048\ ^{\text{mm}}/_{\text{min}}$ up to q_{serv}. *On free soil surface*: Atmospheric load (root_atm.dat)
	2 Atmospheric load only 4-50 [days]	*Lower boundary(1)*: $u_y = 0$ $p_l = 0.15\,\text{MPa}$ $T = 15.4\,°C$	*On free soil surface*: Atmospheric load (root_atm.dat)
	3 Atmospheric load only 50-350 [days]	*Lower boundary(1)*: $u_y = 0$ $p_l = 0.13\,\text{MPa}$ $T = 15.4\,°C$	*On free soil surface*: Atmospheric load (root_atm.dat)
Load Configuration			

Model Configuration at prototype (field) scale	Finite Element Mesh 450 Elements

The load configuration considers an impervious foundation (which may correspond to a good construction practice: (a) rich water-cement ratio, (b) highly compacted and (c) well curing).

7.7.3)   Material Parameters

The material parameters used in the simulation are those summarized in Table 7.43.

7.7.4)   Modeling Results

Fig. 7.183 shows the displacements of the foundation during the early stage of the model: (a) soil vertical displacements due to atmospheric condition in absence of foundation, (b) applied displacement up to service load.
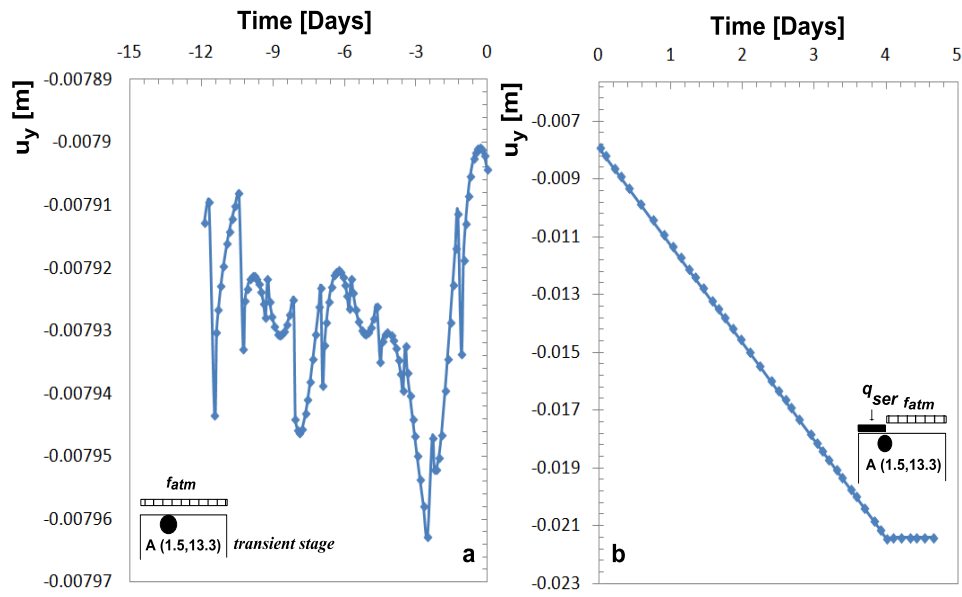
Figure 7.183: Evolution of vertical displacements at the upper soil layer of the silty column: (a) under climatic condition at pre-load stage and (b) under foundation load.

Fig. 7.184 shows a general view of results: (a-b) Time evolution of input wind velocity and atmospheric temperature, (c-d) Soil temperature and soil saturation at 5cm depth, (e-f) Soil surface vertical displacement and differential vertical settlement between foundation and soil surface.
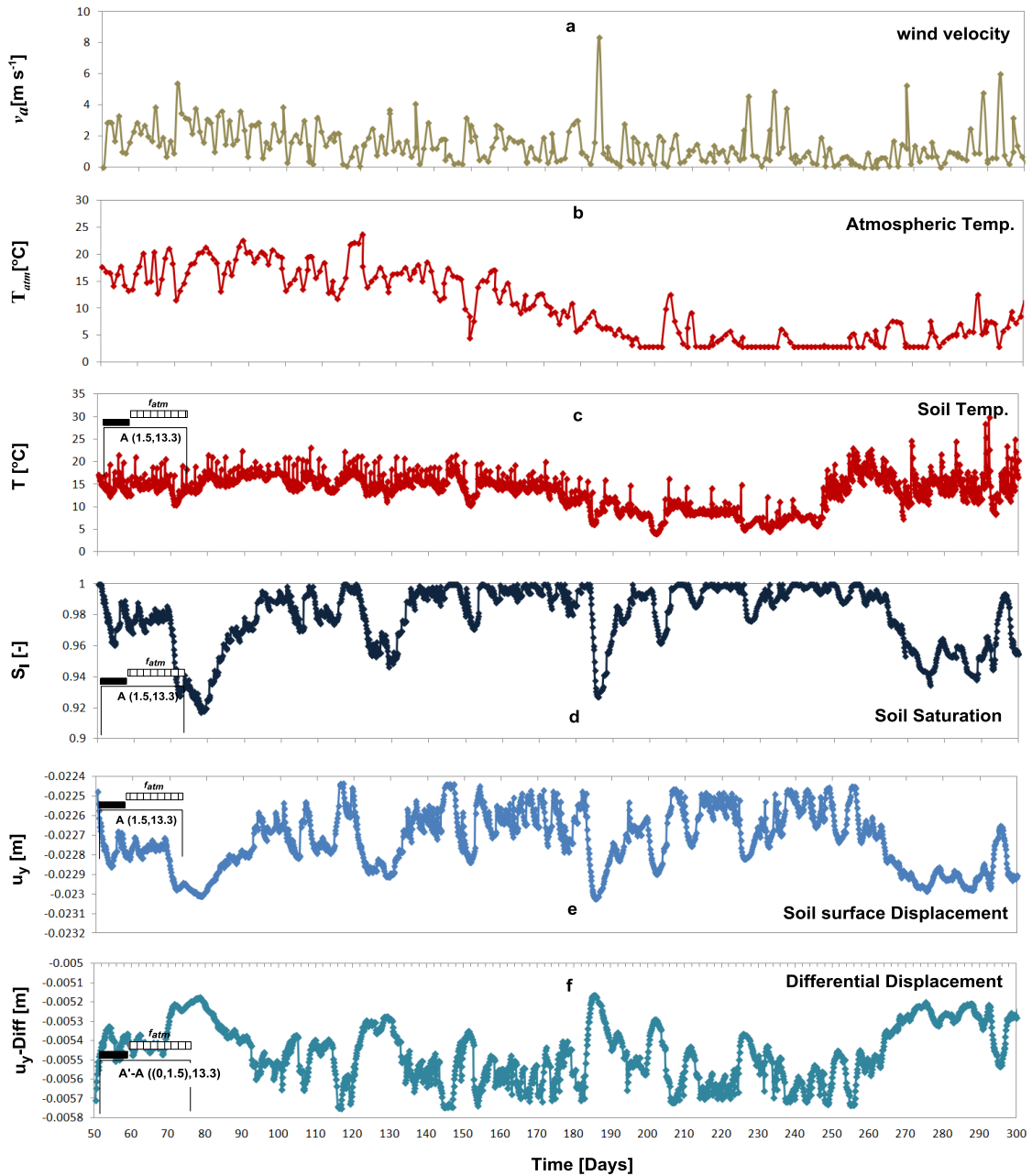
Figure 7.184: Overall view of modeled case. (a-b) wind velocity and atmospheric temperature applied at the soil surface, (c-d) Evolution of soil temperature and Saturation degree at the footing edge, (e) Evolution of Vertical Displacements at the upper soil layer of the silty column and (f) Evolution of Vertical differential displacements observed between the footing center and footing edge.

Soil surface temperature exhibits a variation in agreement with the atmospheric temperature. Variation of the degree of saturation shows a monthly character of dry periods followed by wet periods.

As a result of temperature and degree of saturation, the maximum amplitude of soil displacement is 6mm. This amplitude presents a typical variation in periods of several days.

The relative settlement between the centre and the edge of the foundation is 5.8mm which gives an angular variation of 3E-4.

Figures 7.185 and 7.186 present the stress paths and yield surfaces obtained: (a) at the end of foundation load (b) after 313 days, (c) after 326 days and after 335 days of atmospheric action.
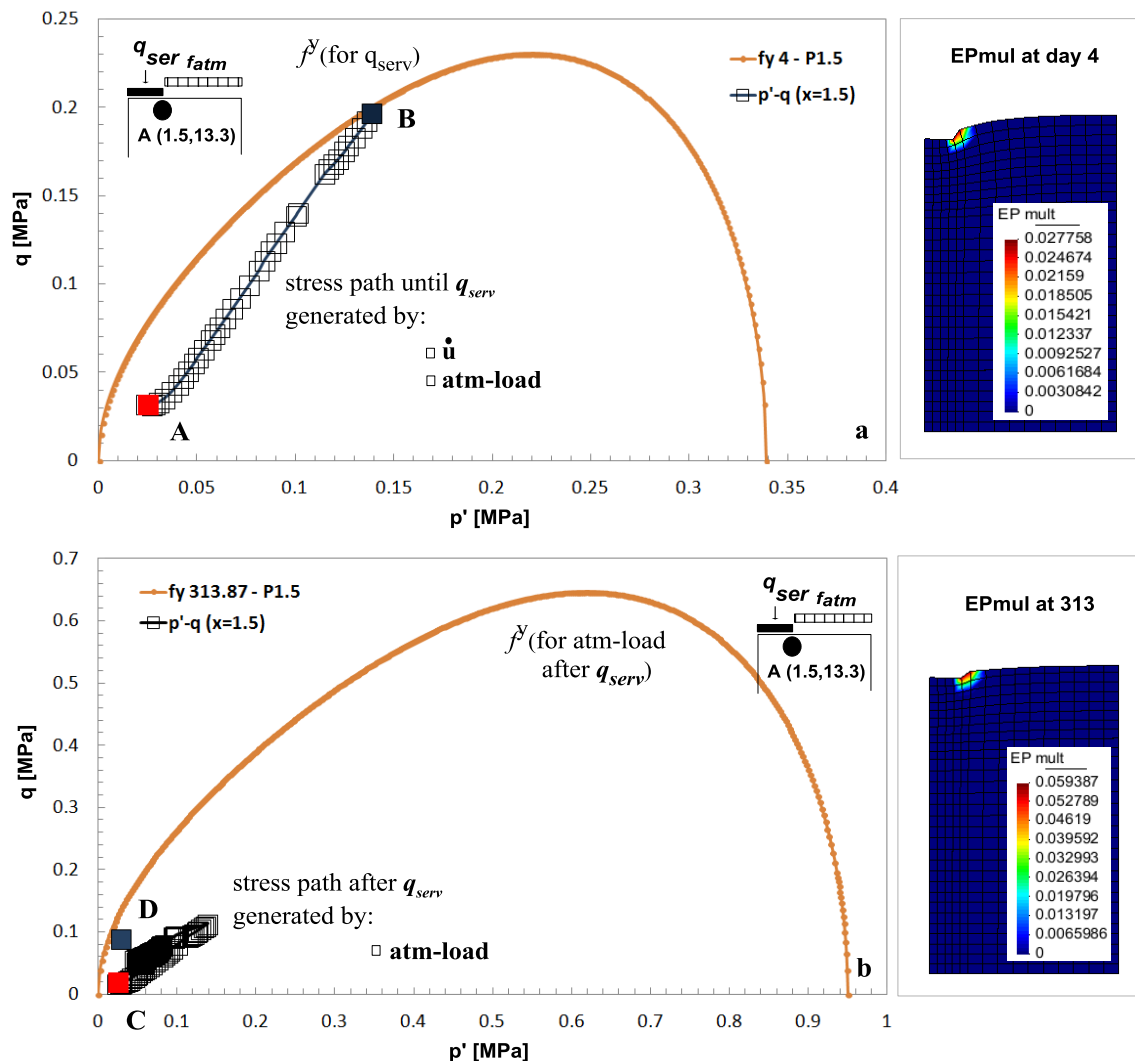
Figure 7.185: Stress paths and yield surfaces at times: (a) of foundation's load at service value and (b) after 313 days under atmospheric load.

During foundation load yield surface is reached at the dilatant side of the critical state producing a softening response of the material.

During the 54 days of atmospheric condition after end of foundation load stress point has moved to an almost isotropic stress state point-C. Henceforward, stress path moves toward the failure locus according to the soil temperature and suction. After 313 days of climatic action the yield surface is reached at the dilatant site point-D for low values of mean stress. At that time a dilatant plastification process occurs below the foundation as a result of atmospheric load only.

As evidenced by the mean Bishop stress / deviatoric stress path depicted in Fig. 7.186, soil is in plastic state at day 326 point-A. Due to increases in suction, caused by the drying of the soil, the stress path moves to point-B enlarging the yield surface by compression and producing a further hardening of the material.

During the next wetting-drying and heating-cooling events, stress path moves alternatively inside the yield locus (elastically) or dragging it (plastically), path B-C-D-C-E-F.

At day 335 yield surface decreases in size due to an increase in temperature reaching the stress state in the dilatant zone point-G with the consequent softening of the material, see Fig. 7.186.

Fig. 7.186 evidences a process of plastification that encompass a zone larger than the foundation influence at t=326 days. At that time, as shown in Fig. 7.184c, soil temperature increases above previous values for a significant period of time as result of latter atmospheric condition.
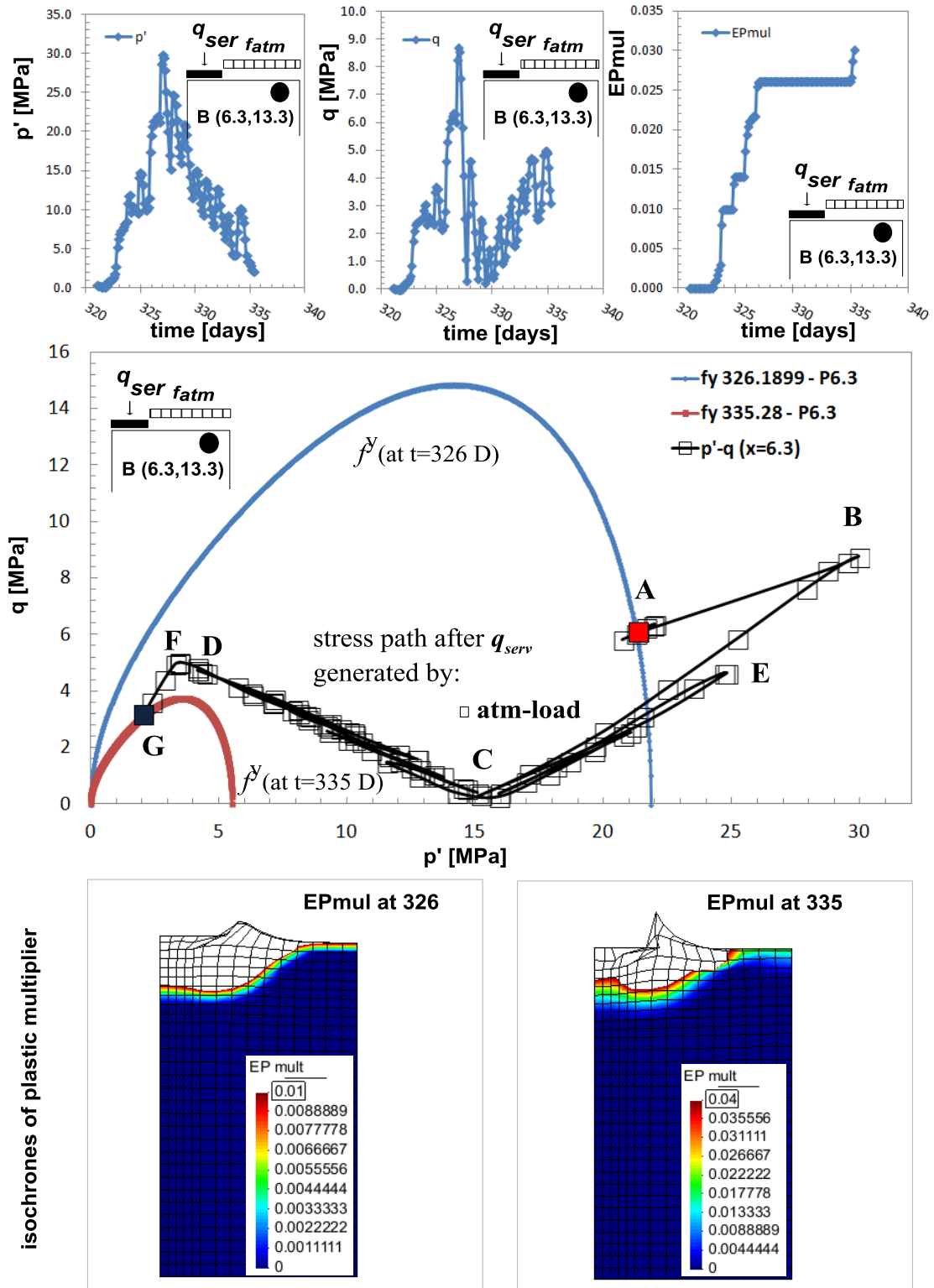
Figure 7.186: Stress path and yield surfaces at times: (a) after 326 days after the atmospheric load onset and (b) after 335 days after the atmospheric load onset.

Fig. 7.187 compares results of: (a) temperature, (b) vapor flux, (c) liquid pressure, (d) saturation degree, and (e) vertical displacement obtained at five different points on the soil surface. Points a-b-c are located below the foundation and thus are not subjected to the atmospheric load. It can be observed that the fluctuations in temperature, pore pressure, degree of saturation and thus displacements are lower in that zone, creating a differential settlement with respect to the edge of the foundation.

Fig. 7.188 shows differential values obtained as the difference between the variables computed at points b, c, d, e and point a (foundation center). Results evidence differential temperatures between -5oC and 9oC, differential pore pressure span between 4kPa and −5kPa, maximum differential degree of saturation reads 6% and corresponding differential settlement between 0.9mm and -1.3mm. Since those differential values may evolve from minimum to maximum in relatively short periods (some days) damage to the structure supported by the foundation is to be evaluated.
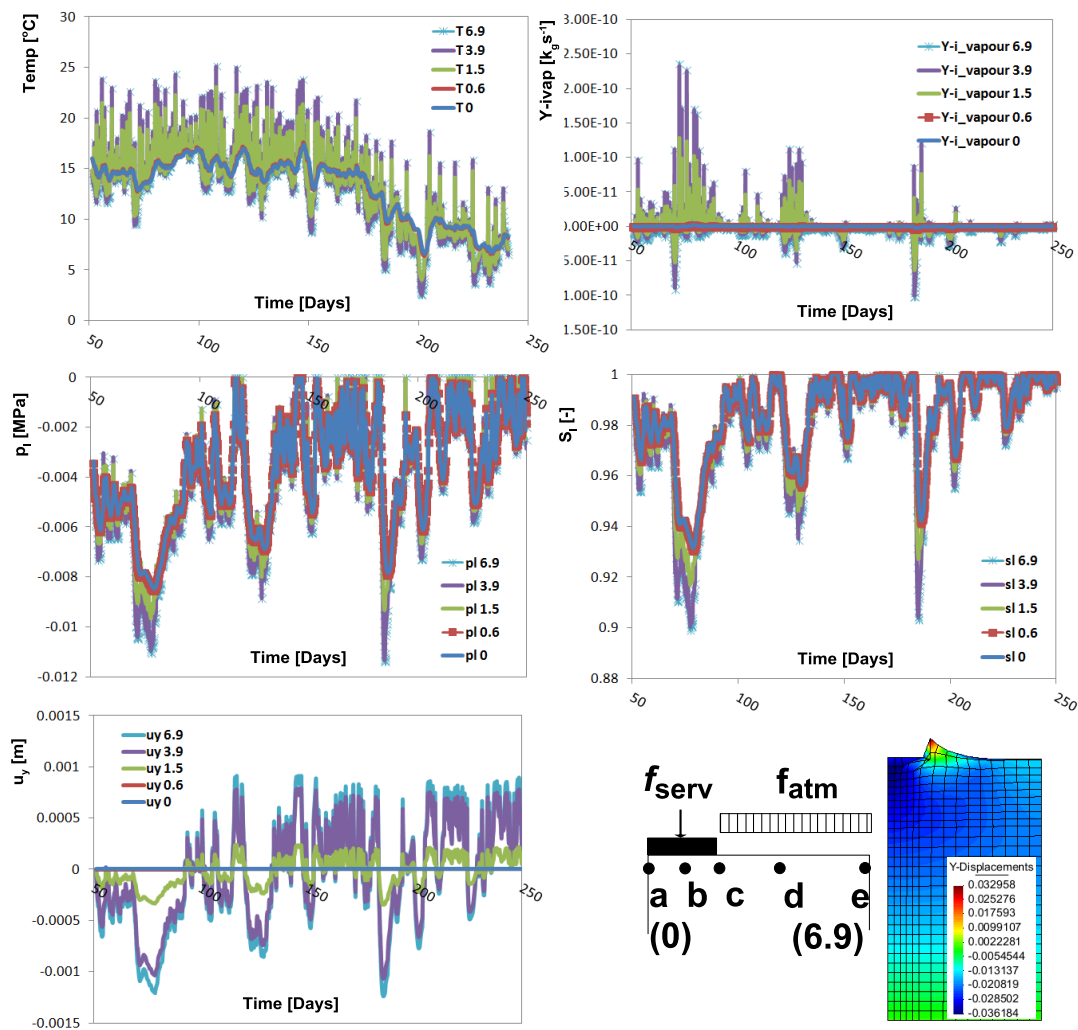
Figure 7.187: Absolute evolutions of: (a) Soil Temperatures, (b) Vapor fluxes exerted surface, (c) Liquid pressures, (d) Liquid saturations and (e) Vertical displacements at five points of the column .
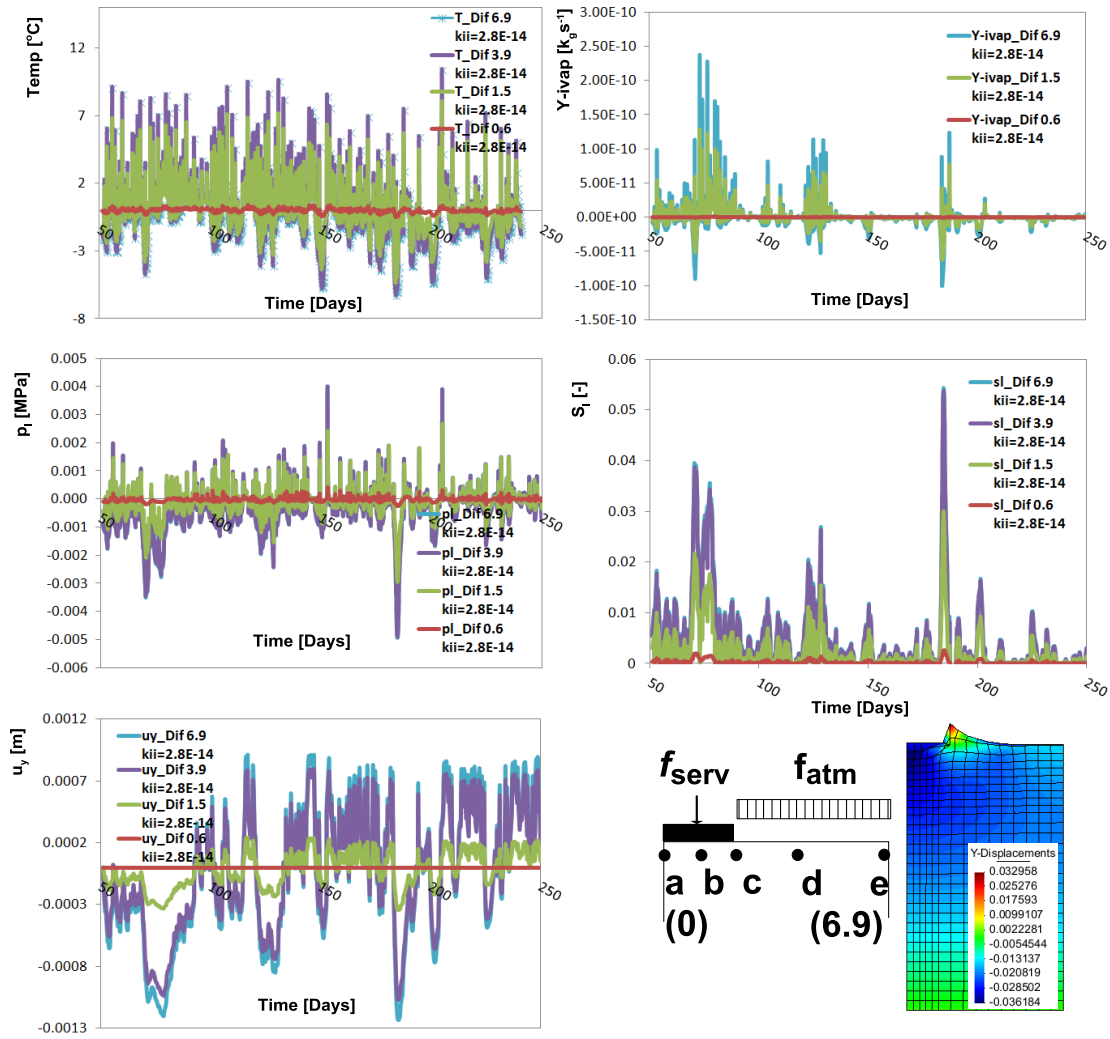
Figure 7.188: Differential evolutions of: (a) Soil Temperatures, (b) Vapor fluxes exerted surface, (c) Liquid pressures, (d) Liquid saturations and (e) Vertical displacements obtained at five points of the column surface.

In order to study the effect of hydraulic conductivity on the response of foundation, two computations have been realized for two values of permeability: (a) $k_{ii} = 2.8E - 14 m^2$ and (b) $k_{ii} = 2.8E - 12 m^2$. Fig. 7.189 shows a comparison of the obtained results for time evolution of: (a) soil temperature, (b) degree of saturation, (c) evaporation flux and (d) vertical displacement.
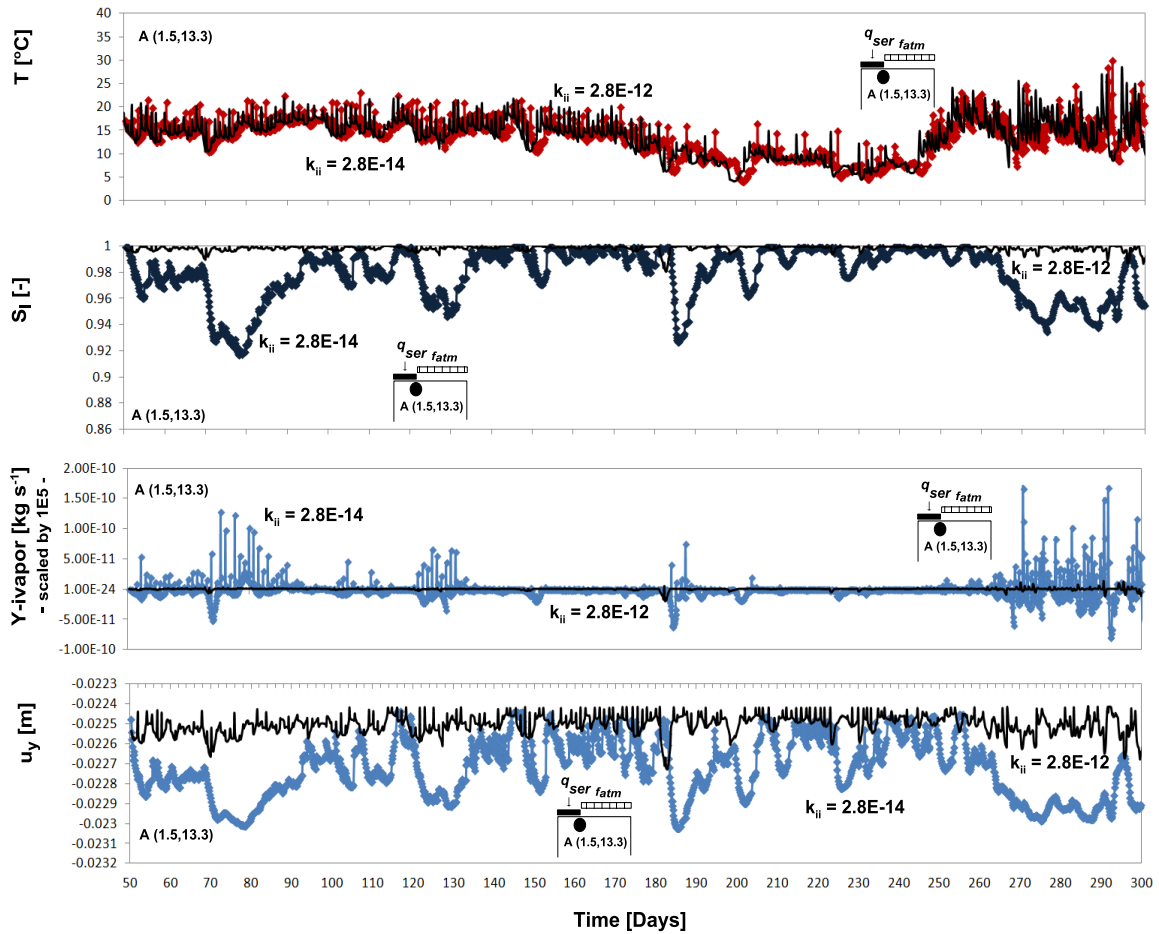
Figure 7.189: Evolutions of: (a) Soil Temperature, (b) Degree of saturation, (c) Vapor flux and (d) Vertical displacement obtained at the column surface for two different values of permeability.

Fig. 7.189 evidences the stronger effect of atmospheric load in lower permeability medium. This is due to the fact that the hydraulic conductivity has a lower control of the vadose zone, which respond more strongly to the soil-atmosphere interaction fluxes.

It is also interesting to note the delay of soil response to the atmospheric load evidenced between the results obtained for each permeability. It is produced due to the higher soil impedance for lower values of hydraulic conductivity.

It can be concluded that the lower the soil permeability the more sensible the soil is to atmospheric fluxes acting at the soil surface. It is stated in view of the magnitude of variations of: (a) displacements, (a) saturation degrees and (c) vapor fluxes obtained at a point in the column surface.

Fig. 7.190 and 7.191 show the differential values between points a-d and a-c, respectively.

In case of higher permeability soil, there is almost no differential desaturation between soil surface and soil beneath the foundation. As consequence differential settlements do not exceed 0.5mm.

Fig.7.190e-f show the pattern of soil deformation at the end of the computation. For the case of the lower permeability, the effect of drying leads to a final lifting of the soil close to the foundation. In the other case, the final deformation pattern is similar to the one obtained after foundation load because of the low effect of atmospheric condition.
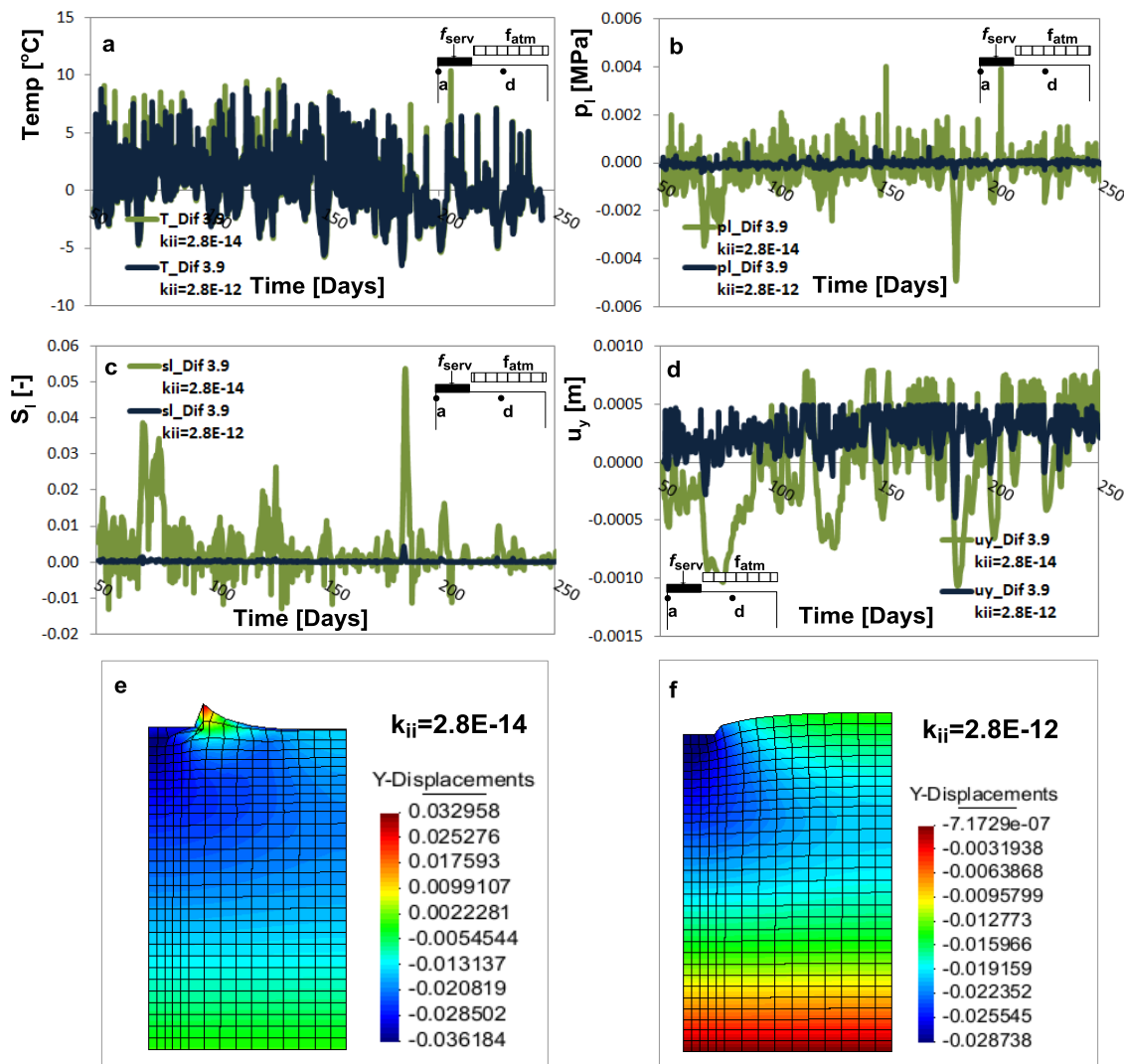
Figure 7.190: Differential evolutions of: (a) Soil Temperatures, (b) Liquid pressures, (c) Liquid saturations, (d) Vertical displacements at the center of the column surface.
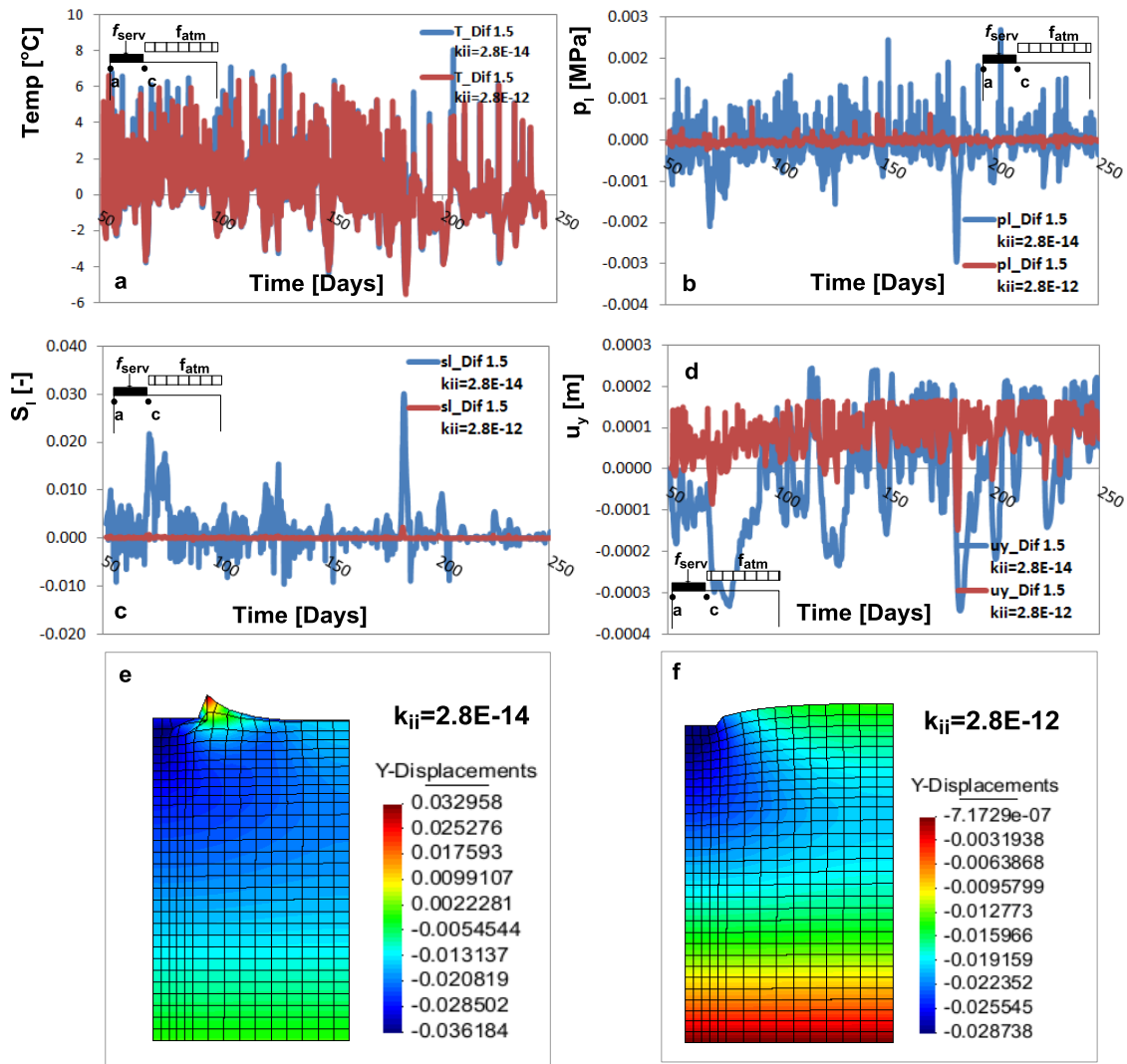
Figure 7.191: Differential evolutions of: (a) Soil Temperatures, (b) Liquid pressures, (c) Liquid saturations, (d) Vertical displacements at the footing edge.

Further insights into deformation patterns can be obtained from profiles of temperature, evaporation flux, pore pressure, degree of saturation and vertical displacement obtained at different times, Fig. 7.192, Fig. 7.193 and Fig. 7.194.

Thus after foundation loading since the same condition has been considered during the loading phase paths are identical.

Afterwards, profiles start to diverge, at 180 days evaporation is much more active in the lower permeability soil leading to lower pore pressures and slightly higher desaturation. As result of the low difference in saturation at that time settlements are still comparable. At time 336 days, the lower permeability case evidence a higher desaturation of about 65% than in the higher permeability case of 95%. Consequently, the pattern of

displacements is completely different, while the lower permeability soil exhibits a soil uplift at the footing edge the higher permeability soil maintains the depressed profile of settlements mainly generated by foundation load.
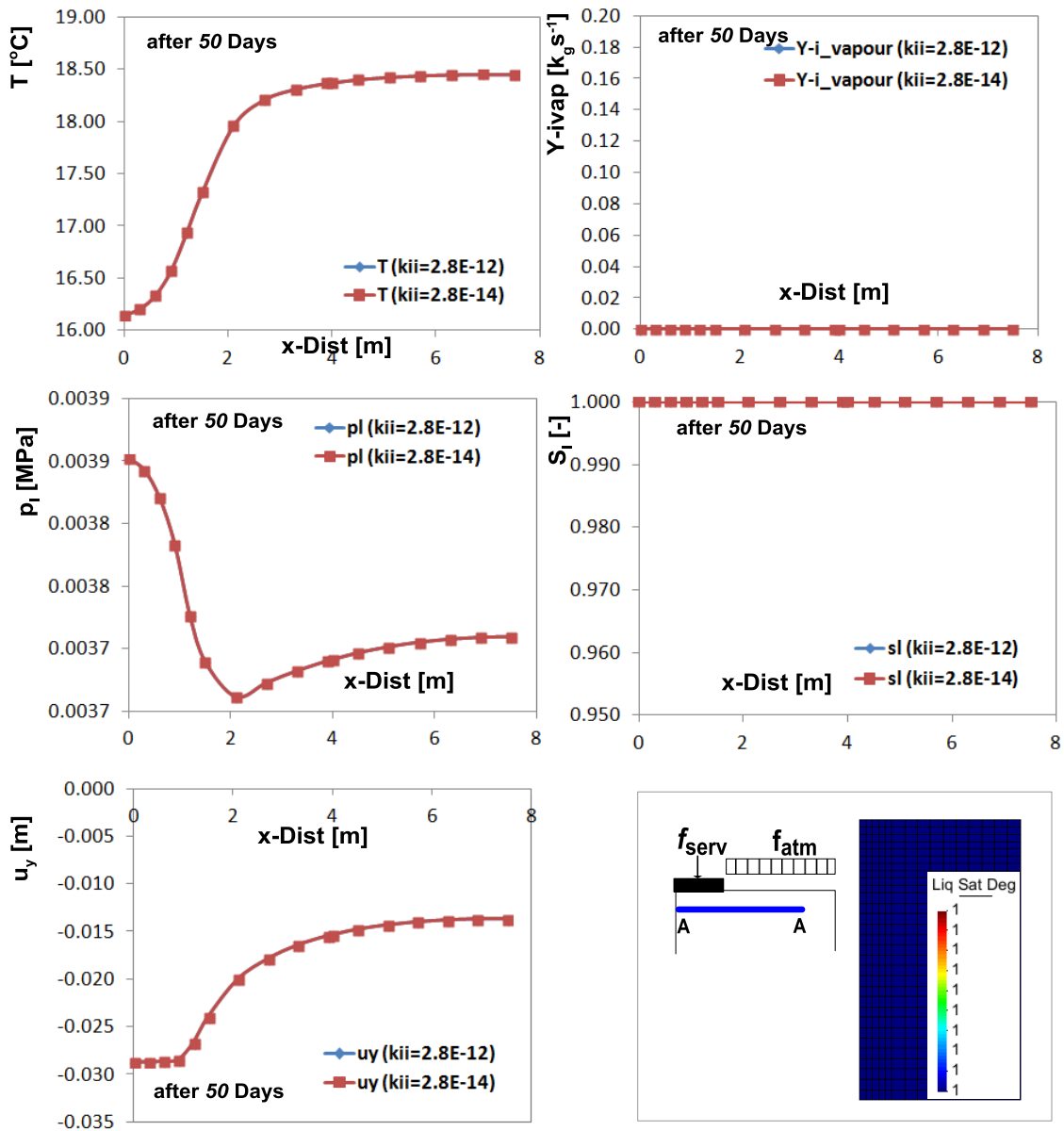
Figure 7.192: Profiles of: (a) vertical displacement, (b) temperature, (c) liquid pressure, (e) saturation degree and (e)vapor flux after 50 days of atmospheric load action.
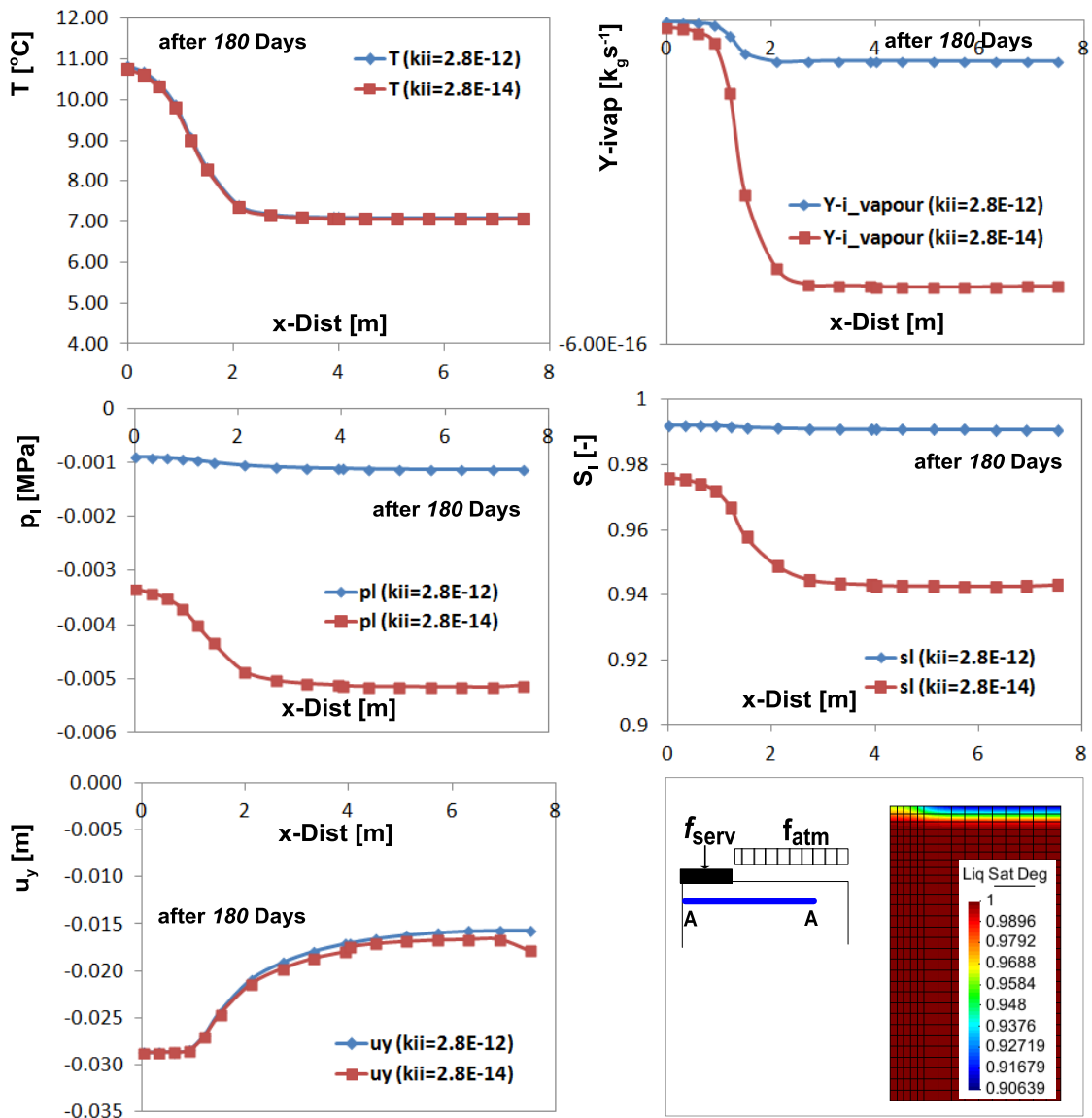
Figure 7.193: Profiles of: (a) vertical displacement, (b) temperature, (c) liquid pressure, (e) saturation degree and (e)vapor flux after 180 days of atmospheric load action.
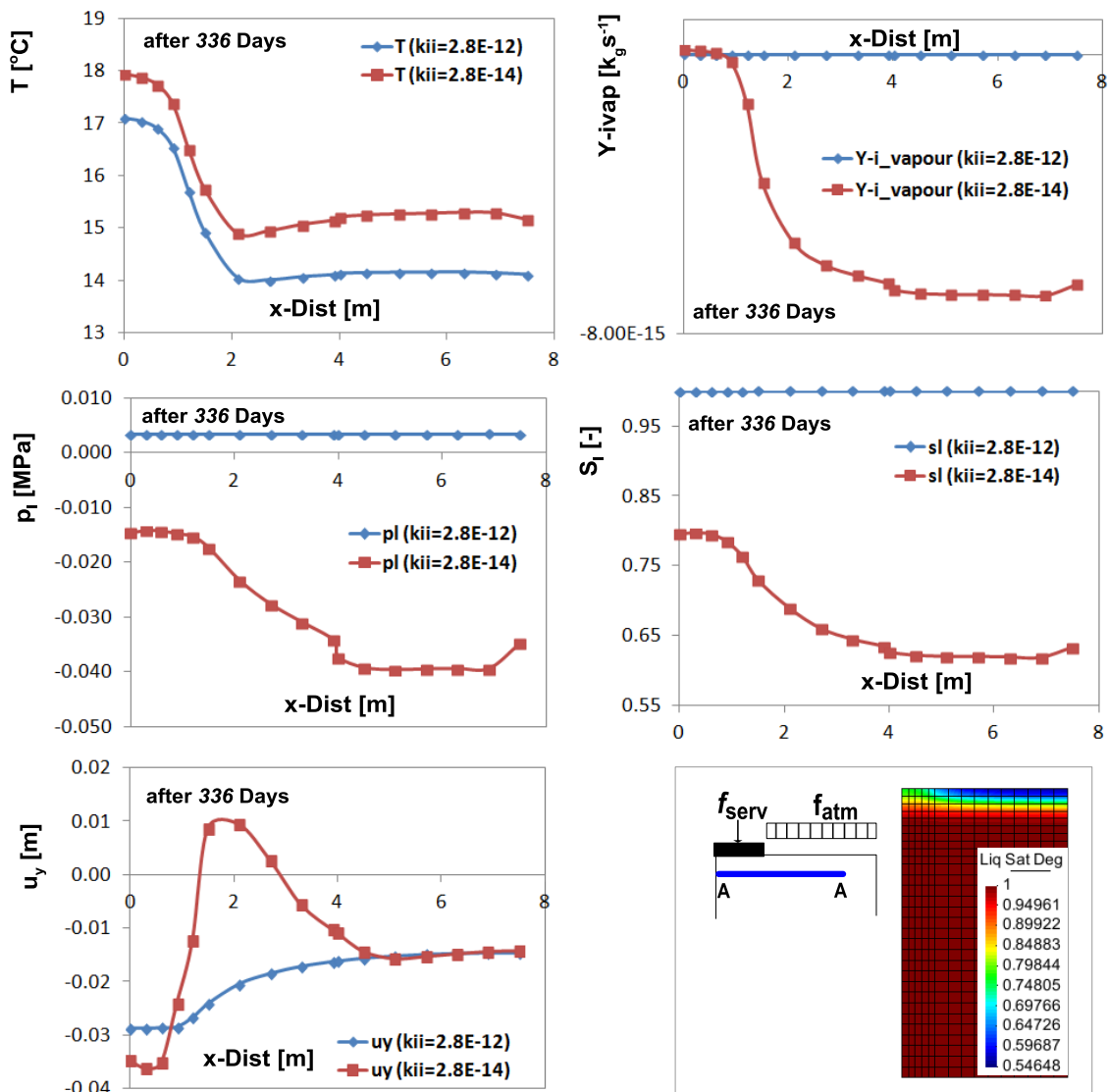
Figure 7.194: Profiles of: (a) vertical displacement, (b) temperature, (c) liquid pressure, (e) saturation degree and (e)vapor flux after 336 days of atmospheric load action.

The particular pattern of deformation in the case of the lower permeability soil can be further investigated by looking at the isochrones of: liquid pressure, vapor flux, shear strain and stress, plastic strains, hardening parameter and displacement, Fig. 7.195 to Fig. 7.199.

Fig. 7.195 shows isochrones of porosity, saturation degree and vapor flux obtained at three different times after the foundation and atmospheric loads action.

Isochrones of degree of saturation and evaporation flux (Fig. 7.195) evidence an active zone of 1m depth while porosity pattern show that the initial compression zone below the foundation turns out into extension zone after the drying event.
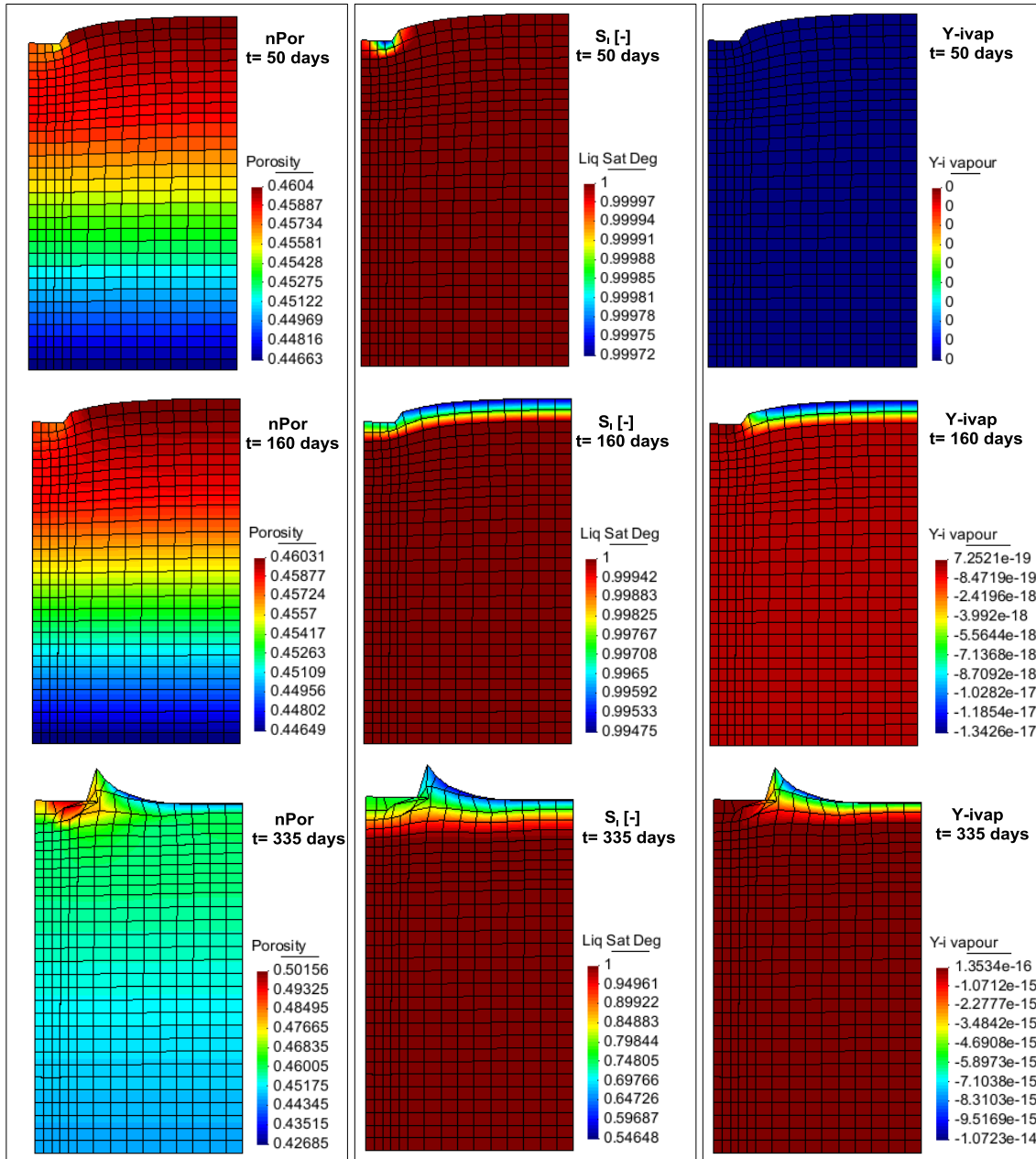
Figure 7.195: Isochrones of: (a) porosity, (b) saturation degree and (c) vapor flux obtained at three different times after the actions of both the foundation's load and the atmospheric load.

_____

Fig. 7.196 shows isochrones of shear strains, shear stress and deviatoric stress obtained at three different times after the foundation and atmospheric loads action.
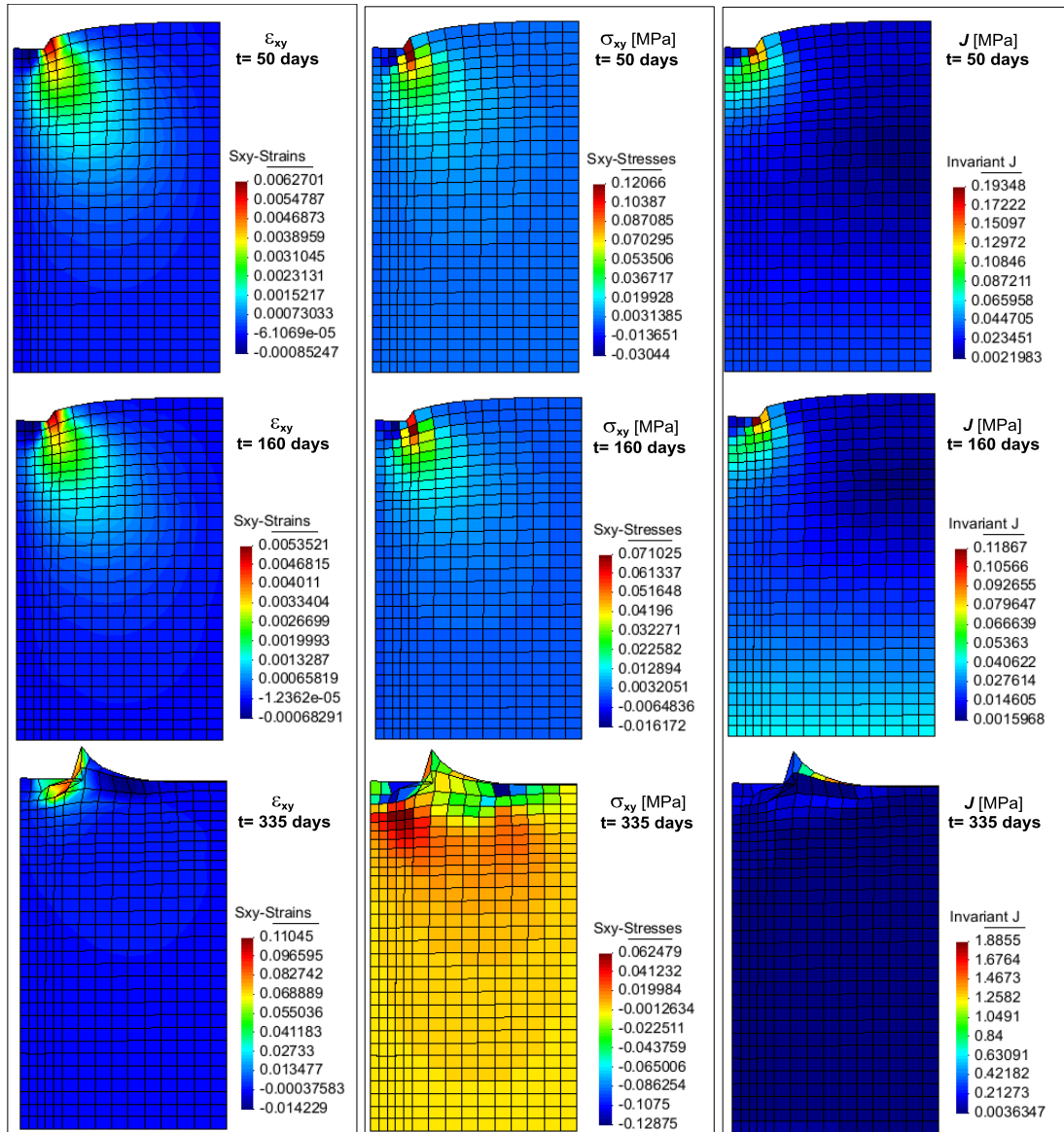
Figure 7.196: Isochrones of: (a) Shear strains, (b) Shear stress, and (c) deviatoric stress invariant obtained at three different times after the actions of both the foundation's load and the atmospheric load.

Fig. 7.197 shows isochrones of plastic strain: (a) normal, (b) shear and (c) vertical obtained at three different times after the actions of both the foundation load and the atmospheric load.

During foundation loading a limited plastic zone develops essentially below the edge of the foundation. It remains basically constant during the application of the atmospheric load before the shown drying cracks. After this event the plastic zone extends significantly around the foundation and vertical plastic extension occurs indicating an uplift of a thin superficial layer from underneath ground.
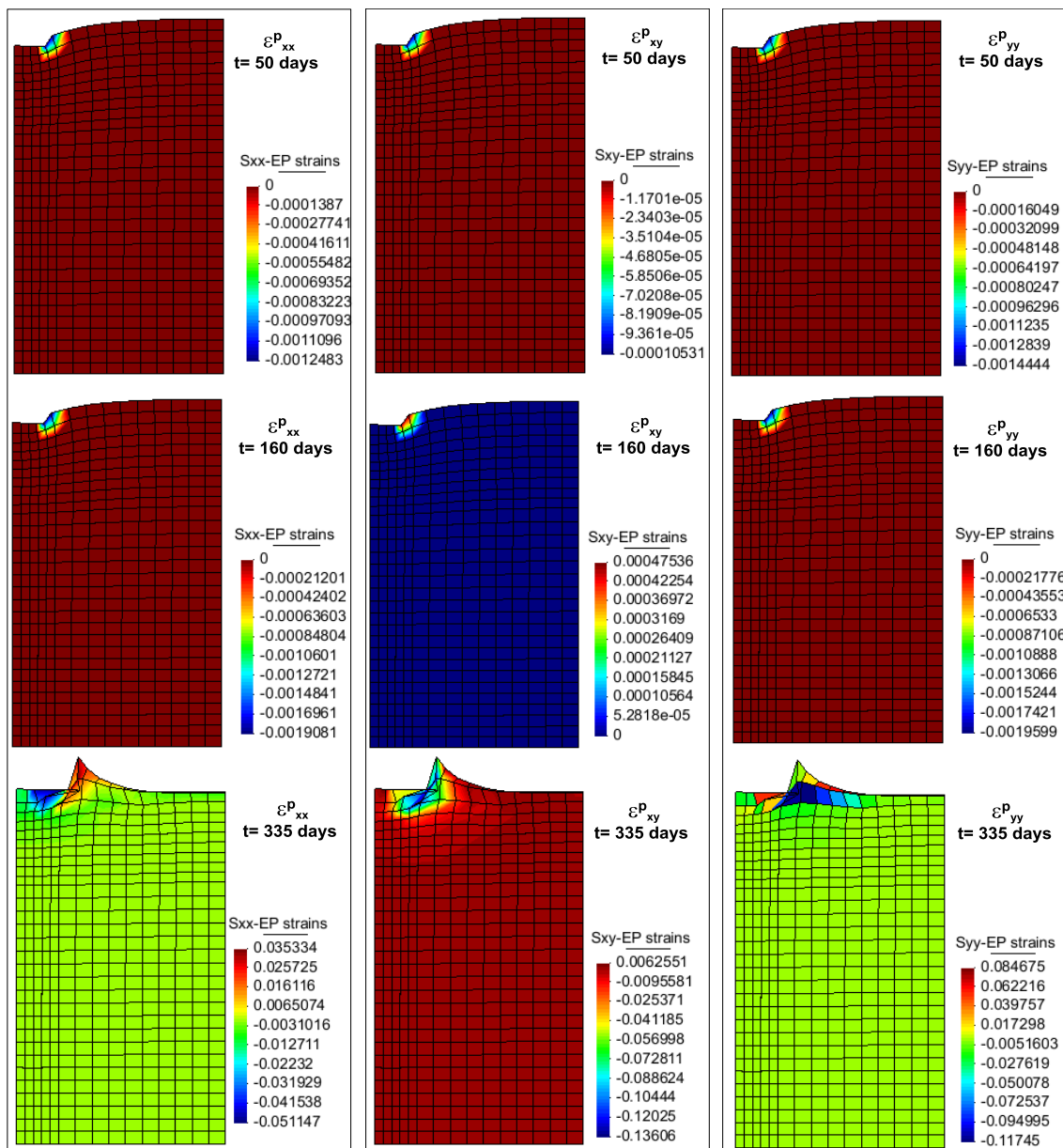
Figure 7.197: Isochrones of: (a) horizontal, (c) shear and (c) vertical plastic strains obtained at three different times after the actions of both the foundation's load and the atmospheric load.

Fig. 7.198 shows isochrones of hardening parameter obtained at three different times after the foundation and atmospheric loads action.

Isochrones of hardening parameter p_o^s evidences the strong hardening due to suction effect which causes an enlargement of the elastic space of about three times the elastic space after the foundation load.
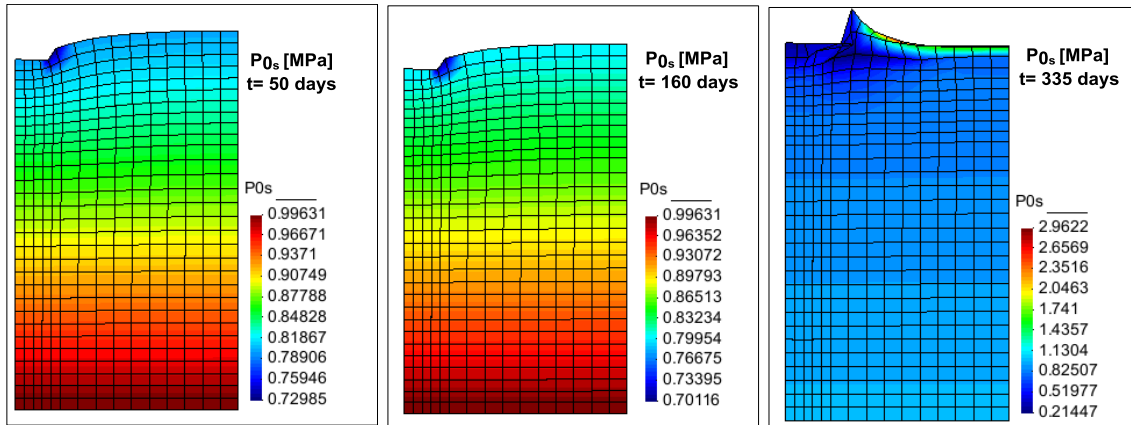
Figure 7.198: Isochrones of hardening parameter obtained at three different times after the actions of both the foundation's load and the atmospheric load.

Fig. 7.199 shows isochrones of vertical displacements at different times after the onset of foundation load and atmospheric load.

The previously observed soil uplift is confirmed here in accordance with the formation of drying cracks.
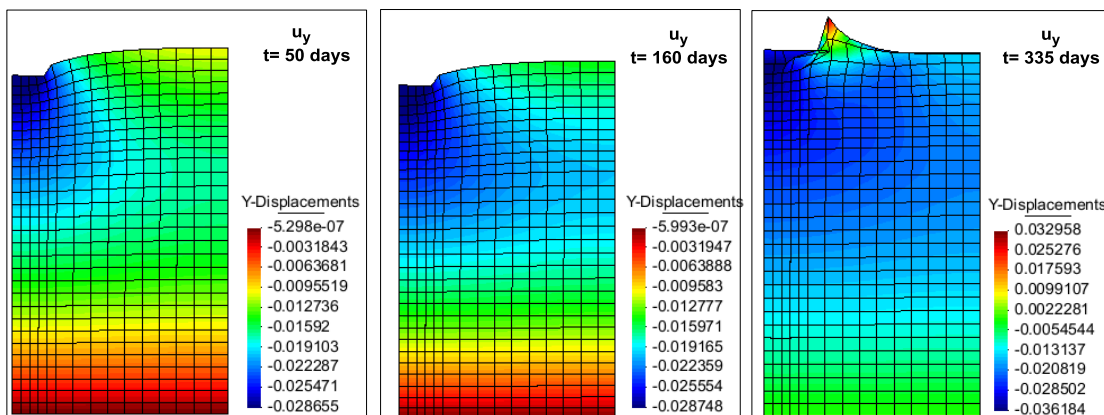
Figure 7.199: Isochrones of vertical displacements at three different times after the actions of both the foundation's load and the atmospheric load.

7.8) Conclusions

In this chapter the response of a shallow foundation under atmospheric condition has been studied.

The model (boundary value) has been calibrated in a physical centrifuge test at laboratory scale. The thermo-hydro-mechanical formulation presented in chapter 2 has been used in order to physically modelize the governing and constitutive equations.

In this regard, the mechanical model BBM2- generalized and the air-liquid interface model simplified van Genuchten retention curve presented in chapter 4 have been used to give a constitutive response at each phase.

Results show that the model is able to reproduce both the hydraulic and the collapse responses of the silty layer. Moreover, the model has also shown to be capable to reproduce the force-displacement curve of the foundation.

A procedure to evaluate the bearing capacity factors in non-saturated conditions has been developed based in Potts proposal, Potts (2001). Then, this procedure has been used to compute the bearing capacity of shallow foundation at the centrifuge test in conditions close to saturation.

The calibrated model (boundary value) has then been applied to the silty layer at field scale in order to study the bearing capacity of the foundation under field scenarios. An atmospheric condition has been applied for a period of two years for the purpose of reproducing real conditions in the soil layer mainly in the upper zone.

To study foundation response particularly concerning displacements under climatic actions, foundation has been loaded until a service load equal to 1/3 of the ultimate load, then two years of atmospheric input have been applied at soil surface under the consideration of an impermeable foundation.

This study shows the development of differential settlements of about 6mm between the footing center and its edge due to the climatic action. During a strong drying process, at the last stage of the atmospheric condition, soil has shown to experiment a vertical displacement in extension of about 3cm.

A sensitivity study shows the implications of soil permeability in this process, where the water table is maintained at a constant depth. In the higher permeability soil the more

open structure prevails over the atmospheric effects leading to low soil suction condition. For the lower permeability soil ($K \approx 1E - 7\,^{m}/_{s}$), the evaporation has a relevant role by generating an active zone of about 1m depth, which affects the superficial settlements.

During this process, tractions stresses have emerged close to the foundation boundary that the model has shown to represent without major problems of convergence.

CHAPTER 8

ANALYSIS OF A ROCK-CLIFF STABILITY UNDER CLIMATIC ACTIONS

8.1) Introduction

In this chapter, a geotechnical problem in stiff material is studied using the constitutive model based on shear failure criterion presented in chapter 4 and implemented using the algorithms presented in chapter 5. A particular attention will be devoted to the modeling of traction failure which occurs in this type of material. It will be shown that such mechanism can be overcame using the interior-point algorithm described in chapter 5.

Since traction failure is a common process occurring in problems of soil response under climatic actions such as soil desiccation, the relevance of the results presented in this chapter is more universal than the modeled case considered.

The case addressed in this chapter arises in 2010 as a public security issue related to the fall of some solids in a cliff above the village La Roque Gageac. The partial collapse of the roof of a troglodyte cavern located in the cliff generate a large concern to the population and the public authorities about the stability of a huge block on top of the village (R.E.G.G., 2011) and the possibility of its fall.

Historical data gathered in Table 8.47 indicates recurrent movements since at least 1920, Fig. 8.200.

Table 8.47: History of observed landslides at La Roque Gageac

1920	Landslide of a neighborhood to the east of the troglodyte cavern
1957	Landslide located to the west of the village
1994	Landslide of the cliff center
2010	Partial collapse of the troglodyte cavern

Figure 8.200: Location of the resent landslides

UPC was in charge of analyzing the possible effect of cyclic thermal load on the stability of the rock massif. In order to consider both temperature and radiation effects the atmospheric condition presented in this thesis has been used.

Due to the dry character of the rock $(1 - \phi)$ and its porosity with no water storage $\left(\phi_g = \phi(1 - S_l) = \phi\right)$, no water mass balance has been considered. A general review of the thermal inputs arising from the land-surface energy balance in absence of water are described in Fig. 8.201.
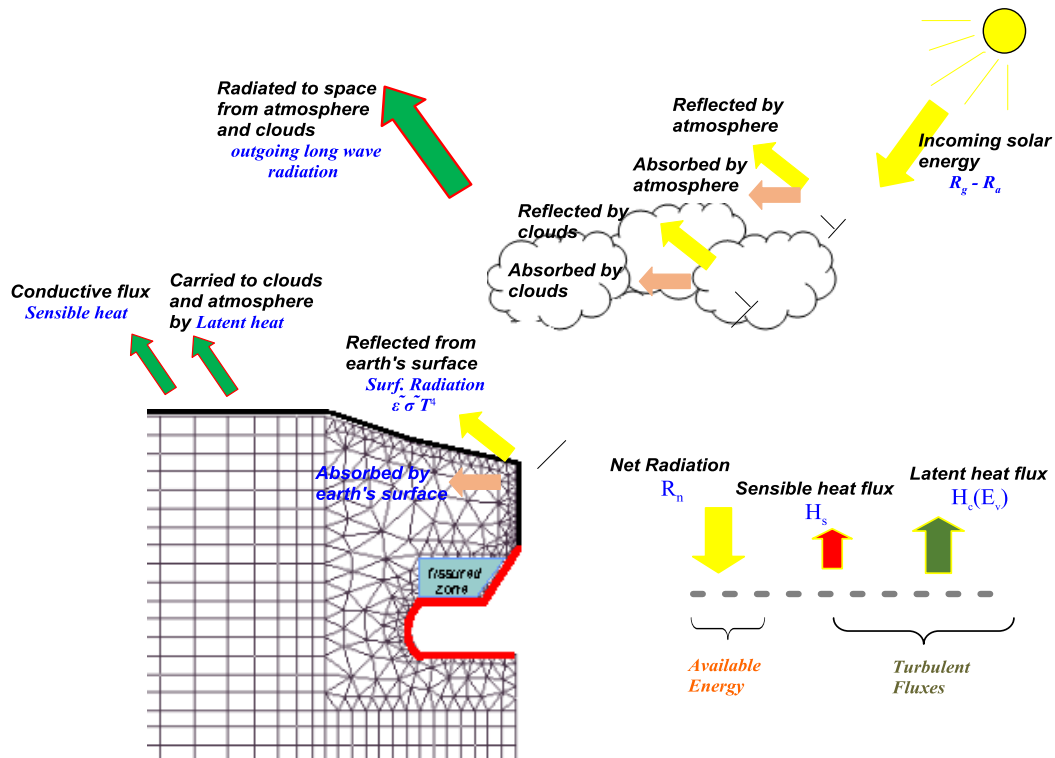
Figure 8.201: Land-surface energy balance over the rock-cliff La Roque Gageac.

It includes:

- Net radiation which is a function of the surface albedo, the atmospheric radiation and the ground emission.
- Sensible heat flux (the heat flowing from one body at higher temperature to another body at lower temperature while they are in direct contact).
- Latent heat flux (the heat energy released by the rock mass during a constant-temperature process).

It is noted once again that because of the dry condition of the rock massif and the negligible variations of gas pressure in relation to the total stress, the latent heat flux in the present case results to be null.

The chapter is organized as follows: firstly the notation and terminology used along the chapter is presented. Secondly, a detailed situation framework of the addressed case and a characterization of the rock-cliff through laboratory tests is presented. Thirdly, the in situ measurements of displacements and temperatures are shown in order to allow a first interpretation of the rock mass behavior. Fourthly, the numerical model of the rock mass "La Roque Gageac" is presented. Fifthly, the modeling results and its comparison with

registered data are shown. Sixthly, a stability analysis of the Cavern roof if addressed and finally, conclusions derived from the study are presented.

8.2) Notation and Terminology

ρ	Unit mass of skeleton
ρ_s	Unit mass of solid phase
ϕ	Porosity
$\dot{u}_i$	Solid skeleton's velocity
E_s	Specific energy of the skeleton
E_l	Specific energy of the liquid phase
E_g	Specific energy of the gas phase
j_{E_s}	Energy flux of the skeleton
j_{E_l}	Energy flux of the liquid phase
j_{E_g}	Energy flux of the gas phase
L	Power input to a porous volume
i_{c_i}	Heat flux vector of the porous medium
$\mathfrak{H}_s$	Entropy of the skeleton
$\mathfrak{H}_l$	Entropy of the liquid phase
$\mathfrak{H}_g$	Entropy of the gas phase
d_s	Specific dissipation of skeleton
σ_{ij}	Stress tensor
ε_{ij}	Strain tensor
α_{ij}	Internal plastic variables
λ	Thermal conductivity

8.3) Geological settings and rock characterization

The village of La Roque Gageac Fig. 8.202 is located on the right bank of the river Dordogne Fig. 8.203, in the heart of Dordogne region at the northwest of Aquitania basin.

It has a population of about 416 inhabitants but is seeds of a large tourist attraction (approx. two million visitors per year) which represents an important aspect of the local economy.

Figure 8.202: (a) View of the Village La Roque Gageac, (b) les Périgords de Dordogne

Figure 8.203: Map and ortho-photography of the study area.

Dordogne region is characterized by a temperate climate with dominant oceanic influence. In winter, it undergoes mountain weather influences due to its proximity to the Central Massif while, in summer, the weather can be subjected to streams of hot air from the Mediterranean. The annual maximum temperatures in the village range between 27ºC and 32ºC and the minimum between -10ºC and -15ºC.

Dordogne river crosses old crystalline rocks in its upper profile formed by deep valleys resulting from erosion of grooves (up to 500m). Then as a result of the tectonic structure of the area, it takes a way towards west where it follows large meanders over jurassic formations of marls and clays. Afterwards in LARG region, it crosses limestone formations belonging to the middle and upper jurassic and its meanders becomes smaller and narrower, Fig. 8.204.

Those formations belong to the coastal depositional features at the toe of Central Massif and as such present generally intercollectors of horizontal permeable and impermeable layers which continuity is laterally interrupted.

Figure 8.204: The Dordogne path.

The rock at LARG consists in its middle and upper part of sandy-limestone rock, divided into three regional zones: (a) a bank of 25m hard sandy limestone at the base of the formation, (b) a soft bed of the same lithology in the middle and (c) 45m of the same hard sandy-limestone with oblique stratification in the upper part. Figure 8.205 shows a geological map of Sarlat-la-Canéda region.

As a result of the tectonic structure and the lateral decompression due to the undergone erosion, the rock massif of LARG is characterized by essentially orthogonal discontinuities parallel and perpendicular to the cliff wall. Such erosion have generated a karstic network which weakens the structure of the massif.
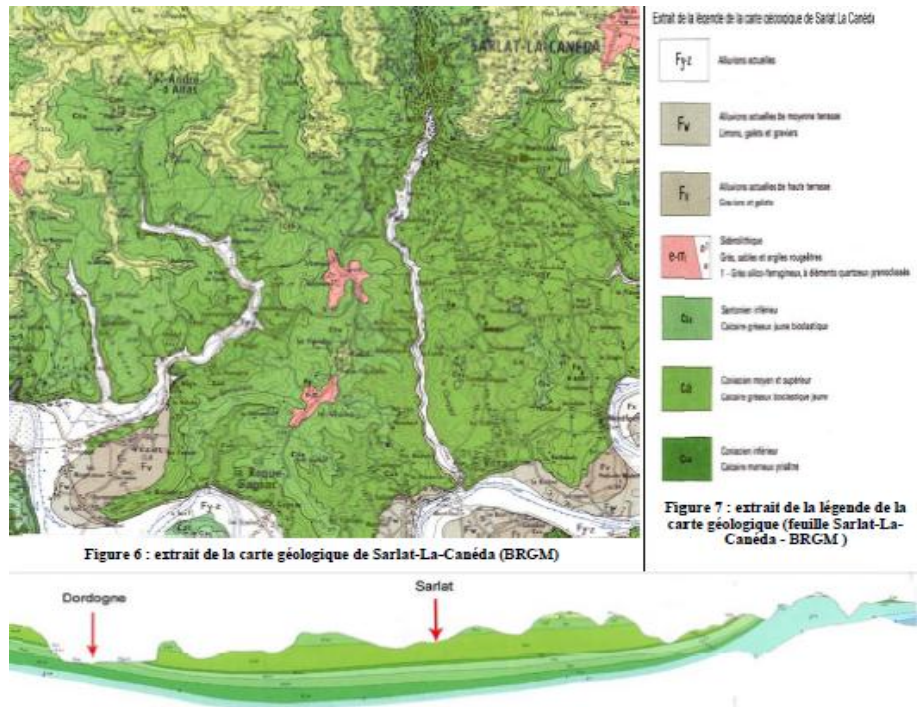
Figure 8.205: Schematic section geologic map (Sarlat-la-Canéda - BRGM)

The cliff at La Roque Gageac has suffered several landslides in recent times with a period of recurrence of about 30 years. In 1957, a part of the cliff of 5000 m^3 fell over the village, Fig. 8.206, and caused the loss of three human lives.

Figure 8.206: Roque Gageac landslide. January - 1957. 5.000 m3 were moved causing the loss of 3 human lives and 12 homes.

451

The landslide occurred in 2010 reported the partial collapse of a troglodyte cavern located on top of the village which removed part of the support of a large block above the cavern, Fig. 8.207. Both, the unstable state of the rock block at the cavern top and the masonry wall which was dragged by the sliding are clearly observed.

Residual risk after the last collapse is controlled by the elements:

- Small blocks fall due to spalling, Fig. 8.207.
- Collapse of the remaining part of the roof.
- Risk of collapse of large blocks over the cavern which may drag the existing debris on top of the village.

Figure 8.207: (a) Blocks capable of slide and require support, (b) Cavern and masonry wall with loose rock blocks

Figure 8.208: Eroded surface of the rock cliff

The cliff rock can be classified as calcareous sandstone of high porosity. Table 8.48 provides a brief description of the rock mass characteristics according to geomechanical classification. Table 8.49 gives experimental values of rock porosities: (a) total (around 18%) and (b) connected. Furthermore, Table 8.50 provides values for elastic parameters, uniaxial shear strength on traction (50 MPa) and wave propagation velocities, obtained in the laboratory.

Table 8.48: Classification of the Rock and the Discontinuities

Property	Value
RQD (rock quality designation)	75% - 90%
Discont. distribution	200mm - 600mm
Nature of Discontinuities	Surface roughness
Water	Dry
RMR (rock mass rating)	71

_____

Table 8.49: Connected and Total porosities

Sample	ϕ_c Connected porosity	ϕ Total porosity	W_{sat} (%)
Mean value	0.112	0.179	4.75

Table 8.50: Results of the blocks tested

Sample	$\rho \left[{}^{kg}/_{m^3} \right]$	$v_p [{}^{m}/_{s}]$	$v_{s_1} [{}^{m}/_{s}]$	$v_{s_2} [{}^{m}/_{s}]$	$\sigma_c [MP_a]$	$\sigma_t [MP_a]$	$E [GP_a]$	v
Mean value	2382	4651	2659	2683	47.37	5.27	42.63	0.14

8.4) In Situ Experimental Program and atmospheric data

Two field campaigns were performed after the rock fell in February 2010. Above the cavern, four crack gages and two horizontal extensometers were installed to follow surface and massif displacements. Each extensometer has a length of 10 m. Measurements of longitudinal (horizontal) displacements were performed at a distance of 6m, 4m and 2m from the cliff wall.

Inside the cavern, a gauge-meter and four crack gages were installed across the main discontinuities delimiting the roof bean. Crack gages were fixed in an horizontal direction measuring the aperture of vertical discontinuity close to the right support of the beam.

Crack gages 2 and 3 were fixed across the horizontal and the vertical discontinuities existing at the vault of the roof. Crack gage 4 measures aperture experienced by the vertical discontinuity in a 45° angle.

Fig. 8.209 shows arrangement of extensometers and crack gages at the cliff. In all the devices measurements were recorded during the period span from July-2010 to March-2011.

_____
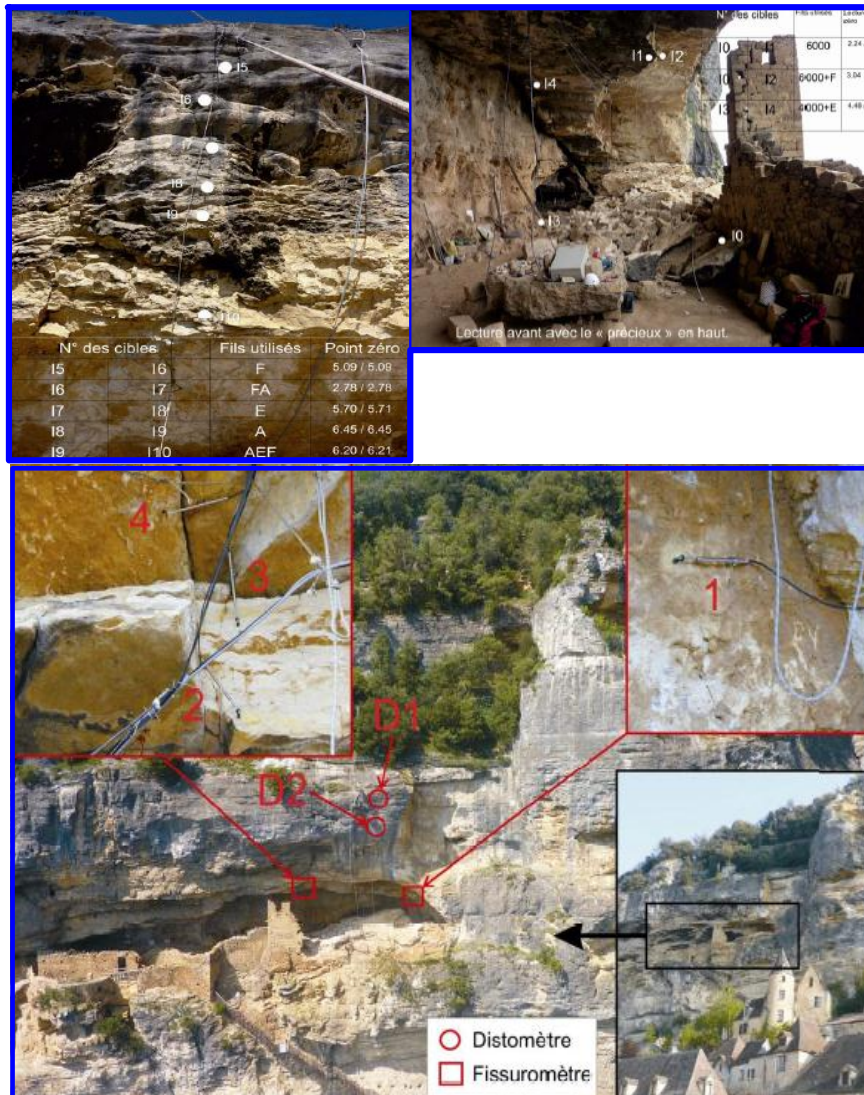
Figure 8.209: Location of Distometers and crack gages at the cliff.

Meteorological data has been available from the meteorological station Sarlat-la-Caneda, located at about 3 km away from the area of interest. To evaluate existence of possible local climate effects, the temperatures recorded at the meteorological station have been compared with those registered on the site by the thermocouples of the extensometers, crack gages and measurements inside the cavern.

Fig. 8.210 presents records of temperature and precipitation registered during the years 2010-2011 at the meteorological station. Temperature and rainfall time series evidence annual fluctuations typical of template climate with low temperatures in winter (typically 5°C) and temperatures around 23°C in summer.
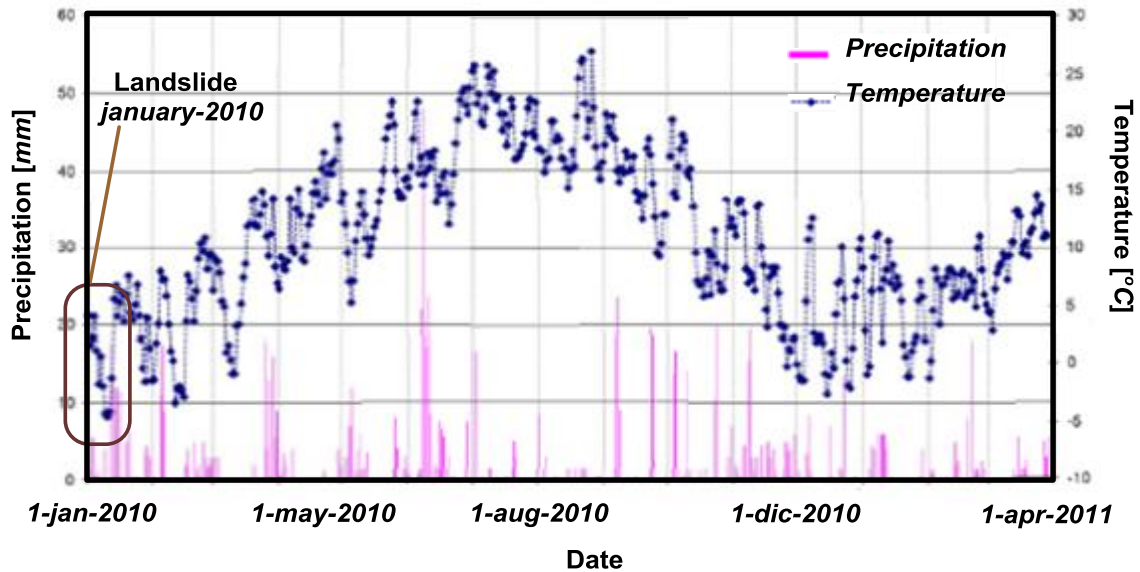
Figure 8.210: Meteorological data recorded at Sarlat-La-Canéda

In winter 2010, after the rock fall, negative temperatures were recorded. Those temperatures were significantly lower in comparison to the temperatures registered in winter 2011.

Fig. 8.211 shows a comparison between local and regional temperatures. They evidence very similar variations validating the use of meteorological data at Sarlat-la-Caneda station to study the cliff response under climatic actions. Lectures of temperature registered at 2m depth from the cliff face and on the cliff face are also compared in Fig. 8.211.

Evolutions and magnitudes recorded shown a delay and a damping in temperature variations. This observations are consistent with the diffusive character of the heat equation, which is defined by its physical constants given by the thermal conductivity and the heat capacity of the rock, Fig. 8.212.

Displacement measurements evidence a similar trend suggesting that they are essentially controlled by the thermal response of the rock, Fig. 8.212.

Crack gages will not be considered in this work since fractures are not represented in the model.
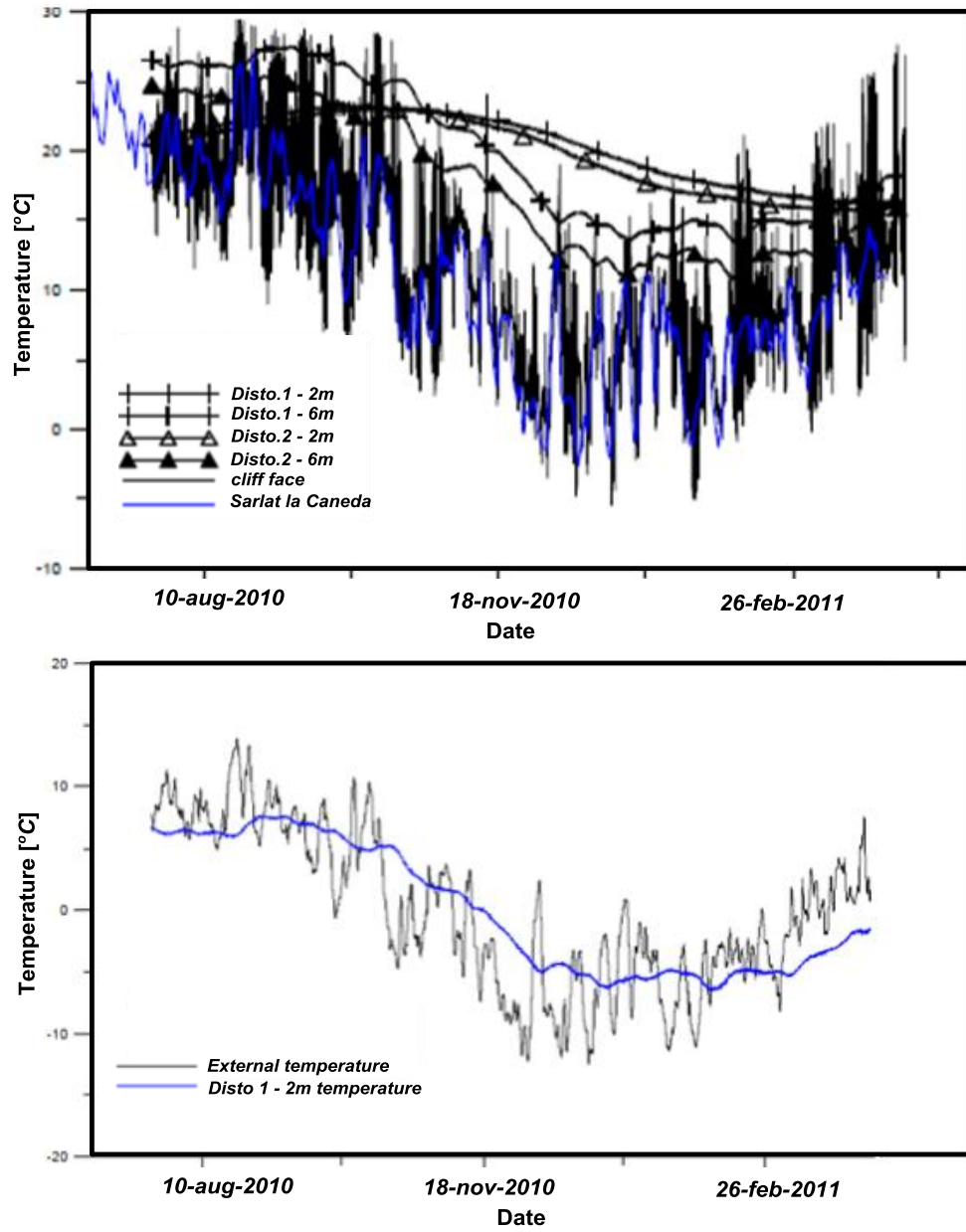
Figure 8.211: Registered temperature at different points of the rock cliff and the temperature recorded at the meteorological station Sarlat la Caneda.
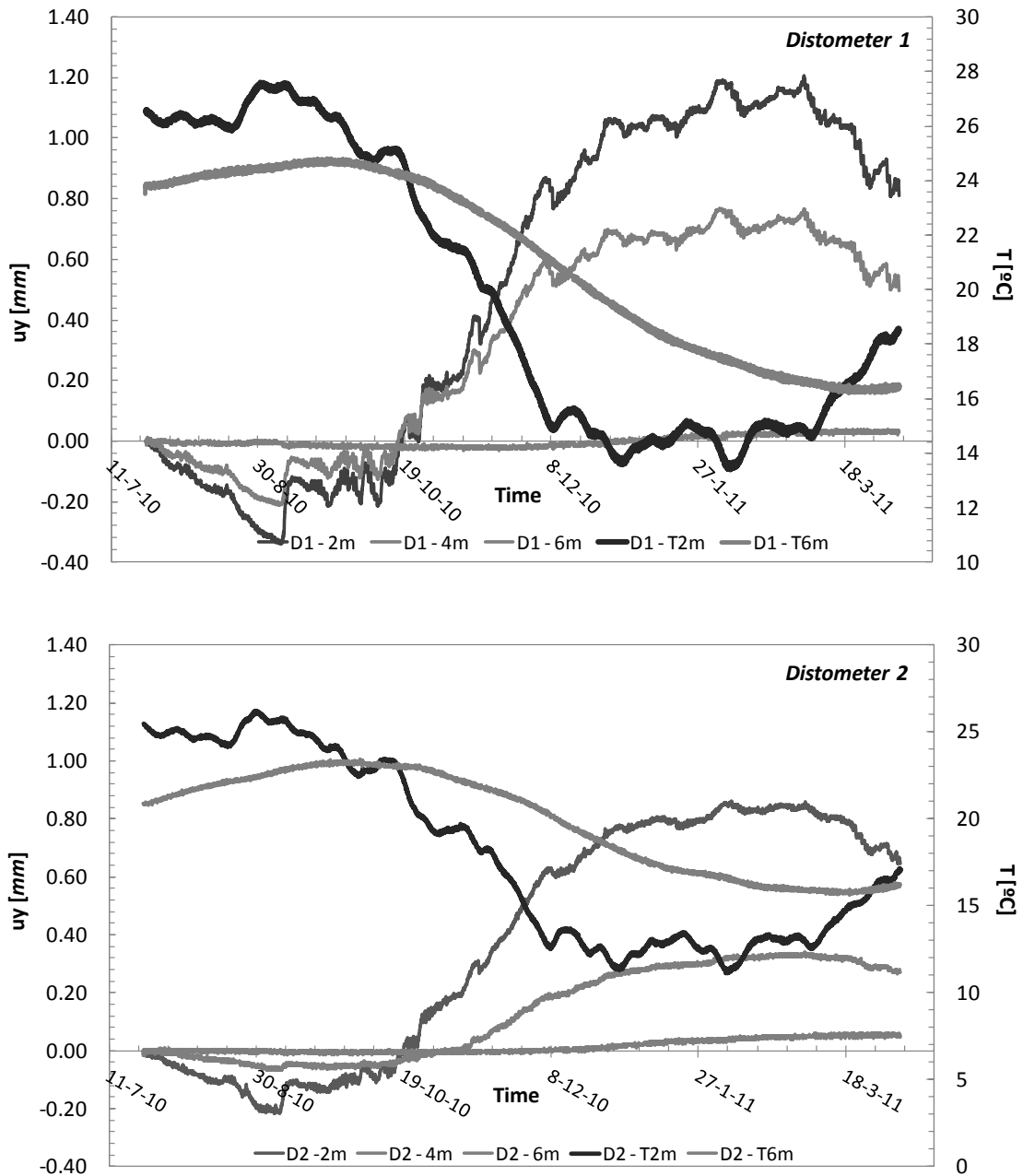
Figure 8.212: Records of Temperature and Displacements obtained at the Distometers.

8.5) Numerical Model for the rock cliff *La Roque Gageac*

In this section, the numerical modeling of the rock-cliff at La Roque Gageac is discussed including the governing equations, geometry, mesh, initial and boundary conditions and material parameters.

458

8.5.1) Derivation of governing equations

8.5.1.1) Thermomechanical approach

In theory of porous media, balance equations are established considering all the phases present in the medium and their interaction.

Ascribing E_s, E_l and E_g as the specific energy of the skeleton, the specific energy of the liquid phase and the specific energy of the gas phase, respectively, the specific internal energy of the porous medium is $E = \widetilde{E}_s + \omega^w E_l + \omega^a E_g$, where $\widetilde{E}$ not only accounts for the solid matrix but also for the interfaces exerted by the interactions between solid, air and liquid.

Thus the local form of the energy balance after application of Gauss divergence theorem is given by the expression (Gens A. , 2010),

$$\frac{\partial}{\partial t}\left(\left(E_s\rho + \phi\rho\sum_{kl} E_i^{kl}\right) + E_l\rho\omega^w S_l\phi + E_g\rho\omega^a(1 - S_l)\phi\right) + \left(j_{\widetilde{E}_s} + j_{E_l} + j_{E_g}\right)_{,j}$$
$$+ f^Q = L - i_{c_{i,j}}$$

(8.1)

where $\rho = \rho_s \cdot (1 - \phi)$ is the dry density of the medium, ω^w and ω^a are the mass fractions of water and air per unit volume of skeleton respectively and E_i^{kl} accounts for the specific interface energy between the phases k and l. Furthermore, *L* is the power input to a porous volume fixed in the space. This power results in the sum of the power input at the boundary and the power exerted by the gravitational forces. The balance Eq. 8.1 states that the sum of the material derivatives of the internal energy equals the power input and the divergence of the heat flux.

Restrictions to the intensive variables defining the energy balance of Eq. 8.1 are introduced invoking the positive character of the dissipation energy of the rock mass (Second law of Thermodynamics). The existence of a state function, the specific entropy $\mathfrak{H}$, is assumed such that the rate of entropy production is non-negative (Houlsby & Puzrin, 2005). Ascribing $\mathfrak{H}_s$, $\mathfrak{H}_l$ and $\mathfrak{H}_g$ as the specific entropy of the skeleton, the specific entropy of pore liquid phase and the specific entropy of pore gas phase, respectively, the specific entropy of the porous medium is $\mathfrak{H} = \widetilde{\mathfrak{H}}_s + \omega^w \mathfrak{H}_l + \omega^a \mathfrak{H}_g$ where $\widetilde{\mathfrak{H}}$ not only accounts for

_____

the entropy of the solid matrix but also for the interface entropies exerted by the interactions between solid, air and liquid.

The convective term of the entropy function of the solid phase $\mathfrak{H}_s$ is given by $j_{\mathfrak{H}_s} = \mathfrak{H}_s \rho \dot{u}$ where $\dot{u}$ is the velocity of the solid phase. Similarly convective terms of the liquid and gas phases are equal to the product of the entropies of each phase by the velocity of the phase.

Fundamental inequality for the entropy is thus:

$$\frac{\partial}{\partial t}\left(\left(\mathfrak{H}_s \rho + \phi\rho \sum_{kl} \mathfrak{H}_i^{kl}\right) + \mathfrak{H}_l \rho\omega^w S_l \phi + \mathfrak{H}_g \rho\omega^a (1 - S_l)\phi\right) + \left(j_{\widetilde{\mathfrak{H}}_s} + j_{\mathfrak{H}_l} + j_{\mathfrak{H}_g}\right)_{,j} \tag{8.2}$$

$$\geq \frac{\partial}{\partial t}\left(\left(\mathfrak{H}_{s_r} \rho + \phi\rho \sum_{kl} \mathfrak{H}_{i_r}^{kl}\right) + \mathfrak{H}_{l_r} \rho\omega^w S_l \phi + \mathfrak{H}_{g_r} \rho\omega^a (1 - S_l)\phi\right)$$

$$+ \left(j_{\widetilde{\mathfrak{H}}_{s_r}} + j_{\mathfrak{H}_{l_r}} + j_{\mathfrak{H}_{g_r}}\right)_{,j} \equiv -\left(\frac{i_{c_i}}{T}\right)_{,j}$$

where the subscript r makes reference to the reversible part of entropy given by the rate of entropy supplied to the porous material element from its surroundings and $\mathfrak{H}_i^{kl}$ accounts for the interface entropy between the phases k and l.

The rate of entropy production within the porous element corresponds to the irreversible part of the entropy. This irreversible part of the entropy defines the dissipation *d* of the porous medium which should satisfy the inequality:

$$d \equiv \begin{aligned} &T\frac{\partial}{\partial t}\left(\left(\mathfrak{H}_{s_i} \rho + \phi\rho \sum_{kl} \mathfrak{H}_{i_i}^{kl}\right) + \mathfrak{H}_{l_i} \rho\omega^w S_l \phi + \mathfrak{H}_{g_i} \rho\omega^a (1 - S_l)\phi\right) + \\ &T\left(j_{\widetilde{\mathfrak{H}}_{si}} + j_{\mathfrak{H}_{li}} + j_{\mathfrak{H}_{gi}}\right)_{,j} \geq 0 \end{aligned} \tag{8.3}$$

$$= \begin{aligned} &T\frac{\partial}{\partial t}\left(\left(\mathfrak{H}_s \rho + \phi\rho \sum_{kl} \mathfrak{H}_i^{kl}\right) + \mathfrak{H}_l \rho\omega^w S_l \phi + \mathfrak{H}_g \rho\omega^a (1 - S_l)\phi\right) + \\ &T\left(j_{\widetilde{\mathfrak{H}}_s} + j_{\mathfrak{H}_l} + j_{\mathfrak{H}_g}\right)_{,j} + i_{c_{k,k}} - \frac{i_{c_k} T_{,k}}{T} \end{aligned}$$

where the subscript i makes reference to the irreversible part of entropy. From Eq. 8.3 the divergence of the thermal flux corresponds to the reversible part of entropy in both the bulk phases and the interfaces in addition to the thermal dissipation:

$$i_{c_{k,k}} = -\left(T\frac{\partial}{\partial t}\left(\left(\mathfrak{H}_{s_r}\rho + \phi\rho\sum_{kl}\mathfrak{H}_{i_r}^{kl}\right) + \mathfrak{H}_{l_r}\rho\omega^w S_l\phi + \mathfrak{H}_{g_r}\rho\omega^a(1-S_l)\phi\right)\right.$$
$$\left. + T\left(j_{\widetilde{\mathfrak{H}}_{s_r}} + j_{\mathfrak{H}_{l_r}} + j_{\mathfrak{H}_{g_r}}\right)_{,j}\right) + \frac{i_{c_k}T_{,k}}{T} \tag{8.4}$$

while the divergence of the heat flux in the solid skeleton $\tilde{\iota}'_{c_{k,k}}$ corresponds to the difference between the total heat flux in the medium $i_{c_{k,k}}$ and the heat flux of the fluid phases in addition to thermal dissipation exerted in those phases:

$$\begin{aligned}
\tilde{\iota}'_{c_{k,k}} &= q_{k,k} + \left(T\left(\frac{\partial}{\partial t}\mathfrak{H}_{l_r}\rho\omega^w S_l\phi + \mathfrak{H}_{g_r}\rho\omega^a(1-S_l)\phi\right) + T\left(j_{\mathfrak{H}_{l_r}} + j_{\mathfrak{H}_{g_r}}\right)_{,j}\right) \\
&\quad - \frac{(i_{c_k}^l + i_{c_k}^g)}{T}T_{,k} \\
&= \underbrace{-\left(T\frac{\partial}{\partial t}\left(\mathfrak{H}_{s_r}\rho + \phi\rho\sum_{kl}\mathfrak{H}_{i_r}^{kl}\right) + Tj_{\widetilde{\mathfrak{H}}_{s_r},j}\right) + \frac{i'_{c_k}T_{,k}}{T}}_{i'_{c_{k,k}}} \tag{8.5}
\end{aligned}$$

Therefore the dissipation of the porous skeleton defined by the difference between the dissipation of the whole medium and the rate of change of entropy production within the bulk fluid phases, reads:

$$\begin{aligned}
d_s &= d - \left(T\frac{\partial}{\partial t}(\mathfrak{H}_{l_i}\rho\omega^w S_l\phi + \mathfrak{H}_{g_i}\rho\omega^a(1-S_l)\phi) + T\left(j_{\mathfrak{H}_{li}} + j_{\mathfrak{H}_{gi}}\right)_{,j}\right) \\
&= T\frac{\partial}{\partial t}\left(\mathfrak{H}_s\rho + \phi\rho\sum_{kl}\mathfrak{H}_i^{kl}\right) + Tj_{\widetilde{\mathfrak{H}}_s,j} + i'_{c_{k,k}} - \frac{i'_{c_k}T_{,k}}{T} \\
&\equiv T\frac{\partial}{\partial t}\left(\mathfrak{H}_{s_i}\rho + \phi\rho\sum_{kl}\mathfrak{H}_{i_i}^{kl}\right) + T\left(j_{\widetilde{\mathfrak{H}}si}\right)_{,j} \geq 0 \tag{8.6}
\end{aligned}$$

In the addressed problem, the hydraulic terms disappear from the specific energy since the rock is considered dry. Moreover under the assumption that the gas pressure remains constant (infinite mobile gas) the specific energy of the porous medium is reduced to $E_s\rho$.

First law of thermodynamics states that the change in energy balance is equal to the mechanical power L plus the divergence of the heat flux. Mechanical power corresponds to the rate of work of tractions in the solid phase $(1-\phi)t_j\dot{u}_j$. Using Green theorem, L can also be stated as $\sigma_{ij}n_i\dot{u}_j$ in terms of the stress tensor and Eq. 8.1 can be re-stated in terms of stresses as:

_____

$$\frac{\partial}{\partial t}(E_s \rho) + \left(j_{E_s}\right)_{,i} + f^Q = \left(\sigma_{ij}\dot{u}_j - i_{c_i}\right)_{,i} + \rho\dot{u}_i g_i \tag{8.7}$$

by use of the material derivative the local statement of the mass conservation law is

$\dot{\rho} + (\rho\dot{u}_i)_{,i} = \dot{\rho} + \rho_{,i}\dot{u}_i + \rho\dot{u}_{i,i} = \frac{d\rho}{dt} + \rho\dot{u}_{i,i} = 0$, which established a relation between the

rate of change of the dry density and the dilation rate of the rock mass. In addition, recognizing that the energy flux of the solid phase is given by $j_{E_s} = E_s\rho\dot{u}_j$, the last equation can be equivalently written as,

$$\rho\frac{dE_s}{dt} + f^Q = \underbrace{\left(\sigma_{ij,i} + \rho g_i \delta_{ij}\right)}_{\text{translation}}\dot{u}_j + \sigma_{ij}\dot{u}_{j,i} - i'_{c_{i,i}} \tag{8.8}$$

As translation movement does not produce change in specific energy: $\sigma_{ij,i} + \rho g_i \delta_{ij} = 0$. Last equation state the momentum balance of the medium. In addition, assuming that small strain develops at the rock mass it can be readily seen that $\sigma_{ij}\dot{u}_{j,i} = \sigma_{ij}\dot{\varepsilon}_{ij}$.

Under the same assumption of dry condition of the rock and constant gas pressure, the skeleton dissipation is reduced to:

$$\begin{aligned} d_s &\equiv T\frac{\partial}{\partial t}\left(\rho\left(\mathfrak{H}_s - \mathfrak{H}_{s_r}\right)\right) + T\left(j_{\mathfrak{H}_s} - j_{\mathfrak{H}_{s_r}}\right)_{,j} \geq 0 \\ &= T\frac{\partial}{\partial t}(\mathfrak{H}_s\rho) + T\left(j_{\mathfrak{H}_s}\right)_{,j} + i'_{c_{i,i}} - \frac{i'_{c_i}T_{,i}}{T} \end{aligned} \tag{8.9}$$

Combining the equations 8.8 and 8.9 leads, after mathematical manipulation, to:

$$\begin{aligned} \frac{dE_s}{dt} + d_s + f^Q &= \frac{1}{\rho}\sigma_{ij}\dot{\varepsilon}_{ij} + T\frac{d\mathfrak{H}_s}{dt} - \frac{1}{\rho}\frac{i'_{c_i}T_{,j}}{T} \\ &= \frac{1}{\rho}\sigma_{ij}\dot{\varepsilon}_{ij} + T\frac{d\mathfrak{H}_s}{dt} - \frac{1}{\rho}\eta_i T_{,j} \end{aligned} \tag{8.10}$$

where $\eta_i = \frac{i'_{c_i}}{T}$. The left hand side of Eq. 8.9 contains the stored terms $\left(\frac{dE_s}{dt}\right)$ and the

dissipated term (d_s).

Under the hypothesis that the specific energy is a function of the strains, the entropy $\mathfrak{H}_s$ and certain internal variables α_{ij}, it is $E_s = E_s(\varepsilon_{ij}, \alpha_{ij}, \mathfrak{H}_s)$, the material derivative can be developed as,

$$\frac{dE_s}{dt} = \frac{\partial E_s}{\partial\varepsilon_{ij}}\dot{\varepsilon}_{ij} + \frac{\partial E_s}{\partial\alpha_{ij}}\dot{\alpha}_{ij} + \frac{\partial E_s}{\partial\mathfrak{H}_s}\frac{d\mathfrak{H}_s}{dt} \tag{8.11}$$

_____

On the other hand, the dissipation function is also postulated as a function of the same state variables, the rate of change of the internal variables α_{ij} and a function of the fluxes: $d_s = d_s(\varepsilon_{ij}, \alpha_{ij}, \mathfrak{H}_s, \eta_i, \dot\alpha_{ij})$.

Due to the characteristics of the dissipation function for modeling rate independent materials: (a) homogeneousness and (b) degree one type, it is possible to write:

$$d_s = \frac{\partial d_s}{\partial \dot\alpha_{ij}} \dot\alpha_{ij} + \frac{\partial d_s}{\partial \eta_i} \eta_i \tag{8.12}$$

Substitution of equations 8.11 and 8.12 in the Eq. 8.10 gives:

$$\frac{\partial E_s}{\partial \varepsilon_{ij}} \dot\varepsilon_{ij} + \frac{\partial E_s}{\partial \alpha_{ij}} \dot\alpha_{ij} + \frac{\partial E_s}{\partial \mathfrak{H}_s} \frac{d\mathfrak{H}_s}{dt} + \frac{\partial d_s}{\partial \dot\alpha_{ij}} \dot\alpha_{ij} + \frac{\partial d_s}{\partial \eta_i} \eta_i + f^Q = \frac{1}{\rho} \sigma_{ij} \dot u_{i,j} + T \frac{d\mathfrak{H}_s}{dt} - \frac{1}{\rho} \eta_i T_{,j} \tag{8.13}$$

or by collecting terms:

$$\left(\frac{\partial E_s}{\partial \varepsilon_{ij}} - \frac{1}{\rho}\sigma_{ij}\right)\dot\varepsilon_{ij} + \left(\frac{\partial E_s}{\partial \alpha_{ij}} + \frac{\partial d_s}{\partial \dot\alpha_{ij}}\right)\dot\alpha_{ij} + \left(\frac{\partial E_s}{\partial \mathfrak{H}_s} - T\right)\frac{d\mathfrak{H}_s}{dt} + \left(\frac{\partial d_s}{\partial \eta_i} + \frac{1}{\rho}T_{,j}\right)\eta_i + f^Q$$
$$= 0 \tag{8.14}$$

Equation 8.13 should be satisfied for any combination of $\dot\varepsilon_{ij}$, $\dot\alpha_{ij}$, $\frac{d\mathfrak{H}_s}{dt}$, η_i, and since all these quantities are independent of each other then each term has to be equal to zero independently. Finally, the constitutive equations for the porous medium obtained from Eq. 8.14 are:

$$\frac{1}{\rho}\sigma_{ij} = \frac{\partial E_s}{\partial \varepsilon_{ij}}; \quad T = \frac{\partial E_s}{\partial \mathfrak{H}_s}; \quad -\frac{\partial d_s}{\partial \dot\alpha_{ij}}(\equiv x_{ij}) = \frac{\partial E_s}{\partial \alpha_{ij}}; \quad -\frac{1}{\rho}T_{,j} = \frac{\partial d_s}{\partial \eta_i} \tag{8.15}$$

where Eq. 8.15a is the hyperelastic constitutive law, Eq. 8.15b is the constitutive law defining the temperature of the medium, Eq. 8.15c is the hardening law (and defines the Ziegler's orthogonality rule) and Eq. 8.15d is the Fourier heat conduction law.

If the dependency $d_s(\eta_i)$ is assumed of the form:

$$d_s(\eta_i) \equiv d_s\left(\frac{i_{c_i}}{T}\right) = \frac{1}{\lambda}\frac{i_{c_i}^2}{T} \underset{\text{then}}{\Longrightarrow} \quad \rho\frac{\partial d_s}{\partial \eta_i} = -T_{,j} = \frac{i_{c_i}}{\lambda} \tag{8.16}$$

Eq. 8.16b is the Fourier's law for an isotropic medium.

_____

8.5.1.2) Constitutive equations

From the previous constitutive equations the most relevant is the one corresponding to the solid phase.

Modelling the solid skeleton (rocky mass) response under climatic actions requires having at hand a thermo-hydro-mechanical model suitable to provide objective numerical solutions. In this regard, the formulation of a constitutive model complying with hyperporoplastic principles must be derived from energy potentials, the internal energy of the solid skeleton E_s and the dissipation function d_s of this phase, as has been seen in chapters 3 and 4.

The internal energy $E_s(\varepsilon_{ij}, \alpha_{ij}, \mathfrak{H}_s)$ being a function of the specific entropy is rarely used and it is often replaced by its complementary function: the Helmholtz energy $f_s(\varepsilon_{ij}, \alpha_{ij}, T) = E_s - T\mathfrak{H}_s$.

Thus the elastic response of the rock mass is given by the expression:

$$f_s(\varepsilon_p, \varepsilon_q, T) = \left(\frac{K\varepsilon_p}{2} + p_o - K\alpha_T \cdot (T - T_i)\right) \cdot \varepsilon_p + \frac{3}{2}G \cdot \varepsilon_q^2 \tag{8.17}$$

where K is the bulk modulus of the rocky mass, G is the shear modulus, α_T is the dilation coefficient and p_o is the initial mean stress.

From energy viewpoint, and as a consequence of the non-dependency of the energy function Eq. 8.17 on the plastic internal variable α_{ij}, the entire generated plastic work will be dissipated $L_s^p = d_s(\dot\alpha_{ij})$.

From Maxwell's equation Eq. 8.15a the expressions for mean stress and deviatoric stress are:

$$p = \frac{\partial f_s}{\partial \varepsilon_p} = K\varepsilon_p + p_o - K\alpha_T \cdot (T - T_i) \tag{8.18}$$

$$q = \frac{\partial f_s}{\partial \varepsilon_q} = 3G\varepsilon_q$$

_____

The model is completed by defining the dissipation function for modeling the inelastic response of the cliff. The Drucker-Prager model sensitivity to thermal effects described in chapter 4 is used to this end.

For the sake of simplicity, the expression for the smoothed yield surface as well as a picture of the yield function are presented here.

$$f^y = \left(\left(\frac{J}{r_c} \right)^2 + \vartheta^2 \right)^{1/2} - Bx_p - (Mp + a(c')) \qquad (8.19)$$
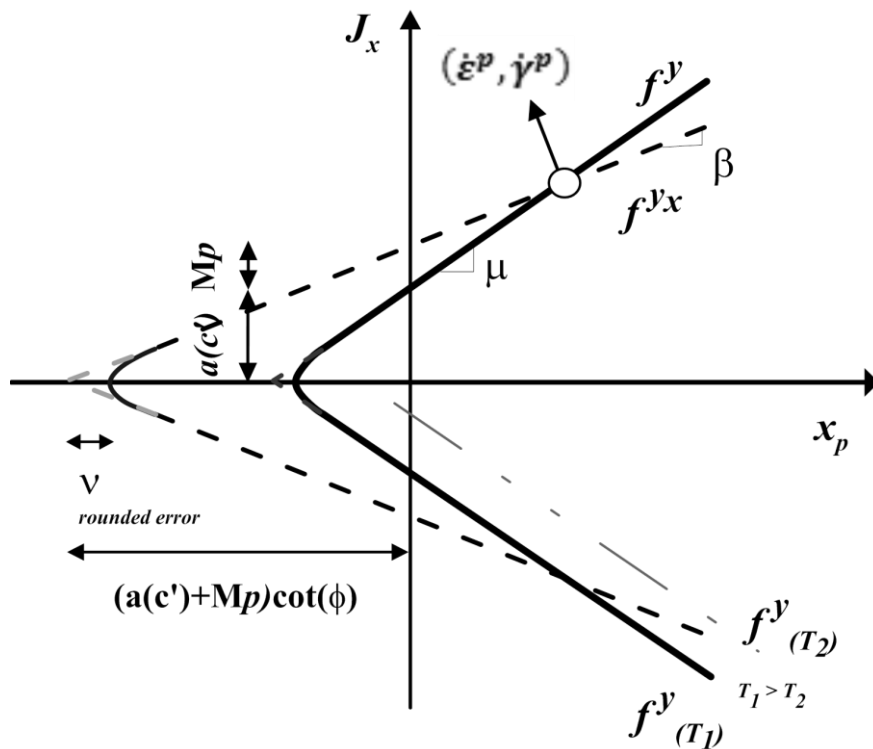
Figure 8.213: Geometrical interpretation of the model's terms. Hyperbolic smoothing at the p-q plane. Yield surface sensibility for two reference temperatures.

8.5.2) Geometry, Mesh, Initial and Boundary Conditions

Figure 8.214a and 8.214b present a picture of the cavern and a profile of the cliff as defined in the remediation project. Fig. 8.214c shows the geometry and dimensions considered in the simulation.

Spatial discretization was performed using linear triangles and quadrilateral elements, resulting in a mesh with 654 nodes, Fig. 8.214d.
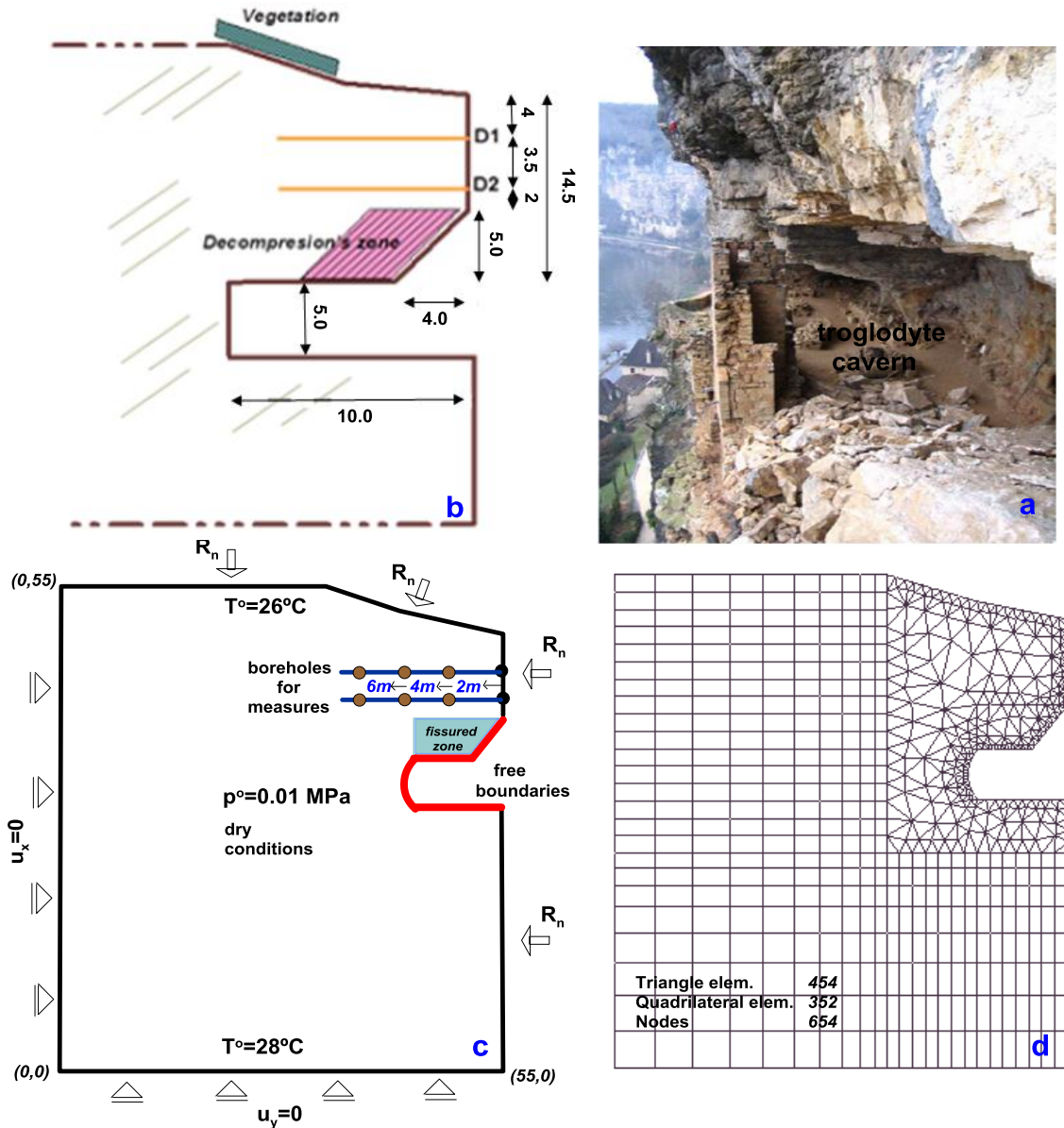
Figure 8.214: a)Profile of the rock cliff, (b) Image of the cavern and the rock mass over the cavern roof, (c) Initial and Boundary conditions of the numerical model, (d) finite element mesh used in the discretization of the rock.

As far as boundary conditions is concerned, normal displacements have been fixed at the bottom and the left side of the rock profile, while cliff's top and right face have been left free of restrictions.

_____

A temperature condition has been applied at the bent wall of the cliff just above the cavern. Inside the cavern only temperature variation was applied. It is considered that there is no radiation nearly this zone.

A temperature equal to 26.4°C was set initially in all the mesh. The initial stress distribution derives from an equilibrium stage performed before the onset of the analysis.

Table 8.51 summarizes the time intervals and initial and boundary conditions assumed in the modeling of the rock-cliff *La Roque Gageac*.

Table 8.51: Intervals, Initial and Boundary conditions considered at the rock-cliff simulation.

Interval	Time [Days]	Initial and Boundary Conditions		
1	-1-0	$\sigma^0 = 0.01$ MPa	In all the mesh	
		$\phi^0 = 0.18$	In all the mesh, except for those elements at the decompression zone.	
		$\phi_d^0 = 0.22$	In all the elements at the decompression zone	
		$T^0 = 26.4\,°C$	In all the mesh	
		Lower bound: $u_y = 0$ $T = 28\,°C$	*Left bound*: $u_x = 0$	
2	0-2168	*Lower bound*: $u_y = 0$ $T = 28\,°C$	*Left bound*: $u_x = 0$	*Cliff -face:* atmospheric load: *root_atm.dat* *Cavern:* Atmospheric Temperature

Table 8.52 summarizes the atmospheric constants used for the parameterization of energy fluxes. A bare ground has been assumed (free of vegetation). Radiation is computed as function of atmospheric temperature, sun position and cloud index provided by Sarlat-la-Caneda station.

Table 8.52: Table of atmospheric constants used in the simulation

Latitude	0.7821
t_{autumn} (s)	0.2255e8
t_{noon} (s)	0.4320e5
H_{main}^{rough} (m)	0.02
H_{stable}^{layer} (m)	1.5
$\emptyset_{factor}$ (kg/m3)	1.00E+00
ρ_g^{atm} (kg/m3)	1.2
$albedo_{dry}$	0.2
$albedo_{wet}$	0.2
rad_{factor}	1
$veg_{fraction}$	0

8.5.3) Material Parameters

Table 8.53 summarizes thermomechanical constitutive law and material properties used in the simulation. The parameters for the interior-point integration are also presented in the table. Table 8.54 presents thermal and phase data parameters used in the modeling.

Output points are indicated in Table 8.55. Points P0-P3 at Disto1 and Disto2 are control points located at different depths along the extensometers 1 and 2, respectively. Points P0-P2 at DZone are control points located in the decompression zone above the cavern.

_____

Table 8.53: Mechanical parameters of the rocky material used to model La Roque Gageac

MECHANICAL DATA		
hyper-thermoplastic model		
Elastic Parameters		$f_s^g(\varepsilon_p, \varepsilon_q, T) = \left(\dfrac{K\varepsilon_p}{2} + p_o - K\alpha_T\right.$
κ	6.1714e-7	
ν	0.14	$\left. \cdot (T - T_i)\right) \cdot \varepsilon_p + \dfrac{3}{2}G$
p_0 [MPa]	0.01	
Thermal Parameters		$\cdot \varepsilon_q^2$
$\alpha_T \left[\dfrac{1}{°C}\right]$	1e-5	
T_0 [°C]	$\equiv T_{initial}$ at the corresponding point	
Plastic Parameters		$f^y = \left(\left(\dfrac{J}{r_c}\right)^2 + \vartheta^2\right)^{1/2} - Bx_p$
r_{c0} [MPa]	40.2	
ϕ [°]	30	$- \left(Mp + a(c')\right)$
c_0 [MPa]	0.065	
ψ [°]	14	
$\gamma_T \left[\dfrac{1}{°C}\right]$	2.46e-3	$r_c = r_{c0} - \gamma_T(T - T_0)$
η [−]	1e-3	
Smoothing Parameters		
ϑ_0 [−]	0.01	
Integration Parameters		
Algorithm index	3 (interior point algorithm)	
Newton tol.	1e-6	
Line_search param. 1	1e-2	
Line_search param. 2	0.1	
Max. iter. barrier	40	
Max. iter. Newton	50	
Max. Line_search iter.	2	

_____

Table 8.54: Thermal and Phase parameters used to model La Roque Gageac

THERMAL AND PHASE DATA		
Conductive Flux of Heat (Fourier's law) $\lambda_{\mathrm{dry}}\ [WmK^{-1}]$	3.0	$\boldsymbol{i}_c = -\lambda\nabla T$
Solid Phase (Density) $C_s\ [Jk_g{}^{-1}K^{-1}]$	800	
$\alpha_T\left[\dfrac{1}{^\circ\mathrm{C}}\right]$	1e-5	
$\rho_s\left[k_g m^{-3}\right]$	2382	

Table 8.55: Control points to evaluate the rock mass response

			coord. X	coord. Y
		CONTROL POINTS		
	Disto. 1	P0	50	46
		P1	48	46
		P2	46	46
		P3	44	46
	Disto. 2	P0	50	42.5
		P1	48	42.5
		P2	46	42.5
		P3	44	42.5
	D. Zone	P0	48	38
		P1	46	38
		P2	44	38

8.6)   Modelling Results

At first instance a thermal analysis has been performed aiming to calibrate rock massif temperature. Then a thermo-mechanical analysis is addressed considering the rock as elastic. This assumption aims to get a preliminary assessment of rock displacement.

Finally, a thermo-mechanical model considering an elastoplastic model for the rock has been approached. It aims to provide further insights into irreversible response of rock massif and its consequences in terms of stability.

For the sake of reducing computing time only monthly time of atmospheric series have been applied. It is believe that the overall rock stability is essentially influenced by relatively long term variation.

8.6.1) Thermal analysis

Two models with different thermal coefficients, thermal conductivity and specific heat has been tested. Table 8.56 summarizes the parameters used for each model.

Table 8.56: Parameters used in the preliminary models of La Roque Gageac

	Thermal coefficient $\alpha[°C^{-1}]$	Thermal Conductivity of the dry Rock media λ_{dry} [Wm/K]	Solid phase specific Heat C_s [J/kg/K]
MODEL *A*	1e-5	2.3	800
MODEL *B*	3e-5	2.5	1000

Results have been compared with in situ measurements. It is noted that in all cases, results belong to the fifth cycle of the total of six cycles which corresponds to outputs in stationary conditions.

Fig. 8.215 shows a comparison of temperature at different points of the rock mass: (a) temperature measured at Sarlat la Caneda meteorological station, which corresponds to the temperature prescribed at the rock-atmosphere interface, (b) temperature measured in situ on the rock face, exposed to radiation, in extensometer D2, (c) temperature measured at the rock surface inside the cavern (crack gage F1), (d) temperatures measured at 2m and 6m from the rock face at extensometers D1 and D2 and (e) computed temperatures at the same points for both model A and model B.

It is observe that results from model A evidence an acceptable agreement in terms of monthly variation. Model A has been selected as the reference thermal model.
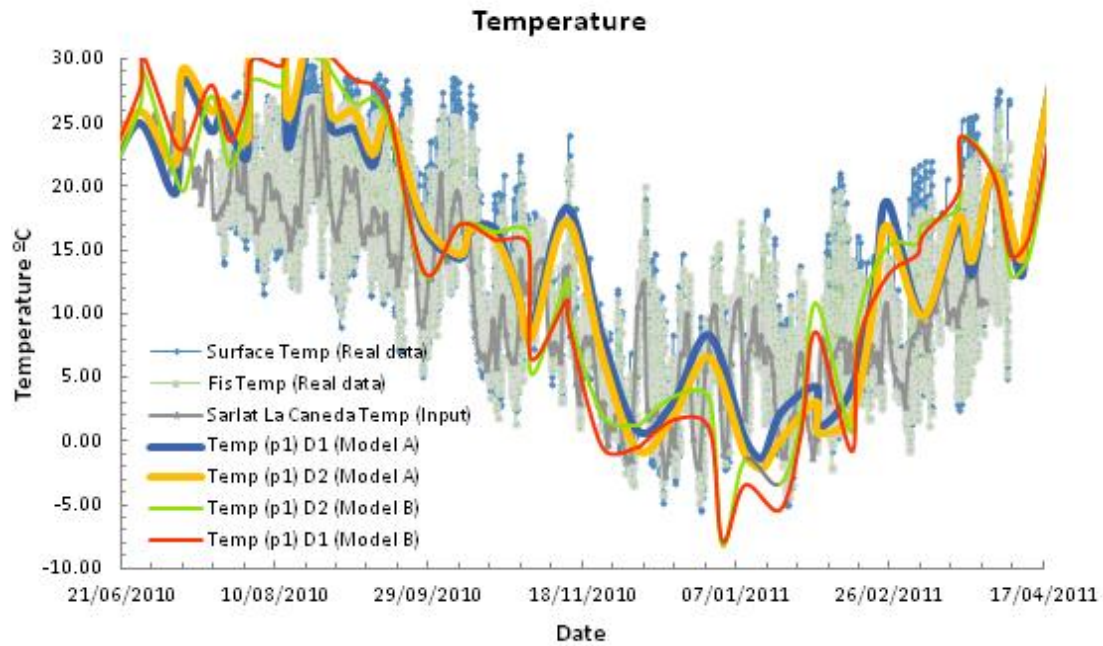
Figure 8.215: Temperature Evolution: (a) measure at the rock mass face, (b) measure at the crack gage, (c) registered at the meteorological station Sarlat la Caneda and (d) resulting from the numerical model at point p1 for the Distometers D1-D2.

Once the model was calibrated regarding the thermal response, the thermo-mechanical calibration was started. Several parameters were tested during the calibration. Evolution of temperature and displacement at different points obtained from the model A are shown below.

8.6.2)   Results of the Elastic Model

Calibration of elastic parameters has been carried out through a sensitivity analysis based on the registered displacements at extensometers D1 and D2 in the field campaign.

At first instance it had been assumed that rock does not plastify at these depths of registration. Then, this assumption has been further confirmed by the elastoplastic analysis.

Figures 8.216 and 8.217 show evolutions of temperature and displacement obtained from the numerical model and compared with in situ measurements.

Results evidence a good agreement between computation and measurements for both temperature and displacement. This fact points out that daily variations of temperature

does not control significantly the variables at depth higher than 2m which validates the atmospheric input considered for the problem.

A clear seasonal variation pattern is observed with negative relative displacements (extension) during summer and with positive relative displacements (compression) during winter.

Curves also evidence the clear diffusive character of heat (and the heat-induced displacement) in the massif. Points located far from the rock-atmosphere boundary experiment an attenuation in magnitude and a shift in time.

Fig. 8.218 complete the overall view of displacements suffered by the rock massif in the near zone of the cliff surface: (a) at 1m depth and (b) at 2m depth from the rock-atmosphere boundary.
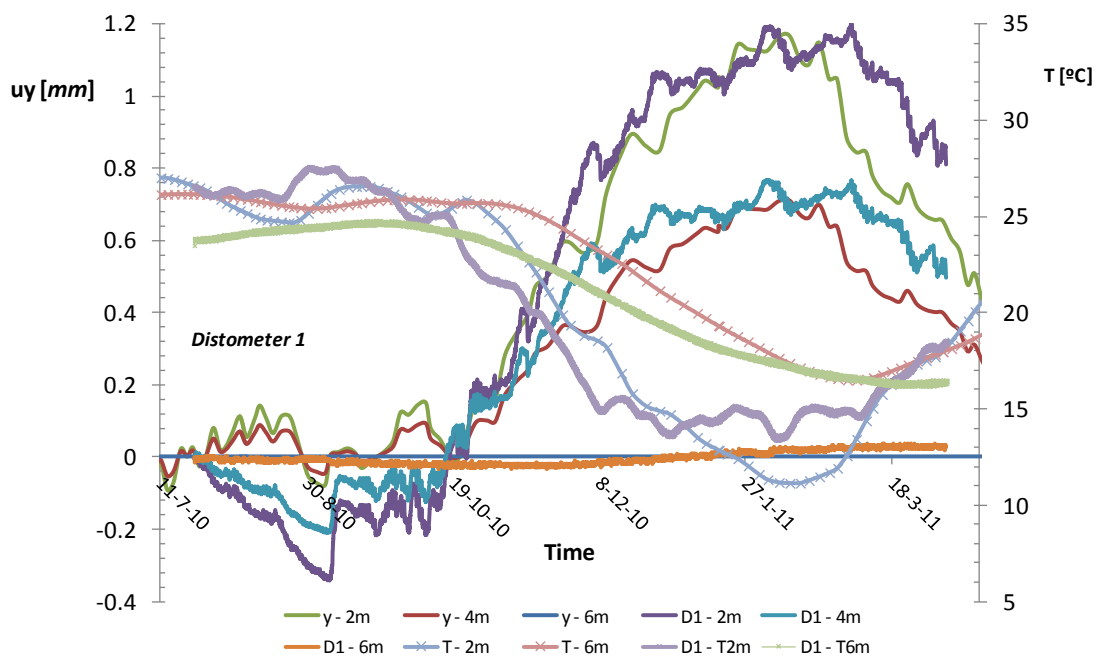
Figure 8.216: Evolution of Displacement and Temperature obtained in the distometer D1. Responses at 2m-4m and 6m depth. Comparison with registered data.
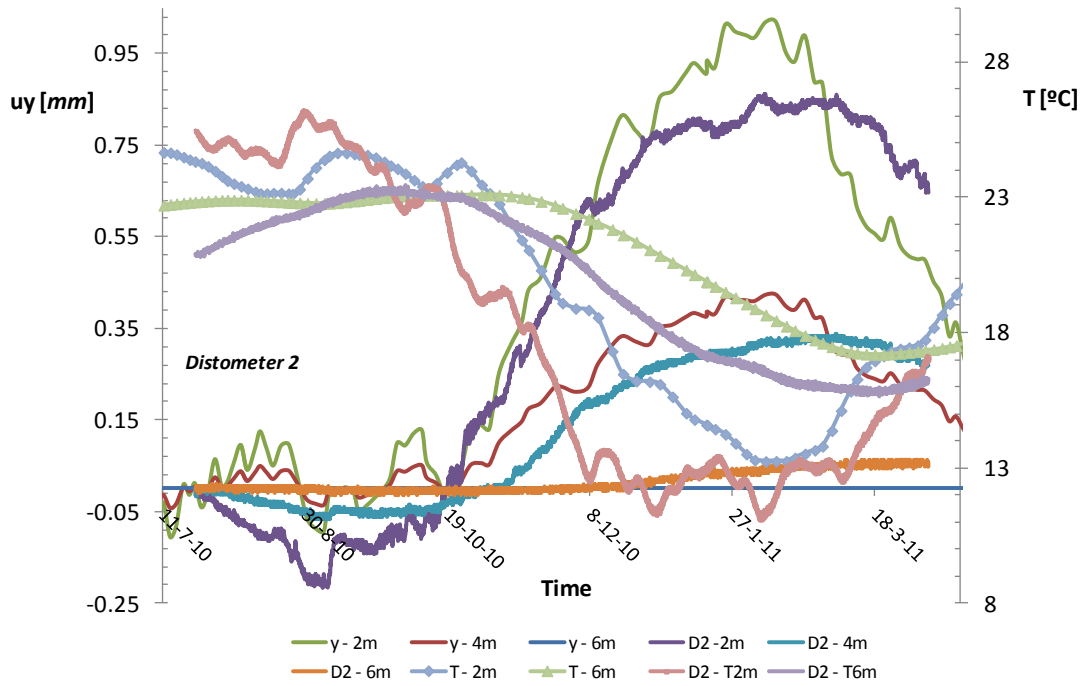
Figure 8.217: Evolution of Displacement and Temperature obtained in the distometer D2. Responses at 2m-4m and 6m depth. Comparison with registered data.
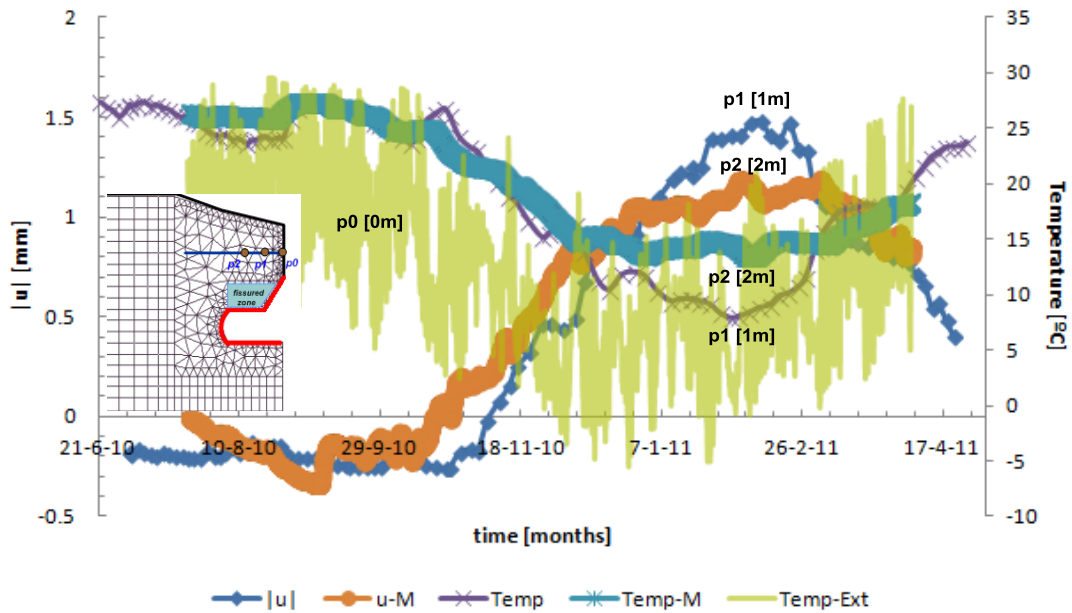
Figure 8.218: Temperature (Temp-M) and displacements (u-M) measures. Obtained results from the numerical simulations at points p0, p1, p2.

474

_____

Finally, Fig. 8.219 shows evolutions of horizontal heat flux and temperature at 2m depth from the cliff face in extensometers D1 and D2.

Positive horizontal heat fluxes (outflow) take place in winter when rock temperature is higher than air temperature. Conversely, negative horizontal heat fluxes (inflow) can be observed in summer when solar radiation is higher at the massif face.
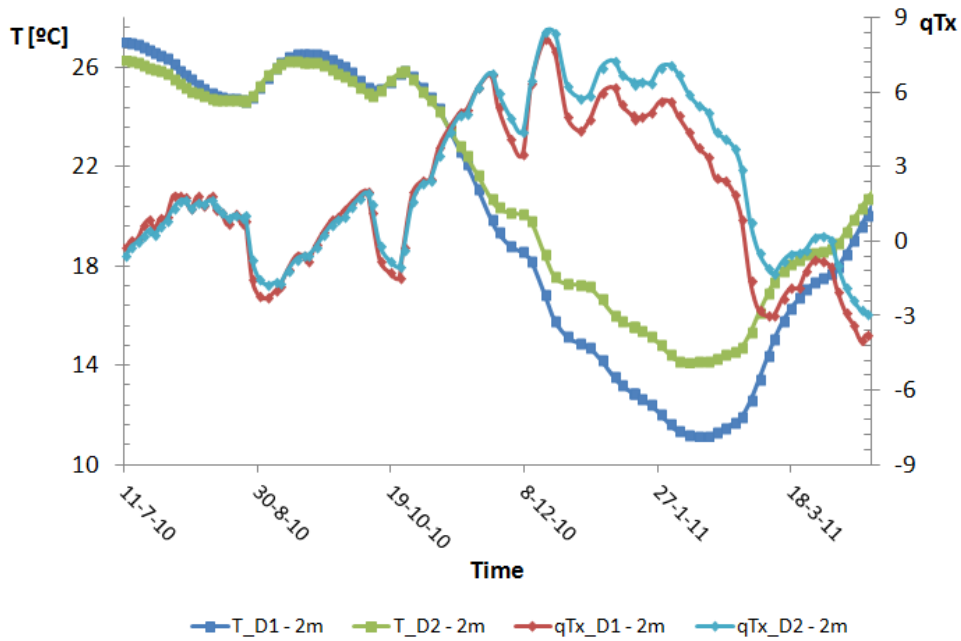
Figure 8.219: Evolution of horizontal heat flux and Temperature at extensometers D1-D2.

Fig. 8.220 shows evolutions of horizontal heat flux and temperature in the cavern of the massif where radiation does not have sensible effects.
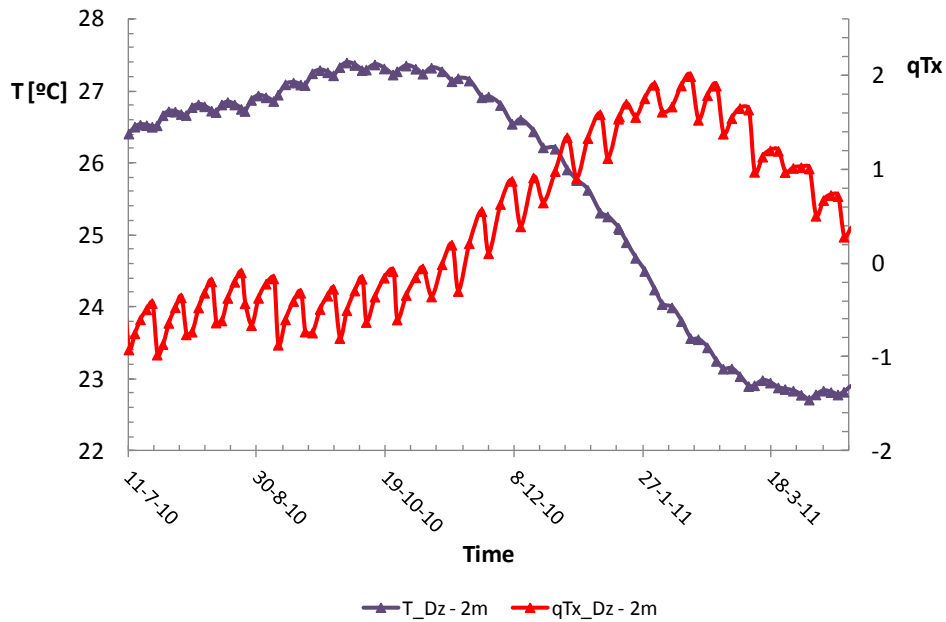
Figure 8.220: Evolution of horizontal heat flux and Temperature at point of the decompression zone.

Variations follow quite well the temperature of the air in the cavern, at the same time that heat fluxes point outwards and inwards in correspondence with seasons of summer and winter, respectively.

A series of isochrones of the most relevant variables governing the porous media response are now presented. Those contours are shown at two different times of maximum (11/07/2010) and minimum (11/02/2011) external temperature.

Figures 8.221 and 8.222 show vectors of heat flux, isochrones of porosity and stress invariants deviatoric and mean stress, obtained during two different seasons: (a) summer and (b) winter.

Fig. 8.221 shows that heat flux vectors point to the interior of the rock mass evidencing a thermal gradient toward the interior of the rock. Isochrones of stress invariants show that the highest values are obtained at the upper right corner of the section.

Fig. 8.222 shows that heat flux vectors point to the exterior of the rock mass determining a thermal gradient toward the exterior of the rock. The highest stresses are observed at the upper right corner of the section.

The mentioned stress concentration could overcome the yield surface of an elastoplastic computation. This fact will be studied in the next section.

Figure 8.223 shows contours of temperature and vertical displacement in the rock cliff profile. It can be seen that contractions are developed at the rock face in accordance with maximum external temperatures while extensions are observed at the rock face in accordance with minimum external temperatures.
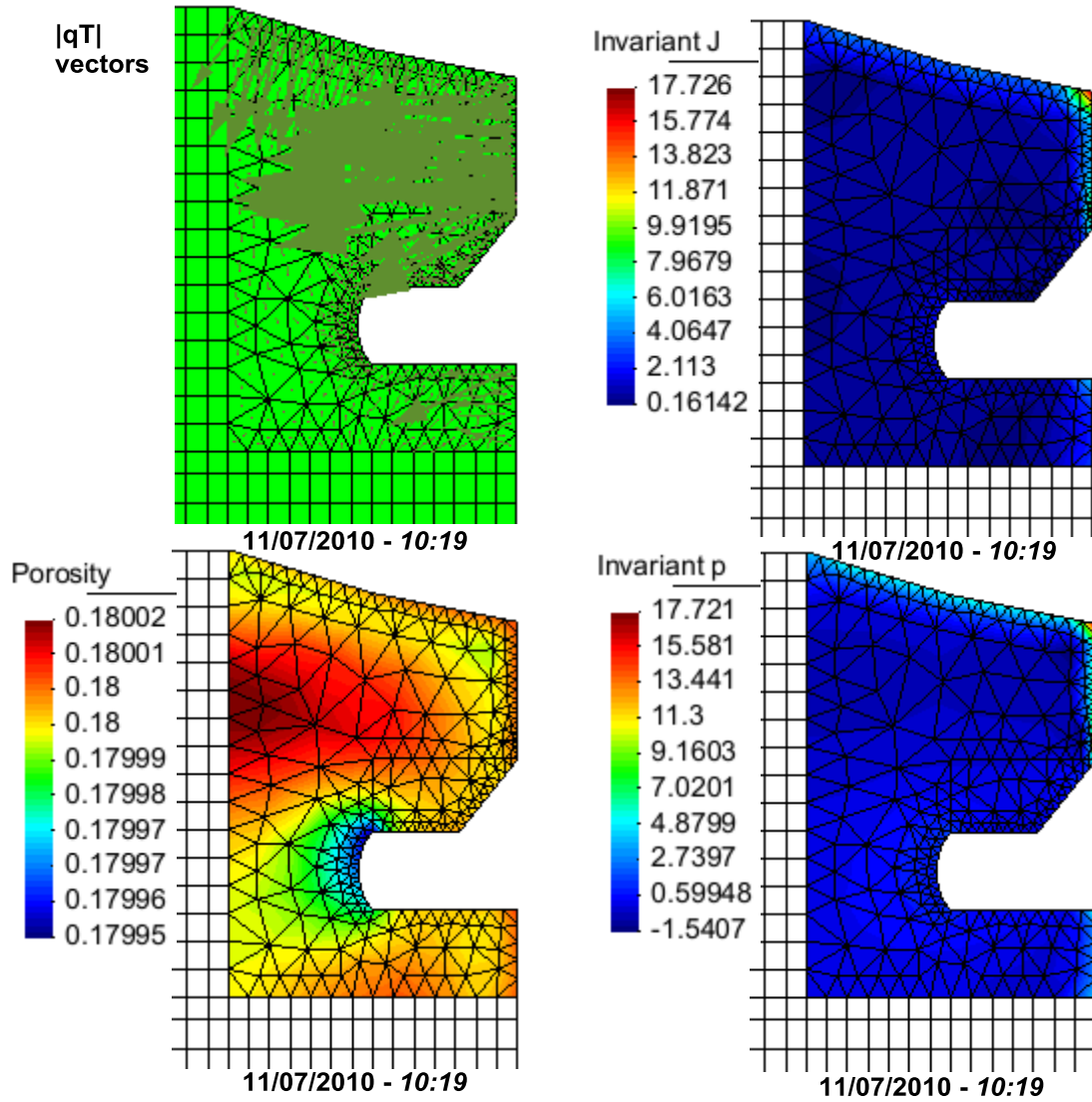
Figure 8.221: Contours of stress invariants, porosity and heat flux vectors at the most exposed section of the rock mass. Contours at a time of maximum temperature registered at the distometers.

477
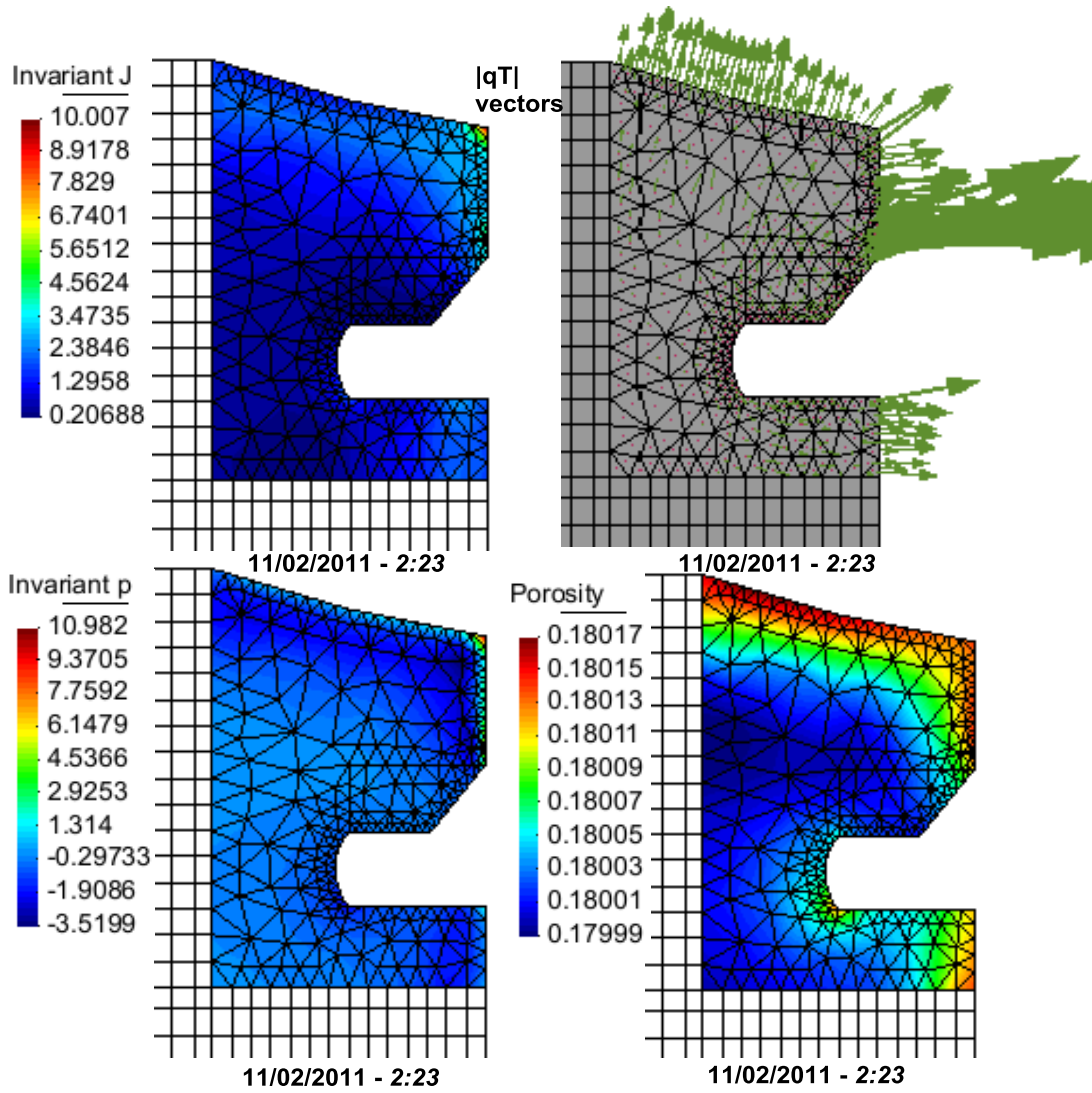
Figure 8.222: Contours of stress invariants, porosity and heat flux vectors at the most exposed section of the rock mass. Contours at a time of minimum temperature registered at the distometers.
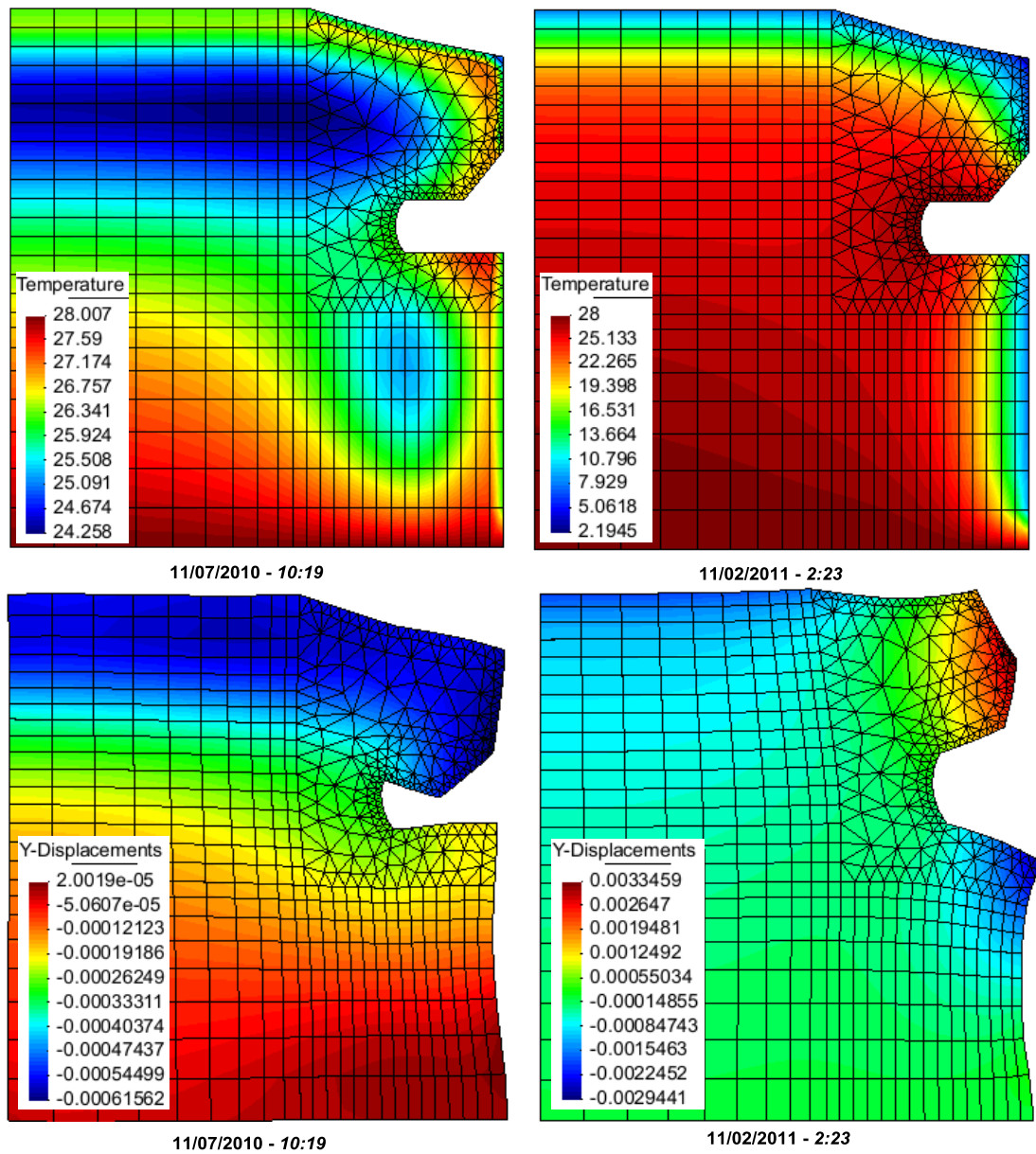
Figure 8.223: Contours of Temperature and Vertical displacement at section of the rock mass. Contours at two different times of maximum and minimum temperatures.

Before proceeding further with the plastic response of the rock cliff, it seems interesting to have an image of the predominant direction of displacements at those points that are most exposed to the atmospheric load. Fig. 8.224 shows the predominant direction of displacements at points D1 and D2 obtained from the elastic model. The vertical displacements at the extensometer D2 (closer to the cavern roof) result in a steepest slope than those at extensometer D1.

479
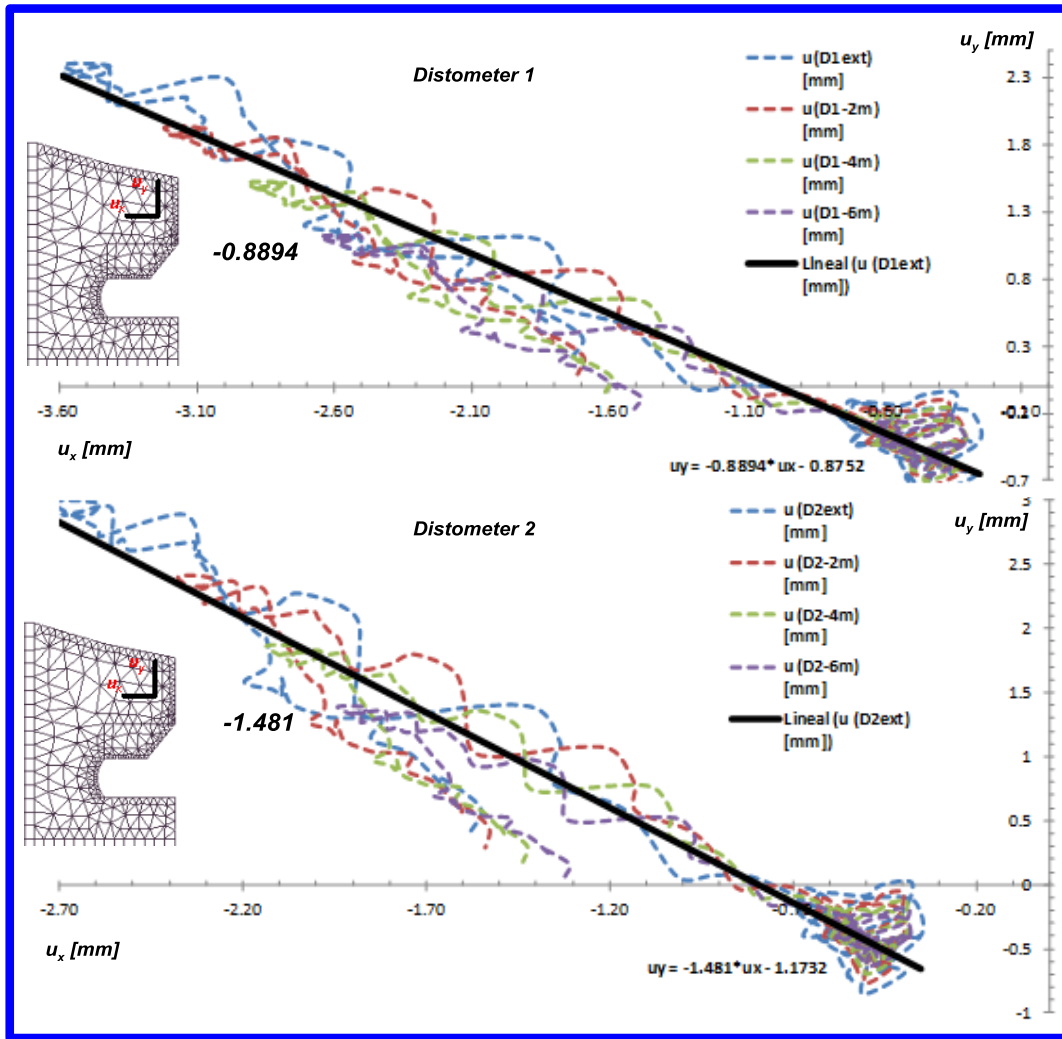
Figure 8.224: Preponderant directions of displacements of the Rock-cliff under the atmospheric load. The vertical Displacements closer to the cavern roof are greater than those closer to the apex.

8.6.3)   Results of the Hyperplastic Model

In the section results of La Roque model considering the rock material response as plastic are presented. In order to analyze the possibility of irreversible strains due either to local shear stress or traction, the plastic response is modeled based on Drucker criterion with thermal degradation.

Numerical model is based on the geometry considered for the elastic model depicted in Fig. 8.214. For the hyperplastic model, an additional division into several material has been considered.

480

In the far field, an elastic material with the same properties as for the elastic numerical model has been considered. In the near field an elastoplastic material with thermal degradation is considered, labeled Drucker-1 and Drucker-2 in Fig. 8.224. Drucker-1 material is provided with a lower strength and a higher sensibility on temperature as the result of the weakening effect acting in the decompression zone.

Moreover, a higher initial porosity is considered at the decompression zone (more open structure) in order to take into account the fissured state of this zone.
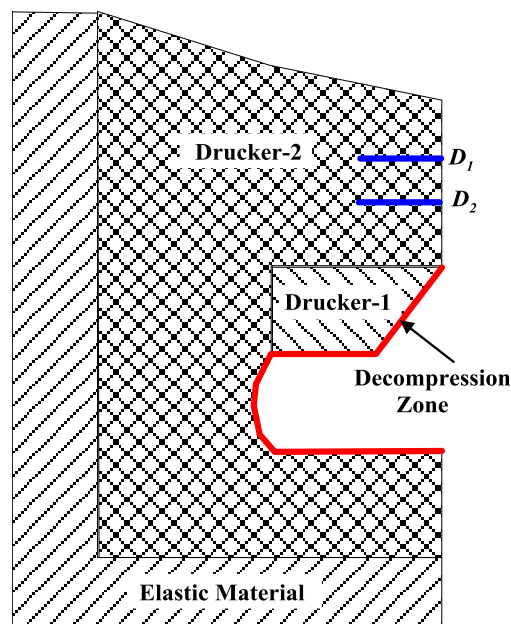
Figure 8.225: Distribution of materials used to model the rock mass response.

A comparison between models results and measurements in extensometers D1 and D2 is presented below, Fig. 8.226 to Fig. 8.233. Fig. 8.234 depicts stress paths computed at critical points of the rock face and cavern.

Figures 8.226 and 8.227 show the evolution of temperature and displacement computed under stationary conditions (5th cycle) in extensometers D1 and D2, respectively. Those results are compared with in situ measurements at 2m, 4m and 6m depths. A good agreement can be observe providing a validation of the model.
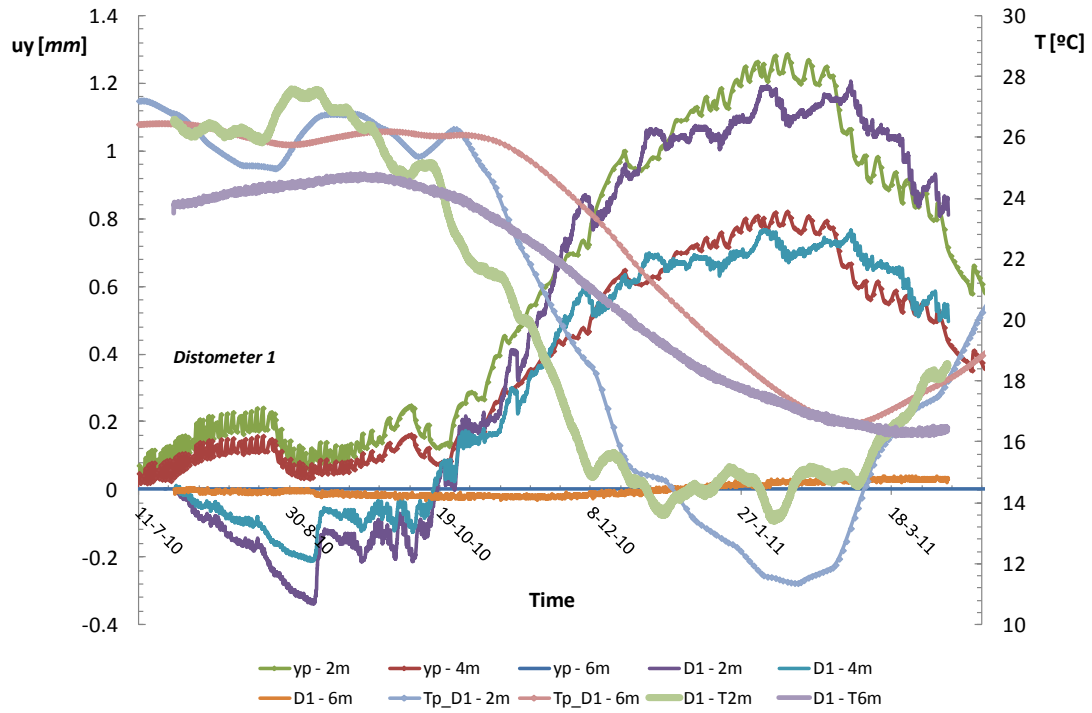
Figure 8.226: Evolution of Displacement and Temperature obtained in the distometer D1 at 2m-4m-6m depth. Results obtained from the Plastic model and comparison with the registered data.
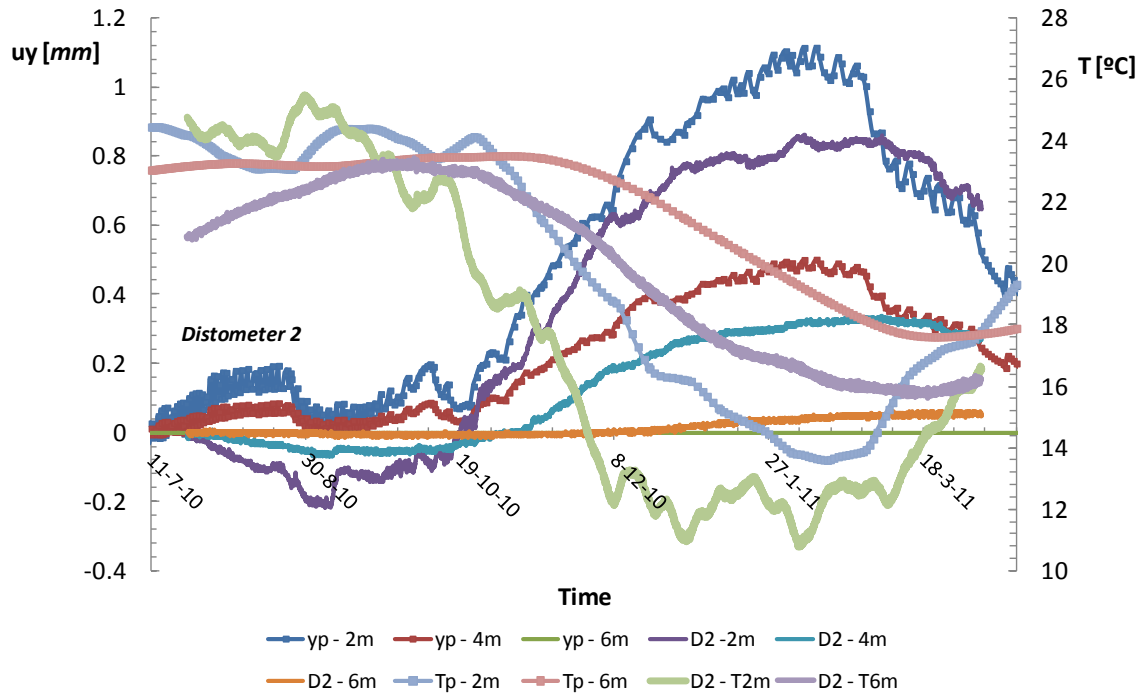
Figure 8.227: Evolution of Displacement and Temperature obtained in the distometer D2 at 2m-4m-6m depth. Results obtained from the Plastic model and comparison with the registered data.

_____

Figures 8.228 to 8.231 present a comparison between temperature and displacements measured at extensometers D1 and D2 and computed by the elastic and the hyperplastic models.
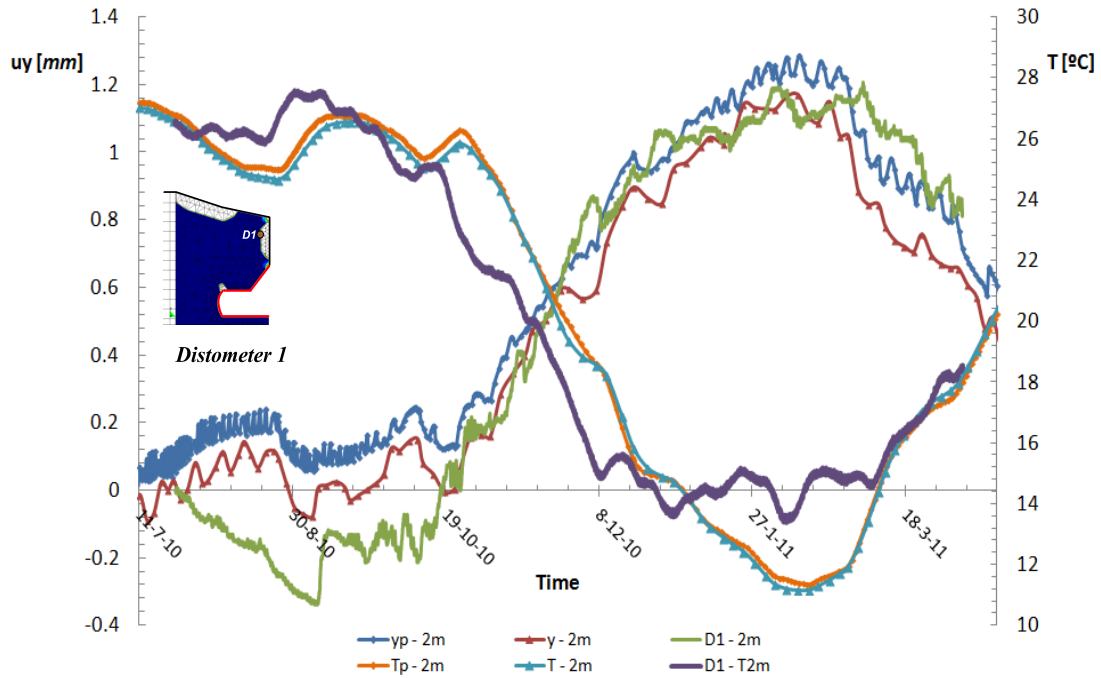
Figure 8.228: Evolution of Displacement and Temperature obtained in the distometer D1 at 2m depth. Results obtained from the Plastic and Elastic models and comparison of the plastic responses and the registered data.
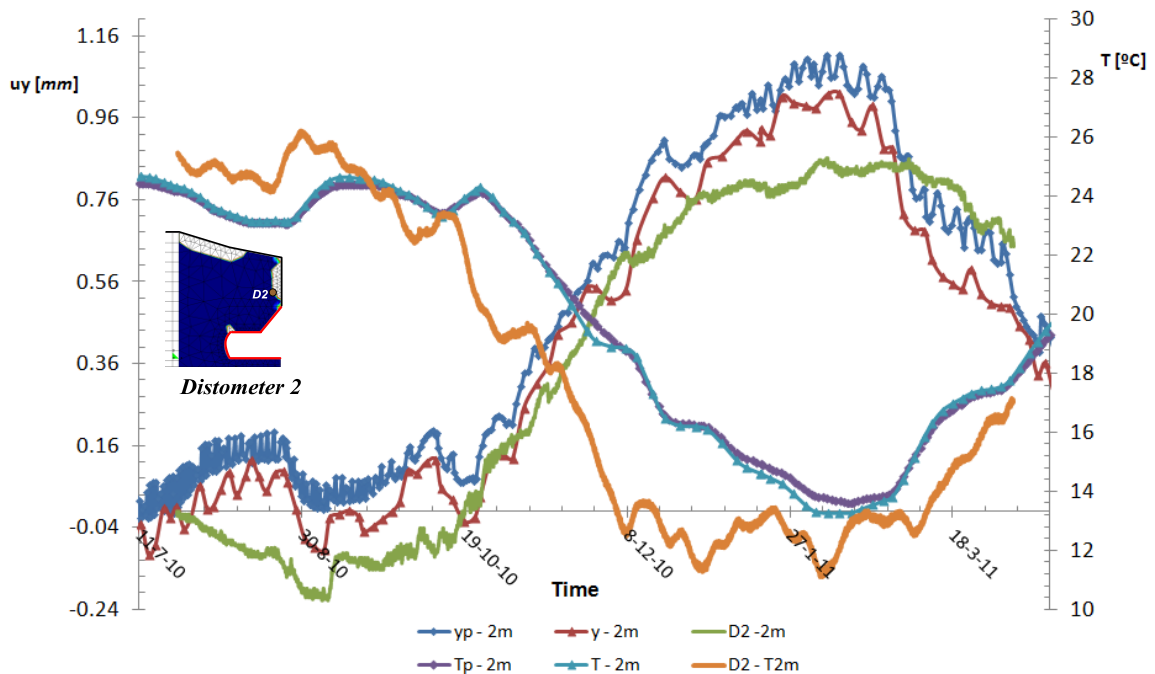
Figure 8.229: Evolution of Displacement and Temperature obtained in the distometer D2 at 2m depth. Results obtained from the Plastic and Elastic models and comparison of the plastic responses and the registered data.
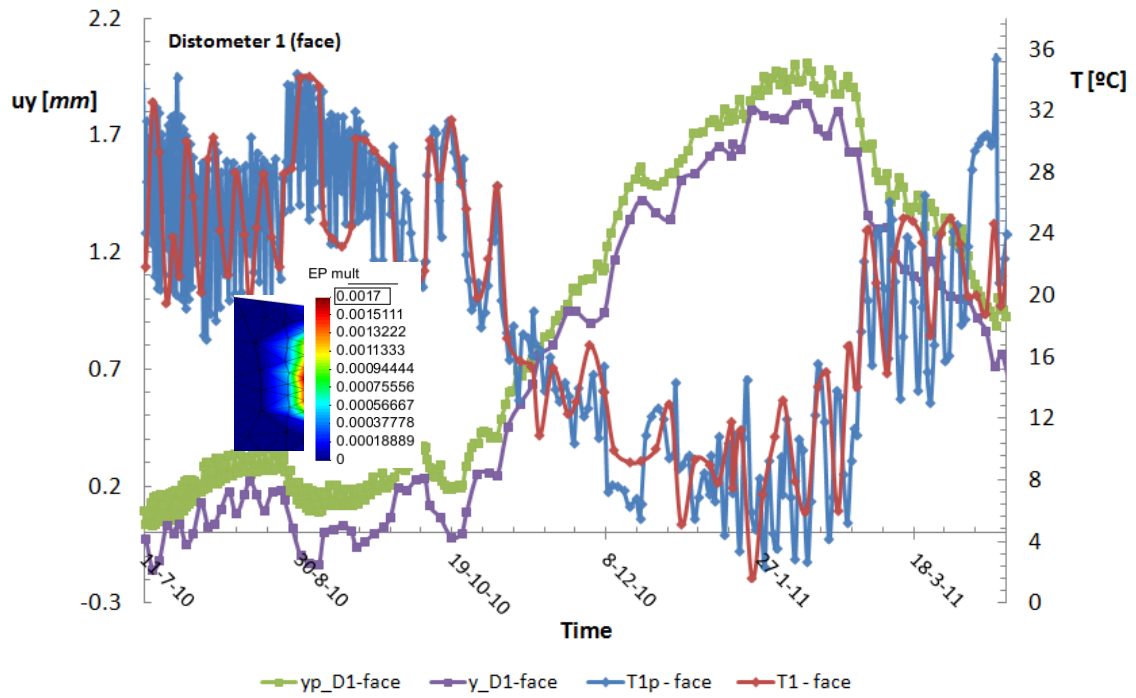
Figure 8.230: Evolution of Displacement and Temperature obtained at the rock-face in the distometer D1. Results obtained from the Plastic model and comparison with results from the elastic model.
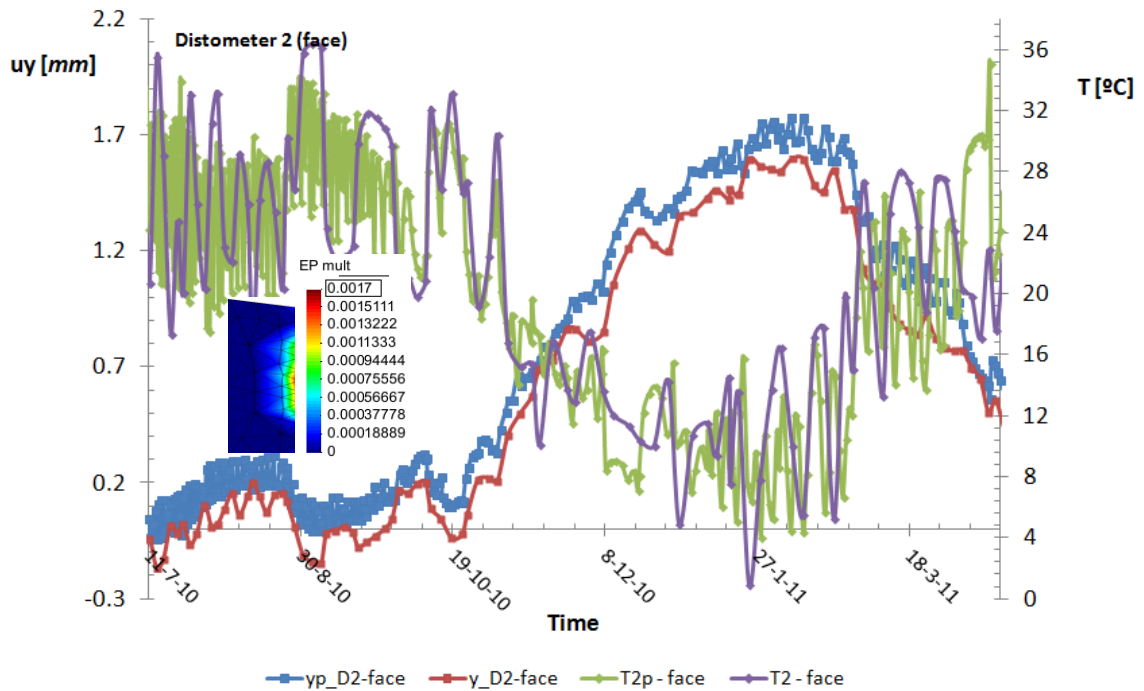
Figure 8.231: Evolution of Displacement and Temperature obtained at the rock-face in the distometer D2. Results obtained from the Plastic model and comparison with results from the elastic model.

484

_____

Temperatures are very similar to that obtained by the elastic model, which is consistent with the fact that the thermal model is not affected by deformations. Displacements predicted by elastic and hyperplastic models are similar indicating that the rock remains in the elastic range at that depth.

Discrepancies are only due to the fact that the plastic model gives a more detailed response as result of the greater number of time steps requires to integrate the mechanical constitutive law.

8.6.3.1)   Decompression Zone (Hyperplastic Model)

Figures 8.232 and 8.233 show evolutions of displacement and temperature computed by both the elastic and the hyperplastic models at point p1 and p2 located at the face of the inclined wall above the cavern and at the cavern roof, respectively.

Fig. 8.232 evidences a superficial plastic zone at point p1. Time evolution of displacements given by the hyperplastic model shows slight discrepancies with respect to the evolution of displacements computed by the elastic model indicating that the effect of plastification is small.

This kind of thermo-mechanical shallow plastification is due to rock degradation in presence of climatic actions and could be associated to the process of spalling observed in the material of the massif face.
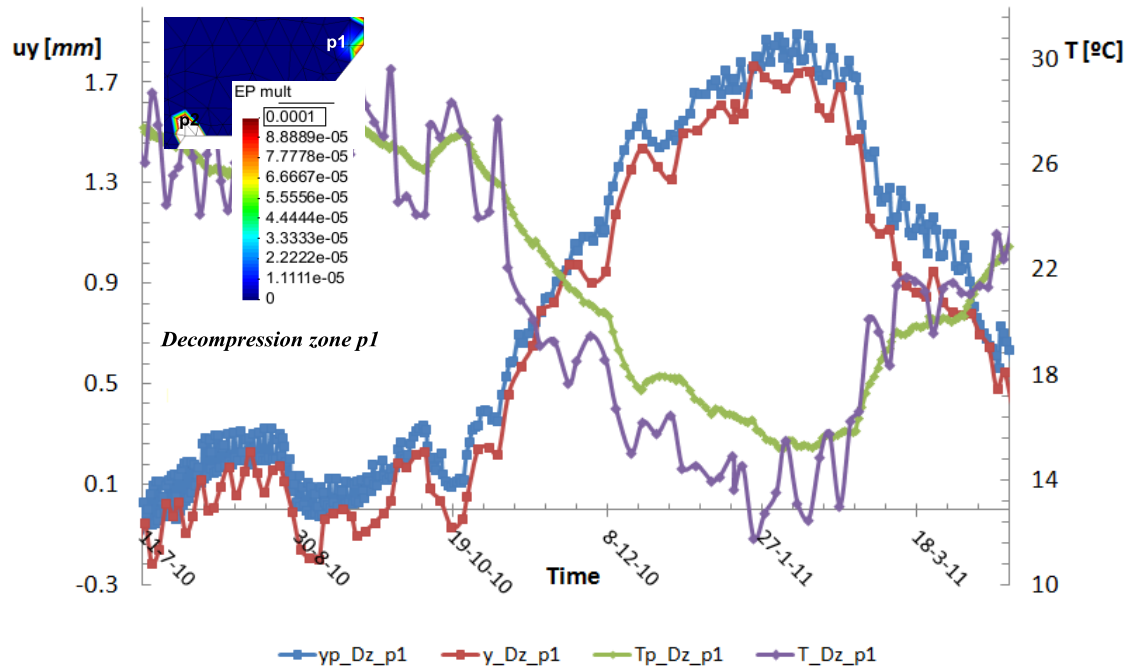
Figure 8.232: Evolution of Displacement and Temperature at point p1 in the inclined plane. Comparison between responses of the plastic model and the elastic model.

Fig.8.233 shows a plastification process with a growing tendency to form a shear band which compromises the support of the rock mass over the troglodyte cavern.
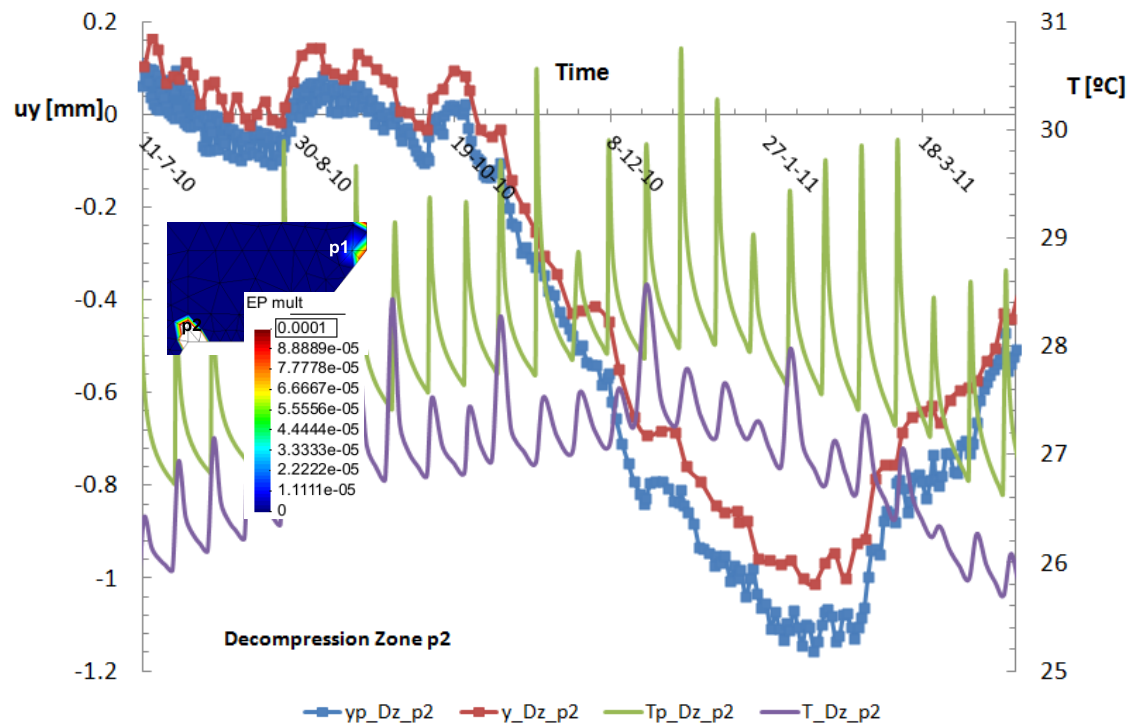
Figure 8.233: Evolution of Displacement and Temperature at point p2 at the bent wall. Comparison between responses of the plastic model and the elastic model.

Figure 8.234 shows stress paths computed in the rock cliff, at the three points: (a) top of cliff, (b) face of cliff and (c) cavern roof, as consequence of the atmospheric actions in cliff's boundary.
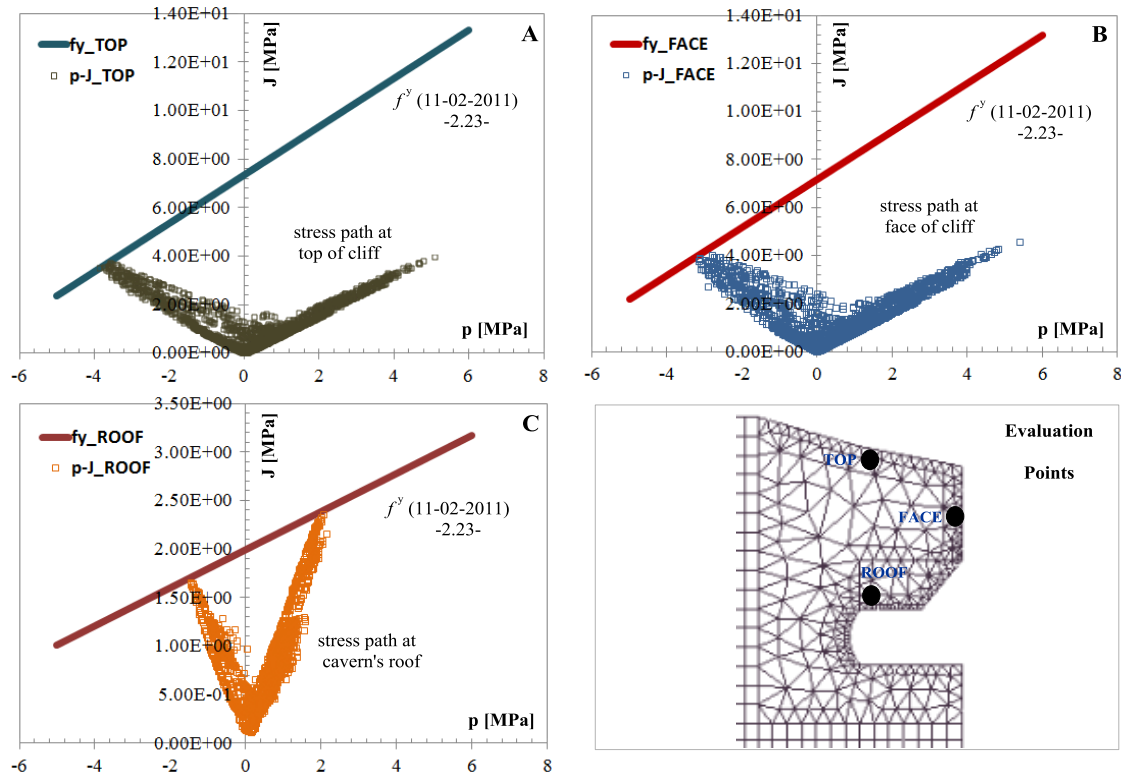
Figure 8.234: Stress paths and Drucker's yield surfaces in the cliff under the atmospheric load.

The stress paths at top and face of the cliff reach yield surfaces in extension states and keep far from plastic developments in compression. On the other side, stress path at the roof of the cavern, in the decompression zone, reaches the yield locus in states of extension and compression due to the degradation law of the rock. Figure 8.236 also validates the yielding criterion and the robustness of the interior-point algorithm to handle numerical problems of convergence observed in this type of stress paths.

Figures 8.235 to 8.243 show isochrones of environmental and mechanical variables at time of higher (11/07/2010) and lower (11/02/2011) external temperatures, respectively.

Fig. 8.235 and Fig. 8.236 show the heat fluxes in the massif in form of vectors and isochrones, respectively. During winter there is an outward flow of heat because the massif is hotter that the atmospheric air. In summer, the isochrones magnitude of heat flux at rock face are typically of 10 $\frac{MJ}{k_g}$ (inward flux) while in winter are typically of 20 $\frac{MJ}{k_g}$ (outward flux).

Temperature isochrones, Fig. 8.237, evidence the delay existing between atmospheric air and rock inner temperature. This process, due to heat diffusion inside the massif, is a cause of differential rock expansion in the massif.
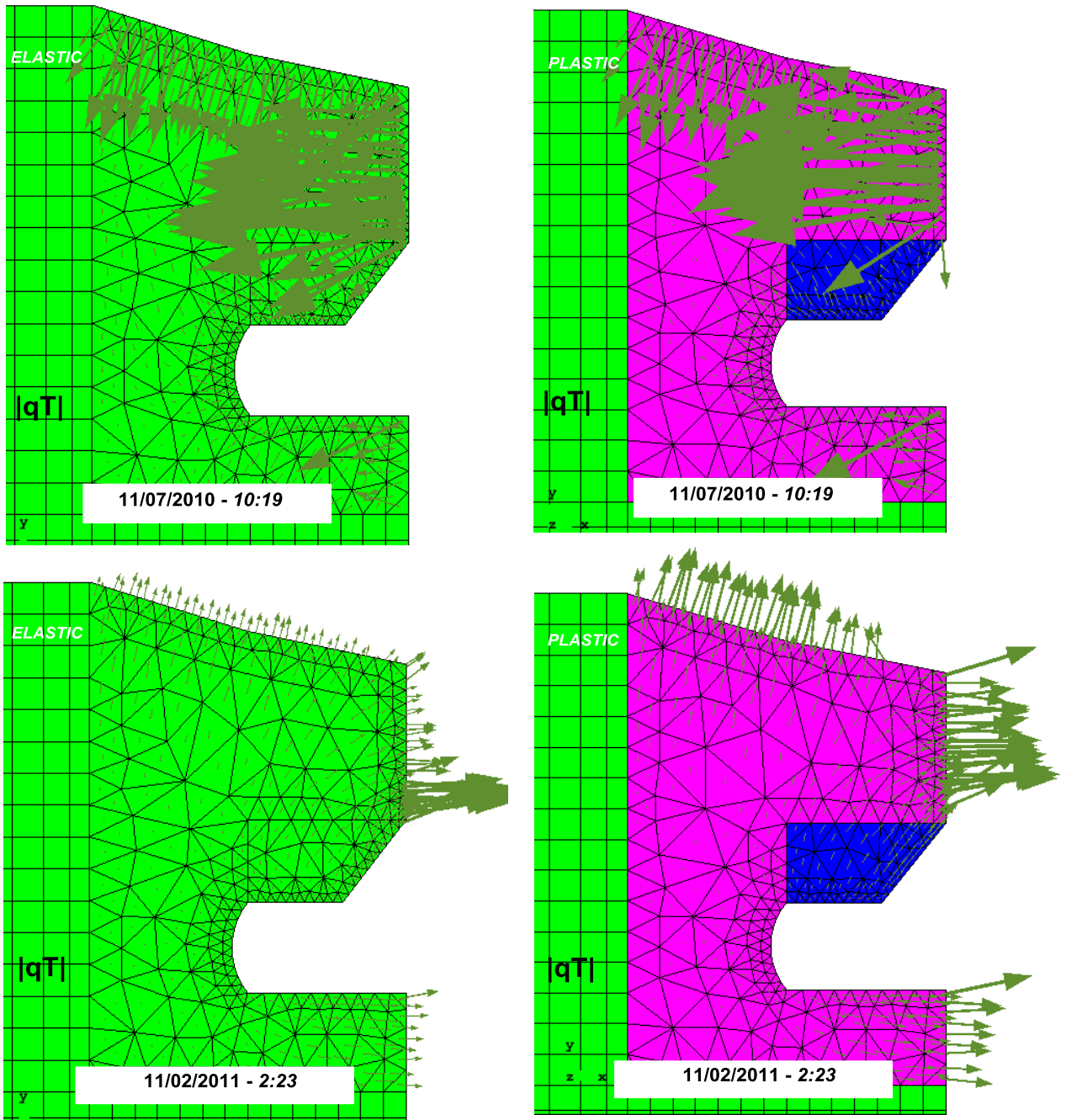
Figure 8.235: Heat flux vectors at two times of maximum and minimum temperatures. Comparison of results obtained by the elastic model and plastic model.

489
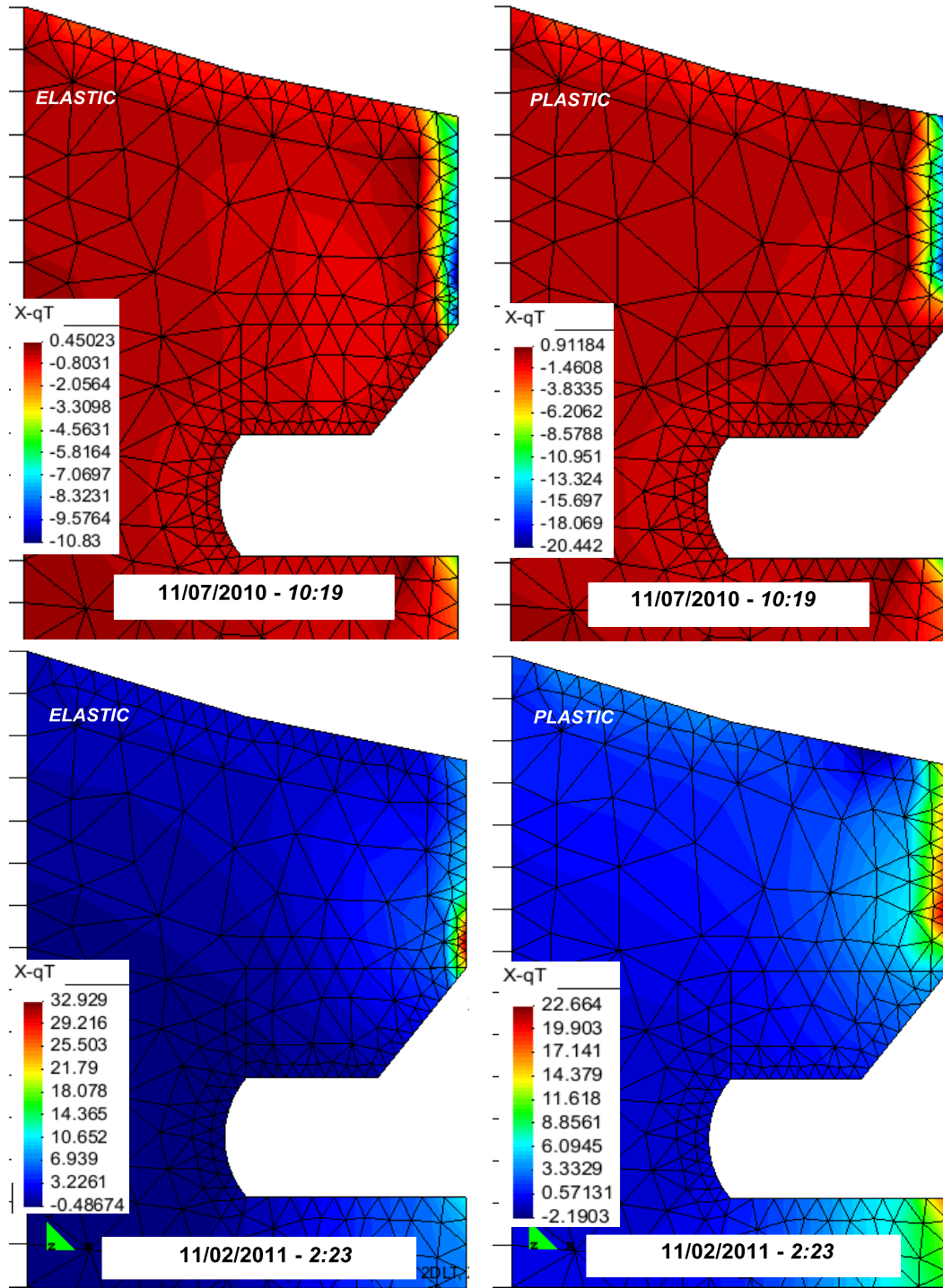
Figure 8.236: Contours of horizontal heat flux at two times of maximum and minimum temperatures. Comparison of results obtained by the elastic model and plastic model.
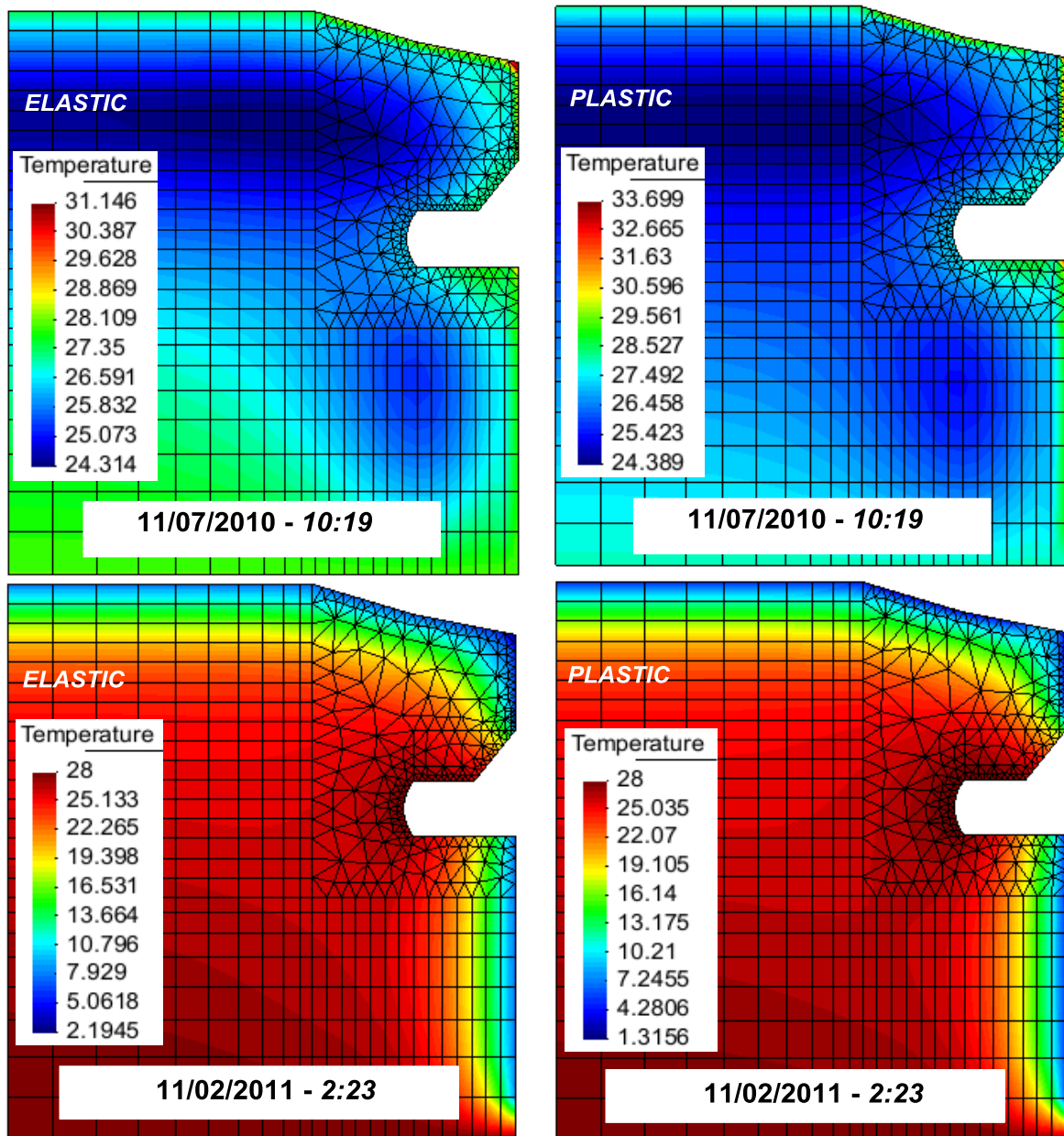
Figure 8.237: Contours of Temperature at two times of maximum and minimum temperatures. Comparison of results obtained by the elastic model and plastic model.

Fig. 8.238 show vertical strains resulting from the differential expansion of the rock. It is observed from the isochrones that in summer a cold bulb is formed inside the massif which acts as a column limiting the vertical displacements. In winter this internal support disappears and vertical deformations reach magnitudes up to two times the magnitudes developed in summer.

491
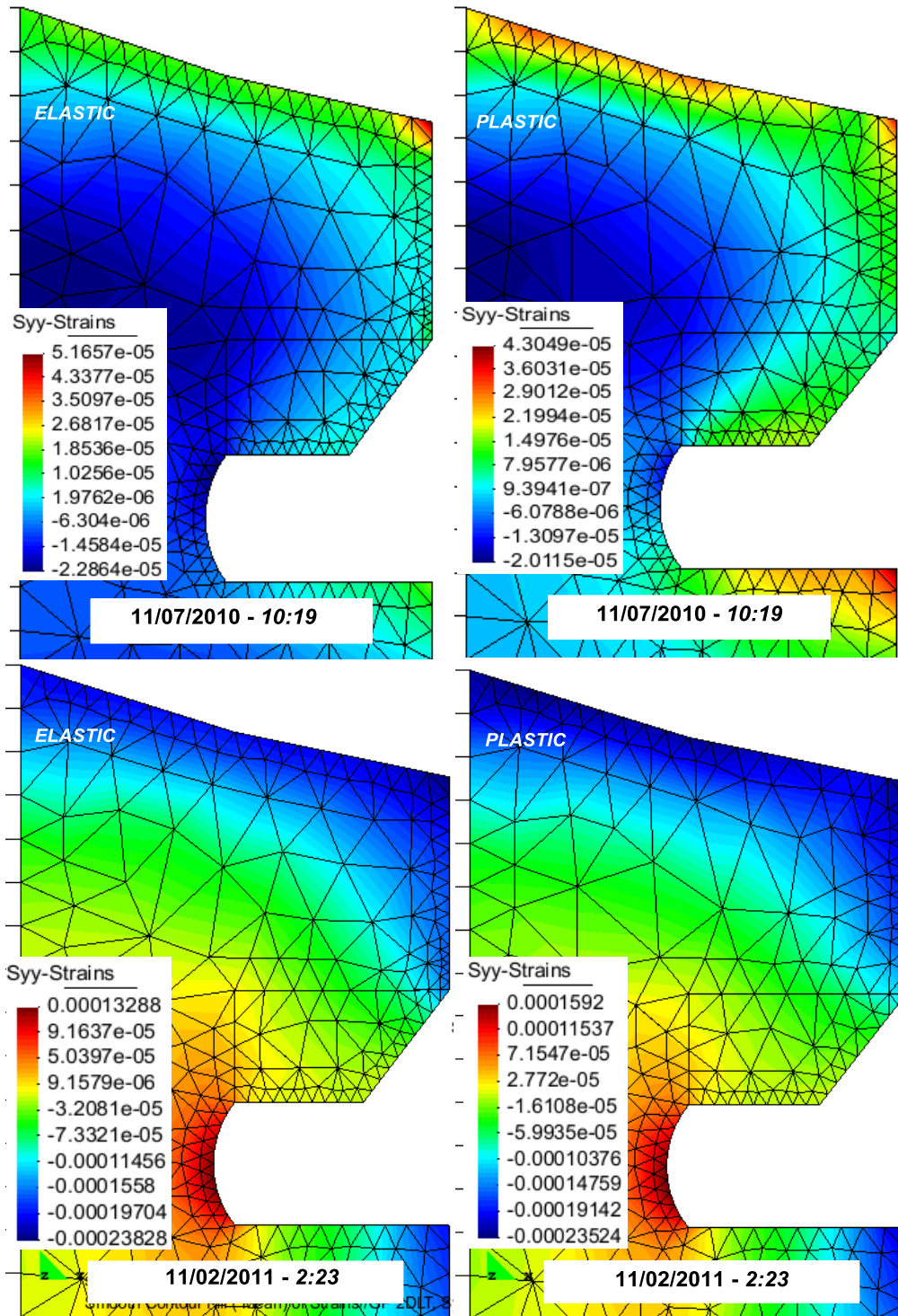
Figure 8.238: Contours of vertical strains at two times of maximum and minimum temperatures. Comparison of results obtained by the elastic model and plastic model.

Figures 8.239 to 8.241 evidence the redistribution of stress that occurs as consequence of plastic zones inside the massif.

Both elastic and hyperplastic model evidence the development of a horizontal compression zone above the cavern, which acts as an arch to support the block. This patterns indicate a cantilever beam type of response that will be studied in the next section.

Deviatoric and shear stresses appear to be very high on rock surface as result of high thermal strains induced by the acting steepest variations of atmospheric temperature. They explain the development of shallow plastic zone on the cliff face. This is confirmed by the isochrones of plastic multiplier, Fig. 8.242.

Isochrones of plastic multiplier also show the development of a failure initiated at both the cavern roof and the upper massif surface. This zones can also be associated to the development of a plastic bending mechanism that encompass the upper block of the cavern.
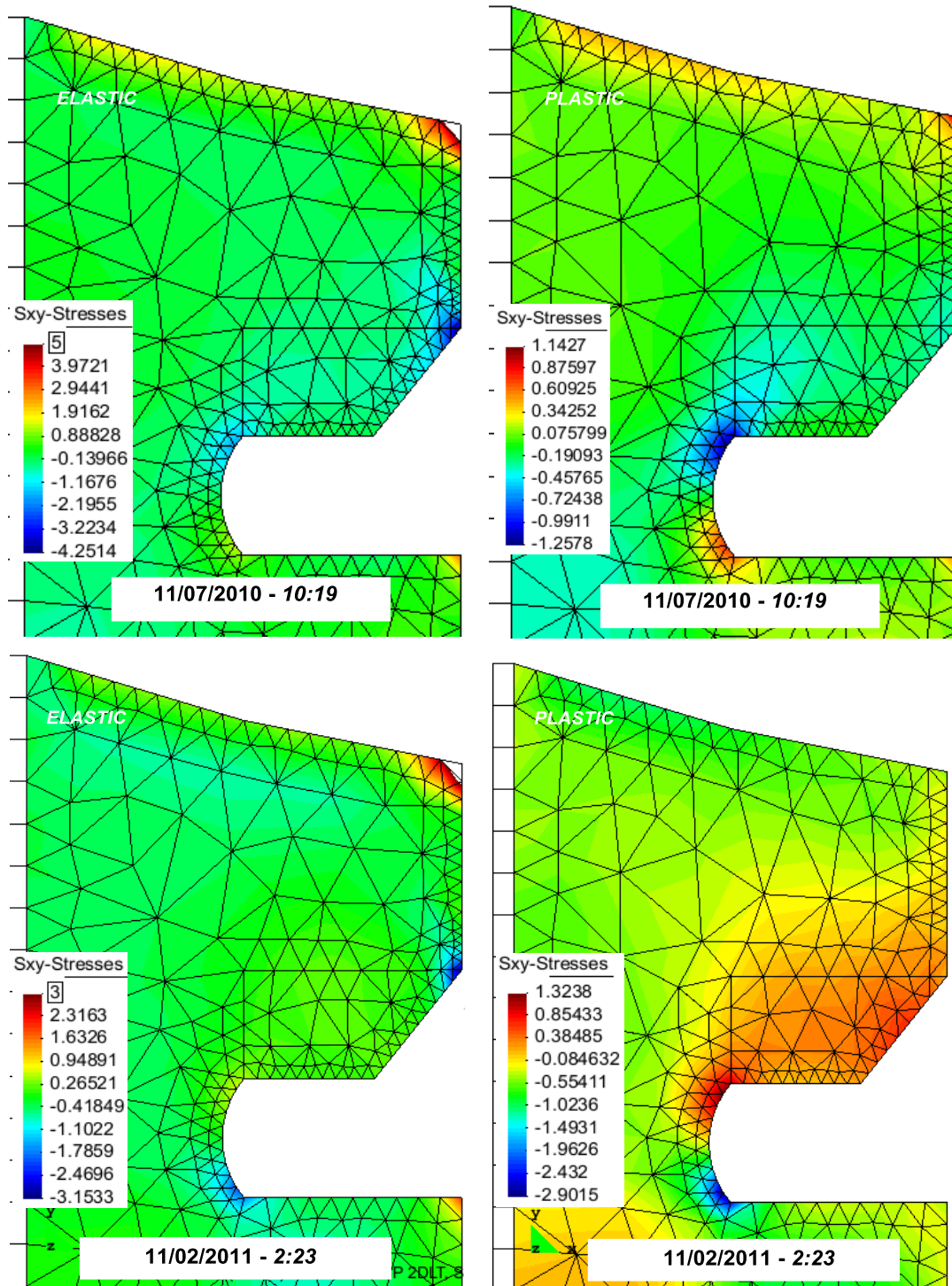
Figure 8.239: Contours of shear strains at two times of maximum and minimum temperatures. Comparison of results obtained by the elastic model and plastic model.
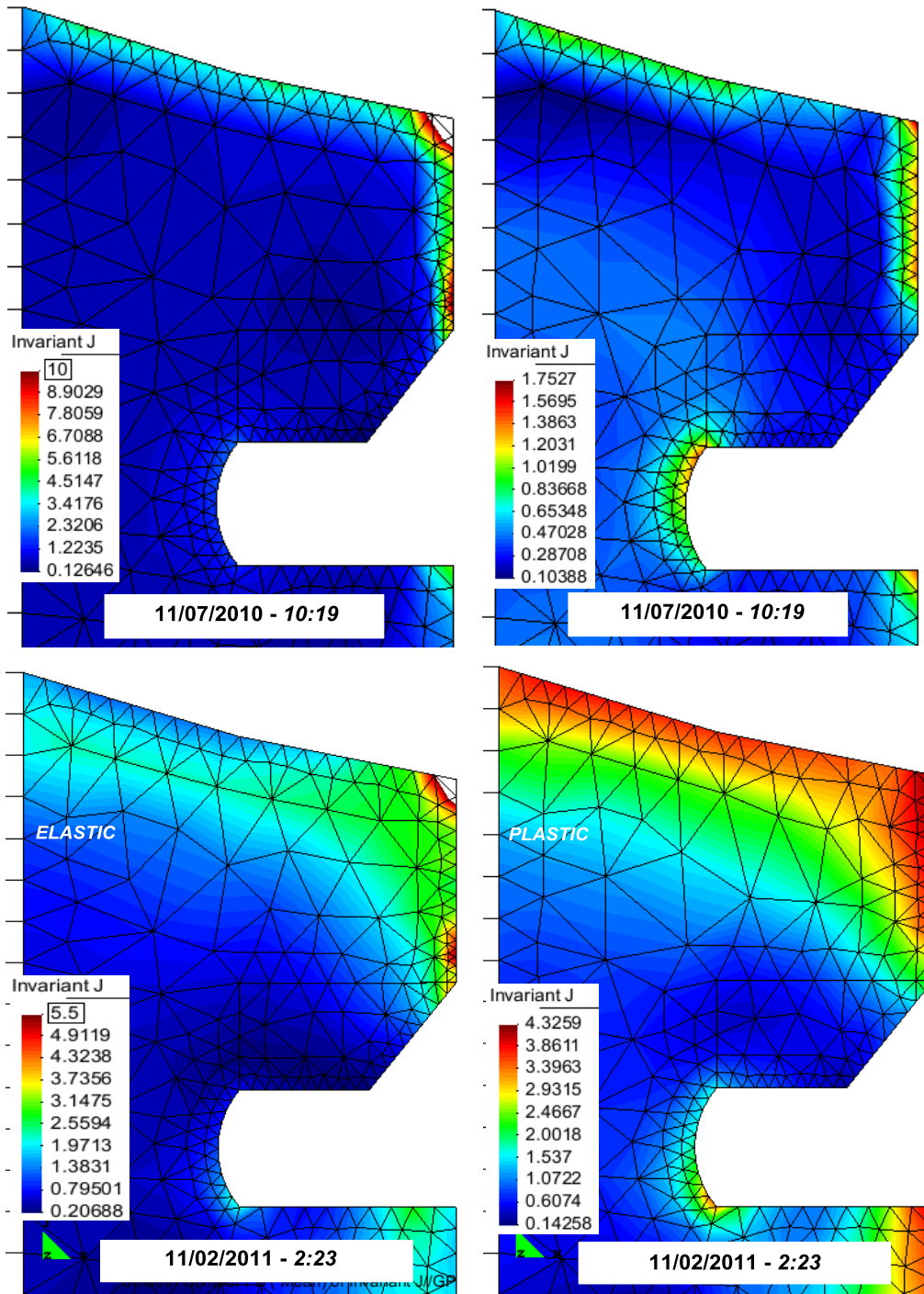
Figure 8.240: Contours of deviatoric stress invariant at two times of maximum and minimum temperatures. Comparison of results obtained by the elastic model and plastic model.
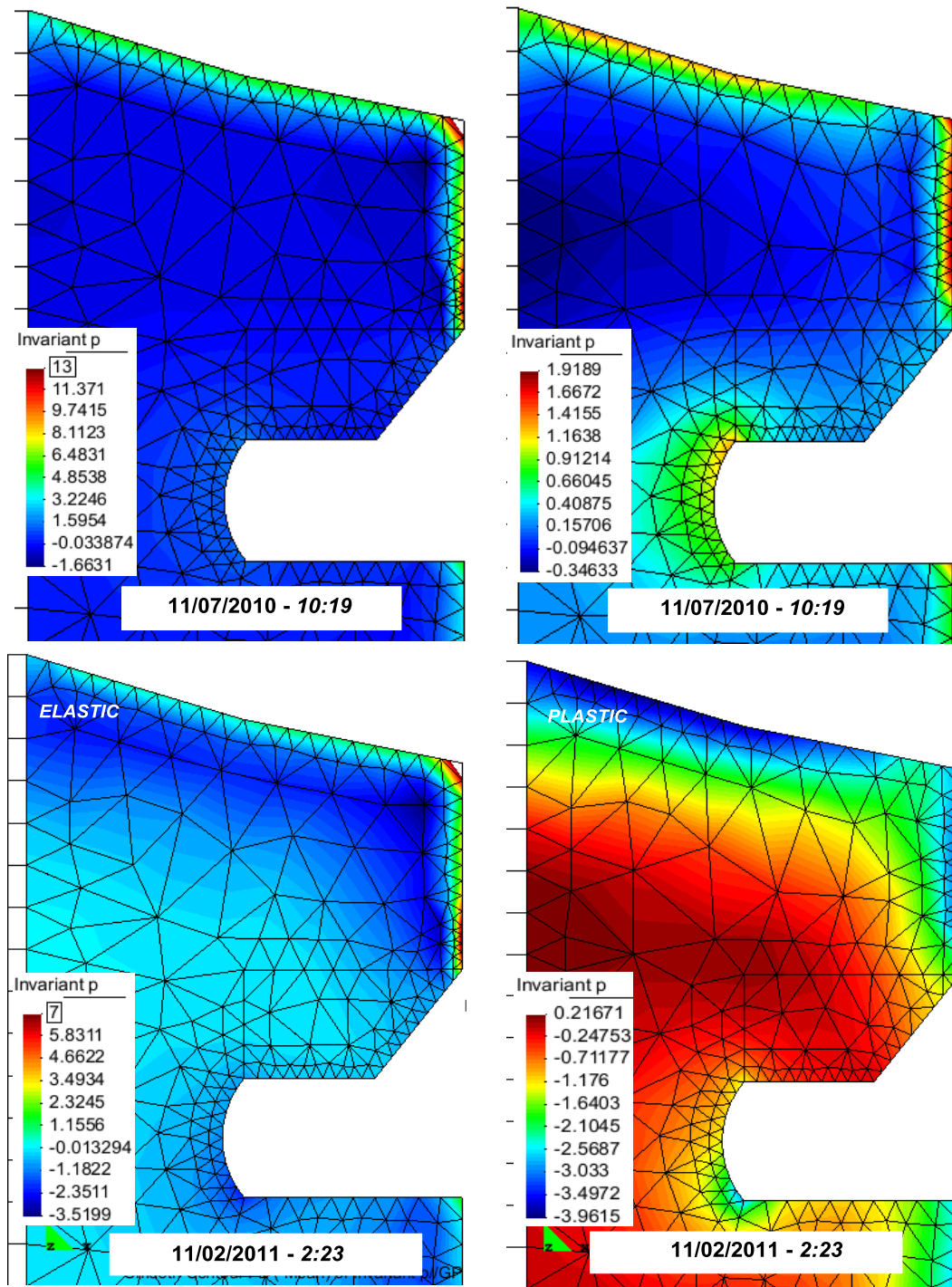
Figure 8.241: Contours of mean stress invariant at two times of maximum and minimum temperatures. Comparison of results obtained by the elastic model and plastic model.
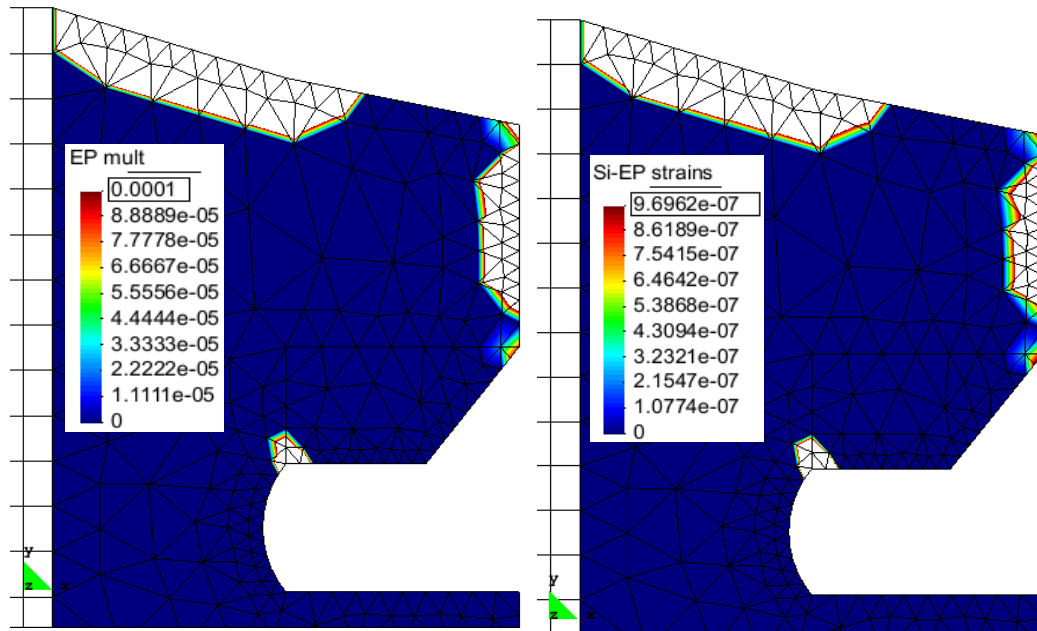
Figure 8.242: Contours of plastic multiplier and principal horizontal plastic strains at two times of maximum and minimum temperatures.

Fig. 8.243 shows the deformed mesh at times of higher and lower external temperatures. Patterns evidence a cyclic divergence and convergence of the cavern roof. Divergence mechanism appears to involve vertical displacements of magnitude 0.0018m at the cavern roof while closure mechanism produces vertical displacements 45% lower at cavern roof. The cyclic bending response of the upper block can also be identified in the figures.
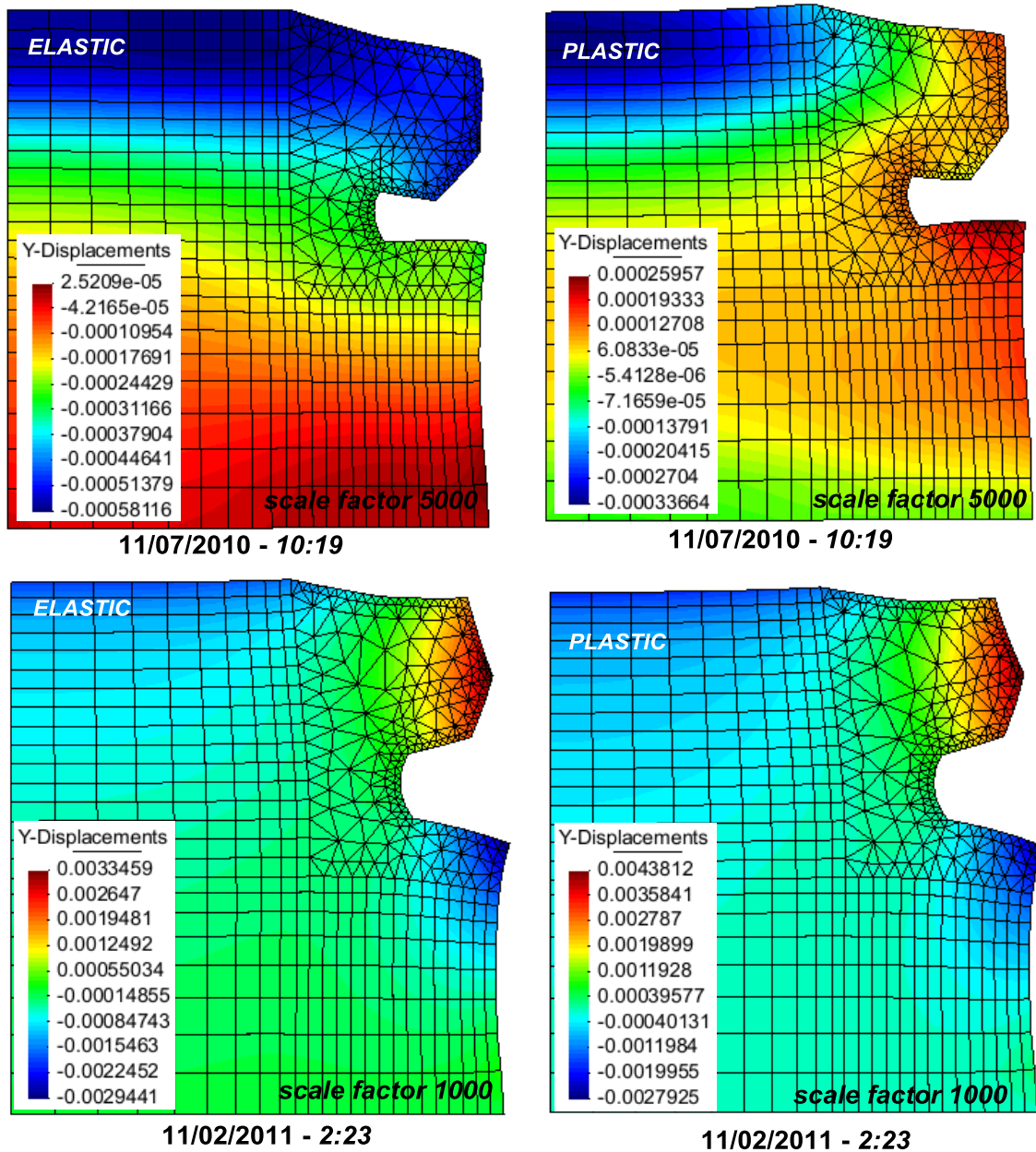
Figure 8.243: Contours of vertical displacements at two times of maximum and minimum temperatures. Comparison of results obtained by the elastic model and plastic model.

8.7)   Stability Analysis of Cavern Roof

In this section, a simple analysis of the block located on top of the cavern is realized. It is based on the Bernoulli beam theory and compare the threshold envelope to the values of axial force, shear force and bending moment computed in the fixed section of the rock-beam due to the developed thermal strains.

Geometry considered in the analysis is shown in Fig. 8.244. It encompasses the block located on top of the cavern. This section is considered as the most critical since it corresponds to the locus of shear stress concentration above the rear part of the cavern.
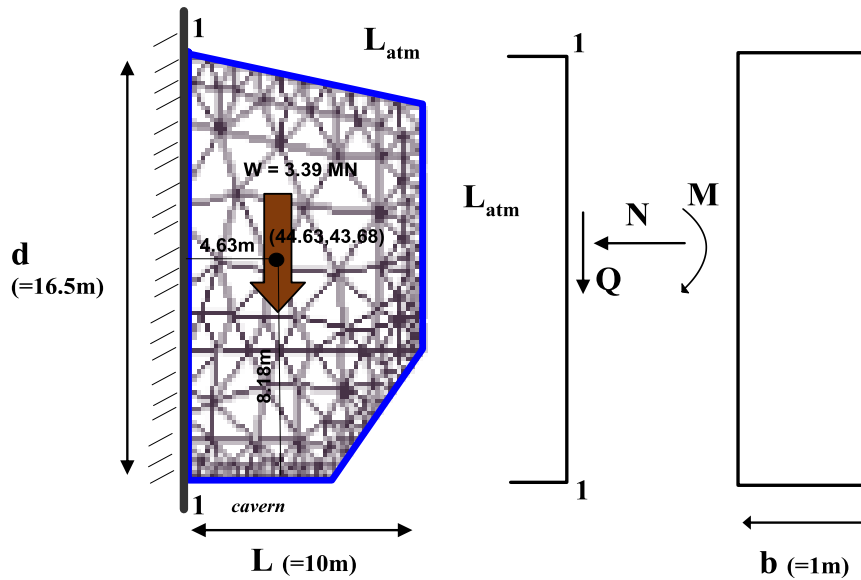
Figure 8.244: Idealized cantilever rock-beam, ceiling of troglodyte cavern.

Potential failure is assumed to take place as result of the development of thermal stresses due to differential strains associated to the gradient of temperature in the cliff. The normal and shear stresses at the plane 1-1 are given by $\sigma_n = \sigma_{xx}$ and $\tau = \tau_{xy}$. By adding up the stresses along the entire area it is possible to compute the time evolution of axial force N, shear force Q and bending moment M at 1-1. Fig. 8.245 shows the cyclic evolution of axial and shear forces, momentum and curvature due to thermal stresses and self-weight in section 1-1.

Profiles of normal stress and shear stress distribution obtained with the numerical model on 11/02/2011 are depicted in Fig. 8.246.

Once remove the bottom part of the diagram which corresponds to the decompression close to the roof of the cavern, they can be favorably compared with the distribution obtained by the elastic beam. Equation 8.20 provides expressions for the axial stress and the shear stress distributions given by this theory, depicted in Fig. 8.248.
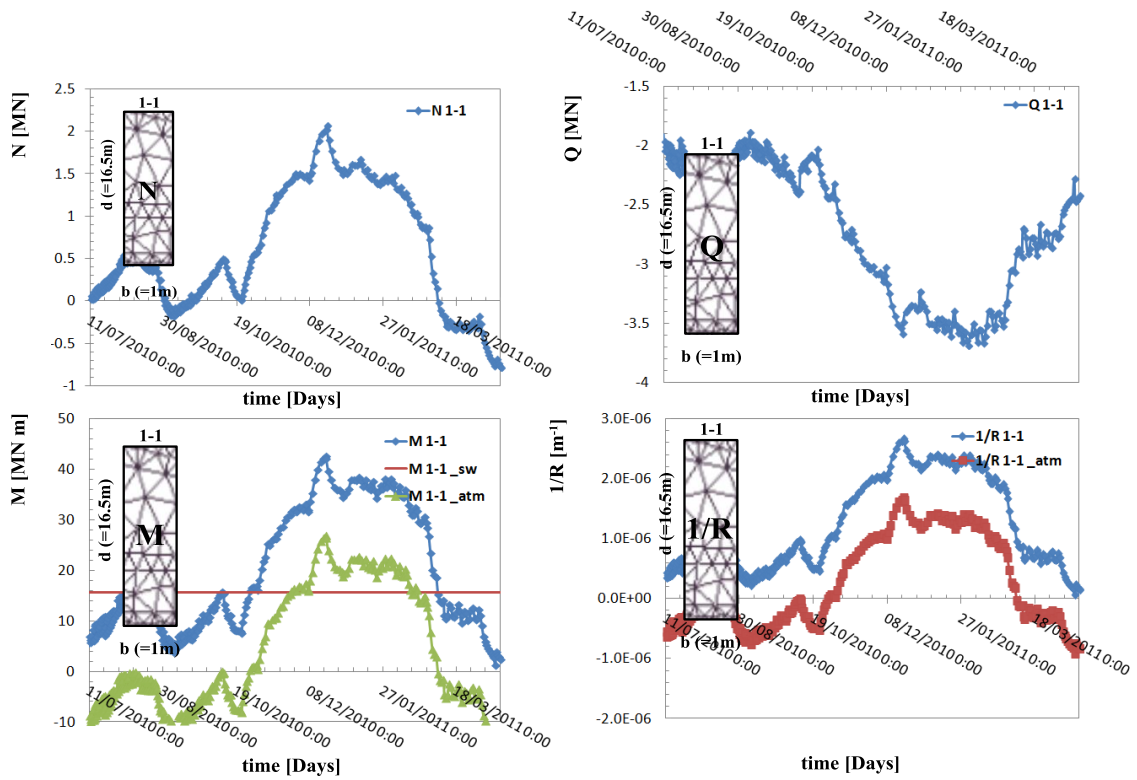
Figure 8.245: Evolution of normal force, shear force, momentum and curvature at fixed section $1-1$ of the rock-beam.
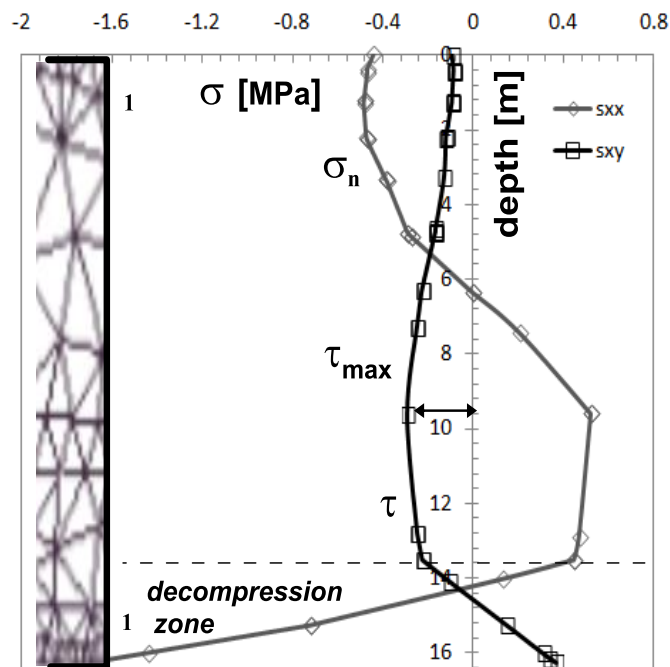
Figure 8.246: Typical profile of normal and shear stress computed in La Roque at section 1-1.

500

$$\sigma_n(L_0, z) = z\frac{M(L_0)}{I(L_0)} + \frac{N(L_0)}{A(L_0)} \qquad (8.20)$$

$$\tau(L_0, z) = \frac{Q(L_0)S_T(L_0)}{I(L_0)b(L_0)}$$

where $L_0 = 0m$, I and A are the moment of inertia and area of cross section 1-1, S_T is the static moment with respect to the centroidal axis.

Fig. 8.247 shows the plastic zones which develop in the rock as the result of the thermal actions. They evidence the development of two weakening zones on top and bottom of section1-1. These weakening zones can be seen as the initiation of a plastic hinge mechanism.
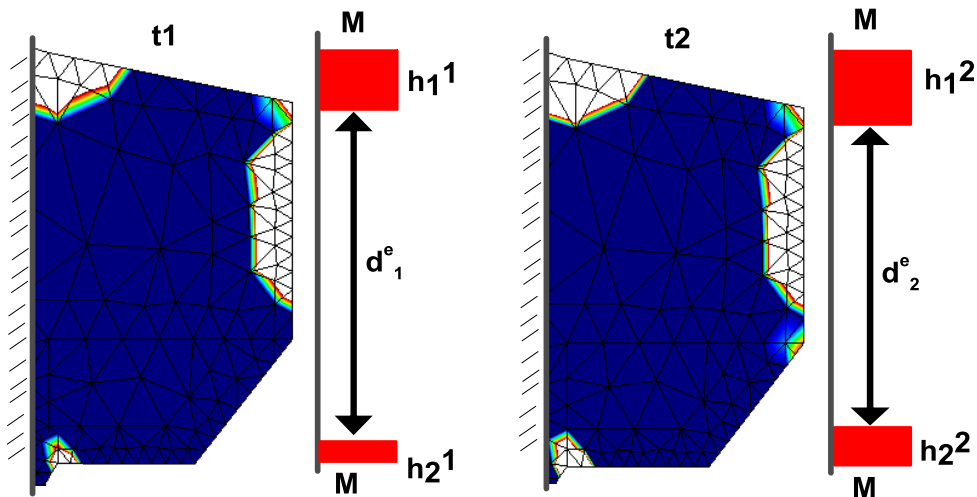
Figure 8.247: Plastification zones in the critical section 1-1 of the rock-beam at two different times.

According to the evidence, the condition of stability of the rock above the cavern will be studied using the theory of plastic bending in a cantilever beam provided with an elastic stress distribution and a yield criterion based on Drucker proposal (Bezukhov referenced by Jirásek (2002)).

In this theory the cross section of a rectangular beam is divided into: (a) a core, where the section remains elastic and (b) plastic regions, in which shear stresses vanish. Fig. 8.248 shows the cross section 1-1 and the idealized stress distribution proposed by Bezukhov.
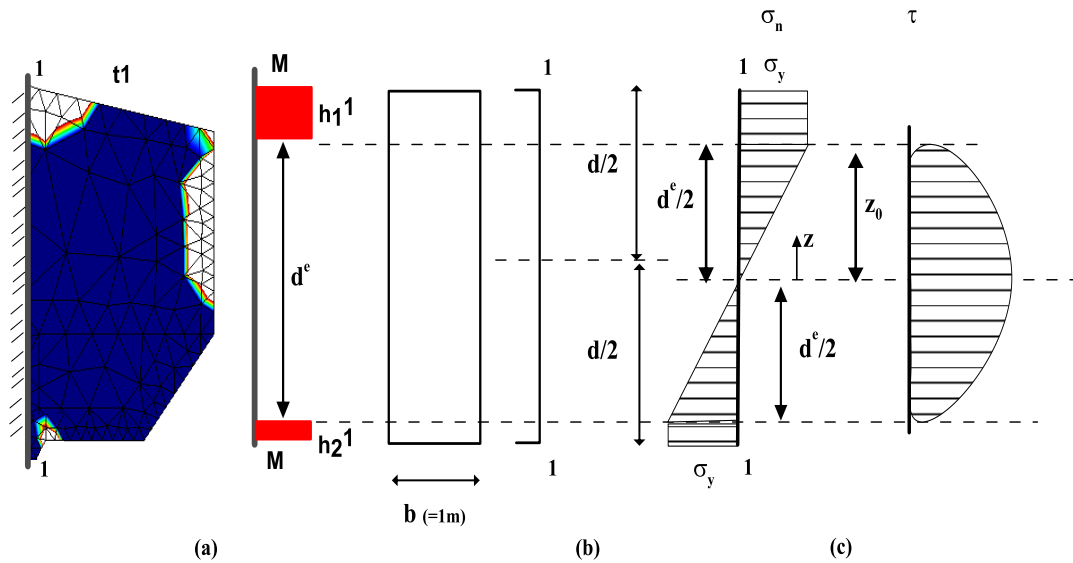
Figure 8.248: Cross section 1-1 and stress distribution according to Bezukhov, after (Jirásek & Bazant, 2002).

The interior approximation (lower limit) of the plastic limit envelope for the cross section 1-1 is obtained by establishing in first instance the bending moment due to the action of axial force, shear force and momentum M.

It is performed in two separate stages that combine: (a) the N-M mechanism and (b) the Q-M mechanism.

If the moment capacity at section 1-1 is computed under the action of N and M only, the influence of the axial force N on the bending moment is obtained, leading to:

$$\mathcal{M} = \underbrace{\frac{\sigma_y b d^2}{4}}_{\mathcal{M}_o}\left(1 - \frac{d^{e^2}}{d^2}\right) = \mathcal{M}_o\left(1 - \frac{N^2}{d^2\sigma_y^2 b^2}\right) \tag{8.21}$$

Eq. 8.21 gives an interaction equation between axial force and bending moment expressed by:

$$\frac{\mathcal{M}}{\mathcal{M}_o} + \left(\frac{N}{d\sigma_y b}\right)^2 = 1 \tag{8.22}$$

Interaction Eq. 8.22 allows to determine the strength of section 1-1 under combined loading N-M. Fig. 8.249 presents the N-M interaction curve for the rectangular section 1-1 of the rock-beam.
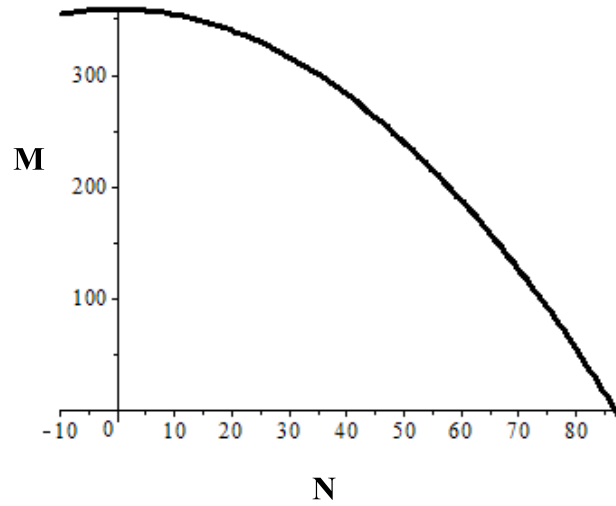
Figure 8.249: N-M interaction curve for the rectangular section 1-1.

Considering the stress distribution in Fig. 8.248, the bending moment regarding Q-M mechanism results:

$$\mathcal{M} = \underbrace{\frac{\sigma_y b d^2}{4}}_{\mathcal{M}_o}\left(1 - \frac{d^{e^2}}{3d^2}\right)$$

(8.23)

where $\mathcal{M}_o$ is the fully plastic moment due to pure bending. Eq. 8.23 gives a direct relation between the high of the elastic core d^e and the bending moment $\mathcal{M}$:

$$d^e = \sqrt{3}\left(1 - \frac{\mathcal{M}}{\mathcal{M}_o}\right)^{1/2} d$$

(8.24)

The moment of inertia and the static moment of the elastic area (Fig. 8.248) are defined by

$I = {bd^{e^3}}/{12}$ and $S_T = {b\left(d^{e^2} - 4z^2\right)}/{8}$, respectively. Thus the shear stress at the elastic

core Eq. 8.20b is rewritten as:

$$\tau = \frac{3}{2}\frac{Q}{bd^{e^3}}\left(d^{e^2} - 4z^2\right)$$

(8.25)

On the other hand, σ_n and τ must satisfy the plastic admissibility condition defined by the Drucker yield surface Eq. 8.19, leading to:

$$\frac{3}{2}\frac{Q}{bd^{e^3}r_c}\left(d^{e^2} - 4z^2\right) - \frac{2(B + M)z}{d^e}\sigma_y - a(c') = 0$$

(8.26)

If this expression holds for the maximum shear stress at $z = 0$ then it holds for the entire elastic core. Then Q must satisfy:

_____

$$\frac{3}{2}\frac{Q}{bd^e r_c} \leq a(c') \tag{8.27}$$

or

$$\frac{3Q}{2b\sqrt{3\left(1-\dfrac{\mathcal{M}}{\mathcal{M}_o}\right)}dr_c} \leq a(c')$$

Eq. 8.27b can be rewritten in the form:

$$\frac{3}{4}\left(\frac{Q}{bdr_c a(c')}\right)^2 + \frac{\mathcal{M}}{\mathcal{M}_o} \leq 1 \tag{8.28}$$

that is the desired plastic limit envelope which defines the maximum allowable shear force Q such that (σ_n, τ) remains plastically admissible within the elastic core (outside this core it is fulfilled by imposition of the yield locus).

It is noted that Eq. 8.24 is valid in the range $\mathcal{M}_E \leq \mathcal{M} \leq \mathcal{M}_o$, where $\mathcal{M}_E$ is the elastic limit moment. For values of $\mathcal{M} \leq \mathcal{M}_E$ the depth of the elastic core would exceed the depth of the cross section.

The obtained failure criterion in the M-Q space provides a safe estimation of the limit shear force given by:

$$|Q| \leq bdr_c a(c')\sqrt{\frac{4}{3}\left(1-\frac{\mathcal{M}}{\mathcal{M}_o}\right)} \tag{8.29}$$

Fig. 8.250 depicts the interior approximation of the plastic limit (interaction $Q, \mathcal{M}$).
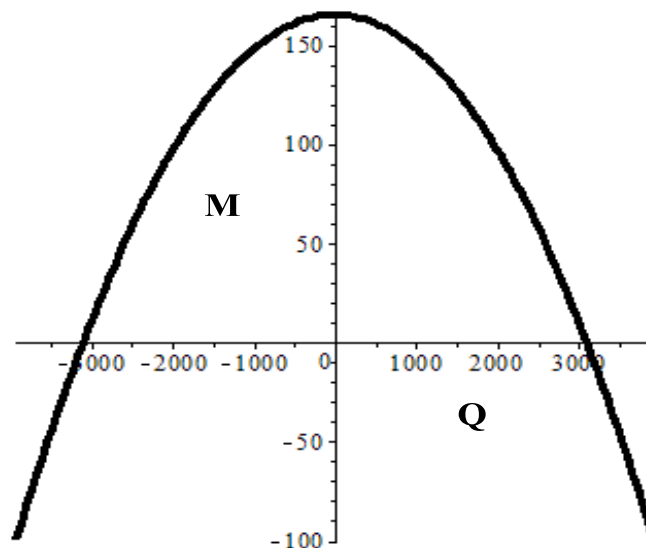
Figure 8.250: Interior approximation of the plastic limit M-Q for stress states within the elastic core at a constant normal force.

_____

Fig. 8.251 presents the shear-moment pairs computed with the numerical model. They lay within the elastic domain delimited by the Q-M plastic limit, as consequence stability of the rock-beam is guaranteed.
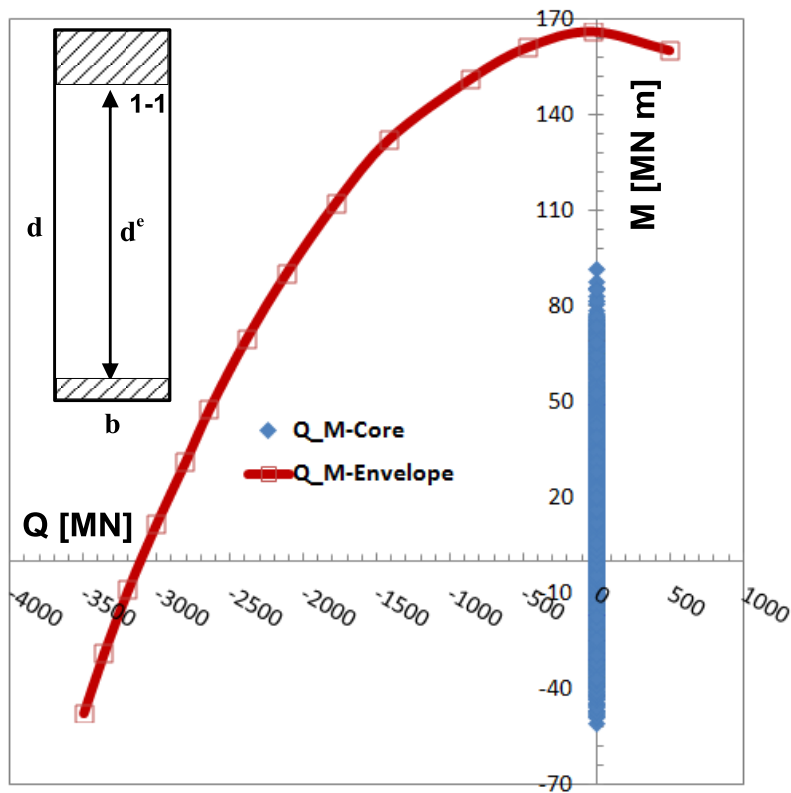
Figure 8.251: (a) Interior interaction envelope of the plastic limit M-Q for stress states within the elastic core at a constant normal force, (b) shear-moment pairs at the elastic core obtained by the model La Roque.

8.8)   Conclusions

This chapter deals with the thermomechanical study of a rock massif located in the south of France, submitted mainly to the action of the solar radiation.

Climatic actions were registered by the meteorological station Sarlat la Caneda, located about 3km from the location of the massif. Extensometers on the cliff face and within the massif allow to follow temperature and displacement in the rock mass.

A numerical model has been built to follow the response of the cliff. The elastic response of the material has been modeled with a hyperelastic linear law, while the plastic response has been modeled with the Drucker-Prager model presented in chapter 4. The interior-point algorithm presented in chapter 5 has been used to integrate the model.

Heat exchange between the massif and the atmosphere generates incoming and outgoing flows of heat coinciding with summer and winter, respectively.

Differential expansions of the rock has been shown to be the result of the diffusion of heat inside the massif. During summer season a cold bulb reseambling a beam developed over the cavern limits the vertical displacements.

Differential deformation has generated stress paths within the massif, which have produced contractions and expansions in the most exposed part of the rock mass. The algorithm has been decisive in providing a proper response to problems of numerical convergence of difficult solution, like the one produced by traction stresses of considerable magnitude. The responses provided by both the elastic and the plastic models show great similarity, being the response of the plastic model more precise due to the greater number of time steps required in order to solve the model.

Irreversible deformations are located in zones of the massif at the rock face, at the top and at the roof of the cavern. Redistribution of stresses due to plastic zones and the concentration of irreversible strains at the top of the massif and at the cavern roof have indicated a cantilever beam type of response of the rock mass over the cavern.

Irreversible strains at the rock face have been associated with the spalling observed in the rock face. The plastification process observed in the cavern roof tends to form a shear band which makes more precarious the stability of the rock mass above the cavern.

Stability study of the rock-beam in the more critical section subjected to: axial force, shear force and momentum generated by the thermal stresses acting in that section, has lead to the conclusion that the beam is stable.

<div align="right">

CHAPTER 9

</div>

<div align="center">

CONCLUSIONS AND FUTURE RESEARCH

</div>

Some general conclusions are drawn from the evidence presented in the preceding Chapters. The most important points are reemphasized and some suggestions for future developments are made.

9.1) Modeling of soil-vegetation-atmosphere interactions

Chapter 2 has addressed the soil-atmosphere interaction in a comprehensive formulation allowing to derive all the equations governing the THM behavior of porous media in a consistent way with the balance equations considered for the continuum.

Heat exchange through Γ^{atm} boundary includes: sensible heat of exchange, heat convected by flows of water and air and net radiation reaching the soil surface. The latter has proved to be of great relevance since it controls the evaporation flux and may cause thermal strains, particularly in rocks. A study case of the later effect is presented in chapter 8.

Water mass flux through Γ^{atm} boundary includes: precipitation, evaporation, vapor flux advected by gas and flux of water drained on soil surface in case of full saturation. Model is able to account for the actual evaporation flux which depends on the magnitudes of current atmospheric variables (wind velocity, relative humidity, atmospheric temperature).

Transpiration flux acts in depth in the root zone of vegetalized areas. Stress factor affecting leaf surface resistance is the main factor controlling the transpiration flux. This factor depends on the soil water content available at the root zone.

Behavior of three-phase porous medium has been approached from a thermomechanical viewpoint. The approach starts establishing the first and the second laws of thermodynamics for the THM coupled problem. Momentum balance equation and balance of air-liquid interface, involving the average stress-like tensor T_{ij}, have been derived from the analysis. Moreover, following standard procedures in thermomechanics, the state equations (constitutive laws) of the three-phase porous medium have been obtained.

The respective effects of these different fluxes has been then studied by sensitive analysis of synthetic problems. A first analysis leads to highlight strong effect of the balance between infiltration and evapotranspiration for the hydric changes in the upper soil layer (active zone).

The effect of the permeability of the topsoil layers has been also illustrated. Low permeability soil are less sensitive to the atmospheric actions than high permeability soils, since they provide a greater resistance to water percolation and favor stronger evaporation flows.

The effect of vegetation has also been illustrated. High density of vegetation cover increases: (a) the relevance of transpiration over evaporation and (b) the depth of the active zone susceptible to pore pressure fluctuations due to the atmospheric action.

As future work, the study of the plant growth at cellular level and its consequent changes in the density of the system is recommended. In this perspective, a cellular growth scenario has been briefly developed at the end of the chapter, highlighting the interest of soil biology model for this research field.

9.2) A Thermomechanical framework for modeling unsaturated soils

Chapter 3 has addressed a review of the theory of plasticity from thermo-mechanical principles. Two consolidated frameworks: (a) poro-elastoplasticity and (b) hyperplasticity have been examined.

The poro-elastoplastic framework offers a formal procedure to separate the skeleton from the pore fluid and formulate independent and coupling equations between each phase.

_____

The hyperplastic framework gives an adequate perspective to address: (a) material hardening and (b) plastic flow direction without losing associativity of the flow rule in the so called dissipative stress space.

Both frameworks have been examined and merged into a thermomechanical consistent framework (hyperporoplasticity) able to model soil response in partially saturated conditions. The hyperporoplasticity maintains the characteristics of the two original theories.

Chapter starts with the hyperporoplastic formulation of two-phase porous materials. The study posses the basis of each approach and introduces the thermomechanical concepts of plasticity as: elastic energy, trapped energy and dissipation energy.

Afterwards the hyperporoplastic formulation for three-phase porous media has been presented. It allowed to derived the constitutive variables commonly used in the modeling of partially saturated soils and to obtain the state equations linking the conjugate variables.

A novel concept introduced by this approach is the kinematical hardening of the retention curve. It extends, to hydraulic variables, the fundamental relationship linking variables in the true and in the dissipative spaces by introducing the concept of shift (or back) suction. This extension leads to a dissipative mechanism which allows to model hysteresis of the capillary curve.

Finally, a general structure has been proposed for the energy functions g_s and f_s in partially saturated conditions.

Although it has not been of mayor interest in this work, the theory supports the development of models with deformable solid phase. This scenario opens a research line to be explored in detail.

9.3)   Formulation of THM models within hyperporoplasticity frame

Along chapter 4 the hyperporoplasticity framework for hydro-mechanical and thermo-mechanical modeling of multiphase media has been applied to several constitutive models that appear to be of importance in practical problems of soil-atmosphere interactions.

They are:

- Water retention with and without hysteresis,
- Thermo-hydro-mechanical elastic law,
- BBM-like models,
- HP-CASM model,
- Drucker-Prager and Matsuoka-Nakai yield criterion with linear elasticity (or also perfectly plastic).

A simplified van Genuchten law has been proposed. This simplified law admits a closed-form integration and therefore the construction of an energy potential for the air-liquid interface. Hysteresis of the retention model has been addressed proposing a proper energy function g_i (or f_i) and a force potential.

Dissipation functions for BBM-like models, formulated in both net stress and effective stress, have been presented and their performances shown at Gauss point level.

Dissipation function for a hyperplastic-CASM model has also been proposed. In this case the hardening parameter has been provided with a thermal dependency in addition to suction.

Generalized elastic potentials proposed by Houlsby (2005) have been extended to consider: (a) suction due to partially saturation of porous media, (b) thermal strains due to temperature changes and (c) water retention dependence on mean stress by an adequate interface energy. The obtained dependencies and couplings for the proposed potentials has led to an extended partition of strains and degree of saturation, beyond the classical elastic and plastic partition.

Drucker-Prager model, derived within the framework of hyperplasticity, has been adapted to consider thermal strength degradation. The presented model has also been smoothed at the apex to avoid the lack of definition of the plastic flow vector at that point.

All the models appear to fit well in hyperporoplasticity framework. The obtained formulations presented the advantage of being susceptible to be implemented in optimization algorithms with good performance (algorithms developed in chapter 5).

The hyperporoplastic formulation of hydro-mechanical constitutive laws considering the hysteretic behavior of the air-liquid interface attached to the solid particles is an interesting research line for future works.

9.4) Numerical Implementation: Implicit Algorithms

The study of the integration of the constitutive models developed in chapters 3 and 4 has been addressed along the chapter 5. The proper integration of the constitutive laws is a key point of the constitutive modeling.

One of the advantages of the elasto-plastic models being derived from the thermo-mechanical principles is that both, internal and dissipation energy functions are known. Those functions include all the information on the models and allow to integrate the constitutive laws trough mathematical programming tools. The minimization of the functionals defined by the sum of the internal energy function and the dissipation function provides with proper variational structures. They allow to determine the optimal points (minimum points) which are the solution to the return plastic mapping where the stress state lies on the yield surface. The study and development of two types of integration algorithm has been carried out:

a)   Return mapping by the closest-point projection
b)   Return mapping by the interior-point method

An additional method to control the step-size during the plastic corrections "the line search method" has been included in both algorithms.

Both algorithms have shown similarities in their performance. They have presented mild difference in convergence properties. In favor of the interior-point algorithm is its versatility in terms of parameterization options, leading to catch the optimal point even when the starting trial point is considerably far from the admissible region. It is a vast and open subject for further exploration.

9.5) Thermo-hydraulic modeling of an experimental fallow field

Chapter 6 has addressed the analysis of an experimental fallow field, intensely instrumented, under climate actions.

The analysis has evidenced that the interaction between the soil and the atmosphere has a great influence on the topsoil layer. The obtained results highlight the predominant action

_____

of transpiration over evaporation in the summer. In winter time the direct evaporation from the soil surface plays the main role.

The modelling of the experimental field Le Fauga has allowed to validate the soil-vegetation-atmosphere boundary condition presented in chapter 2.

9.6) Response of a foundation under atmospheric actions

In chapter 7, the response of a shallow foundation under atmospheric actions has been studied.

The model (boundary value) has been calibrated in a physical centrifuge test at laboratory scale. The thermo-hydro-mechanical formulation presented in chapter 2 has been used in order to physically modelize the governing and constitutive equations.

In this regard, a generalized mechanical model of Barcelona Basic Model, including pure kinematical hardening, coupled with a simplified van Genuchten retention curve, have been used.

Results show that the model is able to reproduce both the hydraulic and the wetting induced collapse responses of the silty layer. Moreover, the model has also shown to be capable to reproduce the force-displacement curve of the foundation.

A procedure to evaluate the bearing capacity factors in non-saturated conditions has been developed on the basis of the proposal from Potts (2001). This procedure has been used to compute the bearing capacity of shallow foundation at the centrifuge test in conditions close to saturation.

The calibrated model (boundary value) has then been applied to the silty layer at field scale in order to study the bearing capacity of the foundation under field scenarios. The atmospheric condition has been applied for a period of two years with the purpose of reproducing real conditions in the soil layer, mainly in the upper zone.

The study of the foundation focuses on the displacements that may occur as the result of climatic actions after its construction. For that, an impervious foundation load until a service load equal to 1/3 of the ultimate load has been modeled during two years of atmospheric actions.

This study shows the development of differential settlements of about 6mm between the footing center and its edge due to the climatic action. At the end of a strong drying period,

_____

the soil has additionally shown to experiment a vertical displacement in extension of about 3cm.

A sensitivity study shows the strong effect caused by the permeability in case in which water table is maintained at low constant depth. In the high permeability soils bottom condition prevails over the atmospheric effect, leading to low suction close to the surface. In the lower permeability soils ($K \approx 1E - 7\,^m/_s$), the evaporation plays a more relevant role, leading to the generation of an active zone of about 1m depth, which may affect the superficial settlements.

Tractions stresses close to the foundation have been easily predicted by the model.

Further investigation about the effects of the hysteretic behavior of the capillary curve on the soil collapse appear to be of high interest. Insights about the wetting collapse for different directions of non associativity of the plastic flow are also an important issue.

9.7) Analysis of a rock cliff stability under climatic actions

Chapter 8 deals with the thermomechanical study of a rock massif located in the south of France, mainly submitted to the action of the solar radiation.

Climatic actions were registered by the meteorological station Sarlat la Caneda, located about 3km from the location of the massif. Extensometers on the cliff face and within the massif allow to follow temperature and displacement in the rock mass.

A numerical model has been built to follow the response of the cliff. The elastic response of the material has been modeled with a hyperelastic linear law, while the plastic response has been modeled with the Drucker-Prager model presented in chapter 4. The interior-point algorithm presented in chapter 5 has been used to integrate the model.

Heat exchange between the massif and the atmosphere generates incoming and outgoing flows of heat coinciding with summer and winter, respectively.

Differential expansions of the rock has been shown to be the result of the diffusion of heat inside the massif. During summer season a cold bulb reseambling a beam developed over the cavern limits the vertical displacements.

Differential deformation has generated stress paths within the massif, which have produced contractions and expansions in the most exposed part of the rock mass. The algorithm has been decisive in providing a proper response to problems of numerical

_____

convergence of difficult solution, like the one produced by traction stresses of considerable magnitude. The responses provided by both the elastic and the plastic models show great similarity, being the response of the plastic model more precise due to the greater number of time steps required in order to solve the model.

Irreversible deformations are located in zones of the massif at the rock face, at the top and at the roof of the cavern. Redistribution of stresses due to plastic zones and the concentration of irreversible strains at the top of the massif and at the cavern roof have indicated a cantilever beam type of response of the rock mass over the cavern.

Irreversible strains at the rock face have been associated with the spalling observed in the rock face. The plastification process observed in the cavern roof tends to form a shear band which makes more precarious the stability of the rock mass above the cavern.

Stability study of the rock-beam in the more critical section subjected to: axial force, shear force and momentum generated by the thermal stresses acting in that section, has lead to the conclusion that the beam is stable.

A further investigation regarding the damage of the rock skeleton is a topic of interest. In future research a dependency of the damage parameter on the current temperature should be introduced. This implementation requires a regularization of the global FEM solution to avoid mesh dependency.

In summary the most important subjects raised in this dissertation are:

> a) Study and development of soil-atmosphere interaction within a coupled thermomechanical analysis for three-phase porous medium.
>
> b) Development and application of thermo-mechanical principles in order to build elastoplastic constitutive models for soils at partially saturated conditions.
>
> c) Use of mathematical optimization techniques for the integration of variational structures of constitutive modeling.
>
> d) Study and development of implicit algorithms of global convergence for the numerical integration of constitutive laws.
>
> e) Application of the model to the study and analysis of geotechnical problems controlled by soil-atmosphere interaction.

APPENDIX

A1)   Mathematical and Physical Formulation of the Coupled Problem

The study of the ground response under atmospheric and vegetation actions requires the consideration of a fully coupled thermo-hydro-mechanical formulation of the porous medium. In this formulation all the studied fluxes have their influence in the medium and act as boundary constraints in an initial boundary value problem. This section presents the coupled formulation for a porous medium on which the finite element code Code_Bright is based. It is in this code where the boundary soil-atmosphere-vegetation condition has been implemented.

Following Olivella (1995), three main species are considered, mineral (h), water(w) and air(a). The mineral is the specie that forms the solid phase. Water is present in the liquid phase and as vapor in the gaseous phase. Air is present in the gas phase (dry air) and in the liquid phase in the dissolved state.

The full description of the Thermo-Hydro-Mechanical state of the partially saturated medium is defined by the set of variables: solid velocity$\left(v_{s_x}, v_{s_y}, v_{s_z}\right)$, liquid pressure($p_l$), gas pressure$\left(p_g\right)$ and temperature(T). Their evolution is constrained by the balance equations (mass, heat and momentum), the constitutive equations and the equilibrium restrictions, see Olivella (1994). The full set of equations has been discretized in the framework of Finite Element formulation and implemented in the code Code-Bright Olivella (1994), Olivella (1996).

Before proceeding further, notation and terminology used in appendix A1 is summarized.

_____

A1.1) Notation and Terminology

Notation for mathematical formulation of THM couple problem	
q_l	Volumetric liquid flux
p_l	Liquid pressure
k_{rl}	Liquid relative permeability
μ_l	Liquid dynamic viscosity
S_r	Effective degree of saturation
p_o	Air entry value
p_g	Gas pressure
k_{rg}	Gas relative permeability
μ_g	Gas dynamic viscosity
i_l^a	Diffusive flux of dissolved air
ω_l^a	Mass fraction of dissolved air
D_m^a	Molecular diffusion of air
T	Coefficient of tortuosity
i_g^w	Diffusive flux of vapor
D_m^w	Molecular diffusion of water
i_c	Conductive heat flux
T	Temperature
Λ	Thermal conductivity
m_s	Mass of solid per unit volume of porous medium
ρ_s	Solid density
j_s	Advective flux of solid
m_w	Mass of water per unit volume of porous medium
ρ_l	Water density
ρ_g	Gas density
ω_l^w	Mass fraction of water in liquid phase
θ_l^w	Apparent mass of liquid
θ_g^w	Apparent mass of vapor (liquid per unit volume of gas phase)

j_l^w	Advective flux of water
j_g^w	Diffusive flux of water
m_a	Mass of air per unit volume
ω_l^a	Mass fraction of air in liquid
ω_g^a	Mass fraction of air in gas
θ_l^a	Apparent mass of dissolved air (per unit volume of liquid phase)
θ_g^a	Apparent mass of dry air
j_l^a	Diffusive flux of dissolved air
j_g^a	Advective flux of dry air
E_m^p	Total internal energy per unit of porous medium
E_s	Specific internal energy per unit mass of solid phase
E_l	Specific internal energy per unit mass of liquid phase
E_g	Specific internal energy per unit mass of gas phase
C_s	Specific heat of solid phase
E_g^w	Specific internal energy of water in the gas phase
E_g^a	Specific internal energy of air in the gas phase
E_l^w	Specific internal energy of water in the liquid phase
E_l^a	Specific internal energy of air in the liquid phase
j_{E_s}	Energy flux of the solid phase
j_{E_l}	Energy flux of the liquid phase
j_{E_g}	Energy flux of the gas phase
Σ	Stress tensor
B	Body forces

A1.2)   Momentum balance (stress equilibrium)

The balance of momentum of the porous medium is reduced to the equilibrium equation for macroscopic total stresses:

$$\frac{\partial \sigma_{ij}}{\partial x_j} + \underbrace{\rho \cdot \left(1 + \phi \left(S_l w_l + (1 - S_l) w_g \right) \right) g_j}_{b_j} = 0 \qquad (A1.1)$$

where $\rho = \rho_s(1 - \phi)$ is the dry density, $w_l = {}^{\rho_l}/_\rho$, $w_g = {}^{\rho_g}/_\rho$ and b_j is the vector of body forces. This equation is completed by the mechanical constitutive relationship of the porous medium that relates "constitutive" stresses to total strain rate, computed from solid velocities v_s through the compatibility equation $\dot{\varepsilon}_{ij} = {}^1/_2 \cdot \left({}^{\partial v_s}/_{\partial x_{ij}} + {}^{\partial v_s}/_{\partial x_{ji}} \right)$.

A1.3) Balance equation of each specie and Energy balance

A1.3.1) Mass balance of solid

Balance equations include the balances of mass for each constituent (solid, water and air), the balance of momentum and the balance of energy. They include interactions effects between phases and species, as derived by Olivella (1995).

The solid mass per unit volume of porous media is $m_s = \rho_s(1 - \phi)$, where ρ_s is the solid density and ϕ is the porosity of the medium. Thus, the mass balance of solid is then expressed as:

$$\frac{\partial}{\partial t}\left(\rho_s(1 - \phi)\right) + (j_s)_{,j} + f^s = 0 \tag{A1.2}$$

where j_s is the advective flux of solid:

$$j_s = \rho_s(1 - \phi)v_s \tag{A1.3}$$

where v_s is the velocity of the solid phase.

A1.3.2) Mass balance of the water

The water mass per unit volume of porous media is defined by $m_w = \phi\left(S_l\rho_l\omega_l^w + S_g\rho_g\omega_g^w\right) = \theta_l^w S_l\phi + \theta_g^w S_g\phi$, where ω_l^w and ω_g^w are the mass fractions of water in the liquid and gas phase, respectively. S_l is the liquid degree of saturation and S_g is the gas degree of saturation. θ_l^w and θ_g^w are the apparent mass of liquid water and vapor in the liquid and gas phases, respectively. The mass balance of water is then expressed as:

$$\frac{\partial}{\partial t}\left(\theta_l^w S_l \phi + \theta_g^w S_g \phi\right) + \left(j_l^w + j_g^w\right)_{,j} + \left(f^w\right) = 0 \tag{A1.4}$$

$$\underbrace{\hspace{4cm}}_{\text{Storage term}} \quad \underbrace{\hspace{2cm}}_{\substack{\text{Advective and} \\ \text{non-advective} \\ \text{flux terms}}} \quad \underbrace{\hspace{1.5cm}}_{\substack{\text{Source/sink} \\ \text{term}}}$$

where j_l^w and j_g^w are the advective and diffusive fluxes of water, given by:

$$j_g^w = \underbrace{i_g^w}_{\substack{\text{Diffusive flux} \\ \text{(given by Fick's} \\ \text{law)}}} + \underbrace{\theta_g^w q_g}_{\substack{\text{Advective flux } (q_g \\ \text{is given by} \\ \text{Darcy's law)}}} + \underbrace{\theta_g^w S_g \phi \, v_s}_{\substack{\text{Solid deformation} \\ \text{influence}}} \tag{A1.5}$$

and

$$j_l^w = i_l^w + \theta_l^w q_l + \theta_l^w S_l \phi v_s$$

Advective fluxes of liquid and gas in liquid phase are modelized by the generalized Darcy's law (Bear J. , 1972),

$$\mathbf{q}_l = -\frac{\mathbf{k} k_{rl}}{\mu_l} \cdot (\nabla p_l - \rho_l \mathbf{g}) \tag{A1.6}$$

$$\mathbf{q}_g = -\frac{\mathbf{k} k_{rg}}{\mu_g} \cdot (\nabla p_g - \rho_g \mathbf{g})$$

where $\mathbf{q}_l$ and $\mathbf{q}_g$ are the volumetric fluxes of liquid gas, p_l and p_g are the liquid pressure and the gas pressure, k_{rl} and k_{rg} are the liquid and gas relative permeabilities and $\mu_l = \rho_l \mathbf{g}$ and $\mu_g = \rho_g \mathbf{g}$ are the liquid and gas dynamic viscosities.

Last term of Darcy's law is due to gravity and includes the effect of liquid and gas densities under changes in pressure and temperature.

Liquid relative permeability is a scalar function of the liquid pressure p_l and can be evaluated though, van Genuchten's law proposal:

$$k_{rl} = \sqrt{S_r}\left[1 - \left(1 - S_r^{1/\lambda}\right)^\lambda\right]^2 \tag{A1.7}$$

where λ is a parameter related to the shape of the retention curve. Eq. A1.7 gives a considerable decrease of the relative permeability (several orders of magnitudes) at low values of saturation's degree.

_____

Relative permeability to gas is obtained as a complement to the permeability of liquid:

$$k_{rg} = 1 - k_{rl} \tag{A1.8}$$

although this law tends to overestimate the value of k_{rg} at high values of degree of saturation.

Degree of saturation S_r is commonly computed by van Genuchten's proposal:

$$S_r = \left[1 + \left(\frac{p_g - p_l}{p_o} \right)^{1/1-\lambda} \right]^{-\lambda} \tag{A1.9}$$

where S_r is the effective degree of saturation and p_o is the air entry value. Retention curve expresses the constitutive relationship between degree of saturation (or water content) and suction. This relation has been extensively addressed in chapter 4 to include hysteresis within the framework of thermo-mechanics.

Species move in the medium through two mechanisms: convection by the phases and diffusion within each phase. Diffusive flux of vapor is computed by Fick's law as:

$$\mathbf{i}_g^w = -\left(\tau \phi \rho_g S_g D_m^w \mathbf{I} \right) \nabla \omega_g^w \tag{A1.10}$$

where ω_g^w is the mass fraction of water vapor, D_m^w is the molecular diffusion of water vapor in the air given by: $\left(D_m^{w\,o} \left(\dfrac{(273.15 + T[°C])^n}{p_g} \right) \right)$.

A1.3.3)   Mass balance of air

The mass balance of air follows a scheme similar to that of water mass balance, where the air mass per unit volume of porous medium is given by,

$$m_a = \phi \left(S_l \rho_l \omega_l^a + S_g \rho_g \omega_g^a \right) = \theta_l^a S_l \phi + \theta_g^a S_g \phi \tag{A1.11}$$

where ω_l^a and ω_g^a are the mass fractions of air in the liquid and gas phase respectively, θ_l^a and θ_g^a the apparent density of dry air and dissolved air in the liquid phase and gas phase respectively, The mass balance of air is then expressed as,

$$\frac{\partial}{\partial t} \left(\theta_l^a S_l \phi + \theta_g^a S_g \phi \right) + \nabla \cdot \left(j_l^a + j_g^a \right) + (f^a) = 0 \tag{A1.12}$$

$$\underbrace{\phantom{\frac{\partial}{\partial t}\left(\theta_l^a S_l \phi\right)}}_{\text{Storage term}} \quad \underbrace{}_{\substack{\text{Advective} - \text{ and} \\ \text{non-advective} \\ \text{flux terms}}} \quad \underbrace{}_{\text{Source-sink}}$$

_____

j_l^a and j_g^a include the advective and diffusive fluxes of dry air in the gas phase, on the one hand, and dissolved air in the liquid phase on the other hand. They are given by:

$$j_g^a = i_g^a + \theta_g^a q_g + \theta_g^a S_g \phi v_s \tag{A1.13}$$

$$j_l^a = \theta_l^a q_l + \theta_l^a S_l \phi v_s$$

As discussed before, in the liquid phase diffusive flux of dissolved air is computed by Fick's law as:

$$\mathbf{i}_l^a = -(\tau \phi \rho_l S_l D_m^a \mathbf{I}) \nabla \omega_l^a \tag{A1.14}$$

where ω_l^a is the mass fractions of dissolved air, D_m^a is the molecular diffusion of air $\left(\text{equal to } \tau D_m^{ao} \exp\left({-Q}/{R \cdot (273.15 + T[°C])} \right)\right)$ and τ is the coefficient of tortuosity.

A1.3.4)   Energy balance

If thermal equilibrium between phases is assumed, the temperature is the same in all the phases. The total internal energy per unit volume of porous medium is then given by,

$$
\begin{aligned}
E \quad &= \quad (E_s \rho_s)(1 - \phi) + S_l(E_l \rho_l)\phi + S_g(E_g \rho_g)\phi \tag{A1.15}\\[6pt]
&= \quad C_s \rho_s T(1 - \phi) + \phi\big(S_l \rho_l E_l + S_g \rho_g E_g\big)
\end{aligned}
$$

where E_s, E_l and E_g are the specific internal energies (internal energy per unit of mass of phase) of each phase and $C_s \left[{J}/{k_g K}\right]$ is the specific heat of the solid phase. According to the mixture theory, the specific internal energy of the gas phase is equal to:

$$E_g \rho_g = \big(E_g^w \omega_g^w + E_g^a \omega_g^a\big)\rho_g \tag{A1.16}$$

where E_g^w and E_g^a are the specific internal energies of water and air in the gas phase respectively. In the same way, the specific internal energy of the liquid phase is given by:

$$E_l \rho_l = \big(E_l^w \omega_l^w + E_l^a \omega_l^a\big)\rho_l \tag{A1.17}$$

where E_l^w and E_l^a are the specific internal energies of air and water in the liquid phase.

Energy balance equation expresses the fact that internal energies variations are equal to the divergence of fluxes plus eventual source/sink terms, which in virtue of Eq. A1.15 is:

_____

$$\frac{\partial}{\partial t}\left(E_s\rho_s\cdot(1-\phi)+E_l\rho_lS_l\phi+E_g\rho_gS_g\phi\right)+\nabla\cdot\left(i_c\underbrace{+j_{E_s}}+j_{E_l}+j_{E_g}\right)+\left(f^Q\right)=0 \qquad \text{(A1.18)}$$

<div align="center">Fourier's law</div>

$$\underbrace{\hspace{7cm}}_{\text{Storage term}} \qquad \underbrace{\hspace{4cm}}_{\substack{\text{Conductive,}\\\text{dispersive and}\\\text{advective terms}}} \qquad \underbrace{\hspace{1.5cm}}_{\substack{\text{Source/sink}\\\text{term}}}$$

where the total energy flux is equal to the sum of the energy flux in each phase:

$$j_{E_s}=E_s\rho_s(1-\phi)v_s \qquad \text{(A1.19)}$$

$$j_{E_l}=(i_l^w+\theta_l^w q_l)E_l^w+(\theta_l^a q_l)E_l^a+E_l\rho_lS_l\phi v_s$$

$$j_{E_g}=\left(i_g^w+\theta_g^w q_g\right)E_g^w+\left(i_g^a+\theta_g^a q_g\right)E_g^a+E_g\rho_gS_g\phi v_s$$

The heat conduction in the porous medium is modeled by Fourier's law:

$$\mathbf{i}_c=-\lambda\nabla T \qquad \text{(A1.20)}$$

where $\mathbf{i}_c$ is the conductive heat flux, T is the temperature of the porous medium and λ the thermal conductivity, function of porosity and degree of saturation. In simplified form, λ can be assumed to vary between two limits, the thermal conductivity of the dry medium λ_{dry} and of the saturated medium λ_{sat}, following the law $\lambda=\lambda_{sat}\sqrt{S_l}+\lambda_{dry}\left(1-\sqrt{S_l}\right)$.

A2)   A cap hyperplastic Model for unsaturated Soils "BBM-cap"

The complex response presented by different type of soils requires a wide range of elasto-plastic models to properly reproduce such a response. One family of proposed models satisfying the necessary requirements to model such a complex behavior are the well known Cap Models (Di Maggio & Sandler , Chen & Mizuno). The first proposed model of this type was presented by Drucker (Drucker et al. 1957). This model suggests a spherical end cap to the Drucker-Prager model, see Chen & Mizuno pag. 270. Another type of Cap model is the generalization of the modified Cam-clay model to consider a cap of the yield ellipse on the contracted side of critical state. This model provides a plastic response for values of the deviator q higher than that defined by the critical state line ($q' - Mp' = 0$) and other for values of the deviator q lower than that defined by the critical state line. That means that a single function allows to reproduce a BBM type response on the dilatant side ($c_a = 1$) and other response given by Cap on the contracted side ($c_a < 1$). Then the BBM-Cap model is derived with thermo-mechanic bases. Consider the following dissipation function:

$$d = \frac{w}{c_a}\left(\frac{\vartheta p^c}{2}\exp\left(\frac{\alpha_p}{\lambda^* - \kappa^*}\right)\right)^b \cdot \sqrt{c_a{}^2\dot{\alpha}_p{}^2 + M^2\dot{\alpha}_q{}^2} \quad \begin{cases} c_a = 1 & q \geq Mp' \\ \\ c_a < 1 & q < Mp' \end{cases} \qquad \text{(A2.1)}$$

where c_a is a positive parameter lower than one and defines the amount of curvature of the cap at the compression side and $\vartheta(c_a, M)$ is a parameter obtained as function of the cap curvature and the slope of the critical state line. The rest of the quantities are defined in chapter 4. Now, following standard procedures in thermo-mechanics the expressions for the generalized mean stress and generalized deviatoric stress are derived,

$$p' - \rho = \frac{\partial d}{\partial \dot{\alpha}_p} = \frac{w^2}{d}\left(\frac{\vartheta p^c}{2}\exp\left(\frac{\alpha_p}{\lambda^* - \kappa^*}\right)\right)^{2b}\dot{\alpha}_p \qquad \text{(A2.2)}$$

$$q' = \frac{\partial d}{\partial \dot{\alpha}_p} = \frac{w^2}{c_a{}^2 \cdot d}\left(\frac{\vartheta p^c}{2}\exp\left(\frac{\alpha_p}{\lambda^* - \kappa^*}\right)\right)^{2b}M^2\dot{\alpha}_q$$

For $q \geq Mp'$ the expression for the generalized mean stress and deviatoric stress without cap are restored ($c_a = 1$). Extracting $\dot{\alpha}_p$ and $\dot{\alpha}_q$ from the previous equations and invoking

_____

the transformation $f^y = (p' - \rho)\dot{\alpha}_p + q'\dot{\alpha}_q - d = 0$ the expression for the yield function is obtained:

$$f^y = \frac{(p' - \rho)^2}{c_a^2} + \frac{q'^2}{M^2} - \frac{w^2}{c_a^2}\left(\frac{\vartheta p^c}{2}\exp\left(\frac{\alpha_p}{\lambda^* - \kappa^*}\right)\right)^{2b} \quad \begin{cases} \vartheta = \dfrac{1 + M}{M \cdot (c_a^2 + 1)} & q \geq Mp' \\[2ex] c_a < 1 & q < Mp' \end{cases} \quad \text{(A2.3)}$$

Figure A2.252 shows the contour of the BBM-Cap model at the p-q plane
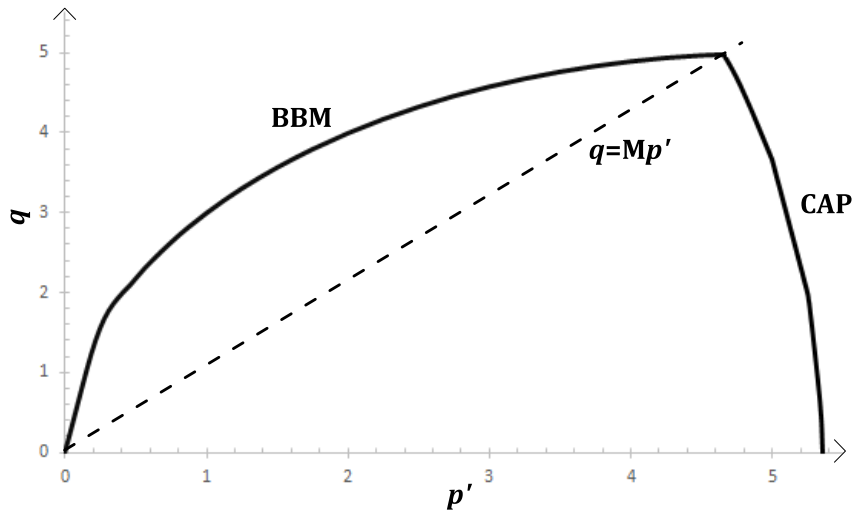
Figure A2.252: BBM-Cap model. The critical state line define the two regions for $c_a = 1$ and for $c_a < 1$.

The expressions for the flow rules results in the equations,

$$\dot{\alpha}_p = \lambda\frac{\partial f^y}{\partial x_p} = \lambda\frac{2(p' - \rho)}{c_a^2} \quad \text{(A2.4)}$$

$$\dot{\alpha}_q = \lambda\frac{\partial f^y}{\partial x_q} = \lambda\frac{2q'}{M^2}$$

It can be seen from the last equation that the volumetric plastic strain rate increases as c_a decreases. A cap model has been presented and derived under hyper-plastic principles. The BBM-Cap model shows again the ability of the hyper-plastic principles to derive elasto-plastic models for soils. Figure A2.253 shows the graph of the yield function BBM-Cap for two different values of cap curvature c_a,

_____
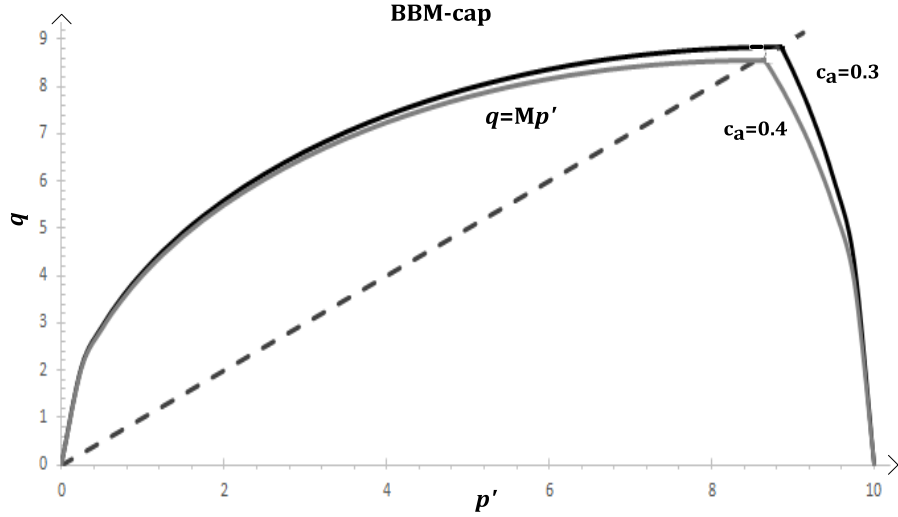
Figure A2.253: Contour of the BBM-cap model for two different values of the cap-curvature parameter c_a and the critical state line.

The model has a unique hardening law. It is activated once a plastic process has been initiated either on the dilatant side or on the contracted side. Experimental evidence reveals that as temperature increases the plastic behavior is mainly volumetric. It means that the magnitude of the mean plastic strain becomes significantly higher than the shear plastic strain component. This fact can be modeled with the BBM-Cap model proposed by introducing a dependence of the cap curvature parameter c_a on the current temperature $\left(\text{a law of type } c_a\left(T/T_0\right)\right)$. The hyperplastic BBM-Cap model is completed defining the Gibbs energy function for the porous medium. If the general nonlinear thermo-elasticity is considered, then the energy function Eq. 4.123 is invoked, but in this case the third component of the function should be added. This term will consider the back stress (kinematic hardening) relating the generalized stress space and the true stress space.

$$g_s = \frac{(1-\beta_s)}{p_o{}^{1-n}\cdot k(1-n)(2-n)}\cdot\left(p'^2+\frac{k(1-n)}{3\varrho}q^2\right)^{\frac{2-n}{2}}-\frac{p'^{(1-\beta_s)}}{k(1-n)}-\left(p'\alpha_p+q\alpha_q\right)$$
$$+w\frac{(\lambda^*-k^*)}{b}\left(\frac{\vartheta p^c}{2}\exp\left(\frac{\alpha_p}{\lambda^*-k^*}\right)\right)^b \tag{A2.5}$$

The same procedure described above allows to express the back stress as,

_____

$$\rho_p' = \frac{\partial g_{s_2}}{\partial \alpha} = w \left(\frac{\vartheta p^c}{2} \exp\left(\frac{\alpha_p}{\lambda^* - k^*} \right) \right)^b \begin{cases} \vartheta = \dfrac{1 + M}{M \cdot (c_a{}^2 + 1)} & q \geq Mp' \\[2mm] \vartheta = 1 & q < Mp' \end{cases} \quad \text{(A2.6)}$$

And then the generalized mean stress becomes,

$$x_p' = p' - \underbrace{w \left(\frac{\vartheta p^c}{2} \exp\left(\frac{\alpha_p}{\lambda^* - k^*} \right) \right)^b}_{\rho_p'} \quad \text{(A2.7)}$$

where the value of ϑ will depend on the deviator's magnitude with respect to the csl. (critical state line). Figure A2.254 shows the contour of the yield surface when transferred to the generalized stress space.
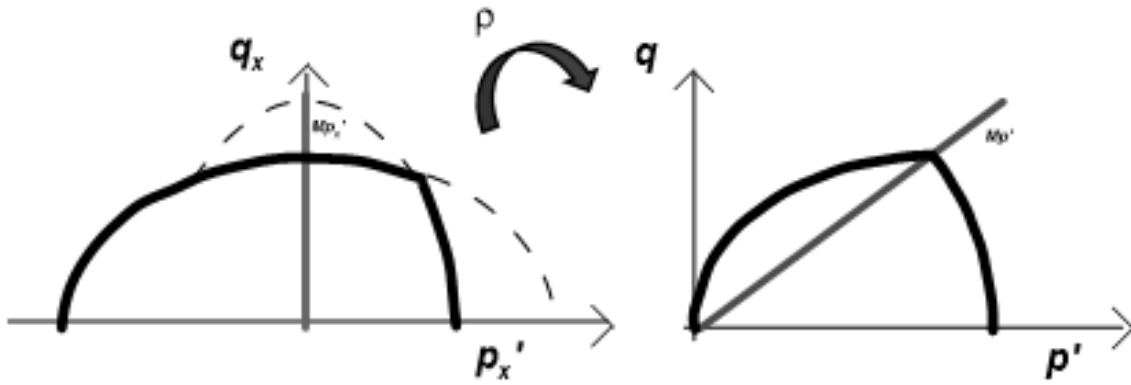
Figure A2.254: Contours of the yield surface at both the generalized stress space and the true stress space. The back or shift stress relating the spaces.

The integration strategy of this model will be the same as the one followed for the previous models. However, an additional question is necessary to define the stress states location with respect to the csl, Fig. A2.255.

_____
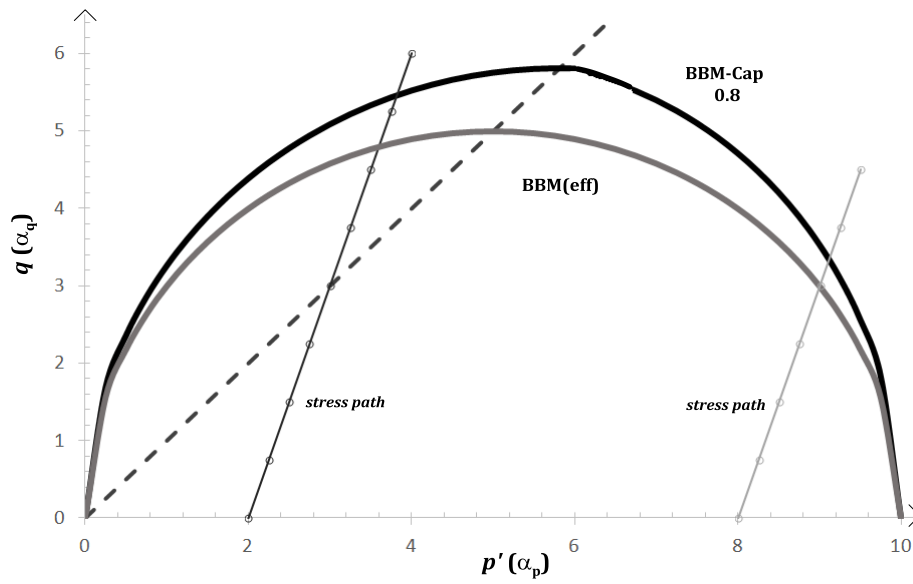
Figure A2.255: Contour of BBM-Cap model with an amount of capping =0.8. Imposed stress paths.

Figure A2.256 shows the model response under triaxial conditions for both samples at lightly overconsolidated condition and heavily overconsolidated condition.

On dry branch, where the contours of BBM-Cap and BBM5 are homothetic, the responses tend to join at the critical state. On the other hand at the wet branch of the critical state, where the contours of BBM-Cap and BBM5 are non-homothetic, the branches evidence a marked difference, being the elastic response larger at the BBM-Cap model.
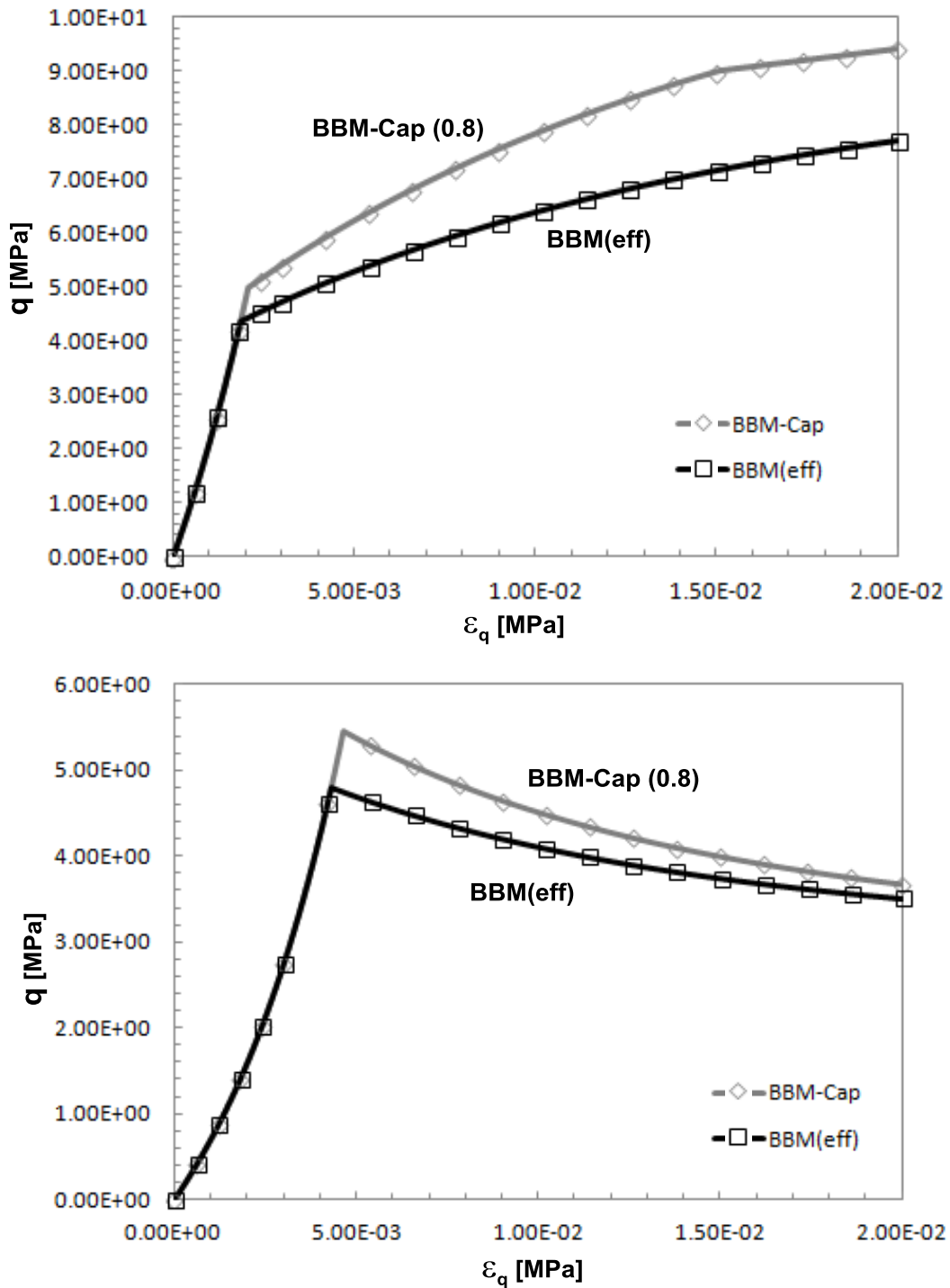
Figure A2.256: Conventional drained triaxial tests on BBM-Cap model. (a)Deviatoric Stress vs. axial strain for lightly overconsolidated sample and heavily overconsolidated sample.

Figure A2.257 shows a comparison between the graph of plastic deviatoric strain vs. plastic volumetric strain for both the BBM-Cap model and BBM5 model. The increase of the plastic volumetric component at the cap of the BBM-Cap model over the same component related to the BBM5 model can be clearly seen.
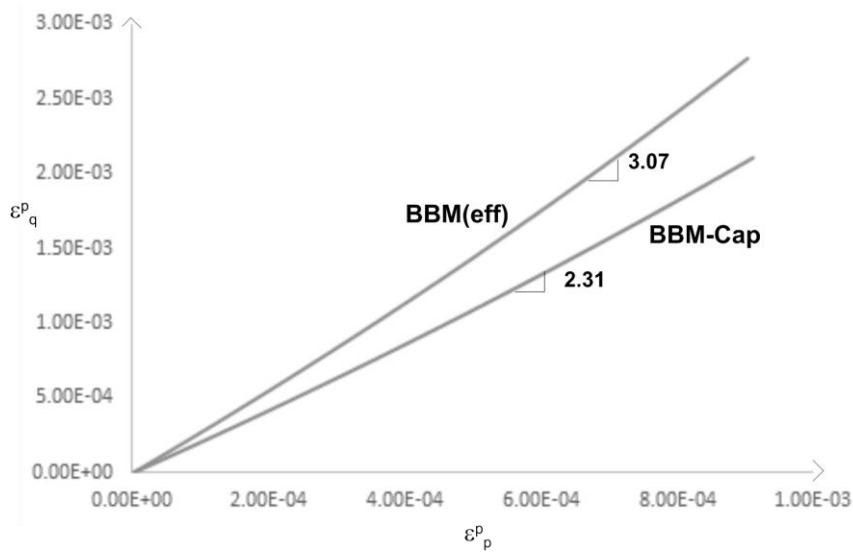
Figure A2.257: Deviatoric plastic strain vs volumetric plastic strain for both BBM-Cap model and BBM5 model. Response to the trial stress path on a lightly consolidated sample.

Finally, I would like to note that this model describes a predominant volumetric plastic response as c_a decreases. This feature would be useful to reproduce the plastic behavior of porous medium under thermal load.

529

_____

A3)   Review of frictional soil models

In this section, two cohesive-frictional models will be reviewed in some detail within the hyper-plastic framework. First, the Drucker-Prager model derived from a dissipation potential by Collins & Houlsby (1997) in case of purely frictional materials will be recalled. This recollection has been extended to consider a cohesive component. Then, the hyperplastic formulation of Matsuoka-Nakai model (Matsuoka & Nakai, 1974) will be described as formulated within hyperplastic framework with special attention devoted to the representation of dilatancy (Houlsby & Puzrin, 2006).

A3.1)   Drucker-Prager Model

The criterion is expressed as a function of the first invariant of the stress tensor ($I_1 = 3p$) and the second invariant of the deviatoric stress tensor $\left(J_2\left(\equiv J = \sqrt{J_2}\right)\right)$ as:

$$f^y = J - Mp - a = 0 \tag{A3.1}$$

where M and a are related to the cohesion and the friction angle of the soil through the expressions (Chen & Mizuno, 1990):

$$M = \frac{6 \cdot \sin \phi'}{\sqrt{3}(3 - \sin \phi')} \tag{A3.2}$$

$$a = \frac{6c' \cdot \cos \phi'}{\sqrt{3}(3 - \sin \phi')}$$

Cohesion is introduced in the model by considering a modified expression of the dissipation function proposed by Collins & Houlsby (1997) for the pure frictional Drucker-Prager model. It takes the form:

$$d = \left[N\frac{\sigma_{kk}}{3} + b\right] \cdot \sqrt{\frac{2}{3}\dot{\alpha}'_{ij}\dot{\alpha}'_{ij}} \tag{A3.3}$$

where $b = \sqrt{3}a$ is a function of cohesion c'. Standard procedure leads to the following expression for the generalized deviatoric stresses:

$$x'_{ij} = x_{ij} - \delta_{ij}x_{kk} = \sqrt{2}\left(M\frac{\sigma_{kk}}{3} + a\right) \cdot \frac{\dot{\alpha}'_{ij}}{\sqrt{\dot{\alpha}'_{ij}\dot{\alpha}'_{ij}}} \tag{A3.4}$$

_____

It can be verified from equation A.2.4 that the internal plastic strains $\dot{\alpha}'_{ij}$ satisfy Drucker-Prager's flow rule.

The dilatant behavior of the material is introduced as an additional constraint by using Lagrange multipliers (Collins & Houlsby, (1997); Houlsby & Puzrin, (2006)):

$$c = \dot{\alpha}_{ii} + B\sqrt{\frac{2}{3}\dot{\alpha}'_{ij}\dot{\alpha}'_{ij}} = 0 \tag{A3.5}$$

where B is a material parameter function of the dilatancy angle and is given by the expression:

$$B = \frac{6\sin\psi}{(3-\sin\psi)} \tag{A3.6}$$

The extended dissipation function reads:

$$d' = d + \Lambda c = \left[\frac{N\sigma_{kk} + 3(b + \Lambda B)}{3}\right]\sqrt{\frac{2}{3}\dot{\alpha}'_{ij}\dot{\alpha}'_{ij}} + \Lambda\dot{\alpha}_{ii} \tag{A3.7}$$

where Λ is the Lagrange multiplier. The standard procedure leads again to the expression of the generalized stress tensor:

$$x_{ij} = \frac{\partial d'}{\partial\dot{\alpha}_{ij}} = \left[\frac{N\sigma_{kk} + 3(b + \Lambda B)}{3}\right]\sqrt{\frac{2}{3}}\frac{\dot{\alpha}'_{ij}}{\sqrt{\dot{\alpha}'_{ij}\dot{\alpha}'_{ij}}} + \Lambda\delta_{ij} \tag{A3.8}$$

And the following expression for the volumetric and deviatoric components of x_{ij}:

$$x_{kk} = 3\Lambda$$

$$x'_{ij} = \left[\frac{N\sigma_{kk} + Bx_{kk}}{3} + b\right]\sqrt{\frac{2}{3}}\frac{\dot{\alpha}'_{ij}}{\sqrt{\dot{\alpha}'_{ij}\dot{\alpha}'_{ij}}} \tag{A3.9}$$

Computation of product $x'_{ij}x'_{ij}$ from the last equation provides the expression for the yield surface in the generalized stress space:

$$\sqrt{\frac{3}{2}x'_{ij}x'_{ij}} - \left(\frac{N\sigma_{kk} + Bx_{kk}}{3}\right) - b = 0 \tag{A3.10}$$

Or, in terms of invariants p and $J = \sqrt{J_2}$:

$$J - Cx_p - Np - a = 0 \tag{A3.11}$$

_____

where $C = {B}/{\sqrt{3}}$. In this equation, the term Np works as an apparent cohesion.

Finally, in absence of kinematical hardening, $x_p = p$. Eq. A3.11 provides thus a yield surface identical to that considered in conventional plasticity Eq. A3.1 with M = C + N. The yield surface and plastic potential for the extended Drucker-Prager model is plotted in Fig. A3.258.
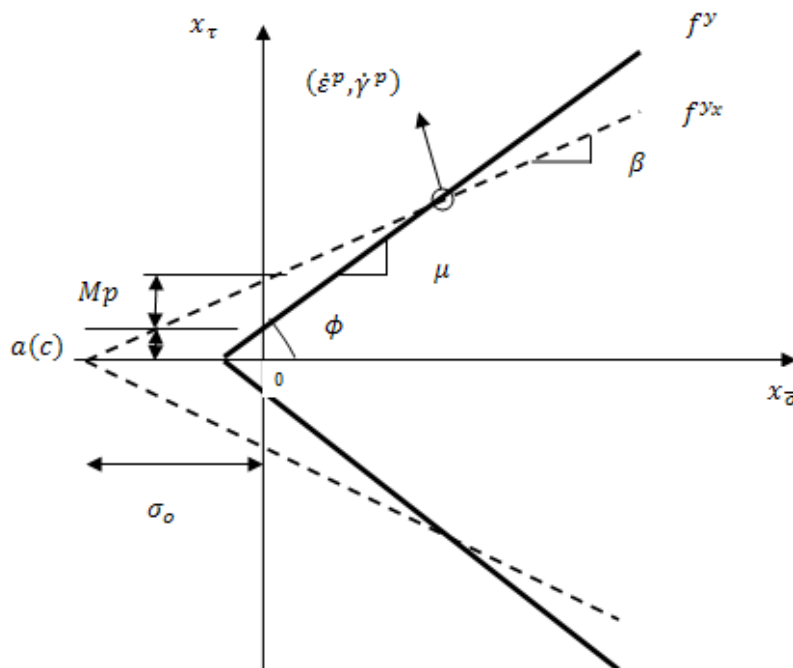
Figure A3.258: Drucker-Prager Yield Surface and Plastic Potential for frictional Plasticity (meridian plane).
M = μ; C = β.

A3.2)   Matsuoka-Nakai Model

The Matsuoka-Nakai yield criterion (Matsuoka & Nakai, (1974)) provides a smooth approximation of Mohr-Coulomb model by the expression:

$$\frac{(\sigma_1 - \sigma_2)^2}{\mu^2 \sigma_1 \sigma_2} + \frac{(\sigma_1 - \sigma_3)^2}{\mu^2 \sigma_1 \sigma_3} + \frac{(\sigma_2 - \sigma_3)^2}{\mu^2 \sigma_2 \sigma_3} = 8 \tag{A3.12}$$

_____

where $\mu = \tan(\phi')$ is the friction coefficient. Alternative expressions of the yield criterion are:

$$(\sigma_1 + \sigma_2 + \sigma_3) \cdot (\sigma_1\sigma_2 + \sigma_2\sigma_3 + \sigma_3\sigma_1) - 9\sigma_1\sigma_2\sigma_3 = 8\mu^2\sigma_1\sigma_2\sigma_3 \qquad (A3.13)$$

$$9I_3 - I_1I_2 + 8\mu^2I_3 = 0 \qquad (A3.14)$$

$$\frac{I_1I_2}{I_3} = 9 + 8\mu^2 \qquad (A3.15)$$

$$k_1^2\bar{\sigma}_1 + k_2^2\bar{\sigma}_2 + k_3^2\bar{\sigma}_3 - 8\bar{\sigma}_1\bar{\sigma}_2\bar{\sigma}_3 = 0 \qquad (A3.16)$$

where I_1, I_2 and I_3 are the 1st, 2nd and 3rd stress invariants, $\bar{\sigma}_i = \mu\sigma_i$ and $k_i = \sigma_j - \sigma_k$, with $i \neq j \neq k$.

The shape of Matsuoka-Nakai criterion is given in Fig. A3.259. It can be observed how it smoothes the apex of Mohr Coulomb criterion, which makes it suitable for numerical implementation.
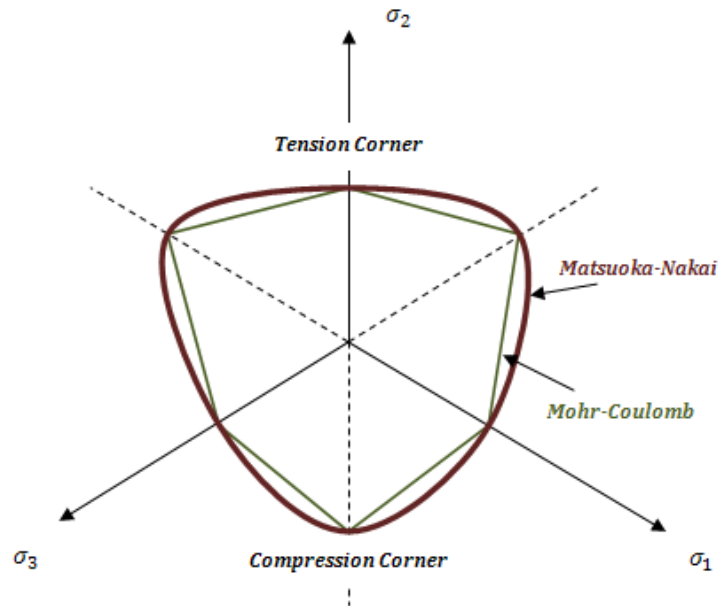
Figure A3.259: Shape of Mohr-Coulomb and Matsuoka-Nakai yield criterion in the deviatoric plane.

According to Coulomb friction law, material does not experiment dilatancy at failure and the flow rule is non-associated in the true stress space. To formulate this model in the framework of hyperplasticity, Houlsby & Puzrin (2006) proposed the following dissipation function:

$$d = \sqrt{\frac{8}{9}[\bar{\sigma}_1\bar{\sigma}_2(\dot{\alpha}_1 - \dot{\alpha}_2)^2 + \bar{\sigma}_2\bar{\sigma}_3(\dot{\alpha}_2 - \dot{\alpha}_3)^2 + \bar{\sigma}_3\bar{\sigma}_1(\dot{\alpha}_3 - \dot{\alpha}_1)^2]} \qquad (A3.17)$$

_____

The generalized stresses are computed from the extended dissipation function $d' = d + \Lambda C$ with the constraint of null dilatancy $C = \dot{\alpha}_1 + \dot{\alpha}_2 + \dot{\alpha}_3 = 0$:

$$x_1 = \frac{\partial(d + \Lambda C)}{\partial \dot{\alpha}_1} = \frac{8}{9d}\left(\overline{\sigma}_1\overline{\sigma}_2(\dot{\alpha}_1 - \dot{\alpha}_2) - \overline{\sigma}_3\overline{\sigma}_1(\dot{\alpha}_3 - \dot{\alpha}_1)\right) + \Lambda \qquad (A3.18)$$

$$x_2 = \frac{\partial(d + \Lambda C)}{\partial \dot{\alpha}_2} = \frac{8}{9d}\left(\overline{\sigma}_2\overline{\sigma}_3(\dot{\alpha}_2 - \dot{\alpha}_3) - \overline{\sigma}_1\overline{\sigma}_2(\dot{\alpha}_1 - \dot{\alpha}_2)\right) + \Lambda$$

$$x_3 = \frac{\partial(d + \Lambda C)}{\partial \dot{\alpha}_3} = \frac{8}{9d}\left(\overline{\sigma}_3\overline{\sigma}_1(\dot{\alpha}_3 - \dot{\alpha}_1) - \overline{\sigma}_2\overline{\sigma}_3(\dot{\alpha}_2 - \dot{\alpha}_3)\right) + \Lambda$$

by summing up the three equations, the following result is obtained: $\Lambda = \frac{x_1+x_2+x_3}{3}$. Now, the condition $\dot{\alpha}_1 + \dot{\alpha}_2 + \dot{\alpha}_3 = 0 = (\dot{\alpha}_1 - \dot{\alpha}_2) + (\dot{\alpha}_3 - \dot{\alpha}_1) + (\dot{\alpha}_2 - \dot{\alpha}_3)$ provides the equation for the yield criterion in the generalized stress space:

$$k_1^2 x_1 + k_2^2 x_2 + k_3^2 x_3 - 8x_1 x_2 x_3 - \frac{(k_1 x_1 + k_2 x_2 + k_3 x_3)^2}{x_1 + x_2 + x_3} = 0 \qquad (A3.19)$$

This yield criterion differs from the yield criterion in the true stress space by the last left-hand term, that can be seen as a stress-dependent cohesion. This term makes the yield criterion perpendicular to the flow rule in the generalized stress space, Fig. A3.260.
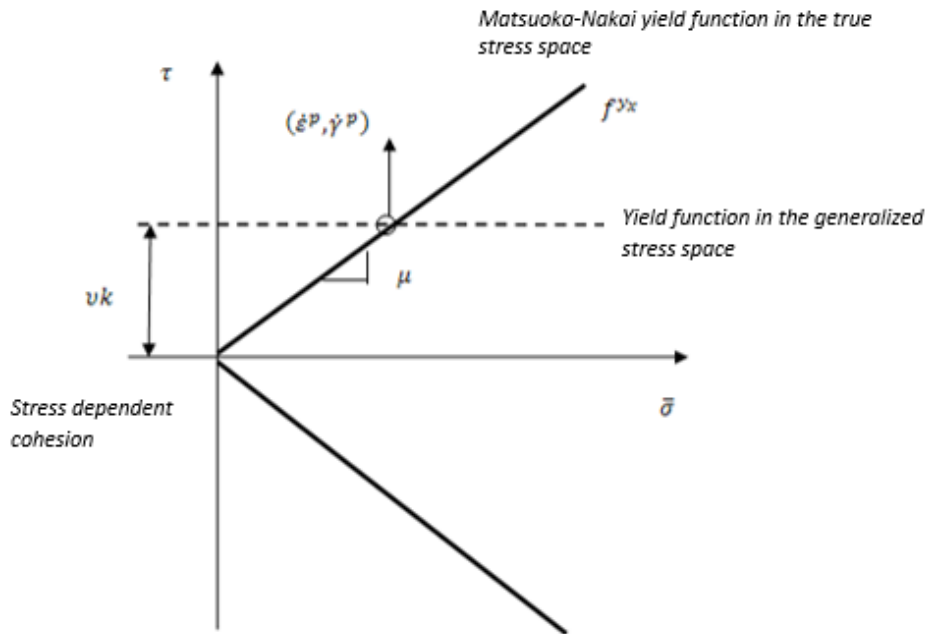
Figure A3.260: Zero Dilatant Matsuoka-Nakai Model at Meridian Plane. The term (vk) works as an apparent cohesion.

_____

Houlsby (1986) proposed a generalization of this criterion, such that it encloses both Tresca (for cohesive materials) and Matsuoka & Nakai (for pure frictional materials) criteria. The equation reads:

$$\frac{(\sigma_1 - \sigma_2)^2}{(c + \mu\sigma_1)(c + \mu\sigma_2)} + \frac{(\sigma_1 - \sigma_3)^2}{(c + \mu\sigma_1)(c + \mu\sigma_3)} + \frac{(\sigma_2 - \sigma_3)^2}{(c + \mu\sigma_2)(c + \mu\sigma_3)} = 8 \tag{A3.20}$$

and can be reformulated into Eq. A3.17 by stating $\overline{\sigma}_i = c + \mu\sigma_i$. Following the same procedure, the dissipation function takes the form (Houlsby & Puzrin, (2006)):

$$d = \sqrt{\frac{8}{9}\begin{bmatrix} (c + \mu\sigma_1)(c + \mu\sigma_2)(\dot{\alpha}_1 - \dot{\alpha}_2)^2 + \\ (c + \mu\sigma_2)(c + \mu\sigma_3)(\dot{\alpha}_2 - \dot{\alpha}_3)^2 + \\ (c + \mu\sigma_3)(c + \mu\sigma_1)(\dot{\alpha}_3 - \dot{\alpha}_1)^2 \end{bmatrix}} \tag{A3.21}$$

_____

Bibliography

Abbo, A. (1997). *Finite Element Algorithms for Elastoplasticity and Consolidation.* Newcastle-Australia: PhD. Thesis.

Abbo, A., Lyamin, A., Sloan, S., & Hambleton, J. (2011). A C2 continuous approximation to Mohr-Coulomb yield surface. *International Journal of Solids and Structues*, 3001-3010.

Alonso, E. G. (1990). A Constitutive Model for Partially Saturated Soils. *Geotechnique, 40, No.3*, 405-430.

Alonso, E., Gens, A., & Josa, A. (1990). A constitutive model for partially saturated soils. *Geotechnique 40, No 3*, 405-430.

Alonso, E., Pereira, J., Vaunat, J., & Olivella, S. (2010). A microstructurally based effective stress for unsaturated soils. *Geotechnique, volume60, Issue 12*, 913-915.

Alonso, E., Pereira, J., Vaunat, J., & Olivella, S. (2010). A microstructurally-based effective stress for unsaturated soils. *Geotechnique, v60, i12*, 913-925.

Avriel, M. (1976). *Nonlinear Programming: Analysis and Methods.* Courier Dover .

Bardet, J. P. (1990). Lode Dependences for Isotropic Pressure-Sensitive Elastoplastic Materials. *Transactions of the ASME*, vol.57, 498-506.

Bear, J. (1972). *Dynamics of fluids in porous media.* Dover.

Bear, J., Zaslavsky, D., & Irmay, S. (1968). *Physical properties of water percolation and seepage.* United Kingdom: Gloucestershire, GLS.

Bendito, E., Carmona, A., Encinas, A., & Gesto, J. (2007). Estimation of Fekete points. *J. Comput. Phys., 225*, 2354-2376.

Benzi, M. (2005). Numerical solution of saddle point problems. *Acta Numerica*, 1-137.

_____

Bertsekas, D. (1986). *Nonlinear Programming.* Athena Scientific.

Biot, M. (1941). General theory of three-dimensional consolidation. *Journal of Applied Physics, 12*, 155-164.

Bishop, A. (1959). The principle of effective stress. *Tecknisk Ukebland*, 177-198.

Blaney, H., & Criddle, W. (1950). Determining water requirements in irrigated areas from climatological and irrigation data. *Technical Publication 96, Washington, DC: US Soil Conservation Service*.

Blight, G. (1997). Interactions between the atmosphere and the Earth. *Geotechnique 47, No.4 ,* 715-767.

Borja, R. (2004). Cam Clay plasticity, Part V: A mathematical framework for three-phase deformation and strain localization analysis of partially saturated porous media. *Computer Methods in Applied Mechanics*, 5301-5338.

Borja, R. I. (2004). Cam-Clay plasticity. Part V: A mathematical framework for three-phase deformation and strain localization analyses of partially saturated porous media. *Comput. Methods Appl. Mech. Engrg., 193*, 5301-5338.

Borja, R., Sama, K. M., & Sanz, P. F. (2003). On the numerical integration of three-invariant elastoplastic constitutive models. *Computer methods in applied mechanics and engineering*, 1227-1258.

Borja, R., Tamagnini, C., & Amorosi, A. (1997). Coupling Plasticity and Energy Conservation Elasticity Models for Clays. *Journal of Geotechnical and Geoenvironmental Engineering, Vol. 123, No 10*, 1-3.

Brooks, R., & Corey, A. (1964). Hydraulic properties of porous media. *Colorado State University Hydrology Papers*, 1-37.

Butterfield, R. (1979). A natural compression law for soils. *Geotechnique, 29*, 469-480.

Carreras, J., Alfageme, H., Galarza, G., Medina, A., & Andres, M. (1991). *Estudio de la infiltracion a traves de la cobetera de la F.U.A.* Barcelona- Espana: Centro Internacional de Metodos Numericos en Ingenieria.

Casini, F. (2008). Effetti del grado di saturazione sul comportamento meccanico di un limo. *PhD Thesis, Università di Roma La Sapienza, Italy*.

_____

Casini, F., Munoz, J., Lorenco, S., Thorel, L., Vaunat, J., & Delage, P. (2013). Centrifuge modelling of a unsaturated collapsible soil.

Chen, W., & Mizuno, E. (1990). *Nonlinear analysis in Soil Mechanics.* Elsevier.

Chiu, C., Cui, Y., Delage, P., De Laure, E., & Haza, E. (2005). Lessons learnt from suction monitoring during centrifuge modeling. *Proc. of Advanced Experimental Unsaturated Soil Mechanics (EXPERUS).*

Choudhury, B., & Idso, S. (1985). An empirical model for stomatal resitance of field-grown wheat. *Agric. for Meteorol., 36*, 65-82.

Coduto, D. (2001). *Foundation Design.* Prentice-Hall.

Collins, I. (2005). The concept of stored plastic work or frozen elastic energy in soil mechanics. *Geotechnique 55, No. 5*, 373-382.

Collins, I., & Houlsby, G. (1997). Application of thermomechanical principles to the modelling of geotechnical materials. *Proc. R. Soc. Lond. A 453*, 1975-2001.

Collins, I., & Houlsby, G. (1997). Application of thermomechanical principles to the modelling of geotechnical materials. *Pro. R. Soc. Lond.* , 1975-2001.

Collins, I., & Kelly, P. (2002). A thermomechanical analysis of a family of soil models. *Géotechnique, 52, No.7*, 507-518.

Coussy, O. (1995). *Mechanics of Porous Continua.* John Wiley & Sons, Ltd. .

Coussy, O. (2004). *Poromechanics.* John wiley & Sons, Ltd. .

Coussy, O., & Fleureau, J. (2002). *Mechanique des sols non satures.* Lavoisier.

Cui, Y. (1993). Etude du comportement d'un limon non saturé et de sa modélisation dans un cadre elasto-plastique. *PhD Thesis, Ecole Nationale des Ponts et Chassées, Paris, France.*

Damon, A., Ward, W., Tosto, P., & Mcgonegal, R. (2007). *Biology.* Heinemann International.

de Ridder, K., & Schayes, G. (1997). The IAGL land surface model. *J. Appl. Meteorol., 36*, 167-182.

_____

Di Donna, A., & Laloui, L. (2013). Introduction in Lagamine of the stress dependency extension for the ACMEG model. *First International Workshop on the Finite Element Code LAGAMINE*.

Dickinson, R. (1984). Modelling Evapotranspiration for three dimensional global climate models.Climate Processes and Climate Sensitivity. *Geophys. Monogr., 29*, 58-72.

Dixon , H., & Joly, J. (1894). On the ascent of sap. *Annals of Botany (8)*, 468-470.

Dobson, M., & Moffat, A. (1995). A re-evaluation of objections to tree planting on containment landfills. *Wate Management Res. 13*, 579-600.

Drucker, D. (1951). A more fundamental approach to plastic stress-strain relations. *Proc. First UN Nat. Confress Appl. Mech.*, 487-491.

Drucker, D., & Prager, W. (1952). Soil mechanics and plastic analysis or limit design. *Appl. Math. 10, No 2*, 157-175.

Einav, I., & Puzrin, A. (2004). Pressure-Dependent Elasticity and Energy Conservation in Elastoplastic Models for Soils. *Journal of Geotechnical and Geoenvironmental Engineering, V 130, No. 1*, 81-92.

Einav, I., Puzrin, A., & Houlsby, G. (2003). Numerical studies of hyperplasticity with single, multiple and a continuous field of yield surfaces. *International journal for numerical and analytical methods in geomechanics, No 27*, 837-858.

Forsgren, A., Gill, P., & Wright, M. (2002). Interior methods for nonlinear optimization. *SIAM Rev., 44(4)*, 535-597.

G.A., M. (1999). *The Thermomechanics of Nonlinear Irreversible Materials.* Singapore and River-Edge, N.J.: World Scientific.

Gallipoli, D., Gens, A., Sharma, R., & Vaunat, J. (2003). An elasto-plastic model for unsaturated soil incorporating the effects of suction and degree of saturation on mechanical behavior. *Geotechnique 53, No 1*, 123-135.

Gallipoli, D., Wheeler, S. J., & Karstunen, M. (2003). Modelling the variation of degree of saturation in a deformable unsaturated soil. *Géotechnique 53, No. 1*, 105-112.

Gens, A. (1995). Effect of structure on the volumetric behaviour of a compacted soils. *Proceedings of the 1st International Conference on Unsaturated Soils. Part 1*, 83.

_____

Gens, A. (2010). Soil-environment interactions in geotechnical engineering. *Geotechnique 60, No. 1*, 3-74.

Gens, A. (2010). Soil-environment interactions in geotechnical engineering. *Geotechnique 60, No. 1*, 3-74.

Gens, A. (2010). Soil-environment interactions in geotechnical engineering. *Géothechnique, V60, 1*, 3-74.

Gesto, J. M., Gens, A., & Vaunat, J. (2011). Smoothing of yield surfaces and a reformulation of multi-surface plasticity. *XI International Conference on Computational Plasticity. Fundamental and Aplications*, 1-11.

Gran, M. (2015). *Coupled heat and water flow dynamics in dry soils: application to a multilayer waste cover.* Barcelona: UPC.

Herskovits, J. (1998). Feasible Direction Interior-Point Technique for Nonlinear Optimization. *Journal of Optimization theory and Applications, v99, N1*, 121-146.

Houlsby, G. (1979). The work input to a granular material. *Geotechnique 29, No. 3*, 354-358.

Houlsby, G. (1981). *A study of plasticity theories and their applicability to soils.* Cambridge: Cambrigde University.

Houlsby, G. (1986). A general failure criterion for frictional and cohesive materials. *Soils Foundation, 26, No 2*, 97-101.

Houlsby, G. (1997). The work input for an unsaturated granular material. *Geotechnique 47, No. 1*, 193-196.

Houlsby, G., & Puzrin, A. (2000). A thermomechanical framework for Constitutive Models for Rate-independent dissipative materials. *International Journal of Plasticity*, 1018-1047.

Houlsby, G., & Puzrin, A. (2005). Thermodynamics of Porous Continua. *Modern Trends in Geomechanics* (pp. 39-60). Viena 27-29 June: Springer.

Houlsby, G., & Puzrin, A. (2006). *Principles of Hyperplasticity.* Springer.

Houlsby, G., & Puzrin, A. (2006). *Principles of Hyperplasticity.* Springer.

_____

Houlsby, G., & Wroth, C. (1991). The Variation of the Shear Modulus of a Clay with Pressure and Overconsolidation Ratio. *Soils and Foundations, Vol. 31, No 3*, 138-143.

Houlsby, G., Amorosi, A., & Rojas, E. (2005). Elastic moduli of soils dependent on pressure. *Géotechnique 55, No.5*, 383-392.

Houlsby, G., Amorosi, A., & Rojas, E. (2005). Elastic moduli of soils dependent on pressure: A hyperplastic formulation. *Geotechnique, 55, No 5*, 383-392.

Houlsby, G., Amorosi, A., & Rojas, E. (2005). Elastic moduli of soils dependent on pressure: A hyperplastic formulation. *Geotechnique, 55, No 5*, 383-392.

Jacquemin, B., & Noilhan, J. (1990). Validation of a land surface parameterization using the HAPEX-MOBILITY data set. *Bound.-Layer Meteorol., 52*, 93-134.

Jarvis, P. (1976). The interpretation of variations in leaf water potential and stomatal conductance found in canopies in the field. *Philos. Trans. R. Soc. London, 273*, 593-610.

Jirásek, M., & Bazant, Z. P. (2002). *Inelastic Analysis of Structures.* England: John Wiley & Sons.

Karmarkar, N. (1984). A new polynomial-time algorithm for linear programming. *Combinatorica 4 (4)*, 373-395.

Krabbenhoft, K., Lyamin, A., Sloan, S., & Wriggers, P. (2007). An interior-point algorithm for elastoplasticity. *International Journal for numerical methods in engineering, No 69*, 592-626.

Leroueil, S. (2001). Cuts and Natural slopes: Movement and failure mechanisms. *Géotechnique, 51(3)*, 195-243.

Lockhart, J. (1965). An analysis of irrevesible plant cell elongation . *J. Theor. Biol. 8*, 264-275.

Lourenço, S., Gallipoli, D., Toll, D., Evans, F., & Medero, G. (2006). Development of a commercial tensiometer for triaxial testing of unsaturated soils. *Geothecnical Special Publication (ASCE), No. 147, Vol. 2*, 1185-1886.

Luenberger, D. (1984). *Linear and Nonlinear Programming.* Massachusetts: Addison-Wesley Publishing Company.

_____

Lynn, B., & Carlson, T. (1990). A stomatal resistance model illustrating plant vs. external control of transpiration. *Agric. For. Meteorol., 52*, 5-43.

Matsuoka, H., & Nakai, T. (1974). Stress-deformation and strength characteristics of soil under three different principal stresses. *Proc. JSCE, 232*, 59-70.

Maugin, G. A. (1999). *The Thermomechanics of Nonlinear Irreversible Behaviors.* Singapore and River Edge, N.J.: World Scientific.

Modaressi, H., Laloui, L., & Aubry, D. (1994). Thermodynamical approach for cam clay family models with Roscoe-type dilatancy rules. *Int. J. Num. Analyt. Meth. Geomech. 18*, 133-138.

Monteith, J. (1965). Evaporation and Environment. *Symposia of the Society for Experimental Biology*, 205-224.

Muñoz, J., De Gennaro, V., & Delaure, E. (2008). Experimental determination of unsaturated hydraulic conductivity in compacted silt. *Proc. of E-UNSAT. Durham, UK*, 123-127.

Nelson, J., & Miller, D. (1992). *Expansive soils - Problems and practice in foundation and pavement engineering.* New York: Wiley-Interscience.

Noilhan, J., & Mahfouf, J. (1996). The ISBA lan surface parameterisation scheme. *Global and Planetary Change 13*, 145-159.

Noilhan, J., & Mahfouf, J. (1996). The ISBA land surface parameterization scheme. *Global and Planetary Change, 13*, 145-159.

Noilhan, J., & Planton, S. (1988). A Simple Parameterization of Land Surface Processes for Meteorological Models. *Monthly Weather Review, 117*, 536-549.

Nuth, M., & Laloui, L. (2008). Advvances in modelling hysteretic water retention curve in deformable soils. *Computers and Geotechnics, 35, No 6*, 835-844.

Olivella, S. (1995). *Nonisothermal Multiphase Flow of Brine and Gas through Saline Media.* Barcelona: Universitat Politecnica de Catalunya.

Olivella, S., Carrera, J., Gens, A., & Alonso, E. (1994). Nonisothermal Multiphase Flow of Brine and Gas Through Saline Media. *Transport in Porous Media 15*, 271-293.

Olivella, S., Gens, A., Carreras, J., & Alonso, E. (1996). Numerical formulation for a simulator (CODE_BRIGHT) for the coupled analysis of saline media. *Engeneering Computations, vol.13 No.7*, 87-112.

Penman, H. (1948). Natural evaporation from open water, bare soil and grass. *Proc. R. Soc. London, Ser. A 193*, 120-146.

Penman, H. (1963). Vegetation and hydrology. *Technical Communication No.53. Harpenden:Commonwealth Agricultural Bureaux.*

Perez-Foguet, A., & Armero, F. (2002). On the formulation of closest-point projection algorithms in elastoplasticity. *International Journal for Numerical Methods in Engineering*, 331-374.

Picarelli, L. (1986). Caratterizzazione geotecnica dei terreni strutturalmente complessi nei problemi di stabilità dei pendii. *Proc. Int. Conf. Landslides- Causes, Impact and Countermeasures, Davos*, 155-170.

Potts, D. M., & Zdravkovic, L. (2001). *Finite Element Analysis in Geotechnical Engineering: Theory and Application.* London: Thomas Telford Ltd.

Puzrin, A., & Houlsby, G. (1999). Fundamentals of Kinematic Hardening Hyperplasticity. *Int. Jour. Solids and Structures*, 3771-3794.

R.E.G.G., G. (2011). *Project DOSMS "La Roque Gageac - Damage to a Rock under Climate Cycles" Report 1.* France: Centre dÉtudes Techniques de lÉquipement du Sud-Ouest. Toulouse.

Richards, L. (1950). Experimental demostration of the Hydraulic criterion for zero water flow in unsaturated soil. *Trans. Int. Congr. Soil Sci. Amsterdan, 1*, 67-68.

Romero, E., & Vaunat, J. (2000). Retention curves of deformable clays. *Experimental evidence and theoretical approaches in unsaturated soils*, 91-106.

Roscoe, K., & Burland, J. (1968). On the generalized stress-strain behavior of 'wet' clay. *Engineering plasticity*, 535-609.

Roscoe, K., & Schofield, A. (1963). Mechanical behavior of an idealised 'wet' clay. *Proc. 2nd Eur. Conf. SMFE, Wiesbaden 1*, 47-54.

Samat, S., & Vaunat, J. (2011). Environmental Actions on Slope Responses. *Code_Bright Workshop.*

_____

Sánchez, M. (2004). *Thermo-Hydro-Mechanical coupled analysis in low permeability media.* Barcelona: UPC.

Sassa, K. (1985). The geotechnical classification of landslides. *Proceedings of IV International Conference and Field Workshop on Landslides.*

Schofield, A., & Wroth, C. (1968). *Critical State Soil Mechanics.* McGraw-Hill.

Sellers, P., Mintz, Y., Sud, Y., & Dalcher, A. (1986). A Simple Biosphere Model (SiB) for Use within General Circulation Models. *Journal of The Atmospheric Sciences*, 505-531.

Sengupta, A., Vaunat, J., Cante, J., Ledesma, A., & Gens, A. (2000). An stress point algorithm for an elastoplastic model in unsaturated soils. *International Journal of Plasticity, Vol 16, No 2*, 121-141.

Simo, J., & Hughes, T. (1998). *Computational Inelasticity.* Springer.

Sivakumar, V. (1993). *A critical state framework for unsaturated soil.* United Kingdom: University of Sheffield.

Taiz, L., & Zeiger, E. (2010). *Plant Physiology.* Sinauer Associates.

Terzaghi, K. (1943). *Theoretical Soil Mechanics.* John Wiley & Sons, Inc.

Thornthwaite, C. (1954). A re-examination of the concept and measurement of potential evapo-transpiration. *The measurement of potential evapo-transpiration. Seabrook, NJ: Pubilcations in Climatology*, 200-209.

Thurairajah, A., & Sithamparapillai, V. (1948). Strength-Deformmation of sand during drained triaxial tests. *Fourth Asian Regional Conf Proc.*

Truesdell, C. (1969). *Rotational Thermodynamics.* New York : MacGraw-Hill.

Turc, L. (1954). Le bilan d'eau des sols. Relation entre les precipitations, l'evaporation et l'ecoulement. *Ann. Agron. 5*, 491-596.

Ulm, F., & Coussy, O. (2003). *Mechanics and durability of solids Vol.1.* MIT, Prentice Hall Series on Civil, Environmental and System Engineering.

Uso, J., Mateu, J., Karjalainen, T., & Salvador, P. (1997). Allometric regression to determine aerial biomasses of Mediterranean shrubs. *Plant Ecology, 132*, 59-69.

_____

van Genuchten, M. T. (1980). A Closed-form Equation for Predicting the Hydraulic Conductivity of Unsaturated Soils. *Soil science society of America*, 892-898.

Vaunat, J., & Romero, E. (2000). An elastoplastic hydro-mechanical model for unsaturated soils. *Proc. Int. work. on Unsaturated Soils, Trento-Italy*, 121-138.

Vaunat, J., Romero, E., & Jomi, C. (2000). An elastoplastic hydro-mechanical model for unsaturated soils. *Proc. Int. Workshop on Unsaturated Soils, Trento-Italy*, 121-138.

Vicol, T. (1990). Comportment hydraulique et mecanique d'un sol fin non sature application a la modelisation. *PhD Thesis, Ecole Nationale des Ponts et Chassées, Paris, France*.

Wetzel, P., & Chang, J. (1987). Concerning the relationship between evapotranspiration and soil moisture. *J. Climate Appl. Meteor., 26*, 18-27.

Wheeler, S., Sharma, R., & Buison, M. (2003). Coupling of hydraulic hysteresis and stress-strain behavior in unsaturated soils. *Geotechnique, 53, No 1*, 41-54.

Wong, H., & Ho, K. (1997). The 23 July 1994 landslide at Kwun Lung Lau, Hong Kong. . *Can. Geotech. J. 34, No. 6*, 825-840.

Wright, S. (1992). An interior point algorithm for linearly constrained optimization. *SIAM J. Optimization*, 450-473.

Wright, S. (1997). *Primal-Dual Interior Point Methods.* Philadelphia, USA: SIAM.

Yu, H. S. (2006). *Plasticity and Geotechnics.* USA: Springer.

Ziegler. (1977). *An Introduction to Thermomechanics.* Amsterdam: North-Holland.

Ziegler, H. (1977). *Introduction to Thermodynamics .* Amsterdan: North-Holland .

Zouain, N., Pontes, I., & Vaunat, J. (2009). Potentials for the Modified Cam-Clay model. *European Journal of Mechanics*.

Zytynski, M., Randolph, M., Nova, R., & Wroth, C. (1978). On modelling the unloading-reloading behavior of soils. *Int. J. Numer. Anal. Methods Geomechanics, 2*, 87-93.